Cinétiques de précipitation de minéraux carbonatés magnésiens, influence de ligands organiques et conséquences pour la séquestration minérale du CO2

Quentin Gautier

UNIVERSITÉ PARIS-EST

Thèse présentée pour obtenir le grade de

Docteur de l'Université Paris-Est

Spécialité : Sciences de l'Univers et Environnement

par

Quentin Gautier

Ecole Doctorale : SCIENCES, INGÉNIERIE ET ENVIRONNEMENT

Cinétiques de précipitation de minéraux carbonatés magnésiens, influence de ligands organiques, et conséquences pour la séquestration minérale du CO_2

Soutenance le 5 décembre 2012 à Toulouse (Observatoire Midi-Pyrénées) devant le jury composé de :

Laurent Charlet (Université Joseph Fourier)	*Rapporteur*
Susan Stipp (Université de Copenhague)	*Rapporteur*
Eric Oelkers (Université Paul Sabatier - OMP)	*Examinateur*
Guntram Jordan (Université Ludwig-Maximilians Munich)	*Examinateur*
Jacques Schott (Université Paul Sabatier - OMP)	*Directeur de thèse*
Jean Sulem (Ecole des Ponts Paris Tech)	*Co-directeur de thèse*
Pascale Bénézeth (Université Paul Sabatier- OMP)	*Co-directrice de thèse*

Résumé

La formation de minéraux carbonatés magnésiens par carbonatation de silicates de magnésium constitue une option pérenne et sûre de séquestration du dioxyde de carbone, dont les estimations les plus optimistes indiquent qu'elle pourrait participer significativement à l'effort global de réduction des émissions de CO_2 d'origine anthropique. À ce jour cependant, ces réactions chimiques se heurtent à de fortes limitations cinétiques, dont l'origine réside dans la faible réactivité des phases minérales en présence. Alors que de nombreuses études se sont intéressées à la phase de dissolution des silicates magnésiens, souvent considérée comme l'étape limitante du processus, ce travail de thèse prend le parti d'étudier expérimentalement les mécanismes et les vitesses de formation des minéraux carbonatés magnésiens qui constituent le produit final des réactions de carbonatation.

Dans une première partie, nous nous intéressons à l'influence sur la cinétique de précipitation de la magnésite $MgCO_3$ de ligands organiques connus pour accélérer la vitesse de dissolution des silicates magnésiens : oxalate, citrate et EDTA. Sur la base d'expériences menées en réacteur à circulation entre 100 et 150°C, nous montrons que ces ligands diminuent significativement la vitesse de précipitation de la magnésite en raison (1) de la complexation des cations Mg^{2+} en solution, estimée grâce à une base de données thermodynamiques établie à partir d'une revue critique de la littérature, et (2) de l'adsorption des ligands au niveau d'un nombre limité de sites à la surface du minéral, avec pour conséquence une diminution de la constante cinétique de précipitation. Cette inhibition de la cristallisation de la magnésite est maximale dans le cas du citrate.

L'utilisation de la microscopie à force atomique en conditions hydrothermales nous a permis de sonder l'origine de l'inhibition observée. Elle nous indique en particulier que le citrate et l'oxalate agissent sur le processus de croissance cristalline à la surface de la magnésite, modifiant la forme des îlots de croissance ainsi que la fréquence de génération des marches cristallines par le processus de croissance en spirale. Nous montrons que ces deux ligands agissent au niveau de sites surfaciques différents, probablement fonction de leurs structures et de leurs propriétés chimiques. Nous proposons que l'inhibition plus forte exercée par le citrate sur la croissance de la magnésite provienne d'une interaction préférentielle du ligand avec les marches cristallines aigües, qui limitent le processus de croissance en spirale de par leur faible vitesse d'avancement.

La description de ces phénomènes à l'aide d'une loi cinétique empirique permet de proposer une modélisation numérique simplifiée de la carbonatation de la forstérite (Mg_2SiO_4) en présence de ligands à 120°C, qui suggère que les ligands organiques étudiés ont une influence défavorable sur le processus global de carbonatation de ce minéral.

La troisième et dernière partie de ce travail s'intéresse à la solubilité et à la cinétique de précipitation d'un carbonate de magnésium hydraté, l'hydromagnésite, entre 25 et 75°C. Les résultats obtenus indiquent que la vitesse de croissance de l'hydromagnésite excède largement celle de la magnésite à affinité chimique comparable, tandis que l'énergie d'activation du processus est beaucoup plus faible que celle de la magnésite. Ces données cinétiques originales confirment que la déshydratation des ions Mg^{2+} est l'étape limitante de la précipitation de la magnésite en solution aqueuse. Toutefois, du fait de sa solubilité plus forte,

l'hydromagnésite n'est susceptible de se former plus rapidement que la magnésite qu'à pH alcalin et basse température. Elle ne peut à ce titre constituer un palliatif à la faible vitesse de précipitation de la magnésite lors de la carbonatation des silicates magnésiens.

Abstract

Forming magnesium carbonate minerals through carbonation of magnesium silicates has been proposed as a safe and durable way to store carbon dioxide, with a possibly high potential to offset anthropogenic CO_2 emissions. To date however, chemical reactions involved in this process are facing strong kinetic limitations, which originate in the low reactivity of both Mg-silicates and Mg-carbonates. Numerous studies have focused on the dissolution of Mg-silicates, under the questionable hypothesis that this step limits the whole process. This thesis work focuses instead on the mechanisms and rates of formation of magnesium carbonates, which are the final products of carbonation reactions.

The first part of the work is dedicated to studying the influence on magnesite precipitation kinetics of three organic ligands known to accelerate Mg-silicates dissolution rates : oxalate, citrate and EDTA. With help of mixed-flow reactor experiments performed between 100 and 150°C, we show that these ligands significantly reduce magnesite growth rates, through two combined mechanisms: (1) complexation of Mg^{2+} cations in aqueous solution, which was rigorously estimated from a thermodynamic database established through a critical review of the literature, and (2) adsorption of ligands to a limited number of surface sites, leading to a decrease of the precipitation rate constant. The observed growth inhibition is maximal with citrate.

We then used hydrothermal atomic force microscopy to probe the origin of the documented growth inhibition. Our observations show that citrate and oxalate interact with the crystal growth process on magnesite surface, modifying the shape of growth hillocks as well as the step generation frequency through spiral growth. We also show that the ligands adsorb preferentially on different kink-sites, which is probably related to their different structures and chemical properties. We propose that the stronger magnesite growth inhibition caused by citrate is related to a preferential interaction of the ligand with acute steps on the magnesite surface, which limit the spiral growth process through their low advancement rate.

The description of these processes with an empirical rate law allows performing simplified numerical simulations of forsterite carbonatation at 120°C in the presence of the ligands. We thus demonstrate that the use of the investigated ligands would clearly be detrimental to the carbonation of forsterite.

The third and last part of this work deals with hydromagnesite solubility and growth kinetics between 25 and 75°C. The obtained results show that hydromagnesite growth rates largely exceed magnesite rates at comparable chemical affinity, while the activation energy of the process is much smaller than for magnesite. This original kinetic dataset thus confirms the long-standing hypothesis that Mg^{2+} dehydration is the rate-limiting step for Mg-carbonate precipitation from aqueous solution. However, due to its higher solubility, hydromagnesite may grow more quickly than magnesite only at low temperature and alkaline pH. Thus, it may not provide a solution to the sluggish precipitation kinetics of magnesite during Mg-silicates carbonation.

Remerciements

Une petite recherche dans d'anciennes archives mailistiques permet de faire remonter l'origine de ce projet de thèse à décembre 2007, lorsque j'avais contacté Jacques Schott en vue d'imaginer un travail de recherche au LMTG sur la réactivité des minéraux, dans le contexte notamment du stockage du CO_2. Ce à quoi Jacques avait répondu: "Nous estimons qu'une des principales limitations actuelles à la modélisation du transport réactif - notamment lors de l'injection du CO_2 - est l'absence de lois et paramètres robustes pour quantifier la vitesse de précipitation abiotique et biotique des minéraux, et tout particulièrement celle des carbonates de Fe/Mg/Ca qu'il est essentiel de connaître lors de l'injection dans les basaltes ou les roches basiques. [...] Nous souhaitons associer autant que possible l'acquisition rigoureuse de données fondamentales et leur application à la description quantitative de processus géologiques ou environnementaux. [...] Je crois que cela correspond bien à la démarche que vous envisagez dans le cadre d'une thèse." Dont acte!

Il appartiendra au lecteur de juger si nous avons contribué à faire progresser cet objectif ambitieux. Pour ma part, je souhaite naturellement remercier sincèrement Jacques, d'abord pour m'avoir accueilli au sein de l'équipe de Geochimie-Biogéochimie-Expérimentale (GBE) du LMTG (devenu GET), ensuite pour m'avoir guidé au travers des joies - et des frustrations - de l'étude de la réactivité minérale, enfin pour avoir supervisé, avec exigence, bienveillance et disponibilité, l'ensemble de ce travail de thèse.

Un grand merci également à Pascale Bénézeth, qui par sa rigueur et son savoir-faire expérimental a fortement contribué à la qualité des données présentées dans ce manuscrit, et de leur interprétation. Je regrette de n'avoir pas travaillé plus tôt et plus souvent avec toi, Pascale, j'aurais certainement pu apprendre avant octobre 2011 que la mesure du pH à 25°C est une science complexe...! Merci tout particulièrement pour ton soutien et tes encouragements au cours des derniers mois de rédaction.

Merci à Vincenzo de Gennaro, de l'Institut Navier à l'Ecole des Ponts ParisTech, pour avoir initialement accepté la co-direction de cette thèse, et à Jean Sulem pour l'avoir reprise au pied levé après le départ de Vincenzo, avec ouverture d'esprit, gentillesse et disponibilité.

De mars à juin 2010, Guntram Jordan m'a accueilli à l'Université Ludwig-Maximilian de Munich, pour y effectuer des expériences de croissance cristalline. Vielen danke für die Führung durch die grundlegenden Konzepte der Theorie des Kristallwachstums, und für Biergarten auch!

C'est un honneur et une fierté d'avoir eu pour rapporteurs Susan Stipp et Laurent Charlet, et ce fut un plaisir de discuter dans le détail avec vous des implications des résultats obtenus. Many thanks also to Eric Oelkers for having accepted to chair my thesis' jury, but also for interesting discussions, animated talks and insightful tips throughout this work.

Giuseppe Saldi terminait sa thèse lorsque j'ai débuté au LMTG. C'est pourtant lui qui m'a enseigné les rudiments du métier et les gestes qui sauvent (les manips). Merci mille fois pour ta disponibilité pendant cette première année de thèse - et pour "quelques" prélévements dominicaux! Merci également à Oleg pour sa mémoire des moindres recoins des salles d'expérimentation, et à Gleb pour m'avoir permis de me familiariser avec les bases de

données et les codes de calcul thermodynamiques.

L'expé peut parfois se transformer en travail fastidieux lorsque le Téflon flue, que le titane fuit, et que le flux d'éthylène s'arrête brutalement. Fort heureusement, une solide équipe veillait au grain: merci au formidable bricoleur/inventeur qu'est Alain, et à Pascal l'artiste de la machine-outil. Merci à Carole pour ses enseignements patients à l'art de l'AAS, et à Stéphanie et Éric pour m'avoir aidé à (presque) apprivoiser la chromato ionique. Merci également à Thierry et Sophie au MEB, Michel à la DRX, Alain pour les analyses granulo, Fabienne pour son franc-parler, Philippe toujours dispo pour agrémenter les longues prises de vue MEB de discussions variées. Merci à Gaelle et Elisabeth pour leur aide administrative efficace - et l'on se rend compte, après quelques mois en administration centrale, pourquoi les ordres de mission sont effectivement si importants! Un grand merci enfin à Marine Daniel puis Cécile Blanchemanche de l'ED SIE, pour m'avoir toujours facilité les choses, avec disponibilité et souplesse.

Dr Mavro, your contribution to this thesis is certainly big - and I'm not talking about sampling mixed-flow reactors. Thanks for your insightful comments, your hard work, your support. To Snorri, who learnt me that an experiment can easily run for 2 months while its designer is 2700km away: thanks for your friendship, great laughs and talks about Iceland and life. I hope we can stay in touch.

À mes fidèles compagnons de bureau Aurélien, Sébastien, Émilie, puis Sylvaine, Vanessa, Sylvain, je souhaiterais exprimer ma gratitude pour avoir permis une cohabitation harmonieuse et divertissante dans 10 m^2. À ceux-là s'ajoutent tous les compagnons d'infortune, en particulier Sophie et Ali, Camille, Irina, Tristan, Guilhem, Joaquín, German, JS, Fx, Jerem, Thomas, Laurent, Elena, Angela, Mélanie, Adrien... Merci à Jérémy, Jean-Louis et Guillaume pour quelques parties de tennis presques mémorables. Et enfin à Alex, partenaire d'expé, je souhaiterais faire promettre que nous ne parlerons plus de vitesse d'agitation et de membrane en Nylon!

Many people passed through the team, some for a few months, others for a few years. Thanks to Chris, Gabbi, Sam "The Boy" Parry, Morgan, Teresa, Therese, Ju for great discussions and quite a few bears. Niklas deserves a special mention: it's been a pleasure to work with you, and I hope I managed to give you a few keys to this sometimes difficult job.

Merci à ceux qui m'ont donné le goût de la minéralogie et de la géochimie : François Guyot, Karim Benzerara, Bruno Goffé. Merci également à Damien Daval, dont la rigueur de raisonnement ne s'exprime jamais mieux que lorsque qu'il tente de donner tort à Jacques! Merci enfin a ceux qui, au labo, m'ont permis d'élargir un peu mon horizon scientifique : Yves, Christophe, Valérie, Christophe, Anne, Bruno, Merlin, Damien ou Anne-Mag. À tous, je souhaiterais dire que bien que j'aie décidé de ne pas poursuivre dans la voie académique, la richesse des rencontres effectuées au cours des 4 dernières années, la rigueur que j'espère avoir acquise et mon attachement au monde de la recherche et à ceux qui l'animent demeureront des points cardinaux pour les années qui viennent.

Merci aux fidèles amis de l'ENS, que je n'ai pas assez vu au cours des dernières années. Mention spéciale à Florian, Nico et au Prince, hôtes récurrents (voire pourvoyeurs d'appartements) lors de mes nombreux séjours parisiens. Merci également à Olivier, qui m'a

fait l'amitié de soutenir sa thèse quelques jours après moi, ce qui nous a permis d'échanger bleus à l'âme et pics de stress pendant la fin de la rédaction...

À Toulouse, un grand merci à Balma et Seb, Sandrine et Fabien, Philippe et Camille pour leur amitié. Marine et Alex, dès que tout sera rentré dans l'ordre, je compte sur vous pour aller faire un tour à la Dent d'Orlu! Une pensée enfin pour Mélanie, dévoreuse de jamón appliquée qui nous a fait l'amitié de venir à intervalles réguliers nous parler de la vie hawaiienne.

Prendre l'air était parfois salutaire. Merci donc au CAF de Toulouse pour m'avoir fait découvrir les Pyrénées à skis, en chaussons ou avec des crampons, et aux apnéistes d'Immersion Libre pour ces bouffées d'oxygène!

Ces remerciements ne seraient pas complets sans mentionner ceux qui, au service de la recherche du Ministère de l'Écologie m'ont permis de terminer ce travail. Merci donc à Laurent Bélanger, Claire Hubert et Patrice Bueso pour leur compréhension et à tous les collègues du SR pour leur soutien au cours des derniers mois de rédaction.

Merci à mes parents bien sûr, pour leur soutien et leur affection constante malgré la distance, et ce jusqu'au pot final. Merci à Greg et Lucas pour leur intérêt poli quand j'essayais de leur expliquer mon sujet de thèse... Mamie et Bonne-Maman auraient certainement aimé voir cette soutenance. Grand-Père m'a fait l'immense plaisir d'être présent. Merci à tous pour votre soutien tout au long de mes études.

La maison d'Elena et Grégoire à Cugnaux fut souvent un refuge dominical chaleureux, merci pour votre accueil et votre générosité, y gracias a los peques por dejarme jugar con vosotros! Gracias a Agnés y Avelino, por vuestra atención y interés, por los fines de semana y las vacaciones en Vilafortuny, Barcelona o en los Pireneos. Y por último, muchas gracias por el suministro en jamónes y embutidos de Béjar, que sin duda contribuyeron a este suceso.

À mon fidèle ordi, je souhaiterais exprimer ma gratitude de n'avoir pas lâché après 4 ans de bons et loyaux services. Merci enfin à FIP, aux Inrocks et à echo/mofo, pour d'innombrables découvertes musicales.

Gracias a Olga por tus talentos informáticos, tu paciencia, tu infatigable apoyo, tu amor. No lo habría conseguido sin tí.

Table des Matières

Liste des figures

Liste des tableaux

Chapitre 1

Introduction Générale

Ce travail de thèse s'inscrit dans le cadre général de la recherche de solutions efficaces pour la séquestration du dioxyde de carbone sous une forme minérale, moyen de lutte potentiel contre les émissions de CO_2 dans l'atmosphère terrestre. Plus précisement, il apporte des contraintes nouvelles sur la formation des minéraux carbonatés magnésiens, cibles de la minéralisation du CO_2 par le biais de la carbonatation de roches basiques ou ultrabasiques. Dans cette introduction, on rappellera quelques fondamentaux relatifs à la nécessité de réduire les émissions mondiales de CO_2, avant de présenter les différentes options de stockage géologique du CO_2 actuellement envisagées à l'échelle internationale. On veillera à replacer la séquestration minérale du CO_2 au sein de ce panel de technologies, notamment en termes de potentialités et de coûts, et l'on présentera plus spécifiquement les enjeux scientifiques relatifs à la formation des carbonates de magnésium.

Sommaire

1.1 Motivations

1.1.1 CO_2 atmosphérique, changement climatique et acidification des océans

La concentration de CO_2 atmosphérique a crû de 40% depuis l'époque pré-industrielle, passant d'environ 280 ppmv à 392 ppmv en 2012 (NOAA, 2012), niveau de concentration qui n'a jamais été atteint depuis au moins 800 000 ans (Lüthi *et al.*, 2008).

L'essentiel de cette augmentation est attribuée aux émissions anthropiques de CO_2, dues en majeure partie à la combustion d'hydrocarbures fossiles (production d'énergie, transports, industrie, bâtiments...), qui ont atteint le niveau record de 34 Gt CO_2/an en 2011 (Oliver *et al.*, 2012), et restent en forte augmentation (Peters *et al.*, 2012). À l'utilisation des combustibles fossiles s'ajoutent les émissions issues du changement d'usage des sols (déforestation et agriculture intensive), de l'ordre de 4.0 Gt de CO_2 par an (Le Quéré *et al.*, 2009 ; Global Carbon Project, 2011), tandis qu'une part plus faible (environ 4% des émissions globales) provient de la calcination de calcaire pour la production de ciment (Oliver *et al.*, 2012).

Bien que la moitié environ des émissions anthropiques de CO_2 soit stockées par dissolution dans les océans ou par photosynthèse (stockage dans la biosphère), la moitié restante s'accumule dans l'atmosphère (Le Quéré *et al.*, 2009 ; Ballantyne *et al.*, 2012), modifiant le cycle du carbone à l'échelle globale.

Du fait de sa concentration dans l'atmosphère, le CO_2 est l'un des principaux gaz à effet de serre terrestres. L'augmentation de sa concentration atmosphérique, ainsi que celle d'autres gaz à effet de serre, conduit donc à une modification de l'équilibre radiatif de la planète, qui est la principale cause du changement climatique en cours, désormais bien documenté. La température moyenne terrestre de surface a ainsi augmenté de 0.76 ± 0.19°C entre le début du XX^{e} siècle et 2005, et beaucoup plus dans les zones arctiques et antarctiques (IPCC, 2007).

Les conséquences de ce changement climatique sont l'objet d'une forte attention scientifique et sociétale. L'augmentation des températures globales s'accompagne en effet d'une augmentation de la fréquence des événements extrêmes, tels que canicules, sécheresses, et fortes précipitations (e.g Coumou et Rahmstorf, 2012 ; Hansen *et al.*, 2012), d'une montée du niveau de la mer en raison de l'expansion thermique des océans et de la fonte des calottes glaciaires (environ 3.1 mm/an entre 1993 et 2012 - IPCC, 2007), d'une fonte de la banquise arctique (e.g Kinnard *et al.*, 2011), et de modifications importantes des écosystèmes et de l'aire de répartition des espèces (e.g Parmesan, 2006).

Face à ces menaces, la communauté internationale a réaffirmé lors des Conférence des Parties de la Convention-cadre des Nations Unies sur les changements climatiques (CCNUCC) à Copenhague (2009) et Cancún (2010) la nécessité de limiter le réchauffement climatique à +2°C par rapport aux niveaux préindustriels.

On estime que le CO_2 contribue pour plus de 60% à l'augmentation de l'effet de serre et au changement climatique associé (IPCC, 2007). Aussi, il concentre la majeure partie des efforts visant à limiter l'étendue du changement climatique. Les modélisations climatiques suggèrent ainsi que pour parvenir à l'objectif fixé par la CCNUCC, les émissions anthropiques cumulées de CO_2 ne devront pas excéder 1000 Gt CO_2 sur la période 2000-2050 (Meinshausen *et al.*, 2009).

Une part importante de ce carbone a d'ores et déjà été émise ; la trajectoire à suivre pour respecter cet objectif final tolère une certaine flexibilité (e.g Van Vuuren et Riahi, 2011), mais il reste que l'ensemble des scénarios envisageables impliquent une réduction substantielle des émissions en 2050 par rapport aux niveaux de 2000, de -20 à -85% (Van Vuuren et Riahi, 2011). Par ailleurs, une concentration atmosphérique de CO_2 de 450 ppmv est considérée comme une limite maximale pour garder une possibilité de ne pas dépasser le seuil de +2°C en température globale (IPCC, 2007).

Nous avons évoqué plus haut le fait que les océans sont un puit majeur des émissions de CO_2. En effet, plus de 20% des émissions anthropiques annuelles sont stockées par dissolution dans les eaux de surface puis exportées dans la circulation thermohaline (Le Quéré *et al.*, 2009 ; Sabine et Tanhua, 2010). Cependant, la dissolution du CO_2 provoque la formation d'un acide faible, l'acide carbonique H_2CO_3, qui se dissocie selon la réaction suivante :

$$H_2CO_3 \rightleftharpoons H^+ + HCO_3^- \rightleftharpoons 2\,H^+ + CO_3^{2-} \tag{1.1}$$

La dissolution du CO_2 a donc pour conséquence l'augmentation de l'acidité des eaux océaniques de surface. Le pH moyen des eaux de surface est ainsi passé d'environ 8.21 à 8.1 depuis l'époque préindustrielle et continue à diminuer au rythme d'environ 0.02 unités par décade (Orr *et al.*, 2005, Doney *et al.*, 2009).

Bien que la réponse globale des écosystèmes océaniques à l'acidification soit encore mal connue, il est établi que les organismes calcificateurs sont affectés diversement par l'augmentation des pressions partielles de CO_2, avec des conséquences très probablement importantes pour la structure et la diversité des écosystèmes associés (e.g Fabry *et al.*, 2008 ; Anthony *et al.*, 2008 ; Ries *et al.*, 2009 ; Beaufort *et al.*, 2011). En effet, cette acidification provoque une diminution de l'indice de saturation des eaux par rapport à la calcite et à l'aragonite, des biominéraux qui constituent l'exosquelette ou la structure de nombreux organismes marins, tels que les coccolithophores, ptéropodes et autres mollusques, échinodermes, coraux et coralligènes (Doney *et al.*, 2009). Le seuil de concentration atmosphérique en CO_2 de 450 ppmv, évoqué plus haut, est considéré comme déja risqué pour les écosystèmes océaniques, notamment dans l'océan Austral, qui pourrait connaitre des périodes de sous-saturation par rapport à l'aragonite dès les années 2030 (McNeil et Matear, 2008 ; Cao et Caldeira, 2008).

Étant donnés les niveaux actuels de CO_2 atmosphérique, et leur taux de croissance supérieur à 2 ppmv/an (NOAA, 2012), on mesure le chemin à parcourir pour stabiliser la concentration à 450 ppmv ou à un niveau inférieur. Toutefois les tendances récentes en matière de consommation d'énergies fossiles ne laissent présager aucun revirement rapide des tendances observées actuellement en matière d'émissions. En 2011, la consommation de charbon, à elle seule responsable de plus de 50% des émissions totales de CO2, a ainsi augmenté de 5% par rapport à 2010, tandis que les consommations de pétrole et de gaz naturel augmentaient respectivement de 1 et 2% (BP World Energy Review 2012).

La réduction des émissions de CO_2 est donc un enjeu majeur, qui requiert d'associer différentes solutions de grande ampleur, à la fois comportementales et technologiques. La capture et stockage du carbone, technologie qui suppose de capter le CO_2 au niveau de grands émetteurs industriels et de le stocker durablement dans le milieu géologique, est susceptible d'être l'une d'entre elles (Pacala et Socolow, 2004 ; Lackner, 2003 ; Van Vuuren et Riahi, 2011).

1.1.2 Capture et séquestration géologique du CO_2

Les techniques de Capture et Stockage du CO_2 (CSC) supposent en premier lieu de piéger le CO_2 dans les effluents gazeux afin d'obtenir un gaz relativement pur. Les différentes méthodes de captage se nomment "pré-combustion", "post-combustion" et "oxy-combustion". Nous ne les détaillerons pas ici ; le lecteur intéressé pourra par exemple se référer au rapport technique publié sur le sujet par l'IPCC en 2005, ou à l'ouvrage de Rackley (2009).

On notera toutefois que ces méthodes de captage occasionnent un coût énergétique important et qu'elles sont d'autant plus efficaces qu'elles sont appliquées à des effluents déjà concentrés en CO_2. Elles ne sont donc pas adaptées à des émetteurs de CO_2 discrets tels que les bâtiments ou les véhicules, mais plutôt à de gros émetteurs ponctuels de CO_2, tels que les centrales thermiques à combustibles fossiles, les cimenteries, ou l'industrie sidérurgique, en particulier les installations émettant plus de 1 Mt de CO_2 par an. Ces gros émetteurs représentent près de 85% des émissions industrielles de CO_2. En 2005, le rapport de l'IPCC estimait ainsi le volume d'émissions de CO_2 potentiellement concernées par les procédés de capture à l'échéance de 2020 entre 2.6 et 4.9 Gt CO_2 par an.

Certains scientifiques proposent de capter le CO_2 directement à partir de l'air, en utilisant des structures filtrant l'air et piégeant le CO_2 soit dans un solvant alcalin, soit sur une résine anionique (e.g Lackner *et al.*, 2001, Lackner, 2009). À ce stade cependant, ces techniques ne sont pas considérées comme viables car les estimations économiques aboutissent à des coûts de capture d'au minimum 200 US$/t CO_2, essentiellement en raison de la régénération des solvants ou résines (Lackner, 2009). Ce montant est à comparer au coût estimé des procédés de capture classiques, de 15 à 75 US$/t CO_2 pour une centrale thermique (IPCC, 2005).

Suite à sa capture, différentes options de séquestration du CO_2 sont envisagées. La figure 1.1 représente les ordres de grandeur des capacités estimées pour différentes méthodes de séquestration ainsi que des durées de temps associées (Lackner, 2003). On n'évoquera ici que les méthodes de séquestration dites "géologiques", qui offrent les meilleures garanties en termes de durée de stockage (IPCC, 2005). Les autres méthodes envisagées (stockage dans la biomasse, stockage océanique) sont décrites par exemple par Rackley (2009).

Le stockage géologique souterrain du CO_2 est envisagé dans quatre types de formations géologiques principales (Bachu, 2008), détaillées ci-dessous.

Les **veines de charbon profondes** sont le support de la technologie appelée "Enhanced Coal Bed Methan" (ECBM). Le charbon présentant une forte affinité pour le CO_2, celui-ci s'adsorbe en désorbant du méthane notamment. Le méthane étant un gaz à effet de serre 21 fois plus fort que le CO_2, l'efficacité du stockage est bien évidemment soumise à la récupération du méthane désorbé et à son utilisation comme source d'énergie. Les capacités de ce type de stockage sont mal connues, et limitées par la faible perméabilité des veines de charbon. Elles sont estimées entre 3 et 200 Gt CO_2 au niveau global (IPCC, 2005).

Le stockage dans des **anciens gisements d'hydrocarbures** est la technologie la plus mature du fait de son utilisation depuis une trentaine d'année par les compagnies pétrolières dans le cadre d'opérations de récupération assistée de pétrole ou de gaz naturel ("Enhanced Oil or Gas Recovery", EOR/EGR). Cette récupération assistée permet de faire baisser significativement le coût de stockage, voire de parvenir à un "coût négatif". Près de 90 projets com-

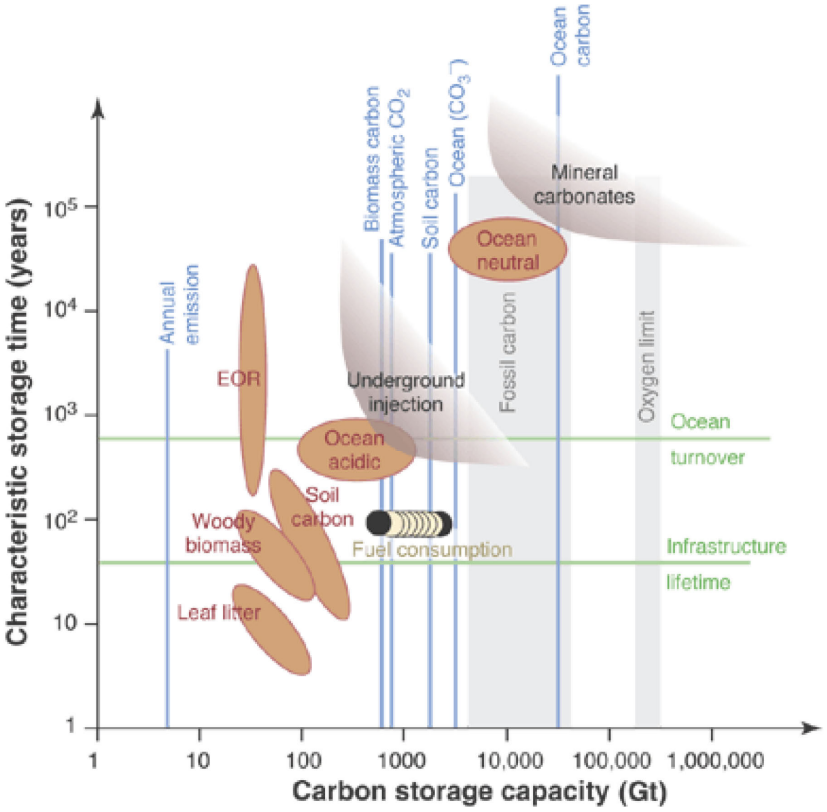

FIGURE 1.1 – Capacités disponibles et durées de temps estimées pour différentes méthodes de séquestration du CO_2. Source : Lackner (2003).
À noter que les émissions annuelles ("annual emission") sont désormais proches de 10 GtC. "EOR" signifie "Enhanced Oil Recovery". "Ocean acidic" et "Ocean neutral" correspondent aux capacités de stockage du CO_2 dans les océans, respectivement sous la forme de gaz, et sous la forme d'ions carbonate ou bicarbonate. "Underground injection" correspond aux capacités estimées de stockage en formation géologique (gisement d'hydrocarbures ou aquifères profonds), tandis que "mineral carbonates" est une estimation du potentiel de stockage de CO_2 sous la forme de minéraux carbonatés, soit *in situ* (dans le milieu géologique), soit *ex situ* (dans le cadre d'un processus industriel, voir section 1.1.3). Enfin, "Fossil carbon" représente le stock estimé de carbone sous la forme d'hydrocarbures fossiles (carbone "émissible"), et "Oxygen limit" désigne la quantité de carbone maximale qui pourrait être brûlée étant donné la quantité de dioxygène disponible.

merciaux d'EOR sont en cours actuellement à l'échelle mondiale, dont le projet de Weyburn (Saskatchewan, Canada), où 2.8 Mt CO_2 provenant d'une usine de gazéification de charbon située au Dakota du Nord (USA) sont injectées annuellement dans un réservoir déplété de pétrole pour en augmenter la productivité. Il s'agit du plus gros projet d'EOR commercial bénéficiant d'un suivi de l'évolution du CO_2 stocké (AIE, 2010). Par ailleurs, les projets de démonstration menés par Total à Lacq, en France, et par le CO2CRC à Otway, en Australie (Jenkins *et al.*, 2012), impliquent l'injection de CO_2 dans des réservoirs de gaz naturel appauvris. L'objectif est alors seulement de tirer parti des pièges géologiques ayant conservé des hydrocarbures pendant plusieurs millions d'années pour y réinjecter du CO_2.

Les capacités mondiales de stockage pour cette technologie sont estimées à 675 à 900 Gt CO_2, avec toutefois de fortes incertitudes dues à l'altération de l'imperméabilité des roches de couverture en raison de l'exploitation pétrolière ou gazière, en raison des forages et de la

dépressurisation des réservoirs (IPCC, 2005).

La technologie la plus prometteuse consiste à injecter le CO_2 dans des **aquifères salins profonds**, au sein de formations géologiques gréseuses ou carbonatées, situées sous une roche de couverture imperméable. Le CO_2 y est préférentiellement injecté sous forme supercritique, à une température supérieure à 31.1°C et une pression supérieure à 7.38 MPa, soit à une profondeur d'au minimum 800 m. La densité et la fluidité du CO_2 ainsi atteintes permettent de maximiser l'injectivité du fluide dans le réservoir ainsi que le volume stocké.

Différents projets de démonstration de grande ampleur sont en cours à l'échelle mondiale, notamment sur le site de Sleipner en Norvège, où près d'1 Mt CO_2 issus de l'exploitation d'un gisement de gaz naturel sont injectées annuellement dans une formation gréseuse située à 800m sous le fond de la Mer du Nord (Korbøl et Kaddour, 1995 ; Arts *et al.*, 2008). Les projets d'In Salah en Algérie (1 Mt CO_2/an) et de Snøhvit en Norvège (700 kt CO_2/an) font également appel à cette technologie (IEA, 2010).

Les capacités estimées à l'échelle mondiale pour ce type de stockage sont de l'ordre de 1000 à 10 000 Gt CO_2 (IPCC, 2005). Outre les importants volumes disponibles, l'attractivité de ce type de sites réside dans l'existence de plusieurs mécanismes permettant d'empêcher la remontée du CO_2 à la surface, contribuant ainsi à la sûreté du stockage à long terme (e.g Bachu *et al.*, 1994 ; Hitchon, 1996 ; Gunter *et al.*, 2004 ; Balashov *et al.*, 2013) :

- Le *stockage structural* ou *stratigraphique* est permis par l'existence d'une roche de couverture ou d'une autre structure géologique à faible perméabilité surmontant la roche réservoir, qui constitue une barrière physique à la remontée du CO_2 supercritique ou gazeux, moins dense que la saumure.

- Une partie du CO_2 gazeux est immobilisé dans l'espace poral par les forces de capillarité, notamment lors de l'imbibition de l'aquifère par la saumure après une phase d'injection de CO_2, un mécanisme appelé *stockage résiduel*.

- Au contact avec la saumure, une partie du CO_2 gazeux ou supercritique se dissout dans l'eau selon la réaction suivante :

$$CO_{2(g)} \longrightarrow CO_{2(aq)} \xrightarrow{H_2O} H_2CO_3 \tag{1.2}$$

  Le temps de résidence de l'eau dans les aquifères profonds pouvant atteindre de l'ordre du million d'années, la dissolution du CO_2 diminue grandement sa mobilité, un phénomène appelé *stockage hydrodynamique*.

- Après dissolution du CO_2 (Eq. 1.2), une partie de l'acide carbonique produit se dissocie selon la réaction 1.1. La dissolution de minéraux silicatés ou carbonatés présents initialement dans la roche réservoir permet de tamponner l'acidité produite, et ainsi de maintenir le CO_2 sous la forme d'ions bicarbonate HCO_3^- ou carbonate CO_3^{2-}. Pour exemple, les réactions de dissolution de la calcite $CaCO_3$ et de l'anorthite $CaAl_2Si_2O_8$ en présence d'acide carbonique sont indiquées ci-dessous :

$$CaCO_3 + H_2CO_3 \longrightarrow Ca^{2+} + 2\,HCO_3^- \tag{1.3}$$

$$CaAl_2Si_2O_8 + 2\,H_2CO_3 \longrightarrow Ca^{2+} + 2\,Al^{3+} + 2\,HSiO_4^{3-} + 2\,HCO_3^- \tag{1.4}$$

Cette séquestration du CO_2 sous forme *ionique* accroît la sécurité du stockage, puisque le CO_2 est moins susceptible de retourner sous sa forme gazeuse ou supercritique, notamment en cas de dépressurisation du réservoir.

- Au sein des réservoirs gréseux, la dissolution de minéraux tels que chlorite, smectites, glauconite, plagioclases sodicalcique, ou oxy-hydroxydes de fer, libère en solution des ions Na^+, K^+, Ca^{2+}, Fe^{2+} et Mg^{2+}. Ces cations métalliques peuvent réagir avec les anions bicarbonate issus de la dissolution du CO_2 pour former différents minéraux carbonatés, notamment l'ankérite $Ca(Fe,Mg)(CO_3)_2$, la calcite $CaCO_3$ ou la sidérite $FeCO_3$, et dans une moindre mesure la dawsonite $NaAlCO_3(OH)_2$, la dolomite $CaMg(CO_3)_2$ et la magnésite $MgCO_3$ (voir la revue récente de Balashov *et al.*, 2013). La réaction s'écrit par exemple pour la calcite :

$$Ca^{2+} + HCO_3^- \longrightarrow H^+ + CaCO_3 \tag{1.5}$$

  Cette *séquestration minérale* du CO_2 est susceptible d'intervenir à l'échéance de plusieurs centaines à plusieurs milliers d'années (e.g Xu *et al.*, 2004, 2005 ; Marini, 2007), et garantit l'immobilisation du CO_2 sur de longues échelles de temps (IPCC, 2005 ; voir également Fig. 1.1).

  Le potentiel de séquestration minérale dépend toutefois bien évidemment de la disponibilité dans la roche réservoir de minéraux réactifs, sources potentielles de cations métalliques. Ces minéraux sont en général présents en faible proportion dans les formations gréseuses, ce qui explique que la formation de minéraux carbonatés ne contribuera dans la majeure partie des cas que de manière marginale au processus de séquestration dans les aquifères salins (e.g Gilfillan *et al.*, 2009 ; Ranganathan *et al.*, 2011).

Le **stockage du CO_2 dans des roches basiques ou ultrabasiques**, telles que basaltes et péridotites, vise justement à optimiser la séquestration minérale "*in situ*" du CO_2 (c'est à dire au sein de formations géologiques). Ces roches contenant moins de 52% de SiO_2 en masse constituent en effet des sources abondantes de cations divalents tels que Ca^{2+}, Mg^{2+} et Fe^{2+}.

Un basalte typique contient ainsi de 7 à 10% en masse de Ca, 5 à 6% de Mg et 7 à 10% de Fe (Oelkers *et al.*, 2008). Sa forte réactivité assure tout à la fois une neutralisation de l'acide carbonique (séquestration ionique du CO_2), et un relargage relativement rapide de cations métalliques en solution. La minéralisation effective d'une partie du CO_2 sous la forme de calcite et de carbonates de Mg-Fe-Ca après une réaction de quelques mois avec un basalte a été démontrée expérimentalement de 40 à 250°C (McGrail *et al.*, 2006 ; Schaef *et al.*, 2009 ; Gysi et Stefánsson, 2012a,b ; Rosenbauer *et al.*, 2012). En outre, les importants volumes de basaltes disponibles à l'échelle internationale rendent cette cible géologique attractive. Pour les seuls trapps de la Columbia River, aux Etats-Unis, le potentiel de stockage de CO_2 a ainsi été estimé à 100 Gt CO_2 (McGrail *et al.*, 2006). Goldberg *et al.* (2008) ont par ailleurs suggéré de tirer profit des vastes volumes de basalte recouvrant le plancher océanique. En Islande, cette méthode de séquestration est actuellement testée à petite échelle dans le cadre du projet CarbFix, sur le site d'Hellisheidi, où du CO_2 d'origine géothermique est injecté depuis juin 2012 dans un aquifère basaltique entre 400 et 800m de profondeur, au rythme de 2200 tonnes/an (Matter *et al.*, 2009, Gislason *et al.*, 2010). Un autre projet de démonstration devrait débuter dans les trapps de la rivière Columbia (Big Sky Carbon Sequestration Partnership).

L'obstacle principal au développement de la séquestration du CO_2 en milieu basaltique réside dans l'identification de réservoirs suffisamment perméables et volumineux, dans des zones géologiquement stables, qui puissent servir de cible pour la séquestration du CO_2. Les trapps basaltiques étant bien moins documentés d'un point de vue géologique que les bassins sédimentaires, la connaissance des sites potentiellement favorables reste lacunaire. Par ailleurs, les travaux récents de Gysi et Stefánsson (2012a,b) indiquent qu'au cours de l'altération du basalte en présence de CO_2, la formation de phases argileuses et de zéolites entre en compétition avec la formation de phases carbonatées, réduisant le potentiel de séquestration minérale.

Du fait de leur forte proportion en MgO, CaO et FeO et de leur réactivité, les péridotites constituent également des cibles privilégiées pour la séquestration minérale du CO_2. L'injection de CO_2 dans les massifs péridotitiques de l'ophiolithe d'Oman a ainsi été proposée par Kelemen et Matter (2008), une suggestion motivée par l'observation de la carbonatation naturelle des péridotites sous la forme de magnésite et dolomite par interaction avec les eaux météoriques (Kelemen *et al.*, 2011). La faible perméabilité des péridotites est toutefois un obstacle évident au stockage de CO_2 en leur sein. Kelemen et Matter (2008) proposent l'usage de la fracturation hydraulique pour initier l'injection, tandis que la variation de volume positive et le caractère exothermique de la réaction de carbonatation pourraient permettre d'auto-entretenir la surface réactive et la température nécessaire à la réalisation de la carbonatation.

Si l'on excepte la séquestration dans les péridotites, à ce stade très hypothétique, les options de stockage géologique de CO_2 détaillées ci-dessus partagent les mêmes technologies et ont donc des coûts d'exploitation proches. Hors récupération assistée d'hydrocarbures, le coût du stockage du CO_2 dans des formations géologiques est estimé de 0.5 à 8 \$/t CO_2, soit largement inférieur au coût de capture du CO_2 (IPCC, 2005). Malgré ce coût relativement modéré, le développement de la séquestration géologique souterraine du CO_2 est soumis à la gestion du risque de fuite hors du stockage, et à la délicate question de l'acceptation publique du stockage (Bachu, 2008).

La séquestration minérale du CO_2 *in situ* offre des garanties de sureté à long terme, mais elle est soumise aux mêmes contraintes que les méthodes plus classiques de stockage souterrain. De plus, le potentiel de séquestration minérale effective des roches basiques reste à préciser ; sa prédiction et son optimisation requièrent de mieux contraindre les mécanismes et vitesses de dissolution des phases silicatées, et les conditions et vitesses de formation des minéraux carbonatés susceptibles de précipiter.
La séquestration minérale *ex situ* du CO_2 donne l'opportunité de mieux contrôler le processus de carbonatation des minéraux.

1.1.3 La séquestration minérale du CO_2 *ex situ* : principe et challenges

Le principe de la séquestration du CO_2 sous la forme de minéraux carbonatés a initialement été proposé par Seifritz (1990), puis repris et détaillé par Lackner *et al.* (1995). Comme nous l'avons vu, il consiste à extraire d'un matériau initial des cations métalliques divalents, afin de former des minéraux carbonatés par réaction avec du CO_2 dissous. La séquestration minérale *ex situ* consiste à réaliser cette réaction de carbonatation dans le cadre d'un processus industriel se déroulant hors du milieu géologique. Schématiquement, au lieu de transporter

le CO_2 vers le site de stockage, il est alors nécessaire d'acheminer vers la source de CO_2 les matériaux primaires servant de substrat à la carbonatation (Zevenhoven *et al.*, 2011).

Les réactions générales de carbonatation en magnésite de différents minéraux magnésiens peuvent ainsi s'écrire :

$$\underset{\text{périclase}}{MgO} + CO_2 \longrightarrow MgCO_3 \tag{1.6}$$

$$\underset{\text{brucite}}{Mg(OH)_2} + CO_2 \longrightarrow MgCO_3 + H_2O \tag{1.7}$$

$$\underset{\text{forstérite}}{Mg_2SiO_4} + 2\,CO_2 \longrightarrow 2\,MgCO_3 + SiO_2 \tag{1.8}$$

$$\underset{\text{serpentine}}{Mg_3Si_2O_5(OH)_4} + 3\,CO_2 \longrightarrow 3\,MgCO_3 + 2\,SiO_2 + 2\,H_2O \tag{1.9}$$

Le principal attrait de la séquestration minérale du CO_2 réside dans le fait que les réactions de carbonatation de nombreux oxydes, hydroxydes et silicates de magnésium, calcium et fer, sont favorisées d'un point de vue thermodynamique jusqu'à des températures élevées, fonction de la pression partielle en CO_2 (Lackner *et al.*, 1995 ; Dufaud, 2006). La figure 1.2 présente ainsi l'évolution de l'énergie libre de la réaction de carbonatation de la forstérite et de la serpentine en fonction de la température, pour deux pressions de CO_2. Elle démontre que ces réactions sont favorisées ($\Delta_r G < 0$) dans un vaste domaine de température.

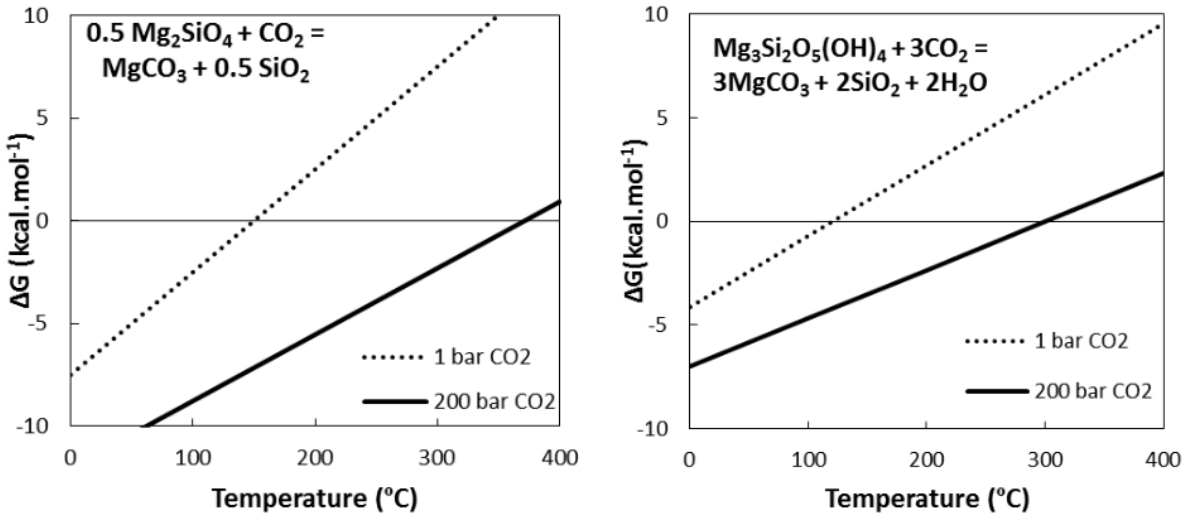

FIGURE 1.2 – Énergie libre de la réaction de carbonatation de la forstérite (gauche) et du chrysotile (droite) en fonction de la température. D'après Declercq et Oelkers (2012).

Par ailleurs, la séquestration industrielle offre la possibilité de recourir à des substrats initiaux variés. Il a ainsi été démontré expérimentalement la possibilité de carbonater des minéraux tels que la forstérite et la serpentine, la brucite (e.g Zhao *et al.*, 2009 ; Schaef *et al.*, 2011), la wollastonite (Daval *et al.*, 2009), l'anorthite (Munz *et al.*, 2011), ou des résidus industriels alcalins tels que les cendres issues de la combustion du charbon (qui contiennent quelques pourcents de CaO - Montes-Hernandez *et al.*, 2009 ; Jo *et al.*, 2012), ou les laitiers d'aciérie (qui contiennent jusqu'à 50% de CaO et MgO - Huijgen *et al.*, 2005).

Toutefois, parmi ces minéraux et matériaux, les ressources les plus abondantes sont de très loin assurées par les silicates de magnésium tels que forstérite et serpentine, présents au sein des unités ultrabasiques situées dans la plupart des orogènes de la planète. La seule ophiolite d'Oman aurait un potentiel de stockage de CO_2 sous la forme de magnésite de 77 000 Gt CO_2 (Kelemen et Matter, 2008). *A contrario*, d'après une analyse récente (Renforth *et al.*, 2011) les résidus industriels alcalins produits annuellement à l'échelle internationale représentent un potentiel de séquestration minérale de seulement 190 à 332 Mt CO_2.

Par conséquent, la séquestration minérale du CO_2 par carbonatation de la forstérite Mg_2SiO_4 et de la serpentine $Mg_3Si_2O_5(OH)_4$ a fait l'objet de nombreuses recherches (e.g O'connor *et al.*, 2001 ; Giammar *et al.*, 2005 ; Béarat *et al.*, 2006 ; Gerdemann *et al.*, 2007 ; Garcia *et al.*, 2010 ; Daval *et al.*, 2011). Le processus peut être décomposé en deux étapes :

1. La dissolution de la phase silicatée en présence de CO_2 dissous, soit dans le cas de la forstérite :

$$Mg_2SiO_4 + 4\,CO_2 + 2\,H_2O \longrightarrow 2\,Mg^{2+} + SiO_{2aq} + 4\,HCO_3^- \tag{1.10}$$

2. La précipitation d'un carbonate de magnésium par réaction des cations Mg^{2+} avec les anions bicarbonate, la magnésite étant la forme la plus stable :

$$2\,Mg^{2+} + 2\,HCO_3^- \longrightarrow 2\,MgCO_3 + 2\,H^+ \tag{1.11}$$

Bien que favorisée d'un point de vue thermodynamique, la réaction de carbonatation des minéraux silicatés magnésiens est particulièrement lente. Afin de rendre le processus compatible avec les échelles de temps industrielles, différentes stratégies ont été proposées :

- Effectuer la carbonatation à haute température afin d'accélérer les cinétiques réactionnelles ;
- Réduire la taille de grain des minéraux silicatés via un broyage intensif afin d'augmenter leur surface réactive (e.g Gerdemann *et al.*, 2007 ; Haug *et al.*, 2010) ;
- Dans le cas de la serpentine, effectuer un traitement thermique à plus de 600°C avant carbonatation afin de déshydrater le minéral, de désorganiser sa structure cristalline, et d'augmenter ainsi sa réactivité (e.g McKelvy *et al.*, 2004 ; Gerdemann *et al.*, 2007) ;
- Séparer le processus de carbonatation en deux phases : dissolution de la phase silicatée dans un acide fort, puis alcalinisation du milieu pour favoriser la précipitation de minéraux carbonatés, un procédé appelé "pH-swing" (e.g Park *et al.*, 2003 ; Teir *et al.*, 2007).

En conséquence, la majeure partie des études de carbonatation directe en solution aqueuse ont été conduites à des températures supérieures à 100°C, sous de fortes pressions de CO_2 (typiquement 20 à 150 bars). Les rendements maximaux de carbonatation ont ainsi été obtenus par Gerdemann *et al.* (2007) dans des solutions contenant 0.64 M de $NaHCO_3$ et 1 M de NaCl à 185°C et 150 bars P_{CO_2} pour la forstérite, et 155°C et 40 bars P_{CO_2} pour la serpentine pré-traitée thermiquement. Ce dernier procédé va être testé dans le cadre d'un projet industriel pilote mené par l'Université de Newcastle et le groupe GreenMag dans l'état australien de Nouvelle-Galles-du-Sud.

Par ailleurs, à température ambiante, le procédé de "pH-swing" permet d'obtenir une carbonatation quasi-complète de serpentines non traitées thermiquement sous la forme de carbonates de magnésium hydratés tels que hydromagnésite $Mg_5(CO_3)_4(OH)_2{\cdot}4\,H_2O$ ou nesquéhonite $MgCO_3{\cdot}3\,H_2O$ (Teir *et al.*, 2007, 2009).

L'analyse des coûts énergétiques et financiers associés à ces stratégies de carbonatation permet d'éliminer certaines solutions et d'illustrer les défis auxquels reste confrontée la séquestration minérale *ex situ* du CO_2. Le procédé de "pH-swing" nécessite ainsi de grandes quantités de réactifs, dont la production ou la régénération est très énergivore. Ainsi, Teir *et al.* (2009) ont estimé que le procédé entraine l'émission d'environ trois fois plus de CO_2 que la quantité minéralisée si l'énergie utilisée est d'origine carbonée. Gerdemann *et al.* (2007) ont par ailleurs montré que le pré-traitement de la serpentine introduit un surcoût énergétique inacceptable. Seule la carbonatation directe de la forstérite semble réalisable, avec un coût estimé à 54 US$/t CO_2 minéralisée pour une centrale thermique au charbon de 1GW, en intégrant l'extraction du minéral, son transport, son broyage et sa carbonatation. Le surcoût énergétique représente de plus 15 à 30 % de la production électrique de la centrale, ce qui amène à une estimation globale d'environ 80 US$/t CO_2 évitée.

Ces estimations restent très largement supérieures aux estimations du coût du stockage géologique souterrain du CO_2. Aussi, il est nécessaire de trouver des moyens supplémentaires d'accélérer la réaction, de manière à en diminuer les besoins énergétiques.

Il est en général considéré dans la littérature que l'étape limitante de la réaction de carbonatation réside dans la phase de dissolution des silicates magnésiens (e.g Park *et al.*, 2003 ; Prigiobbe *et al.*, 2009 ; Zevenhoven *et al.*, 2011). Dans ce contexte, accélérer la dissolution des silicates devient crucial pour accélérer la réaction de carbonatation. Partant du fait que de nombreux ligands organiques ont la propriété d'augmenter la vitesse de dissolution des minéraux silicatés (voir la revue de Ganor *et al.*, 2009), plusieurs auteurs ont ainsi proposé d'utiliser des ligands organiques, en particulier l'acide oxalique, l'acide citrique et l'EDTA, pour accélérer l'extraction du Mg^{2+} de la forstérite ou de la serpentine (Park *et al.*, 2003 ; Hänchen *et al.*, 2006 ; Krevor et Lackner, 2011 ; Prigiobbe et Mazzotti, 2011).

En revanche, la question de l'influence de ces ligands organiques sur la précipitation des minéraux carbonatés magnésiens n'a encore jamais été abordée. Cette question est d'autant plus importante que les études expérimentales récentes de Saldi *et al.* (2009), et Saldi *et al.* (2012) (en annexe du manuscrit) ont montré que la précipitation de la magnésite est particulièrement lente, et est susceptible de limiter l'avancée de la réaction de carbonatation de la forstérite.

Quantifier et comprendre l'influence de ligands organiques sur la cinétique et le mécanisme de la croissance minérale de la magnésite sera donc l'un des objectifs principaux de ce travail de thèse.

Un dernier point mérite d'être mentionné - bien qu'il ne s'agisse pas à proprement parler de séquestration minérale *ex situ*.

Sans pré-traitement thermique, la carbonatation directe de la serpentine en magnésite est beaucoup plus lente que celle de la forstérite (Gerdemann *et al.*, 2007). Pourtant, l'altération à basse température de résidus miniers de serpentine disposés à l'air libre au Canada (Colom-

bie Britannique, Yukon, Québec) ou dans l'Ouest de l'Australie (Mont Keith Mine), conduit à la formation au sein des talus miniers de carbonates de magnésium hydratés tels que l'hydromagnésite $Mg_5(CO_3)_4(OH)_2{\cdot}4\,H_2O$ (Wilson *et al.*, 2006, 2009 ; Pronost *et al.*, 2011). Wilson *et al.* (2009) ont estimé la quantité de CO_2 ainsi fixée annuellement par carbonatation passive des résidus de chrysotile de la mine de Clinton Creek, au Yukon à plus de 6000 t CO_2 par an. L'abondance de ce type de résidus miniers laisse cependant présager un potentiel beaucoup plus important de réduction des émissions de CO_2 de l'industrie minière (Bea *et al.*, 2012).

La quantification et l'optimisation de ces processus de séquestration minérale du CO_2 requièrent de mieux contraindre la vitesse et les conditions de formation des minéraux carbonatés magnésiens hydratés susceptibles de précipiter. Ce sera la seconde ambition de ce travail de thèse.

1.1.4 Particularités du sytème des minéraux carbonatés magnésiens

Bien que partageant avec la calcite $CaCO_3$ un même système cristallin (trigonal), une chimie proche, et une solubilité comparable, la magnésite $MgCO_3$ est incomparablement moins présente que son homologue calcique dans les environnements sédimentaires. Sursaturée dans la plupart des eaux superficielles Hostetler (1964), la magnésite ne se forme généralement pas à température ambiante (Lippmann, 1973 ; Deelman, 2011), tandis que la calcite précipite sans difficulté, et constitue le principal biominéral à la surface de la planète.

Expérimentalement, la magnésite n'a été précipitée directement à partir de solutions aqueuses qu'à des températures supérieures à environ 80°C (e.g Giammar *et al.*, 2005 ; Hänchen *et al.*, 2006 ; Saldi *et al.*, 2009). Des travaux récents ont confirmé que la vitesse de précipitation de la magnésite est particulièrement lente, de 5 à 6 ordres de grandeur inférieure à celle de la calcite (Saldi *et al.*, 2009, 2012). Aussi, bien que la magnésite soit le carbonate de magnésium le plus stable (Königsberger *et al.*, 1999, Bénézeth *et al.*, 2011), une grande diversité de minéraux carbonatés magnésiens plus ou moins hydratés, métastables, se forment à sa place à température ambiante (Davies et Bubela, 1973 ; Hopkinson *et al.*, 2012). Les plus courants sont représentés dans le diagramme ternaire de la Figure 1.3 : hydromagnésite $Mg_5(CO_3)_4(OH)_2{\cdot}4\,H_2O$, nesquéhonite $MgCO_3{\cdot}3\,H_2O$, dypingite $Mg_5(CO_3)_4(OH)_2{\cdot}5\,H_2O$, artinite $Mg_2(CO_3)(OH)_2{\cdot}3\,H_2O$, lansfordite $MgCO_3{\cdot}5\,H_2O$, et barringtonite $MgCO_3{\cdot}2\,H_2O$.

Parallèlement, la magnésite est également connue pour sa faible vitesse de dissolution parmi les minéraux carbonatés (Pokrovsky et Schott, 1999, Pokrovsky *et al.*, 2009 ; Saldi *et al.*, 2010). Cette caractéristique rend le minéral attractif pour la séquestration minérale du CO_2, puisque la magnésite peut ainsi stocker du carbone sans risque de re-dissolution.

La faible réactivité de la magnésite résulte de facteurs cinétiques qui ont souvent été reliés au caractère très hydraté du cation Mg^{2+} constitutif du minéral (e.g Lippmann, 1973 ; Sayles et Fyfe, 1973). Petit et fortement chargé, l'ion Mg^{2+} a une forte densité de charges qui conduit à la structuration de "sphères d'hydratation" fermement liées à l'ion. La première sphère d'hydratation (ou sphère de coordination) est constituée de six molécules d'eau en configuration octaédrique, tandis que la seconde sphère contient 12 à 13 molécules d'eau (Hamm *et al.*, 2010 ; Di Tommaso et de Leeuw, 2010).

On considère généralement que la précipitation de minéraux carbonatés est contrôlée par l'échange d'une molécule d'eau dans la sphère de coordination du métal avec un ion carbonate ou bicarbonate de la solution, ceci conduisant à la formation d'un complexe

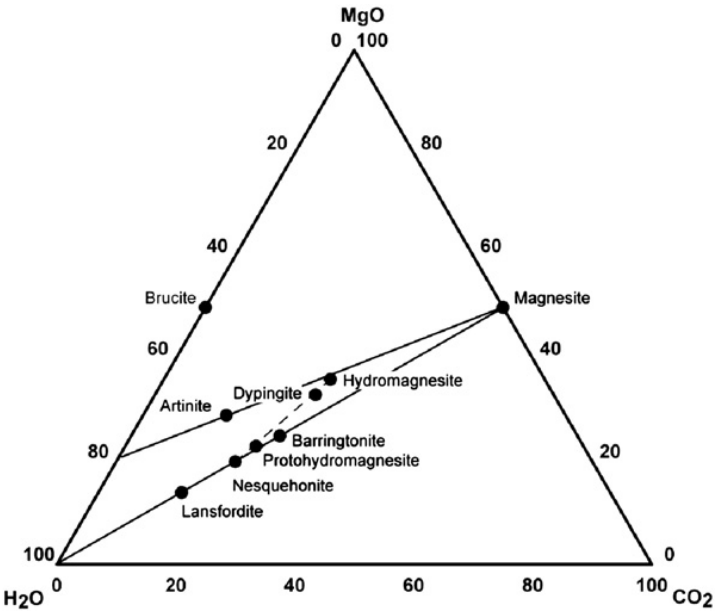

FIGURE 1.3 – Diagramme compositionnel représentant les phases minérales principales se formant dans le système MgO-CO_2-H_2O. La ligne pointillée représente les phases intermédiaires précipitées par Davies et Bubela (1973). Source : Bénézeth *et al.* (2011).

métal-carbonate, dont la vitesse de formation est proportionnelle à la vitesse d'échange des molécules d'eau entre la solution et la sphère de coordination du métal (Lincoln et Merbach, 1995 ; Schott *et al.*, 2009). Par ailleurs, Pokrovsky et Schott (2002) ont montré que la vitesse de dissolution des différents minéraux carbonatés est directement corrélée à cette vitesse d'échange. Or la fréquence d'échange de molécules d'eau depuis la sphère d'hydratation du Mg^{2+} est inférieure de près de 4 ordres de grandeur à celle de Ca^{2+} (Bleuzen *et al.*, 1997 ; Larentzos et Criscenti, 2008), ce qui explique la faible réactivité générale de la magnésite, et notamment sa propension limitée à précipiter.

Deux questions fondamentales se posent donc :

- Connaissant l'influence de l'hydratation du Mg^{2+} sur la faible réactivité de la magnésite, est-il possible d'imaginer des méthodes pour accélérer la vitesse de précipitation de ce minéral ?
- Quels sont les facteurs thermodynamiques et cinétiques qui contrôlent la précipitation des minéraux carbonatés magnésiens hydratés en lieu et place de la magnésite à température ambiante ?

Pour répondre à la première question, deux solutions sont envisageables : soit influencer directement l'hydratation du Mg^{2+} en diminuant l'activité chimique de l'eau, soit augmenter la vitesse d'échange des molécules d'eau dans la sphère de coordination du Mg.

Il est possible de diminuer l'activité de l'eau en ajoutant à la solution aqueuse un solvant organique tel que le méthanol. Cette solution a été testée à température ambiante par Teng et Wang (2011), qui ont constaté que la présence de méthanol accélère la formation de carbonates de magnésium hydratés, mais ne permet pas à elle seule la précipitation de carbonate de magnésium anhydre. Kowacz *et al.* (2007) avaient également constaté pour des raisons analogues une augmentation de la cinétique de croissance cristalline de la barite $BaSO_4$ en présence d'une faible proportion de méthanol.

Pour le second cas, la complexation d'un cation métallique avec un ligand organique ou inorganique pourrait avoir pour conséquence une augmentation de la fréquence d'échange des

molécules d'eau. La complexation du cation a en effet pour conséquence une déstabilisation de la sphère d'hydratation, qui entraîne une plus grande labilité des molécules d'eau. Cela a notamment été vérifié dans le cas des cations Al^{3+} par Phillips *et al.* (1997a,b) et Sullivan *et al.* (1999). Par ailleurs, Mirsal et Zankl (1985) ont proposé un mécanisme par lequel un complexe constitué par un ligand organique (oxalate, malonate ou citrate) et un cation métallique annexe faciliterait la formation de carbonates magnésiens tel que la dolomite. Bien que ces résultats aient été contestés (Deelman, 1988), ils interrogent sur **le rôle que pourraient avoir des ligands organiques aussi simples que l'oxalate ou le citrate sur la réactivité de Mg^{2+}, et peut-être de la magnésite**. On accordera une attention particulière à cette question dans le cadre de ce travail.

La seconde question est motivée par la méconnaissance du système des carbonates magnésiens. Bien que les propriétés thermodynamiques des phases minérales principales soient relativement bien contraintes, la précipitation des carbonates magnésiens hydratés à température ambiante semble dictée par des facteurs essentiellement cinétiques (Hänchen *et al.*, 2006 ; Hopkinson *et al.*, 2012). Or **il existe à ce stade très peu de données sur la cinétique de précipitation des carbonates de magnésium hydratés**. L'hypothèse selon laquelle l'état d'hydratation du minéral influerait sur sa cinétique de précipitation n'a pas été formellement prouvée, de même que le lien proposé entre énergie d'activation et état d'hydratation (Lippmann, 1973).

Outre leur intérêt fondamental, de nouvelles données sur la réactivité des différentes phases de carbonates de magnésium seraient utiles à l'optimisation des stratégies de séquestration minérale du CO_2. Elles permettraient également de mieux comprendre les mécanismes de précipitation des carbonates de magnésium dans le milieu naturel, notamment au sein de biofilms ou stromatolites (e.g Thompson et Ferris, 1990 ; Power *et al.*, 2007 ; Shirokova *et al.*, 2012).

1.2 Objectifs de la thèse et stratégies expérimentales

Nous l'avons vu, la compréhension et le développement des techniques de séquestration minérale du carbone, qu'elles soient *in situ* ou *ex situ*, requièrent une connaissance précise de la réactivité des minéraux carbonatés, notamment magnésiens. Le processus de précipitation d'un cristal à partir d'une solution aqueuse est composé de deux phases : la nucléation de germes cristallins à partir de la solution, puis leur croissance. Les travaux présentés ici concernent uniquement l'étude de la croissance cristalline, et nous n'évoquerons pas les phénomènes de nucléation des carbonates de magnésium. Le lecteur intéressé par les bases théoriques et les méthodes d'étude des phénomènes de nucléation pourra se référer par exemple à Fritz et Noguera (2009).

Le premier objectif de ce travail de thèse sera de quantifier et de comprendre l'influence de ligands organiques sur la précipitation de la magnésite, en vue d'évaluer si l'utilisation de tels ligands est envisageable pour accélérer la réaction de carbonatation de minéraux silicatés magnésiens.

Les ligands organiques les plus utilisés dans la littérature pour accélérer la cinétique de dissolution de la forstérite ou de la serpentine sont l'oxalate $(COO)_2^{2-}$ (et son acide conjugué l'acide oxalique), le citrate $C_3H_5O(COO)_3^{3-}$ (et son acide conjugué l'acide citrique), et l'acide éthylène diamine tétraacétique (EDTA) ou sa base conjuguée $C_{10}H_{12}N_2O_8^{4-}$. Mes efforts se sont donc naturellement portés sur l'étude de ces trois ligands, représentés Fig. 1.4, qui diffèrent de par leurs propriétés chimiques et la nature et la stabilité des complexes qu'ils forment avec les cations métalliques.

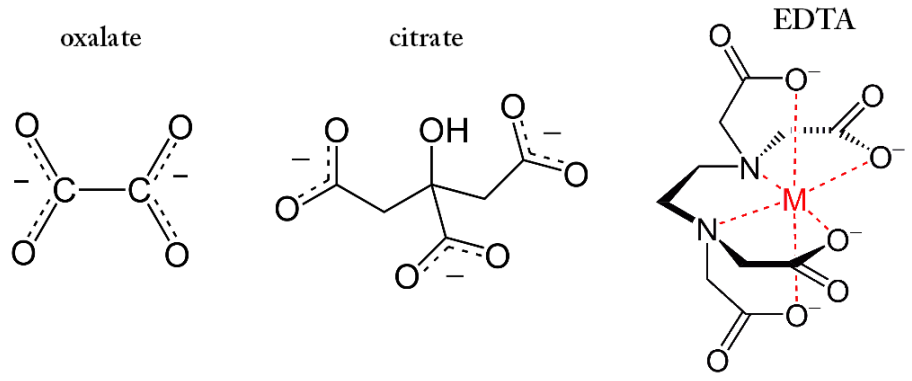

FIGURE 1.4 – Représentation squelettique des trois ligands utilisés dans cette étude. L'atome M représenté dans la structure de l'EDTA est un cation métallique chelaté par le biais de six liaisons faibles, représentées en rouge.

L'approche retenue pour l'étude est essentiellement expérimentale, basée sur la réalisation d'essai de croissance cristalline suivies par le biais de différentes méthodes expérimentales. Du fait de la faible cinétique de croissance cristalline de la magnésite, ces expériences ont été réalisées à des températures supérieures ou égales à 100°C.
L'originalité du travail réside dans l'association de méthodes d'études à différentes échelles :

- La réalisation d'expériences en réacteur à flux continu permet de caractériser l'influence des ligands à l'échelle "macroscopique", en déterminant la loi de croissance du minéral

pour différentes conditions physico-chimiques. Cette même technique expérimentale a notamment été utilisée par Shiraki et Brantley (1995) pour étudier la cinétique de précipitation de la calcite, par Devidal *et al.* (1997) pour la kaolinite, ou Saldi *et al.* (2012) pour la magnésite en conditions inorganiques. Ces données cinétiques ont ensuite été intégrées dans un modèle cinétique simple visant à déterminer l'influence des ligands sur le processus global de carbonatation, incluant la phase de dissolution du silicate de magnésium.

- Par ailleurs, l'utilisation de la microscopie à force atomique en conditions hydrothermales permet d'étudier dans des conditions analogues le processus de croissance cristalline directement à l'échelle surfacique, et de caractériser la manière dont les ligands l'influencent. Cette technique a été utilisée au cours de mon séjour au Département de Cristallographie de l'Université Ludwig Maximilian de Munich (LMU). Les données obtenues fournissent des informations améliorant notre compréhension fondamentale de l'interaction entre ligands organiques et croissance cristalline de la magnésite.

Le second objectif est d'apporter des données nouvelles sur la réactivité des carbonates de magnésium hydratés, dans le but d'une part de mieux comprendre les raisons pour lesquelles la magnésite ne se forme pas à température ambiante, et d'autre part de mieux prédire, voire d'optimiser, la séquestration minérale du CO_2 à basse température par carbonatation de roches (ultra)basiques et la formation de ces minéraux au sein des environnements naturels.

Dans ce but, mon étude a porté sur la cinétique de croissance cristalline de l'hydromagnésite $Mg_5(CO_3)_4(OH)_2{\cdot}4\,H_2O$, le carbonate de magnésium le plus courant après la magnésite (Deelman, 2011). Afin de déterminer l'énergie d'activation du processus, des expériences de croissance cristalline ont été conduites entre 25 et 75°C, de manière à permettre une comparaison avec la cinétique de précipitation de la magnésite, étudiée à plus haute température. À 50 et 75°C, les expériences ont été réalisées en utilisant les mêmes dispositifs expérimentaux que pour la magnésite (réacteurs à flux continu). À 25°C ont été utilisés des réacteurs "à flux discontinu", qui seront décrits dans la partie dédiée du manuscrit. Enfin, du fait de la disparité des données de solubilité de l'hydromagnésite, l'interprétation des données cinétiques a requis la mesure expérimentale du produit de solubilité de l'hydromagnésite naturelle utilisée pour conduire les expériences de croissance cristalline.

1.3 Structure du manuscrit

Le manuscrit est organisé en 7 chapitres, dont l'introduction génerale (Chapitre 1).
Les chapitres 3, 4, 5 et 6 sont écrits en anglais. Les chapitres 4, 5 et 6 sont présentés sous la forme d'articles prochainement soumis à la publication, au sein desquels sont décrites en détail les méthodes expérimentales utilisées.

Le chapitre 2 présente les matériaux minéraux, dispositifs expérimentaux et techniques analytiques utilisés dans les chapitres 3 à 6.

Le chapitre 3 présente la constitution d'une base de données thermodynamiques pertinente pour le calcul de la spéciation chimique des solutions expérimentales, qui sera utilisée dans la suite du travail. En effet, les bases de données usuelles de PHREEQC, le code de calcul géochimique avec lequel seront effectués les calculs de spéciation chimique (Parkhurst et Appelo,

1999), ne comportent pas l'ensemble des données pertinentes au système étudié, notamment en présence des ligands organiques en conditions hydrothermales. Ce chapitre présente donc une revue des données pertinentes de la littérature et explique leur extrapolation en température, en vue de construire une base de données thermodynamiques aussi exhaustive et juste que possible.

On y présentera par ailleurs les résultats d'une expérience de mesure de la solubilité de la magnésite en présence de citrate effectuée afin de préciser la valeur de la constante de complexation entre les espèces du citrate et Mg^{2+} à haute température.

Les chapitres 4 et 5 présentent l'étude de l'influence de l'oxalate, du citrate et de l'EDTA sur le processus et la cinétique de croissance cristalline de la magnésite en conditions hydrothermales, selon deux approches complémentaires.

Le chapitre 4 présente les résultats des expériences effectuées en réacteur à circulation et vise à quantifier et à modéliser l'influence de l'oxalate, du citrate et de l'EDTA sur la cinétique de précipitation de la magnésite, entre 100 et 146°C. Les résultats obtenus sont la base d'une modélisation cinétique simple de l'influence de l'oxalate sur la carbonatation de la forstérite, présentée en discussion de l'article.

Dans le chapitre 5, on présentera les résultats de l'étude effectuée à l'échelle surfacique sur le même système par le biais de la microscopie à force atomique. Ces résultats expérimentaux permettent de confirmer et de préciser certaines hypothèses émises dans le chapitre 4 quant au mode d'interaction des ligands organiques avec le processus de croissance cristalline de la magnésite.

Le chapitre 6 présente les résultats de l'étude menée sur la solubilité et la cinétique de précipitation de l'hydromagnésite entre 25 et 75°C. Ces données originales seront comparées aux données analogues acquises pour la magnésite, dans le but de tirer des enseignements fondamentaux sur le rôle de l'hydratation des cations Mg^{2+} dans la formation des carbonates de magnésium et afin de déterminer le rôle potentiel joué par l'hydromagnésite dans l'optimisation de la séquestration minérale du CO_2.

Un chapitre de Conclusions et Perspectives (chapitre 7) viendra, classiquement, clore ce manuscrit, en en rappelant les résultats principaux et leurs conséquences scientifiques et sociétales.

Enfin, une annexe contient un article dont je suis coauteur, publié en 2012 dans la revue *Geochimica et Cosmochimica Acta* (Saldi *et al.*, 2012). L'article présente une étude détaillée de la cinétique de précipitation de la magnésite en fonction de la chimie des solutions, interprétée grâce à un modèle de complexation de surface. Ces résultats établissent pour la première fois le fait que la précipitation de la magnésite est potentiellement limitante dans le cadre du processus de carbonatation de la forstérite et constituent de ce fait l'une des motivations du travail effectué avec les ligands organiques. En outre, ils constituent une référence pour la cinétique de précipitation de la magnésite en conditions inorganiques et seront à ce titre fréquemment cités et discutés, notamment dans le cadre du Chapitre 4.

Bibliographie

Anthony, K. R. N., Kline, D. I., Diaz-Pulido, G., Dove, S. et Hoegh-Guldberg, O. (2008). Ocean acidification causes bleaching and productivity loss in coral reef builders. *Proceedings of the National Academy of Sciences*, 105(45), 17442–17446.

Arts, R., Chadwick, A., Eiken, O., Thibeau, S. et Nooner, S. (2008). Ten years' experience of monitoring CO_2 injection in the Utsira Sand at Sleipner, offshore Norway. *First Break*, 26, 65–72.

Bachu, S. (2008). CO_2 storage in geological media : Role, means, status and barriers to deployment. *Progress in Energy and Combustion Science*, 34(2), 254–273.

Bachu, S., Gunter, W. et Perkins, E. (1994). Aquifer disposal of CO_2 : Hydrodynamic and mineral trapping. *Energy Conversion and Management*, 35(4), 269–279.

Balashov, V. N., Guthrie, G. D., Hakala, J. A., Lopano, C. L., Rimstidt, J. D. et Brantley, S. L. (2013). Predictive modeling of CO_2 sequestration in deep saline sandstone reservoirs : Impacts of geochemical kinetics. *Applied Geochemistry*, (30), 41–56.

Ballantyne, A. P., Alden, C. B., Miller, J. B., Tans, P. P. et White, J. W. C. (2012). Increase in observed net carbon dioxide uptake by land and oceans during the past 50 years. *Nature*, 488(7409), 70–72.

Béarat, H., McKelvy, M. J., Chizmeshya, A. V. G., Gormley, D., Nunez, R., Carpenter, R. W., Squires, K. et Wolf, G. H. (2006). Carbon sequestration via aqueous olivine mineral carbonation : Role of passivating layer formation. *Environ. Sci. Technol.*, 40(15), 4802–4808.

Bea, S. A., Wilson, S. A., Mayer, K. U., Dipple, G. M., Power, I. M. et Gamazo, P. (2012). Reactive transport modeling of natural carbon sequestration in ultramafic mine tailings. *Vadose Zone Journal*, 11(2).

Beaufort, L., Probert, I., Garidel-Thoron, T., Bendif, E. M., Ruiz-Pino, D., Metzl, N., Goyet, C., Buchet, N., Coupel, P., Grelaud, M., Rost, B., Rickaby, R. E. M. et Vargas, C. d. (2011). Sensitivity of coccolithophores to carbonate chemistry and ocean acidification. *Nature*, 476(7358), 80–83.

Bleuzen, A., Pittet, P. A., Helm, L. et Merbach, A. E. (1997). Water exchange on Magnesium(II) in aqueous solution : a variable temperature and pressure ^{17}O NMR study. *Magnetic Resonance in Chemistry*, 35, 765–773.

Bénézeth, P., Saldi, G. D., Dandurand, J. L. et Schott, J. (2011). Experimental determination of the solubility product of magnesite at 50 to 200°C. *Chemical Geology*, 286, 21–31.

BP (2012). BP statistical review of World Energy June 2012. Rapport technique.

Cao, L. et Caldeira, K. (2008). Atmospheric CO_2 stabilization and ocean acidification. *Geophysical Research Letters*, 35(19).

Coumou, D. et Rahmstorf, S. (2012). A decade of weather extremes. *Nature Climate Change*.

Daval, D., Martinez, I., Corvisier, J., Findling, N., Goffé, B. et Guyot, F. (2009). Carbonation of ca-bearing silicates, the case of wollastonite : Experimental investigations and kinetic modeling. *Chemical Geology*, 265(1), 63–78.

Daval, D., Sissmann, O., Menguy, N., Saldi, G. D., Guyot, F., Martinez, I., Corvisier, J., Garcia, B., Machouk, I., Knauss, K. G. et Hellmann, R. (2011). Influence of amorphous silica layer formation on the dissolution rate of olivine at 90 °C and elevated pCO_2. *Chemical Geology*, 284(1-2), 193–209.

Davies, P. J. et Bubela, B. (1973). The transformation of nesquehonite into hydromagnesite. *Chemical Geology*, 12, 289–300.

Declercq, J. et Oelkers, E. (2012). Thermodynamic and kinetic constraints on the carbonation of forsterite and serpentine. *Submitted to Environmental Science & Technology*.

Deelman, J. C. (1988). Some phenomenological aspects of carbonate geochemistry. The control effect of transition metals - Discussion. *Geologische Rundschau*, 77(2), 609–611.

Deelman, J. C. (2011). *Low-temperature formation of magnesite and dolomite*. Geology Series. Compact Disc Publications, Eindhoven, The Netherlands, 2.3 édition. E-book first published online in May 2003. Version 2.3 updated in 2011. www.jcdeelman.demon.nl/dolomite/bookprospectus.html.

Devidal, J.-L., Schott, J. et Dandurand, J.-L. (1997). An experimental study of kaolinite dissolution and precipitation kinetics as a function of chemical affinity and solution composition at 150°C, 40 bars, and pH 2, 6.8, and 7.8. *Geochimica et Cosmochimica Acta*, 61(24), 5165–5186.

Di Tommaso, D. et de Leeuw, N. H. (2010). First principles simulations of the structural and dynamical properties of hydrated metal ions Me^{2+} and solvated metal carbonates (Me = Ca, Mg, and Sr). *Crystal Growth & Design*, 10(10), 4292–4302.

Doney, S. C., Fabry, V. J., Feely, R. A. et Kleypas, J. A. (2009). Ocean acidification : The other CO_2 problem. *Annual Review of Marine Science*, 1(1), 169–192.

Dufaud, F. (2006). *Etude expérimentale des réactions de carbonatation minérale du CO_2 dans les roches basiques et ultrabasiques*. Thèse de doctorat, Institut de Physique du Globe, Paris, France.

Fabry, V. J., Seibel, B. A., Feely, R. A. et Orr, J. C. (2008). Impacts of ocean acidification on marine fauna and ecosystem processes. *ICES Journal of Marine Science*, 65(3), 414–432.

Fritz, B. et Noguera, C. (2009). Mineral precipitation kinetics. *Reviews in Mineralogy and Geochemistry*, 70(1), 371–410.

Ganor, J., Reznik, I. et Rosenberg, Y. (2009). Organics in water-rock interactions. *Reviews in Mineralogy and Geochemistry*, 70(1), 259.

Garcia, B., Beaumont, V., Perfetti, E., Rouchon, V., Blanchet, D., Oger, P., Dromart, G., Huc, A.-Y. et Haeseler, F. (2010). Experiments and geochemical modelling of CO_2 sequestration by olivine : Potential, quantification. *Applied Geochemistry*, 25(9), 1383–1396.

Gerdemann, S. J., O'Connor, W. K., Dahlin, D. C., Penner, L. R. et Rush, H. (2007). Ex situ aqueous mineral carbonation. *Environ. Sci. Technol.*, 41(7), 2587–2593.

Giammar, D. E., Bruant, R. G. et Peters, C. A. (2005). Forsterite dissolution and magnesite precipitation at conditions relevant for deep saline aquifer storage and sequestration of carbon dioxide. *Chemical Geology*, 217(3-4), 257–276.

Gilfillan, S. M. V., Lollar, B. S., Holland, G., Blagburn, D., Stevens, S., Schoell, M., Cassidy, M., Ding, Z., Zhou, Z., Lacrampe-Couloume, G. et Ballentine, C. J. (2009). Solubility trapping in formation water as dominant CO_2 sink in natural gas fields. *Nature*, 458(7238), 614–618.

Gislason, S. R., Wolff-Boenisch, D., Stefansson, A., Oelkers, E. H., Gunnlaugsson, E., Sigurdardottir, H., Sigfusson, B., Broecker, W. S., Matter, J. M., Stute, M. *et al.* (2010). Mineral sequestration of carbon dioxide in basalt : A pre-injection overview of the CarbFix project. *International Journal of Greenhouse Gas Control*, 4(3), 537–545.

Global Carbon Project (2011). Carbon budget and trends 2010. Rapport technique. www.globalcarbonproject.org.

Goldberg, D. S., Takahashi, T. et Slagle, A. L. (2008). Carbon dioxide sequestration in deep-sea basalt. *Proceedings of the National Academy of Sciences*.

Gunter, W. D., Bachu, S. et Benson, S. (2004). The role of hydrogeological and geochemical trapping in sedimentary basins for secure geological storage of carbon dioxide. *Geological Society, London, Special Publications*, 233(1), 129–145.

Gysi, A. P. et Stefánsson, A. (2012a). CO_2-water-basalt interaction. Low temperature experiments and implications for CO_2 sequestration into basalts. *Geochimica et Cosmochimica Acta*, 81(0), 129–152.

Gysi, A. P. et Stefánsson, A. (2012b). Mineralogical aspects of CO2 sequestration during hydrothermal basalt alteration - An experimental study at 75 to 250°C and elevated pCO2. *Chemical Geology*, 306-307, 146–159.

Hamm, L. M., Wallace, A. F. et Dove, P. M. (2010). Molecular dynamics of ion hydration in the presence of small carboxylated molecules and implications for calcification. *The Journal of Physical Chemistry B*, 114, 10488–10495.

Hansen, J., Sato, M. et Ruedy, R. (2012). Perception of climate change. *Proceedings of the National Academy of Sciences*, 109(37), E2415–E2423.

Haug, T. A., Kleiv, R. A. et Munz, I. A. (2010). Investigating dissolution of mechanically activated olivine for carbonation purposes. *Applied Geochemistry*, 25(10), 1547–1563.

Hitchon, B. (1996). *Aquifer disposal of carbon dioxide : hydrodynamic and mineral trapping : proof of concept*. Geoscience Pub., Alberta Research Council édition.

Hänchen, M., Prigiobbe, V., Storti, G., Seward, T. et Mazzotti, M. (2006). Dissolution kinetics of fosteritic olivine at 90 - 150°C including effects of the presence of CO_2. *Geochimica et Cosmochimica Acta*, 70(17), 4403–4416.

Hopkinson, L., Kristova, P., Rutt, K. et Cressey, G. (2012). Phase transitions in the system MgO-CO_2-H_2O during CO_2 degassing of Mg-bearing solutions. *Geochimica et Cosmochimica Acta*, 76, 1–13.

Hostetler, P. B. (1964). The degree of saturation of magnesium and calcium carbonate minerals in natural waters. *Intern. Assoc. Sci. Hydrol., Comm. Subterranean Waters, Publ*, 64, 34–49.

Huijgen, W. J. J., Witkamp, G.-J. et Comans, R. N. (2005). Mineral CO_2 sequestration by steel slag carbonation. *Environmental Science & Technology*, 39(24), 9676–9682.

IEA (2010). IEA/CSLF Report to the Muskoka 2010 G8 Summit - Carbon Capture and Storage. Rapport technique, International Energy Agency.

IPCC (2005). *Carbon Dioxide Capture and Storage : Special Report of the Intergovernmental Panel on Climate Change*. Cambridge University Press.

IPCC (2007). *Climate Change 2007 - The Physical Science Basis : Working Group I. Contribution to the Fourth Assessment Report of the IPCC*. Cambridge University Press.

Jenkins, C. R., Cook, P. J., Ennis-King, J., Undershultz, J., Boreham, C., Dance, T., de Caritat, P., Etheridge, D. M., Freifeld, B. M., Hortle, A. *et al.* (2012). Safe storage and effective monitoring of CO_2 in depleted gas fields. *Proceedings of the National Academy of Sciences*, 109(2), E35–E41.

Jo, H. Y., Kim, J. H., Lee, Y. J., Lee, M. et Choh, S.-J. (2012). Evaluation of factors affecting mineral carbonation of CO_2 using coal fly ash in aqueous solutions under ambient conditions. *Chemical Engineering Journal*, 183, 77–87.

Kelemen, P. B. et Matter, J. (2008). In situ carbonation of peridotite for CO_2 storage. *Proceedings of the National Academy of Sciences*, 105(45), 17295–17300.

Kelemen, P. B., Matter, J., Streit, E. E., Rudge, J. F., Curry, W. B. et Blusztajn, J. (2011). Rates and mechanisms of mineral carbonation in peridotite : Natural processes and recipes for enhanced, in situ CO_2 capture and storage. *Annual Review of Earth and Planetary Sciences*, 39(1), 545–576.

Kinnard, C., Zdanowicz, C. M., Fisher, D. A., Isaksson, E., Vernal, A. et Thompson, L. G. (2011). Reconstructed changes in arctic sea ice over the past 1450 years. *Nature*, 479(7374), 509–512.

Königsberger, E., Königsberger, L. et Gamsjäger, H. (1999). Low-temperature thermodynamic model for the system Na_2CO_3-$MgCO_3$-$CaCO_3$-H_2O. *Geochimica et Cosmochimica Acta*, 63(19-20), 3105–3119.

Korbøl, R. et Kaddour, A. (1995). Sleipner vest CO_2 disposal - injection of removed CO_2 into the Utsira formation. *Energy Conversion and Management*, 36(6), 509–512.

Kowacz, M., Putnis, C. et Putnis, A. (2007). The effect of cation :anion ratio in solution on the mechanism of barite growth at constant supersaturation : Role of the desolvation process on the growth kinetics. *Geochimica et Cosmochimica Acta*, 71(21), 5168–5179.

Krevor, S. C. et Lackner, K. S. (2011). Enhancing serpentine dissolution kinetics for mineral carbon dioxide sequestration. *International Journal of Greenhouse Gas Control*, 5(4), 1073–1080.

Lackner, K. (2009). Capture of carbon dioxide from ambient air. *The European Physical Journal - Special Topics*, 176(1), 93–106.

Lackner, K. S. (2003). A guide to CO_2 sequestration. *Science*, 300(5626), 1677–1678.

Lackner, K. S., Grimes, P. et Ziock, H. J. (2001). Capturing carbon dioxide from air. *In Proceedings of the First National Conference on Carbon Sequestration*.

Lackner, K. S., Wendt, C. H., Butt, D. P., Joyce Jr., E. L. et Sharp, D. H. (1995). Carbon dioxide disposal in carbonate minerals. *Energy*, 20(11), 1153–1170.

Larentzos, J. P. et Criscenti, L. J. (2008). A molecular dynamics study of alkaline earth metal-chloride complexation in aqueous solution. *The Journal of Physical Chemistry B*, 112(45), 14243–14250.

Le Quéré, C., Raupach, M. R., Canadell, J. G., Marland, G. et *et al* (2009). Trends in the sources and sinks of carbon dioxide. *Nature Geoscience*, 2(12), 831–836.

Lincoln, S. F. et Merbach, A. E. (1995). Substitution reactions of solvated metal ions. *Advances in inorganic chemistry*, 42, 1–88.

Lippmann, F. (1973). *Sedimentary carbonate minerals*. Springer-Verlag Berlin.

Lüthi, D., Le Floch, M., Bereiter, B., Blunier, T., Barnola, J.-M., Siegenthaler, U., Raynaud, D., Jouzel, J., Fischer, H., Kawamura, K. et Stocker, T. F. (2008). High-resolution carbon dioxide concentration record 650.000 - 800.000 years before present. *Nature*, 453(7193), 379–382.

Marini, L. (2007). *Geological sequestration of carbon dioxide : thermodynamics, kinetics, and reaction path modeling*, volume 11. Elsevier Science Limited.

Matter, J. M., Broecker, W., Stute, M., Gislason, S., Oelkers, E., Stefánsson, A., Wolff-Boenisch, D., Gunnlaugsson, E., Axelsson, G. et Björnsson, G. (2009). Permanent carbon dioxide storage into basalt : The CarbFix pilot project, iceland. *Energy Procedia*, 1(1), 3641–3646.

McGrail, B. P., Schaef, H. T., Ho, A. M., Chien, Y. J., Dooley, J. J. et Davidson, C. L. (2006). Potential for carbon dioxide sequestration in flood basalts. *Journal of Geophysical Research*, 111, B12201.

McKelvy, M. J., Chizmeshya, A. V. G., Diefenbacher, J., Béarat, H. et Wolf, G. (2004). Exploration of the role of heat activation in enhancing serpentine carbon sequestration reactions. *Environ. Sci. Technol.*, 38(24), 6897–6903.

McNeil, B. I. et Matear, R. J. (2008). Southern ocean acidification : A tipping point at 450-ppm atmospheric CO_2. *Proceedings of the National Academy of Sciences*, 105(48), 18860–18864.

Meinshausen, M., Meinshausen, N., Hare, W., Raper, S. C. B., Frieler, K., Knutti, R., Frame, D. J. et Allen, M. R. (2009). Greenhouse-gas emission targets for limiting global warming to 2°C. *Nature*, 458(7242), 1158–1162.

Mirsal, I. A. et Zankl, H. (1985). Some phenomenological aspects of carbonate geochemistry. the control effect of transition metals. *Geologische Rundschau*, 74(2), 367–377.

Montes-Hernandez, G., Pérez-López, R., Renard, F., Nieto, J. et Charlet, L. (2009). Mineral sequestration of CO_2 by aqueous carbonation of coal combustion fly-ash. *Journal of Hazardous Materials*, 161(2-3), 1347–1354.

Munz, I., Brandvoll, O., Haug, T., Iden, K., Smeets, R., Kihle, J. et Johansen, H. (2011). Mechanisms and rates of plagioclase carbonation reactions. *Geochimica et Cosmochimica Acta*.

O'connor, W. K., Dahlin, D. C., Rush, G. E., Dahlin, C. L. et Collins, W. K. (2001). Carbon dioxide sequestration by direct mineral carbonation : process mineralogy of feed and products. *Minerals & metallurgical processing*, 19(2), 95–101.

Oelkers, E. H., Gislason, S. R. et Matter, J. (2008). Mineral carbonation of CO_2. *Elements*, 4(5), 333–337.

Oliver, J., Janssens-Maenhout, G. et Peters, J. (2012). Trends in global CO_2 emissions ; 2012 report. Rapport technique, The Hague : PBL Netherlands Environmental Assessment Agency ; Ispra : Joint Research Centre.

Orr, J. C., Fabry, V. J., Aumont, O., Bopp, L., Doney, S. C., Feely, R. A., Gnanadesikan, A., Gruber, N., Ishida, A., Joos, F., Key, R. M., Lindsay, K., Maier-Reimer, E., Matear, R., Monfray, P., Mouchet, A., Najjar, R. G., Plattner, G.-K., Rodgers, K. B., Sabine, C. L., Sarmiento, J. L., Schlitzer, R., Slater, R. D., Totterdell, I. J., Weirig, M.-F., Yamanaka, Y. et Yool, A. (2005). Anthropogenic ocean acidification over the twenty-first century and its impact on calcifying organisms. *Nature*, 437(7059), 681–686.

Pacala, S. et Socolow, R. (2004). Stabilization wedges : Solving the climate problem for the next 50 years with current technologies. *Science*, 305(5686), 968–972.

Park, A. H. A., Jadhav, R. et Fan, L. S. (2003). CO_2 mineral sequestration : chemically enhanced aqueous carbonation of serpentine. *The Canadian Journal of Chemical Engineering*, 81(3-4), 885–890.

Parkhurst, D. et Appelo, C. A. J. (1999). User's guide to PHREEQC (version 2) : a computer program for speciation, batch-reaction, one-dimensional transport, and inverse geochemical calculations. *US Geological Survey Water-Resources Investigations Report*, 99(4259), 312.

Parmesan, C. (2006). Ecological and evolutionary responses to recent climate change. *Annual Review of Ecology, Evolution, and Systematics*, 37, 637–669.

Peters, G. P., Marland, G., Quéré, C. L., Boden, T., Canadell, J. G. et Raupach, M. R. (2012). Rapid growth in CO_2 emissions after the 2008-2009 global financial crisis. *Nature Climate Change*, 2(1), 2–4.

Phillips, B. L., Casey, W. H. et Crawford, S. N. (1997a). Solvent exchange in $AlF_x(H_2O)^{3-x}_{6-x\ (aq)}$ complexes : Ligand-directed labilization of water as an analogue for ligand-induced dissolution of oxide minerals. *Geochimica et cosmochimica acta*, 61(15), 3041–3049.

Phillips, B. L., Crawford, S. N. et Casey, W. H. (1997b). Rate of water exchange between $Al(C_2O_4)(H_2O)^+_{4\ (aq)}$ complexes and aqueous solutions determined by ^{17}O-NMR spectroscopy. *Geochimica et cosmochimica acta*, 61(23), 4965–4973.

Pokrovsky, O., Golubev, S., Schott, J. et Castillo, A. (2009). Calcite, dolomite and magnesite dissolution kinetics in aqueous solutions at acid to circumneutral pH, 25 to 150°C and 1 to 55 atm pCO2 : new constraints on CO_2 sequestration in sedimentary basins. *Chemical Geology*, 265(1-2), 20–32.

Pokrovsky, O. et Schott, J. (1999). Processes at the magnesium-bearing carbonates/solution interface. II. kinetics and mechanism of magnesite dissolution. *Geochimica et cosmochimica acta*, 63(6), 881–897.

Pokrovsky, O. S. et Schott, J. (2002). Surface chemistry and dissolution kinetics of divalent metal carbonates. *Environmental science & technology*, 36(3), 426–432.

Power, I., Wilson, S., Thom, J., Dipple, G. et Southam, G. (2007). Biologically induced mineralization of dypingite by cyanobacteria from an alkaline wetland near atlin, british columbia, canada. *Geochemical transactions*, 8, 13.

Prigiobbe, V., Costa, G., Baciocchi, R., Hänchen, M. et Mazzotti, M. (2009). The effect of and salinity on olivine dissolution kinetics at salinity at 120°C. *Chemical Engineering Science*, 64(15), 3510–3515.

Prigiobbe, V. et Mazzotti, M. (2011). Dissolution of olivine in the presence of oxalate, citrate, and CO_2 at 90°C and 120°C. *Chemical Engineering Science*, 66(24), 6544–6554.

Pronost, J., Beaudoin, G., Tremblay, J., Larachi, F., Duchesne, J., Hébert, R. et Constantin, M. (2011). Carbon sequestration kinetic and storage capacity of ultramafic mining waste. *Environmental Science & Technology*, 45(21), 9413–9420.

Rackley, S. (2009). *Carbon Capture and Storage*. Gulf Professional Publishing.

Ranganathan, P., van Hemert, P., Rudolph, E. S. J. et Zitha, P. Z. (2011). Numerical modeling of CO_2 mineralisation during storage in deep saline aquifers. *Energy Procedia*, 4(0), 4538–4545.

Renforth, P., Washbourne, C.-L., Taylder, J. et Manning, D. A. C. (2011). Silicate production and availability for mineral carbonation. *Environmental Science & Technology*, 45(6), 2035–2041.

Ries, J. B., Cohen, A. L. et McCorkle, D. C. (2009). Marine calcifiers exhibit mixed responses to CO_2-induced ocean acidification. *Geology*, 37(12), 1131–1134.

Rosenbauer, R. J., Thomas, B., Bischoff, J. L. et Palandri, J. (2012). Carbon sequestration via reaction with basaltic rocks : Geochemical modeling and experimental results. *Geochimica et Cosmochimica Acta*, 89(0), 116–133.

Sabine, C. L. et Tanhua, T. (2010). Estimation of anthropogenic CO_2 inventories in the ocean. *Annual Review of Marine Science*, 2(1), 175–198.

Saldi, G. D., Jordan, G., Schott, J. et Oelkers, E. H. (2009). Magnesite growth rates as a function of temperature and saturation state. *Geochimica et Cosmochimica Acta*, 73(19), 5646–5657.

Saldi, G. D., Schott, J., Pokrovsky, O. S., Gautier, Q. et Oelkers, E. H. (2012). An experimental study of magnesite precipitation rates at neutral to alkaline conditions and 100-200°C as a function of pH, aqueous solution composition and chemical affinity. *Geochimica et Cosmochimica Acta*, 83, 93–109.

Saldi, G. D., Schott, J., Pokrovsky, O. S. et Oelkers, E. H. (2010). An experimental study of magnesite dissolution rates at neutral to alkaline conditions and 150 and 200°C as a function of pH, total dissolved carbonate concentration, and chemical affinity. *Geochimica et Cosmochimica Acta*, 74, 6344–6356.

Sayles, F. et Fyfe, W. (1973). The crystallization of magnesite from aqueous solution. *Geochimica et Cosmochimica Acta*, 37(1), 87–99.

Schaef, H., McGrail, B. et Owen, A. (2009). Basalt-CO_2-H_2O interactions and variability in carbonate mineralization rates. *Energy Procedia*, 1(1), 4899–4906.

Schaef, H., Windisch, C., McGrail, B., Martin, P. et Rosso, K. (2011). Brucite [$Mg(OH_2)$] carbonation in wet supercritical CO_2 : An in situ high pressure x-ray diffraction study. *Geochimica et Cosmochimica Acta*, 75(23), 7458–7471.

Schott, J., Pokrovsky, O. et Oelkers, E. (2009). The link between mineral dissolution/precipitation kinetics and solution chemistry. *Reviews in Mineralogy and Geochemistry*, 70(1), 207–258.

Seifritz, W. (1990). CO_2 disposal by means of silicates. *Nature*, 345(6275), 486–486.

Shiraki, R. et Brantley, S. (1995). Kinetics of near-equilibrium calcite precipitation at 100°C : an evaluation of elementary reaction-based and affinity-based rate laws. *Geochimica et Cosmochimica Acta*, 59(8), 1457–1471.

Shirokova, L. S., Mavromatis, V., Bundeleva, I. A., Pokrovsky, O. S., Bénézeth, P., Gérard, E., Pearce, C. R. et Oelkers, E. H. (2012). Using Mg isotopes to trace cyanobacterially mediated magnesium carbonate precipitation in alkaline lakes. *Aquatic Geochemistry*.

Sullivan, D. J., Nordin, J. P., Phillips, B. L. et Casey, W. H. (1999). The rates of water exchange in Al(III)-salicylate and Al(III)-sulfosalicylate complexes. *Geochimica et cosmochimica acta*, 63(10), 1471–1480.

Teir, S., Eloneva, S., Fogelholm, C. et Zevenhoven, R. (2009). Fixation of carbon dioxide by producing hydromagnesite from serpentinite. *Applied Energy*, 86(2), 214–218.

Teir, S., Kuusik, R., Fogelholm, C. et Zevenhoven, R. (2007). Production of magnesium carbonates from serpentinite for long-term storage of CO_2. *International Journal of Mineral Processing*, 85(1-3), 1–15.

Teng, H. et Wang, J. (2011). Solvent effect on the precipitation of Mg-carbonate. *Mineralogical Magazine*, 75(3), 1997.

Thompson, J. B. et Ferris, F. G. (1990). Cyanobacterial precipitation of gypsum, calcite, and magnesite from natural alkaline lake water. *Geology*, 18(10), 995–998.

Van Vuuren, D. et Riahi, K. (2011). The relationship between short-term emissions and long-term concentration targets. *Climatic Change*, 104(3), 793–801.

Wilson, S. A., Dipple, G. M., Power, I. M., Thom, J. M., Anderson, R. G., Raudsepp, M., Gabites, J. E. et Southam, G. (2009). Carbon dioxide fixation within mine wastes of ultramafic-hosted ore deposits : Examples from the Clinton Creek and Cassiar chrysotile deposits, Canada. *Economic Geology*, 104(1), 95–112.

Wilson, S. A., Raudsepp, M. et Dipple, G. M. (2006). Verifying and quantifying carbon fixation in minerals from serpentine-rich mine tailings using the Rietveld method with X-ray powder diffraction data. *American Mineralogist*, 91(8-9), 1331–1341.

Xu, T., Apps, J. A. et Pruess, K. (2004). Numerical simulation of CO_2 disposal by mineral trapping in deep aquifers. *Applied Geochemistry*, 19(6), 917–936.

Xu, T., Apps, J. A. et Pruess, K. (2005). Mineral sequestration of carbon dioxide in a sandstone-shale system. *Chemical Geology*, 217(3-4), 295–318.

Zevenhoven, R., Fagerlund, J. et Songok, J. K. (2011). CO_2 mineral sequestration : developments toward large scale application. *Greenhouse Gases : Science and Technology*, 1(1), 48–57.

Zhao, L., Sang, L., Chen, J., Ji, J. et Teng, H. H. (2009). Aqueous carbonation of natural brucite : Relevance to CO_2 sequestration. *Environmental Science & Technology*, 44(1), 406–411.

Chapitre 2

Matériaux et Méthodes Expérimentales

L'essentiel de ce travail de thèse repose sur un important travail expérimental mobilisant différents dispositifs expérimentaux et techniques analytiques. L'objectif de ce chapitre est de présenter succinctement les matériaux minéraux, méthodes expérimentales et techniques analytiques utilisés pour effectuer les expériences de croissance minérale et de solubilité.

Sommaire

2.1 Matériaux

2.1.1 Méthodes de caractérisation des solides

Les minéraux (magnésite et hydromagnésite) utilisés pour les expériences de croissance minérale et de solubilité ont systematiquement été caractérisés, avant et après expérimentation, en utilisant des techniques analytiques classiques.

Contrôle de la minéralogie et de la chimie des échantillons

La minéralogie de tous les échantillons minéraux a été contrôlée par diffractométrie des rayons X sur un appareil INEL CPS, en utilisant une source au cobalt dont la radiation Kα (1.78897 Å) est générée à 40 kV et 25 mA.

En parallèle, la microscopie électronique à balayage a été largement utilisée afin de vérifier la morphologie des cristaux et la chimie des minéraux. Après métallisation au carbone des échantillons, les observations en électrons secondaires (observation du relief) ou rétrodiffusés (visualisation des constrastes chimiques) ont été menées sur un microscope Jeol de type JSM 6360LV. Un détecteur EDS (Energy Dispersive X-ray spectroscopy) permettait d'effectuer des analyses chimiques semi-quantitatives des matériaux, et de vérifier ainsi la pureté chimique des phases minérales.

Plus ponctuellement, des analyses à la microsonde électronique ont été effectuées pour mesurer quantitativement la composition chimique de cristaux naturels d'hydromagnésite (voir section 2.1.3). Ces analyses ont été effectuées avec un appareil Cameca SX50 sur des fragments d'hydromagnésite inclus dans un bloc de resine époxy puis polis.

Enfin, des analyses thermo-gravimétrique ont été conduites sur des échantillons d'hydromagnésite dont nous souhaitions vérifier la stœchiométrie. Cette technique consiste à chauffer un échantillon réduit en poudre sous atmosphère contrôlée, et à en mesurer l'évolution de la masse en fonction de la température. La perte de masse est dûe au dégagement de gaz (typiquement H_2O et CO_2 pour un carbonate) provenant de la destructuration du système cristallin du minéral sous l'effet de la temperature. La magnitude des pertes de masses successives ainsi que la température à laquelle elles interviennent sont caractéristiques du minéral, et renseignent donc sur la nature de la phase minérale et sur sa teneur en eau et en CO_2. Ces analyses ont été effectuées sur un appareil Netzsch STA449-F3 TG/DSC Analyser, sous atmosphère d'argon, avec une vitesse de chauffage de 10°C.min^{-1} entre 30 and 1000°C, sur des échantillons broyés d'environ 800 mg de minéral.

Détermination de la surface spécifique des échantillons

La surface spécifique des échantillons minéraux est utilisée pour normaliser les cinétiques de précipitation mesurées expérimentalement, en considérant que la surface spécifique est un bon proxy de la surface réactive des substrats minéraux.

Les surfaces spécifiques avant et après expérience ont été mesurées par l'intermédiaire de la méthode BET (Brunauer *et al.*, 1938), qui consiste à mesurer l'isotherme de sorption d'un gaz

(azote ou krypton) sur un échantillon, à une température donnée. Connaissant la dimension des molécules de gaz ainsi que la quantitée sorbée à la surface, et faisant l'hypothèse que le gaz est adsorbé sous la forme d'une monocouche, il est possible d'en déduire la surface spécifique du matériau.

Les mesures ont été effectuées sur un appareil AUTOSORB 1 de la société Quantachrome instruments. Afin d'éliminer les molécules d'eau susceptibles d'être présentes à la surface des particules, un dégazage sous vide à des températures supérieures à 150°C est effectué avant la mesure. La mesure d'adsorption est ensuite effectuée à la température de l'azote liquide (T < 77.4 K). Le krypton a été utilisé pour les mesures sur les poudres de magnésite, de faible surface spécifique, tandis que l'azote a été utilisé pour l'hydromagnésite, de surface spécifique plus importante. L'erreur sur les mesures BET, liée en partie à la calibration de l'appareil est estimée à 10%, alors que la reproductibilité des mesures est de l'ordre de 5%.

Des mesures de granulométrie laser ont été réalisées sur des poudres de magnésite avec un appareil Coulter LS100Q en vue d'en déterminer la surface spécifique géométrique. À partir de la distribution granulométrique des grains, il est en effet possible d'estimer la surface spécifique géométrique de l'échantillon, en assimilant les grains à des cubes, et en utilisant la formule suivante :

$$S_{\text{GEO}} = \sum_i \frac{6}{\rho \cdot \mathrm{d}_i} x_i \tag{2.1}$$

où ρ est la densité de la magnésite (3.01 g/cm^3), et x_i et d_i sont respectivement la fraction volumique et la valeur médiane de la distribution granulométrique pour chaque quantile de taille de grain.

2.1.2 Magnésite

Synthèse

Les échantillons de magnésite utilisés pour les expériences de solubilité (Chapitre 4) et les expériences de croissance cristalline en réacteur à circulation (Chapitre 3) ont été synthétisés selon la procédure décrite par Saldi *et al.* (2010, 2012).

Pour chaque synthèse, environ 20 g de carbonate de magnésium hydraté (magnesium hydroxide carbonate, Merck Chemicals) sont placés dans un autoclave en titane de 400 mL muni d'une vanne, en présence de 250 mL d'eau déminéralisée et de 15 à 20 g de glace carbonique. L'autoclave est scellé et chauffé de 220 à 250°C, la pression interne demeurant inférieure à 80 bars. Après deux à trois semaines, le chauffage est arrêté, la vanne ouverte et la solution aqueuse évacuée au travers d'un fritté en titane d'une porosité de 2 µm. Les poudres sont récupérées, rinsées à l'eau déminéralisée, puis séchées dans une étuve à 60°C. Les observations MEB indiquent que les poudres sont constituées de cristaux rhomboédriques de 1 à 25 µm d'arête. Un exemple en est présenté figure 2.1. Diffractogrammes et analyses EDS confirment que les échantillons sont constitués exclusivement de magnésite. Un diffractogramme représentatif est ainsi présenté Fig. 2.2.

De manière à obtenir des poudres homogènes et à en ôter les plus fines particules, les poudres synthétisées sont soumises à un tri granulométrique : des échantillons d'environ

3 g sont placés dans des béchers en polypropylène dans 100 mL d'eau deminéralisée, ultrasonisés, puis sédimentent pendant 3 minutes. Le surnageant est évacué, puis la procédure est répétée 3 fois pour chaque aliquot. Finalement les poudres sont à nouveau séchées à 60°C. La figure 2.1 montre la morphologie typique des cristaux utilisés pour les expériences.

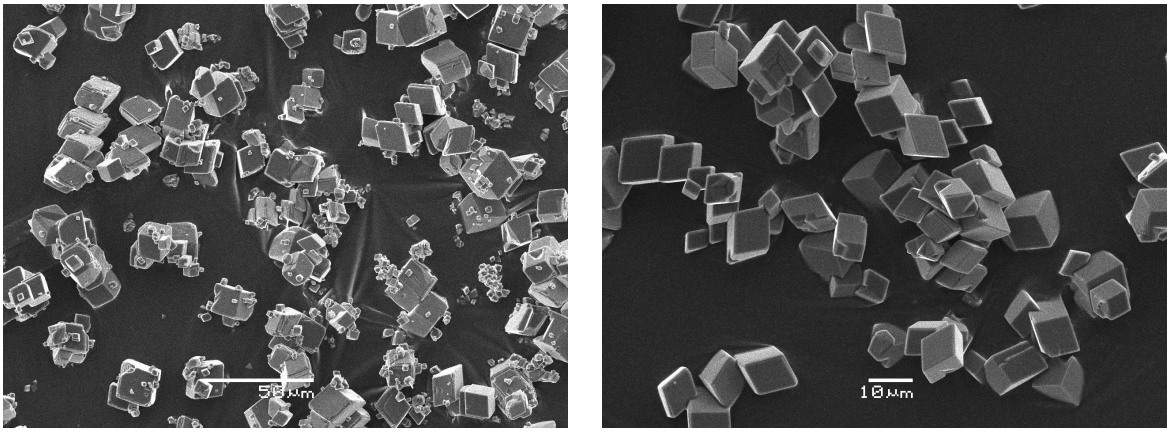

FIGURE 2.1 – Images MEB (électrons secondaires) de cristaux de magnésite synthétisés au cours de cette étude. À gauche, cristaux synthétisés à 225°C avant sélection granulométrique. À droite, exemple de cristaux obtenus après sélection granulométrique, et utilisés pour les expériences.

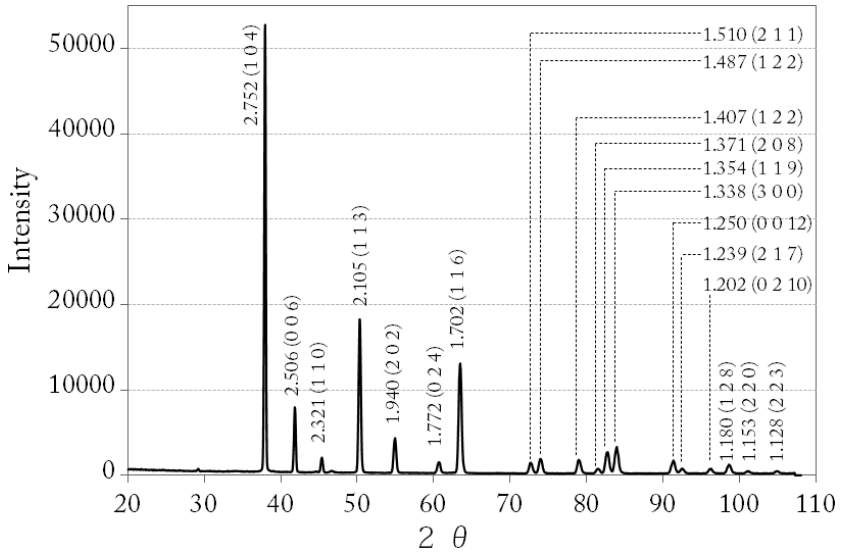

FIGURE 2.2 – Diffractogramme typique d'un échantillon de magnésite synthétisée. La distance réticulaire et l'indexation cristallographique des pics sont reportés. Tous les pics correspondent à la magnésite.

Les résultats de mesure de surface spécifique par la méthode BET et par granulométrie sont présentés Table 2.1 pour les trois échantillons de magnésite synthétisés au cours de cette étude. Les surfaces obtenues par les deux techniques diffèrent peu, ce qui implique que les cristaux synthétiques ne présentent pas de forte rugosité de surface, ni d'importante microporosité.

Échantillon	S_{BET} (cm^2/g)	S_{GEO} (cm^2/g)
Mgs 1	1940	n.d.
Mgs 2	1750	1114
Mgs 3	2100	1330

TABLE 2.1 – Mesures de surface spécifique des échantillons de magnésite synthétisés par la méthode BET (S_{BET}) et par la méthode granulométrique, qui donne une estimation de la surface spécifique géométrique (S_{GEO}).

Échantillons naturels (HAFM)

Les cristaux de magnésite utilisés pour les expériences de microscopie à force atomique sont issus de macrocristaux de magnésite naturelle en provenance de Brumado, au Brésil. Des analyses à la microsonde électronique ont été publiées par Jordan *et al.* (2001) et indiquent que les cristaux contiennent moins de 0.15% de métaux autre que du magnésium (Ca, Fe essentiellement).

2.1.3 Hydromagnesite

L'hydromagnésite utilisée dans cette étude est un minéral naturel provenant du réseau de grottes André Lachambre, dans le département des Pyrénées Orientales. La percolation d'eau météorique dans une formation dolomitique conduit à la formation de concrétions d'aragonite et d'hydromagnésite dont un exemple est présenté Fig. 2.3.

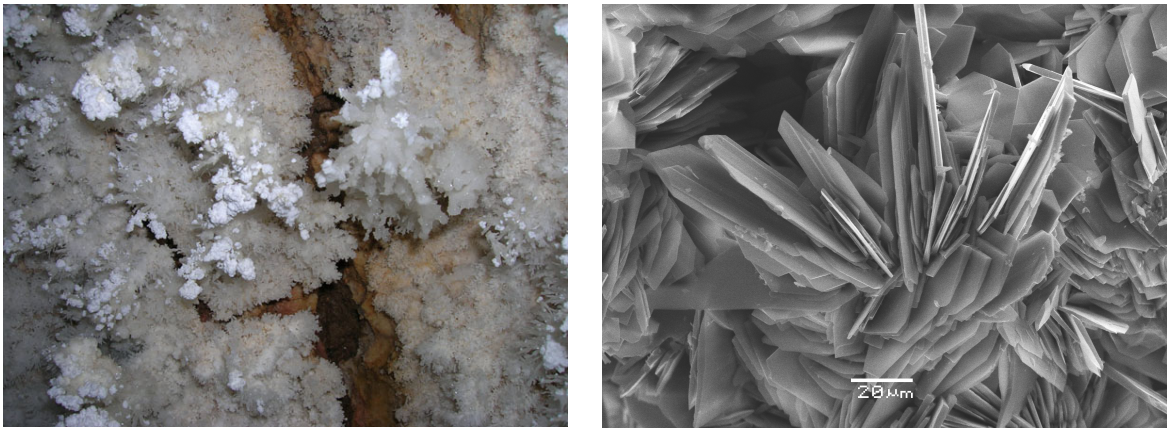

FIGURE 2.3 – Images des cristaux d'hydromagnésite naturelle utilisés dans l'étude.
Gauche : efflorescences d'hydromagnésite sur concrétions d'aragonite dans les grottes du réseau André Lachambre. Droite : image MEB (électrons secondaires) des cristaux d'hydromagnésite constituant les efflorescences.

Les observations MEB montrent que les agglomérats centimétriques d'hydromagnésite sont constitués de nombreux cristaux de forme rectangulaire à hexagonale, allongés, mesurant jusqu'à 80 µm de long, 60 µm en largeur et 2 à 3 µm d'épaisseur (Fig. 2.3). Quelques rares cristaux d'aragonite étaient présents dans le matériau initial, toutefois non repérables

sur les diffractogrammes, qui correspondent exclusivement à l'hydromagnésite (voir Fig. 6.2). Des analyses à la microsonde électronique, dont les résultats sont présentés dans la table 6.1, indiquent que les cristaux d'hydromagnésite comportent des quantités mineures d'impuretés métalliques (Ca, Mn, Fe, Sr). Des analyses thermogravimétriques ont permis de vérifier que le minéral correspond bien à la formule structurale de l'hydromagnésite : $Mg_5(CO_3)_4(OH)_2 \cdot 4\,H_2O$ (voir Chapitre 6).

De manière à disposer d'un matériau homogène pour les expériences, les efflorescences d'hydromagnésite ont été délicatement broyées dans un mortier en agathe, et la poudre obtenue a été utilisée sans modifications pour les expériences de solubilité et de croissance cristalline.

2.2 Dispositifs expérimentaux

2.2.1 Étude de la cinétique de précipitation

Réacteur à circulation

Les réacteurs à circulation hydrothermaux en titane ont été utilisés pour réaliser l'ensemble des expériences de croissance cristalline de la magnésite (Chapitre 4) ainsi que les expériences de croissance d'hydromagnésite aux températures supérieures à 50°C (Chapitre 6).

Un réacteur à circulation est un système ouvert de volume fixé (200 ou 300 mL dans le cas présent) au travers duquel circule un fluide parfaitement mélangé à débit constant. La composition chimique de l'effluent est la même que celle de la solution contenue dans le réacteur. Les réacteurs à circulation (ou "mixed-flow reactors") présentent l'avantage de permettre une détermination directe de la cinétique de réaction sur la base de l'analyse de la chimie des solutions. Ils ont, pour cette raison, été largement utilisés pour des études de cinétique de dissolution minérale (e.g Rimstidt et Dove, 1986 ; Dove et Crerar, 1990 ; Berger *et al.*, 1994 ; Oelkers et Schott, 1995 ; Gudbrandsson *et al.*, 2011 ; Schott *et al.*, 2012) et dans une moindre mesure pour des études de précipitation (e.g Nagy *et al.*, 1991, Nagy et Lasaga, 1992 ; Shiraki et Brantley, 1995 ; Devidal *et al.*, 1997 ; Saldi *et al.*, 2009, 2012).

L'évolution de la concentration d'un traceur i au cours du temps est donnée par l'équation suivante :

$$C(t) = C_0(1 - e^{-\frac{t}{\tau}}) \tag{2.2}$$

où C_0 est la concentration du traceur dans le fluide d'entrée et τ le temps de résidence du fluide dans le réacteur (rapport du volume du réacteur au début de fluide). D'après l'équation 2.2, la solution dans le réacteur est renouvelée à 99% au bout de 4.6τ, ce qui correspond à un état stationnaire "mécanique".

La réaction de la solution avec le minéral contenu dans le réacteur induit une modification de la chimie de la solution. La composition chimique de l'effluent diffère donc naturellement de la chimie de la solution pénétrant dans le réacteur. L'état stationnaire "chimique" est atteint lorsque la composition chimique de l'effluent est stable (marqué par un minimum de 3 échantillons de composition chimique identique sur une durée correspondant au minimum à 3τ). Il s'agit d'un état d'"équilibre" entre le renouvellement de la solution et la réaction de cette solution avec le minéral. Il est alors possible de déterminer la cinétique de croissance ou de dissolution du minéral à partir de la formule suivante :

$$R = \frac{\mathrm{FR} \cdot \Delta[X]}{m \cdot S \cdot \nu_i} \tag{2.3}$$

où FR représente le débit de fluide, $\Delta[X]$ est la différence entre la concentration d'entrée et de sortie (à l'état stationnaire) d'un élément X constitutif du minéral étudié, ν_i est le coefficient stœchiométrique de l'élément X dans le minéral étudié, m est la masse de minéral placée initialement dans le réacteur, S la surface spécifique de ce minéral.

Dans mes expériences, l'état stationnaire chimique est obtenu rapidement après l'atteinte de l'état stationnaire mécanique. Toutefois, les expériences ont été systematiquement menées

pendant une durée minimale de 7τ.

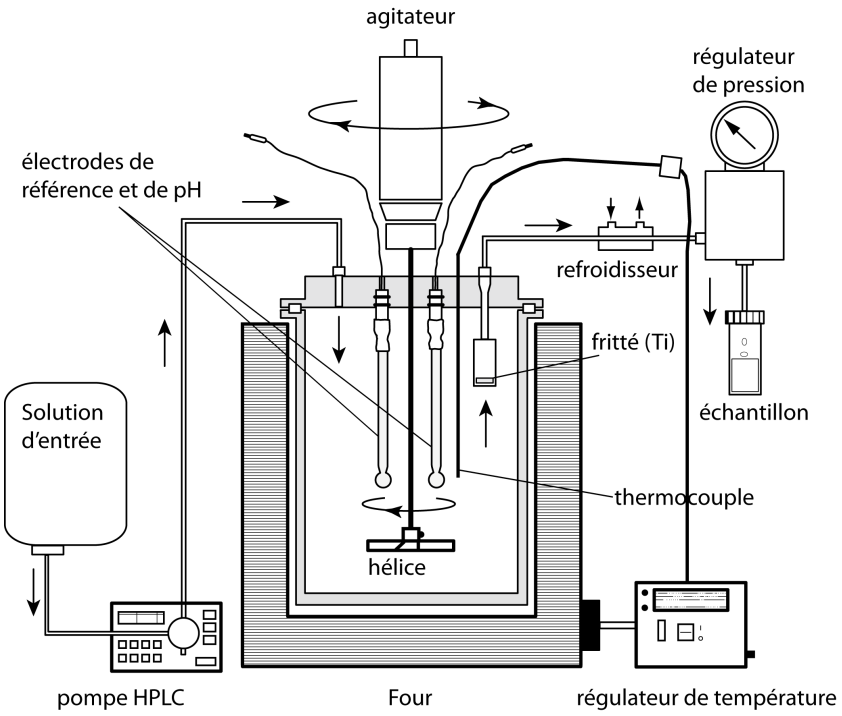

FIGURE 2.4 – Schéma d'un réacteur à circulation hydrothermal, utilisé pour les expériences de croissance cristalline de magnésite et d'hydromagnésite. Modifié d'après Saldi (2009).

La figure 2.4 présente un schéma du dispositif expérimental, tandis qu'une photo de l'un des réacteurs utilisés est montrée Fig. 2.5. Le réacteur est muni d'un système d'agitation magnétique permettant la mise en suspension de la poudre minérale et la bonne homogénéisation du fluide. Un régulateur de pression à membrane est positionné en sortie de réacteur afin de maintenir la pression interne à un niveau supérieur à la pression de vapeur saturante, ceci en vue d'éviter la formation de bulles. Un four circulaire, relié à un régulateur électronique et à un thermocouple introduit dans un doigt en titane plongé dans la solution, permet de maintenir la température à $\pm$ 2°C de la température visée. La solution réactive, contenue dans une poche flexible de 5 à 10 L en polypropylène à température ambiante, est injectée dans le réacteur par l'intermédiaire d'une pompe HPLC (High pressure liquid chromatography), à débit constant (de 0.4 à 3 mL/min dans mes expériences). La solution quitte le réacteur par l'intermédiaire d'un fritté en titane muni de pores de 2 µm de diamètre, et est refroidie via un système de circulation d'eau avant d'être évacuée ou échantillonnée. Enfin, pour un nombre limité d'expériences, une mesure in situ du pH a été effectuée grace à des électrodes à contact solide insérées dans la tête du réacteur.

L'ensemble des parties métalliques du dispositif en contact avec la solution à haute température sont en titane, afin d'éviter tout risque de contamination des solutions et solides étudiés.

En début d'expérience, 0.5 à 1.5 g de poudre minérale (magnésite ou hydromagnésite) sont déposés dans le réacteur en titane, qui est ensuite rempli soit avec de l'eau déminéralisée,

FIGURE 2.5 – Photographie de l'un des réacteurs à circulation de marque Parr® utilisé au cours de cette étude, muni d'une pompe HPLC, d'un régulateur de température et d'un four, d'un système de réfrigération et d'un régulateur de pression.

soit avec la solution réactive. Le réacteur est ensuite fermé, connecté à la pompe HPLC ainsi qu'au régulateur de pression, puis la solution réactive est mise en circulation. Une fois la température expérimentale atteinte, des échantillons sont collectés à intervalles réguliers en vue de contrôler l'évolution du pH, de la concentration en Mg et en carbone inorganique dissous. Une fois l'état stationnaire atteint, il est possible de modifier le débit, ou la solution d'entrée, afin de réaliser plusieurs expériences en série sur une même poudre initiale.

À la fin d'une expérience (ou d'une série d'expériences), la solution contenue dans le réacteur est filtrée et la poudre minérale collectée et séchée avant caractérisation. Le réacteur est nettoyé, puis une solution acide de rinçage (HCl + HNO_3 à pH = 1.5) est mise en circulation pendant au moins 24 heures dans le réacteur en vue de dissoudre les résidus carbonatés.

Les réacteurs à circulation permettent donc une détermination simple de la cinétique de croissance d'un minéral. Tirant profit de la solubilité rétrograde des minéraux carbonatés, le dispositif expérimental permet de stocker à température ambiante une seule solution réactive sous-saturée, qui deviendra sursaturée lorsque elle est injectée dans le réacteur à la température de l'expérience. En outre, en modifiant le débit de fluide ou la composition chimique de la solution initiale, il est possible de modifier l'écart à l'équilibre thermodynamique de la solution réactive, et ainsi de collecter des données pour des conditions variables de sursaturation.

On notera toutefois quelques limites à ce type d'expériences pour les études de croissance cristalline :

- Il est difficile de contrôler précisément la sursaturation des solutions. En effet, si la composition de la solution d'entrée est connue, la composition de la solution dans le réacteur à l'état stationnaire, et donc sa sursaturation, résulte d'un équilibre entre vitesse de renouvellement de la solution et cinétique de croissance cristalline. S'il est aisé de faire varier l'état de saturation à partir d'un point de départ, il est en revanche très complexe de fixer *a priori* cet état de saturation. Les dispositifs expérimentaux dits "à composition constante", utilisés notamment pour étudier à basse température les cinétiques de précipitations minérales rapides, permettent de s'affranchir de cette contrainte (voir par exemple Witkamp

et al., 1990 pour le gypse, Westin et Rasmuson, 2005, Lakshtanov *et al.*, 2011 ou Ukrainczyk *et al.*, 2012 pour la calcite). Toutefois, la technique de "composition constante" n'a à ma connaissance pas été utilisée dans des conditions hydrothermales.

- À l'intérieur du réacteur, une partie de la poudre minérale tend à précipiter à l'aplomb de l'hélice utilisée pour agiter la solution. Ce phénomène hydrodynamique peut engendrer dans les expériences à précipitation rapide une certaine cimentation de la poudre sous l'effet de la croissance cristalline, ce qui influence la surface réactive. Il est donc nécessaire de renouveler assez fréquemment les substrats minéraux de la précipitation.
- Lorsque la sursaturation de la solution d'entrée est trop importante, la solution, chauffée en arrivant à proximité du réacteur, tend à nucléer des germes cristallins. Ces germes peuvent influencer la surface réactive s'ils sont acheminés à l'intérieur du réacteur, ou, s'ils demeurent dans le capillaire d'injection, provoquent en général un bouchage du capillaire. Ce phénomène pose une limite supérieure aux sursaturations qu'il est possible d'étudier en utilisant un réacteur à circulation muni d'une seule entrée de fluide.

Ces différents phénomènes expliquent probablement une partie de la variabilité expérimentale présentée dans la Section 4.3.1.

Dispositif expérimental à basse température : réacteur à circulation discontinue

À 25°C, la sursaturation doit être créée par l'ajout dans un réacteur de deux solutions indépendantes. Les expériences de croissance cristalline de l'hydromagnésite à 25°C ont donc été réalisées en utilisant un réacteur muni de deux entrées de solution, que nous avons appelé "à circulation discontinue" en raison du mode de prélèvement discontinu des effluents.

Un schéma du dispositif expérimental est présenté Fig. 6.4. Le réacteur en polypropylène, d'un volume de 1000 mL, est alimenté par deux solutions, l'une contenant des ions Mg^{2+}, l'autre des ions CO_3^{2-}. Les solutions sont acheminées à un débit constant et identique par deux pompes péristaltiques, par l'intermédiaire de capillaires en Tygon®. Le réacteur est positionné dans un bain thermostaté sur un agitateur magnétique, et un barreau aimanté flottant disposé dans le réacteur permet d'homogénéiser la solution.

Une fois par jour, un volume correspondant à la somme des volumes ajoutés depuis les deux solutions d'entree est échantillonné des réacteurs avec une seringue, limitant ainsi la variation journalière de volume à environ 5 %. L'effluent est filtré et sa composition chimique contrôlée. Le principe est donc le même que pour les réacteurs à circulation hydrothermaux, et, lorsque l'état stationnaire est atteint, on utilise l'équation 2.3 pour calculer la cinétique de précipitation.

Toutefois, l'échantillonnage manuel des effluents suppose de garder des débits d'entrée faibles afin de limiter la variation de volume dans le réacteur. Aussi, le renouvellement du fluide dans le réacteur est particulierement lent, et l'état stationnaire est estimé atteint lorsque la concentration en Mg de l'effluent est constante sur une durée minimale de 6 jours consécutifs.

Du fait des prélévements ponctuels quotidiens, il est par ailleurs possible d'estimer la cinétique de précipitation entre deux prélèvements successifs sur la base d'un calcul de bilan

de quantité de matière, sous réserve de connaître précisément les débits d'entrée et les quantités prélevées. Le calcul, détaillé Section 6.3.3, est affecté par d'importantes incertitudes, en parties compensées par la grande quantité de données accessibles par cette méthode.

2.2.2 Mesures de solubilité : réacteurs fermés

Les mesures de solubilité et d'adsorption ont été effectuées dans des réacteurs fermés (également appelés réacteurs batch). Quelle que soit la température, le principe consiste à mettre en présence une poudre minérale avec une solution aqueuse en prélevant des échantillons de solution à intervalles régulier en vue de vérifier l'atteinte de l'équilibre thermodynamique.

Dispositif hydrothermal

La mesure de la solubilité de la magnésite à 120°C en présence de citrate, détaillée Section 3.7.4, a été effectuée à l'aide d'un réacteur fermé en titane d'un volume de 400 mL, dont un schéma est présenté Fig. 2.6. Le même dispositif a été utilisé pour la mesure de l'adsorption de l'oxalate et du citrate sur la magnésite à 120°C (Section 4.3.4).

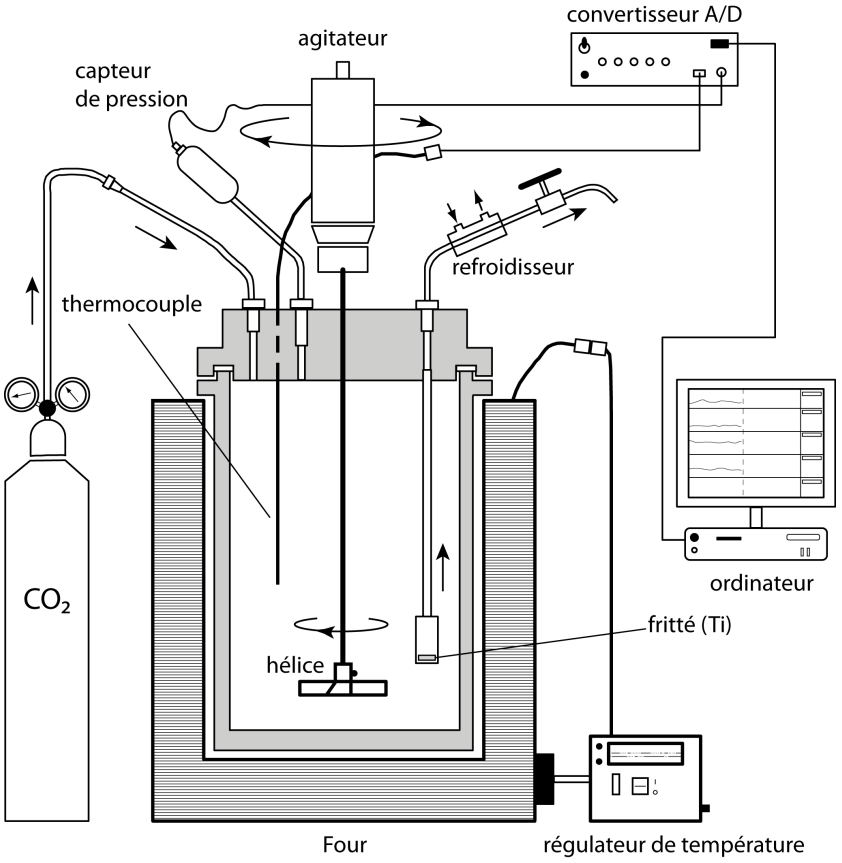

FIGURE 2.6 – Schéma d'un réacteur fermé en titane, utilisé pour la mesure de la solubilité de la magnésite en présence de citrate. Modifié d'après Saldi (2009).

Le réacteur est muni d'un dispositif d'agitation magnétique, et la température est ajustée à $\pm$ 1°C grâce à une console de régulation électronique reliée à un four circulaire et à un

thermocouple plongé dans le réacteur. Le réacteur est relié à une bouteille de CO_2 qui permet le cas échéant de pressuriser la solution une fois atteinte la température visée. L'évolution de la pression dans le système est suivie en continu grace à un transducteur de pression. Une ligne de prélèvement de fluide munie d'un filtre en titane (porosité 2 µm de diamètre) plonge dans la solution et permet d'effectuer des prélèvements réguliers (3 à 6 mL) pour contrôler la composition chimique de la solution et verifier l'atteinte de l'équilibre thermodynamique (pour les expériences de solubilité) ou la quantité de ligand adsorbée (pour les expériences d'adsorption).

À basse température

Les expériences de solubilité de l'hydromagnésite à 25 et 50°C ont éte effectuées dans des béchers en polypropylène de marque Azlon, fermés par un couvercle en polypropylène muni d'un joint torique réalisé à l'atelier mécanique du GET. Les béchers fermés sont placés dans des bains thermostatés et agités avec des barreaux aimantés placés dans des cages en Teflon. Les couvercles possèdent deux ouvertures : la première est fermée par une vis en polypropylène et permet l'introduction d'une électrode pH pour mesurer le pH *in situ*. La seconde est fermée par un septum en silicone recouvert de Teflon® et maintenu par une vis en acier trouée. C'est au travers de ce trou et du septum que sont prélevés les échantillons grâce à des seringues munies d'aiguilles d'une dizaine de centimètres de long.

Les échantillons prélevés (environ 6 mL) sont filtrés au travers de filtres Millipore® en Nylon de 0.22 µm de porosité. Un aliquot est réservé à la mesure rapide du pH (après refroidissement si nécessaire), un second est acidifié pour la mesure du Mg et le troisième est réfrigéré pour une mesure ultérieure de l'alcalinité.

En fin d'expérience (après une soixantaine de jours), le contenu des réacteurs est filtré , lyophilisé, puis caractérisé par les méthodes détaillées ci-dessus.

2.2.3 Microscopie à force atomique hydrothermale

Les réacteurs à circulation, dont le principe de fonctionnement a été détaillé ci-dessus, donnent des informations quantitatives sur la cinétique de croissance cristalline, en relation notamment avec les paramètres physico-chimiques des solutions réactives. Le processus de croissance cristalline étant controlé par les processus se déroulant à l'interface solide-solution, la compréhension globale des mécanismes de croissance requiert toutefois également des informations acquises à l'échelle surfacique.

Principes

La microscopie à force atomique (Atomic Force Microscopy AFM) permet l'observation de la topographie ainsi que de différents paramètres de la surface de matériaux. Elle appartient aux techniques de microscopie à champ proche, au même titre que la microscopie à effet tunel (Scanning Tunneling Microscopy STM), dont le développement depuis les années 1980 a révolutionné les nanosciences. Le premier microscope à force atomique a été développé par Binnig et collaborateurs au milieu des années 80 (Binnig *et al.*, 1986).

Dans son principe, la microscopie à force atomique consiste à faire circuler à très faible distance de la surface d'un échantillon une pointe très fine supportée par un micro-levier (cantilever), en général en silice ou en nitrure de silicium. En fonction de la distance de la pointe à la surface, celle-ci subit une force répulsive ou attractive qui provoque la déflection du micro-levier. En maintenant constante cette déflection par l'intermédiaire d'une boucle d'asservissement, on obtient une image "iso-force" de la surface qui reflète sa topographie.

La figure 2.7 présente un schéma général de l'AFM. Outre la pointe et son micro-levier, le système comprend un élément piézoélectrique, et un laser qui se réfléchit sur le micro-levier, et dont les mouvements sont enregistrés par une photodiode. Dans la configuration utilisée, la pointe et le levier sont immobiles, et c'est l'échantillon qui se déplace de manière très précise dans les trois dimensions spatiales grâce au tube piézoélectrique sur lequel il repose.

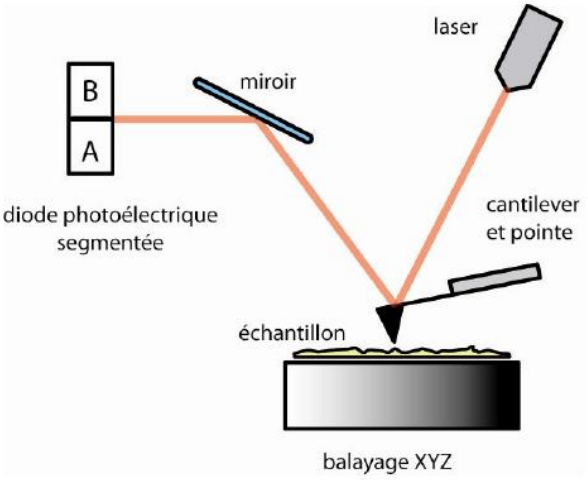

FIGURE 2.7 – Schéma de principe de la microscopie à force atomique. La surface de l'échantillon est scannée par une pointe très fine supportée par un micro-levier, dont les déplacements verticaux par rapport à la surface sont restitués par l'intermédiaire d'un faisceau laser dont les mouvements sont enregistrés par un détecteur photoélectrique et permettent de reconstituer la topographie de surface. Tiré de Saldi (2009).

On distingue trois modes d'interaction entre pointe et surface :

- le mode contact, dans lequel la pointe sondeuse est en contact avec la surface, et est soumise à des forces répulsives. C'est le mode le plus adapté pour l'imagerie dans des liquides, et le plus utilisé pour l'étude des surfaces minérales. C'est le mode d'imagerie que nous utiliserons.
- le mode non-contact, où la pointe est positionnée à faible distance de la surface, et est soumise à de faibles forces attractives. Ce mode est plutôt utilisé pour l'imagerie de matériaux fragiles.
- le mode intermittent (tapping), qui permet notamment de caractériser la force des interactions pointe-surface.

Les déplacements verticaux du levier dûs aux interactions entre le relief de surface et la pointe engendrent des modifications de la réflection de la lumière laser, enregistrées par la photodiode. Une boucle de rétroaction permet d'agir sur le tube piézoélectrique en vue d'ajuster la position de l'échantillon, afin que la déflection du levier revienne à son niveau

initial. La tension du courant appliqué à l'élément piézoélectrique en vue d'ajuster sa hauteur constitue donc une mesure quantitative du relief de surface, et est utilisée pour produire des *images en hauteur*.

Par ailleurs, du fait du caractère imparfait de la boucle de rétroaction, la déflection du micro-levier enregistrée par la photodiode permet de produire des images contrastées du relief, appelées *images en déflection*. Une comparaison des deux types d'images est proposée Figure 2.8.

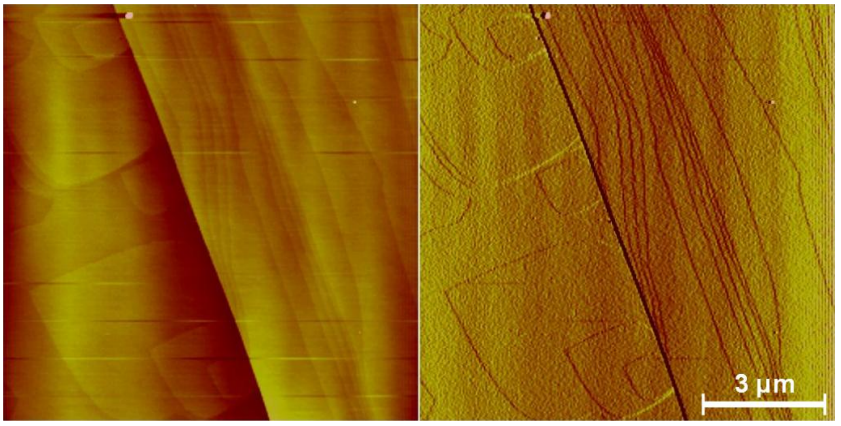

FIGURE 2.8 – Comparaison entre une image "en hauteur" (à droite) et "en déflection" (à gauche) de marches cristallines observées pendant une expérience de croissance de la magnésite à 100°C. L'image en hauteur, reconstituée d'après les ajustements verticaux du tube piézoélectrique, contient des informations quantitatives sur la hauteur relative des différentes structures, tandis que l'image en déflection, reconstituée d'après l'enregistrement de la déflection du microlevier, permet d'observer un relief plus contrasté.

Dispositif expérimental

Pour étudier les cinétiques réactionnelles lentes d'un minéral peu réactif tel que la magnésite, il est nécessaire de travailler dans des conditions hydrothermales, où une pressurisation du système est nécessaire en vue d'éviter la formation de bulles de vapeur. Le microscope à force atomique hydrothermal permet ainsi de travailler jusqu'à une température d'environ 150°C et une pression de 50 bars. Le premier exemplaire en a été développé par Higgins *et al.* (1998). Le modèle disponible à l'Université Ludwig Maximilian de Munich est une amélioration de ce prototype, construit et assemblé par Guntram Jordan, Werner Rammensee et Wolfgang W. Schmahl.

Le microscope, dont des photographies sont présentées Fig. 2.9, est constitué d'une cellule d'environ 500 µL de volume dont les constituants métalliques en contact avec le fluide sont en titane. Le porte-échantillon y est séparé du tube piézoélectrique par une membrane flexible étanche. La partie supérieure est fermée hermétiquement par une vitre en saphir, au travers de laquelle passe la lumière laser. La source laser, le miroir ainsi que le détecteur photoélectrique sont disposés sur un trépied qui surmonte la cellule. Le chauffage est assuré par un four circulaire qui entoure la cellule et dont la température est contrôlée par l'intermédiaire d'un thermocouple. Un schéma détaillé du cœur du dispositif est disponible

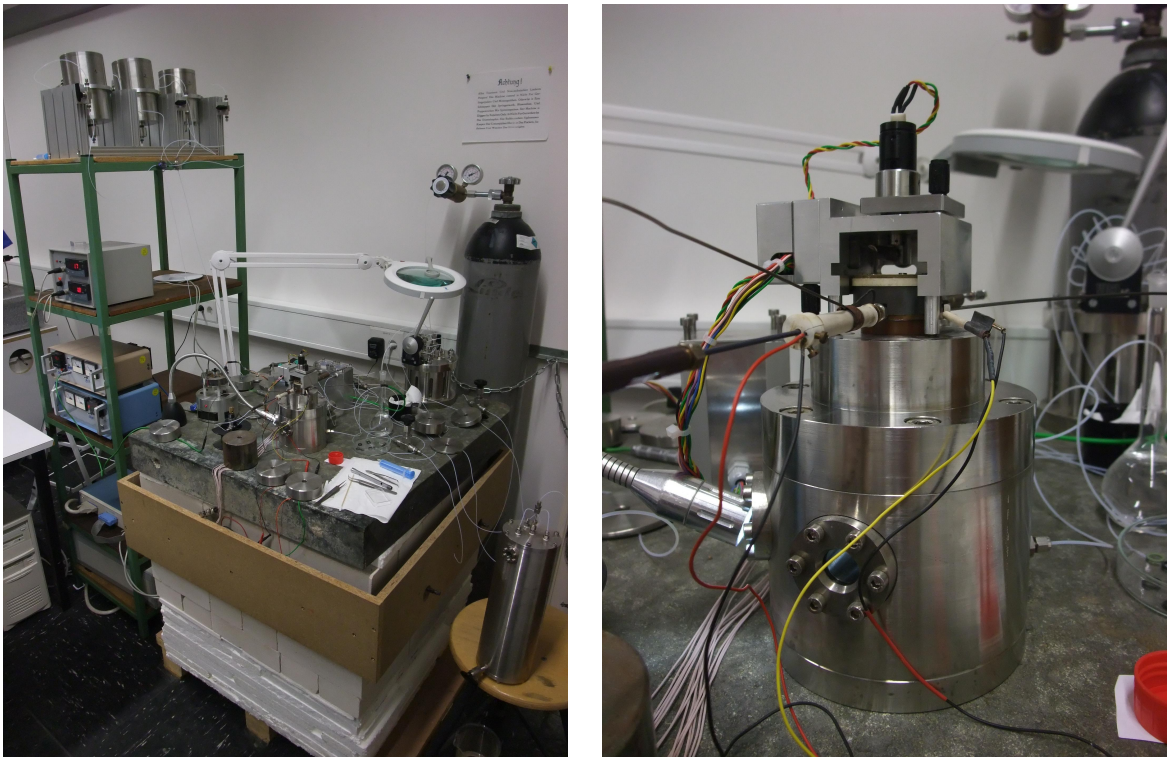

FIGURE 2.9 – Photographies du microscope à force atomique hydrothermal. À gauche, on distingue en hauteur les trois récipients pouvant contenir des solutions aqueuses. La photographie de droite est une vue de détail de la cellule hydrothermale dans laquelle est positionnée l'échantillon.

dans Saldi (2009).

Les solutions sont disposées dans trois récipients flexibles en Viton® situés en hauteur par rapport à la cellule. L'un des récipients est uniquement destiné à contenir de l'eau déionisée afin de nettoyer le circuit. Les deux autres réservoirs contiennent des solutions réactives, et permettent de changer de solution en cours d'expérience. Les solutions circulent par gravité, le débit pouvant être ajusté par l'intermédiaire d'une vanne. Les effluents sont collectés dans un récipient muni d'un robinet d'évacuation, ou bien échantillonnés dans des cylindres en PVC grâce à un cylindre échantillonneur. L'ensemble du système est pressurisé avec de l'azote à une pression homogène en tout point (typiquement quelques bars).

La résolution maximale des observations AFM est obtenue sur des surfaces avec une faible densité de marches cristallines (e.g Pina et Jordan, 2010). Les observations sont réalisées sur des cristaux de magnésite de quelques mm^2, clivés au scalpel selon leur plan de clivage. Seuls les cristaux apparaissant parfaitement plats à la loupe sont observés en AFM (Fig. 2.10). Dans ce but, les cristaux sont manipulés avec une pince fine et disposés sous un fil en titane qui les maintient pendant les observations. Les cristaux sont d'abord observés à l'air, avant que le système ne soit mis en eau, puis scellé, pressurisé et enfin chauffé.

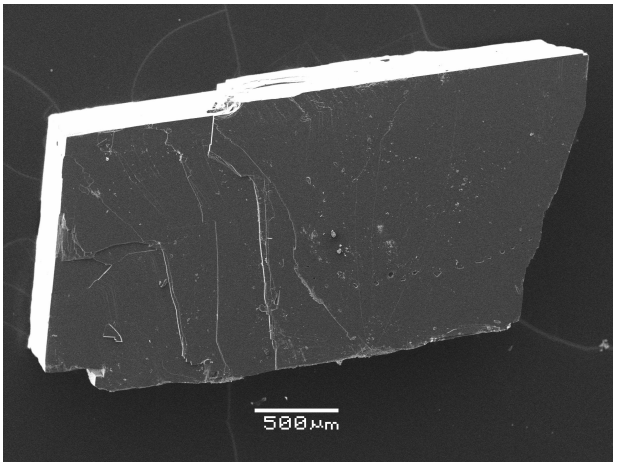

FIGURE 2.10 – Exemple de crystal de magnésite clivé au scalpel utilisé pour les expériences HAFM (image MEB). La surface plane correspond au plan (1 0 4) et l'on y observe de nombreuses fractures de clivage. Les observations AFM ont été menées sur la partie la plus plane.

Types d'observations et principales limites

La résolution latérale de l'AFM correspond au rayon de courbure de la pointe sondeuse, et atteint de l'ordre de quelques dizaines de nanomètres. Verticalement, la résolution verticale est déterminée par la résolution du déplacement vertical du tube piézoélectrique, de l'ordre de 1 Å. Ces résolutions sont suffisantes pour permettre de résoudre individuellement des couches monomoléculaires (d'une épaisseur de 0.27 nm pour la magnésite), et d'obtenir des données quantitatives sur la forme et la position des ilôts de croissance et des marches cristallines.

Les images successives acquises pendant la croissance du minéral permettent donc d'assister en temps réel et *in situ* à la production et à l'avancée de marches cristallines. Afin de traduire ses observations en données quantitatives, il existe différentes méthodes de mesure rappelées par Pina et Jordan (2010). La plus courante - et celle que nous avons majoritairement utilisée - consiste à utiliser un marqueur supposé immobile à la surface (impureté, imperfection du cristal...) comme point de référence à partir duquel on mesure la progression des marches.

Toutefois, ces observations peuvent être affectées par différents biais. En premier lieu, l'acquisition peut être affectée par une dérive instrumentale qui conduit à une distortion des images (Henriksen et Stipp, 2002). Cette dérive peut être estimée et corrigée lorsque l'on dispose d'un point de référence fixe, mais elle occasionne parfois la perte de ces points de référence. Pour l'HAFM, la dérive a essentiellement lieu pendant la phase de chauffage, ce qui nécessite un temps de stabilisation du système une fois la température expérimentale atteinte.

Par ailleurs, la vitesse de balayage à la surface de l'échantillon est limitée par la capacité du tube piézoélectrique ainsi que par la résolution souhaitée, de telle sorte que les marches cristallines avancent significativement pendant que les scans successifs sont acquis. Ceci occasionne des différences significatives entre la forme et l'orientation observée des structures, qui diffèrent selon la direction dans laquelle est prise le scan, et leur forme et orientation réelles. Ces phénomenes ont largement été décrits dans la littérature (e.g Land *et al.*, 1997, Pina et Jordan, 2010, Yoshino *et al.*, 2010). La mesure des vitesses d'avancement peut en être dans une certaine mesure corrigée en utilisant des relations géométriques simples, si un point de référence fixe existe.

Enfin, comme nous l'avons vu, la résolution spatiale de l'AFM est limitée par le rayon de courbure de la micro-pointe. Si la densité de marches cristallines est trop forte, et que l'espacement entre marches successives est de l'ordre de ce rayon de courbure, l'AFM ne sera pas capable de résoudre de manière satisfaisante chacune des marches. Une topographie trop tourmentée provoque de plus une usure accélérée de la pointe, avec une perte de résolution en cours d'expérience. La combinaison d'une résolution spatiale et d'une vitesse de balayage limitées rend difficile la mesure de phénomènes transitoires à petite échelle, tels que la génération de marches cristallines au niveau de dislocations vis par le processus de croissance en spirale (Higgins et Hu, 2006).

Outre la vitesse d'avancement des marches cristallines, l'observation d'une surface en croissance permet d'accéder à son taux de croissance macroscopique. Différentes méthodes ont été proposées, la plus simple consistant à mesurer la fréquence de passage de marches cristallines au niveau d'un point de référence fixe. La vitesse de croissance macroscopique est alors calculée par le produit de cette fréquence et de la hauteur d'une marche monomoléculaire, divisé par le volume molaire du minéral (voir Section 5.2). L'avantage de cette méthode est que la source des marches cristallines (par exemple, une dislocation du réseau cristallin) ne doit pas nécessairement se situer dans l'aire d'observation. On suppose que la fréquence de passage reflète la fréquence de génération de marches cristallines par un mécanisme inconnu, et la mesure de cette fréquence dépend peu de la résolution spatiale de l'AFM, ou d'éventuelles distortions de l'image réelle.

En revanche, la surface accessible à la pointe sondeuse est limitée et atteint environ 1000 μm^2, soit moins de 0.1% de la surface typique des cristaux utilisés. Dès lors, la généralisation des phénomènes observés dans l'aire accessible suppose que ceux-ci soient représentatifs de l'ensemble du cristal.

Pendant la croissance d'un minéral, les sources de marches cristallines avec la fréquence de génération la plus forte tendent à recouvrir les sources moins actives. Par conséquent, la croissance d'une surface est contrôlée par les sources de marches les plus actives, à la condition que le mécanisme à leur origine soit pérenne. À l'échelle d'une aire d'observation, on considérera donc la source la plus active et régulière comme représentative de l'ensemble du cristal, mais ces observations doivent être répétées dans différentes zones du cristal.

Enfin, l'une des principales limites potentielles de l'imagerie en mode contact provient des interactions entre le balayage de la surface par la pointe sondeuse et les processus de croissance. La pointe peut en effet exercer une influence mécanique sur la propagation des steps ou la répartition d'éventuelles impuretés (voir par exemple Pina *et al.*, 2009), ou bien un effet chimique en perturbant le champ de concentration à proximité de la surface. On peut appréhender cet effet potentiel en "dézoomant" après observation d'une zone réduite, afin d'apprécier une éventuelle différence de vitesse de croissance des marches ou de morphologie des structures surfaciques.

En fixant la déflection du levier au minimum nécessaire pour obtenir des images d'une bonne résolution, on minimise les interactions pointe-surface. Dans le cas des expériences menées sur la magnésite, nous n'avons pas observé de conséquences visibles de ces interactions.

2.3 Méthodes d'analyse des solutions aqueuses

2.3.1 Spectroscopie d'absorption atomique flamme

La concentration en magnésium des solutions expérimentales a été mesurée par spectrométrie d'absorption atomique (SAA) à la flamme, sur un appareil Perkin-Elmer AAnalyst 400. Le principe consiste à nébuliser l'échantillon que l'on souhaite analyser dans une flamme air-acétylène. Une lampe à cathode creuse émet une lumière dont la longueur d'onde est caractéristique du magnésium. En traversant la flamme, une partie des photons sont absorbés par les atomes de magnésium présents. Un détecteur mesure l'absorption de la flamme, qui est directement reliée à la concentration de l'élément dissous. Une courbe de calibration, établie avec des standards de 0.1 à 0.6 ppm Mg préparés dans la même matrice que les échantillons (0.1 M NaCl), permet de remonter à la concentration de l'échantillon.

Avant analyse, les échantillons sont donc dilués pour rentrer dans la gamme d'étalons (extensible à 1 ppm en modifiant la position de la flamme et son absorbance), et acidifiés par ajout d'acide nitrique bi-distillé. Une solution d'oxyde de lanthane est ajoutée en faible quantité (30 µl par 10 ml d'échantillon), dans le but d'éliminer de possibles interférences. La limite de détection de la concentration en magnésium est de l'ordre de 0.020 ppm, avec une incertitude de $\pm$ 1%.

2.3.2 Mesure des concentrations en ligands organiques

2.3.2.1 Mesure du Carbone Organique Dissous (COD)

La mesure du carbone organique dissous a été utilisée pour contrôler la bonne préparation des solutions expérimentales contenant des ligands organiques, ainsi que dans le cadre des expériences préliminaires d'adsorption de l'oxalate et du citrate sur la magnésite (Section 4.3.4).

Les analyses ont été effectuées sur un appareil Shimatzu TOC-BCSN. Les échantillons sont dilués avec de l'eau déminéralisée jusqu'à une concentration inférieure à 30 ppm, et disposés dans des tubes en verre munis d'un septum en silicone. Un échantillonneur automatique prélève un volume d'échantillon (50 ou 136 µL) qui, après dégazage du carbone inorganique dissous, est chauffé jusqu'à plus de 680°C. La combustion du carbone organique provoque un dégagement de CO_2 qui est suivi par spectroscopie infra-rouge (voir ci-dessous). La concentration en carbone organique est déterminée grâce à deux droites de calibration (soit 0-3 ppm, soit 3-30 ppm, selon la concentration de l'échantillon). La limite de détection est de 0.15 ppm, l'incertitude de 2 à 3%.

2.3.2.2 Chromatographie ionique

La chromatographie ionique a été utilisée beaucoup plus ponctuellement, afin de vérifier que les ligands organiques oxalate et citrate ne se dégradaient pas lors des expériences menées à des températures supérieures à 100°C.

La chromatographie ionique permet de séparer différents constituants ioniques d'une solution aqueuse en injectant cette solution dans une résine échangeuse d'ions, puis en faisant circuler un éluant (10 mM ou 20 mM KOH). Les ions vont être entraînés par l'éluant avec

un temps de rétention dépendant de leur affinité pour la résine, les ions les plus petits et les moins chargés étant élués en premier. Les différents ions sont détectés à la sortie de la colonne chromatographique par conductimétrie, et identifiés d'après leur temps de rétention.

Les analyses ont été effectuées sur un système Dionex ICS-2000, équipé d'une colonne d'analyse IonPac® AS11 adaptée par l'analyse des anions organiques, et d'une pré-colonne AG11 permettant d'éliminer certains contaminants potentiels de la colonne d'analyse. En comparant les solutions expérimentales avant et après expérience, nous n'avons pas constaté d'apparition de nouvelles espèces qui auraient pu signaler une dégradation des ligands organiques. En revanche, nous n'avons pas procédé à des analyses quantitatives des concentrations de ligands par chromatographie ionique, les courbes d'étalonnage s'avérant peu précises (en particulier pour le citrate).

2.3.3 Mesure du carbone inorganique dissous

La mesure du carbone inorganique dissous, cruciale pour estimer la spéciation chimique des solutions et leur indice de saturation par rapport aux minéraux étudiés, a été effectuée en utilisant deux techniques différentes. L'alcalinité a été mesurée sur la majeure partie des échantillons dépourvus de ligands organiques, tandis que la spectroscopie infra-rouge non-dispersive, qui est une mesure directe du carbone inorganique dissous, a été utilisée pour les échantillons contenant des concentrations significatives de ligands organiques, ou lorsque les volumes d'échantillons disponibles étaient trop faibles pour envisager une analyse d'alcalinité.

2.3.3.1 Mesures d'alcalinité

L'alcalinité mesure la capacité d'une solution aqueuse à neutraliser au cours d'une titration acidimétrique des ions H^+ jusqu'au pH équivalent du couple HCO_3^-/CO_3^{2-} (pH $\sim$ 4.5). En pratique, l'alcalinité, exprimée en eq/L, correspond à la somme stoichiométrique des concentrations des bases en solution. Lorsque seules les espèces carbonatées contribuent à l'alcalinité, celle-ci s'exprime donc :

$$A = 2 \cdot [CO_3^{2-}] + [HCO_3^-] + [OH^-] - [H^+] \tag{2.4}$$

L'alcalinité n'est donc pas une mesure directe de la concentration en carbone inorganique dissous (CID). Cependant, connaissant l'alcalinité et le pH d'une solution, il est possible de calculer la quantité de CID. La présence de ligands organiques, qui sont des bases faibles, affecte la mesure de l'alcalinité, qui ne peut donc être utilisée lorsque la concentration en ligands excède 1% de la concentration en CID.

L'alcalinité des solutions expérimentales a été mesurée par titration à l'acide chlorhydrique de concentration 0.001 à 0.1 M, en utilisant un titrateur automatique Schott TA 10plus. La limite de détection est de l'ordre de 5×10^{-5} eq/L et l'incertitude de $\pm1\%$. La quantité de CID et la spéciation carbonatée sont ensuite calculées en utilisant le code de calcul géochimique PHREEQC (voir Chapitre 3).

2.3.3.2 Spectroscopie infrarouge non dispersive

La concentration en carbone inorganique total dissous a été mesurée directement par spectroscopie infra-rouge non dispersive (NDIR) en utilisant un analyseur de CO_2 LI-820 (Licor Inc.). La méthode est basée sur la mesure de l'absorbance d'un gaz à une longueur d'onde infra-rouge caractéristique du CO_2. L'absorbance est directement proportionnelle à la concentration en CO_2. La méthode et le dispositif expérimental sont décrits de manière détaillée par Bénézeth *et al.* (2011). Un schéma et une photo du dispositif sont présentés Fig 2.11.

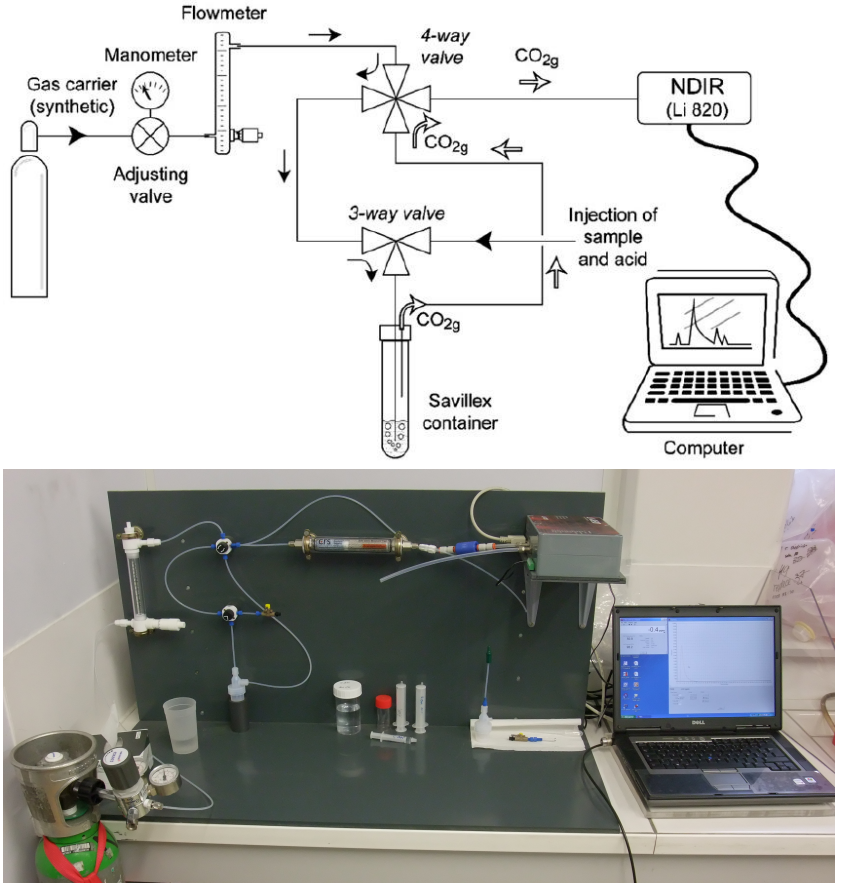

FIGURE 2.11 – Schéma (tiré de Bénézeth *et al.*, 2011) et photo du dispositif analytique utilisé pour la mesure du carbone inorganique dissous par spectroscopie infrarouge non-dispersive.

En pratique, un volume connu de solution provenant d'un échantillon à analyser (0.5 à 2 mL en fonction de la concentration en CID) est injecté avec l'aide d'une seringue dans un bécher Savillex®, par l'intermédiaire d'une valve à trois voies qui isole la solution de l'air extérieur. Un volume de 0.5 à 1.5 mL de solution de HCl 1 M est injecté par la même voie et convertit l'ensemble des espèces carbonatées en CO_2 gazeux, qui est évacué de la solution par l'intermédiaire d'un gaz porteur (air synthétique sans CO_2). Le gaz porteur, qui circule à un débit constant contrôlé par un débit-mètre, amène le CO_2 jusqu'à une cellule optique de 5 cm de long, au sein de laquelle est effectuée la mesure en continu de l'absorbance IR du gaz. Celle-ci est mesurée par un détecteur pyroélectrique maintenu à 50°C précisément. L'absorbance est convertie en concentration instantanée en CO_2 (ppmv), qui est enregistrée

au cours du temps pendant l'évacuation du CO_2 depuis l'échantillon contenu dans le Savillex.

On obtient donc une courbe d'évolution de la concentration en CO_2 après injection d'acide chlorhydrique, dont un exemple est représenté Fig. 2.12. L'aire d'intégration du pic permet de calculer la quantité de CO_2 de l'échantillon initial par l'intermédiaire d'une droite de calibration, établie en analysant des standards de concentration en CID connue, préparés à partir de $NaHCO_3$ et Na_2CO_3 purs et séchés. La courbe de calibration relie l'aire d'intégration du pic obtenu pour chaque échantillon à la quantité de CO_2 contenu dans l'échantillon initial. Un exemple en est présenté Fig. 2.12.

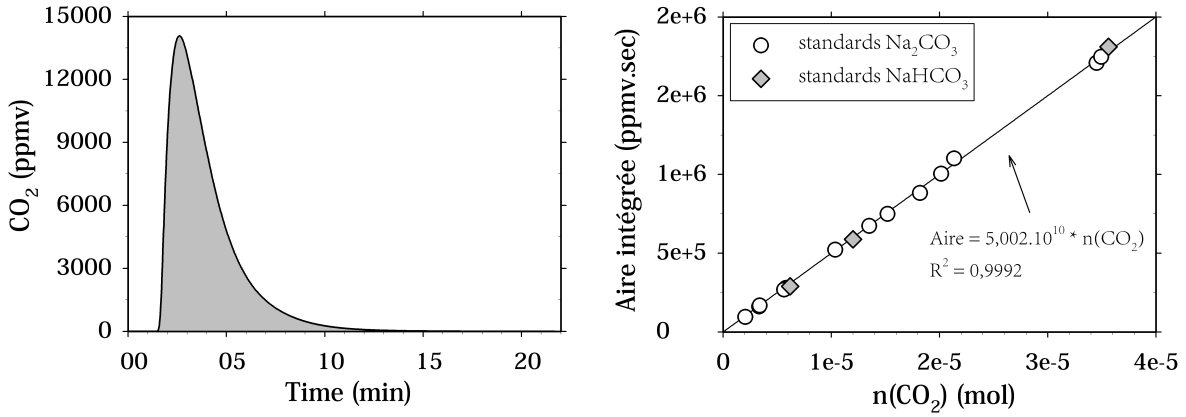

FIGURE 2.12 – Gauche : Évolution de la concentration en CO_2 dans le gaz porteur au cours du temps, après injection d'HCl dans l'échantillon à analyser. La droite de calibration (à droite) est établie en reliant la surface de l'aire grisée à la quantité de CO_2 dans l'échantillon.

Il est à noter que le détecteur est particulièrement stable au cours du temps, puisque les courbes de calibration successives établies sur une durée de 2 ans n'ont jamais différé de manière significative. Pour chaque échantillon analysé, un minimum de deux analyses a été réalisé. La variabilité moyenne des mesures est inférieure à 3%, tandis que l'incertitude est estimée à environ 5%.

Lorsque des mesures d'alcalinité et de spectroscopie NDIR ont éte réalisées sur les mêmes échantillons, la différence entre les concentrations en DIC mesurées directement et celles re-calculées à partir de l'alcalinité n'a jamais excédé 5%, attestant de la qualité des mesures NDIR.

Bibliographie

Berger, G., Cadore, E., Schott, J. et Dove, P. M. (1994). Dissolution rate of quartz in lead and sodium electrolyte-solutions between 25°C and 300°C - effect of the nature of surface complexes and reaction affinity. *Geochimica et Cosmochimica Acta*, 58(2), 541–551.

Binnig, G., Quate, C. F. et Gerber, C. (1986). Atomic force microscope. *Physical Review Letters*, 56(9), 930–933.

Bénézeth, P., Saldi, G. D., Dandurand, J.-L. et Schott, J. (2011). Experimental determination of the solubility product of magnesite at 50 to 200°C. *Chemical Geology*, 286, 21–31.

Brunauer, S., Emmett, P. H. et Teller, E. (1938). Adsorption of gases in multimolecular layers. *Journal of the American Chemical Society*, 60(2), 309–319.

Devidal, J.-L., Schott, J. et Dandurand, J.-L. (1997). An experimental study of kaolinite dissolution and precipitation kinetics as a function of chemical affinity and solution composition at 150°C, 40 bars, and pH 2, 6.8, and 7.8. *Geochimica et Cosmochimica Acta*, 61(24), 5165–5186.

Dove, P. M. et Crerar, D. A. (1990). Kinetics of quartz dissolution in electrolyte-solutions using a hydrothermal mixed flow reactor. *Geochimica et Cosmochimica Acta*, 54(4), 955–969.

Gudbrandsson, S., Wolff-Boenisch, D., Gislason, S. R. et Oelkers, E. H. (2011). An experimental study of crystalline basalt dissolution from 2 < pH < 11 and temperatures from 5 to 75°C. *Geochimica et Cosmochimica Acta*, 75(19), 5496–5509.

Henriksen, K. et Stipp, S. L. S. (2002). Image distortion in scanning probe microscopy. *American Mineralogist*, 87(1), 5–16.

Higgins, S. R., Eggleston, C. M., Knauss, K. G. et Boro, C. O. (1998). A hydrothermal atomic force microscope for imaging in aqueous solution up to 150°c. *Review of scientific instruments*, 69, 2994.

Higgins, S. R. et Hu, X. (2006). Near molecular-scale growth of natural minerals : Experimental methods and errors in length-dependent step speeds with scanning probe microscopy. *Journal of electron spectroscopy and related phenomena*, 150(2-3), 235–247.

Jordan, G., Higgins, S. R., Eggleston, C. M., Knauss, K. G. et Schmahl, W. W. (2001). Dissolution kinetics of magnesite in acidic aqueous solution, a hydrothermal atomic force microscopy (HAFM) study : step orientation and kink dynamics. *Geochimica et Cosmochimica Acta*, 65(23), 4257–4266.

Lakshtanov, L. Z., Bovet, N. et Stipp, S. L. S. (2011). Inhibition of calcite growth by alginate. *Geochimica et Cosmochimica Acta*, 75(14), 3945–3955.

Land, T. A., DeYoreo, J. J. et Lee, J. D. (1997). An in-situ AFM investigation of canavalin crystallization kinetics. *Surface Science*, 384(1-3), 136–155.

Nagy, K. L., Blum, A. E. et Lasaga, A. C. (1991). Dissolution and precipitation kinetics of kaolinite at 80°c and pH 3 ; the dependence on solution saturation state. *American Journal of Science*, 291(7), 649–686.

Nagy, K. L. et Lasaga, A. C. (1992). Dissolution and precipitation kinetics of gibbsite at 80°c and pH 3 - the dependence on solution saturation state. *Geochimica et Cosmochimica Acta*, 56(8), 3093–3111.

Oelkers, E. H. et Schott, J. (1995). Experimental study of anorthite dissolution and the relative mechanism of feldspar hydrolysis. *Geochimica Et Cosmochimica Acta*, 59(24), 5039–5053.

Pina, C. et Jordan, G. (2010). Reactivity of mineral surfaces at nano-scale : kinetics and mechanisms of growth and dissolution. *EMU Notes in Mineralogy*, 8, 239–323.

Pina, C., Merkel, C. et Jordan, G. (2009). On the bimodal effects of silicic acids on calcite growth. *Crystal Growth & Design*, 9(9), 4084–4090.

Rimstidt, J. D. et Dove, P. M. (1986). Mineral solution reaction-rates in a mixed flow reactor - wollastonite hydrolysis. *Geochimica et Cosmochimica Acta*, 50(11), 2509–2516.

Saldi, G., Jordan, G., Schott, J. et Oelkers, E. (2009). Magnesite growth rates as a function of temperature and saturation state. *Geochimica et Cosmochimica Acta*, 73(19), 5646–5657.

Saldi, G. D. (2009). *Les cinétiques de dissolution et précipitation de la magnésite aux conditions hydrothermales*. Thèse de doctorat, Université Paul Sabatier, Toulouse.

Saldi, G. D., Schott, J., Pokrovsky, O. S., Gautier, Q. et Oelkers, E. H. (2012). An experimental study of magnesite precipitation rates at neutral to alkaline conditions and 100-200°C as a function of pH, aqueous solution composition and chemical affinity. *Geochimica et Cosmochimica Acta*, 83, 93–109.

Saldi, G. D., Schott, J., Pokrovsky, O. S. et Oelkers, E. H. (2010). An experimental study of magnesite dissolution rates at neutral to alkaline conditions and 150 and 200°C as a function of pH, total dissolved carbonate concentration, and chemical affinity. *Geochimica et Cosmochimica Acta*, 74, 6344–6356.

Schott, J., Pokrovsky, O. S., Spalla, O., Devreux, F., Gloter, A. et Mielczarski, J. A. (2012). Formation, growth and transformation of leached layers during silicate minerals dissolution : The example of wollastonite. *Geochimica Et Cosmochimica Acta*, 98, 259–281.

Shiraki, R. et Brantley, S. L. (1995). Kinetics of near-equilibrium calcite precipitation at 100°C : an evaluation of elementary reaction-based and affinity-based rate laws. *Geochimica et Cosmochimica Acta*, 59(8), 1457–1471.

Ukrainczyk, M., Gredičak, M., Jerić, I. et Kralj, D. (2012). Interactions of salicylic acid derivatives with calcite crystals. *Journal of Colloid and Interface Science*, 365(1), 296–307.

Westin, K.-J. et Rasmuson, A. C. (2005). Crystal growth of aragonite and calcite in presence of citric acid, DTPA, EDTA and pyromellitic acid. *Journal of Colloid and Interface Science*, 282(2), 359–369.

Witkamp, G. J., Van der Eerden, J. P. et Van Rosmalen, G. M. (1990). Growth of gypsum : I. Kinetics. *Journal of Crystal Growth*, 102(1-2), 281–289.

Yoshino, T., Kagi, H., Kamiya, N. et Kokawa, R. (2010). Relation between etch-pit morphology and step retreat velocity on a calcite surface in aspartic acid solution. *Journal of Crystal Growth*, 312(9), 1590–1598.

Chapter 3

Thermodynamic dataset and chemical speciation calculation

Sommaire

3.1 Introduction

Calculating accurately aqueous chemical speciation is a prerequisite to correctly estimate the saturation state of aqueous solutions with respect to various minerals. As will be seen in the following chapters, this information is needed to interpret the results of mineral growth experiments. A few geochemical softwares may be used to perform these calculations. However, more important than the software is the chemical activity model and the thermodynamic database behind it. In my study, this is particularly important since my experiments were performed at relatively high temperatures, while many databases are focused on low-temperature environments.

In addition, I will be using organic "ligands", which by definition have the ability to form complexes in solution with other ions. Oxalate, citrate and EDTA are indeed known to complex aqueous metal cations (Me^{n+}) with the following effectiveness: oxalate < citrate < EDTA and $Me^{+} < Me^{2+} < Me^{3+}$. As such, these organic ligands have the ability to reduce the chemical activity in solution of free cations, and therefore to reduce the saturation state of the solution with respect to the minerals containing these cations.

In the case of magnesite, in order to accurately calculate the saturation state of the solution, we need to correctly account for the extent of complexation between the organic ligands and Mg^{2+} in solution. We therefore need to know which complexes are forming (depending of the protonation of the ligand, its concentration and that of Mg^{2+}), what are their stability constants, and how these stability constants evolve with temperature.

Many carboxylic ligands, their dissociation constants, the type of complexes they form with metal cations and their stability constants, have been studied at ambient temperature. This is however much less the case at higher temperature, for instance at 100 to 150°C, where my experiments have been performed.

The goal of the present chapter is first to present the geochemical code PHREEQC and its thermodynamic databases and activity model, recall some basic thermodynamics relationships and summarize the existing strategies to extrapolate low-temperature stability and dissociation constants to higher temperatures and zero ionic strength. I will then review the existing data for oxalic acid, citric acid and EDTA dissociation and complexation with Mg^{2+} and Na^{+}, and present the data that have been selected to calculate chemical speciation throughout this thesis. In addition, I will present additional experimental work I performed to determine poorly known stability and solubility constants.

3.2 Temperature extrapolation

3.2.1 Thermodynamic relationships

In the following, I will consider a generic chemical reaction in an homogeneous system involving aqueous species and water:

$$\nu_{\mathrm{a}}\mathrm{A} + \nu_{\mathrm{b}}\mathrm{B} \rightleftharpoons \nu_{\mathrm{c}}\mathrm{C} + \nu_{\mathrm{d}}\mathrm{D} \tag{3.1}$$

A and B are the reactants, C and D the products, and the $\nu_{a,b,c,d}$ are the stoichiometric coefficients of components A, B, C, D.

The equilibrium constant of reaction (3.1) is defined by the law of mass action:

$$K = \frac{a(C)^{\nu_c}\, a(D)^{\nu_d}}{a(A)^{\nu_a}\, a(B)^{\nu_b}} \tag{3.2}$$

where $a(i)$ designates the chemical activity of component i at equilibrium.

Most generally, the chemical reaction (3.1) can be written

$$\sum_i \nu_i C_i = 0 \tag{3.3}$$

with C_i the chemical components. Here, by convention, the stoichiometric coefficients ν_i are positive for products, and negative for reactants. The law of mass action is then written:

$$K = \prod_i a_i^{\nu_i} \tag{3.4}$$

The equilibrium constant is related to the standard molar Gibbs free energy of reaction at the temperature of the experiment $\Delta_r G^0$ through:

$$K = e^{-\Delta_r G^0/RT} \Leftrightarrow \log K = \frac{-\Delta_r G^0}{RT \ln 10} \tag{3.5}$$

with T the absolute temperature and R the gas constant (8.31451 J·K^{-1}·mol $^{-1}$).

$\Delta_r G^0$ is defined as $\Delta_r G^0 = \sum \nu_i \Delta G_i^0$, where ΔG_i^0 designates the standard partial molal Gibbs free energy of component i in reaction (3.3). ΔG_i^0 is defined with respect to the thermodynamic standard state of component i. For water, the standard state adopted in this study is that of unit activity for pure H_2O at any temperature and pressure. For other aqueous species, the standard state is of unit activity in an hypothetical 1 molal solution referenced to infinite dilution at any temperature and pressure. The standard state of solids is that of the pure substance. The ΔG_i^0 are functions of the chemical composition of the system, temperature as well as pressure. Because all our experiments were performed at pressures close to the atmospheric one, pressure negligibly affects the chemical equilibrium in our system, and will not be discussed further. In what follows, we will focus on the temperature dependence of thermodynamic properties and equilibrium constants.

According to the second law of thermodynamics, $\Delta_r G^0$ can be expressed at any given temperature as a function of the standard molar reaction enthalpy $\Delta_r H^0$ and the standard

molar reaction entropy $\Delta_r S^0$, according to:

$$\Delta_r G^0 = \Delta_r H^0 - T\Delta_r S^0 \tag{3.6}$$

The temperature derivatives of the reaction enthalpy and entropy are given by:

$$\left(\frac{\partial \Delta_r H^0}{\partial T}\right)_P = \Delta_r C_p^0 \tag{3.7}$$

$$\left(\frac{\partial \Delta_r S^0}{\partial T}\right)_P = \frac{\Delta_r C_p^0}{T} \tag{3.8}$$

where $\Delta_r C_p^0$ is the molar calorific capacity (or heat capacity) of the reaction.

From the three preceding equations, it is possible to express $\Delta_r G^0$ as a function of temperature and $\Delta_r C_p^0$:

$$\Delta_r G^0(T) = \Delta_r G^0(T_r) - (T - T_r)\Delta_r S^0(T_r) + \int_{T_r}^{T} \Delta_r C_p^0 \, \mathrm{d}T - T\int_{T_r}^{T} \frac{\Delta_r C_p^0}{T} \, \mathrm{d}T \tag{3.9}$$

T_r is the reference temperature, usually taken at 298.15 K. $\Delta_r G^0(T_r)$, $\Delta_r S^0(T_r)$ and $\Delta_r H^0(T_r)$ therefore are the standard thermodynamic properties of the reaction at the reference temperature.

Using eqn. (3.6), eqn. (3.9) can also be written as a function of reaction enthalpy:

$$\Delta_r G^0(T) = \frac{T}{T_r}\Delta_r G^0(T_r) - \Delta_r H^0(T_r)\left(\frac{T}{T_r} - 1\right) + \int_{T_r}^{T} \Delta_r C_p^0 \, \mathrm{d}T - T\int_{T_r}^{T} \frac{\Delta_r C_p^0}{T} \, \mathrm{d}T \tag{3.10}$$

And therefore, eqn. (3.5) gives us a general expression of the equilibrium constant as a function of temperature:

$$\log K(T) = \log K(T_r) - \frac{\Delta_r H^0(T_r)}{R\ln 10}\left(\frac{1}{T} - \frac{1}{T_r}\right) - \frac{1}{RT\ln 10}\int_{T_r}^{T} \Delta_r C_p^0 \, \mathrm{d}T + \frac{1}{R\ln 10}\int_{T_r}^{T} \frac{\Delta_r C_p^0}{T} \, \mathrm{d}T \tag{3.11}$$

Therefore, the equilibrium constant of a chemical reaction may be calculated at any temperature, provided that:

- The equilibrium constant is known at the reference temperature (298.15 K);
- The temperature dependence of $\Delta_r C_p^0$ is known;
- Either $\Delta_r H^0(298.15K)$ or $\Delta_r S^0(298.15K)$ is known.

Heat capacities and reaction enthalpies may be determined experimentally with a good accuracy by mean of calorimetric techniques. Alternatively, they can be estimated from an experimental study of the equilibrium constant as a function of temperature. Indeed:

$$\left(\frac{\partial \ln K}{\partial T}\right)_P = \frac{\Delta_r H^0(T)}{RT^2}$$

$\Delta_r C_p^0(T)$ can then be estimated according to eqn. (3.7).

However, reaction heat capacities and enthalpies have usually been determined over a limited temperature range, which seldom extends to hydrothermal temperatures. Worse, in many cases, heat capacites are unknown, and reaction enthalpies have been determined only at one temperature (usually the reference temperature 298.15K). It is therefore necessary to use approximations.

If $\Delta_r C_p^0$ is estimated to be a constant as a function of temperature, eqn. (3.11) becomes:

$$\boxed{\log K(T) = \log K(T_r) + \frac{\Delta_r H^0(T_r)}{R \ln 10}\left(\frac{1}{T_r} - \frac{1}{T}\right) + \frac{\Delta_r C_p^0}{R \ln 10}\left(\ln \frac{T}{T_r} + \frac{T_r}{T} - 1\right)} \tag{3.12}$$

According to Helgeson (1967), this approximation could lead to a fair estimation of equilibrium constants in the temperature range between 273 and 373 to 423K.

In the absence of an accurate value of $\Delta_r C_p^0$, one may assume it is equal to zero, and therefore $\Delta_r H^0$ is temperature-independent. In this case, eqn. (3.12) is further simplified and leads to the well-known, and widely used, Van't Hoff equation:

$$\boxed{\log K(T) = \log K(T_r) + \frac{\Delta_r H^0(T_r)}{R \ln 10}\left(\frac{1}{T_r} - \frac{1}{T}\right)} \tag{3.13}$$

The validity of such an approximation highly depends on the accuracy of the determination of $\Delta_r H^0(T_r)$. According to Puigdomenech *et al.* (1997), the use of the Van't Hoff equation should be limited to $\pm$ 10K from the reference temperature.

3.2.2 Isoelectric and isocoulombic reactions

The range of temperature for which the "constant-enthalpy" (eqn. 3.13) and the "constant-heat capacity" (eqn. 3.12) approximations can be extended in the case of isoelectric and isocoulombic chemical reactions.

Definition

"Isoelectric" reactions are reactions in which the total number of positive and negative charges is balanced between reactants and products. For example, in the case of a generic metal (M)-ligand (L) complexation reaction:

$$\mathrm{M^{m+} + L^{n-} \rightleftharpoons ML^{(m-n)+}}$$

is not isoelectric, whereas:

$$\mathrm{M^{m+} + H_nL \rightleftharpoons ML^{(m-n)+} + nH^+} \tag{3.14}$$

is isoelectric (there are "m" positive charges in both sides of the chemical equilibrium).

Similarly, for a generic acid dissociation reaction:

$$\mathrm{H_nA \rightleftharpoons nH^+ + A^{n-}} \tag{3.15}$$

is not isoelectric, whereas:

$$H_nA + nOH^- \rightleftharpoons nH_2O + A^{n-} \tag{3.16}$$

is (equilibrated number of negative charges in both sides of the chemical equilibrium).

The term "isocoulombic" (Lindsay, 1980) is used for isoelectric aqueous reactions for which the electrical charges are not only balanced globally between reactants and products, but also individually between each ionic species. Reactions (3.14) and (3.16) are isocoulombic if $m = n = 1$: one positive charge (or negative charge) is carried by one ionic species on both sides of the chemical equilibrium. Strictly speaking, the term "isocoulombic" is limited to chemical reactions with the same number of reactants and products. If this number differs (but electrical charges are still balanced), the reaction is referred to as "pseudo-isocoulombic".

Interest

Mesmer & Baes (1974) and Lindsay (1980) observed that the equilibrium constants of isocoulombic and isoelectric reactions exhibit very regular dependences on temperature, i.e $\Delta_r C_p^0$ is small and constant.

The reason for this smooth dependence on temperature lies in the mainly electrostatic nature of reaction enthalpy: electrostatic interactions of dissolved ionic species between themselves and with the solvent make up the largest contribution to the reaction heat capacity, and therefore to the temperature variation of reaction enthalpy (Puigdomenech *et al.*, 1997 and references therein). In the case of isoelectric reactions, these electrostatic contributions to the temperature dependence of reaction enthalpy will balance out to a large extent, which leads to small reaction heat capacities. It the case of truly isocoulombic reactions, the reaction heat capacity term may simply be neglected (Lindsay, 1980).

Therefore, in the case of isoelectric and isocoulombic reactions, eqn. (3.12, $\Delta_r C_p^0 = constant$) and (3.13, $\Delta_r C_p^0 = 0$) are valid in a much greater temperature range compared to the normal case. Such approximations were therefore widely used in the literature (e.g Lindsay, 1980; Cobble *et al.*, 1982; Mesmer *et al.*, 1988).

Practical use

In order to write isocoulombic reactions, a chemical equilibrium can be combined with another well-known chemical reaction in order to equilibrate charges and number of components. For instance, reaction (3.15) in the case were $n = 2$ can be combined with the reaction for total dissociation of carbonic acid:

$$H_2CO_3 \rightleftharpoons 2H^+ + CO_3^{2-} \tag{3.17}$$

to generate the following isocoulombic reaction:

$$H_2A + CO_3^{2-} \rightleftharpoons H_2CO_3 + A^{2-} \tag{3.18}$$

The equilibrium constant of the isocoulombic reaction (3.18) can be extrapolated to higher temperatures thanks to eqs. (3.12) or (3.13), and the equilibrium constant of reaction (3.15) can be calculated for different temperatures by adding the equilibrium constant of reaction (3.17), which is quite precisely known as a function of temperature (Millero *et al.*, 2007).

In what follows, when thermodynamic data of interest are not available as a function of temperature, we will use isoelectric or isocoulombic writing of chemical equilibrium, so as to guarantee a maximum accuracy for our temperature extrapolations. Of course, the temperature extrapolation presented above rely upon the existence of reliable thermodynamic constants at ambient temperature for the chemical reaction of interest. Published values for $K(T_r)$, $\Delta_r H^0(T_r)$, and if possible $\Delta_r C_p^0(T_r)$ will serve as a basis for our extrapolations.

The general procedure for temperature extrapolation of equilibrium constants by mean of the isoelectric method is summarized in Fig. (3.1). A comparison of the different extrapolation methods (isoelectric vs. non-isoelectric, constant heat capacity or constant enthalpy approximation) has been drawn in Fig.(3.5) for the example of Mg^{2+} complexation by $Oxalate^{2-}$.

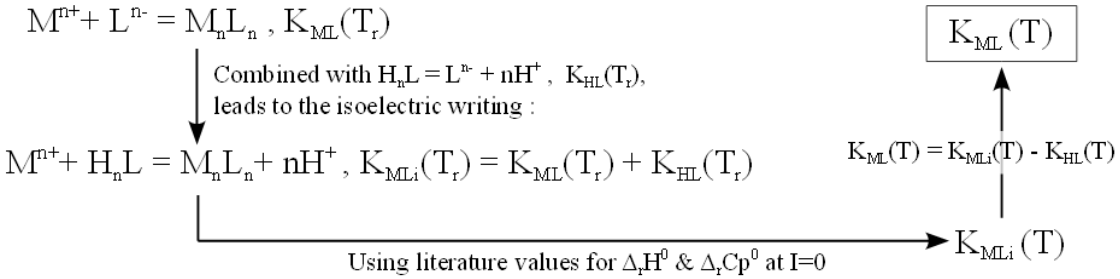

Figure 3.1 – General procedure for extrapolation of equilibrium constants to higher temperatures. K_{ML} is the equilibrium constant of the given complexation reaction, K_{HL} is the constant of the dissociation reaction used to write the isoelectric form of the complexation reaction, K_{MLi} is the equilibrium constant of the isoelectric reaction.

3.2.3 Additional temperature extrapolation methods

There are other methods, more complex and more accurate, to extrapolate existing equilibrium constants to a different temperature range. Among them, the revised Helgeson-Kirkham-Flowers (HKF) model (Tanger & Helgeson, 1988; Shock & Helgeson, 1988) is the most well-known and widely used. In particular, it served as a basis to build internally consistent thermodynamic databases, such as the `slop07.dat` database which is used by the SUPCRT92 software (Johnson *et al.*, 1992). When available, we will use these estimations to complete our thermodynamic dataset (see Section 3.5.2 below).

However, such a model requires a number of empirical ion-dependent parameters, which are not available for complex organic ligands such as citrate or EDTA. It is therefore not readily applicable to our system. Furthermore, the temperature extrapolation we intend to make is still within a limited temperature range, in which the classical "constant-enthalpy" or "constant-heat capacity" approximations should yield reliable results, particularly in the case of isoelectric or isocoulombic equilibria.

For more details about additional methods for extrapolation of thermodynamic data (revised HKF, but also the DQUANT equation (Helgeson, 1967), and the density model (Anderson *et al.*, 1991)), the reader can refer to reviews by Puigdomenech *et al.* (1997) and Oelkers *et al.* (2009).

3.3 Extrapolation to zero ionic strength

Thermodynamic data should be reported in their standard state, i.e at 298.15 K, atmospheric pressure, and infinite dilution. Experimentally however, standard thermodynamic data are not directly accessible, and should be extrapolated from measurements made at non-zero ionic strengths. In some literature sources, this extrapolation to infinite dilution has not been made, and thermodynamic data are reported at the experimental ionic strength. In this case, equilibrium quotients are reported in lieu of equilibrium constants.

For reaction (3.1), the equilibrium quotient is defined as:

$$Q = \frac{m_C^{\nu_c}\, m_D^{\nu_d}}{m_A^{\nu_a}\, m_B^{\nu_b}}$$

where m_i designates the component molality, which is related to chemical activity through:

$$a_i = \gamma_i \frac{m_i}{m_0}$$

with γ_i the activity coefficient of component i, and m_0 the standard molality (1 mol·kg^{-1}). It follows that the equilibrium constant K can be expressed as a function the equilibrium quotient Q according to:

$$K = Q \times \frac{\gamma_C^{\nu_c}\, \gamma_D^{\nu_d}}{\gamma_A^{\nu_a}\, \gamma_B^{\nu_b}} \tag{3.19}$$

In order to extrapolate equilibrium quotients to infinite dilution, all we need to know are the values of the activity coefficients.

In the present study, individual ionic activity coefficients were estimated based on the mean background electrolyte stoichiometric activity coefficient, under the assumption that for an ion i of charge z:

$$\gamma(i, z) = \gamma_{\pm(NaCl)}^{z^2} \tag{3.20}$$

$\gamma_{\pm(NaCl)}$ is the mean molal stoichiometric activity coefficient of NaCl, which was derived from the Meissner equation (Meissner & Tester, 1972; Lindsay, 1989). The values for NaCl were calculated at the ionic strength and temperature of interest with a software based on Archer (1992). The main interest of this method is that it allows an easy calculation of activity coefficients at different temperatures in a NaCl-dominated medium.

If the reaction enthalpy $\Delta_r H$ and heat capacity $\Delta_r C_p$ have not been reported at infinite dilution in the literature, the equilibrium quotient Q reported at the same ionic strength is used instead of the equilibrium constant K for temperature extrapolation. Chemical reactions are expressed in an isoelectric or isocoulombic form (see Section 3.2.2), and eqs. (3.12) or (3.13) expressed for Q are used. After temperature extrapolation, equilibrium quotients are extrapolated to zero ionic strength using eqs. (3.19) and (3.20), to yield the true equilibrium constants as a function of temperature. This extrapolation procedure is summarized in Fig. 3.2.

It should be noted that in some instances, equilibrium quotients reported in the literature were retrieved experimentally in a different media than NaCl (usually tetraalkyl ammonium,

or KCl). In these cases, extrapolation to infinite dilution using eqn. (3.20) may lead to inconsistencies. To limit these problems, only the literature data acquired at ionic strength [1] equal or lower to 0.1 mol·kg^{-1} were considered for extrapolation. In this ionic strength range, activity coefficients can be considered to depend only on the ionic strength of the solution, and not on the type of background electrolyte, so the use of eqn. (3.20) should not lead to erroneous results.

Note also that the mean salt method for the estimation of activity coefficients agrees closely with the widely used Davies equation (eqn. 3.22) (Davies, 1962).

The use of more complex and more accurate activity models, such as the Specific ion Interaction Theory (SIT) model (Scatchard, 1936; Guggenheim, 1966) or the Pitzer model (Pitzer & Mayorga, 1973) was not possible here because such models require the knowledge of ion interaction coefficients, which are unknown for the organic species and complexes we are dealing with.

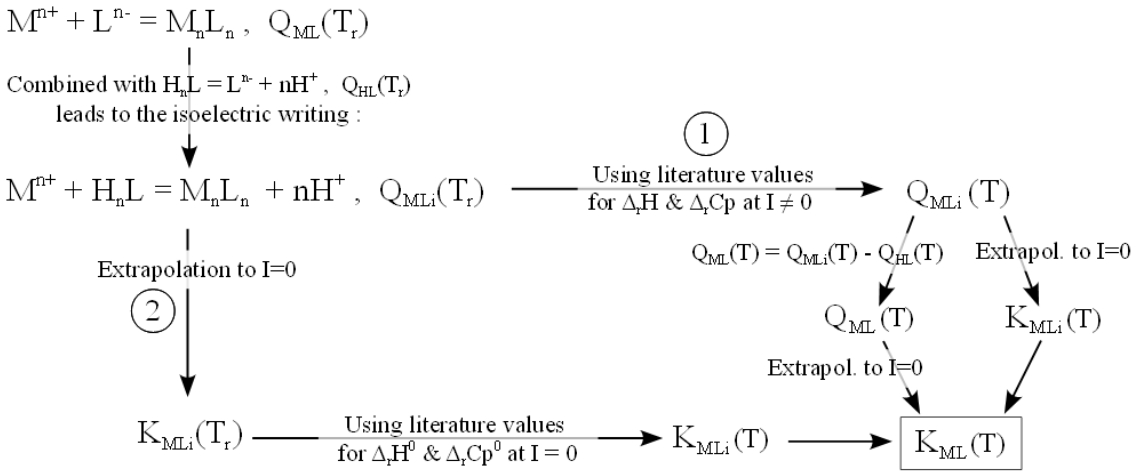

Figure 3.2 – Extrapolation procedure when thermodynamic data are only available at a given ionic strength $I \neq 0$. Q designates the concentration quotients at equilibrium. If reaction enthalpy and heat capacity are only available at the same ionic strength, then the temperature extrapolation needs to be done on the concentration quotients, and extrapolation to infinite dilution is done afterwards (pathway 1). If reaction enthalpy and heat capacity have been reported at infinite dilution, then the extrapolation of the equilibrium constant to infinite dilution is done first, either on the initial concentration quotient Q_{ML}, or on the isoelectric quotient Q_{MLi}. Temperature extrapolation is done afterwards (pathway 2).

[1] The ionic strength I is defined as:

$$I = \frac{1}{2}\sum_i m_i {z_i}^2$$

where the summation is over all charged aqueous species, m_i are components molalities and z_i designates their electrical charge.

3.4 Chemical speciation calculation : the PHREEQC geochemical code

Throughout this study, chemical speciation calculations were performed with the **PHREEQC** geochemical code (Parkhurst & Appelo, 1999). The code solves the Law of Mass Action for all chemical equilibria involving aqueous and mineral species specified in the input file.

3.4.1 Thermodynamic database

The PHREEQC software comes along with different thermodynamic databases. The `llnl.dat` database is derived from the `slop98.dat` database, a former database of the SUPCRT92 software (Johnson *et al.*, 1992). It was built upon the numerous works by Helgeson, Shock and coworkers on mineral and aqueous species equilibria, and gathers experimentally determined as well as extrapolated and estimated thermodynamic constants. It is the most complete database concerning inorganic complexes, and allows calculation of chemical speciation up to high temperatures for most species (up to 300°C). It does not however contain many organic species, and was not updated since it was included with the PHREEQC distribution. Some thermodynamic data may therefore be lacking, or could be modified (for a short review on how the `slop98.dat` database was built, please refer to Oelkers *et al.*, 2009).

The `minteq.dat` database is derived from the MINTEQA2 software (Allison *et al.*, 1991) database. It contains many organic species and their complexes with metal cations, but it is mainly intended to be used at low temperature. Temperature extrapolation is limited to the simple Van't Hoff equation, and in many cases, reaction enthalpy is not reported.

Therefore, for the accuracy of high temperature speciation calculations, and for consistency with the study by Saldi (2009), the `llnl.dat` database will be used throughout this study. Some modifications will however be introduced and will be detailed below.

3.4.2 Activity model

The `llnl.dat` database comes with a built-in activity model based on the B-dot equation of Helgeson (1969). Activity coefficients are calculated according to:

$$\log \gamma_i = -\frac{A z_i^2 \sqrt{I}}{1 + \mathring{a}_i B \sqrt{I}} + \dot{B} I \tag{3.21}$$

where $\mathring{a}_i$ is the "ion-size" parameter of species i, A, B and $\dot{B}$ are constants depending only on temperature, and I is the ionic strength.

Neutral solute species are attributed the activity coefficient of aqueous CO_2 in pure sodium chloride solutions of the same ionic strength. This activity coefficient is expressed as a function of temperature and ionic strength using an expression from Drummond (1981).

This activity model was developed to span a wide range of temperature (up to 300°C), and is therefore well suited for our high temperature calculations.

For a number of species, the "ion-size" parameter å$_i$ is not known. In these cases, the Davies equation is used to calculate activity coefficients (valid for ionic strengths up to 0.1M):

$$\log \gamma_i = -Az_i^2 \left(\frac{\sqrt{I}}{1+\sqrt{I}} - 0.3I \right) \tag{3.22}$$

3.4.3 Temperature dependence of equilibrium constants

In PHREEQC, the temperature dependence of equilibrium constants is defined analytically, via a 5-coefficients expression:

$$\log K = A_1 + A_2 T + \frac{A_3}{T} + A_4 \log T + \frac{A_5}{T^2} \tag{3.23}$$

where T is in Kelvin.

Therefore, after temperature extrapolation of equilibrium constants for newly defined chemical reactions, the analytical expression (3.23) was fitted on the retrieved $\log K$ for different temperatures by mean of a least-square fitting algorithm. The A_1-A_5 coefficients were then included in the PHREEQC database. They are listed together with the reported thermodynamic constants of newly defined chemical reactions in Table 3.4.

3.5 Oxalate species

Oxalic acid (ethanedioic acid), of formula HOOC−COOH, forms upon complete acidic dissociation the oxalate conjugate base, $^{-}$OOC−COO^{-}, which is a known complexing substance. Oxalate forms bidentate complexes with metal cations, binding them with both carboxylic groups (e.g Kondoh & Oi, 1998). Both species are widely encountered in natural systems, and used for industrial applications. As a result, the acidic and complexing properties of oxalic acid have been studied in some details.

3.5.1 Oxalic acid dissociation constants

The two dissociation reactions of oxalic acid are written:

$$\mathrm{H_2Oxalate} \rightleftharpoons \mathrm{HOxalate^-} + \mathrm{H^+}, \qquad K_{a1}(Ox) = \frac{h \cdot a(\mathrm{HOxalate^-})}{a(\mathrm{H_2Oxalate})}$$

$$\mathrm{HOxalate^-} \rightleftharpoons \mathrm{Oxalate^{2-}} + \mathrm{H^+}, \qquad K_{a2}(Ox) = \frac{h \cdot a(\mathrm{Oxalate^{2-}})}{a(\mathrm{HOxalate^-})}$$

where $K_{a1}(Ox)$ and $K_{a2}(Ox)$ are the first and the second dissociation constants of oxalic acid, respectively, and h designates the activity of the proton.

Based on experimental investigations and reevaluation of former data, Kettler *et al.* (1998) proposed an expression for both dissociation constants as a function of ionic strength and temperature (5 to 175°C).

SUPCRT92 also provides estimates of oxalic acid dissociation constants, based on Shock (1995). SUPCRT92 estimates are in excellent agreement with Kettler *et al.* (1998) concerning $K_{a2}(Ox)$, but they are higher by ca. 0.1 log unit for $K_{a1}(Ox)$ (Fig. 3.3). Recent estimates

between 0 and 60°C from Partanen *et al.* (2009) are in close agreement for both dissociation constants with SUPCRT92 estimates. However, these latest data are based mostly on a reevaluation of older data which also served as a basis for Kettler *et al.* (1998) and Shock (1995).

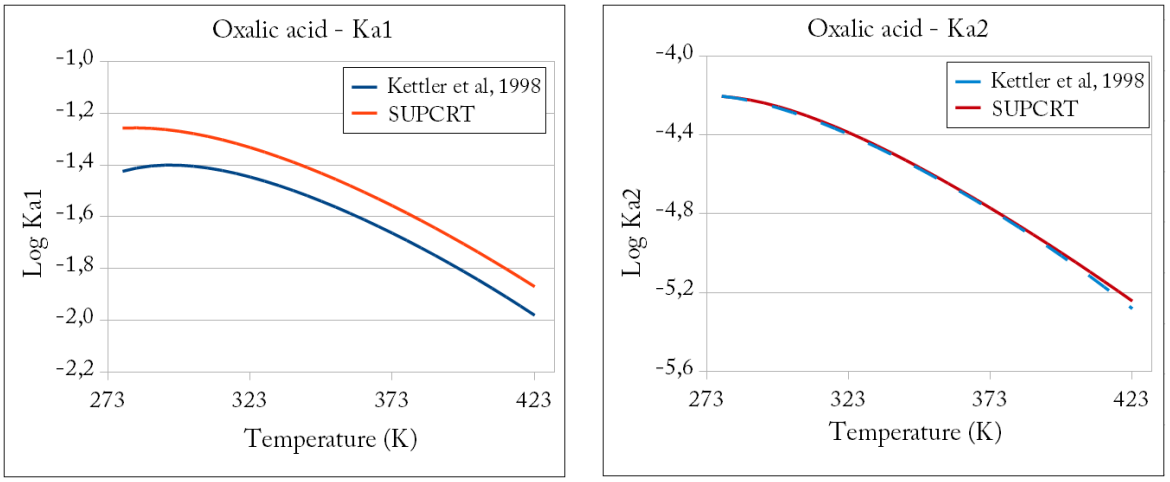

Figure 3.3 – First and second dissociation constants of oxalic acid as a function of temperature. The agreement between Kettler *et al.* (1998) data and SUPCRT92 estimates is good for K_{a2}, but some differences exist for K_{a1}.

Because the Kettler *et al.* (1998) estimates span a big temperature range, and were fitted on most of the previously published measurements of oxalic acid dissociation, they were selected to introduce oxalate species in our thermodynamic database. Possible discrepancies on the first dissociation constant do not have any impact on our speciation calculations, since our experiments were performed in alkaline conditions, where oxalic acid is mainly in its fully dissociated form (see speciation diagram in Fig. 3.4).

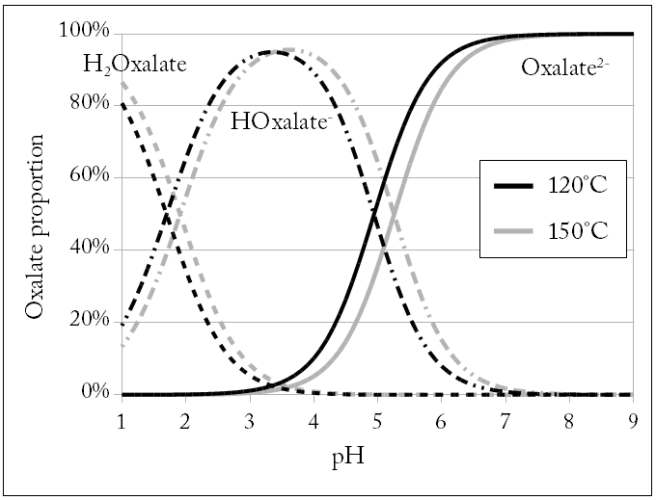

Figure 3.4 – Speciation diagram of oxalic acid at 120 and 150°C according to Kettler *et al.* (1998). The speciation is largely dominated by $Oxalate^{2-}$ at pH > 7.

3.5.2 Oxalate complexation with Mg^{2+} and Na^{+}

Data for $Oxalate^{2-}$ complexation with Mg^{2+} and Na^{+} were retrieved from SUPCRT92. The following reactions were considered:

$$\begin{aligned} Oxalate^{2-} + Mg^{2+} &\rightleftharpoons MgOxalate, \qquad K_{MgOx} \\ Oxalate^{2-} + Na^{+} &\rightleftharpoons NaOxalate^{-}, \qquad K_{NaOx} \end{aligned} \tag{3.24}$$

The SUPCRT92 estimates come from Prapaipong *et al.* (1999), who extrapolated published low-temperature data for both stability constants based on the revised HKF model.

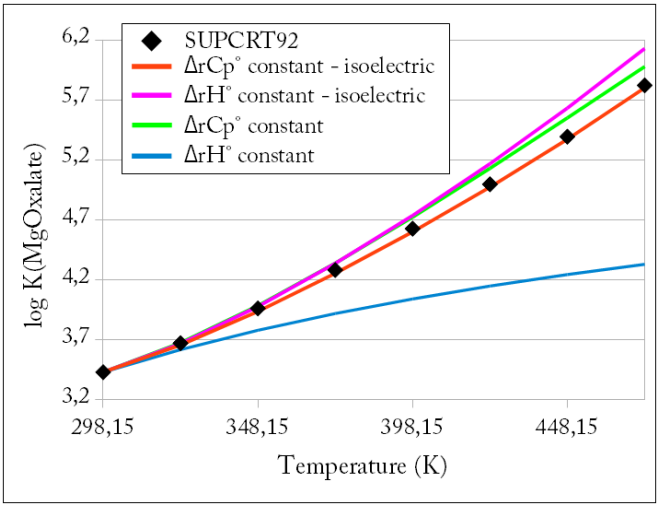

Figure 3.5 – Complexation constant of $Oxalate^{2-}$ with Mg^{2+}, from SUPCRT92 (black rhombs). The results of the different temperature extrapolation methods outlined in Section 3.2 have been drawn for comparison. The constant heat capacity approximation obtained via isoelectric writing of reaction (3.24) gives the best results (see text).

The temperature extrapolation for K_{MgOx} is based on an experimental value at 25°C by Money & Davies (1932) ($\log K_{MgOx}(25°C) = 3.43$). The standard-state reaction entropy $\Delta_r S^0$ is estimated through a correlation with the standard partial molal entropy of the complexed cation. Although the formation of the MgOxalate complex itself has not been studied experimentally as a function of temperature, the correlation proposed by Prapaipong *et al.* (1999) is based on a number of other oxalate complexes, which allows to have a reasonable confidence in the estimation of the authors for K_{MgOx}. Furthermore, the extrapolated value at 37°C is in good agreement with the experimental determination of Finlayson *et al.* (1975). The SUPCRT92 data have been plotted as a function of temperature in Fig. (3.5).

Prapaipong *et al.* (1999) mention the existence of the $MgOxalate_2^{2-}$ complex, and report the following value for its formation constant at 25°C: $\log K_{MgOxalate_2^{2-}} = 4.38$ (from Barney *et al.*, 1951). Its temperature dependence is however unknown. Using the reported stability constant at ambient temperature, speciation calculations indicate that this complex is unlikely to play a big role in the chemical speciation of our experimental solutions. It was therefore not included in our database.

Estimation for K_{NaOx} by Prapaipong *et al.* (1999) is based on experimentally measured standard thermodynamic data for $NaOxalate^{-}$ formation (Daniele *et al.*, 1981, 1983), and can therefore be considered as reliable.

The result of speciation calculation using this dataset is illustrated at 120°C as a function of total Mg^{2+} molality in Fig. (3.6), for a solution at pH 8.0 containing 1mM oxalate, with 90mM

NaCl as background electrolyte fixing the ionic strength to $\sim$ 0.1M (composition approaching some of our experimental solutions). Despite its relatively low stability constant, NaOxalate$^-$ complexes make up a big part of oxalate speciation due to the high NaCl concentration in our experimental solutions. In the range of chemical compositions investigated in our study (represented by vertical dashed lines in Fig. 3.6), MgOxalate never represents more than 40% of the total oxalate.

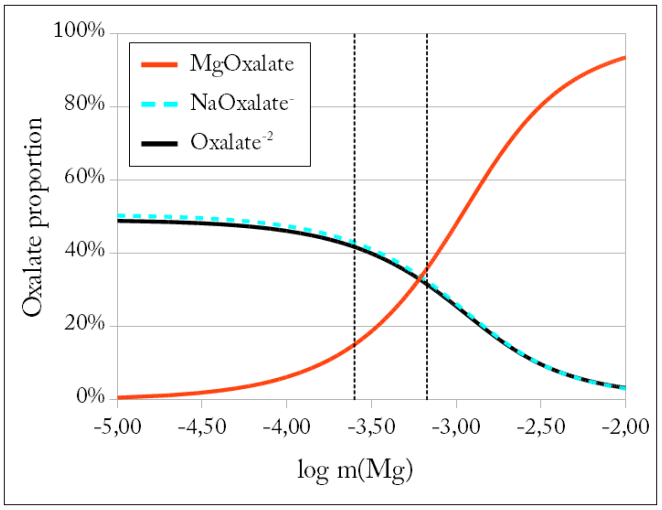

Figure 3.6 – Speciation of 1mM of oxalic acid at 120°C as a function of total magnesium molality (in mol·kgw^{-1}). The present example was drawn at pH 8, with 90mM of NaCl as background electrolyte. Ionic strength is close to 0.1M. H_2Oxalate and HOxalate$^-$ are present in negligibly small quantities. Vertical dashed lines indicate the range of Mg^{2+} molality in our experiments with 1mM oxalate.

MgOxalate formation constant was used as an example to illustrate the results of different temperature extrapolation methods outlined in Section 3.2. Four different methods were used: the Van't Hoff equation (eq. 3.13) and the constant heat capacity approximation (eqn. 3.12) were first applied directly on $K_{MgOx}(25°C)$. Then reaction (3.24) was written in an isoelectric form: H_2Oxalate + $Mg^{2+} \rightleftharpoons$ MgOxalate + 2 H^+, and the extrapolation procedure outlined in Fig. (3.1) was used. Values for $K_{MgOx}(25°C)$, $\Delta_r H^0$ and $\Delta_r Cp^0$ for the reactions of interest were taken from SUPCRT92. The results of the different extrapolations are plotted in Fig. (3.5).

Temperature extrapolation for the isoelectric reaction gives the best results. In this case, the constant heat capacity hypothesis gives excellent results, within 0.03 log units from the original SUPCRT92 data. The constant reaction enthalpy approximation gives results which are acceptable (within 0.1 log units from the original data) up to 120°C. When extrapolation is done directly on the initial stability constant, the constant heat capacity approximation gives fairly accurate estimations (within 0.1 log units from the original data up to 130°C), whereas the Van't Hoff equation may only be used below 60°C.

3.6 EDTA species

Ethylediaminetetraacetate is widely used for industrial applications due to the strong hexadentate chelates it forms with metallic cations. Its protonation and complexation reactions have therefore been thoroughly studied.

3.6.1 Protonation

Numerous experimental studies have focused on EDTA protonation at ambient conditions. The NIST CRITICAL database (Smith *et al.*, 1998) reports critically selected thermodynamic constants, and served as a basis for our literature evaluation.

Here, we will refer to $EDTA^{4-}$ as ethylediaminetetraacetate, the fully deprotonated form of ethylediaminetetraacetatic acid H_4EDTA. The different protonation steps of EDTA may be written generally:

$$H_{(n-1)}EDTA^{n-5} + H^+ \rightleftharpoons H_nEDTA^{n-4}, \qquad K_{H_{n-1}EDTA^{n-5}} \tag{3.25}$$

with n going from 1 ($EDTA^{4-}$ protonation) to 6 ($HEDTA^{+}$ protonation).

A quick review of the literature reveals that protonation of H_2EDTA^{2-} or more protonated species will be negligible in the alkaline conditions of our experiments. Indeed, according to the CRITICAL database, at $I = 0.1M$, $\log Q_{H_2EDTA^{2-}} = 2.7$, $\log Q_{H_3EDTA^{-}} = 2.0$, and protonation of H_4EDTA and H_5EDTA^{+} occurs at even more acidic conditions. Furthermore, reported reaction enthalpies are small, maximum 7 kJ·mol^{-1} for $n = 3$ (reaction 3.25), and according to Hovey *et al.* (1988), $\log Q_{H_2EDTA^{2-}}(0.1\text{ M})$ does not exceed 3.18 at 125°C.

Therefore, only the first and second protonation reaction of EDTA ($n = 1$ and 2) will matter to our calculations.

Reported equilibrium constants at infinite dilution for EDTA first and second protonation reactions at 25°C are listed in Table 3.1, together with their literature source.

$\log K_{EDTA^{4-}}$	$\log K_{HEDTA^{3-}}$	source
10.95	6.27	Carini & Martell (1953)
11.09	6.71	Daniele *et al.* (1985)
10.19	6.88	Mizera *et al.* (1999)
10.36	6.89	Thakur *et al.* (2007)

Table 3.1 – Equilibrium constants for the first and the second protonation of EDTA (reaction 3.25) reported in the literature. Values were extrapolated to infinite dilution by the authors, except for Daniele *et al.* (1985), where equilibrium constants were generated using a precise fitting equation proposed by the authors.

Table 3.1 reveals an important variability of the listed values for both protonation constants, which likely stems from the different methods used for extrapolation to zero ionic strength, as well as from the difficult estimation of EDTA complexation with the background electrolyte (Hummel *et al.*, 2005).

A number of additional data were reported for ionic strengths of 0.1M, with various background electrolytes. For the first protonation reaction, constants extrapolated to infinite dilution agree well with the range of values listed in Table 3.1. The values reported by Mizera *et al.* (1999) and Daniele *et al.* (1985) were chosen for speciation calculation because they represent extreme estimates for the first protonation constant.

For the second protonation reaction, the value of Carini & Martell (1953) appears to be significantly lower than the rest of the literature body. The values reported by Daniele *et al.* (1985) and Mizera *et al.* (1999) were chosen here as well in order to span the entire range of likely values for the second protonation constant.

However, as will be shown later, the value selected eventually impacts negligibly speciation calculation for our solutions.

Several studies have focused on the variation of protonation constants as a function of temperature. However, only Carini & Martell (1953) reported standard reaction enthalpies for the first and second protonation reactions (reaction 3.25) : $\Delta_r H^0_{\mathrm{EDTA}^{4-}} = -22.36$ kJ/mol and $\Delta_r H^0_{\mathrm{HEDTA}^{3-}} = -15.45$ kJ/mol, respectively.

Hovey *et al.* (1988) determined calorimetrically the standard partial molal heat capacities associated with various EDTA species at 25°C. Their data result in $\Delta_r Cp^0_{\mathrm{EDTA}^{4-}} = 228 \pm 20$ J·K^{-1}·mol^{-1} and $\Delta_r Cp^0_{\mathrm{HEDTA}^{3-}} = 163 \pm 2$ J·K^{-1}·mol^{-1}. These values were used for temperature extrapolation.

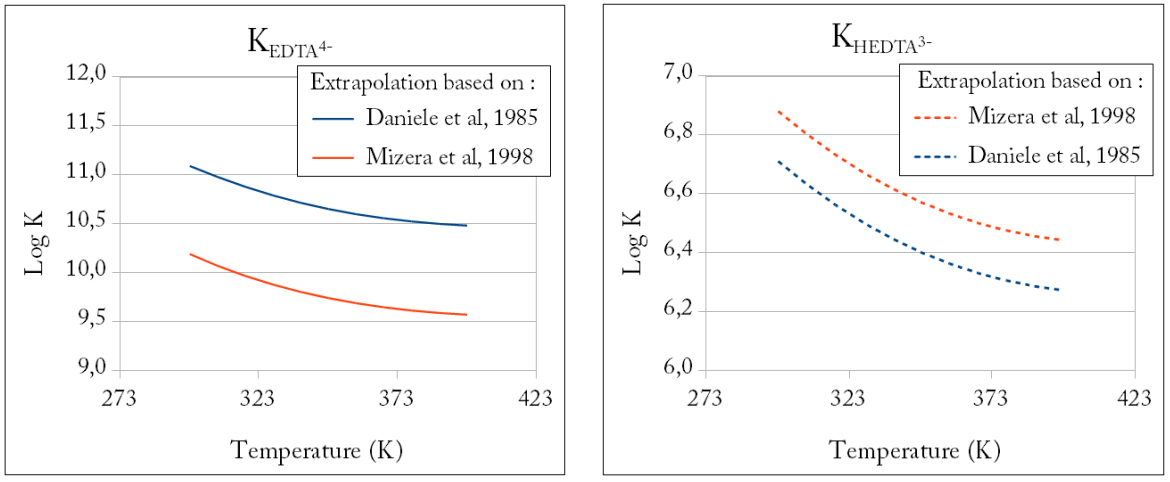

Figure 3.7 – First and second protonation constants of EDTA as a function of temperature.

Protonation reactions were written in an isoelectric form by combining them with the water dissociation reaction:

$$\mathrm{EDTA}^{4-} + \mathrm{H_2O} \rightleftharpoons \mathrm{HEDTA}^{3-} + \mathrm{OH}^-$$
$$\mathrm{HEDTA}^{3-} + \mathrm{H_2O} \rightleftharpoons \mathrm{H_2EDTA}^{2-} + \mathrm{OH}^-$$

The standard thermodynamic constants for water dissociation needed to calculate the standard thermodynamic constants of the isoelectric reactions were taken from Busey & Mesmer (1976, 1978). Temperature extrapolation of the protonation constants was done

according to the procedure detailed in Section 3.2.

The extrapolated protonation constants are plotted as a function of temperature in Figure 3.7. The speciation diagram at 100 and 120°C, plotted in Fig. 3.8, indicates that in our pH conditions, and in the absence of any metal cations, $HEDTA_3^-$ would dominate the speciation.

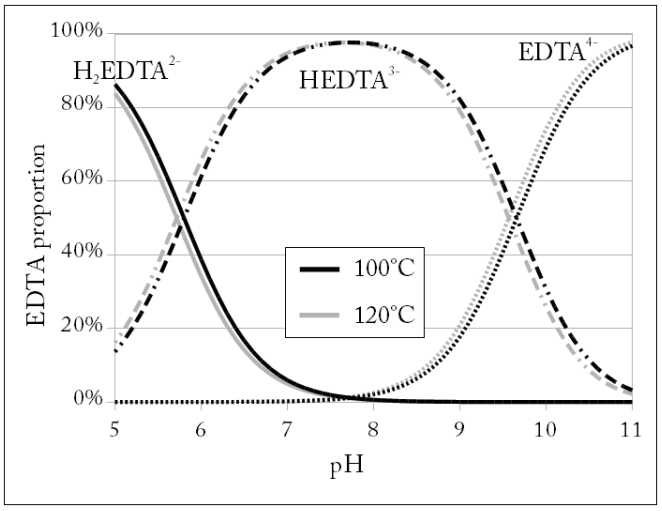

Figure 3.8 – Speciation diagram of EDTA at 100 and 120°C, at $I \simeq 0.1$ M, using the data from Daniele *et al.* (1985) for $K_{\mathrm{EDTA^{4-}}}$ and Thakur *et al.* (2007) for $K_{\mathrm{HEDTA^{3-}}}$. In our chemical conditions, the speciation is largely dominated by $HEDTA^{3-}$.

3.6.2 Complexation with Mg^{2+} and Na^+

The following complexation reactions were considered:

$$\mathrm{EDTA^{4-} + Mg^{2+} \rightleftharpoons MgEDTA^{2-}}, \qquad K_{\mathrm{MgEDTA^{2-}}} \tag{3.26}$$

$$\mathrm{EDTA^{4-} + Na^{+} \rightleftharpoons NaEDTA^{3-}}, \qquad K_{\mathrm{NaEDTA^{3-}}} \tag{3.27}$$

The corresponding isocoulombic reactions are :

$$\mathrm{H_2EDTA^{2-} + Mg^{2+} \rightleftharpoons MgEDTA^{2-} + 2\,H^{+}} \tag{3.28}$$

$$\mathrm{HEDTA^{3-} + Na^{+} \rightleftharpoons NaEDTA^{3-} + H^{+}} \tag{3.29}$$

According to the CRITICAL database (Smith *et al.*, 1998) version 8.0 and additional literature review, $\log K_{\mathrm{MgEDTA^{2-}}}$ ranges between 10.45 (extrapolated to infinite dilution from a value listed by Smith & Martell, 1987) and 10.71 (Arena *et al.*, 1983). $\Delta_r H^0_{\mathrm{MgEDTA^{2-}}}$ for reaction (3.26) is 18 kJ · mol^{-1} according to the CRITICAL database. Calorimetric studies by Hovey & Tremaine (1985) allow to estimate for the same reaction $\Delta_r Cp^0_{\mathrm{MgEDTA^{2-}}} = 432.8\,\mathrm{J \cdot K^{-1} \cdot mol^{-1}}$.

Temperature extrapolation through the isoelectric reaction (3.28), according to the procedure detailed in Fig. 3.1, requires to precisely know the standard thermodynamic properties of the following reaction :

$$\mathrm{H_2EDTA^{2-} \rightleftharpoons EDTA^{4-} + 2\,H^{+}}$$

These were estimated based on the data presented in the precedent section, and listed in Table 3.4. Figure 3.9a presents the calculated evolution of $K_{\mathrm{MgEDTA^{2-}}}$ as a function of temperature.

The formation of the $\mathrm{MgHEDTA^-}$ complex is known from experimental studies (e.g Arena *et al.*, 1983), and its formation constant according to the following reaction:

$$\mathrm{Mg^{2+} + HEDTA^{3-} \rightleftharpoons MgHEDTA^-}$$

is estimated to be 4.5 ± 0.2 according to the literature review by Hummel *et al.* (2005). This complex would therefore negligibly affect the results of our speciation calculation. Furthermore, the temperature dependence of its stability constant is not known. Consequently, it was not included in our database.

Estimations for $\log K_{\mathrm{NaEDTA^{3-}}}$ agree within uncertainties with that of Felmy & Mason (2003): $\log K_{\mathrm{NaEDTA^{3-}}} = 2.7$, which was therefore selected.

There is a much greater scatter on the estimations of the enthalpy of reaction (3.27) (e.g Daniele *et al.*, 1985 ; Smith & Martell, 1987 ; Hovey *et al.*, 1988). The value recommended by Hummel *et al.* (2005) should be used : $\Delta_r H^0_{\mathrm{NaEDTA^{2-}}} = 4 \pm 3\ \mathrm{kJ \cdot mol^{-1}}$. The heat capacity for the same reaction was estimated from Hovey *et al.* (1988) : $\Delta_r Cp^0_{\mathrm{NaEDTA^{3-}}} = 243.2\ \mathrm{J \cdot K^{-1} \cdot mol^{-1}}$. The result of the temperature extrapolation of $K_{\mathrm{NaEDTA^{3-}}}$ is plotted in Figure 3.9b.

The formation of the $\mathrm{NaHEDTA^{2-}}$ complex was reported by several authors (e.g Daniele *et al.*, 1985), but its stability constant is low ($K_{\mathrm{NaHEDTA^{2-}}} < 1$) and the complex may therefore be neglected in the present case.

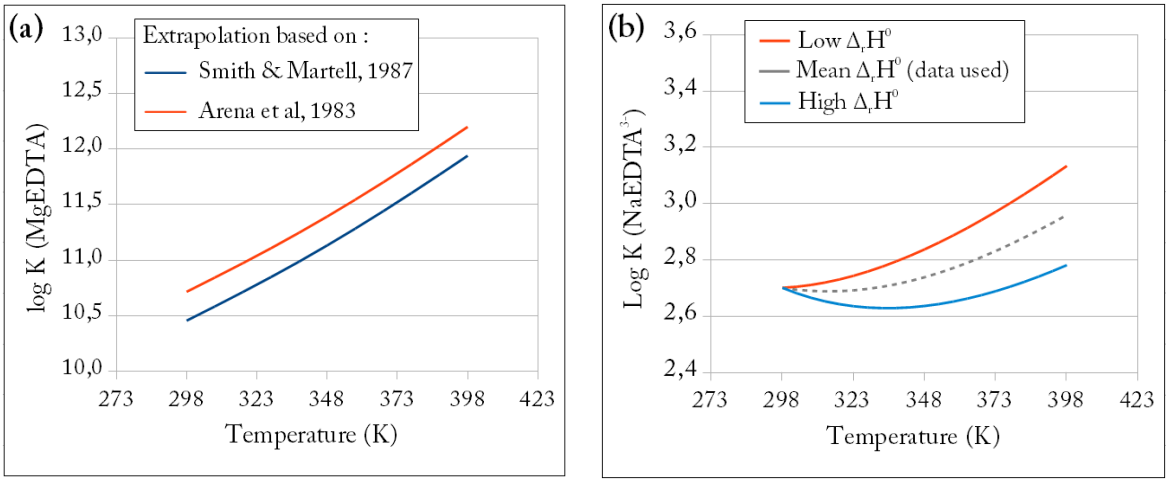

Figure 3.9 – (a) Stability constant of the $\mathrm{MgEDTA^{2-}}$ complex as a function of temperature (reaction 3.26). The two estimations are based on different initial $\log K$ at 25°C, but uncertainty on reaction enthalpy and heat capacity was not taken into account. (b) Stability constant of the $\mathrm{NaEDTA^{3-}}$ complex as a function of temperature (reaction 3.27). Only one estimate at 25°C was selected, but the important uncertainty on reaction enthalpy was considered.

There obviously are significant uncertainties on the respective stability constants of the different EDTA species at high temperature. However, the extremely high complexation constant between $\mathrm{Mg^{2+}}$ and EDTA has a simple consequence : in the presence of $\mathrm{Mg^{2+}}$ in the

experimental solution, an overwhelming part of the total EDTA gets complexed with the cation. Figure 3.10 represents a speciation diagram of EDTA in the presence of varying total Mg molality. The fraction of $MgEDTA^{2-}$ increases linearly with Mg molality, and reaches nearly 100% of the total EDTA as soon as $m(Mg) = m(EDTA)$. In order for the solution to be supersaturated with respect to magnesite, Mg^{2+} has to be introduced in significant excess compared to EDTA. The finally selected thermodynamic data for EDTA species are listed in Table 3.4.

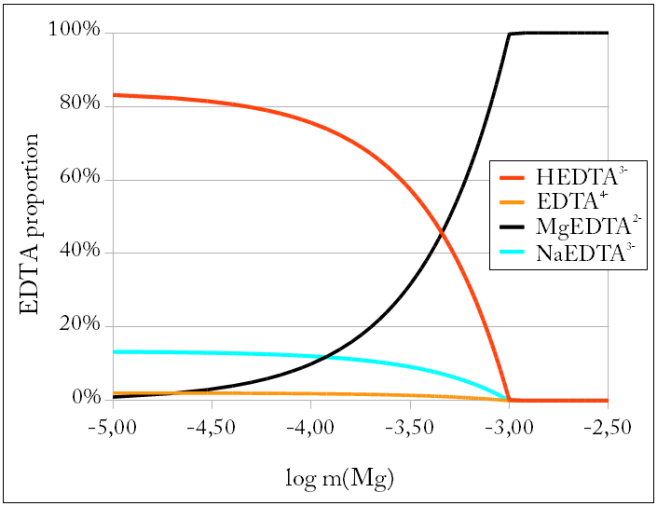

Figure 3.10 – Speciation of 1mM of EDTA at 120°C as a function of total magnesium molality (in mol·kgw^{-1}). The present example was drawn at pH 8, with 90mM of NaCl as background electrolyte. Ionic strength is close to 0.1M. The proportion of $MgEDTA^{2-}$ increases linearly with the Mg molality, leading to a complete domination of $MgEDTA^{2-}$ on EDTA speciation in solution supersaturated with respect to magnesite.

3.7 Citrate species

Citric acid is a common metabolite of live beings, and is widely used for industrial purposes due to its complexing and buffering capacity. Citrate has the ability to bind metal cations in tridentate fashion involving two carboxyl groups and the central hydroxyl group (Glusker, 1980; Kondoh & Oi, 1998). Because of its importance for biological processes, its chemical properties are well known at ambient temperature to 37°C. There is however a scarcity of data concerning its complexing properties at higher temperatures.

3.7.1 Citric acid dissociation constants

The three step-wise citric acid dissociation equilibria are :

$$H_3Citrate \rightleftharpoons H_2Citrate^- + H^+, \qquad K_{a1} \tag{3.30}$$

$$H_2Citrate^- \rightleftharpoons HCitrate^{2-} + H^+, \qquad K_{a2} \tag{3.31}$$

$$HCitrate^{2-} \rightleftharpoons Citrate^{3-} + H^+, \qquad K_{a3} \tag{3.32}$$

with K_{a1}, K_{a2}, K_{a3} their respective equilibrium constants.

These equilibria were studied by Bénézeth *et al.* (1997) from 5 to 150°C, in a NaCl media. The authors determined the equilibrium constants at varying temperatures, which were

used without modifications in the present study. The evolution of the three dissociation constants as a function of temperature, and the corresponding speciation diagram at 120°C are represented in Fig. 3.11a and b, respectively. In the pH conditions of our experiments, $Citrate^{3-}$ dominates the citric acid speciation.

The standard thermodynamic constants determined by Bénézeth *et al.* (1997) and the corresponding PHREEQC parameters are listed in Table 3.4.

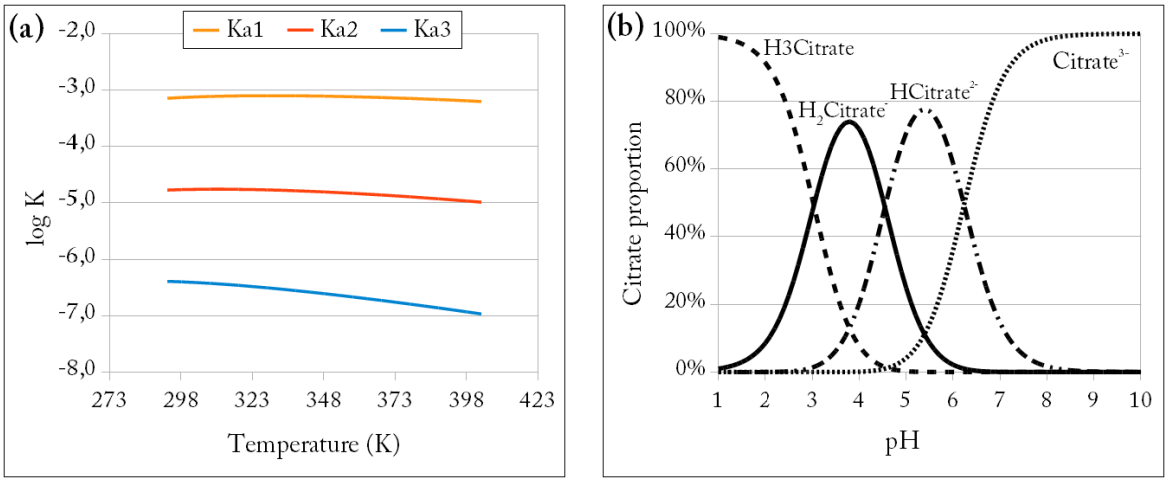

Figure 3.11 – (a) Dissociation constants of citric acid as a function of temperature, from Bénézeth *et al.* (1997). (b) Citric acid speciation diagram at 120°C in a 0.1M ionic strength solution. There is little difference with the speciation diagram at 100°C.

3.7.2 Citrate complexation with Na^+

The following complexation reactions between Na^+ and citrate species were considered:

$$Citrate^{3-} + Na^+ \rightleftharpoons NaCitrate^{2-}, \qquad K_{NaCitrate^{2-}} \tag{3.33}$$

$$Citrate^{3-} + 2\,Na^+ \rightleftharpoons Na_2Citrate^-, \qquad K_{Na_2Citrate^-} \tag{3.34}$$

$$Citrate^{3-} + H^+ + Na^+ \rightleftharpoons NaHCitrate^-, \qquad K_{NaHCitrate^-} \tag{3.35}$$

The stability constants of $NaCitrate^{2-}$ and $Na_2Citrate^-$ were studied by Zelenina & Zelenin (2005), who also determined by mean of calorimetric methods the standard enthalpy and heat capacity of reaction (3.33). These data were used to calculate the temperature dependence of $K_{NaCitrate^{2-}}$ according to the procedure detailed in Fig. 3.1, by mean of the following isocoulombic reaction:

$$HCitrate^{2-} + Na^+ \rightleftharpoons NaCitrate^{2-} + H^+$$

where the data for the third dissociation constant of citric acid were taken from Bénézeth *et al.* (1997). The calculated extrapolated stability constants are plotted as a function of temperature in Fig. 3.12b.

The reaction enthalpy of reaction 3.34 at 25°C is reported in the `minteq.dat` database of PHREEQC, as well as the stability constant and reaction enthalpy of reaction 3.35. The original source of these data could not be determined. They were introduced directly in our database, the temperature extrapolation being therefore calculated with the Van't Hoff law. Because $NaCitrate^{2-}$ is by far the most important Na^+- citrate complex, uncertainties associated with reactions (3.34) and (3.35) do not significantly affect the result of our calculations.

All thermodynamic constants and corresponding PHREEQC parameters are summarized in Table 3.4.

3.7.3 Citrate complexation with Mg^{2+}

The following complexation reactions between Mg^{2+} and citrate species were considered:

$$\mathrm{Citrate^{3-}} + \mathrm{Mg^{2+}} \rightleftharpoons \mathrm{MgCitrate^{-}}, \qquad K_{\mathrm{MgCitrate^-}} \tag{3.36}$$

$$\mathrm{HCitrate^{2-}} + \mathrm{Mg^{2+}} \rightleftharpoons \mathrm{MgHCitrate}, \qquad K_{\mathrm{MgHCitrate}} \tag{3.37}$$

$$\mathrm{H_2Citrate^{-}} + \mathrm{Mg^{2+}} \rightleftharpoons \mathrm{MgH_2Citrate^{+}}, \qquad K_{\mathrm{MgH_2Citrate^+}} \tag{3.38}$$

$$2\,\mathrm{Citrate^{3-}} + \mathrm{Mg^{2+}} \rightleftharpoons \mathrm{Mg(Citrate)_2^{4-}}, \qquad K_{\mathrm{MgCitrate_2^{4-}}} \tag{3.39}$$

According to the literature, the strongest complex is $MgCitrate^-$ (reaction 3.36). The CRITICAL database (Smith *et al.*, 1998) reports values for $\log Q_{\mathrm{MgCitrate^-}}$ at an ionic strength of 0.1M ranging from 3.43 to 3.64.

There is to our knowledge no calorimetric study of the reaction enthalpy and heat capacity of reaction (3.36). CRITICAL mentions for $\Delta_r H_{\mathrm{MgCitrate^-}}$ a value of ~ 8 kJ $\cdot$ mol^{-1} at a 0.1M ionic strength, but we were not able to determine the original literature source of this data.

Amico *et al.* (1982) proposed a value of 21.8 kJ $\cdot$ mol^{-1} for $\Delta_r H^0_{\mathrm{MgCitrate^-}}$, but this value was based on a literature review of complexation constants determined by various authors using different investigation techniques, and over a limited temperature range (25-37°C). Therefore this value should be considered of little significance (P.G. Daniele *pers. com.*).

Additional estimates of $\Delta_r H$ exist for other citrate complexes with identical stoichiometry, such as $CaCitrate^-$, $NiCitrate^-$, $ZnCitrate^-$, $CdCitrate^-$. Although there have been a few attemps to draw correlations between the thermodynamic properties of complexation reactions and cations properties (e.g Smith & Martell, 1987; Daniele *et al.*, 2008), such correlations cannot give more than a very rough estimate of unknown stability constants or reaction enthalpies. In the case of $MgCitrate^-$, correlations would at least require a good knowledge of complexation reactions with other alkaline earth cations than Ca^{2+} (e.g Be^{2+}, Sr^{2+}, Ba^{2+}), which are not available.

We therefore decided to keep the value selected by the CRITICAL database. Because $\Delta_r H_{\mathrm{MgCitrate^-}}$ is only available at an ionic strength of 0.1M, the procedure detailed in Figure 3.2, pathway ①, was used for temperature extrapolation. The isoelectric reaction corresponding to reaction (3.36) is :

$$\mathrm{H_2Citrate^{-}} + \mathrm{Mg^{2+}} \rightleftharpoons \mathrm{MgCitrate^{-}} + 2\,\mathrm{H^{+}}$$

where the necessary knowledge of citric acid dissociation constants were taken from Bénézeth *et al.* (1997) (see precedent section).

In order to take into account the uncertainties associated with this extrapolation, we considered the whole range of reported values for the complexation constant at 25°C and 0.1M: $\log Q_{\mathrm{MgCitrate^-}} = 3.43$ to 3.64. The two corresponding extrapolations have been drawn in Fig. 3.12a. In the following section (section 3.7.4), these two extrapolations will be tested against experimental results of magnesite solubility in the presence of citrate.

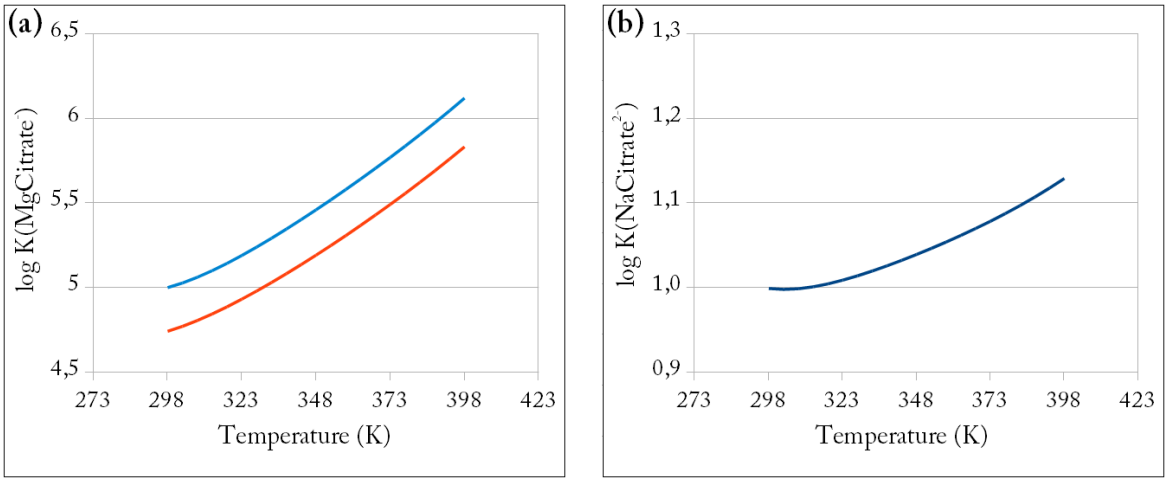

Figure 3.12 – (a) Calculated evolution of $K_{\mathrm{MgCitrate^-}}$ as a function of temperature. The two extrapolations represent a range of plausible values for the complexation constant. (b) Calculated evolution of $K_{\mathrm{NaCitrate^{2-}}}$ as a function of temperature, based on Zelenina & Zelenin (2005).

The formation of additional Mg-citrate complexes (reactions 3.37 to 3.39) was reported by a number of studies (see for instance Field *et al.*, 1975), but their temperature dependency is unknown. Complexation constants for reactions (3.37) and (3.38) were taken from CRITICAL, while that of reaction (3.39) was extrapolated to zero ionic strength from data reported at 37°C and 0.15M ionic strength by Covington & Danish (2009) (data summarized in Table 3.4). Because these species are not expected to play an important role on the speciation of our alkaline solution, the associated uncertainties will likely not significantly affect our calculations.

3.7.4 Experimental study of magnesite solubility at 120°C with 1mM citrate

Motivations

In order to gain confidence in the thermodynamic dataset used to describe Mg^{2+}- citrate complexation, we performed one solubility experiment of magnesite in the presence of 1mM citrate, at 120°C.

Magnesite solubility product, $K_{sp(Mgs)}$, is the equilibrium constant of the following reaction:

$$\mathrm{MgCO_{3(s)}} \rightleftharpoons \mathrm{Mg^{2+} + CO_3^{2-}}, \qquad K_{sp(Mgs)} = a(\mathrm{Mg^{2+}}) \cdot a(\mathrm{CO_3^{2-}})$$

In the presence of citrate, Mg^{2+} complexation induces an increase of magnesite solubility (a higher amount of magnesite can be dissolved in an aqueous solution). On the contrary,

the solubility product, which is a thermodynamic constant, does not change. Therefore, an accurate chemical speciation calculation in the presence of citrate should allow us to retrieve the exact magnesite solubility product measured experimentally by Bénézeth *et al.* (2011) on similar hydrothermally synthesized magnesite seeds.

Experimental methods

The solubility experiment at 120°C was carried out in a 400 mL titanium batch reactor which was continuously stirred with a magnetically driven stirrer (Parr Instrument Company). A description of the reactor is given in the Materials and Methods section. The method follows that used for magnesite solubility product determination by Bénézeth *et al.* (2011), for a few of their experiments).

4.22 g of synthetic magnesite seeds (see Chapter 4 for the synthesis of magnesite) were disposed in the reactor, which was filled up with approximately 300mL of freshly prepared initial solution, containing 0.07 mol/L NaCl, 0.03 mol/L $NaHCO_3$ and 0.001 mol/L of Na_3Citrate. The ionic strength was therefore fixed at ∼0.1M, $NaHCO_3$ being added in order to better control the pH of the solution. The initial solution was prepared out of ultrapure deionized water (resistivity 18.2 MΩ·cm), NaCl and $NaHCO_3$ were added in the form of reagent grade powdered chemicals, while citrate was added from a 995 ± 5 ppm Na_3Citrate certified stock solution (SCP Sciences), corresponding to a $3.856 \cdot 10^{-3} \pm 0.019 \cdot 10^{-3}$M citrate concentration. Citrate concentration in the inlet solution was confirmed by mean of DOC measurements.

The reactor vessel was then quickly sealed and connected to a CO_2 bottle via a Ti-tube, before heating up to the desired temperature. Pure CO_2 was then added to the vessel, while the exact pressure was monitored by mean of a solid-state pressure transducer (pressure reading precision: 0.1 bar). This allowed us to control and keep the gas pressure constant inside the reactor and adjust it to the desired value after each sampling procedure. The CO_2 pressure is then equal to the total pressure as read by the pressure transducer, *minus* the water steam pressure at the given temperature.

The temperature was controlled and monitored by mean of a calibrated thermocouple. Solution samples of approximately 6mL were taken periodically through a titanium valve and an *in situ* titanium 2 μm filter. Samples were analyzed for Mg concentration by flame atomic absorption spectroscopy (AAS) using a range of Mg standard solutions from 0.1 to 0.6 ppm prepared with the same experimental matrix solution, with an uncertainty of ±2% and a detection limit of $6 \cdot 10^{-7}$ mol·kg^{-1}.

Results

Achievement of equilibrium was verified by the measurement of constant dissolved magnesium concentrations within analytical uncertainties in successive solution samples, as shown in Fig.3.13.

In order to calculate the chemical speciation of the solution, it is assumed that the solution is in equilibrium with the applied CO_2 partial pressure, thus fixing pH and the total dissolved

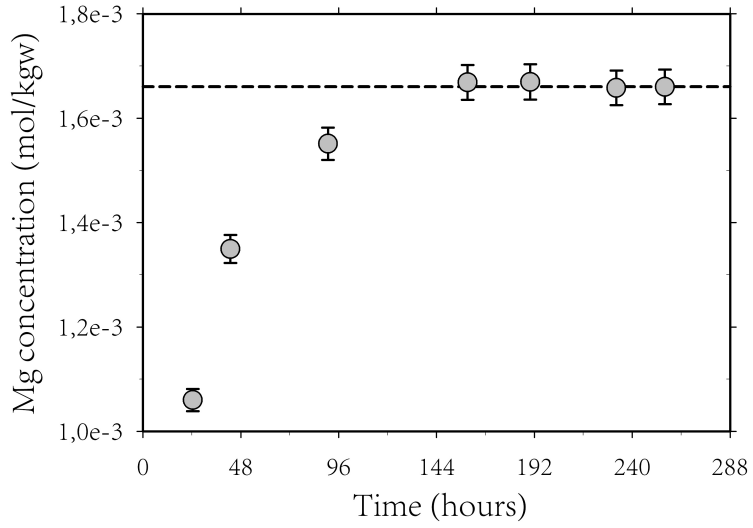

Figure 3.13 – Evolution of Mg concentration with time during the course of the magnesite solubility experiment. Stability of Mg concentration (as symbolized by the dashed line) indicates equilibrium is reached.

inorganic carbon (TDIC) concentration. The parameters of the solution at equilibrium are summarized in Table 3.2.

T(°C)	[Citrate] (mol/kg)	[Mg_{tot}] (mol/kg)	pCO_2 (bars)
120	10^{-3}	$1.660 \cdot 10^{-3} \pm 2.5 \cdot 10^{-5}$	15.2 ± 0.1

Table 3.2 – Result of the solubility experiment performed in a Ti-batch reactor.

In their study, Bénézeth *et al.* (2011) used the Lindsay (1989) activity model to derive magnesite solubility product directly from their experimental results, assuming Mg complexation with carbonate species is negligible in hydrogen electrode concentration cell experiments, at low pCO_2. In this case, $[Mg_{tot}] \sim [Mg^{2+}]$, and carbonate speciation can be calculated directly from chemical equilibria.

In our case, at high pCO_2, and in the presence of citrate, the use of a chemical speciation code is mandatory to calculate the activity of Mg^{2+} and CO_3^{2-}. In order to allow for a direct comparison with the results of Bénézeth *et al.* (2011), it is important that the activity model used for speciation calculation is close to the Lindsay (1989) model used by the authors.

The speciation calculations were performed with PHREEQC with its `llnl.dat` database, which was modified in order to use the classical Davies model for activity coefficients, which gives closer results to the Lindsay (1989) model then the B-dot activity model normally used with the `llnl.dat` database. The database was also modified to include Patterson *et al.* (1982, 1984) data for carbonic acid dissociation, and Brown *et al.* (1996) data for Mg^{2+} hydrolysis (see section 3.8), in accordance with the thermodynamic dataset used by Bénézeth *et al.* (2011). The database also includes the data described above for Mg-citrate complexation (summarized in Table 3.4). In particular, the calculations were run with the two selected

hypothesis for $MgCitrate^-$ stability constants (see Fig. 3.12).

The apparent solubility product $Q_{sp(Mgs)} = [Mg^{2+}][CO_3^{2-}]$ is calculated from the result of the speciation calculation. The solubility product is then expressed as:

$$K_{sp(Mgs)} = Q_{sp(Mgs)}\ \gamma_{Mg^{2+}}\gamma_{CO_3^{2-}}$$

where γ_i is the activity coefficient of the subscripted species, and is determined according to eq. (3.20) (see Section 3.3). The results of the calculations with our two hypothesis for $K_{MgCitrate^-}$ are summarized in Table 3.3.

$\log K_{MgCitrate^-}$ (120°C)	pH	I (mol/kg)	[TDIC] (mol/kg)	$[Mg^{2+}]$ (mol/kg)	$[CO_3^{2-}]$ (mol/kg)	$\log Q_{sp(Mgs)}$	γ_{NaCl}	$\log K_{sp(Mgs)}$
6.05	5.70	0.1035	$1.829.10^{-1}$	$6.293.10^{-4}$	$2.934.10^{-6}$	**-8.734**	0.7313	**-9.82 ± 0.04**
5.76	5.70	0.1039	$1.829.10^{-1}$	$7.054.10^{-4}$	$2.947.10^{-6}$	-8.682	0.7310	-9.77 ± 0.04

Table 3.3 – Results of the chemical speciation calculation performed from the solution chemistry detailed in Table 3.2, and determination of $K_{sp(Mgs)}$ with two hypothesis for $MgCitrate^-$ stability constant. Values for $K_{MgCitrate^-}$ were calculated based on data summarized in Table 3.4. Uncertainties on $\log K_{sp(Mgs)}$ were calculated based on estimated uncertainties on $[Mg^{2+}]$ and pCO_2.

The value of $\log K_{sp(Mgs)}$ determined at 120°C from the fit proposed by Bénézeth *et al.* (2011) is **-9.824 ± 0.15**. The results of their two batch reactor solubility experiments at 120°C were recalculated using the exact same procedure as here, giving $\log K_{sp(Mgs)}$ of -9.84 and -9.77 at 30 and 15 bars pCO_2, respectively [2].

It can therefore be concluded that :

- Our estimation of Mg-citrate speciation is fairly accurate, leading to a magnesite solubility product in excellent agreement with the experimental determination of Bénézeth *et al.* (2011).
- **The higher hypothesis for $MgCitrate^-$ stability constant ($\log K_{MgCitrate^-}$ (120°C) = 6.05 and $\log K_{MgCitrate^-}$ (25°C) = 5.00) gives the best agreement with the global estimation by Bénézeth *et al.* (2011)**. It will therefore be used for chemical speciation calculation of solutions containing Mg^{2+} and citrate.

[2] It should be noted that, although Bénézeth *et al.* (2011) used *in situ* pH electrodes to better constrain the pH of their experimental solutions, calculations based on only pCO_2 give extremely close results for $K_{sp(Mgs)}$ - within 0.01 log units.

Based on this choice, the speciation diagram presented in Fig. 3.14 was plotted. It indicates that in the investigated conditions, citrate speciation is dominated by $MgCitrate^{-}$, with $Citrate^{3-}$ and $NaCitrate^{-}$ present in smaller quantities. All other citrate species and complexes are present in negligible quantities.

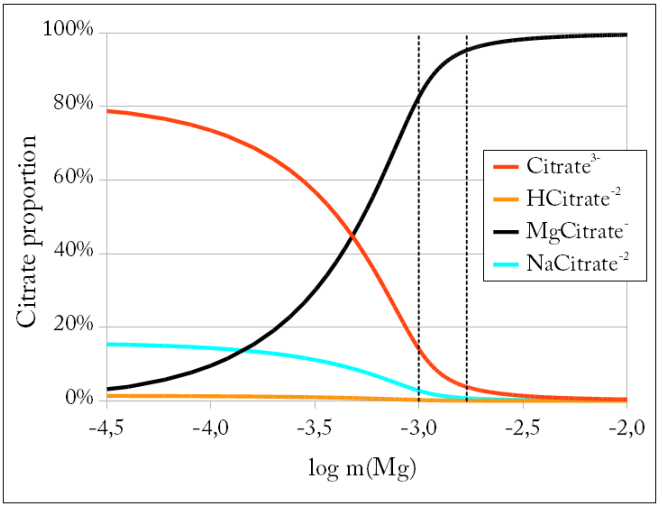

Figure 3.14 – Speciation of 1mM of citrate at 120°C as a function of total magnesium molality (in $mol{\cdot}kgw^{-1}$). The present example was drawn at pH 8, with 90mM of NaCl as background electrolyte. Ionic strength is close to 0.1M. Vertical dashed lines indicate the range of Mg^{2+} molality investigated in our experiments with 1mM citrate.

3.8 Additional modifications of the thermodynamic database

Besides the integration of the organic species presented above, two additional modifications were done to the `llnl.dat` database :

Carbonic acid dissociation

An accurate calculation of carbonate speciation is crucial for a precise determination of saturation indices of carbonate minerals. Carbonic acid dissociation follows the following chemical reactions:

$$CO_{2(aq)} + H_2O \rightleftharpoons HCO_3^- + H^+, \qquad K_{a1} \tag{3.40}$$

$$HCO_3^- \rightleftharpoons CO_3^{2-} + H^+, \qquad K_{a2} \tag{3.41}$$

Figure 3.15 presents a comparison between the `llnl.dat` estimation of K_{a1} and K_{a2}, and the data from Millero *et al.* (2007), which propose a fit valid up to 250°C, based on the widely accepted experimental data of Patterson *et al.* (1982, 1984). Fig. 3.15 reveals that there are significant differences between the two datasets concerning the second dissociation constant, above ca. 80°C. We therefore used the data of Millero *et al.* (2007), which were fitted according to the PHREEQC analytical expression (eqn. 3.23), with coefficients listed in Table 3.4.

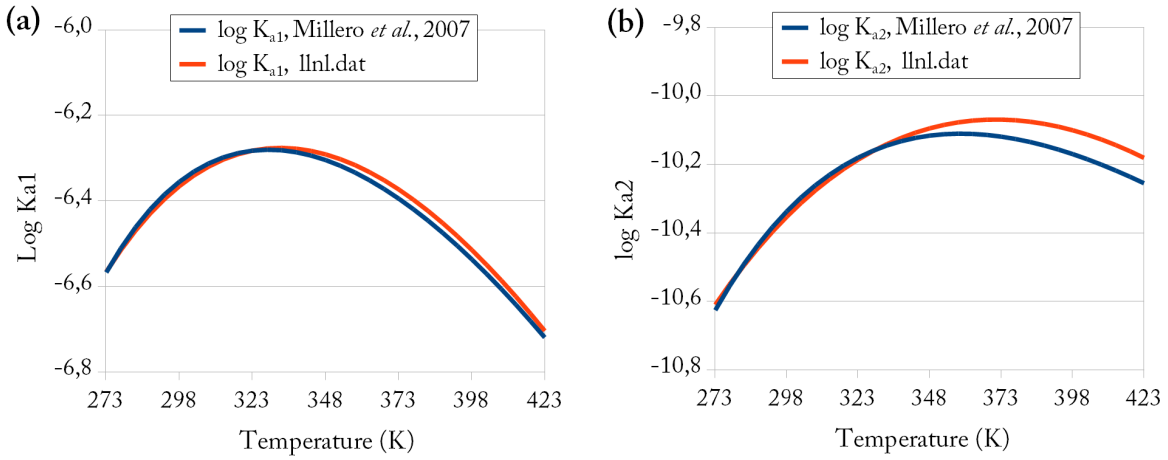

Figure 3.15 – (a) Carbonic acid first dissociation constant as a function of temperature. The data of the `llnl.dat` database are in good agreement with Millero *et al.* (2007). (b) Carbonic acid second dissociation constant as a function of temperature. There are substantial differences between the `llnl.dat` data and Millero *et al.* (2007), reaching up to 0.07 log units at 120°C.

Mg^{2+} hydrolysis

The data for Mg^{2+} first hydrolysis constant according to the following reaction :

$$Mg^{2+} + H_2O \rightleftharpoons MgOH^+ + H^+$$

were taken from Brown *et al.* (1996). The corresponding data are listed in Table 3.4.

Chemical reaction	$\log K^0$(25°C)	$\Delta_r H^0$ (kJ/mol)	$\Delta_r Cp^0$ (J/K/mol)	$\log K$(100°C)	$\log K$(120°C)	PHREEQC parameters A1	A2	A3	A4	A5
$H_2Oxalate = HOxalate^- + H^+$	-1.401[a]	-0.7 ± 0.7[a]	-231± 6[a]	-1.66	-1.78	-739.3678	-0.119019	41387.414	268.140027	-2565187
$HOxalate^- = Oxalate^{2-} + H^+$	-4.264[a]	-7.3 ± 0.5[a]	-229 ± 27[a]	-4.78	-4.97	-917.1163	-0.158607	48446.628	335.08197	-2799098
$Mg^{2+} + Oxalate^{2-} = MgOxalate$	3.430[b]	13.89[b]	347.1[b]	4.28	4.56	875.623	0.148736	-48542.17	-318.05465	2958184
$Na^+ + Oxalate^{2-} = NaOxalate^-$	0.860[b]	4.88[b]	344.6[b]	1.38	1.58	570.1005	0.0951661	-33325.7	-206.3708	2205606
$EDTA^{4-} + H^+ = HEDTA^{3-}$	**11.09**[c]	**-22.36**[d]	**228 ± 20**[e]	**10.54**	**10.49**	-1425.172	-0.197970	81143.415	515.299	-4617282
	10.19[f]	-22.36[d]	228 ± 20[e]	9.63	9.58	221.094	0.044402	-10500.70	-79.9084	782793
$HEDTA^{3-} + H^+ = H_2EDTA^{2-}$	6.71[c]	-15.45[d]	163 ± 2[e]	6.49	6.45	-199.8294	-0.01590	13957.336	70.2891	-825650
	6.88[f]	**-15.45**[d]	**163 ± 2**[e]	**6.32**	**6.28**	-199.9995	-0.01590	13957.341	70.2891	-825650
$Mg^{2+} + EDTA^{4-} = MgEDTA^{2-}$	10.45[g]	18 ± 1[h]	432.8[i]	11.52	11.85	-623.588	-0.051327	40081.480	219.8435	-2585156
	10.71[j]	**18 ± 1**[h]	**432.8**[i]	**11.78**	**12.11**	-623.329	-0.051327	40081.50	219.8437	-2585157
$Na^+ + EDTA^{4-} = NaEDTA^{3-}$	2.7[k]	4 ± 3[l]	243.2[e]	2.83	2.93	-716.294	-0.092745	39965.868	257.5537	-2195631
$H_3Citrate = H_2Citrate^- + H^+$	-3.127[m]	4.1 ± 0.2[m]	-162 ± 7[m]	-3.137	-3.176	-629.0840	-0.097611	35073	227.0593	-2170870
$H_2Citrate^- = HCitrate^- + H^+$	-4.759[m]	2.2 ± 0.1[m]	-192 ± 15[m]	-4.874	-4.945	-620.2920	-0.097611	34692	223.3623	-2170870
$HCitrate^{2-} = Citrate^{3-} + H^+$	-6.397[m]	-3.6 ± 0.3[m]	-231 ± 7[m]	-6.761	-6.896	-609.3330	-0.097611	34388	218.6843	-2170870
$Mg^{2+} + Citrate^{3-} = MgCitrate^-$	4.74[h]	8.7	-	5.49	5.76	2904.3237	0.45882	-158646.72	-1054.377	9308149.6
	5.00[h]	**7.7**	**-**	**5.77**	**6.05**	3780.587	0.58618	-207969.83	-1370.2973	12257385.1
$HCitrate^{2-} + Mg^{2+} = MgHCitrate$	2.59[h]	-	-	-	-	-	-	-	-	-
$H_2Citrate^- + Mg^{2+} = MgH_2Citrate^+$	1.0[h]	-	-	-	-	-	-	-	-	-
$2\,Citrate^{3-} + Mg^{2+} = Mg(Citrate)_2^{4-}$	5.49[n]	-	-	-	-	-	-	-	-	-
$Na^+ + Citrate^{3-} = NaCitrate^{2-}$	1.00[O]	-0.47 ± 0.36[O]	120 ± 30[O]	1.08	1.12	1434.9759	0.219719	-78510.05	-520.379	4576387
$Citrate^{3-} + 2\,Na^+ = Na_2Citrate^-$	1.81[h]	-5.1[p]	-	-	-	-	-	-	-	-
$Na^+ + Citrate^{3-} + H^+ = NaHCitrate^-$	6.45[p]	-3.6[p]	-	-	-	-	-	-	-	-
$CO_2 + H_2O = HCO_3^- + H^+$	-6.355[q]	-	-	-6.395	-6.505	-276.7773	-0.055589	15540.60	100.31795	-1187414
$HCO_3^- = CO_3^{2-} + H^+$	-10.337[q]	-	-	-10.119	-10.157	125.8913	0.012673	-5974.26	-48.51880	7752.9
$Mg^{2+} + H_2O = MgOH^+ + H^+$	-11.682[r]	-	-	-9.399	-8.925	257.2578	0.0367237	-18601.93	-92.37876	985628

Table 3.4 – Summary of the selected thermodynamic data for the present study. Where two possibilities of temperature extrapolation existed, both are reported here. The bold characters designate which of the two was actually used for chemical speciation calulations. Parameters A1 - A5 refer to eqn. 3.23 and describe analytically the temperature dependence of the equilibrium constant. Superscripted letters refer to the literature source of the selected data, as follows : a = Kettler *et al.* (1998); b = SUPRCT92 (Johnson *et al.* (1992)); c = Daniele *et al.* (1985); d = Carini & Martell (1953); e = Hovey *et al.* (1988); f = Mizera *et al.* (1999); g = Smith & Martell (1987); h = CRITICAL (Smith *et al.* (1998)); i = Hovey & Tremaine (1985); j = Arena *et al.* (1983); k = Felmy & Mason (2003); l = Hummel *et al.* (2005); m = Bénézeth *et al.* (1997); n = Covington & Danish (2009); O = Zelenina & Zelenin (2005); p = `minteq.dat`; q = Millero *et al.* (2007); r = Brown *et al.* (1996).

Appendix: Selected data by Hummel *et al.* (2005)

While going through the writing of this chapter, I found out that a book entitled "*Chemical thermodynamics of compounds and complexes of U, Np, Pu, Am, Tc, Se, Ni, and Zr, with selected organic ligands*" by Wolfgang Hummel and coauthors, published by the OECD Nuclear Energy Agency, contained a thorough and extensive critical review of existing thermodynamic data concerning a few organic acids - including oxalic acid, citric acid, and EDTA - and their interactions with a number of actinides, as well as with Na^+, K^+, Mg^{2+} and Ca^{2+}.

The literature review is tremendous, and exceeds by far what we have been able to review for our own thermodynamic data selection. Furthermore, after critical selection of valuable experimental data, the authors derived the standard thermodynamic constants using the Specific Interaction Theory (SIT) for extrapolation to infinite dilution, by fitting ion interaction coefficients to the data acquired in different background electrolytes and at different ionic strength. The method therefore stands on a stronger basis than our method for extrapolation to zero ionic strength, and the data selected by Hummel *et al.* (2005) should be regarded as more trustful than our choices.

Selected data for our chemical reactions of interest are listed in Table 3.5, and it is insightful to compare our data selection with this dataset.

Chemical reaction	$\log K^0$(25°C)	$\pm$	$\Delta_r H^0$ (kJ/mol)	$\pm$	$\Delta_r Cp^0$ (J/K/mol)	$\pm$
$H_2Oxalate = HOxalate^- + H^+$	-1.40	0.03	-3.3	0.5	-	
$HOxalate^- = Oxalate^{2-} + H^+$	-4.25	0.01	-7.3	0.1	-	
$Mg^{2+} + Oxalate^{2-} = MgOxalate$	3.56	0.04	-		-	
$Mg^{2+} + 2\,Oxalate^{2-} = Mg(Oxalate)_2^{2-}$	5.17	0.08	-		-	
$Na^+ + Oxalate^{2-} = NaOxalate^-$			no recommendation			
$EDTA^{4-} + H^+ = HEDTA^{3-}$	11.24	0.03	-19.8	0.5	228	20
$HEDTA^{3-} + H^+ = H_2EDTA^{2-}$	6.80	0.02	-15.2	0.4	163	2
$H_2EDTA^{2-} + H^+ = H_3EDTA^-$	3.15	0.02	7.1	0.4	-	
$H_3EDTA^- + H^+ = H_4EDTA$	2.23	0.05	1.9	1.5	-	
$H_4EDTA + H^+ = H_5EDTA^+$	1.30	0.1	-		-	
$H_5EDTA^+ + H^+ = H_6EDTA^{2+}$	-0.50	0.2	-		-	
$Mg^{2+} + EDTA^{4-} = MgEDTA^{2-}$	10.90	0.1	19.8	0.4	-	
$Mg^{2+} + HEDTA^{3-} = MgHEDTA^-$	4.50	0.2	-		-	
$Na^+ + EDTA^{4-} = NaEDTA^{3-}$	2.80	0.2	-4.0	3	243	25
$Na^+ + HEDTA^{3-} = NaHEDTA$	< 1					
$H_3Citrate = H_2Citrate^- + H^+$	-3.13	0.01	4.5	0.3	-116	6
$H_2Citrate^- = HCitrate^- + H^+$	-4.78	0.01	2.4	0.3	-167	8
$HCitrate^{2-} = Citrate^{3-} + H^+$	-6.36	0.02	-3.3	0.3	-222	14
$Mg^{2+} + Citrate^{3-} = MgCitrate^-$	4.81	0.03	-		-	
$HCitrate{-}2 + Mg^{2+} = MgHCitrate$	2.60	0.07	-		-	
$H_2Citrate^- + Mg^{2+} = MgH_2Citrate^+$	1.31	0.16	-		-	
$Na^+ + Citrate^{3-} = NaCitrate^{2-}$			no recommendation			

Table 3.5 – Critically selected data by Hummel *et al.* (2005).

It appears that most data selected by Hummel *et al.* (2005) are in close agreement with the data used for our speciation calculations. There is a significant difference concerning

$K_{\mathrm{MgOxalate}}$, Hummel *et al.* (2005) recommending a higher complexation constant compared to the value selected by Prapaipong *et al.* (1999), and reported in SUPCRT92. This implies that Mg^{2+} complexation by $Oxalate^{2-}$ could be slightly higher than calculated.

Small differences concerning EDTA species (equilibrium constants and reaction enthalpies) do not, as exposed above, impact significantly the result of speciation calculations, which remain dominated by $MgEDTA^{2-}$ in our experimental conditions.

The recommended value for $K_{\mathrm{MgCitrate^-}}$ should be used instead of the two estimations we used, but because Mg-Citrate complexation was validated at high temperature by mean of a solubility experiment, we believe our calculations are accurate.

It should be noted that the review by Hummel *et al.* (2005) is limited in most cases to data published up to 2001, and therefore lacks more recent valuable data we have been using in some cases. In addition, little attention has been paid to extrapolation to high temperature, and reaction heat capacities are seldom reported.

Finally, the good agreement between Hummel *et al.* (2005) recommendations based on a thorough and extensive literature review, and our data selection, gives confidence that our chemical speciation calculations are reasonably accurate over a large temperature range.

Bibliography

Allison, J.D., Kevin, J., Gradac, N., & Brown, D.S. 1991. *MINTEQA2/PRODEFA2: A Geochemical Assessment Model for Environmental Systems: Version 3.0 User's Manual*. National Technical Information Service.

Amico, P., Daniele, P.G., Rigano, C., & Sammartano, S. 1982. Stability of calcium- and magnesium-citrate complexes in aqueous solutions. *Annali di chimica*, 12, 1–24.

Anderson, G.M., Castet, S., Schott, J., & Mesmer, R.E. 1991. The density model for estimation of thermodynamic parameters of reactions at high temperatures and pressures. *Geochimica et Cosmochimica Acta*, 55(7), 1769–1779.

Archer, D. G. 1992. Thermodynamic properties of the NaCl+H_2O system. II. Thermodynamic properties of NaCl(aq), NaCl·$2H_2O$(cr), and phase equilibria. *Journal of Physical and Chemical Reference Data*, 21(4), 793–829.

Arena, G., Musumeci, S., Purrello, R., & Sammartano, S. 1983. Calcium- and magnesium-EDTA complexes. Stability constants and their dependence on temperature and ionic strength. *Thermochimica Acta*, 61(1-2), 129–138.

Barney, J.E., Argersinger Jr, W.J., & Reynolds, C.A. 1951. A study of some complex chlorides and oxalates by solubility measurements. *Journal of the American Chemical Society*, 73(8), 3785–3788.

Bénézeth, P., Palmer, D.A., & Wesolowski, D.J. 1997. Dissociation quotients for citric acid in aqueous sodium chloride media to 150°C. *Journal of Solution Chemistry*, 26(1), 63–84.

Bénézeth, P., Saldi, G.D., Dandurand, J.L., & Schott, J. 2011. Experimental determination of the solubility product of magnesite at 50 to 200°C. *Chemical Geology*, 286, 21–31.

Brown, P.L., Drummond, S.E., & Palmer, D.A. 1996. Hydrolysis of magnesium (II) at elevated temperatures. *J. Chem. Soc., Dalton Trans.*, 3071–3075.

Busey, R.H., & Mesmer, R.E. 1976. The ionization of water in NaCl media to 300°C. *Journal of Solution Chemistry*, 5(2), 147–152.

Busey, R.H., & Mesmer, R.E. 1978. Thermodynamic quantities for the ionization of water in sodium chloride media to 300°C. *Journal of Chemical & Engineering Data*, 23(2), 175–176.

Carini, F.F., & Martell, A.E. 1953. Thermodynamics of metal chelate formation. I. The third and fourth dissociation constants of ethylenediaminetetraacetic acid. *Journal of the American Chemical Society*, 75(19), 4810–4813.

Cobble, J.W., Murray Jr, R.C., Turner, P.J., & Chen, K. 1982. High-temperature thermodynamic data for species in aqueous solution. *Electric Power Research Institute (EPRI NP-2400)*.

Covington, A.K., & Danish, E.Y. 2009. Measurement of magnesium stability constants of biologically relevant ligands by simultaneous use of pH and ion-selective electrodes. *Journal of Solution Chemistry*, 38(Oct.), 1449–1462.

Daniele, P.G., Rigano, C., & Sammartano, S. 1981. The formation of proton and alkali-metal complexes with ligands of biological interest in aqueous solution. Thermodynamics of H^+, Na^+ and K^+-oxalate complexes. *Thermochimica Acta*, 46(2), 103–116.

Daniele, P.G., Rigano, C., & Sammartano, S. 1983. The formation of proton and alkali metal complexes with ligands of biological interest in aqueous solution. Thermodynamics of Li^+, Na^+ and K^+-dicarboxylate complex formation. *Thermochimica Acta*, 62(1), 101–112.

Daniele, P.G., Rigano, C., & Sammartano, S. 1985. Ionic strength dependence of formation constants. Alkali metal complexes of ethylenediaminetetraacetate, nitrilotriacetate, diphosphate, and tripolyphosphate in aqueous solution. *Analytical Chemistry*, 57(14), 2956–2960.

Daniele, P.G., Foti, C., Gianguzza, A., Prenesti, E., & Sammartano, S. 2008. Weak alkali and alkaline earth metal complexes of low molecular weight ligands in aqueous solution. *Coordination Chemistry Reviews*, 252(10-11), 1093–1107.

Davies, C.W. 1962. *Ion association*. Butterworths London.

Drummond, S.E. 1981. *Boiling and mixing of hydrothermal fluids: chemical effects on mineral precipitation*. Ph.D. thesis, Pennsylvania State University.

Felmy, A.R., & Mason, M.J. 2003. An aqueous thermodynamic model for the complexation of sodium and strontium with organic chelates valid to high ionic strength. I. Ethylenedinitrilotetraacetic acid (EDTA). *Journal of solution chemistry*, 32(4), 283–300.

Field, T.B., Coburn, J., McCourt, J.L., & McBryde, WAE. 1975. Composition and stability of some metal citrate and diglycolate complexes in aqueous solution. *Analytica Chimica Acta*, 74(1), 101–106.

Finlayson, B., Smith, A., & DuBois, L. 1975. The stability constants of magnesium oxalate complexes. *Investigative Urology*, 13(1), 20–24.

Glusker, J.P. 1980. Citrate conformation and chelation: enzymic implications. *Accounts of Chemical Research*, 13(10), 345–352.

Guggenheim, E.A. 1966. *Applications of statistical mechanics*. Clarendon P.

Helgeson, H.C. 1967. Thermodynamics of complex dissociation in aqueous solution at elevated temperatures. *The Journal of Physical Chemistry*, 71(10), 3121–3136.

Helgeson, H.C. 1969. Thermodynamics of hydrothermal systems at elevated temperatures and pressures. *American Journal of Science*, 267(7), 729–804.

Hovey, J.K., & Tremaine, P.R. 1985. Thermodynamics of the complexes of aqueous iron (III), aluminum and several divalent cations with EDTA: heat capacities, volumes, and variations in stability with temperature. *The Journal of Physical Chemistry*, 89(25), 5541–5549.

Hovey, J.K., Hepler, L.G., & Tremaine, P.R. 1988. Thermodynamics of aqueous EDTA systems: Apparent and partial molar heat capacities and volumes of aqueous $EDTA^{4-}$, $HEDTA^{3-}$, H_2EDTA^{2-}, $NaEDTA^{3-}$, and $KEDTA^{3-}$ at 25°C. Relaxation effects in mixed aqueous electrolyte solutions and calculations of temperature dependent equilibrium constants. *Canadian Journal of Chemistry*, 66(4), 881–896.

Hummel, W., Anderegg, G., Puigdomènech, I., Rao, L., & Tochiyama, O. 2005. *Chemical thermodynamics of compounds and complexes of U, Np, Pu, Am, Tc, Se, Ni, and Zr, with selected organic ligands*. OECD Nuclear Energy Agency edn. Chemical Thermodynamics, vol. 9. Elsevier Science.

Johnson, J.W., Oelkers, E.H., & Helgeson, H.C. 1992. SUPCRT92: A software package for calculating the standard molal thermodynamic properties of minerals, gases, aqueous species, and reactions from 1 to 5000 bar and 0 to 1000°C. *Computers & Geosciences*, 18(7), 899–947.

Kettler, R. M., Wesolowski, D. J., & Palmer, D. A. 1998. Dissociation constants of oxalic acid in aqueous sodium chloride and sodium trifluoromethanesulfonate media to 175°C. *Journal of Chemical & Engineering Data*, 43(3), 337–350.

Kondoh, A., & Oi, T. 1998. Interaction of alkaline earth metal ions with carboxylic acids aqueous solutions studied by ^{13}C NMR spectroscopy. *Zeitschrift für Naturforschung*, 53a, 77–91.

Lindsay, W.T. 1980. Estimation of concentration quotients for ionic equilibria in high temperature water: The model substance approach. *Pages 284–294 of: Proceedings of the 41st International Water Conference*.

Lindsay, W.T. 1989. Chemistry of steam cycle solutions: principles. *Pages 341–544 of: The ASME Handbook on Water Technology for Thermal Power Systems*, Paul Cohen edn. ASME.

Meissner, H.P., & Tester, J.W. 1972. Activity coefficients of strong electrolytes in aqueous solutions. *Industrial & Engineering Chemistry Process Design and Development*, 11(1), 128–133.

Mesmer, R.E., & Baes, C.F. 1974. Phosphoric acid dissociation equilibria in aqueous solutions to 300°C. *Journal of Solution Chemistry*, 3(4), 307–322.

Mesmer, R.E., Marshall, W.L., Palmer, D.A., Simonson, J.M., & Holmes, H.F. 1988. Thermodynamics of aqueous association and ionization reactions at high temperatures and pressures. *Journal of Solution Chemistry*, 17(8), 699–718.

Millero, F., Huang, F., Graham, T., & Pierrot, D. 2007. The dissociation of carbonic acid in NaCl solutions as a function of concentration and temperature. *Geochimica et Cosmochimica Acta*, 71(1), 46–55.

Mizera, J., Bond, A.H., Choppin, G.R., & Moore, R.C. 1999. Dissociation constants of carboxylic acids at high ionic strengths. *Pages 113–124 of:* Reed, Donald Timothy, Clark, Sue B., & Rao, Linfeng (eds), *Actinide Speciation in High Ionic Strength Media*. Springer.

Money, R.W., & Davies, C.W. 1932. The extent of dissociation of salts in water. Part IV.: bi-bivalent salts. *Trans. Faraday Soc.*, 28, 609–614.

Oelkers, E.H., Benezeth, P., & Pokrovski, G.S. 2009. Thermodynamic databases for water-rock interaction. *Reviews in Mineralogy and Geochemistry*, 70(1), 1.

Parkhurst, D.L., & Appelo, C.A.J. 1999. User's guide to PHREEQC (version 2) : a computer program for speciation, batch-reaction, one-dimensional transport, and inverse geochemical calculations. *US Geological Survey Water-Resources Investigations Report*, 99(4259), 312.

Partanen, J.I., Juusola, P.M., & Covington, A.K. 2009. Re-evaluation of the First and Second Stoichiometric Dissociation Constants of Oxalic Acid at Temperatures from 0 to 60°C in Aqueous Oxalate Buffer Solutions with or without Sodium or Potassium Chloride. *Journal of Solution Chemistry*, 38(11), 1385–1416.

Patterson, C.S., Slocum, G.H., Busey, R.H., & Mesmer, R.E. 1982. Carbonate equilibria in hydrothermal systems: first ionization of carbonic acid in NaCl media to 300°C. *Geochimica et Cosmochimica Acta*, 46(9), 1653–1663.

Patterson, C.S., Busey, R.H., & Mesmer, R.E. 1984. Second ionization of carbonic acid in NaCl media to 250°C. *Journal of solution chemistry*, 13(9), 647–661.

Pitzer, K.S., & Mayorga, G. 1973. Thermodynamics of electrolytes. II. Activity and osmotic coefficients for strong electrolytes with one or both ions univalent. *The Journal of Physical Chemistry*, 77(19), 2300–2308.

Prapaipong, P., Shock, E. L, & Koretsky, C. M. 1999. Metal-organic complexes in geochemical processes: Temperature dependence of the standard thermodynamic properties of aqueous complexes between metal cations and dicarboxylate ligands. *Geochimica et cosmochimica acta*, 63(17), 2547–2577.

Puigdomenech, I., Joseph, A., Plyasunov, A.V., & Grenthe, I. 1997. Chapter X: Temperature Corrections to Thermodynamic data and Enthalpy Calculations. *Pages 438–494 of: Modelling in Aquatic Geochemistry*. OECD Publications.

Saldi, Giuseppe D. 2009. *Les cinétiques de dissolution et précipitation de la magnésite aux conditions hydrothermales*. Ph.D. thesis, Université Paul Sabatier, Toulouse.

Scatchard, G. 1936. Concentrated Solutions of Strong Electrolytes. *Chemical Reviews*, 19(3), 309–327.

Shock, E.L. 1995. Organic acids in hydrothermal solutions: standard molal thermodynamic properties of carboxylic acids and estimates of dissociation constants at high temperatures and pressures. *American Journal of Science*, 295(5), 496.

Shock, E.L., & Helgeson, H.C. 1988. Calculation of the thermodynamic and transport properties of aqueous species at high pressures and temperatures: Correlation algorithms for ionic species and equation of state predictions to 5 kb and 1000°C. *Geochimica et Cosmochimica Acta*, 52(8), 2009–2036.

Smith, R.M., & Martell, A.E. 1987. Critical stability constants, enthalpies and entropies for the formation of metal complexes of aminopolycarboxylic acids and carboxylic acids. *Science of the Total Environment*, 64(1-2), 125–147.

Smith, R.M., Martell, A.E., & Motekaitis, R.J. 1998. *NIST critically selected stability constants of metal complexes database*. National Institute of Standards & Technology.

Tanger, J.C., & Helgeson, H.C. 1988. Calculation of the thermodynamic and transport properties of aqueous species at high pressures and temperatures; revised equations of state for the standard partial molal properties of ions and electrolytes. *American Journal of Science*, 288(1), 19.

Thakur, P., Mathur, J.N., Moore, R.C., & Choppin, G.R. 2007. Thermodynamics and dissociation constants of carboxylic acids at high ionic strength and temperature. *Inorganica Chimica Acta*, 360(12), 3671–3680.

Zelenina, T.E., & Zelenin, O.Y. 2005. Complexation of citric and tartaric acids with Na and K ions in aqueous solution. *Russian Journal of Coordination Chemistry*, 31(4), 235–242.

Chapter 4

Magnesite growth inhibition by organic ligands: an experimental study at 100 to 150°C

Sommaire

Magnesite growth inhibition by organic ligands: an experimental study at 100 to 150°C *

Quentin Gautier[1,2], Pascale Bénézeth[1], Jacques Schott[1]

[1] Géosciences Environnement Toulouse, Observatoire Midi-Pyrénées, CNRS, Université de Toulouse, 14, avenue Edouard Belin, 31400 Toulouse, France
[2] Université Paris-Est, Laboratoire Navier, 6/8, avenue Blaise Pascal, Champs-sur-Marne, 77455 Marne-La-Vallée, France

Abstract

It has been proposed that simple organic ligands which accelerate Mg-silicates dissolution could be used to accelerate CO_2 mineral sequestration through mineral carbonation. The influence of these ligands on magnesite growth has however never been studied.
In this work, we investigate the influence of three organic ligands: oxalate, citrate and EDTA on magnesite growth in alkaline conditions and at hydrothermal temperatures (100, 120 and 146°C). We show that the studied carboxylates decrease magnesite growth rates, due to two converging mechanisms:

- Complexation of Mg^{2+} in solution, which decreases the saturation state of the solution. This effect was carefully taken into account by building a thermodynamic database relevant for the studied system and valid and the experimental temperatures (presented in Chapter 3). EDTA being the stronger chelate of the three investigated ligands, it has the strongest influence on solution saturation state.
- Adsorption of the ligand on magnesite surface growth sites, which decreases the kinetic rate constant of magnesite growth. We observed the following inhibition effectiveness of investigated organic ligands: citrate > EDTA > oxalate.

While citrate exerts the strongest growth inhibition due to adsorption, it does not apparently lead to a complete interruption of magnesite growth. Preliminary adsorption experiments suggest that citrate adsorbs to active growth sites at the mineral surface with a much higher affinity than for the bulk of the surface.

Using experimentally retrieved magnesite growth rate laws and published forsterite dissolution rate low, we performed numerical simulations in order to estimate the overall influence of the investigated ligands on the carbonation rates of forsterite. We observe that all ligands will clearly be detrimental to forsterite carbonation rates in typical conditions foreseen for Mg-silicates mineral carbonation. Their use may be positive for the carbonation of less reactive Mg-silicate minerals, but the delayed formation of magnesite could as well trigger the formation of secondary Mg-bearing phases which would reduce the maximal carbonation extent.

*This work will be submitted for publication to *Geochimica et Cosmochimica Acta* in a revised version.

4.1 Introduction

Mg or Ca-bearing silicate minerals carbonation has been proposed as a possible mitigation strategy against the emission of large amounts of CO_2 of industrial origin (Seifritz, 1990; Lackner *et al.*, 1995; IPCC, 2005). Because of their widespread abundance at the Earth's surface, Mg-silicates have received much attention as potential sources of cations for subsequent CO_2 mineralization under the form of Mg-carbonates (magnesite $MgCO_3$ being the most stable form). An extensive amount of work has thus been devoted to defining the best physico-chemical conditions for forsterite or serpentine carbonation (e.g O'connor *et al.*, 2001; McKelvy *et al.*, 2004; Chen *et al.*, 2006; Gerdemann *et al.*, 2007; Garcia *et al.*, 2010), as well as to understand the mechanism and kinetics of Mg-silicates dissolution (Pokrovsky & Schott, 2000; Rosso & Rimstidt, 2000; Liu, 2006; Hänchen *et al.*, 2006, 2007; Teir *et al.*, 2007b; Prigiobbe *et al.*, 2009), magnesite precipitation (Saldi *et al.*, 2009, 2012), and the whole carbonation process (Giammar *et al.*, 2005; Béarat *et al.*, 2006; King *et al.*, 2010; Daval *et al.*, 2011).

However, industrialization of mineral carbonation is still facing the high energy demand and high costs of the process (Newall *et al.*, 2000). The slow kinetics of the carbonation reaction is one crucial barrier to overcome. A number of studies have thus focused on how to accelerate the dissolution of the Mg-silicate phase, with the assumption that this step is limiting for the whole carbonation process. Heating, fine grinding or thermal pre-treatment of the initial material have proven to efficiently accelerate the dissolution (Park *et al.*, 2003; McKelvy *et al.*, 2004 ; Gerdemann *et al.*, 2007; Haug *et al.*, 2010), but are associated with high energetic costs (Huijgen *et al.*, 2007). Alternatively, it has been suggested that strong acids could be used to quickly dissolve the silicate mineral as part of a two-step process involving a strong pH shift for the subsequent magnesite precipitation (so-called "pH-swing process", Park & Fan, 2004; Teir *et al.*, 2007a, 2009). Here as well, the process is however limited by the high consumption of concentrated acids, and high associated costs.

Some organic ligands have the ability to enhance the rate of silicate minerals dissolution through surface complexation of surface metal groups facilitating their detachment from the crystal structure, a phenomenon known as "ligand-promoted dissolution" (see Ganor *et al.*, 2009 and references therein). Several authors have thus suggested that organic ligands could be used to accelerate Mg-silicates dissolution. Park *et al.* (2003) for instance noticed that a mixture of orthophosphoric acid, oxalic acid and EDTA greatly enhanced serpentine dissolution rate. Similarly, Krevor & Lackner (2011) have shown that high concentrations (0.1 to 15 M) of oxalate, citrate and EDTA enhance serpentine dissolution rate by one to three orders of magnitude in slightly acidic conditions, while acetate has little effect (Teir *et al.*, 2007b). Moreover, a number of studies demonstrated that forsterite dissolution rate is significantly enhanced in the presence of various organic ligands, including oxalate, citrate and EDTA, both at ambient (Grandstaff, 1986; Wogelius & Walther, 1991; Olsen & Rimstidt, 2008) and at higher temperatures (Hänchen *et al.*, 2006; Prigiobbe & Mazzotti, 2011), in a wide range of pH conditions.

Surprisingly, not a single study has addressed the question of the influence of the same organic ligands on magnesite precipitation thermodynamics and kinetics. The view that Mg-

silicate dissolution is the limiting step of CO_2 mineral sequestration has however recently been challenged in the case of forsterite carbonation by Saldi *et al.* (2012), who thoroughly studied magnesite growth kinetics as a function of temperature, solution chemistry and saturation state. The results indicate that magnesite growth is sufficiently slow that it may limit the direct carbonation of forsterite, unless the solution is highly supersaturated with respect to magnesite ($\Omega_{Mgs} = \frac{IAP}{K_{sp}} > 50$), and/or the surface area of the precipitating magnesite is much higher than that of the forsterite initial material.

It is thus essential to characterize magnesite precipitation kinetics in the presence of organic ligands, in order to estimate the global influence of dissolution enhancers on the whole carbonation process. This need is comforted by the recent study of Bonfils *et al.* (2012), who performed direct carbonation of a forsteritic olivine in the presence of high concentrations (0.1 M) of oxalate, citrate and EDTA. No magnesite was formed, although the extraction of Mg from the silicate was enhanced in the presence of the ligands. The authors attributed this observation to complexation of the dissolved magnesium by the abundant ligands, thus reducing or suppressing solution supersaturation with respect to magnesite.

Although, to our knowledge, the influence of organic ligands on Mg-carbonates precipitation has not yet been studied experimentally, insights on this problem may be gained from the abundant literature which exists on calcite ($CaCO_3$) precipitation kinetics in the presence of various organic substances. Numerous studies have indeed been performed with natural organic material such as humic and fulvic substances (Lebron & Suarez, 1996, 1998; Hoch *et al.*, 2000; Zuddas *et al.*, 2003; Lin *et al.*, 2005), polysaccharides (e.g Lakshtanov *et al.*, 2011), complex organics designed to prevent scale formation (e.g Reddy & Nancollas, 1973), natural and synthetic polypeptides (Fu *et al.*, 2005; Elhadj *et al.*, 2005, 2006; Njegic-Dzakula *et al.*, 2009; Chen *et al.*, 2011), and simple (poly)carboxylic acids (Meyer, 1984; Giannimaras & Koutsoukos, 1988; Reddy & Hoch, 2001; Westin & Rasmuson, 2005a; Lee & Reeder, 2006; Schmidt *et al.*, 2008).

The overwhelming majority of these studies, including those performed with simple carboxylates such as oxalate or citrate, points towards a reduction of calcite growth rate in the presence of the ligands, which cannot be explained only by complexation of aqueous Ca^{2+} by the ligands, but was rather attributed to adsorption of the organic substances at the mineral surface. Due to the structural and chemical similarity between calcite and magnesite, such an effect is therefore likely to be also present in the interaction between magnesite growth and organic substances.

However, a few studies performed with proteins extracted from seashell nacre (Fu *et al.*, 2005; Kim *et al.*, 2005; Heinemann *et al.*, 2011), synthetic polypeptides rich in acidic residues (Elhadj *et al.*, 2006), or peptoids (poly-N-substituted glycines, Chen *et al.*, 2011) have shown that at very low concentrations, such molecules have the ability to significantly *enhance* calcite growth, an effect that has been attributed to the facilitated desolvation of the Ca^{2+} cation at the mineral surface (Hamm *et al.*, 2010). Indeed, desolvation of the building cation is thought to play a key role in the precipitation of ionic crystals (Nielsen, 1984; Piana *et al.*, 2006), and simple molecules that are able to facilitate cation dehydration, could as well accelerate crystal growth (Piana *et al.*, 2007).

Carbonate minerals reactivity has been shown to be nicely correlated with the hydration state of the forming cation - i.e, the rate of exchange of water molecules in its coordination sphere, Pokrovsky & Schott (2002). The slow precipitation kinetics of anhydrous Mg-carbonates is indeed thought to result from the difficulties to dehydrate the strongly hydrated Mg^{2+} cation (Lippmann, 1973). On the other hand, simple organic ligands are known to accelerate the rate of water exchange rates from the hydration sphere of dissolved cations (Phillips *et al.*, 1997a,b; Sullivan *et al.*, 1999). Thus, this possible positive influence of ligands on Mg^{2+} reactivity could be favorably expressed in the rate of magnesite precipitation.

In the present study, we examine the influence of three simple organic ligands: oxalate, citrate and EDTA, on the kinetics of magnesite growth at hydrothermal temperatures. These three polycarboxylates have been chosen for their known enhancing influence of forsterite and serpentine dissolution kinetics, but also because they differ by their number of carboxylate groups, structure, and complexing properties of the Mg^{2+} cations (EDTA being the strongest chelate, and oxalate, the weakest, as presented in Chapter 3). Thus, they provide an opportunity to assess the influence of various carboxylates on the overall carbonation process of Mg-silicates.

4.2 Experimental Methods

4.2.1 Seed material

The synthetic magnesite samples used in this study were synthesized following the procedure described in Saldi *et al.* (2010, 2012). 20 g of analytical grade hydrated Mg-carbonate (magnesium hydroxide carbonate, Merck Chemicals) were placed into a 400 ml titanium rocking autoclave, together with 250 ml of high purity deionized water, and 15 to 20 g of carbonic ice. The autoclave was sealed and heated to 220 to 250°C.

After two to three weeks, the solids were recovered, rinsed in deionized water, and dried in an oven at 60°C. The synthesized magnesite crystals consisted of 2 to 30 µm rhombohedral shaped crystals. X-ray diffraction (XRD) and energy dispersive X-ray spectroscopic (EDS) analysis confirmed that the obtained powders were pure magnesite.

In order to remove the finest particles, small amounts of powder (approximately 3 g) were placed in 150 mL polypropylene beakers filled with 100 mL high purity deionized water, ultrasonized, and then left for sedimentation for 3 minutes. The supernatant was discarded, and the procedure was repeated three times for each powder aliquot. The final powders were collected, and dried again at 60°C.

The specific surface area of all synthesized magnesite powders was determined by multipoint krypton adsorption according to the BET method (Brunauer *et al.*, 1938), with an estimated uncertainty of 10%. Laser granulometry analysis, performed on a Coulter LS100Q laser particle size analyzer, indicates that the grain size distribution is relatively narrow, with a mean grain size of 17.7 to 20.5 µm (Table 4.1). The geometric surface area estimated from this grain size repartition, assuming crystals are cubic, is only slightly smaller than the BET surface area, indicating that the crystals have little microporosity and surface roughness.

Representative SEM pictures of the magnesite seeds are shown in Fig. 4.1a & b. The BET surface area measurements, results of granulometry analysis, and geometric surface area estimations for the three sets of synthetic magnesite seeds used throughout the study are reported in Table 4.1.

Magnesite seeds	S_{BET} (cm^2/g)	Mean diameter (µm)	s.d. (µm)	Variance (µm)	Median (µm)	S_{GEO} (cm^2/g)
Mgs 1	1940	-	-	-	-	n.d.
Mgs 2	1750	20.5	1.6	2.5	22.2	1114
Mgs 3	2100	17.7	1.7	2.9	18.6	1330

Table 4.1 – Results of BET specific surface area (S_{BET}) measurements and volumetric granulometry analysis on the magnesite powders used in this study. "s.d." stands for "standard deviation". The geometric specific surface area (S_{GEO}) is estimated from the grain size distribution.

4.2.2 Mixed-flow reactor experiments

Steady-state magnesite growth rates were determined from mixed-flow reactor experiments using 200 and 300 ml titanium reactors similar to those described by Gautier *et al.* (1994), following the procedure detailed by Saldi *et al.* (2012). A sketch of the experimental setting can be found in Chapter 2.

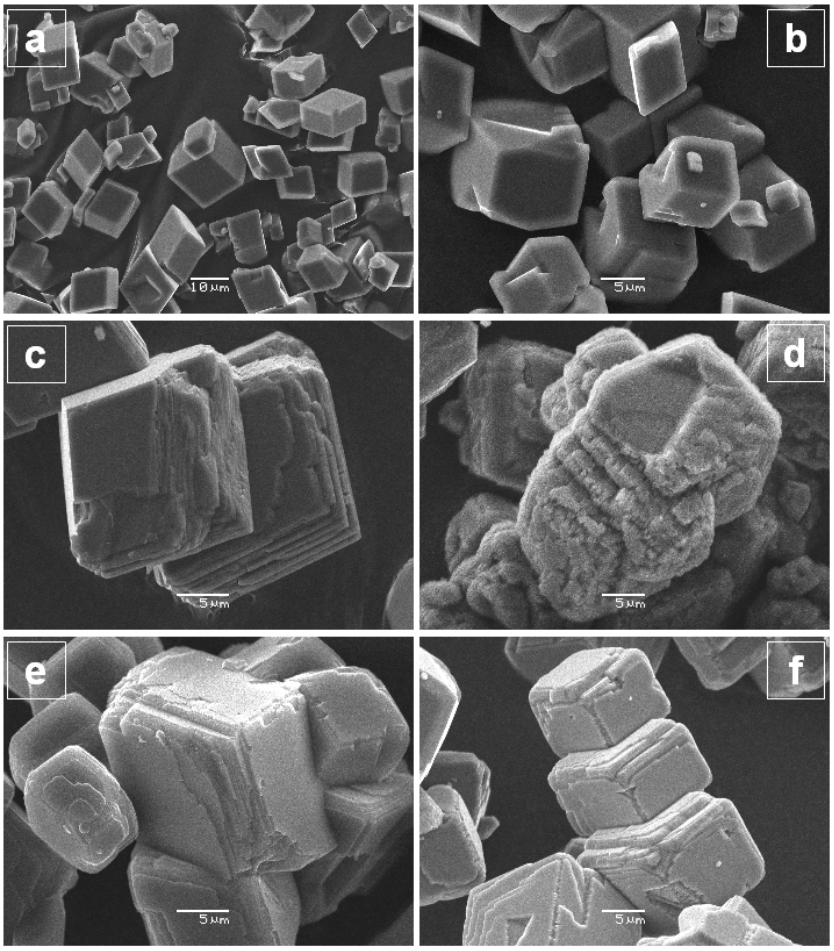

Figure 4.1 – Secondary electron SEM pictures of [a] & [b] synthesized magnesite seeds, [c] crystals grown at 120°C in the absence of ligands (exp. M24), [d] crystals grown at 120°C in the presence of 1 mM of citrate (exp. Cit8), [e] crystals grown at 146°C in the absence of ligands (exp. M28), and [f] crystals grown at 146°C in the presence of 10 mM of oxalate (exp. M9). Note the highly serrated aspect of the overgrown layers in the presence of citrate, whereas oxalate does not strongly affect the shape of precipitated layers.

At the beginning of the experiments, a small amount of seed material (Fig. 4.1a & b) was disposed into the reactors, which were filled either with high purity deionized water, or with the inlet reactive solution. Inlet solutions were stored in 5 to 10 L compressible polyethylene containers at ambient temperature, and injected into the reactor by a high pressure liquid chromatography (HPLC) pump at flow rates ranging from 0.4 to 3 ml/min. Inside the reactor, the solution was stirred at a constant rate (200 to 240 rpm) with a Parr magnetic stirrer, and kept at constant temperature $\pm$ 2°C by a furnace connected to a calibrated thermocouple. The fluid left the reactor through a 2 µm titanium filter and was cooled before passing through a back-pressure regulator which constantly maintained throughout the system a pressure higher than the water vapor pressure at the temperature of the experiment.

Experiments were in general run in series, at 146, 120 and 100°C. Series consisted of experiments with distinct fluid flow rates and/or distinct inlet solutions with a single magnesite powder. Each experimental series is noted by a distinct prefix in Tables 4.2.

Steady-state growth rates, indicated by a constant outlet Mg concentration, were calculated using:

$$R = \frac{\mathrm{FR} \cdot \Delta[Mg]_{\mathrm{tot}}}{m_{\mathrm{Mgs}} \cdot S_{\mathrm{BET}}} \tag{4.1}$$

where FR represents the fluid flow rate, $\Delta[Mg]_{\mathrm{tot}}$ stands for the difference between the inlet and outlet fluid Mg concentration at steady-state, m_{Mgs} is the initial magnesite seeds mass, S_{BET} is the initial specific BET surface area.

Experimental steady-state was verified with a minimum of three outlet fluid samples with identical Mg concentrations (within analytical uncertainties) taken over several residence times. The time necessary to reach steady-state varied from a few hours to 5 days, depending on the experimental conditions. After steady-state was confirmed, fluid flow rate and/or inlet fluid solution were changed to the next desired experimental conditions. Figure 4.2 presents an example of Mg concentration evolution during the course of such an experimental sequence.

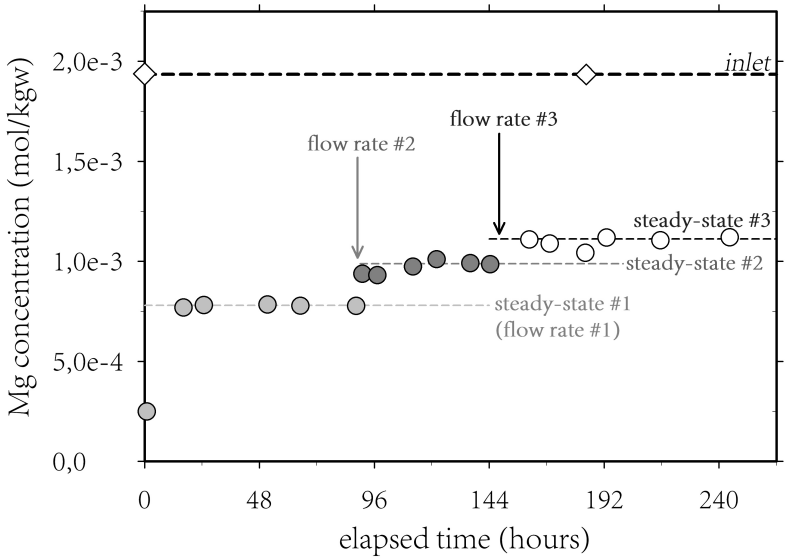

Figure 4.2 – Evolution of Mg concentration in the outlet fluid during experiments Cit5A to Cit5C. White rhombs represent the inlet solution Mg concentration. Inlet flow rate is modified after achievement of steady-state, which is verified with a minimum of 3 successive samples with identical concentrations over several residence times. In the present examples, flow rate # 1 is 0.5 mL/min, # 2 is 1.0 mL/min, and # 3 is 1.5 mL/min. The analytical uncertainty is less than the symbol size.

During a series of experiments, mineral growth leads to an increase of mineral mass, while BET measurements performed on a few final powders indicate that the specific surface area of the powders decreases during the course of the experiment. This is attributed to an increase of the grain size and to grain agglomeration (see for instance Fig. 4.1e). Both tendencies tend to compensate each other, such that the total surface area does not change by more than 25% during the experimental series. We therefore normalized the measured growth rates with respect to the initial surface area, as outlined in eq. 4.1.

The validity of this assumption was verified in a few experimental series (exp. M28 at 146°C; M40, Cit5, Edta5 at 120°C): at the end of the series, the flow rate and fluid composition were changed back to the conditions of the first experiment of the series, which had been performed on pristine powders. The obtained final growth rate, normalized to the initial surface area, always agreed closely with the initial rate, which confirms that the total reactive surface area did not significantly change during the course of the experimental series.

4.2.3 Solution preparation and chemical analyses

Experimental solutions were prepared with high purity deionized water (resistivity 18.2 MΩ), reagent grade NaCl, $MgCl_2 \cdot 6\,H_2O$, $NaHCO_3$, Na_2Oxalate, Na_3Citrate$\cdot 2\,H_2O$, Na_2H_2EDTA$\cdot 2\,H_2O$, and high purity 1M HCl and NaOH solutions (throughout the manuscript, the symbol "M" is used for "mol/L"). Organic ligands were either used directly as salts, or pre-dissolved in concentrated stock solutions stored at 4°C, from which the experimental solutions were later prepared. The NaCl concentration was adjusted to obtain an ionic strength close to 0.1 M in all experiments. Experiments were designed so as to obtain relatively low, and constant, carbonate anion chemical activities, while keeping the $a(Mg^{2+})/a(CO_3^{2-})$ ratio relatively close to one (in practical between 0.1 and 5, cf. Tables 4.7 to 4.10). Indeed, as shown by Saldi *et al.* (2012), carbonate anion exert an inhibiting influence on magnesite growth rates at high activities. On the contrary, the range of variation of the $a(Mg^{2+})/a(CO_3^{2-})$ ratio should not significantly affect the experimental results (Saldi *et al.*, 2012).

pH measurement

pH at the experimental temperature was kept between 7.6 to 8.1 for all experiments. Solution pH measurements were performed at ambient temperature for inlet solutions as well as for outlet solutions immediately after sampling using a standard glass electrode calibrated against 4.01, 6.86, and 9.18 NIST pH buffers (25°C), with an uncertainty of 0.02 units. These pH measurements were used together with measured fluid compositions and the PHREEQC geochemical code (Parkhurst & Appelo, 1999) to calculate the pH at the temperatures of the experiments.

Solution pH was also measured *in situ* during few experiments performed at 146°C, using a solid contact Li-Sn alloy commercial pH electrode coupled to a Na-selective glass reference electrode providing a constant potential in Na^+-rich solutions. Descriptions of potentiometric measurements using these electrodes are provided by Pokrovski *et al.* (1995) and Saldi *et al.* (2012). The pH values obtained using the high temperature electrodes were in excellent agreement (within maximum 0.03 units) with those calculated from outlet pH measured at ambient temperature. Due to the low durability of the high temperature electrodes, pH calculation from the outlet measurements was preferred for most of the experiments.

Mg concentration and carbon content

All inlet solutions and outlet samples were analysed for magnesium concentration by flame atomic absorption spectroscopy (AAS) with an uncertainty of $\pm 1\%$ and a detection limit of 6×10^{-7} M. The total dissolved inorganic carbon (TDIC) content of the solutions was either

estimated from alkalinity measurements, or directly measured by mean of non-dispersive infrared (NDIR) spectroscopy.

Alkalinity was measured by mean of automatic HCl titration using a Schott automatic volumetric titrator (TA10plus), with an uncertainty of $\pm 1\%$ and a detection limit of 5×10^{-5} M. TDIC and carbonate speciation were subsequently calculated from the measured alkalinity and pH, using PHREEQC together with a modified `llnl.dat` database described below. Alkalinity measurements were performed on solutions containing organic ligands at concentrations lower than 10^{-4}M, as dissolved organic acids contribute to the titrated alkalinity, and may therefore significantly interfere with the TDIC determination at higher concentrations (e.g Willey *et al.*, 1975; Cantrell *et al.*, 1990; Zhang & Dawe, 1996).

For solutions containing organic ligands, TDIC was analyzed using a LI-820 (LICOR Inc.) non dispersive infra-red (NDIR) CO_2 gas analyser. A detailed description of the principles of the technique and the analytical procedure was provided by Bénézeth *et al.* (2011). The present analyses were performed with a 5 cm optical bench, and the calibration curve was established from standard solutions freshly prepared from dried reagent grade Na_2CO_3 and $NaHCO_3$. It should be noted that the analyser proved to be particularly stable, as the several calibration curves established throughout this study (over a duration of two years) never significantly differed. A minimum of two analysis were performed on each analysed sample, the mean of which was taken as representative of the TDIC of the sample. The average variability of the measurements was lower than 3%. The uncertainty of the analyses performed in this study is estimated to be lower than 5%.

On samples were both alkalinity measurements and NDIR spectroscopy analysis were performed, the difference dissolved inorganic carbon concentrations calculated from alkalinity and direct TDIC measurements never exceeded 5%.

Organic ligands

Organic ligands concentrations were measured in inlet as well as selected outlet samples, by mean of total dissolved organic carbon (DOC) analysis, using a Shimatzu TOC-BCSN analyser, with an uncertainty of $\pm 2\%$ and a detection limit of 0.15 mg/L. Outlet samples never showed differences to the inlet exceeding analytical uncertainties, but in one case (exp. M22), during which precipitation of glushinskite (MgOxalate $\cdot$ $2H_2O$) occurred (see Table 4.8).

One may express concerns regarding the thermal stability of the investigated ligands at the relatively high temperatures of our experiments. Experimental studies indicate that oxalate degradation is very slow in aqueous solution at temperatures lower than 160°C, and that its thermal stability is increased at pH higher than 7, and when it is complexed to metal cations (Crossey, 1991; Fein, 1991). Studies on EDTA indicate that this compound degrades rapidly at temperatures of 175°C or higher in basic solutions (Martell *et al.*, 1975), but no significant degradation is noticed at 125°C (Boles *et al.*, 1987), particularly when EDTA is complexed with metal cations (Motekaitis *et al.*, 1982). There seems to exist less information on citrate thermal degradation rates, but Bénézeth *et al.* (1997) reported that the thermal stability limit of citric acid in aqueous solution is about 125 to 150°C, on the basis of potentiometric measurements. Our experiments with oxalate have been performed up to 146°C, and citrate and EDTA have been used up to 120°C. In addition, complete renewal of the experimental solu-

tions in the mixed-flow reactors takes maximum 87 hours (300 mL reactors, 0.4 mL/min flow rate). Therefore, significant degradation of the organics during the experiments is unlikely.

Ion chromatography (IC) analysis were performed in order to verify this assumption for oxalate and citrate. Indeed, polycarboxylic acids degradation leads to the formation of smaller organics, such as formate or acetate (e.g Crossey, 1991), which would be detectable with IC. Analysis were performed on a Dionex ICS-2000 system, equipped with an IonPac® AS11 column and an IonPac® AG11 pre-column, under a 10 mM KOH eluent for solutions containing oxalate, and a 20 mM KOH eluent for solutions containing citrate. Analysis of inlet solutions containing organic ligands were compared with the analysis of selected outlet samples from experiments performed at the lowest flow rates (i.e the highest residence times). The results indicate no significant difference between inlet and outlet samples, therefore confirming the absence of significant degradation of oxalate and citrate during our experiments.

The chemical composition of all experimental solutions is summarized in Table 4.2.

4.2.4 Chemical speciation calculation

Aqueous solution speciation, pH and saturation states in the experimental conditions were computed from Mg^{2+} concentration, alkalinity or DIC, organic ligand concentration, solution ionic strength, and pH measured at room temperature, using the PHREEQC computer code together with its `llnl.dat` database. The B-dot activity model (Helgeson, 1969) was used to compute activity coefficients. The database was modified to include the dissociation constants of carbonic acid of Millero *et al.*, 2007 and the equilibrium constant for the first Mg^{2+} hydrolysis (Palmer & Wesolowski, 1997), as presented in Chapter 3.

Saturation state of the experimental solutions with respect to magnesite is defined as:

$$\Omega = \frac{a_{Mg^{2+}} a_{CO_3^{2-}}}{K_{sp(Mgs)}} \tag{4.2}$$

where $a_{Mg^{2+}}$ and $a_{CO_3^{2-}}$ represent the activity of the subscripted species, and $K_{sp(Mgs)}$ stands for magnesite solubility product. In this study the value for $K_{sp(Mgs)}$ is taken from the `llnl.dat` database, which was shown to be consistent with the recent experimental determination of Bénézeth *et al.* (2011).

The ligands used in this study are known to form aqueous complexes with Mg^{2+} and Na^{+}. It is therefore crucial to accurately calculate the chemical speciation of the organic acids, so as to properly estimate the saturation state of the experimental solutions with respect to magnesite. The values of their dissociation constants and of the formation constants of the complexes they form with Mg^{2+} and Na^{+} were taken from the literature when available, or approximated as described in the Chapter 3 of this thesis. These constants were introduced in the database according to the procedure detailed in Chapter 3. A measurement of magnesite solubility in the presence of 1 mM citrate at 120°C, detailed in Chapter 3, allowed to select the most appropriate estimation of Mg-citrate complexation.

The selected thermodynamic data used for chemical speciation calculations are listed in Table 3.4 of Chapter 3. Despite uncertainties, this thermodynamic dataset is thought to accurately represent the most important chemical species present at the temperature of our experiments. Throughout the manuscript, reported error bars in saturation states stem from analytical uncertainties (pH, alkalinity and TDIC, ligand concentration and magnesium concentration at steady state). Ω is termed "saturation state", while "supersaturation" refers to $\Omega - 1$ (the solution is supersaturated, and may precipitate magnesite, when $\Omega - 1 > 0$).

4.2.5 Ligand adsorption experiments

Preliminary adsorption experiments of oxalate and citrate on magnesite were carried out at 120°C in conditions similar to those of the growth experiments.

Synthetic magnesite seeds were first grounded in a Retsch MM 200 agate mixer mill for 90 minutes at 30 Hz. The grounded powder was then aged for 48 h at 120°C in a titanium batch reactor, in a solution containing 0.1 M NaCl and 0.02 M $NaHCO_3$. Aging aimed at dissolving the smallest particles, and removing surface defects created by heavy grinding. The final powder had a BET surface area of 16.12 $m^2 \cdot g^{-1}$ (mean of 2 measurements, estimated uncertainty $\pm$ 5%).

Sorption experiments were conducted in a 300 mL titanium batch reactor equipped with a magnetic stirring system (a sketch of the reactor can be found in Chapter 2). Solutions contained 0.1 M NaCl, 0.02 M $NaHCO_3$ and 10^{-3} M of oxalate or citrate, added from standard stock solutions. Initial solution pH was adjusted at ambient temperature to 7.81, in order to reach a pH of 8.00 at 120°C. 2 to 3 g of carefully weighted and homogenized magnesite powder were then disposed into the reactor, which was filled with 200 mL of experimental solution. The reactor was sealed, weighted, heated, and pressurized to a few bars with pure nitrogen, in order to permit fluid sampling.

The solution left the reactor through a 2 µm titanium filter, and was cooled down before sampling with a running water refrigerating system. The first sample was collected soon after a temperature of 120°C was reached in the reactor, and several additional samples were collected at regular time intervals during the following 24 hours. Each sample was carefully weighted in order to keep track of the solution volume. pH was measured just after sampling, at ambient temperature, then solutions were filtered through a 0.22 µm nylon filter, and samples were analysed for Mg concentration, dissolved CO_2 (with NDIR spectroscopy) and total dissolved organic carbon. Successive samples indicate adsorption equilibrium was reached in less than 5 hours. Measured pH, Mg concentration, dissolved CO_2 and DOC, were used to estimate the solution speciation at 120°C, using PHREEQC with the above-mentioned database.

Experiments	T (°C)	pH (25°C)	Ligand type	[Ligand]*10^3 (mol/kg)	$MgCl_2$*10^4 (mol/kg)	$NaHCO_3$ (mol/kg)	NaCl (mol/kg)	HCl*10^4 (mol/kg)	NaOH*10^4 (mol/kg)
M5	146	7.77	-	-	3.858	0.018	0.0993	32.30	-
M5B	146	7.47	-	-	3.802	0.018	0.0993	32.00	-
M11	146	7.66	-	-	3.926	0.018	0.0993	32.80	-
M11B	146	7.66	-	-	4.481	0.018	0.0993	7.00	-
M11C	146	7.80	-	-	4.129	0.018	0.0993	7.00	-
M13	146	7.98	-	-	6.241	0.018	0.0993	7.00	-
M15	146	8.16	-	-	6.720	0.020	0.1000	6.95	-
M23A-C	146	7.97	-	-	8.730	0.018	0.0993	6.90	-
M23D	146	7.97	-	-	8.927	0.018	0.0993	6.90	-
M28A-B	146	7.52	-	-	3.677	0.018	0.0993	7.30	-
M28C-E	146	7.52	-	-	3.587	0.018	0.0993	7.30	-
M10A-B	146	7.66	Oxalate	0.01	3.938	0.018	0.0993	32.90	-
M8	146	7.44	Oxalate	0.10	4.200	0.018	0.0993	34.60	-
M6A	146	7.65	Oxalate	0.80	6.189	0.018	0.0993	7.00	-
M6B-C	146	7.81	Oxalate	0.80	6.355	0.018	0.0993	7.00	-
M7A-B	146	7.86	Oxalate	1.50	8.571	0.018	0.0993	7.00	-
M9A-B	146	7.70	Oxalate	9.17	31.239	0.018	0.0993	6.20	-
M18	146	8.22	Oxalate	10.00	31.001	0.018	0.0793	6.70	-
M19	146	8.20	Oxalate	10.00	15.276	0.018	0.0793	6.80	-
M20	146	8.17	Oxalate	10.00	46.544	0.018	0.0793	6.50	-
M22	146	7.93	Oxalate	10.00	75.091	0.020	0.0742	7.60	-
M14	120	7.96	-	-	8.622	0.018	0.0993	7.00	-
M24B	120	7.61	-	-	8.660	0.018	0.0993	6.90	-
M25A-B	120	8.01	-	-	7.353	0.020	0.1000	6.95	-
M27	120	7.83	-	-	10.190	0.018	0.0993	6.80	-
M31A-B	120	7.74	-	-	3.586	0.020	0.1000	8.93	-
M32A-C	120	7.68	-	-	6.422	0.020	0.1000	9.00	-
M32D	120	7.71	-	-	6.960	0.020	0.1000	9.00	-
M33A-C	120	7.64	-	-	6.424	0.020	0.1000	9.00	-
M34A-B	120	7.64	-	-	9.653	0.018	0.0993	6.80	-
M35A-B	120	7.75	-	-	6.326	0.020	0.1000	9.00	-
M37	120	7.82	-	-	9.941	0.018	0.0993	6.80	-
M39A-B	120	7.77	-	-	6.476	0.020	0.1000	9.00	-
M40A-B	120	8.07	-	-	11.055	0.020	0.0976	2.30	-
M40D-F	120	8.37	-	-	10.996	0.020	0.0976	2.30	-
M41	120	7.73	-	-	10.011	0.018	0.0993	6.80	-
Oxl1	120	7.73	Oxalate	0.10	9.954	0.018	0.0993	6.80	-
Oxl2	120	7.70	Oxalate	1.00	9.947	0.018	0.0973	7.10	-
Oxl3	120	7.73	Oxalate	5.00	10.057	0.018	0.0903	7.40	-
Oxl4	120	7.72	Oxalate	10.00	10.095	0.018	0.0803	7.50	-
M22	120	7.93	Oxalate	10.00	75.091	0.020	0.0742	7.60	-
M29A	120	7.56	Oxalate	10.00	15.675	0.018	0.0793	6.80	-
M29E	120	7.56	Oxalate	10.00	15.994	0.018	0.0793	6.80	-
M36A-C	120	7.54	Oxalate	10.00	24.798	0.018	0.0793	7.40	-
M36D	120	7.54	Oxalate	10.00	24.888	0.018	0.0793	7.40	-
Oxl5A-B	120	8.17	Oxalate	9.81	38.316	0.020	0.0623	1.00	-
Oxl5C-D	120	8.18	Oxalate	9.81	38.206	0.020	0.0623	1.00	-
Oxl6B	120	8.13	Oxalate	1.00	7.960	0.020	0.0833	0.90	-
Oxl6C-D	120	8.02	Oxalate	1.00	8.135	0.020	0.0833	0.90	-
Cit1	120	7.55	Citrate	0.01	9.965	0.018	0.0993	6.80	-
Cit2	120	7.55	Citrate	0.10	9.487	0.018	0.0993	6.90	-
Cit3	120	7.55	Citrate	1.00	9.876	0.018	0.0973	7.40	-
Cit4	120	7.55	Citrate	10.00	9.787	0.018	0.0490	10.39	-
Cit5A-B	120	8.37	Citrate	0.21	19.398	0.018	0.0775	2.05	-
Cit5C2-D1	120	8.25	Citrate	0.21	19.338	0.018	0.0775	2.05	-
Cit5D2-F	120	8.25	Citrate	0.21	19.410	0.018	0.0775	2.05	-
Cit8A-B	120	8.19	Citrate	1.05	14.171	0.021	0.0776	0.90	-
Cit8C-D	120	8.20	Citrate	1.05	14.238	0.021	0.0776	0.90	-
Cit9A-B	120	8.10	Citrate	0.105	6.440	0.021	0.0836	0.90	-
Edta1	120	7.73	Edta	0.01	9.947	0.018	0.0993	6.60	-
Edta2	120	7.72	Edta	0.10	9.911	0.018	0.0994	4.90	-
Edta3	120	7.71	Edta	0.50	9.929	0.018	0.0998	-	2.90
Edta4	120	7.75	Edta	1.00	9.870	0.018	0.1000	-	12.50
Edta5A-B	120	8.04	Edta	1.00	15.948	0.020	0.0938	-	17.20
Edta5D-F	120	7.86	Edta	1.00	15.839	0.020	0.0938	-	17.20
M38A-B	100	8.37	-	-	7.879	0.020	0.080	-	9.00
M38C-E	100	8.37	-	-	7.950	0.020	0.080	-	9.00
Cit6A-B	100	8.36	Citrate	1.044	16.032	0.020	0.0781	-	8.60
Cit6C-E	100	8.37	Citrate	1.044	16.112	0.020	0.0761	-	8.60
Cit7A-B	100	8.38	Citrate	0.105	10.021	0.020	0.0788	-	9.60
Cit7C-E	100	8.39	Citrate	0.105	10.256	0.020	0.0788	-	9.60

Table 4.2 – Composition of inlet fluid solutions used for magnesite growth experiments in this study.

4.3 Results

4.3.1 Magnesite inorganic growth rates

Comparison with results from Saldi *et al.* (2012)

According to Saldi *et al.* (2012), magnesite growth rates at pH > 6 are consistent with a second-order rate law, expressed as follows:

$$R_{Mgs} = k_{Mgs} \left\{ > \mathrm{MgOH_2^+} \right\}^2 \cdot \left(\Omega^2 - 1 \right) \tag{4.3}$$

where k_{Mgs} represents the "absolute" growth rate constant, $\left\{ > \mathrm{MgOH_2^+} \right\}$ is the surface concentration of protonated magnesium centers, and Ω, the saturation state, is defined according to equation 4.2. k_{Mgs} depends on temperature according to an Arrhenius-type law of the form:

$$k_{Mgs} = A \cdot e^{\frac{-Ea}{RT}} \tag{4.4}$$

with Ea the apparent activation energy, A a so-called pre-exponential factor, R the gas constant.

In equation 4.3, $\left[> \mathrm{MgOH_2^+} \right]$ is assumed to be the rate-controlling surface species in neutral to alkaline conditions, according to the surface complexation model (SCM) of Pokrovsky *et al.* (1999). Its surface concentration can be calculated within the framework of the SCM (Saldi *et al.*, 2010, 2012):

$$\{ > \mathrm{MgOH_2^+} \} \simeq \left(\frac{K_{CO3} K_{OH}}{K_{CO3} K_{OH} + a_{\mathrm{CO_3^{2-}}} K_{OH} + K_{CO3} a_{\mathrm{OH^-}}} \right) \tag{4.5}$$

with K_{CO3} and K_{OH} the equilibrium constant corresponding respectively to the following surface reactions: $>\mathrm{MgCO_3^-} + \mathrm{H_2O} = >\mathrm{MgOH_2^+} + \mathrm{CO_3^{2-}}$ and $>\mathrm{MgOH^0} + \mathrm{H_2O} = >\mathrm{MgOH_2^+} + \mathrm{OH^-}$.

At nearly constant pH and carbonate activity, $\left[> \mathrm{MgOH_2^+} \right]$ is approximately a constant, and rate law 4.3 can be approximated to:

$$R_{Mgs} = k_{Mgs} \left\{ > \mathrm{MgOH_2^+} \right\}^2 \cdot \left(\Omega^2 - 1 \right) \simeq k'_{Mgs} \cdot \left(\Omega^2 - 1 \right) \tag{4.6}$$

where k'_{Mgs} is the "apparent" kinetic rate constant.

The squared exponent of Ω in equation 4.3 and 4.6 is interpreted in the crystal growth literature to stem from a spiral growth mechanism (e.g Shiraki & Brantley, 1995). This was confirmed by Saldi *et al.* (2009), who observed with hydrothermal atomic force microscopy (HAFM) that spiral growth is the dominant growth mechanism on magnesite [104] surface between 80 and 120°C, in a wide range of saturation states.

It should be noted that equation 4.3 is a rate law derived from the transition state theory (Lasaga, 1981; Aagaard & Helgeson, 1982). Based on experimental results as well as theoretical derivations, the crystal growth literature (e.g Nielsen, 1984; Blum & Lasaga, 1987; Shiraki

& Brantley, 1995; Saldi *et al.*, 2009) usually refers rather to rate laws of the type :

$$R = k' \cdot (\Omega - 1)^n \tag{4.7}$$

with k' an apparent growth rate constant and n the rate order, which equals 2 in the case of spiral growth controlled growth mechanism.

In the present study, for consistency with the crystal growth literature, and the HAFM study presented in Chapter 4, we will therefore use the following rate law:

$$R_{Mgs} = k'_{Mgs} \cdot (\Omega - 1)^2 \tag{4.8}$$

It should however be noted that rate laws 4.6 and 4.8 give close results, particularly when $\Omega > 10$. In the range of saturation states investigated by Saldi *et al.* (2012), and given experimental uncertainties, both rate laws fit equally well the measured growth rates, and the rate constants derived by Saldi *et al.* (2012) using rate law 4.3 may be applied without modification with eq. 4.8 .

The results of 48 experiments performed without ligands at 100, 120 and 146°C are summarized in Appendix A in Tables 4.7, 4.8, 4.9 and 4.10. The measured growth rates are compared with the results obtained by Saldi *et al.* (2012) in similar conditions of temperature and carbonate activity in Figure 4.3. The dashed lines drawn in Fig. 4.3(a to c) are best fits of the data according to equation 4.8, and confirm that, despite some scatter, the measured growth rates are satisfyingly fitted with a parabolic rate law in the saturation range $1 < \Omega < 80$.

However, it can be seen that the growth rates measured in this study are consistently and significantly higher than the rates obtained by Saldi *et al.* (2012). Apparent kinetic rate constant k'_{Mgs} derived from plots 4.3(a to c) were used to calculate the true kinetic rate constant k_{Mgs} using equations 4.5 and 4.6 with surface equilibrium constants listed by Saldi *et al.* (2012), and mean carbonate activity and pH from our experiments at a given temperature. The retrieved rate constants are listed in Table 4.4. Fig. 4.3d presents an Arrhenius plot of k_{Mgs}, which shows that our rate constants are higher by 0.4 to 0.5 log units. The retrieved activation energy is 85.1 $\pm$ 7.7 kJ/mol, which is consistent with the value obtained in the former study (80.1 kJ/mol).

The source of this consistent discrepancy in similar chemical conditions and using identical experimental settings is unknown, but may be related to variations of the intrinsic reactivity of the synthesized magnesite seeds, or to a defective temperature control in the study by Saldi *et al.* (2012). Note that with the reported apparent activation energy, an increase of temperature of 10°C at about 120°C would result in a nearly two times higher growth rate constant.

As a result, we used the newly determined inorganic growth rates as a basis to estimate the influence of ligands studied in the following sections of this manuscript.

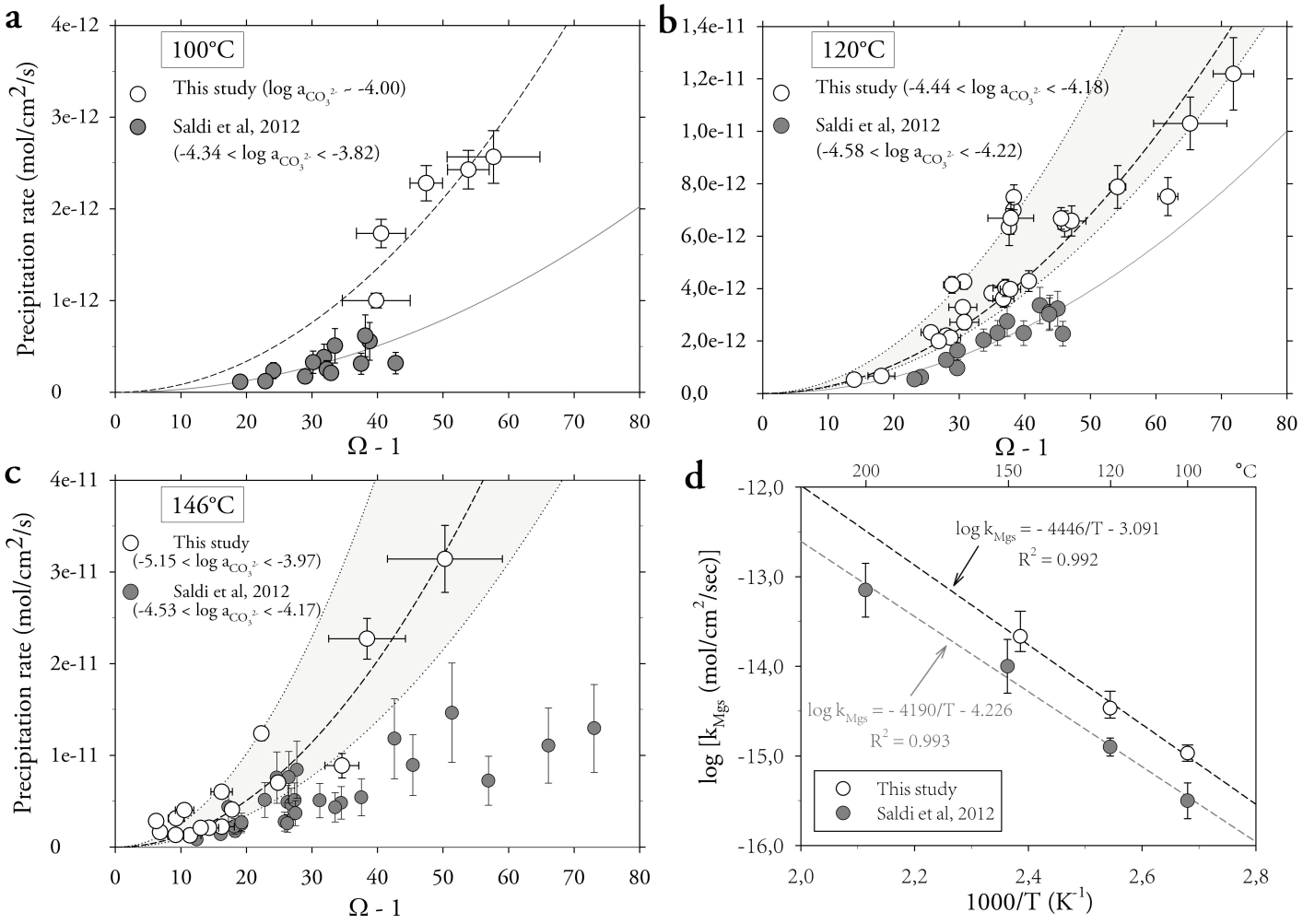

Figure 4.3 – (a) to (c): Magnesite growth rate as a function of the degree of supersaturation (Ω -1) at (a) 100, (b) 120, (c) 146°C. Dashed lines are best fits according to eq. 4.8. Grey-shaded areas limited by dotted lines in (b) and (c) highlight the observed variability. Rates measured by Saldi *et al.* (2012) in comparable chemical conditions are represented as dark grey circles. Fig. (d) represents an Arrhenius plot of retrieved rate constants as a function of reciprocal temperature. Dashed lines are linear least square fits of the rate constants. The slopes are consistent with an activation energy of 85.1 $\pm$ 7.7 kJ/mol in the present study, 80.1 kJ/mol in the study by Saldi *et al.* (2012).

Reproducibility of the results

Data plotted in Fig. 4.3 exhibit a rather important dispersion, which exceeds the estimated experimental uncertainty. A particular attention was given to characterizing the influence of different potential sources of variability on the reproducibility of measured growth rates: reactor type (200 mL or 300 mL titanium Parr reactors), nature of the initial filling solution (deionized water or reactive solution), seed material. Test experiments were reproduced with identical inlet solutions, while changing experimental parameters. Operating conditions of two test experiments are summarized in Table 4.3, and their results have been plotted in Figure 4.4.

Table 4.3 – Operating conditions of test experiments performed at 120°C.

Exp.	Seeds	Initial filling solution	Reactor type	Stirring rate
M27	Mgs 2	deionized water	200 mL	200 rpm
M37	Mgs 2	deionized water	200 mL	200 rpm
M41	Mgs 3	deionized water	200 mL	200 rpm
M32A	Mgs 2	NaCl 0.1M	200 mL	200 rpm
M33A	Mgs 2	deionized water	300 mL	200 rpm
M35A	Mgs 2	inlet "reactive" solution	300 mL	200 rpm
M39A	Mgs 3	deionized water	300 mL	200 rpm

Experiments M27 and M37 were performed at 120°C from the same inlet solution composition (Table 4.2), in identical experimental conditions (same reactor, stirring rate, seed material and mass). The obtained growth rates and calculated saturation states (Table 4.8) agree within experimental uncertainties. Experiment M41 was performed from the same inlet solution composition, but with a different starting seed material (see Table 4.1). The resulting BET surface area-normalized growth rate is in close agreement with those obtained from exp. M27 and M37, but the corresponding saturation state is significantly lower ($\Omega = 38.9 \pm 3.5$ against 46.8 ± 1.0, respectively).

Experiments M32A, M33A, M35A and M39A were all performed at 120°C from close starting solutions (Table 4.2). Different experimental parameters were varied: reactor type, nature of the initial filling solution, seed material (Table 4.3). All measured growth rates and calculated saturation states agreed within experimental uncertainty (Fig. 4.4, Table 4.8).

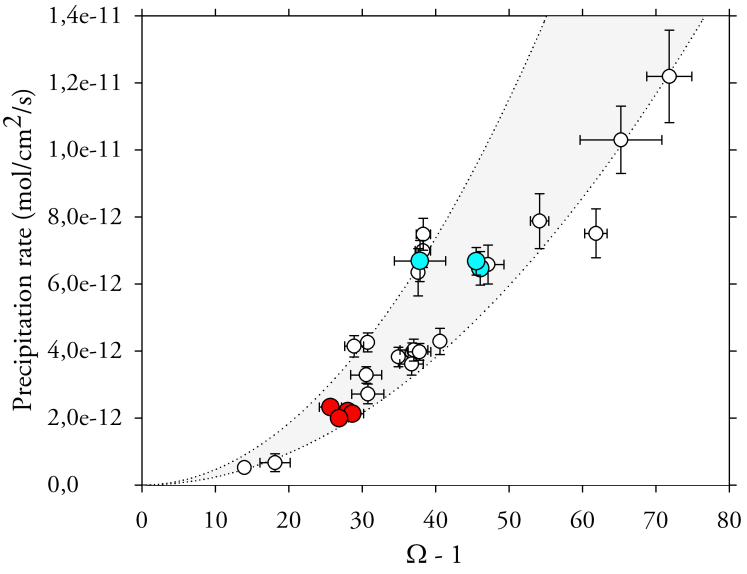

Figure 4.4 – Magnesite growth rates at 120°C, as a function of the degree of supersaturation.
Blue: test experiments M27, M37 and M41.
Red: test experiments M32A, M33A, M35A and M39A.

The results indicate that the reproducibility of experiments performed at constant inlet chemistry is excellent, including when using different experimental settings and initial filling solutions. The use of different seed material may impact to some extent the BET surface area-normalized rates. However, it should be noted that most experiments at a given temperature were performed with a single type of seed material (Table 4.7 to 4.10).

Thus, the observed variability does not appear to be consistently linked with any of the above-mentioned experimental parameters. It may however be linked to a misestimation of the reactive surface area of the seed material, and its evolution during the course of growth experiments, or to a certain variability of the intrinsic reactivity of individual seed samples.

4.3.2 Bulk influence of ligands on magnesite growth kinetics at 120°C

In order to evaluate the bulk influence of the ligands on magnesite growth kinetics, growth experiments were performed at constant Mg concentration, TDIC, pH and ionic strength, and identical experimental conditions, with increasing ligand concentrations.

The chemical composition of experiments M27/M37/M41 (1 mM Mg, 18 mM $NaHCO_3$, pH 7.71-7.76) was selected as a starting point, and magnesite inorganic growth experiments were performed to serve as a reference (see section 4.3.1). Four experiments were then performed in series on the starting seeds, with increasing ligand concentrations, between 0.1 and 10 mM of oxalate (exp. Oxl1-Oxl4), 0.01 and 10 mM of citrate (exp. Cit1-Cit4), and 0.01 and 1 mM of EDTA (exp. Edta1-Edta4).

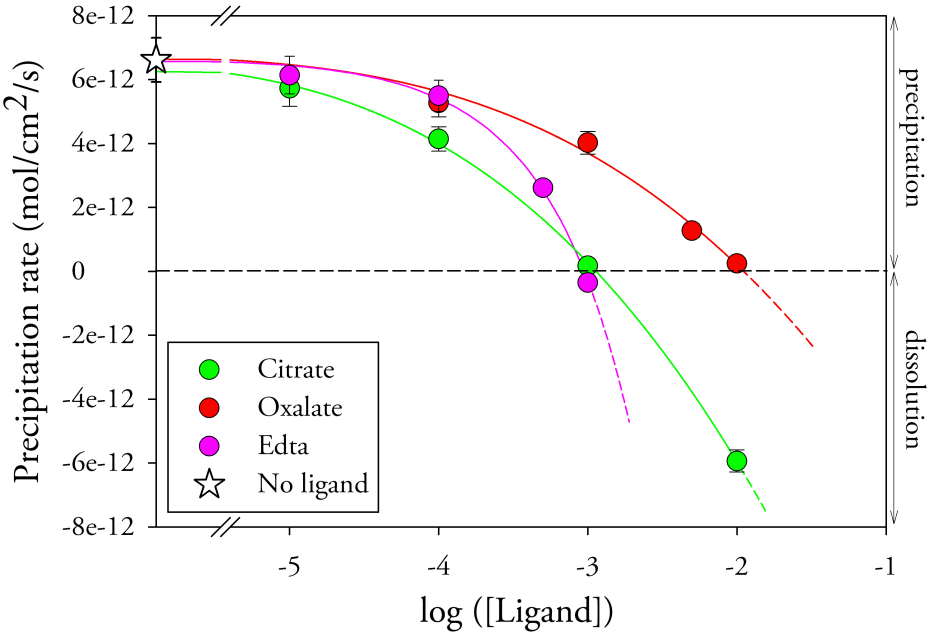

Figure 4.5 – Magnesite surface area normalized growth rates at 120°C as a function of the logarithm of total ligand concentration, at otherwise constant solution composition. The white star symbolizes the growth rate measured in the absence of ligands from a reference solution containing 1 mM Mg, 18 mM $NaHCO_3$, at pH 7.71-7.76 and ionic strength 0.116 M. Plain coloured lines are guides to the eyes.

The measured rates are plotted as a function of ligand concentration in Figure 4.5, and show a significant decrease of magnesite growth rates in the investigated conditions when ligand concentration exceeds 10^{-5} (citrate) to 10^{-4} M (oxalate, EDTA). As citrate and EDTA concentrations are increased above approximately 1 mM, magnesite dissolution is observed to take place. This indicates that the observed growth rate decrease is related at least in part to a decrease in solution supersaturation due to Mg^{2+} complexation by the ligands since the solution becomes undersaturated as the ligand concentration is increased. Influence

of complexation is further suggested by the fact that citrate and EDTA, which form strong complexes with Mg^{2+}, decrease growth rates more than oxalate, which forms weaker magnesium complexes (see Chapter 3). Chemical speciation calculations (Tables 4.8 and 4.9) indeed demonstrate a decrease of solution saturation state as ligand concentration is increased.

Two points are worth noting:

- The growth rate in the presence of citrate is decreased slightly more than in the presence of EDTA, at ligand concentrations lower than 1 mM, although EDTA more strongly binds to Mg^{2+} cations (Chapter 3).
- Calculations predict a slightly positive supersaturation of the solutions in the presence of 1 mM EDTA ($\Omega = 3.1 \pm 0.5$) and 10 mM citrate ($\Omega = 1.5 \pm 0.1$), although experimental results indicate magnesite dissolution. This reveals imprecisions in the thermodynamic database and/or speciation calculation, particularly concerning pH estimation, magnesite solubility product and carbonate speciation (as already noticed by Saldi *et al.*, 2010; Bénézeth *et al.*, 2011). Possible uncertainties in the knowledge of magnesium-ligand complexation at high temperature are not sufficient to account for these incorrect calculations.

4.3.3 Influence of oxalate, citrate and EDTA on magnesite growth kinetics as a function of saturation state

In order to examine the impact of the three investigated carboxylic ligands on magnesite growth rates independently of their influence on saturation state, a total of 67 experiments were performed with various concentrations of oxalate, citrate and EDTA, at temperatures of 146, 120 and 100°C. Their results are summarized in Tables 4.7 to 4.10 (in Appendix A), and plotted as a function of saturation state in Figures 4.6 to 4.8.

Growth rates measured in the presence of the investigated organic ligands are accurately described by the empirical second-order rate law (eq. 4.8), as shown by the good agreement between dashed lines in Fig.4.6 to 4.8 and the respective datapoints. This suggests that magnesite growth in the presence of ligands is controlled by spiral growth on the mineral surface in a large range of saturation states, as in the absence of additives (Saldi *et al.*, 2010). However, the apparent rate constant k'_{Mgs} is decreased in the presence of the ligands. In other words, magnesite growth is inhibited at constant saturation state in the presence of organic ligands. The extent of inhibition depends on the nature of the additive and its concentration. Table 4.4 summarizes the apparent kinetic rate constants fitted on the measured rates according to eq. 4.8.

In the presence of oxalate, growth inhibition is limited. At 146°C (Fig. 4.6), rates measured in the presence of oxalate at concentrations between 0.1 and 10 mM do not markedly differ from those measured in oxalate-free solutions. Growth rates with 10 mM oxalate compare well with the lower range of the rates measured in the absence of ligands, which are affected by an important scatter.

At 120°C (Fig. 4.7), oxalate at concentrations equal or lower than 5 mM do not significantly affect magnesite growth rates, whereas the apparent rate constant k'_{Mgs} is decreased twofold in the presence of 10 mM oxalate.

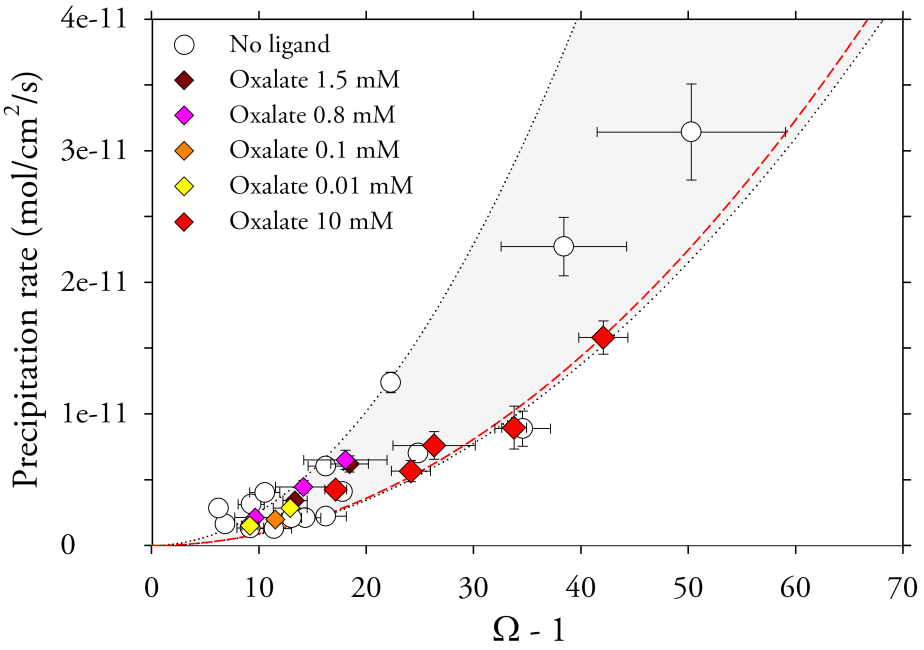

Figure 4.6 – Magnesite growth rates as a function of the degree of supersaturation at 146°C in the absence of ligands, and in presence of various concentrations of oxalate. The grey shaded area represents the range of variability of inorganic rates, while the red dashed line is a best fit according to rate law 4.8 of rates measured in the presence of 10 mM oxalate.

This rate constant decrease is similar to that measured at 120°C in the presence of 1 mM of EDTA, which is predominantly under the form of $MgEDTA^{2-}$ complexes. Lower concentrations of this strong chelate do not visibly affect growth rates (Fig. 4.8).

Citrate is a more efficient inhibitor of magnesite growth. Both at 100°C (Fig. 4.9) and 120°C (Fig. 4.10), concentrations of 0.1 mM are sufficient to lower magnesite growth rates. At 100°C, the apparent rate constant decreases by a factor of 2.4 in the presence of 1 mM citrate.

Inhibition is more pronounced at 120°C: a three to four-fold decrease of the rate constant is observed with as little as 0.2 mM citrate. Surprisingly, increasing citrate concentration to 1 mM does not further decrease magnesite growth rates, which suggests that growth inhibition reaches a plateau.

Besides, at 120°C in the presence of 1 mM citrate, crystal growth seems to be prevented at Ω lower than *ca.* 20. This observation of a "no-growth zone" would however require additional data to be firmly confirmed.

Overall, the measured inhibition of magnesite is limited, since relatively high concentrations of ligands are necessary to affect growth rates (0.1 mM for citrate, 1mM for EDTA and 10 mM for oxalate). As a comparison, aspartic acid-rich polypeptides were reported to completely halt calcite growth at concentrations lower than 10^{-6} M (Elhadj *et al.*, 2005).

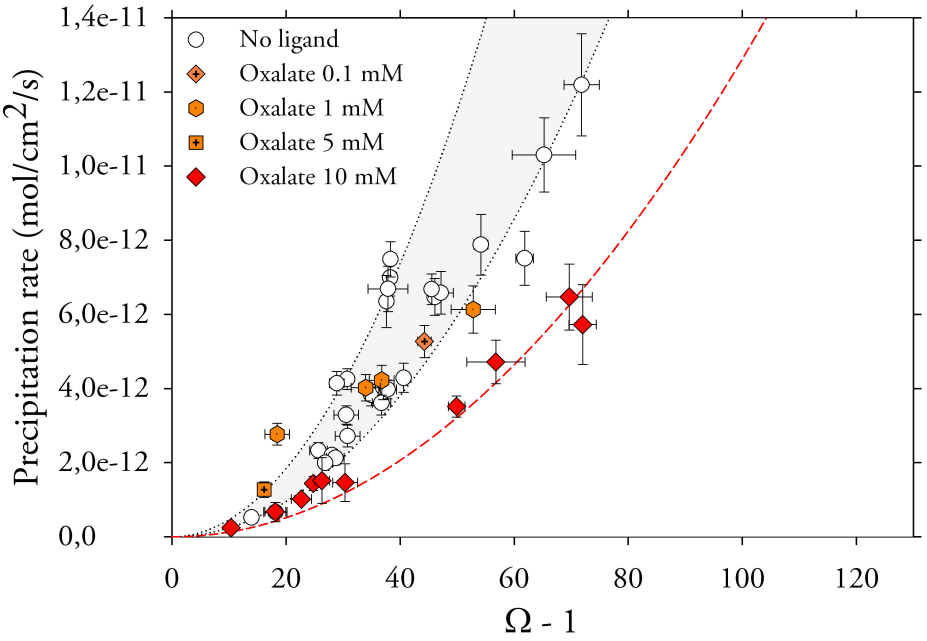

Figure 4.7 – Magnesite growth rates as a function of the degree of supersaturation at 120°C in the absence of ligands, and in presence of various concentrations of oxalate. The grey shaded area represents the range of variability of inorganic rates, while the red dashed line is a best fit according to rate law 4.8 of rates measured in the presence of 10 mM oxalate.

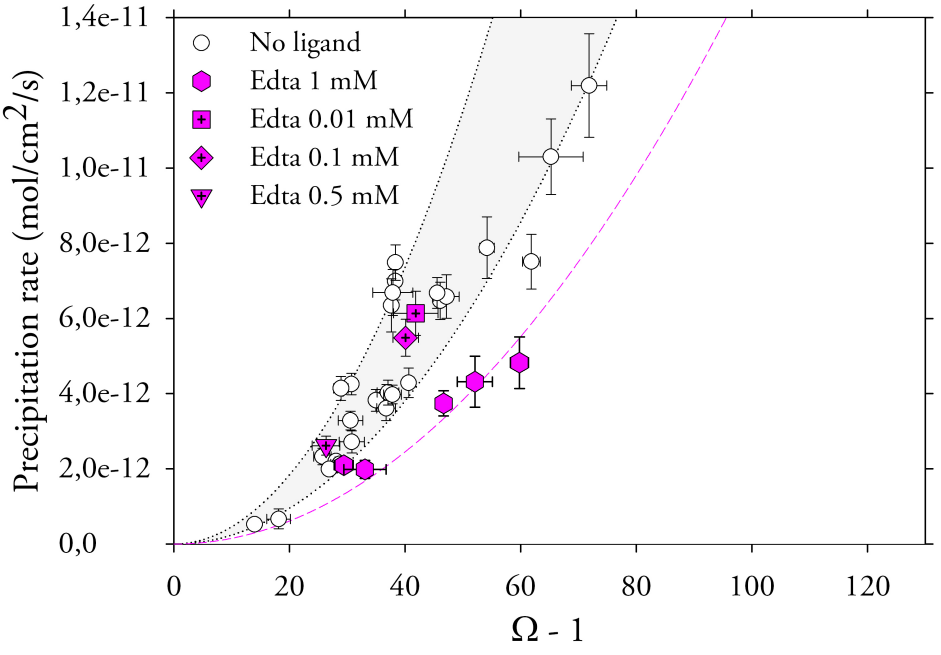

Figure 4.8 – Magnesite growth rates at 120°C in the absence of ligands, and in presence of various concentrations of EDTA. Growth rates measured in the presence of 1 mM EDTA are satisfyingly fitted by rate law 4.8, as shown by the pink dashed line.

These are the first measurements of magnesite growth kinetics in the presence of dissolved carboxylates. Our observations are in qualitative agreement with calcite experiments per-

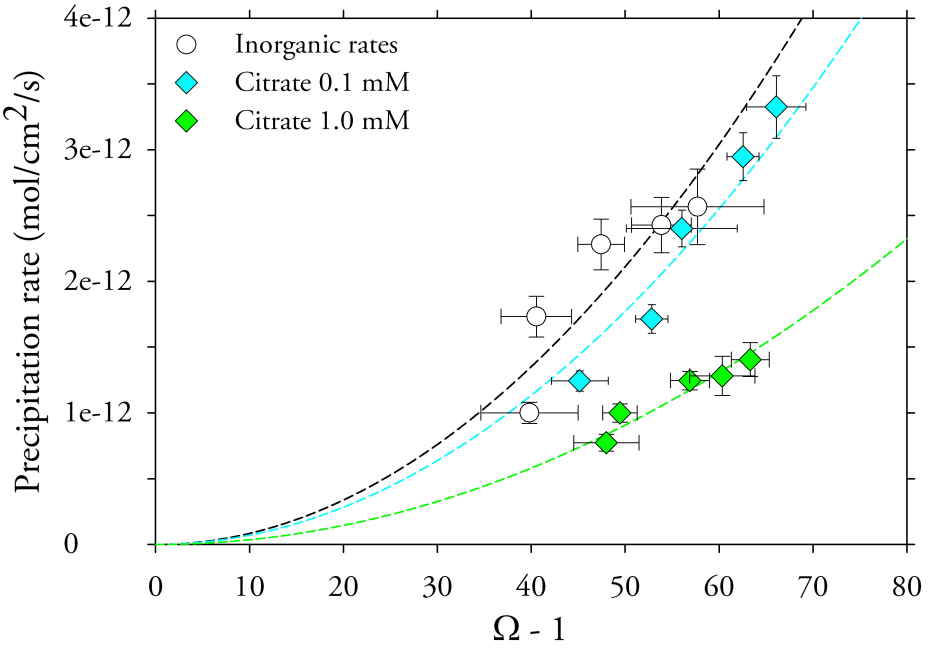

Figure 4.9 – Magnesite growth rates at 100°C in the absence and presence of citrate at concentrations 0.1 and 1 mM. Dashed lines are best fits of the results according to rate law 4.8. The apparent kinetic rate constant k'_{Mgs} is significantly decreased in the presence of citrate.

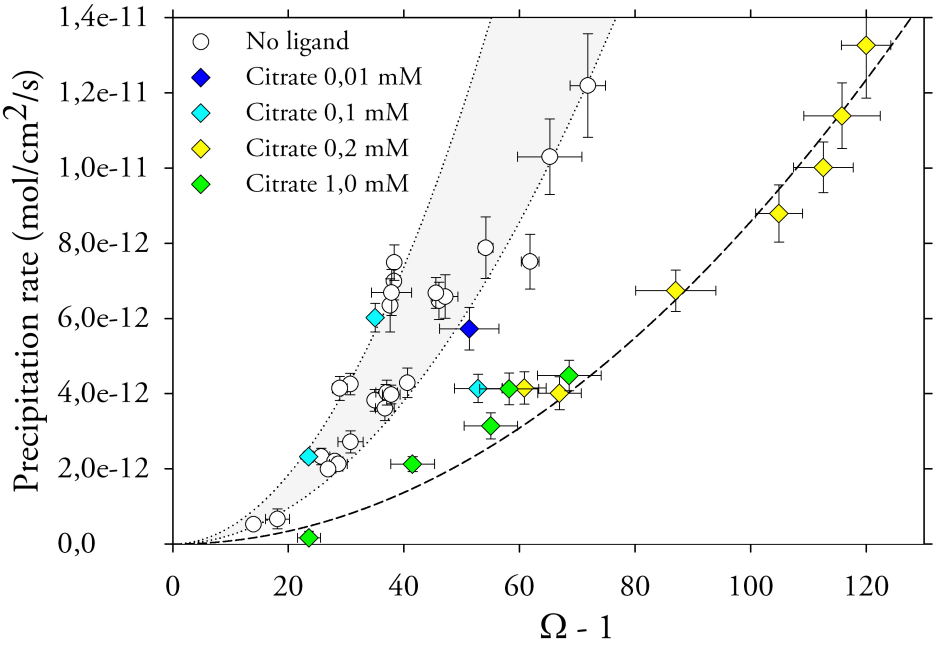

Figure 4.10 – Magnesite growth rates as a function of the degree of supersaturation at 120°C in the absence of ligands, and in presence of various concentrations of citrate. The dashed line is a best fit according to rate law 4.8 of rates measured in the presence of 0.2 mM citrate, and satisfyingly fits the rates obtained with 1 mM citrate.

formed at lower temperature in the presence of citrate.. Westin & Rasmuson (2005a) indeed reported that citrate is a moderate calcite growth inhibitor, causing a 60 % reduction of growth

Table 4.4 – Values of rate constants obtained in the present study by fitting experimental datapoints according to eq. 4.8, in the absence and in presence of various concentrations of organic ligands. The minimum (min.) and maximum (max.) values of the rate constants usually correspond to a 95% confidence interval. At 120 and 146°C without ligands, and at 120°C in the presence of 0.1 mM citrate, due to the important data scatter, these min. and max. values represent rather the whole range of measured rates.

T(°C)	Ligand conc.	k'_{Mgs} (mol/cm^2/s)	min. * 10^{15}	max. * 10^{15}	{>MgOH$^+$} (mean)	k_{Mgs} (mol/cm^2/s)
100	No ligand	$0.88 * 10^{-15}$	0.71	1.05	0.818 ± 0.006	$1.07 * 10^{-15}$
100	**Citrate** 0.1 mM	$0.73 * 10^{-15}$	0.64	0.81		
100	**Citrate** 1 mM	$0.36 * 10^{-15}$	0.33	0.39		
120	No ligand	$2.98 * 10^{-15}$	2.32	4.61	0.873 ± 0.018	$3.41 * 10^{-15}$
120	**Oxalate** 1 mM	$2.57 * 10^{-15}$	1.18	3.96		
120	**Oxalate** 10 mM	$1.29 * 10^{-15}$	1.15	1.43		
120	**Edta** 1 mM	$1.53 * 10^{-15}$	1.22	1.84		
120	**Citrate** 0.01 mM	$2.18 * 10^{-15}$	-	-		
120	**Citrate** 0.1 mM	$3.05 * 10^{-15}$	1.48	4.61		
120	**Citrate** 0.2 mM	$0.86 * 10^{-15}$	0.80	0.92		
120	**Citrate** 1 mM	$1.05 * 10^{-15}$	0.87	1.23		
146	No ligand	$12.7 * 10^{-15}$	8.60	25.0	0.589 ± 0.052	$2.16 * 10^{-14}$
146	**Oxalate** 10 mM	$8.95 * 10^{-15}$	7.47	10.5		

rate at a concentration of 0.2 mM at pH 8.5 and $\Omega = 4$. A further increase of citrate concentration only slightly further enhanced growth inhibition, supporting the idea of an "inhibition plateau". A similar conclusion was reached by Reddy & Hoch (2001). Concerning the growth rate law, a decrease of calcite growth rate constant was observed by Lee & Reeder (2006) with 0.5 mM citrate. This feature was also noticed with more complex organic molecules such as humic acids (Zuddas *et al.*, 2003), salicylic acid derivatives (Ukrainczyk *et al.*, 2012) or alginate (Lakshtanov *et al.*, 2011), though in the latter case the decrease in the rate constant was accompanied by a change in the rate order (n in eq. 4.7).

These observations were systematically interpreted as resulting from the interaction of the organic additives with the surface of the mineral, decreasing the number of active growth-controlling sites.

Support for this hypothesis in the case of magnesite growth comes from the observation of magnesite crystals after growth in the presence of organics (Fig. 4.1). While EDTA and oxalate did not affect much the aspect of the overgrown layers (Fig. 4.1f), citrate caused the apparition of laterally discontinuous planes of growth, giving a "burgeoning" aspect to the magnesite seeds (Fig. 4.1d). These observations resembles those made for instance by Reddy & Hoch (2001) on calcite crystals grown in the presence of cyclic polycarboxyclic acids, and clearly point towards adsorption of the organics at the crystal surface.

4.3.4 Preliminary adsorption experiments

In order to evaluate the extent of ligand adsorption onto magnesite surface in our experiments, we performed preliminary adsorption experiments at 120°C, in chemical conditions close to the growth experiments (0.02 M $NaHCO_3$, pH 8.0 to 9.0).

Two experiments were performed with 1 mM citrate, and one with 1 mM oxalate. Their results are summarized in Table 4.5. Oxalate adsorption was below detection limit. The amount of citrate adsorbed on magnesite surface was estimated from a simple mass balance calculation. The corresponding surface coverage was calculated assuming that negatively charged citrate molecules only bind to positively charged surface magnesium (Pokrovsky *et al.*, 2009), whose geometric surface sites density is 9.84 µmol/m^2 (Pokrovsky *et al.*, 1999).

Bearing in mind the uncertainties associated with such a procedure (e.g Davis & Kent, 1990), we may define a preliminary Langmuir adsorption constant K_L:

$$K_L = \frac{\Gamma}{(S_T - \Gamma) * \left[\mathrm{Cit}^{3-}\right]} \tag{4.9}$$

where Γ represents the adsorbed ligand surface concentration (in mol/m^2), S_T is the maximum amount of adsorbed ligand, taken to be equal to the surface density of magnesium surface functional groups, and $\left[\mathrm{Cit}^{3-}\right]$ is the solution free citrate concentration, calculated by taking into account the complete solution speciation.

Because the exact citrate species adsorbing at the mineral surface is unknown, the same expression can be written referring to the total citrate concentration in lieu of $Citrate^{3-}$ concentration; the corresponding Langmuir constant is written K'_L. Both values have been reported in Table 4.5.

Table 4.5 – Results of adsorption experiments. Molalities (in brackets) are given in mol/kg. [Cit^{3-}] refers to the free (uncomplexed) citrate molality, calculated at the experimental temperature from solution speciation. K'_L and K_L are tentative Langmuir adsorption constants (see text).

Ligand	T(°C)	initial [Lig.]	pH (20°C)	S (m^2)	final [Lig.]	ads. ligand (mol/m^2)	Surface coverage	pH (120°C)	[Cit^{3-}] (mol/kgw)	K'_L	K_L
Citrate	120	$1.04*10^{-3}$	8.76	31.18	$9.80*10^{-4}$	$5.84*10^{-7}$	5.9%	8.46	$6.96*10^{-4}$	64 ± 20	91 ± 29
Citrate	120	$9.94*10^{-4}$	8.72	48.60	$8.42*10^{-4}$	$6.49*10^{-7}$	6.6%	8.31	$5.85*10^{-4}$	84 ± 14	121 ± 20
Oxalate	120	$1.03*10^{-3}$	9.10	45.03	1 mM	-				< 30	

The two experiments performed with citrate gave concording results, although the second experiment, performed with a higher magnesite surface, should be more reliable. In the case of oxalate, considering a ±2% uncertainty in COD analysis, we evaluated the tentative adsorption constant K'_L to be lower than ca. 30. These experiments thus indicate that citrate adsorbs more than oxalate on the magnesite surface, in accordance with its obviously bigger influence on growth rates. Both ligands however have a very limited affinity for the magnesite surface.

Altough little data exist on the adsorption of carboxylates onto carbonates surfaces, our observations may be compared to informations available for calcite.
According to Geffroy *et al.* (1999) and adsorption experiments performed on calcite at ambient temperature and pH 9, adsorption of di- and tri-carboxylates proceeds through the binding to surface calcium in a bidentate way involving two carboxylate groups, or a carboxylate and a hydroxyl group. Five-membered chelate rings are most stable, leading to a stronger adsorption of oxalate compared to citrate. Plank & Bassioni (2007) also came to the conclusion that citrate adsorbs less onto calcite than simpler carboxylates such as benzoate or tartrate at pH 9. However, it is shown that the adsorbed quantity decreases upon temperature increase up to 60°C, and the adsorption enthalpy for citrate is less negative than for the dicarboxylate tartrate. If the same applies for magnesite with the oxalate/citrate couple, this could provide an explanation as to why citrate adsorbs more than oxalate at high temperature.

Besides, Pokrovsky *et al.* (2009) performed magnesite dissolution experiments at 60°C in the presence of various ligands in slightly acidic conditions, and interpreted the results based on a surface complexation model involving adsorption of the ligands on the magnesite surface. The fitted adsorption constants are of the order of oxalate < citrate < EDTA, in accordance with our observations, but the magnitude of the adsorption constants is significantly higher than ours, which may be explained by the different chemical conditions and temperature.

4.4 Discussion

4.4.1 Influence of adsorption on magnesite growth kinetics

Quantitative description of magnesite kinetic inhibition through citrate adsorption

The role of adsorption in the inhibition of crystal growth in the presence of impurities is usually established by showing that the reduction of growth rate as a function of ligand concentration follows a Langmuir-type adsorption isotherm. Kubota & Mullin (1995) proposed a modified Langmuir model taking into account the inhibition effectiveness of the impurity. The model has been widely used in the crystal growth literature to interpret growth rate reduction (e.g Westin & Rasmuson, 2005a; Ukrainczyk *et al.*, 2012, to cite just a few examples on calcite). It postulates that growth inhibition in the presence of impurities can be described according to the following equation:

$$\frac{R}{R_0} = 1 - \frac{\alpha * K_L C}{1 + K_L C} \tag{4.10}$$

where R_0 is the initial growth rate at a particular saturation state, R is the growth rate at the same saturation state in the presence of impurities at a concentration C, K_L is a Langmuir adsorption constant, and α an "effectiveness factor" describing the efficiency of growth inhibition. When $\alpha > 1$, complete growth inhibition is obtained before the surface coverage is complete, while $\alpha < 1$ indicate incomplete growth inhibition. In the model by Kubota & Mullin (1995), both K_L and α may be fitted onto the experimental dataset, or K_L may be retrieved from independent adsorption experiments.

It should be noted that among the numerous studies investigating crystal growth inhibition, few have focused on the influence of impurities at varying saturation states. Our observations suggest that the influence of ligands on magnesite growth rate can be described through a reduction of magnesite growth rate constant; we therefore expressed the Kubota & Mullin (1995) model in terms of rate constants:

$$\frac{k'_{Mgs}}{k'^{0}_{Mgs}} = 1 - \frac{\alpha * K_L C}{1 + K_L C} \tag{4.11}$$

with k'^{0}_{Mgs} the apparent rate constant in the absence of impurities.

Retrieved magnesite growth rate constants in the presence of citrate at 120°C are plotted in Figure 4.11, (a) as a function of $Citrate^{3-}$ concentration and (b) as a function of total citrate concentration. The evolution of the rate constant as a function of citrate concentration does resemble a Langmuir isotherm, with a steep decrease of the rate constant at relatively low citrate concentration, and an inhibition plateau corresponding to approximately a 70 % reduction of the growth rate constant.

Equation 4.11 was fitted onto these plots; the best fit on plot (a) gives $\log K_L = 5.92$ and $\alpha = 0.72$, and $\log K'_L = 4.79$ and $\alpha' = 0.71$ on plot (b). The fit could not be attempted for other ligands (oxalate, EDTA) or at a different temperature due to an insufficient number of investigated concentrations. Bearing in mind the observed data scatter, a generalized rate

law can therefore be proposed for magnesite growth at 120°C and pH $\simeq$ 8 in the presence of citrate:

$$R_{Mgs}^{Cit} = k'^{0}_{Mgs} \cdot \left[1 - \frac{\alpha * K_L C}{1 + K_L C}\right] \cdot (\Omega - 1)^2 \tag{4.12}$$

where C designates either the total citrate concentration or only Citrate^{3-} concentration, and α and K_L should be chosen accordingly. The version written in terms of Citrate^{3-} concentration should be preferred since it allows to take into account solution chemical speciation. k'^{0}_{Mgs} can be converted into an "absolute" rate constant using relationship 4.6.

One should however keep in mind that such a relationship is only valid at a given pH, and for Mg and dissolved CO_2 concentrations relatively close to those of the original experiments. Important changes in the solution chemistry and pH could indeed lead to a modification of magnesite surface chemistry, and thus of ligand adsorption.

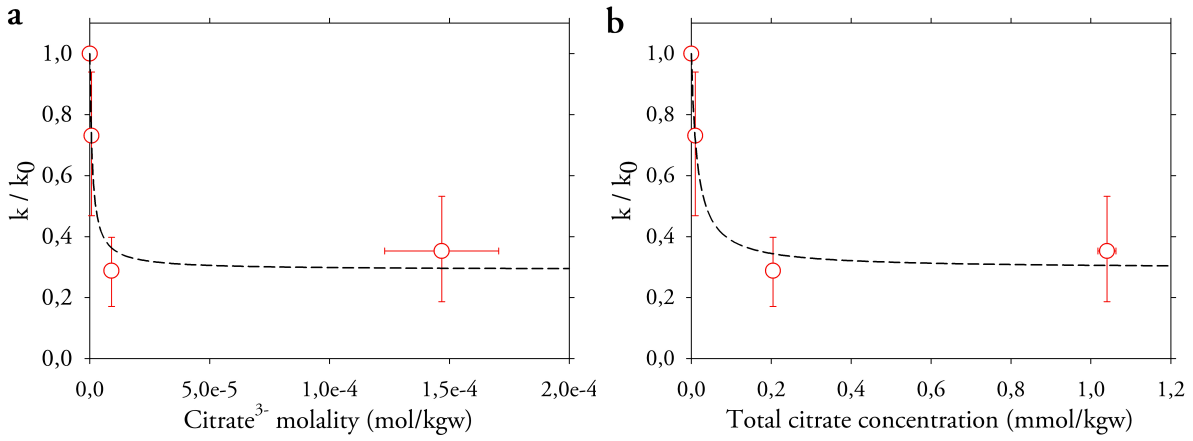

Figure 4.11 – Magnesite growth rate constants at 120°C normalized to the ligand-free constant k_0, plotted as a function of (a) the free Citrate^{3-} molality and (b) the total citrate concentration. Black dashed lines are best fits of the data according to eq. 4.11. Datapoints corresponding to 0.1 mM citrate concentration (exp. Cit2 and Cit9) have been voluntarily omitted from these graphs due to important uncertainties on the rate constant.

Site-specific adsorption and inhibition plateau

Langmuir adsorption constants retrieved from kinetic data with citrate are orders of magnitude higher than those measured directly on the bulk of the magnesite surface in similar chemical conditions, while the saturation of inhibition is reached well before total coverage of the bulk surface with adsorbed citrate. This clearly indicates that growth inhibition results from the adsorption of citrate not on the bulk of the magnesite surface, but rather onto limited surface sites for which it has a much higher affinity. Such an observation is not uncommon in the crystal growth literature: since growth proceeds through the addition of crystal units at specific active sites called "kinks" (Burton *et al.*, 1951), growth inhibition indeed results from the interaction of the additives with these specific sites (see the review by Ganor *et al.*, 2009 and references therein). In particular, it is known that many organic substances have a higher affinity for non-planar environments such as steps and kinks at the mineral surface (e.g Orme *et al.*, 2001 or de Leeuw & Cooper, 2003 for the calcite surface, or Pina *et al.*, 2004 for barite).

Because the number of kink sites is limited, growth rate reduction is obtained for a low total surface coverage by inhibitors, as observed for instance by Reddy & Hoch (2001) on calcite, or Pina *et al.* (2004) on barite, and confirmed in our experiments. The observed "inhibition plateau" thus corresponds to saturation of these existing adsorption sites, which is reached all the more quickly that the affinity of the adsorbate for these sites is high and the number of sites limited. The retrieved value of the inhibition effectiveness factor α, lower than 1, indicates that although citrate binds to growth controlling sites, this does not lead to a complete inhibition of the growth process. Such a feature has been interpreted as resulting from a large spacing of kink sites and adsorbed inhibitors along the steps (Kubota & Mullin, 1995), or from a weak attachement of the molecule to growth sites therefore allowing frequent detachment and limited growth (Pina *et al.*, 2004).

Why do different ligands inhibit magnesite growth to a different extent?

Adsorption and growth inhibition results from highly specific interactions between impurities and the growth surface (Ganor *et al.*, 2009). The behaviour of organic ligands on carbonate surfaces have indeed been related to their number of carboxylate groups and chemical functionalities, the length of their hydrocarbon chain, the distance between functional groups, and the rigidity of the molecules (e.g Zullig & Morse, 1988; Geffroy *et al.*, 1999; Hoch *et al.*, 2000). It is therefore no surprise that oxalate, citrate and EDTA influence magnesite growth to a different extent. The particularities of ligand interactions with magnesite surface will be further discussed on the basis of atomic force microscopy observation in the following Chapter 5.

In addition, ligand complexation with metal cations in aqueous solution has been shown to affect their adsorption on mineral surfaces. Johnson *et al.* (2004) for instance reported that oxalate complexation with Al(III) decreases its affinity for aluminum oxide surface under acidic pH conditions, while Davis & Kent (1990) reported that EDTA complexed to metal cations adsorbs very little on mineral surfaces. As a result, Jones *et al.* (2007) noticed that the growth inhibiting influence of EDTA on barite growth is suppressed upon addition of Ca^{2+}, which forms strong complexes with EDTA. This could provide an explanation as to why EDTA affects little magnesite growth although it was reported to adsorb more strongly than oxalate and citrate on surface magnesium of magnesite and brucite under its uncomplexed form (Pokrovsky *et al.*, 2005, 2009).

Evolution of adsorption with solution chemistry and temperature

Finally, it should be remembered that our measurements have been obtained in alkaline conditions, between 100 and 150°C. CO_2 mineral sequestration through carbonation of Mg-silicates is most favorable in slightly acidic conditions, under high CO_2 pressure. Changes in the physico-chemical conditions of magnesite growth are likely to modify as well the adsorption and the growth modifying influence of the investigated organic ligands.

pH, in particular, is a crucial parameter influencing adsorption, through modification of surface chemistry and surface charge (Stumm, 1992). Adsorption of negatively charged carboxylates is electrostatically favored on positively charged surfaces. Thus, the adsorption

maximum depends on the protonation state of both the ligand and the surface. For most small carboxylates, adsorption on clays or metal oxides reaches a maximum in slightly acidic to circumneutral pH (3 < pH < 6) (e.g Kummert & Stumm, 1980; Filius *et al.*, 1997; Evanko & Dzombak, 1999; Lackovic *et al.*, 2003; Alliot *et al.*, 2005). In the case of carbonates, adsorption studies have only been performed in basic conditions, and little variation of the adsorption was observed between pH 9 and 12 (Geffroy *et al.*, 1999; Plank & Bassioni, 2007).

According to Pokrovsky *et al.* (1999), the pH of zero charge of magnesite surface at low pCO_2 and 25°C is equal to 8.7 $\pm$ 0.2. It decreases with increasing pCO_2 as a result of carbonate adsorption. Thus, it is likely that a pH decrease to slightly acidic conditions would favor ligand adsorption thanks to a more positive surface charge. Increase of Mg^{2+} concentration could produce a similar effect thanks to adsorption of the magnesium cations to surface carbonate groups. Such an analysis is however highly qualitative, and only a consistent surface complexation model of magnesite surface at high temperature could help predicting precisely the evolution of growth inhibition at lower pH than those investigated.

Concerning temperature, few adsorption studies have focused on temperatures other than 25°C. Plank & Bassioni (2007) investigated the adsorption of several carboxylates on calcite between 20 and 60°C at pH 9, and observed a clear decrease of the sorbate concentration upon temperature increase. Similarly, Liu & Nancollas (1975) remarked that an increase of temperature provokes a marked decrease of gypsum growth inhibition in the presence of scale inhibitors. Our own kinetic measurements show that magnesite growth inhibition due to oxalate is higher at 120°C than 146°C. For citrate, our data indicate a slightly higher inhibition at 120°C compared to 100°C. Data scatter however render these observations hardly conclusive. In addition, Angove *et al.* (2006a,b) have shown that the evolution of adsorption of mellitic acid on kaolinite and goethite as a function of temperature between 10 and 70°C depends on the pH: adsorption increases with temperature at low pH, but decreases when temperature increases at basic pH. On the contrary Fein (1995) observed an increase of oxalate adsorption on alumina at pH > 9 between 25 and 60°C, and a decrease at 6 < pH < 9. It is thus difficult to conclude on the potential influence of temperature on the inhibiting influence of carboxylates on magnesite growth; thorough adsorption studies as a function of temperature and pH are needed.

4.4.2 Consequences for Mg-silicates carbonation

Oxalate, citrate and EDTA are known to enhance Mg-silicates dissolution rates, including forsterite (Olsen & Rimstidt, 2008; Prigiobbe & Mazzotti, 2011) and serpentine (Park *et al.*, 2003; Krevor & Lackner, 2011). Using magnesite growth rates determined in the present study, and Mg-silicates dissolution rates from the literature, it is possible to simulate the overall carbonation of forsterite in the presence of ligands, and thus determine their net influence on the carbonation process.

Numerical simulation of forsterite carbonation: setting the scene

Here, we focused on the widely studied case of direct aqueous forsterite carbonation (e.g Giammar *et al.*, 2005; Béarat *et al.*, 2006; Dufaud *et al.*, 2009; Garcia *et al.*, 2010; Daval *et al.*, 2011; Bonfils *et al.*, 2012), which may be summarized using the following set of chemical reactions:

$$Mg_2SiO_4 + 4\,H^+ \longrightarrow 2\,Mg^{2+} + H_4SiO_4 \tag{4.13}$$

$$Mg^{2+} + HCO_3^- \longrightarrow MgCO_3 + H^+ \tag{4.14}$$

where HCO_3^- is produced by CO_2 dissolution into the aqueous solution.
Magnesian olivine dissolution mechanism and kinetics (corresponding to eq. 4.13) is indeed well known in a wide range of pH and temperature (Wogelius & Walther, 1991; Pokrovsky & Schott, 2000; Rosso & Rimstidt, 2000; Golubev *et al.*, 2005; Hänchen *et al.*, 2006; Prigiobbe *et al.*, 2009), including in the presence of various organic ligands (Grandstaff, 1986; Wogelius & Walther, 1991; Olsen & Rimstidt, 2008; Prigiobbe & Mazzotti, 2011).

In particular, Prigiobbe & Mazzotti (2011) proposed a semi-empirical rate law for far-from-equilibrium forsterite dissolution rates in the presence of oxalate, valid in the temperature range 25 < T < 120°C and in the pH range 2 < pH < 8:

$$R_{Fo} = r'_{Fo} * \frac{1}{1 + K_H a_{H^+}^n} \left(\frac{1 + \beta K_{ox} a_{ox}}{1 + K_{ox} a_{ox}} \right) \tag{4.15}$$

with a_{H^+} is the proton activity, a_{ox} is the Oxalate^{2-} activity, K_H is the protonation constant of forsterite surface oxygens, K_{ox} is the surface complexation constant of forsterite surface magnesium with oxalate anions, and r'_{Fo} is the pH-dependent ligand-free far-from-equilibrium dissolution rate. At 120°C, $\beta = 71$, $K_H = 0.2$ and $K_{ox} = 10$. At the same temperature, r'_{Fo} is a function of pH only and may be expressed in the range 2 < pH < 8 as (Prigiobbe *et al.*, 2009):

$$\log r'_{Fo} = -0.52 * \mathrm{pH} - 7.59 \tag{4.16}$$

Such rate laws can be directly included into geochemical codes. Although the enhancing influence of citrate and EDTA on forsterite dissolution has been evidenced experimentally (Grandstaff, 1986 at low temperature; Hänchen *et al.*, 2006 and Prigiobbe & Mazzotti, 2011 for citrate at high temperature), experimental results are more scarce for these ligands, and generalizable rate laws are currently lacking. Thus, numerical simulations were limited to the case of oxalate.

Kinetic simulations were performed using PHREEQC (Parkhurst & Appelo, 1999) with the updated `llnl.dat` database used throughout the study (see Chapter 3). They consisted in simulating the evolution of a 10 g (0.07108 mol) of forsterite placed in a stirred batch reactor containing one kilogram of water at 120°C, under a given constant CO_2 pressure. The initial forsterite specific surface area was taken to be 0.1 m^2/g, corresponding to micrometer-sized spherical forsterite grains.

Two experimental cases were investigated; in both cases, simulations were performed both in the absence of any organic ligand, and in the presence of 10 mM of oxalate :

- The first set of simulations was performed under a constant 10 bars CO_2 pressure, and with 0.07 M NaCl as a background salt in order to fix the ionic strength close to 0.1 M. These conditions correspond roughly to some experimental studies (Giammar *et al.*, 2005; Bonfils *et al.*, 2012; Declercq & Oelkers, 2012). In order to minimize the differences in pH introduced by oxalate, the initial pH in the ligand-free simulation was adjusted with NaOH to the initial pH obtained in the presence of oxalate (4.766). This pH adjustment had very minor consequences on the final results. The corresponding dissolved carbon concentration varied during the progress of the reaction between 0.1 and 0.16 M.

- The second set of simulations was performed at a constant CO_2 pressure of 1 bar, without sodium chloride, under which conditions the pH of the system was initially adjusted to 7.5 by adding sodium hydroxide. The ionic strength was close to 0.15 M and the dissolved carbon concentration was stable and equal to about 0.155 M.

  Such chemical conditions are not favorable for forsterite carbonation, since forsterite dissolution rate is much slower than at lower pH. However, the advantage of these simulations is twofold: 1) pH conditions are close to the pH conditions used to investigate magnesite growth kinetics in the present study, such that the corresponding rate laws may be used without modifications, and 2) these simulations present an interesting conceptual case study where the overall carbonation rate is likely to be limited by the slower forsterite dissolution kinetics. In addition, forsterite carbonation at high PCO_2 and slightly basic pH has been tested by O'connor *et al.* (2001) and Gerdemann *et al.* (2007) by using 0.64 M $NaHCO_3$ as an additive to increase alkalinity. High pH solutions may as well be produced through alteration of ultramafic bodies (e.g Kelemen *et al.*, 2011).

The rate expression used to describe forsterite dissolution is :

$$R_{tot,Fo} = R_{Fo} * A_0 \left(\frac{m}{m_0}\right)^{\frac{2}{3}} \tag{4.17}$$

where R_{Fo} is the specific rate (mol/m^2/s) given by eq. 4.15, A_0 the initial surface area of the mineral (1 m^2), m_0 its initial mass (10 g) and m its mass at a given time. The term $\left(\frac{m}{m_0}\right)^{2/3}$ accounts for the evolution in surface area of uniformly dissolving forsterite spheres (Parkhurst & Appelo, 1999). Here, it should be noted that no term describing the dependence of forsterite dissolution rate on chemical affinity was introduced in eq. 4.17. Reasons for this omission are given below.

For magnesite growth in the absence of ligands, eq. 4.3 was used with magnesite surface complexation constants determined by Saldi *et al.* (2012) and rate constants listed in Table 4.4 at 120°C.

In the presence of 10 mM oxalate, we used the empirical rate law described by eq. 4.8 together with rate constants listed in Table 4.4. The assumption here is that this rate law determined in alkaline conditions is applicable in different chemical conditions (lower pH, higher magnesium and carbon concentrations, higher extent of oxalate complexation). However, as outlined in Section 4.3.4, the evolution of oxalate adsorption on magnesite surface as a function of pH, Mg^{2+} and carbonate concentration is somehow uncertain. In the absence of a complete surface complexation model at 120°C taking oxalate into account, it is not possible to explicitly account for these effects. Thus, in both investigated case studies, we only performed additional simulations with 10 mM oxalate, assuming oxalate did not affect magnesite precipitation kinetics through adsorption (labelled below "no adsorption"). In this case, equation 4.3 was used with the ligand-free rate constants.

Several additional simplifying assumptions were used:

- Dissolved silica produced by forsterite dissolution (eq. 4.13) is assumed to precipitate only under the form of amorphous silica $SiO_{2(am)}$. Although this product has been identified as the main sink of silica during forsterite carbonation experiments (e.g Béarat *et al.*, 2006; Daval *et al.*, 2011), a few experimental studies have outlined the formation of hydrated Mg-silicate phases, particularly at high temperature (Dufaud *et al.*, 2009; King *et al.*, 2010; Bonfils *et al.*, 2012). The thermodynamics and precipitation kinetics of such phases are however poorly constrained, and they were therefore not included in the simulations.

- Amorphous silica is assumed to precipitate at equilibrium, which is a strongly simplifying assumption (Rimstidt & Barnes, 1980; Carroll *et al.*, 1998).

- Experimental studies of forsterite carbonation in unstirred batch reactors have shown the passivating influence of dense amorphous silica layers precipitated at the surface of forsterite grains (Béarat *et al.*, 2006; Daval *et al.*, 2011). The formation of such silica layers is apparently prevented in stirred batch reactors (Gerdemann *et al.*, 2007; Bonfils *et al.*, 2012). Here, we do not take into account the possible inhibiting influence of precipitated amorphous silica on olivine dissolution.

- No dependence on chemical affinity was introduced into forsterite dissolution rate equation (eq. 4.17). According to the classical transition state theory, dependence to forsterite saturation state Ω_{Fo} may be described via a term $(1 - \Omega_{Fo}^{n})^{m}$, with n and m constant exponents determined experimentally (Lasaga, 1981). However, such a relationship has never been verified experimentally (Daval *et al.*, 2011), and as mentioned above, it is likely that upon extensive forsterite dissolution, disordered Mg-silicate phases will precipitate, thus limiting the approach of forsterite equilibrium.

  In simulations with 10 bars of CO_2 pressure, the solution never gets close to forsterite equilibrium, and thus the introduction of a chemical affinity dependence term would not significantly change the results. In simulations with 1 bar of CO_2 however, the solution does get close to forsterite saturation. In order to limit this effect, the results presented below were limited to the first 24 hours of reaction.

- For simplicity sake, it is assumed that the precipitating phases (magnesite and amorphous silica) have a surface area equivalent to the initial forsterite surface area (1 m^2). The nucle-

ation kinetics of these phases, poorly constrained, is not taken into account. Thus, magnesite and amorphous silica may precipitate on a 1 m^2 surface area as soon as the solution is supersaturated with respect to these phases.

Therefore, it should be kept in mind that such simulations do not aim at accurately representing the extent and the rate of forsterite carbonation under given conditions, but rather provide an integrated view of the influence of ligands on the coincident forsterite dissolution and magnesite precipitation.

Results and conclusions

The evolution of the amount of the different minerals, as well as of the carbonation rate during forsterite carbonation at 120°C have been plotted in Fig. 4.12 (10 bars PCO_2, free pH) and 4.13 (1 bar PCO_2, pH 7.5). Evolution of pH, Mg and Si concentration, and Mg and oxalate speciation have been plotted in Appendix B (Fig. 4.14 and 4.15). Table 4.6 summarizes the extent of carbonation simulated at different timesteps for the different case studies.

Run with 10 bars PCO_2			
Time (hours)	no ligand	Oxalate 10 mM	Oxl 10 mM - no adsorption
24	9.03 %	5.16 %	7.79 %
100	57.02 %	48.39 %	53.94 %
1200	95.32 %	91.05 %	91.95 %
Run with 1 bar PCO_2, initial pH 7.5			
Time (hours)	no ligand	Oxalate 10 mM	Oxl 10 mM - no adsorption
24	3.67 %	4.61 %	5.13 %

Table 4.6 – Extent of forsterite carbonation (% of conversion into magnesite of the total Mg available in 10 g of forsterite) for different timesteps.

In the absence of oxalate, forsterite carbonation appears to be a lot more efficient under a 10 bars CO_2 pressure than under 1 bar, in accordance with the literature. Indeed, the carbonation rate is half an order of magnitude higher at the highest CO_2 pressure (Fig. 4.12b and 4.13c).

Under a 10 bars CO_2 pressure, addition of 10 mM of oxalate initially leads to an enhanced forsterite dissolution rate (Fig. 4.12c), while magnesite formation rate is reduced compared to the ligand-free case (Fig. 4.12d), leading to a 43% reduction of the carbonation extent after 24h (Table 4.6). As the reaction progresses in the presence of oxalate, an increase of pH coupled to an increase of total magnesium concentration lowering the amount of free oxalate, leads to a decrease of forsterite dissolution rate which further lowers magnesite growth rate.

Thus, in the period between 15 and 85 h, the mean carbonation rate is equal to $2.68 \cdot 10^{-7}$ mol Mgs/s in the absence of ligands, while it is reduced by 12 % in the presence of 10 mM oxalate ($2.37 \cdot 10^{-7}$ mol Mgs/s), despite a slightly higher pH and a significantly higher dissolved carbon concentration (see Fig. 4.14a in Appendix B).
Finally, the maximum extent of forsterite carbonation is reduced as well in the presence of oxalate, due to the persistence of MgOxalate complexes.

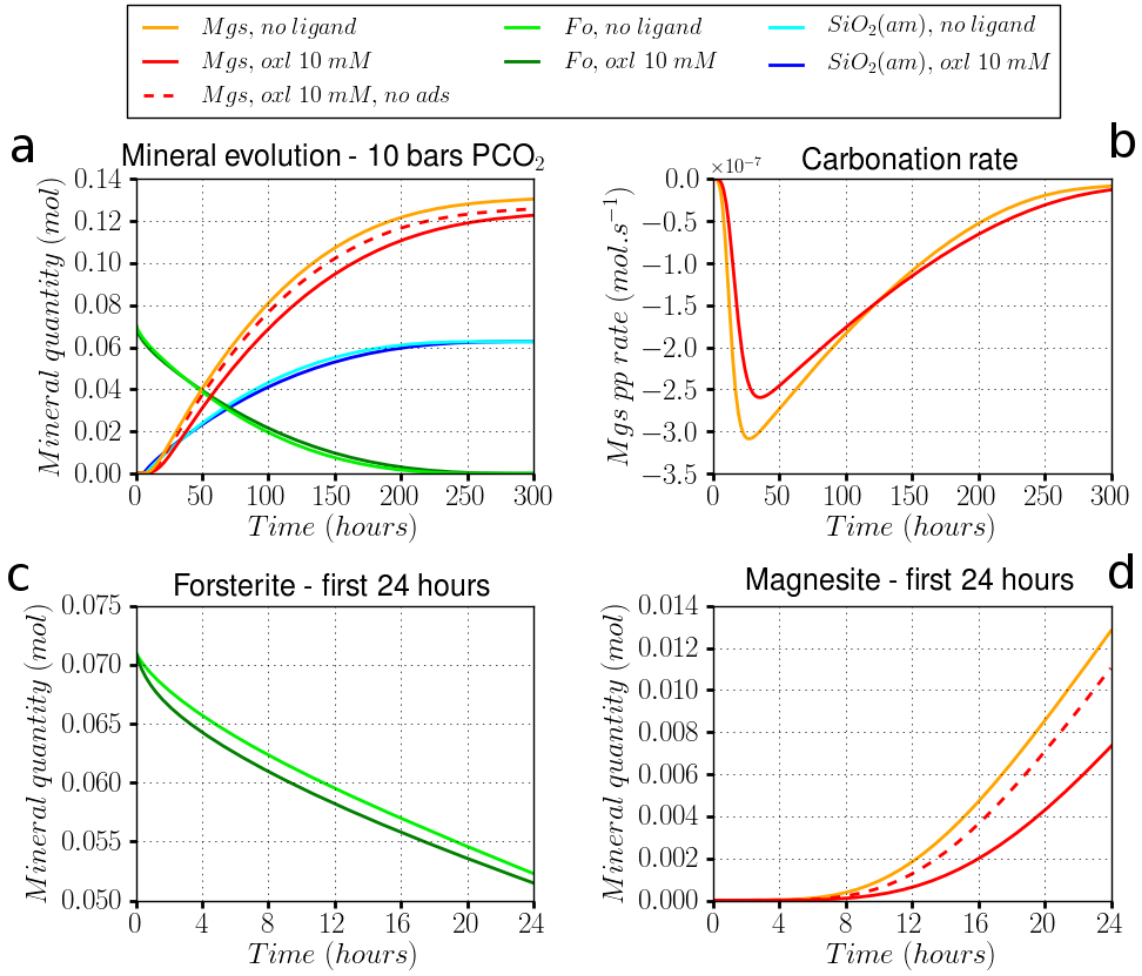

Figure 4.12 – Simulation of the carbonation of 10g of forsterite in one kilogram of water under a 10 bars CO_2 pressure, in the absence of any ligands and in the presence of 10 mM of oxalate: (a) Evolution of the quantity of forsterite, magnesite, and amorphous silica during a 300h carbonation simulation. The dashed line represents the evolution of precipitated magnesite in the presence of 10 mM oxalate, when the inhibiting influence of oxalate on magnesite precipitation due to adsorption at the mineral surface is not taken into account. (b) Carbonation rate (rate of magnesite formation) as a function of time. (c) and (d) Detail of the evolution of forsterite and magnesite during the first 24h of the simulation.

If the inhibiting influence of oxalate on magnesite precipitation is not taken into account, as represented by dashed lines in Fig. 4.12, the addition of 10 mM oxalate is still detrimental to forsterite carbonation, which can then only be attributed to the thermodynamic effect of magnesium complexation by oxalate anions.

The extent of the reduction of carbonation rate and carbonation extent in the presence of oxalate of course depends on the respective amounts of forsterite and the ligand. If the same simulations are performed with 1 g of forsterite instead of 10 g, under otherwise identical conditions, the inhibiting influence of oxalate on forsterite carbonation is more important (see Fig. 4.16 in Appendix B).

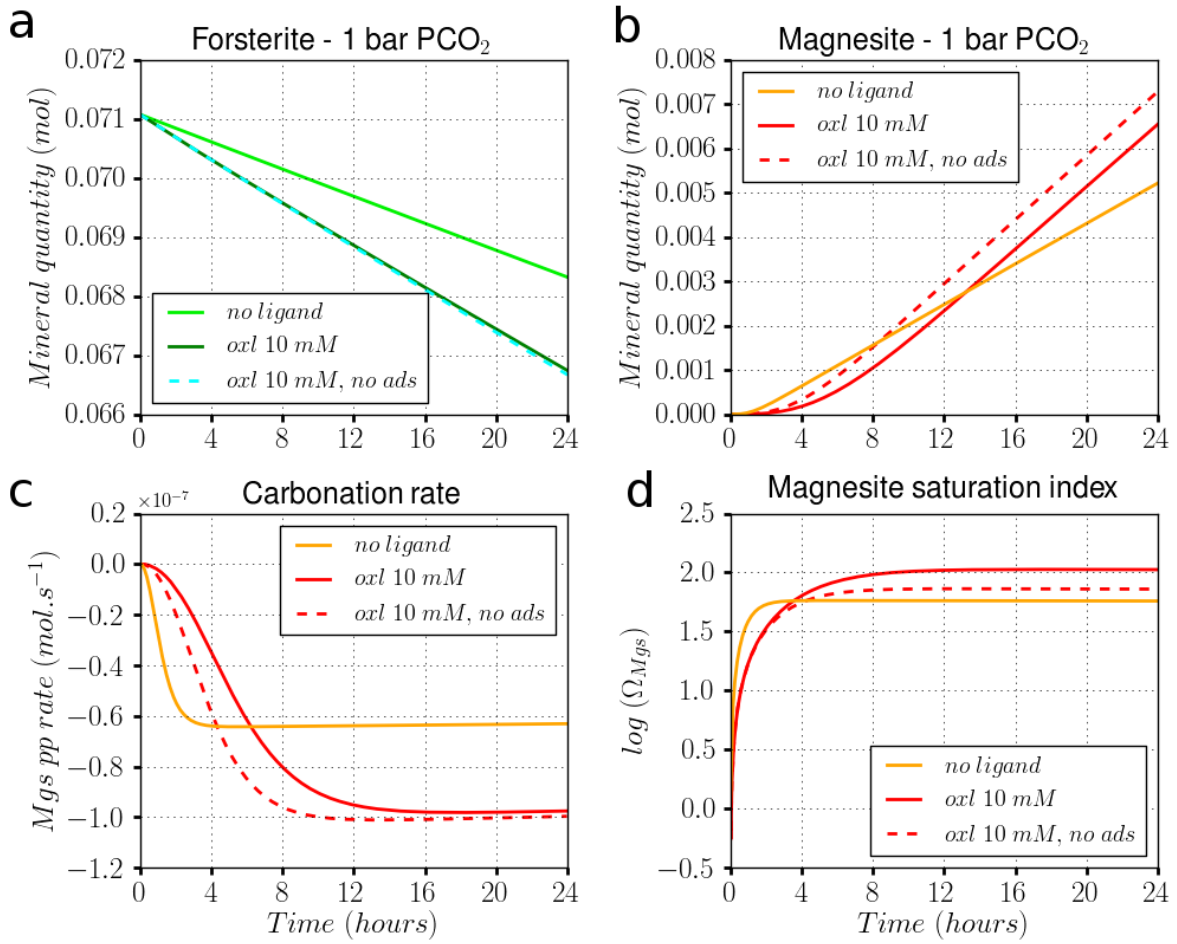

Figure 4.13 – Simulation of the carbonation of 10g of forsterite in one kg of water under a 1 bar CO_2 pressure, with and without 10 mM of oxalate, with an initial pH fixed to 7.5: (a) and (b) Evolution of the quantity of forsterite and magnesite during the first 24h of the simulation. Amorphous silica did not form within this time frame. Dashed lines represent the evolution of minerals amounts in the presence of 10 mM oxalate, when the inhibiting influence of oxalate on magnesite precipitation is not taken into account. (c) Carbonation rate, with and without oxalate. (d) Corresponding evolution of magnesite saturation index ($SI = \log \Omega_{Mgs}$).

Only the first 24 hours of the second run (1 bar CO_2 pressure, initial pH 7.5) have been represented on Fig. 4.13, which assumes that forsterite dissolution rate is not limited by the approach of thermodynamic equilibrium. In this case, forsterite dissolution is significantly accelerated by 10 mM of oxalate (Fig. 4.13a). Formation of magnesite is initially delayed, but as forsterite dissolution proceeds at higher rate than in the absence of ligands, the solution saturation state with respect to magnesite soon exceeds that in the absence of ligands (Fig. 4.13d), and carbonation rate increases accordingly. Indeed, between 12 and 20 hours, the mean carbonation rate in the absence of ligands is calculated to be $6.36 \cdot 10^{-8}$ mol Mgs/s, while it would be $9.78 \cdot 10^{-8}$ mol Mgs/s in the presence of 10 mM oxalate (54 % more). Thus, surprisingly, after approximately 14 hours, magnesite production in the presence of 10 mM of oxalate exceeds that in the absence of ligands.

If adsorption of oxalate onto magnesite is not taken into account (dashed lines), forsterite dissolution is not affected, but the carbonation rate is further increased (Fig. 4.13c). However, because in both cases a majority of dissolved magnesium is stored under the MgOxalate

complexed form (Fig. 4.15), it is likely that the maximum extent of carbonation will be reduced in the presence of oxalate.

Although conceptual, this case study indicates that under conditions were slow Mg-silicate dissolution may limit the rate of mineral carbonation, the use of additives which enhance sufficiently silicates dissolution may have a positive effect on carbonation rate, even if the ligand slows down magnesite formation. This observation could be useful to optimize the carbonation of slowly dissolving Mg-containing silicates such as talc or serpentine (Guyot *et al.*, 2011).

Limitations and extrapolation to other ligands

In addition to the simplifying hypothesis already presented above, several factors may lead to a reduction of forsterite carbonation rate and carbonation extent compared to our simulations:

- As a result of quicker forsterite dissolution and delayed magnesite precipitation in the presence of oxalate, solution saturation state with respect to other Mg-containing phases increase as well. It is likely that disordered Mg-silicate phases will precipitate in addition to magnesite, as observed experimentally (King *et al.*, 2010). Such precipitations will store part of the magnesium extracted from forsterite, thus reducing magnesite precipitation. This effect is particularly likely in alkaline conditions (Declercq & Oelkers, 2012), which limits the validity of our simulation results at high pH to the very first hours of the carbonation reaction. The possibly positive effect of oxalate could then quickly be overreached by secondary phases precipitation.
- Phase nucleation has not been represented in the present simulations, but constitute a major challenge in accurately representing mineral carbonation processes. It is anyhow likely that the addition of organic ligands will delay the nucleation of carbonates (as well as other phases) due to reduction of the saturation state, and possible effects on the interfacial tension of newly formed nuclei. Citrate for instance has been shown to retard nucleation of calcium carbonate (Westin & Rasmuson, 2005b; Gebauer *et al.*, 2009).

Despite these limitations, and although comprehensive rate laws describing the influence of citrate and EDTA on forsterite dissolution rates are currently lacking, it is possible to speculate from the simulations performed on the global influence of citrate and EDTA on the forsterite carbonation process.

Prigiobbe & Mazzotti (2011) have shown that the enhancement of forsterite dissolution is less important with citrate than with oxalate. As shown in this study, the inhibition of magnesite growth is more pronounced in the presence of citrate than with oxalate. In addition, Mg^{2+} complexation by citrate anions is significantly stronger than with oxalate. Thus, citrate will be more detrimental to forsterite carbonation than oxalate is. In addition, it should not be forgotten that concentrations of 1mM of citrate or higher may create "no-growth" zones preventing magnesite growth at positive supersaturations (see Section 4.3.3). Such dead zones would further delay magnesite formation and slow down carbonation rate.

Although EDTA has been shown to be an efficient promoter of Mg-silicates dissolution (e.g Park *et al.*, 2003; Krevor & Lackner, 2011), it is as well a very strong chelate of Mg^{2+}.

Thus, if EDTA is present in excess with respect to dissolved magnesium, it will bind most of the available Mg^{2+} (see Chapter 3), therefore hindering completely magnesium precipitation through reduction of the saturation state. If Mg^{2+} is present in excess, all EDTA will be under the $MgEDTA^{2-}$ form, which is less likely to adsorb on mineral surfaces than the free EDTA (Davis & Kent, 1990), and may therefore less enhance forsterite dissolution. Therefore, although EDTA has the ability to enhance forsterite dissolution, this ability will be limited by complexation with the resulting cations. At the same time, we have seen that, even under its magnesium-complexed form, EDTA inhibits magnesite growth more than oxalate (Section 4.3.3). Thus, EDTA will most certainly be detrimental to forsterite carbonation.

Overall, the quantitative influence of organic ligands on carbonation rate and maximum carbonation extent will depend on the respective ligand concentration and the solid/solution ratio. Rigorous predictions can only be attempted if models describing the influence of the ligands on both silicate dissolution and carbonate precipitation are available. Such models should take into account the aqueous speciation of the ligand as well as the surface speciation of mineral surfaces, in order to determine how the ligand influence may evolve with evolving solution chemistry, in a wide range of physico-chemical conditions. The model proposed by Prigiobbe & Mazzotti (2011) for forsterite dissolution in the presence of oxalate is a first step in this direction, but we are still far from being able to propose a consistent surface complexation model to describe the influence of ligands on magnesite precipitation kinetics.

4.5 Conclusion

Simple polycarboxylates such as oxalate, citrate and EDTA decrease magnesite growth rates in slightly basic conditions and at hydrothermal temperatures investigated in this study. This rate decrease results in part from complexation of Mg^{2+} by the ligands, which reduces the aqueous solution supersaturation with respect to magnesite. This effect was carefully taken into account by compiling a complete thermodynamic database describing Mg^{2+}-ligand interactions at high temperature (presented in Chapter 3).

In addition, we evidenced that the investigated organic ligands inhibit magnesite growth through adsorption onto the growth-controlling sites at the mineral surface. While growth rates in the presence of ligands can still be expressed with a second-order rate law, inhibition translates into a reduction of the growth rate constant, which in the case of citrate at 120°C can be described via a Langmuir adsorption isotherm. This growth inhibition was verified at different temperatures. Among the ligands studied, citrate is the most efficient at inhibiting growth, with up to 70 % reduction of the growth rate constant with 0.2 mM of ligand. EDTA affects growth rate from 1 mM concentrations, while high concentrations of oxalate (10 mM) are necessary to influence magnesite growth rates.

Although the measured growth inhibition is overall relatively limited, it has important consequences on the rate and extent of Mg-silicates carbonation. We performed numerical kinetic simulations of forsterite carbonation in the presence of oxalate, using published expressions for forsterite dissolution rate in the presence of oxalate. Our results indicate that under typical carbonation conditions (PCO_2 = 10 bars, 120°C, slightly acidic pH), the use of 10 mM of oxalate to accelerate forsterite dissolution is likely to result in a delayed magnesite formation, a significant 12 % decrease of carbonation rates, as well as in a decrease of the maximal extent of carbonation. Citrate and EDTA will also be detrimental to forsterite carbonation. Only in cases where the carbonation process is strongly limited by the dissolution of the silicate phase could ligands prove to be useful to accelerate the initial stages of magnesite production. However, delayed magnesite formation could as well lead to more secondary Mg-silicate phases formation, which would be detrimental to carbonation.

Our results suggest that using organic ligands accelerating silicates dissolution in order to accelerate mineral carbonation is not a promising pathway. Although a positive influence of organic ligands on Mg^{2+} reactivity through an acceleration of water exchange rates cannot be ruled out, this possible favourable effect is overprinted by inhibition resulting from adsorption. Accelerating Mg-carbonate formation with organic molecules is not yet possible, and future research should focus on more complex bio- or bio-inspired molecules which could further impact Mg^{2+} solvation while interacting little with the mineral surface (Hamm *et al.*, 2010; Chen *et al.*, 2011).

Finally, small dicarboxylates such as oxalate are widely spread in formation waters of sedimentary basins, with citrate also present in minor quantities (Means & Hubbard, 1987; Kharaka *et al.*, 1993; Kharaka & Hanor, 2003). The results obtained here may thus be of some relevance for the understanding of the reactivity of Mg-containing carbonate minerals (e.g dolomite) found in sedimentary basins were CO_2 injection is foreseen.

Although our results suggest that magnesite growth inhibition by carboxylates proceeds through preferential binding of the organics to surface growth sites, the exact inhibition mechanism has not yet been determined. Insights on this problem can be gained from nanoscale observations of growth processes at the mineral surface through atomic force microscopy (Pina *et al.*, 2004; Saldi *et al.*, 2009). This will be the subject of the next chapter.

Bibliography

Aagaard, P. & Helgeson, H. C. (1982). Thermodynamic and kinetic constraints on reaction rates among minerals and aqueous solutions; i. theoretical considerations. *American Journal of Science*, 282(3), 237–285.

Alliot, C., Bion, L., Mercier, F., & Toulhoat, P. (2005). Sorption of aqueous carbonic, acetic, and oxalic acids onto α-alumina. *Journal of Colloid and Interface Science*, 287(2), 444–451.

Angove, M. J., Wells, J. D., & Johnson, B. B. (2006a). The influence of temperature on the adsorption of mellitic acid onto goethite. *Journal of Colloid and Interface Science*, 296(1), 30–40.

Angove, M. J., Wells, J. D., & Johnson, B. B. (2006b). Influence of temperature on the adsorption of mellitic acid onto kaolinite. *Langmuir*, 22(9), 4208–4214.

Béarat, H., McKelvy, M. J., Chizmeshya, A. V. G., Gormley, D., Nunez, R., Carpenter, R. W., Squires, K., & Wolf, G. H. (2006). Carbon sequestration via aqueous olivine mineral carbonation: Role of passivating layer formation. *Environmental Science & Technology*, 40(15), 4802–4808.

Blum, A. & Lasaga, A. (1987). Monte carlo simulations of surface reaction rate laws. In *Aquatic Surface Chemistry* (pp. 255–292). New York: John Wiley and Sons.

Bénézeth, P., Palmer, D. A., & Wesolowski, D. J. (1997). Dissociation quotients for citric acid in aqueous sodium chloride media to 150°C. *Journal of Solution Chemistry*, 26(1), 63–84.

Bénézeth, P., Saldi, G. D., Dandurand, J. L., & Schott, J. (2011). Experimental determination of the solubility product of magnesite at 50 to 200°C. *Chemical Geology*, 286, 21–31.

Boles, J. S., Ritchie, K., & Crerar, D. A. (1987). Reducing the potential for migration of radioactive waste: aqueous thermal degradation of the chelating agent disodium edta. *Nuclear and Chemical Waste Management*, 7(2), 89–93.

Bonfils, B., Julcour-Lebigue, C., Guyot, F., Bodénan, F., Chiquet, P., & Bourgeois, F. (2012). Comprehensive analysis of direct aqueous mineral carbonation using dissolution enhancing organic additives. *International Journal of Greenhouse Gas Control*, 9(0), 334–346.

Brunauer, S., Emmett, P. H., & Teller, E. (1938). Adsorption of gases in multimolecular layers. *Journal of the American Chemical Society*, 60(2), 309–319.

Burton, W. K., Cabrera, N., & Frank, F. C. (1951). The growth of crystals and the equilibrium structure of their surfaces. *Philosophical Transactions of the Royal Society of London. Series A, Mathematical and Physical Sciences*, 243(866), 299–358.

Cantrell, K. J., Serkiz, S. M., & Perdue, E. M. (1990). Evaluation of acid neutralizing capacity data for solutions containing natural organic acids. *Geochimica et Cosmochimica Acta*, 54(5), 1247–1254.

Carroll, S., Mroczek, E., Alai, M., & Ebert, M. (1998). Amorphous silica precipitation (60 to 120°C): comparison of laboratory and field rates. *Geochimica et Cosmochimica Acta*, 62(8), 1379–1396.

Chen, C. L., Qi, J., Zuckermann, R. N., & DeYoreo, J. J. (2011). Engineered biomimetic polymers as tunable agents for controlling CaCO3 mineralization. *Journal of the American Chemical Society*.

Chen, Z.-Y., O'Connor, W. K., & Gerdemann, S. J. (2006). Chemistry of aqueous mineral carbonation for carbon sequestration and explanation of experimental results. *Environmental Progress*, 25(2), 161–166.

Crossey, L. J. (1991). Thermal degradation of aqueous oxalate species. *Geochimica et Cosmochimica Acta*, 55(6), 1515–1527.

Daval, D., Sissmann, O., Menguy, N., Saldi, G. D., Guyot, F., Martinez, I., Corvisier, J., Garcia, B., Machouk, I., Knauss, K. G., & Hellmann, R. (2011). Influence of amorphous silica layer formation on the dissolution rate of olivine at 90 °C and elevated pCO2. *Chemical Geology*, 284(1-2), 193–209.

Davis, J. A. & Kent, D. B. (1990). Surface complexation modeling in aqueous geochemistry. *Reviews in Mineralogy and Geochemistry*, 23(1), 177.

de Leeuw, N. H. & Cooper, T. G. (2003). A computer modeling study of the inhibiting effect of organic adsorbates on calcite crystal growth. *Crystal Growth & Design*, 4(1), 123–133.

Declercq, J. & Oelkers, E. H. (2012). Thermodynamic and kinetic constraints on the carbonation of forsterite and serpentine. *submitted*.

Dufaud, F., Martinez, I., & Shilobreeva, S. (2009). Experimental study of mg-rich silicates carbonation at 400 and 500 °C and 1 kbar. *Chemical Geology*, 265(1-2), 79–87.

Elhadj, S., De Yoreo, J. J., Hoyer, J. R., & Dove, P. M. (2006). Role of molecular charge and hydrophilicity in regulating the kinetics of crystal growth. *Proceedings of the National Academy of Sciences*, 103(51), 19237–19242.

Elhadj, S., Salter, E. A., Wierzbicki, A., De Yoreo, J. J., Han, N., & Dove, P. M. (2005). Peptide controls on calcite mineralization: polyaspartate chain length affects growth kinetics and acts as a stereochemical switch on morphology. *Crystal Growth & Design*, 6(1), 197–201.

Evanko, C. R. & Dzombak, D. A. (1999). Surface complexation modeling of organic acid sorption to goethite. *Journal of Colloid and Interface Science*, 214(2), 189–206.

Fein, J. B. (1991). Experimental study of aluminum-, calcium-, and magnesium-acetate complexing at 80 c. *Geochimica et Cosmochimica Acta*, 55(4), 955–964.

Fein, J. B. (1995). Mineral surface controls on the diagenetic transport of oxalate and aluminum. *Chemical Geology*, 121(1-4), 11–18.

Filius, J. D., Hiemstra, T., & Van Riemsdijk, W. H. (1997). Adsorption of small weak organic acids on goethite: Modeling of mechanisms. *Journal of Colloid and Interface Science*, 195(2), 368–380.

Fu, G., Qiu, S. R., Orme, C. A., Morse, D. E., & De Yoreo, J. J. (2005). Acceleration of calcite kinetics by abalone nacre proteins. *Advanced Materials*, 17(22), 2678–2683.

Ganor, J., Reznik, I. J., & Rosenberg, Y. O. (2009). Organics in water-rock interactions. *Reviews in Mineralogy and Geochemistry*, 70(1), 259.

Garcia, B., Beaumont, V., Perfetti, E., Rouchon, V., Blanchet, D., Oger, P., Dromart, G., Huc, A.-Y., & Haeseler, F. (2010). Experiments and geochemical modelling of CO_2 sequestration by olivine: Potential, quantification. *Applied Geochemistry*, 25(9), 1383–1396.

Gautier, J. M., Oelkers, E. H., & Schott, J. (1994). Experimental study of k-feldspar dissolution rates as a function of chemical affinity at 150°C and pH 9. *Geochimica et Cosmochimica Acta*, 58(21), 4549–4560.

Gebauer, D., Calfen, H., Verch, A., & Antonietti, M. (2009). The multiple roles of additives in CaCO3 crystallization: A quantitative case study. *Advanced Materials*, 21(4), 435–439.

Geffroy, C., Foissy, A., Persello, J., & Cabane, B. (1999). Surface complexation of calcite by carboxylates in water. *Journal of Colloid and Interface Science*, 211(1), 45–53.

Gerdemann, S. J., O'Connor, W. K., Dahlin, D. C., Penner, L. R., & Rush, H. (2007). Ex situ aqueous mineral carbonation. *Environmental Science & Technology*, 41(7), 2587–2593.

Giammar, D. E., Bruant, R. G., & Peters, C. A. (2005). Forsterite dissolution and magnesite precipitation at conditions relevant for deep saline aquifer storage and sequestration of carbon dioxide. *Chemical Geology*, 217(3-4), 257–276.

Giannimaras, E. K. & Koutsoukos, P. G. (1988). Precipitation of calcium carbonate in aqueous solutions in the presence of oxalate anions. *Langmuir*, 4(4), 855–861.

Golubev, S. V., Pokrovsky, O. S., & Schott, J. (2005). Experimental determination of the effect of dissolved CO_2 on the dissolution kinetics of mg and ca silicates at 25 °C. *Chemical Geology*, 217(3-4), 227–238.

Grandstaff, D. E. (1986). The dissolution rate of forsteritic olivine from hawaiian beach sand. *Rates of chemical weathering of rocks and minerals*, (pp. 41–59).

Guyot, F., Daval, D., Dupraz, S., Martinez, I., Ménez, B., & Sissmann, O. (2011). CO_2 geological storage: The environmental mineralogy perspective. *Comptes Rendus Geoscience*, 343(2-3), 246–259.

Hamm, L. M., Wallace, A. F., & Dove, P. M. (2010). Molecular dynamics of ion hydration in the presence of small carboxylated molecules and implications for calcification. *The Journal of Physical Chemistry B*, 114, 10488–10495.

Haug, T. A., Kleiv, R. A., & Munz, I. A. (2010). Investigating dissolution of mechanically activated olivine for carbonation purposes. *Applied Geochemistry*, 25(10), 1547–1563.

Heinemann, F., Gummich, M., Radmacher, M., & Fritz, M. (2011). Modification of $CaCO_3$ precipitation rates by water-soluble nacre proteins. *Materials Science and Engineering: C*, 31(2), 99–105.

Helgeson, H. C. (1969). Thermodynamics of hydrothermal systems at elevated temperatures and pressures. *American Journal of Science*, 267(7), 729–804.

Hänchen, M., Krevor, S., Mazzotti, M., & Lackner, K. S. (2007). Validation of a population balance model for olivine dissolution. *Chemical Engineering Science*, 62(22), 6412–6422.

Hänchen, M., Prigiobbe, V., Storti, G., Seward, T., & Mazzotti, M. (2006). Dissolution kinetics of fosteritic olivine at 90 - 150°C including effects of the presence of CO_2. *Geochimica et Cosmochimica Acta*, 70(17), 4403–4416.

Hoch, A. R., Reddy, M. M., & Aiken, G. R. (2000). Calcite crystal growth inhibition by humic substances with emphasis on hydrophobic acids from the florida everglades. *Geochimica et Cosmochimica Acta*, 64(1), 61–72.

Huijgen, W. J., Comans, R. N., & Witkamp, G.-J. (2007). Cost evaluation of CO_2 sequestration by aqueous mineral carbonation. *Energy Conversion and Management*, 48(7), 1923–1935.

IPCC (2005). *Carbon Dioxide Capture and Storage: Special Report of the Intergovernmental Panel on Climate Change*. Cambridge University Press.

Johnson, S. B., Yoon, T. H., Slowey, A. J., & Brown, G. E. (2004). Adsorption of organic matter at Mineral/Water interfaces: 3. implications of surface dissolution for adsorption of oxalate. *Langmuir*, 20(26), 11480–11492.

Jones, F., Jones, P., Ogden, M., Richmond, W., Rohl, A., & Saunders, M. (2007). The interaction of EDTA with barium sulfate. *Journal of Colloid and Interface Science*, 316(2), 553–561.

Kelemen, P. B., Matter, J., Streit, E. E., Rudge, J. F., Curry, W. B., & Blusztajn, J. (2011). Rates and mechanisms of mineral carbonation in peridotite: Natural processes and recipes for enhanced, in situ CO2 capture and storage. *Annual Review of Earth and Planetary Sciences*, 39(1), 545–576.

Kharaka, Y. K., Ambats, G., & Thordsen, J. J. (1993). Distribution and significance of dicarboxylic acid anions in oil field waters. *Chemical Geology*, 107(3-4), 499–501.

Kharaka, Y. K. & Hanor, J. S. (2003). Deep fluids in the continents: I. Sedimentary basins. In *Treatise on geochemistry*, volume 5 chapter 5.16, (pp. 499–540). Elsevier Ltd.

Kim, I. W., Darragh, M. R., Orme, C., & Evans, J. S. (2005). Molecular tuning of crystal growth by nacre-associated polypeptides. *Crystal Growth & Design*, 6(1), 5–10.

King, H. E., Plümper, O., & Putnis, A. (2010). Effect of secondary phase formation on the carbonation of olivine. *Environmental Science & Technology*, 44(16), 6503–6509.

Krevor, S. C. & Lackner, K. S. (2011). Enhancing serpentine dissolution kinetics for mineral carbon dioxide sequestration. *International Journal of Greenhouse Gas Control*, 5(4), 1073–1080.

Kubota, N. & Mullin, J. (1995). A kinetic model for crystal growth from aqueous solution in the presence of impurity. *Journal of Crystal Growth*, 152(3), 203–208.

Kummert, R. & Stumm, W. (1980). The surface complexation of organic acids on hydrous γ-Al_2O_3. *Journal of Colloid and Interface Science*, 75(2), 373–385.

Lackner, K. S., Wendt, C. H., Butt, D. P., Joyce Jr., E. L., & Sharp, D. H. (1995). Carbon dioxide disposal in carbonate minerals. *Energy*, 20(11), 1153–1170.

Lackovic, K., Johnson, B. B., Angove, M. J., & Wells, J. D. (2003). Modeling the adsorption of citric acid onto muloorina illite and related clay minerals. *Journal of Colloid and Interface Science*, 267(1), 49–59.

Lakshtanov, L. Z., Bovet, N., & Stipp, S. L. S. (2011). Inhibition of calcite growth by alginate. *Geochimica et Cosmochimica Acta*, 75(14), 3945–3955.

Lasaga, A. C. (1981). Transition state theory. *Reviews in Mineralogy and Geochemistry*, 8(1), 135–168.

Lebron, I. & Suarez, D. L. (1996). Calcite nucleation and precipitation kinetics as affected by dissolved organic matter at 25 c and pH> 7.5. *Geochimica et Cosmochimica Acta*, 60(15), 2765–2776.

Lebron, I. & Suarez, D. L. (1998). Kinetics and mechanisms of precipitation of calcite as affected by pco2 and organic ligands at 25 c. *Geochimica et Cosmochimica Acta*, 62(3), 405–416.

Lee, Y. J. & Reeder, R. J. (2006). The role of citrate and phthalate during Co(II) coprecipitation with calcite. *Geochimica et Cosmochimica Acta*, 70(9), 2253–2263.

Lin, Y., Singer, P. C., & Aiken, G. R. (2005). Inhibition of calcite precipitation by natural organic material: Kinetics, mechanism, and thermodynamics. *Environmental Science & Technology*, 39(17), 6420–6428.

Lippmann, F. (1973). *Sedimentary carbonate minerals*. Springer-Verlag Berlin.

Liu, S. T. & Nancollas, G. H. (1975). A kinetic and morphological study of the seeded growth of calcium sulfate dihydrate in the presence of additives. *Journal of Colloid and Interface Science*, 52(3), 593–601.

Liu, Y. (2006). Mechanism for the dissolution of olivine series minerals in acidic solutions. *American Mineralogist*, 91(2-3), 455–458.

Martell, A. E., Motekaitis, R. J., Fried, A. R., Wilson, J. S., & MacMillan, D. T. (1975). Thermal decomposition of EDTA, NTA, and nitrilotrimethylenephosphonic acid in aqueous solution. *Canadian Journal of Chemistry*, 53(22), 3471–3476.

McKelvy, M. J., Chizmeshya, A. V. G., Diefenbacher, J., Béarat, H., & Wolf, G. (2004). Exploration of the role of heat activation in enhancing serpentine carbon sequestration reactions. *Environmental Science & Technology*, 38(24), 6897–6903.

Means, J. L. & Hubbard, N. (1987). Short-chain aliphatic acid anions in deep subsurface brines: a review of their origin, occurrence, properties, and importance and new data on their distribution and geochemical implications in the Palo Duro Basin, Texas. *Organic geochemistry*, 11(3), 177–191.

Meyer, H. J. (1984). The influence of impurities on the growth rate of calcite. *Journal of Crystal Growth*, 66(3), 639–646.

Millero, F., Huang, F., Graham, T., & Pierrot, D. (2007). The dissociation of carbonic acid in NaCl solutions as a function of concentration and temperature. *Geochimica et Cosmochimica Acta*, 71(1), 46–55.

Motekaitis, R. J., Cox, X. B., Taylor, P., Martell, A. E., Miles, B., & Tvedt Jr, T. J. (1982). Thermal degradation of EDTA chelates in aqueous solution. *Canadian Journal of Chemistry*, 60(10), 1207–1213.

Newall, P. S., Clarke, S. J., Haywood, H. M., Scholes, H., Clarke, N. R., King, P. A., & Barley, R. W. (2000). CO_2 storage as carbonate minerals, report PH3/17 for IEA greenhouse gas R&D programme.

Nielsen, A. E. (1984). Electrolyte crystal growth mechanisms. *Journal of Crystal Growth*, 67(2), 289–310.

Njegic-Dzakula, B., Brecevic, L., Falini, G., & Kralj, D. (2009). Calcite crystal growth kinetics in the presence of charged synthetic polypeptides. *Crystal Growth & Design*, 9, 2425–2434.

O'connor, W. K., Dahlin, D. C., Rush, G. E., Dahlin, C. L., & Collins, W. K. (2001). Carbon dioxide sequestration by direct mineral carbonation: process mineralogy of feed and products. *Minerals & metallurgical processing*, 19(2), 95–101.

Olsen, A. A. & Rimstidt, D. J. (2008). Oxalate-promoted forsterite dissolution at low pH. *Geochimica et Cosmochimica Acta*, 72(7), 1758–1766.

Orme, C. A., Noy, A., Wierzbicki, A., McBride, M. T., Grantham, M., Teng, H. H., Dove, P. M., & DeYoreo, J. J. (2001). Formation of chiral morphologies through selective binding of amino acids to calcite surface steps. *Nature*, 411(6839), 775.

Palmer, D. A. & Wesolowski, D. J. (1997). Potentiometric measurements of the first hydrolysis quotient of magnesium (II) to 250 c and 5 molal ionic strength (NaCl). *Journal of solution chemistry*, 26(2), 217–232.

Park, A. H. A. & Fan, L. S. (2004). CO_2 mineral sequestration: physically activated dissolution of serpentine and pH swing process. *Chemical Engineering Science*, 59(22), 5241–5247.

Park, A. H. A., Jadhav, R., & Fan, L. S. (2003). CO_2 mineral sequestration: chemically enhanced aqueous carbonation of serpentine. *The Canadian Journal of Chemical Engineering*, 81(3-4), 885–890.

Parkhurst, D. L. & Appelo, C. A. J. (1999). User's guide to PHREEQC (version 2): a computer program for speciation, batch-reaction, one-dimensional transport, and inverse geochemical calculations. *US Geological Survey Water-Resources Investigations Report*, 99(4259), 312.

Phillips, B. L., Casey, W. H., & Crawford, S. N. (1997a). Solvent exchange in $AlF_x(H_2O)^{3-x}_{6-x\ (aq)}$ complexes: Ligand-directed labilization of water as an analogue for ligand-induced dissolution of oxide minerals. *Geochimica et cosmochimica acta*, 61(15), 3041–3049.

Phillips, B. L., Crawford, S. N., & Casey, W. H. (1997b). Rate of water exchange between $Al(C_2O_4)(H_2O)^+_{4\ (aq)}$ complexes and aqueous solutions determined by ^{17}o-nmr spectroscopy. *Geochimica et cosmochimica acta*, 61(23), 4965–4973.

Piana, S., Jones, F., & Gale, J. (2006). Assisted desolvation as a key kinetic step for crystal growth. *Journal of the American Chemical Society*, 128(41), 13568–13574.

Piana, S., Jones, F., & Gale, J. D. (2007). Aspartic acid as a crystal growth catalyst. *CrystEngComm*, 9(12), 1187–1191.

Pina, C. M., Putnis, C. V., Becker, U., Biswas, S., Carroll, E. C., Bosbach, D., & Putnis, A. (2004). An atomic force microscopy and molecular simulations study of the inhibition of barite growth by phosphonates. *Surface Science*, 553(1-3), 61–74.

Plank, J. & Bassioni, G. (2007). Adsorption of carboxylate anions on a $CaCO_3$. *Zeitschrift für Naturforschung B*, 62b, 1277–1284.

Pokrovski, G. S., Schott, J., & Sergeyev, A. S. (1995). Experimental determination of the stability constants of $NaSO_4^-$ and $NaB(OH)_4^0$ in hydrothermal solutions using a new high-temperature sodium-selective glass electrode - Implications for boron isotopic fractionation. *Chemical Geology*, 124(3), 253–265.

Pokrovsky, O., Schott, J., & Thomas, F. (1999). Processes at the magnesium-bearing carbonates/solution interface. i. a surface speciation model for magnesite. *Geochimica et cosmochimica acta*, 63(6), 863–880.

Pokrovsky, O. S., Golubev, S. V., & Jordan, G. (2009). Effect of organic and inorganic ligands on calcite and magnesite dissolution rates at 60 c and 30 atm pCO2. *Chemical Geology*, 265(1-2), 33–43.

Pokrovsky, O. S. & Schott, J. (2000). Kinetics and mechanism of forsterite dissolution at 25°C and pH from 1 to 12. *Geochimica et Cosmochimica Acta*, 64(19), 3313–3325.

Pokrovsky, O. S. & Schott, J. (2002). Surface chemistry and dissolution kinetics of divalent metal carbonates. *Environmental science & technology*, 36(3), 426–432.

Pokrovsky, O. S., Schott, J., & Castillo, A. (2005). Kinetics of brucite dissolution at 25°C in the presence of organic and inorganic ligands and divalent metals. *Geochimica et Cosmochimica Acta*, 69(4), 905–918.

Prigiobbe, V., Costa, G., Baciocchi, R., Hänchen, M., & Mazzotti, M. (2009). The effect of and salinity on olivine dissolution kinetics at salinity at 120°C. *Chemical Engineering Science*, 64(15), 3510–3515.

Prigiobbe, V. & Mazzotti, M. (2011). Dissolution of olivine in the presence of oxalate, citrate, and CO2 at 90°C and 120°C. *Chemical Engineering Science*, 66(24), 6544–6554.

Reddy, M. M. & Hoch, A. R. (2001). Calcite crystal growth rate inhibition by polycarboxylic acids. *Journal of Colloid and Interface Science*, 235(2), 365–370.

Reddy, M. M. & Nancollas, G. H. (1973). Calcite crystal growth inhibition by phosphonates. *Desalination*, 12(1), 61–73.

Rimstidt, J. D. & Barnes, H. L. (1980). The kinetics of silica-water reactions. *Geochimica et Cosmochimica Acta*, 44(11), 1683–1699.

Rosso, J. J. & Rimstidt, J. (2000). A high resolution study of forsterite dissolution rates. *Geochimica et Cosmochimica Acta*, 64(5), 797–811.

Saldi, G. D., Jordan, G., Schott, J., & Oelkers, E. H. (2009). Magnesite growth rates as a function of temperature and saturation state. *Geochimica et Cosmochimica Acta*, 73(19), 5646–5657.

Saldi, G. D., Schott, J., Pokrovsky, O. S., Gautier, Q., & Oelkers, E. H. (2012). An experimental study of magnesite precipitation rates at neutral to alkaline conditions and 100-200°C as a function of pH, aqueous solution composition and chemical affinity. *Geochimica et Cosmochimica Acta*, 83, 93–109.

Saldi, G. D., Schott, J., Pokrovsky, O. S., & Oelkers, E. H. (2010). An experimental study of magnesite dissolution rates at neutral to alkaline conditions and 150 and 200°C as a function of pH, total dissolved carbonate concentration, and chemical affinity. *Geochimica et Cosmochimica Acta*, 74, 6344–6356.

Schmidt, M. H., Ellison, I., Holliday, K., Kubin, M., & Trujillo, F. (2008). Selective inhibition of aragonite growth by citrate and isocitrate at moderate supersaturations, as measured by an optical-microscope flow-cell assay. *Journal of Crystal Growth*, 310(4), 804–815.

Seifritz, W. (1990). CO_2 disposal by means of silicates. *Nature*, 345(6275), 486–486.

Shiraki, R. & Brantley, S. L. (1995). Kinetics of near-equilibrium calcite precipitation at 100°C: an evaluation of elementary reaction-based and affinity-based rate laws. *Geochimica et Cosmochimica Acta*, 59(8), 1457–1471.

Stumm, W. (1992). *Chemistry of the Solid-Water Interface*. John Wiley & Sons, New York.

Sullivan, D. J., Nordin, J. P., Phillips, B. L., & Casey, W. H. (1999). The rates of water exchange in Al(III)-salicylate and Al(III)-sulfosalicylate complexes. *Geochimica et cosmochimica acta*, 63(10), 1471–1480.

Teir, S., Eloneva, S., Fogelholm, C., & Zevenhoven, R. (2009). Fixation of carbon dioxide by producing hydromagnesite from serpentinite. *Applied Energy*, 86(2), 214–218.

Teir, S., Kuusik, R., Fogelholm, C., & Zevenhoven, R. (2007a). Production of magnesium carbonates from serpentinite for long-term storage of CO2. *International Journal of Mineral Processing*, 85(1-3), 1–15.

Teir, S., Revitzer, H., Eloneva, S., Fogelholm, C., & Zevenhoven, R. (2007b). Dissolution of natural serpentinite in mineral and organic acids. *International Journal of Mineral Processing*, 83(1-2), 36–46.

Ukrainczyk, M., Grebičak, M., Jerić, I., & Kralj, D. (2012). Interactions of salicylic acid derivatives with calcite crystals. *Journal of Colloid and Interface Science*, 365(1), 296–307.

Westin, K.-J. & Rasmuson, A. C. (2005a). Crystal growth of aragonite and calcite in presence of citric acid, DTPA, EDTA and pyromellitic acid. *Journal of Colloid and Interface Science*, 282(2), 359–369.

Westin, K.-J. & Rasmuson, A. C. (2005b). Nucleation of calcium carbonate in presence of citric acid, DTPA, EDTA and pyromellitic acid. *Journal of Colloid and Interface Science*, 282(2), 370–379.

Willey, L., Kharaka, Y., Presser, T., Rapp, J., & Barnes, I. (1975). Short chain aliphatic acid anions in oil field waters and their contribution to the measured alkalinity. *Geochimica et Cosmochimica Acta*, 39(12), 1707–1711.

Wogelius, R. A. & Walther, J. V. (1991). Olivine dissolution at 25°C: effects of pH, CO_2, and organic acids. *Geochimica et Cosmochimica Acta*, 55(4), 943–954.

Zhang, Y. & Dawe, R. (1996). Effect of organic acids on the determination of carbonate species in solutions. *Analytica Chimica Acta*, 318(2), 239–249.

Zuddas, P., Pachana, K., & Faivre, D. (2003). The influence of dissolved humic acids on the kinetics of calcite precipitation from seawater solutions. *Chemical Geology*, 201(1-2), 91–101.

Zullig, J. J. & Morse, J. W. (1988). Interaction of organic acids with carbonate mineral surfaces in seawater and related solutions: I. fatty acid adsorption. *Geochimica et Cosmochimica Acta*, 52(6), 1667–1678.

Appendix

A Results of mixed flow reactor experiments

Exp.	[Ligand] (mmol/kg)	Ω	pH outlet	pH (100°C)	I (mol/kg)	Δ[Mg]$*10^4$ (mol/kg)	Alk.*100 (eq/kg)	TDIC*100 (mol/kg)	FR (g/min)	BET (cm^2/g)	seeds (g)	Rate $*10^{12}$ ($mol/cm^2/s$)	a(Mg^{2+}) $*10^5$	a(CO_3^{2-}) $*10^5$	$\frac{a(Mg^{2+})}{a(CO_3^{2-})}$	m(Cit^{3-}) (mol/kg)	a(Cit^{3-})	$\frac{Cit^{3-}}{\text{total Cit.}}$	$\frac{MgCit^{-}}{\text{total Mg}}$
M38A	-	41.5 ± 3.8	8.22(1)	7.99	0.100	3.347	1.924	-	0.979	2100	1.5021	1.73 ± 0.15	1.29	0.99	1.31	-	-	-	-
M38B	-	48.4 ± 2.5	8.28(1)	8.02	0.100	2.941	1.940	-	1.467	2100	1.5021	2.28 ± 0.17	1.40	1.07	1.30	-	-	-	-
M38C	-	54.9 ± 3.2	8.27	8.01	0.100	2.312	1.954	-	1.986	2100	1.5021	2.43 ± 0.19	1.59	1.06	1.50	-	-	-	-
M38D	-	58.7 ± 7.1	8.28(2)	8.02	0.100	1.956	1.958	-	2.483	2100	1.5021	2.57 ± 0.33	1.69	1.07	1.58	-	-	-	-
M38E	-	40.8 ± 5.2	8.29(1)	8.03	0.100	3.848	1.921	-	0.492	2100	1.5021	1.00 ± 0.07	1.16	1.08	1.07	-	-	-	-
Cit7A	Citrate 0.105	53.8 ± 1.7	8.30(1)	7.98	0.100	3.320	-	1.990	0.975	2100	1.4997	1.71 ± 0.06	1.64	1.02	1.61	$9.91 \cdot 10^{-6}$	$7.20 \cdot 10^{-7}$	9.4 %	13.8 %
Cit7B	Citrate 0.105	57 ± 5.9	8.33(2)	7.99	0.100	3.113	-	2.018	1.458	2100	1.4997	2.40 ± 0.05	1.69	1.05	1.61	$9.49 \cdot 10^{-6}$	$7.02 \cdot 10^{-7}$	9.0 %	13.5 %
Cit7C	Citrate 0.105	63.6 ± 1.7	8.33(1)	8.01	0.100	2.868	-	1.982	1.942	2100	1.4997	2.95 ± 0.08	1.82	1.08	1.68	$9.06 \cdot 10^{-6}$	$6.57 \cdot 10^{-7}$	8.6%	12.7%
Cit7D	Citrate 0.105	67.1 ± 3.2	8.34	8.02	0.100	2.565	-	1.973	2.450	2100	1.4997	3.32 ± 0.16	1.90	1.09	1.74	$8.65 \cdot 10^{-6}$	$6.31 \cdot 10^{-7}$	8.2%	12.3%
Cit7E	Citrate 0.105	46.2 ± 3	8.36(2)	8.03	0.099	4.756	-	1.920	0.494	2100	1.4997	1.24 ± 0.04	1.30	1.10	1.18	$1.21 \cdot 10^{-5}$	$8.82 \cdot 10^{-7}$	11.6%	16.4%
Cit6A	Citrate 1.044	50.5 ± 1.8	8.22(1)	8.04	0.102	1.917	-	1.987	0.993	2100	1.5114	1.00 ± 0.04	1.34	1.16	1.15	$1.19 \cdot 10^{-4}$	$8.50 \cdot 10^{-6}$	11.4%	65.0%
Cit6B	Citrate 1.044	57.9 ± 2.1	8.23(6)	8.06	0.102	1.585	-	2.001	1.496	2100	1.5114	1.25 ± 0.02	1.48	1.21	1.23	$1.08 \cdot 10^{-4}$	$7.78 \cdot 10^{-6}$	10.4%	62.9%
Cit6C	Citrate 1.044	61.4 ± 3.5	8.27(1)	8.05	0.102	1.221	-	1.989	1.999	2100	1.5114	1.28 ± 0.18	1.59	1.19	1.33	$1.02 \cdot 10^{-4}$	$7.33 \cdot 10^{-6}$	9.8%	61.5%
Cit6D	Citrate 1.044	64.3 ± 2	8.28(1)	8.06	0.102	1.068	-	2.026	2.507	2100	1.5114	1.41 ± 0.13	1.61	1.23	1.31	$1.01 \cdot 10^{-4}$	$7.22 \cdot 10^{-6}$	9.6%	61.0%
Cit6E	Citrate 1.044	49 ± 3.5	8.29(2)	8.08	0.102	2.980	-	1.990	0.493	2100	1.5114	0.77 ± 0.05	1.19	1.27	0.93	$1.33 \cdot 10^{-4}$	$9.40 \cdot 10^{-6}$	12.7%	67.0%

Table 4.7 – Summary of the results of magnesite growth experiments performed in this study at 100°C. Uncertainty on outlet pH measurements third figure is given in parenthesis, and corresponds to 1σ variability of outlet pH at steady state. Uncertainty on saturation state was calculated by taking into account the measured 1σ variability on pH, Mg concentration, and alkalinity or TDIC at steady-state. The uncertainties reported on rates result from error propagation based on 1σ variability or estimated uncertainty on the different terms contributing to eq. 4.1. The same procedure was used to estimate uncertainties in the other results tables.

Exp.	[Ligand] (mmol/kg)	Ω	pH outlet	pH (120°C)	I (mol/kg)	Δ[Mg]$*10^4$ (mol/kg)	Alk.*100 (eq/kg)	TDIC*100 (mol/kg)	FR (g/min)	BET (cm^2/g)	seeds (g)	Rate $*10^{12}$ ($mol/cm^2/s$)	$a(Mg^{2+})$ $*10^5$	$a(CO_3^{2-})$ $*10^5$	$\frac{a(Mg^{2+})}{a(CO_3^{2-})}$	$m(Oxl^{2-})$ (mol/kg)	$a(Oxl^{2-})$	$\frac{Oxl^{2-}}{\text{total Oxl.}}$	$\frac{MgOxl}{\text{total Mg}}$
M14	-	**31.5 ± 2.1**	7.72(4)	7.72	0.116	5.188	1.628	-	0.511	1750	0.7685	**3.29 ± 0.25**	8.95	4.14	2.16	-	-	-	-
M24B	-	**37.8 ± 0.5**	7.86	7.80	0.116	5.116	1.614	-	0.499	1750	0.6139	**3.96 ± 0.29**	9.13	4.87	1.87	-	-	-	-
M25A	-	**31.8 ± 2.2**	7.89(3)	7.83	0.118	4.008	1.821	-	0.497	1750	0.6976	**2.72 ± 0.29**	6.34	5.88	1.08	-	-	-	-
M25B	-	**55.2 ± 1.3**	7.98(2)	7.88	0.118	3.295	1.859	-	1.752	1750	0.6976	**7.88 ± 0.82**	9.78	6.63	1.48	-	-	-	-
M27	-	**47.1 ± 0.7**	7.71	7.71	0.116	4.792	1.595	-	0.996	1750	0.7029	**6.47 ± 0.5**	14.18	3.90	3.63	-	-	-	-
M31A	-	**15 ± 0.3**	7.87(1)	7.82	0.118	2.369	1.847	-	0.405	1750	1.7492	**0.52 ± 0.04**	3.02	5.83	0.52	-	-	-	-
M31B	-	**19.1 ± 2.1**	7.89(1)	7.83	0.118	2.056	1.847	-	0.596	1750	1.7492	**0.67 ± 0.26**	3.78	5.93	0.64	-	-	-	-
M32A	-	**26.7 ± 1.5**	7.74(1)	7.73	0.118	3.802	1.817	-	0.489	1750	0.7611	**2.33 ± 0.22**	6.63	4.73	1.40	-	-	-	-
M32B	-	**31.7 ± 0.1**	7.78	7.76	0.118	3.445	1.818	-	0.987	1750	0.7611	**4.26 ± 0.28**	7.50	4.98	1.51	-	-	-	-
M32C	-	**39.3 ± 1.1**	7.87(2)	7.81	0.118	3.129	1.823	-	1.786	1750	0.7611	**6.99 ± 0.5**	8.20	5.63	1.46	-	-	-	-
M32D	-	**38.6 ± 0.7**	7.69(1)	7.69	0.118	2.801	1.832	-	1.812	1750	0.7611	**6.35 ± 0.7**	10.59	4.29	2.47	-	-	-	-
M33A	-	**29 ± 0.6**	7.74(1)	7.73	0.118	3.563	1.815	-	0.494	1750	0.7609	**2.2 ± 0.17**	7.24	4.72	1.54	-	-	-	-
M33B	-	**35.9 ± 0.3**	7.78(1)	7.75	0.118	3.046	1.829	-	1.003	1750	0.7609	**3.83 ± 0.29**	8.60	4.92	1.75	-	-	-	-
M33C	-	**48.1 ± 2.2**	7.83(4)	7.78	0.118	2.193	1.844	-	2.398	1750	0.7609	**6.58 ± 0.58**	10.63	5.33	2.00	-	-	-	-
M34A	-	**29.9 ± 1.3**	7.69(2)	7.69	0.115	6.142	1.585	-	0.498	1750	0.7028	**4.14 ± 0.32**	9.41	3.73	2.52	-	-	-	-
M34B	-	**39.3 ± 1**	7.77(2)	7.74	0.116	5.517	1.601	-	1.001	1750	0.7028	**7.49 ± 0.47**	10.94	4.23	2.59	-	-	-	-
M35A	-	**29.7 ± 1.5**	7.77(3)	7.75	0.118	3.442	1.822	-	0.494	1750	0.7609	**2.13 ± 0.19**	7.13	4.89	1.46	-	-	-	-
M35B	-	**37.7 ± 1.6**	7.79(3)	7.76	0.118	2.879	1.822	-	1.002	1750	0.7609	**3.61 ± 0.33**	8.78	5.05	1.74	-	-	-	-
M37	-	**46.5 ± 0.5**	7.77(1)	7.74	0.116	4.954	1.617	-	0.994	1750	0.7021	**6.68 ± 0.41**	13.00	4.21	3.09	-	-	-	-
M39A	-	**27.9 ± 0.9**	7.78(2)	7.75	0.117	3.840	1.801	-	0.498	2100	0.7613	**1.99 ± 0.12**	6.67	4.91	1.36	-	-	-	-
M39B	-	**41.6 ± 1.6**	7.82(1)	7.78	0.117	2.767	1.825	-	1.486	2100	0.7613	**4.29 ± 0.39**	9.31	5.26	1.77	-	-	-	-
M40A	-	**38 ± 1.9**	7.79(3)	7.766	0.116	7.551	1.800	-	0.395	1750	0.7050	**4.03 ± 0.33**	8.87	5.04	1.76	-	-	-	-
M40B	-	**62.8 ± 1.5**	7.96(1)	7.855	0.116	6.251	1.823	-	0.889	1750	0.7050	**7.51 ± 0.73**	11.90	6.21	1.92	-	-	-	-
M40D	-	**66.2 ± 5.6**	7.81(4)	7.771	0.116	5.074	1.850	-	1.503	1750	0.7050	**10.3 ± 1**	14.89	5.22	2.85	-	-	-	-
M40E	-	**72.8 ± 3.1**	7.86(2)	7.798	0.116	4.818	1.856	-	1.873	1750	0.7050	**12.19 ± 1.38**	15.44	5.54	2.79	-	-	-	-
M40F	-	**38.8 ± 1.6**	7.84(3)	7.794	0.115	7.619	1.799	-	0.386	1750	0.7050	**3.98 ± 0.25**	8.51	5.36	1.59	-	-	-	-
M41	-	**38.9 ± 3.5**	7.80(4)	7.762	0.115	6.055	1.598	-	0.977	2100	0.7019	**6.69 ± 0.61**	10.30	4.43	2.32	-	-	-	-
Oxl1	Oxalate 0.10	**45.3 ± 1.2**	7.66(1)	7.67	0.116	3.974	1.632	-	0.978	1750	0.7021	**5.27 ± 0.44**	14.39	3.70	3.89	$2.78{\cdot}10^{-5}$	$7.71{\cdot}10^{-6}$	27.8%	6.62%
Oxl2	Oxalate 1.00	**35 ± 2.5**	7.72(4)	7.72	0.115	3.030	-	1.680	0.979	1750	0.7021	**4.02 ± 0.36**	9.94	4.14	2.40	$3.16{\cdot}10^{-4}$	$8.79{\cdot}10^{-5}$	31.6%	44.53%
Oxl3	Oxalate 5.00	**17.1 ± 0.7**	7.82(1)	7.78	0.116	0.934	-	1.732	1.006	1750	0.7021	**1.27 ± 0.21**	4.07	4.95	0.82	$1.94{\cdot}10^{-3}$	$5.37{\cdot}10^{-4}$	38.7%	82.82%
Oxl4	Oxalate 10.00	**11.4 ± 0.3**	7.97	7.87	0.116	0.180	-	1.718	0.996	1750	0.7021	**0.24 ± 0.13**	2.20	6.07	0.36	$4.21{\cdot}10^{-3}$	$1.17{\cdot}10^{-3}$	42.1%	91.17%
M22	Oxalate 10.00	**precipitation MgOxalate · $2H_2O$**																	
M29A	Oxalate 10.00	**19.1 ± 1.9**	8.01(4)	7.90	0.116	0.999	-	1.737	0.497	1750	0.6993	0.68 ± 0.07	3.41	6.60	0.52	$4.02{\cdot}10^{-3}$	$1.12{\cdot}10^{-3}$	40.2%	90.71%
M29E	Oxalate 10.00	**23.7 ± 1.8**	8.18(4)	7.99	0.116	1.497	-	1.768	0.498	1750	0.6993	**1.02 ± 0.09**	3.36	8.29	0.40	$4.02{\cdot}10^{-3}$	$1.11{\cdot}10^{-3}$	40.2%	90.41%
M36A	Oxalate 10.00	**25.8 ± 0.7**	7.88(1)	7.82	0.115	2.157	-	1.694	0.491	1750	0.7001	**1.44 ± 0.19**	5.67	5.35	1.06	$3.69{\cdot}10^{-3}$	$1.03{\cdot}10^{-3}$	36.9%	90.20%
M36C	Oxalate 10.00	**31.4 ± 2.2**	7.94(4)	7.86	0.115	0.715	-	1.743	1.505	1750	0.7001	**1.46 ± 0.51**	6.18	5.96	1.04	$3.62{\cdot}10^{-3}$	$1.01{\cdot}10^{-3}$	36.2%	89.89%
M36D	Oxalate 10.00	**27.3 ± 1.3**	7.81(1)	7.79	0.116	0.555	-	1.789	2.006	1750	0.7001	**1.51 ± 0.62**	6.23	5.16	1.21	$3.61{\cdot}10^{-3}$	$1.00{\cdot}10^{-3}$	36.1%	89.96%
Oxl5A	Oxalate 9.81	**50.9 ± 1.5**	7.97(1)	7.88	0.101	5.305	-	1.905	0.502	1750	0.7218	**3.51 ± 0.29**	8.70	6.88	1.26	$3.32{\cdot}10^{-3}$	$9.68{\cdot}10^{-4}$	33.9%	89.59%
Oxl5B	Oxalate 9.81	**73 ± 2.4**	8.16(1)	7.98	0.102	2.884	-	1.976	1.504	1750	0.7218	**5.72 ± 1.08**	9.57	8.97	1.07	$3.22{\cdot}10^{-3}$	$9.37{\cdot}10^{-4}$	32.9%	88.87%

Table 4.8 – Summary of the results of magnesite growth experiments performed in this study at 120°C (Part 1).

Exp.	[Ligand] (mmol/kg)	Ω	pH outlet	pH (120°C)	I (mol/kg)	Δ[Mg]$*10^4$ (mol/kg)	Alk.*100 (eq/kg)	TDIC*100 (mol/kg)	FR (g/min)	BET (cm^2/g)	seeds (g)	Rate $*10^{12}$ (mol/cm^2/s)	a(Mg^{2+}) $*10^5$	a(CO_3^{2-}) $*10^5$	$\frac{a(Mg^{2+})}{a(CO_3^{2-})}$	m(Oxl^{2-}) (mol/kg)	a(Oxl^{2-})	$\frac{Oxl^{2-}}{\text{total Oxl.}}$	$\frac{MgOxl}{\text{total Mg}}$
Oxl5C	Oxalate 9.81	**57.8 ± 5.1**	8.00(5)	7.89	0.101	3.625	-	1.973	0.986	1750	0.7218	**4.72 ± 0.58**	9.20	7.38	1.25	$3.26{\cdot}10^{-3}$	$9.49{\cdot}10^{-4}$	33.3%	89.26%
Oxl5D	Oxalate 9.81	**70.7 ± 4**	8.13(4)	7.96	0.101	2.452	-	1.956	2.000	1750	0.7218	**6.47 ± 0.89**	9.73	8.54	1.14	$3.21{\cdot}10^{-3}$	$9.33{\cdot}10^{-4}$	32.7%	88.92%
Oxl6B	Oxalate 1.00	**19.4 ± 2.2**	7.97(2)	7.88	0.104	5.268	-	1.909	0.395	1750	0.7163	**2.77 ± 0.29**	3.31	6.88	0.48	$4.08{\cdot}10^{-4}$	$1.18{\cdot}10^{-4}$	40.8%	50.79%
Oxl6C	Oxalate 1.00	**37.8 ± 2.2**	8.04(2)	7.91	0.104	3.576	-	1.951	0.888	1750	0.7163	**4.22 ± 0.4**	5.85	7.59	0.77	$3.69{\cdot}10^{-4}$	$1.06{\cdot}10^{-4}$	36.9%	47.87%
Oxl6D	Oxalate 1.00	**53.8 ± 3.9**	8.16(2)	7.97	0.104	2.575	-	1.954	1.791	1750	0.7163	**6.13 ± 0.64**	7.22	8.76	0.82	$3.51{\cdot}10^{-4}$	$1.01{\cdot}10^{-4}$	35.1%	46.11%
																m(Cit^{3-})	a(Cit^{3-})	$\frac{Cit^{3-}}{\text{total Cit.}}$	$\frac{MgCit^{-}}{\text{total Mg}}$
Cit1	Citrate 0.01	**52.3 ± 5.1**	7.78(5)	7.74	0.116	4.328	-	1.625	0.977	1750	0.7029	**5.73 ± 0.57**	14.48	4.25	3.41	$7.32{\cdot}10^{-7}$	$4.10{\cdot}10^{-8}$	7.3%	1.61%
Cit2	Citrate 0.10	**53.8 ± 4.1**	7.78(4)	7.75	0.116	3.095	-	1.684	0.987	1750	0.7029	**4.14 ± 0.38**	14.18	4.46	3.18	$7.48{\cdot}10^{-6}$	$4.17{\cdot}10^{-7}$	7.5%	14.16%
Cit3	Citrate 1.00	**24.6 ± 2**	7.94(3)	7.85	0.117	0.126	-	1.711	0.988	1750	0.7029	**0.17 ± 0.17**	5.08	5.69	0.89	$1.79{\cdot}10^{-4}$	$9.96{\cdot}10^{-6}$	17.9%	79.32%
Cit4	Citrate 10.00	**1.5 ± 0.1**	8.04(2)	7.95	0.117	-4.437	-	1.789	0.988	1750	0.7029	**-5.94 ± 0.35**	0.23	7.58	0.03	$7.08{\cdot}10^{-3}$	$3.92{\cdot}10^{-4}$	70.8%	98.01%
Cit5A	Citrate 0.205	**61.8 ± 3.8**	7.80(3)	7.76	0.096	11.730	-	1.646	0.498	1750	1.3403	**4.15 ± 0.43**	15.97	4.55	3.51	$1.22{\cdot}10^{-5}$	$7.88{\cdot}10^{-7}$	5.9%	24.29%
Cit5B	Citrate 0.205	**88 ± 6.9**	7.87(3)	7.79	0.096	9.393	-	1.639	1.009	1750	1.3403	**6.74 ± 0.55**	21.41	4.84	4.43	$9.25{\cdot}10^{-6}$	$5.99{\cdot}10^{-7}$	4.5%	19.53%
Cit5C2	Citrate 0.205	**105.9 ± 4**	7.91(1)	7.80	0.097	8.216	-	1.689	1.506	1750	1.3403	**8.79 ± 0.77**	24.47	5.09	4.81	$8.18{\cdot}10^{-6}$	$5.27{\cdot}10^{-7}$	4.0%	17.48%
Cit5D1	Citrate 0.205	**116.8 ± 6.6**	7.97(2)	7.83	0.097	7.992	-	1.703	2.006	1750	1.3403	**11.39 ± 0.87**	24.83	5.54	4.48	$8.08{\cdot}10^{-6}$	$5.20{\cdot}10^{-7}$	4.0%	17.13%
Cit5D2	Citrate 0.205	**113.6 ± 5.2**	7.89(1)	7.79	0.097	7.040	-	1.723	2.003	1750	1.3403	**10.02 ± 0.67**	26.36	5.07	5.20	$7.64{\cdot}10^{-6}$	$4.91{\cdot}10^{-7}$	3.7%	16.44%
Cit5E	Citrate 0.205	**121 ± 4.3**	7.87	7.79	0.097	6.216	-	1.709	3.003	1750	1.3403	**13.27 ± 1.41**	28.61	4.97	5.76	$7.06{\cdot}10^{-6}$	$4.54{\cdot}10^{-7}$	3.5%	15.44%
Cit5F	Citrate 0.205	**67.9 ± 3.8**	7.80	7.75	0.096	11.398	-	1.643	0.495	1750	1.3403	**4.01 ± 0.44**	17.94	4.45	4.03	$1.09{\cdot}10^{-5}$	$7.07{\cdot}10^{-7}$	5.3%	22.41%
Cit8A	Citrate 1.051	**42.5 ± 3.8**	8.14(2)	7.97	0.101	3.398	-	2.019	0.492	1750	0.7476	**2.13 ± 0.2**	5.52	9.04	0.61	$1.63{\cdot}10^{-4}$	$1.02{\cdot}10^{-5}$	15.5%	78.66%
Cit8B	Citrate 1.051	**59.2 ± 5.1**	8.24(2)	8.02	0.101	2.226	-	2.058	1.456	1750	0.7476	**4.13 ± 0.42**	6.74	10.31	0.65	$1.39{\cdot}10^{-4}$	$8.63{\cdot}10^{-6}$	13.2%	75.34%
Cit8C	Citrate 1.051	**56.1 ± 4.6**	8.15(2)	7.97	0.101	2.474	-	2.049	0.998	1750	0.7476	**3.14 ± 0.35**	7.14	9.21	0.78	$1.32{\cdot}10^{-4}$	$8.23{\cdot}10^{-6}$	12.6%	74.79%
Cit8D	Citrate 1.051	**69.6 ± 5.5**	8.22(2)	8.01	0.102	1.769	-	2.096	1.989	1750	0.7476	**4.48 ± 0.4**	7.96	10.27	0.77	$1.21{\cdot}10^{-4}$	$7.49{\cdot}10^{-6}$	11.5%	72.59%
Cit9A	Citrate 0.105	**36 ± 0.7**	7.97(2)	7.88	0.103	3.204	-	1.998	1.386	1750	0.7022	**6.02 ± 0.38**	5.89	7.20	0.82	$1.57{\cdot}10^{-5}$	$9.60{\cdot}10^{-7}$	14.9%	26.40%
Cit9B	Citrate 0.105	**24.5 ± 0.9**	8.13(1)	7.96	0.103	4.323	-	1.965	0.397	1750	0.7022	**2.33 ± 0.15**	3.30	8.73	0.38	$2.43{\cdot}10^{-5}$	$1.49{\cdot}10^{-6}$	23.2%	35.27%
																m($Edta^{4-}$)	a($Edta^{4-}$)	$\frac{Edta^{4-}}{\text{total Edta}}$	$\frac{MgEdta^{2-}}{\text{total Mg}}$
Edta1	Edta 0.01	**43.6 ± 3.9**	7.80(4)	7.76	0.115	5.566	-	1.637	0.975	2100	0.7019	**6.14 ± 0.59**	11.26	4.54	2.48	$6.72{\cdot}10^{-12}$	$4.00{\cdot}10^{-14}$	0.0001%	2.25%
Edta2	Edta 0.10	**41.1 ± 2.2**	7.85(2)	7.79	0.115	4.968	-	1.620	0.977	2100	0.7019	**5.49 ± 0.49**	10.20	4.73	2.15	$7.41{\cdot}10^{-11}$	$4.42{\cdot}10^{-13}$	0.0001%	20.23%
Edta3	Edta 0.50	**27.3 ± 2.4**	7.84(5)	7.79	0.118	2.414	-	1.694	0.959	2100	0.7019	**2.62 ± 0.25**	6.47	4.96	1.31	$5.95{\cdot}10^{-10}$	$3.46{\cdot}10^{-12}$	0.0001%	66.34%
Edta4	Edta 1.00	**3.1 ± 0.5**	7.93	7.85	0.120	-0.323	-	1.735	0.968	2100	0.7019	**-0.35 ± 0.1**	0.62	5.82	0.11	$1.30{\cdot}10^{-8}$	$7.38{\cdot}10^{-11}$	0.0013%	97.59%
Edta5A	Edta 1.00	**30.4 ± 1.6**	8.03(3)	7.91	0.117	3.932	-	1.900	0.394	1750	0.7026	**2.1 ± 0.16**	4.89	7.31	0.67	$1.57{\cdot}10^{-9}$	$9.18{\cdot}10^{-12}$	0.0002%	83.19%
Edta5B	Edta 1.00	**47.6 ± 1.2**	8.13(1)	7.96	0.117	3.069	-	1.892	0.899	1750	0.7026	**3.74 ± 0.34**	6.86	8.16	0.84	$1.12{\cdot}10^{-9}$	$6.53{\cdot}10^{-12}$	0.0001%	77.64%
Edta5D	Edta 1.00	**53.1 ± 3**	8.00(2)	7.88	0.117	2.126	-	1.904	1.499	1750	0.7026	**4.32 ± 0.68**	9.05	6.89	1.31	$8.45{\cdot}10^{-10}$	$4.96{\cdot}10^{-12}$	0.0001%	72.91%
Edta5E	Edta 1.00	**60.8 ± 1.6**	8.07	7.92	0.117	1.877	-	1.920	1.895	1750	0.7026	**4.82 ± 0.69**	9.53	7.50	1.27	$8.04{\cdot}10^{-10}$	$4.70{\cdot}10^{-12}$	0.0001%	71.63%
Edta5F	Edta 1.00	**34 ± 3.7**	8.07(5)	7.93	0.117	3.671	-	1.905	0.399	1750	0.7026	**1.99 ± 0.24**	5.21	7.66	0.68	$1.47{\cdot}10^{-9}$	$8.61{\cdot}10^{-12}$	0.0001%	82.17%

Table 4.9 – Summary of the results of magnesite growth experiments performed in this study at 120°C (Part 2).

Exp.	[Ligand] (mmol/kg)	Ω	pH outlet	pH (120°C)	I (mol/kg)	Δ[Mg]$*10^4$ (mol/kg)	Alk.*100 (eq/kg)	TDIC*100 (mol/kg)	FR (g/min)	BET (cm^2/g)	seeds (g)	Rate $*10^{12}$ ($mol/cm^2/s$)	a(Mg^{2+}) $*10^5$	a(CO_3^{2-}) $*10^5$	$\frac{a(Mg^{2+})}{a(CO_3^{2-})}$	m(Oxl^{2-}) (mol/kg)	a(Oxl^{2-})	$\frac{Oxl^{2-}}{\text{total Oxl.}}$	$\frac{MgOxl}{\text{total Mg}}$
M5A	-	12.4 ± 1.7	7.84(3)	7.87	0.113	3.406	1.563	-	0.490	1938	1.1216	**1.28 ± 0.17**	0.89	4.50	0.20	-	-	-	-
M5B	-	17.2 ± 1.9	7.49(2)	7.68	0.113	2.899	1.548	-	0.999	1938	1.1216	**2.22 ± 0.24**	1.88	2.94	0.64	-	-	-	-
M11A	-	10.2 ± 1.3	7.51(5)	7.70	0.113	3.407	1.537	-	0.244	1750	0.5956	**1.33 ± 0.1**	1.08	3.03	0.36	-	-	-	-
M11B	-	10.3 ± 1.2	7.85(3)	**7.85(3)**	0.114	4.106	1.644	-	0.473	1750	0.5892	**3.14 ± 0.28**	0.73	4.53	0.16	-	-	-	-
M11C	-	7.8 ± 0.8	7.74(3)	7.83	0.114	3.831	1.630	-	0.458	1750	1.0188	**1.64 ± 0.31**	0.58	4.30	0.14	-	-	-	-
M13	-	7.2 ± 0.7	7.84(2)	**7.85(3)**	0.114	5.975	1.622	-	0.485	1750	0.9695	**2.85 ± 0.26**	0.52	4.47	0.12	-	-	-	-
M15	-	11.6 ± 1.4	8.05(3)	**7.98(5)**	0.117	6.409	1.827	-	0.502	1750	0.7611	**4.03 ± 0.23**	0.55	6.72	0.08	-	-	-	-
M23A	-	17.2 ± 1.6	7.68	7.80	0.114	7.792	1.572	-	0.500	1750	0.6140	**6.04 ± 0.61**	1.45	3.82	0.38	-	-	-	-
M23B	-	23.3 ± 0.3	7.68	7.79	0.114	7.962	1.577	-	1.003	1750	0.6140	**12.38 ± 0.78**	1.97	3.79	0.52	-	-	-	-
M23C	-	39.4 ± 5.8	7.74(2)	7.82	0.115	7.369	1.589	-	1.988	1750	0.6140	**22.72 ± 2.22**	3.13	4.04	0.78	-	-	-	-
M23D	-	51.3 ± 8.8	7.68(1)	7.79	0.115	6.763	1.596	-	2.995	1750	0.6140	**31.42 ± 3.64**	4.33	3.80	1.14	-	-	-	-
M28A	-	15.3 ± 1.5	7.77(5)	7.84	0.114	3.108	1.646	-	0.497	1750	0.6993	**2.1 ± 0.19**	1.11	4.43	0.25	-	-	-	-
M28B	-	18.8 ± 0.7	7.82(1)	7.86	0.114	3.003	1.651	-	1.002	1750	0.6993	**4.1 ± 0.27**	1.31	4.63	0.28	-	-	-	-
M28C2	-	25.8 ± 0.1	7.71	7.81	0.114	2.571	1.657	-	2.003	1750	0.6993	**7.01 ± 0.44**	2.00	4.15	0.48	-	-	-	-
M28D	-	35.6 ± 2.6	7.75	7.83	0.114	2.233	1.663	-	2.922	1750	0.6993	**8.88 ± 1.33**	2.65	4.32	0.61	-	-	-	-
M28E	-	14 ± 0.9	7.99(4)	7.93	0.114	3.145	1.643	-	0.489	1750	0.6993	**2.09 ± 0.2**	0.83	5.41	0.15	-	-	-	-
M10A	Oxalate 0.01	10.2 ± 0.8	7.66(2)	7.79	0.113	3.498	1.554	-	0.496	1938	0.9904	**1.51 ± 0.12**	0.88	3.72	0.24	$3.09 \cdot 10^{-6}$	$7.831 \cdot 10^{-7}$	30.9%	1.31%
M10B	Oxalate 0.01	13.9 ± 1.6	7.70(2)	7.81	0.113	3.357	1.548	-	0.978	1938	0.9904	**2.85 ± 0.33**	1.15	3.87	0.30	$3.03 \cdot 10^{-6}$	$7.696 \cdot 10^{-7}$	30.3%	1.28%
M8	Oxalate 0.10	12.5 ± 0.5	7.70(2)	7.81	0.113	3.614	-	1.583	0.492	1938	0.7710	**1.98 ± 0.23**	1.04	3.86	0.27	$3.05 \cdot 10^{-5}$	$7.741 \cdot 10^{-6}$	30.5%	11.57%
M6A	Oxalate 0.80	10.7 ± 1.9	7.70(10)	7.85	0.115	5.381	-	1.628	0.482	1938	1.0507	**2.12 ± 0.28**	0.86	3.97	0.22	$2.46 \cdot 10^{-4}$	$6.200 \cdot 10^{-5}$	30.8%	50.89%
M6B	Oxalate 0.80	15.2 ± 2.6	7.79(2)	**7.81(4)**	0.115	5.119	-	1.620	0.985	1938	0.9734	**4.45 ± 0.48**	1.22	3.96	0.31	$2.404 \cdot 10^{-4}$	$6.056 \cdot 10^{-5}$	30.0%	49.96%
M6C	Oxalate 0.80	19.1 ± 3.9	7.86(3)	**7.86(4)**	0.115	4.969	-	1.619	1.480	1938	0.9734	**6.5 ± 0.73**	1.36	4.45	0.31	$2.382 \cdot 10^{-4}$	$6.000 \cdot 10^{-5}$	29.8%	49.39%
M7	Oxalate 1.50	14.4 ± 1.1	7.67(1)	7.79	0.116	6.789	-	1.598	0.505	1938	0.8645	**3.41 ± 0.37**	1.23	3.74	0.33	$4.49 \cdot 10^{-4}$	$1.128 \cdot 10^{-4}$	30.0%	65.54%
M7B	Oxalate 1.50	19.5 ± 1.8	7.69(4)	7.80	0.117	6.247	-	1.605	0.998	1938	0.8645	**6.2 ± 0.62**	1.63	3.83	0.43	$4.38 \cdot 10^{-4}$	$1.100 \cdot 10^{-4}$	29.2%	64.89%
M9	Oxalate 9.17	25.2 ± 1.8	7.33(2)	7.57	0.129	11.186	-	1.531	0.502	1938	0.8538	**5.66 ± 0.81**	3.90	2.07	1.88	$2.31 \cdot 10^{-3}$	$5.580 \cdot 10^{-4}$	25.2%	90.86%
M9B	Oxalate 9.17	34.8 ± 1.2	7.43	7.65	0.129	8.904	-	1.552	0.999	1938	0.8538	**8.96 ± 1.63**	4.45	2.51	1.77	$2.25 \cdot 10^{-3}$	$5.427 \cdot 10^{-4}$	24.5%	90.43%
M18	Oxalate 10.00	27.3 ± 3.8	7.61	**7.74(3)**	0.113	14.069	-	1.610	0.488	1750	0.8608	**7.6 ± 1.05**	2.62	3.35	0.78	$2.813 \cdot 10^{-3}$	$7.136 \cdot 10^{-4}$	28.1%	92.51%
M19	Oxalate 10.00	18.2 ± 1	7.85(2)	7.87	0.112	6.411	-	1.641	0.488	1750	0.6996	**4.26 ± 0.39**	1.25	4.67	0.27	$3.08 \cdot 10^{-3}$	$7.835 \cdot 10^{-4}$	30.8%	92.83%
M20	Oxalate 10.00	43.1 ± 2.3	7.47(1)	7.66	0.113	16.362	-	1.521	0.517	1750	0.5095	**15.8 ± 1.26**	5.39	2.57	2.10	$2.41 \cdot 10^{-3}$	$6.115 \cdot 10^{-4}$	24.1%	91.72%

Table 4.10 – Summary of the results of magnesite growth experiments performed in this study at 146°C. In situ pH measurements at 146°C with solid contact electrodes are reported in bold characters in column 5.

B Simulation of carbonation experiments - Evolution of elemental concentrations, and Mg and oxalate speciation

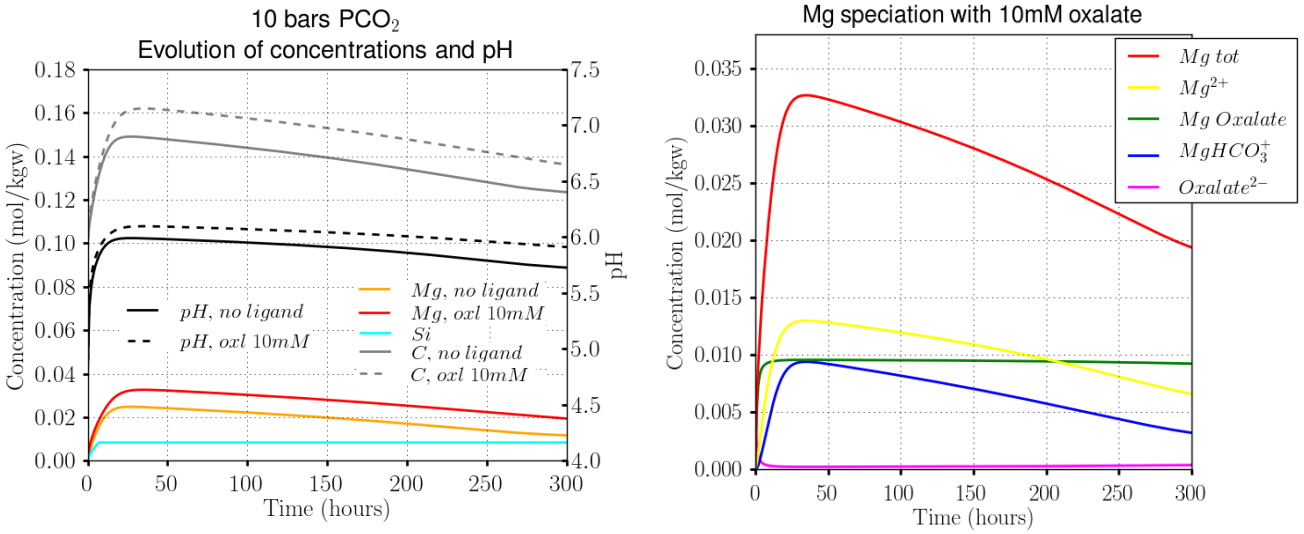

Figure 4.14 – (Left) Evolution of pH, and Mg and Si concentration during carbonation of 10g of forsterite in 1kg of water under a CO_2 pressure of 10 bars, in the absence and in presence of 10 mM oxalate. For Si, the introduction of oxalate did not have significant consequences. Thus, only one curve has been represented. (Right) Corresponding evolution of magnesium and oxalate chemical speciation in the presence of 10 mM oxalate. Only the main species have been represented. In conditions were Mg is in large excess compared to oxalate, a substantial proportion of the total Mg is present under the free Mg^{2+} form.

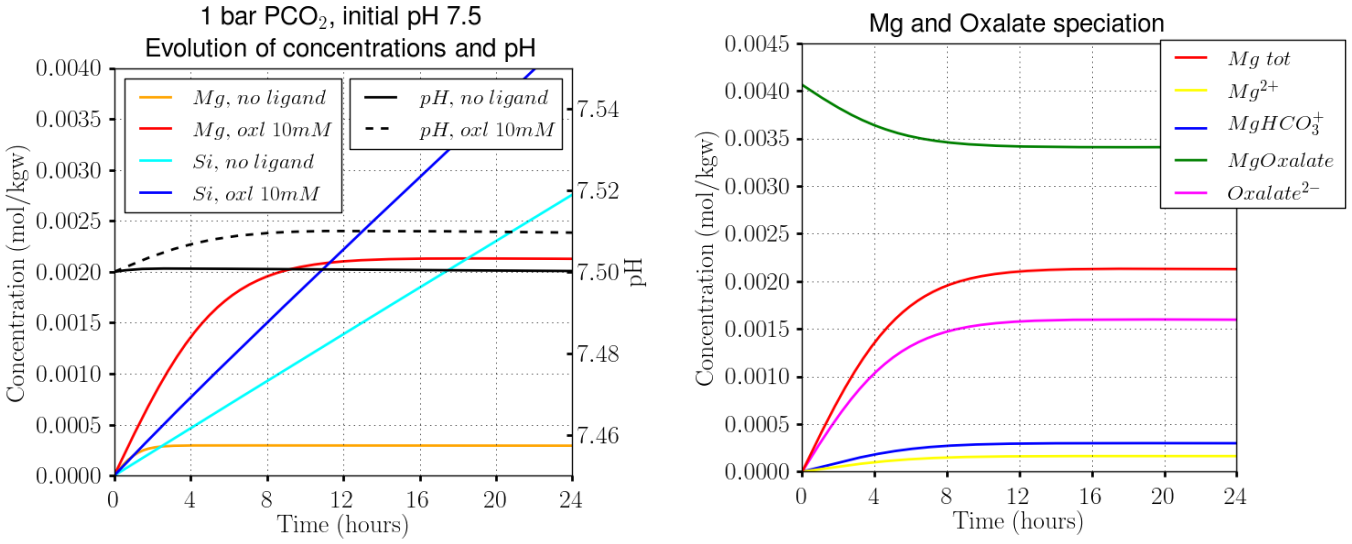

Figure 4.15 – (Left) Evolution of pH, Mg and Si concentration during carbonation of 10g of forsterite in 1kg of water under a CO_2 pressure of 1 bar, in the absence and in presence of 10 mM oxalate, at an initial pH of 7.5. Only the first 24h are represented here, corresponding to the results shown in Fig. 4.13.
(Right) Corresponding evolution of magnesium and oxalate chemical speciation in the presence of 10 mM oxalate. Mg speciation is largely dominated by MgOxalate. $NaOxalate^-$ has not been represented here, but makes up most of the oxalate speciation.

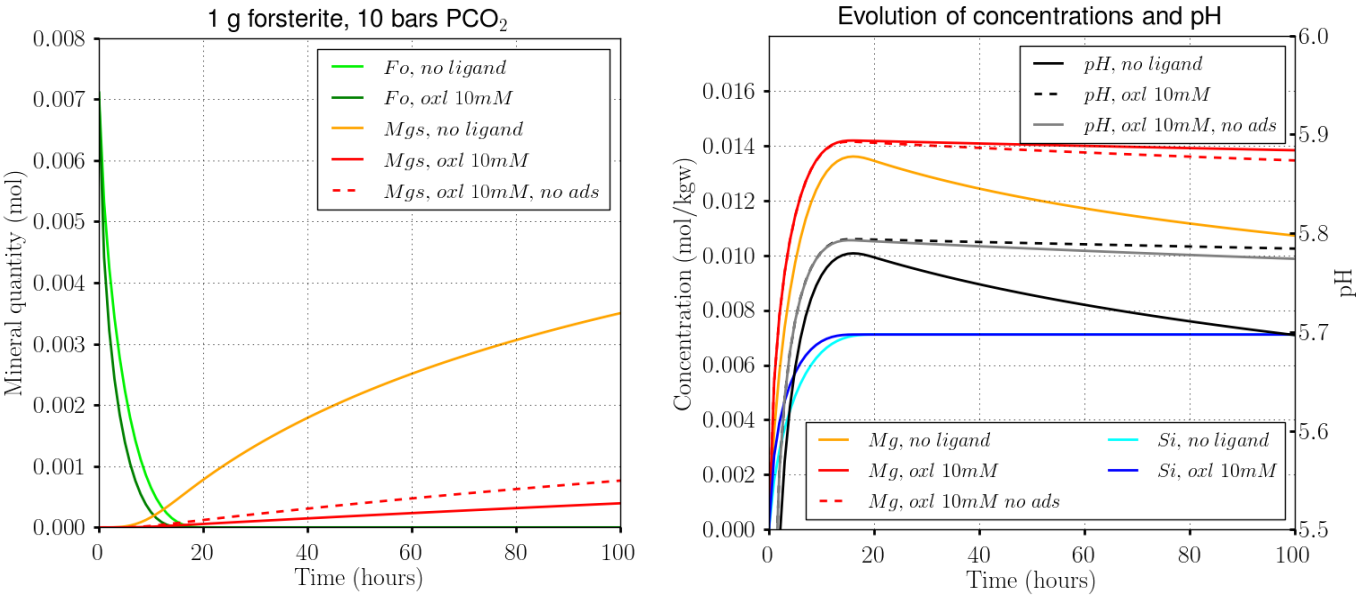

Figure 4.16 – (Left) Evolution of forsterite and magnesite during carbonation of 1 g of forsterite at a CO_2 pressure of 10 bars, in one kilogram of water, without ligands as well as in the presence of 10 molal oxalate. Here, magnesite formation strongly limits the carbonation process. Oxalate accelerates forsterite dissolution substantially, but delays magnesite formation more strongly, even if its inhibiting influence of magnesite growth kinetics is not taken into account (dashed red line). (Right) Corresponding evolution of Mg and Si concentrations and pH.

Chapter 5

Influence of organic ligands on magnesite growth: A hydrothermal Atomic Force Microscopy study

Sommaire

Influence of organic ligands on magnesite growth: A hydrothermal Atomic Force Microscopy study *

Quentin Gautier[1,3], Ulf-Niklas Berninger[2], Jacques Schott[1], Guntram Jordan[2]

[1] Géosciences Environnement Toulouse, Observatoire Midi-Pyrénées, CNRS, Université de Toulouse, 14, avenue Edouard Belin, 31400 Toulouse, France

[2] Department für Geo- und Umweltwissenschaften, Ludwig-Maximilians-Universität, Theresienstr. 41, 80333 München, Germany

[3] Université Paris-Est, Laboratoire Navier, 6/8, avenue Blaise Pascal, Champs-sur-Marne, 77455 Marne-La-Vallée, France

Abstract

In order to understand the processes controlling magnesite growth inhibition by carboxylic ligands at high temperature (Chapter 4), magnesite growth processes on the [104] surface have been investigated using hydrothermal atomic force microscopy (HAFM) at 100°C, at alkaline conditions, in the presence of various concentrations of oxalate, citrate and EDTA.

Crystal growth rates generated from step generation frequencies by spiral growth are in good agreement with bulk precipitation rates, and confirm that 1 mM of citrate decreases growth rates by a factor of 3, whereas EDTA do not appear to have a significant effect on magnesite growth.

We show that citrate and oxalate at high concentration (1 to 10 mM) exert a significant but different effect on the morphology of growth hillocks, revealing specific interaction with the crystal step edges. These shape modifications can be understood in terms of a preferential adsorption of the two ligands to specific kink-sites at the crystals steps, due to their different conformation and chemical functionalities.

Despite these pronounced morphological changes, obtuse steps velocity are not decreased by any of the three investigated ligands, which may be explained within the framework of the kink-blocking model for low kink density crystals from De Yoreo *et al.* (2009).

Inhibition of crystal growth stems from a decreased spiral growth generation rate, which may originate either from a decrease of the acute step velocity (not easily accessible to the HAFM probe), or from an increase in the step critical length. Preferential interaction of citrate with acute steps could explain its relatively higher inhibition efficiency compared to oxalate.

Overall, the observed inhibition of magnesite growth is limited, which may be due both to the relatively low adsorption of the ligands to the mineral surface, and to their complexation with Mg^{2+} in aqueous solution, which leaves only a small amount of free ligand to interact with magnesite crystal surface.

*This work will be submitted in a revised version to *Journal of Crystal Growth* or *Crystal Growth and Design*.

5.1 Introduction

In the Chapter 4, we have seen that oxalate, citrate and EDTA inhibit magnesite precipitation, due to Mg^{2+} complexation by the ligands, which reduces solution supersaturation, and a decrease of the apparent kinetic rate constant for magnesite growth, likely stemming from adsorption at the mineral surface. The highest growth inhibition is obtained with citrate, which adsorbs more strongly to the magnesite surface. In addition, we have seen that citrate likely adsorbs preferentially to growth-controlling sites at the magnesite surface. However, the mechanisms by which these organic ligands hinder magnesite growth remain to be understood.

Atomic force microscopy offers the possibility to probe surface processes at the nano-scale, and has been widely used to study interactions between a number of organic additives and mineral growth and dissolution processes (e.g Gratz & Hillner, 1993; Bosbach & Hochella Jr., 1996; Teng & Dove, 1997; Orme *et al.*, 2001; Qiu *et al.*, 2004; Elhadj *et al.*, 2005; Wu *et al.*, 2011, to cite just a few).

Such observations have helped to partly unravel the source of the control exerted by organic molecules on common (bio)minerals crystallization. For instance, the long-standing observation that calcite crystals shape may be strongly modified by simple carboxylates (Mann *et al.*, 1990; Didymus *et al.*, 1993; Meldrum & Hyde, 2001) or aminoacids (Orme *et al.*, 2001), has been explained by preferential interaction of the organic molecules with particular steps on calcite $[104]$ surface, which results in a modified crystal shape via *"the self-replicating process of crystal growth"* (De Yoreo & Dove, 2004). Similarly, the growth-modifying influence of citrate on Calcium Oxalate Monohydrate has been shown to proceed from a preferential adsorption of citrate on the $[\bar{1}01]$ face, resulting in a strong alteration of hillocks morphology on this face (Qiu *et al.*, 2005).

Most of this work has focused on minerals commonly forming at ambient temperature, such as calcite, barite, gypsum, hydroxyapatite, brushite or calcium oxalates, in order to better understand processes involved in biomineralization (Yoreo *et al.*, 2007; Qiu & Orme, 2008), or to design efficient growth inhibitors for the prevention of industrial scale formation (e.g Bosbach & Hochella Jr., 1996; Pina *et al.*, 2004). However, to our knowledge, no study has been dedicated to the interactions between organic additives and mineral growth at higher temperature.

In the present study, we wish to elucidate the surface-scale mechanisms which leads to magnesite growth inhibition at 100°C in the presence of carboxylic ligands. To this aim, we have used hydrothermal atomic force microscopy to study magnesite growth on its $[104]$ face under well constrained chemical conditions, varying ligand concentration, and varying saturation state.

The extensive work that has been published on magnesite dissolution (Jordan *et al.*, 2001; Higgins *et al.*, 2002), including in the presence of organic ligands (Jordan *et al.*, 2007), and on magnesite growth at hydrothermal conditions (Saldi *et al.*, 2009), provides a solid framework to which our observations can be compared. In addition, we wish to compare our measurements with the existing models for crystal-impurity interaction, which have mostly been developed for lower temperature processes.

5.2 Experimental methods

5.2.1 Hydrothermal Atomic Force Microscopy (HAFM)

Experiments were performed with a self-constructed continuous-flow hydrothermal atomic force microscope operating in contact mode. The apparatus, which has been described elsewhere (Higgins *et al.*, 1998), allows to investigate the mineral surfaces in solution, at temperatures up to 150°C, under moderate pressure. Our experiments were performed mostly at 100°C, occasionally at 80°C, with confining pressures never exceeding 4 bars. Experimental aqueous solutions were contained in compressible bladders placed above the HAFM cell, allowing a gravitational flow. Of the three available bladders, one was filled with high purity deionized water (resistivity 18.2 MΩ·cm) in order to clean the system between experiments. Flow rates were of the order of 10 µL/s, therefore allowing a quick renewal of the ca. 500 µL cell volume. This way, the solution chemistry was negligibly affected by growth on the mineral surface, and could thus be assumed to be equivalent to that of the inlet reactive solution.

HAFM experiments were performed on the (1 0 4) cleavage surface of transparent magnesite monocrystals from Brumado, Brazil. An electron microprobe analysis of the crystals revealed only minor amounts of Ca, Cu and Fe (Saldi *et al.*, 2009). The macrocrystals were cleaved with a scalpel immediately before the beginning of the experiments, leading to crystals of a few mm^2 in geometrical surface area.
Cleaved crystals were fixed under a titanium wire inside the HAFM cell. The crystal surface was first imaged in the experimental solution at ambient temperature. If the accessible surface was estimated sufficiently flat for imaging, the system was pressurized, and the cell heated to the desired temperature with a circular heater controlled via a thermocouple placed within the cell.

The cantilevers used throughout the study were uncoated silicon cantilevers from Nanosensors. At the high temperature of the experiments, silicon nitride coated cantilevers proved to be little durable, probably due to an uplift of the metallic coating. With silicon cantilevers, we experienced in alkaline conditions periodic fluctuations of the signal quality (period ca. 1 hour), due to shifts in the signal intensity recorded by the photo-diode. Such fluctuations were more pronounced in higher pH solutions, and essentially absent in neutral or acidic solutions. We interpret them as interferences with the laser light occurring because of dissolution of the silicon cantilever.

Step velocities were obtained by measuring the step advancement perpendicularly to the step orientation, from images taken in the same scan direction, using a surface landmark as fixed reference. When such a reference was not available perpendicularly to the step, available reference points were used, and the step advancement was corrected geometrically to obtain the true step velocity. Image distortions are frequent because steps advance during the scanning of the image, and because of instrumental artifacts. As a result, reported step velocities are the average of measurements taken on different islands, at different scan angles (0/90°), and different scanning directions (upward/downward and trace/retrace).

Magnesite growth rates R were derived from the layer formation frequency I measured in the accessible scan area:

$$R = I \cdot \frac{h}{V_M} \tag{5.1}$$

where h stands for the elementary layer thickness, equal to 2.74 Å on the $[104]$ face, and V_M represents the magnesite molar volume (28.1 cm^3/mol). I can be accessed directly by counting steps generated at a particular step generating point, or by counting steps passing a fixed reference point, during a given time frame (Higgins *et al.*, 2002).

5.2.2 Solution preparation and analysis

Experimental solutions were prepared with high purity deionized water (resistivity 18.2 MΩ·cm), reagent grade NaCl, $MgCl_2 \cdot 6H_2O$,$NaHCO_3$, Na_2Oxalate, Na_3Citrate·2 H_2O, Na_2H_2EDTA·2 H_2O, and high purity 1M HCl and NaOH solutions (throughout the manuscript, the symbol "M" is used for "mol/L"). Organic ligands were either used directly as salts, or pre-dissolved in concentrated stock solutions, from which the experimental solutions were later prepared. The NaCl concentration was adjusted to obtain an ionic strength close to 0.1M in all experiments.

pH of the solutions was measured just before the beginning of the experiments by means of a standard glass electrode calibrated against NIST standard buffers, with an uncertainty of 0.02 units. pH was kept within a narrow range, from 7.95 to 8.17 at 100°C for all experiments. This pH range was chosen for consistency with the study by Saldi *et al.* (2009), and in order to limit signal fluctuations due to cantilever dissolution at higher pH.

As much as possible, the activity ratios $a_{Mg^{2+}}/a_{CO_3^{2-}}$ were kept close to 1. However, reactive solutions with the highest saturation states were prepared with a $a_{Mg^{2+}}/a_{CO_3^{2-}}$ ratio significantly higher than 1 (typically 3 to 5), in order to obtain higher saturation states without significantly changing the pH nor increasing the total carbon content (which would have caused difficulties in keeping a stable pH).

Experimental solutions were analysed for magnesium concentration by flame atomic absorption spectroscopy (AAS) with an uncertainty of $\pm$1% and a detection limit of 6×10^{-7} M. In order to verify the carbon content of the solutions, alkalinity was measured by means of automatic HCl titration, with an uncertainty of $\pm$1% and a detection limit of 5×10^{-5} M. Alkalinity was measured only on samples with organic ligands concentrations less than 10^{-4}M, in which case the influence of the organic molecules on the alkalinity titration was negligible. Dissolved inorganic carbon (DIC) as calculated from alkalinity and pH measurement at ambient temperatures always agreed closely with DIC as estimated from the solution preparation. Organic ligand concentrations were verified by means of DOC analysis on a Shimatzu TOC-BCSN, with an uncertainty of $\pm$2% and a detection limit of 0.15ppm. Effluents collected downstream of the HAFM cell were chemically analysed, and never showed differences to the inlet solutions exceeding analytical uncertainties, therefore confirming that growth of the crystal does not significantly affect the chemistry of the fluid in the cell. The chemical composition of all experimental solutions is summarized in Table 5.1.

Solution	pH (25°C)	Ligand type	[Ligand] (mol/L)	$MgCl_2$ (mol/L)	$NaHCO_3$ (mol/L)	NaCl (mol/L)	HCl (mol/L)	NaOH (mol/L)	Alk. (eq/L)
Mgs2	8.45	-	-	$4.00 \cdot 10^{-4}$	0.0200	0.100	-	-	0.0201
Mgs3	8.43	-	-	$3.38 \cdot 10^{-4}$	0.0180	0.083	-	$1.20 \cdot 10^{-4}$	0.0179
Mgs3_3	8.29	-	-	$3.76 \cdot 10^{-4}$	0.0180	0.083	-	-	0.0180
Mgs3_4	8.21	-	-	$3.76 \cdot 10^{-4}$	0.0180	0.083	$3.00 \cdot 10^{-4}$	-	0.0178
Mgs5	8.18	-	-	$3.35 \cdot 10^{-4}$	0.0180	0.083	-	-	0.0184
M38	8.43	-	-	$7.98 \cdot 10^{-4}$	0.0200	0.080	-	$1.80 \cdot 10^{-4}$	0.0200
M38A	8.53	-	-	$4.53 \cdot 10^{-4}$	0.0192	0.081	-	$2.50 \cdot 10^{-4}$	0.0193
M38B	8.46	-	-	$4.93 \cdot 10^{-4}$	0.0194	0.081	-	$1.73 \cdot 10^{-4}$	0.0193
Oxl2	8.42	Oxalate	$1.02 \cdot 10^{-2}$	$2.64 \cdot 10^{-3}$	0.0180	0.100	-	-	
Oxl3	8.39	Oxalate	$1.06 \cdot 10^{-3}$	$5.83 \cdot 10^{-4}$	0.0180	0.081	-	$1.00 \cdot 10^{-4}$	
Cit1_1	8.29	Citrate	$9.83 \cdot 10^{-3}$	$8.07 \cdot 10^{-3}$	0.0180	0.045	-	-	
Cit1_2	8.26	Citrate	$1.00 \cdot 10^{-2}$	$9.13 \cdot 10^{-3}$	0.0180	0.047	-	-	
Cit1_3	8.19	Citrate	$1.01 \cdot 10^{-2}$	$1.13 \cdot 10^{-2}$	0.0180	0.048	$2.20 \cdot 10^{-4}$	-	
Cit2	8.27	Citrate	$1.04 \cdot 10^{-3}$	$1.24 \cdot 10^{-3}$	0.0180	0.079	-	-	
Cit6	8.4	Citrate	$1.21 \cdot 10^{-3}$	$1.58 \cdot 10^{-3}$	0.0200	0.076	-	$1.72 \cdot 10^{-4}$	
Cit6C	8.49	Citrate	$1.05 \cdot 10^{-3}$	$1.47 \cdot 10^{-3}$	0.0199	0.076	-	$6.50 \cdot 10^{-5}$	
Cit6D	8.49	Citrate	$1.04 \cdot 10^{-3}$	$1.50 \cdot 10^{-3}$	0.0202	0.076	-	$1.70 \cdot 10^{-4}$	
Cit6E	8.28	Citrate	$9.85 \cdot 10^{-4}$	$1.33 \cdot 10^{-3}$	0.0199	0.076	$3.05 \cdot 10^{-4}$	-	
Cit7	8.46	Citrate	$1.07 \cdot 10^{-4}$	$1.02 \cdot 10^{-3}$	0.0200	0.079	-	$1.92 \cdot 10^{-4}$	
Cit7A	8.32	Citrate	$1.02 \cdot 10^{-4}$	$6.67 \cdot 10^{-4}$	0.0199	0.079	$3.70 \cdot 10^{-4}$	-	
Cit7D	8.38	Citrate	$1.02 \cdot 10^{-4}$	$7.70 \cdot 10^{-4}$	0.0197	0.079	-	$1.60 \cdot 10^{-5}$	
Cit7E	8.41	Citrate	$1.02 \cdot 10^{-4}$	$5.51 \cdot 10^{-4}$	0.0192	0.080	-	$9.20 \cdot 10^{-5}$	
Edta1	8.27	EDTA	$9.90 \cdot 10^{-3}$	$1.16 \cdot 10^{-2}$	0.0180	0.032	-	$8.48 \cdot 10^{-3}$	
Edta2	8.2	EDTA	$9.83 \cdot 10^{-3}$	$1.13 \cdot 10^{-2}$	0.0180	0.032	-	$2.00 \cdot 10^{-2}$	
Edta3	8.23	EDTA	$9.83 \cdot 10^{-3}$	$1.19 \cdot 10^{-2}$	0.0180	0.032	-	$1.93 \cdot 10^{-2}$	
Edta4	8.2	EDTA	$9.83 \cdot 10^{-3}$	$1.10 \cdot 10^{-2}$	0.0180	0.032	-	$1.96 \cdot 10^{-2}$	
Edta6	8.21	EDTA	$1.00 \cdot 10^{-4}$	$4.32 \cdot 10^{-4}$	0.0180	0.082	-	$2.00 \cdot 10^{-2}$	
Edta7	8.21	EDTA	$1.00 \cdot 10^{-5}$	$3.42 \cdot 10^{-4}$	0.0180	0.083	-	$2.00 \cdot 10^{-2}$	

Table 5.1 – Composition of the solutions used for magnesite growth experiments.

5.2.3 Chemical speciation calculation

The experimental results are reported as a function of the saturation state of the experimental solutions with respect to magnesite, defined as:

$$\Omega = \frac{a_{Mg^{2+}} a_{CO_3^{2-}}}{K_{sp(Mgs)}} \tag{5.2}$$

where $K_{sp(Mgs)}$ stands for the solubility product of magnesite. The organic molecules used in this study, that are known to form aqueous complexes with Mg^{2+} and Na^{+}, therefore decrease the saturation state of the solution with respect to magnesite. Thus, it is crucial to accurately quantify this complexation effect, in order to witness directly the influence of ligands on magnesite growth, apart from their effect on saturation state.

Chemical activities, pH, and saturation state in the experimental conditions were computed from Mg^{2+} concentration, alkalinity or DIC, organic ligand concentration and pH measured at room temperature, using the PHREEQC computer code and its `llnl.dat` database, derived from the slop98.dat database of the SUPCRT92 software (Johnson *et al.*, 1992). The B-dot activity model (Helgeson, 1969) is used to compute activity coefficients. The magne-

site solubility product used in this study is taken from the `llnl.dat` database, which is consistent with the experimental determination of Bénézeth *et al.* (2011). The database was modified to include the dissociation constants of carbonic acid of Millero *et al.*, 2007 and the equilibrium constant for the first Mg^{2+} hydrolysis (Palmer & Wesolowski, 1997). The dissociation constants of organic acids and their complexation constants with metal cations were taken from the literature, and introduced in the database according to the procedure detailed in Chapter 3 of the thesis.

The selected thermodynamic data used for chemical speciation calculation are listed in Chapter 3, Table 4. Despite uncertainties, this thermodynamic dataset is thought to accurately represent the most important chemical species at the temperature of our experiments, and allow for an accurate calculation of chemical speciation and saturation states at the temperature of the experiments. Reported error bars in saturation states stem from analytical uncertainties (pH, alkalinity, magnesium and ligand concentration).

5.3 Results

5.3.1 Step generation mechanism and macroscopic growth rates

In the absence of ligands, Saldi *et al.* (2009) concluded that the main step generation mechanism controlling growth on the magnesite $[104]$ surface in a large range of temperatures and saturation states is spiral growth initiated at screw dislocations.

We performed ligand-free experiments in order to complete the results obtained by Saldi *et al.*, 2009, and to establish a consistent baseline serving as a reference to which experiments with ligands can be compared. In our experiments at 100°C, spiral growth initiated at screw dislocations with a Burgers vector of 1 was often witnessed within the scan area for Ω higher than ~ 50. At lower saturation states, steps were usually generated along surface features such as cleavage macrosteps (in which case the exact step-generating mechanism could not be imaged), or generated at impurities attaching to the mineral surface. Step generation by means of these defect-assisted 2D nucleation mechanisms was irregular in frequency, and variable spatially. On the contrary, spiral growth was the only mechanism able to generate steps at a constant frequency within the time frame of our experiments (typically: a few hours). Furthermore, when an active spiral was visible within the scan area (or propagating into the scan area from a screw dislocation located outside), its step generation frequency was significantly higher than that of other step-generating mechanisms. As a result, spiral growth was always the mechanism dominating growth at the surface scale, and likely to control steady-state growth at the macroscopic scale. We therefore agree with the observations of Saldi *et al.* (2009).

The presence of ligands did not alter the step generation mechanism. Spiral growth was observed in the presence of citrate and EDTA (see for instance Fig. 5.5a, c, 5.6a), but not unambiguously in the presence of oxalate. This however, is probably due to the low saturation states investigated in the presence of oxalate ($\Omega < 50$) and to the limited number of observations, rather than a consequence of oxalate itself. Furthermore, precipitation experiments in mixed-flow reactors (MFR) presented in Chapter 4, led to the conclusion that magnesite precipitation in the presence of oxalate, citrate and EDTA obeys to a second-order rate law of

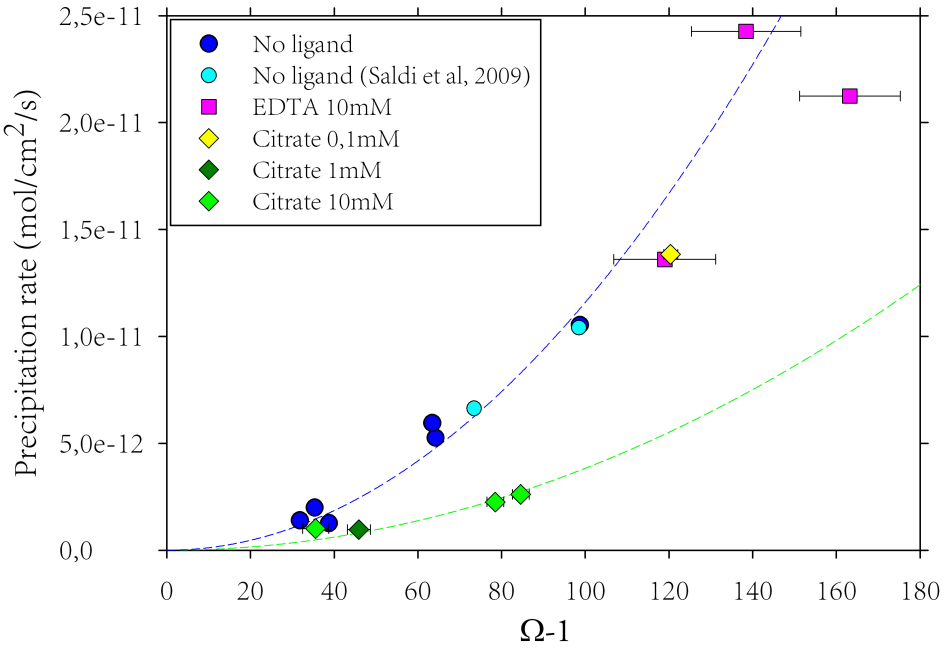

Figure 5.1 – HAFM-based magnesite growth rates at 100°C, plotted as a function of saturation state, in the absence and presence of organic ligands (citrate and EDTA). Experiments with citrate at concentrations of 1 mM or higher show a reduced growth rate of magnesite compared to the ligand-free case, whereas EDTA at a concentration of 10 mM does not affect growth rates. The dotted lines are best fits of the HAFM rates without ligand (blue), and with 1 mM citrate (green), according to equation (5.3).

the type:

$$R = k(\Omega - 1)^2 \tag{5.3}$$

where k stands for the apparent kinetic rate constant. Such a rate law has been interpreted to reveal a spiral growth mechanism (e.g Blum & Lasaga, 1987; Shiraki & Brantley, 1995). Therefore, we consider spiral growth to be the controlling mechanism for magnesite growth in the presence and absence of organic ligands, in the investigated conditions.

Observations regarding step-generating mechanisms are listed in Table 5.2, together with measured step generation frequencies and step velocities. Magnesite growth rates calculated from step generation frequency according to equation (5.1), are reported in Fig. 5.1 and 5.2 as a function of saturation state, together with data from Saldi *et al.* (2010). Please note that only step generation by regular step generating mechanism (proven spiral growth, or regular step generation at macrosteps when the step generating point could not be imaged) has been considered here, which explains the reduced scatter compared to Saldi *et al.* (2010). These surface-based rates are compared to MFR rates in analogous conditions (Chapter 4), normalized to the seeds geometrical surface area estimated from laser granulometry.

Several important outcomes of these experiments deserve to be highlighted:

First, HAFM-derived rates are satisfyingly fitted with a second-order rate law, in accordance with spiral growth being the rate-controlling mechanism.

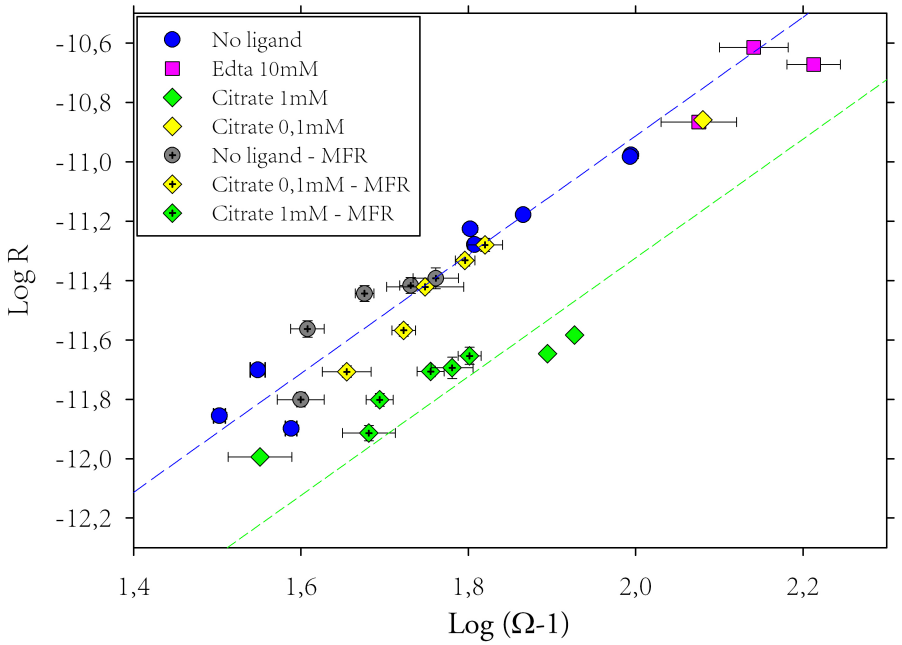

Figure 5.2 – Comparison between HAFM and MFR-based magnesite growth rates at 100°C in the absence and presence of organic ligands. MFR data were presented in Chapter 4. There is a good agreement between MFR rates normalized to geometrical surface area, and HAFM rates. In both cases, experiments with 1 mM citrate exhibit a reduced growth rate compared to ligand-free experiments. The dotted lines are best fits of the HAFM rates in ligand-free solutions (blue), and in the presence of 1 mM citrate (green), according to the log version of equation 5.3. The fits are consistent with a second-order rate law.

Second, growth rates derived from HAFM are in good agreement with geometrical surface-normalized MFR rates. This observation was already made by Saldi *et al.* (2009) for ligand-free experiments, but the agreement is also satisfying for experiments with 1 mM of citrate (cf Fig. 5.2). Bearing in mind the uncertainties related to seeds geometrical surface estimation, this nonetheless suggests that processes observed at the surface scale with HAFM are likely to control the overall growth rate of magnesite.

Third, magnesite growth rate in the presence of citrate appears reduced compared to ligand-free experiments. The apparent kinetic rate constant k (cf equation 5.3) is $1.16\times10^{-15}\pm 6\times10^{-17}$ mol·cm^{-2}·s^{-1} without ligands ($R^2 = 0.96$), whereas it is $0.38\times10^{-15}\pm6\times10^{-17}$ mol·cm$^{-2}\cdot$ s^{-1} in the presence of 1 mM citrate. The apparent kinetic rate constant is therefore decreased by a factor of about 3.
In addition, one datapoint acquired with 0.1 mM citrate at high saturation state ($\Omega = 121$) does not depart significantly from the ligand-free baseline, which suggests that citrate at concentrations of 0.1 mM or lower does not appreciably affect magnesite growth (Fig. 5.1), in accordance with MFR results (Chapter 4). Eventually, one experiment with 10 mM citrate gave rates comparable to those obtained with 1 mM citrate. Therefore, the observation based on MFR experiments that citrate inhibits magnesite growth at concentrations higher than 0.2 mM is confirmed by HAFM measurements. As a result, surface scale observations are likely to give insights into the origin of growth inhibition by citrate.

Fourth and last point, experiments ran with 10 mM of EDTA, despite being at much higher saturation states, led growth rates which are in agreement with the rate law derived from

ligand-free experiments (Figure 5.1). Thus, EDTA in the investigated conditions does not appreciably affect magnesite growth rates, an observation in contradiction with MFR experiments (Chapter 4), which revealed a small decrease of the kinetic rate constant at 120°C with 1 mM EDTA. Possible origins of this discrepancy will be discussed later.

5.3.2 Islands morphologies

Without ligands

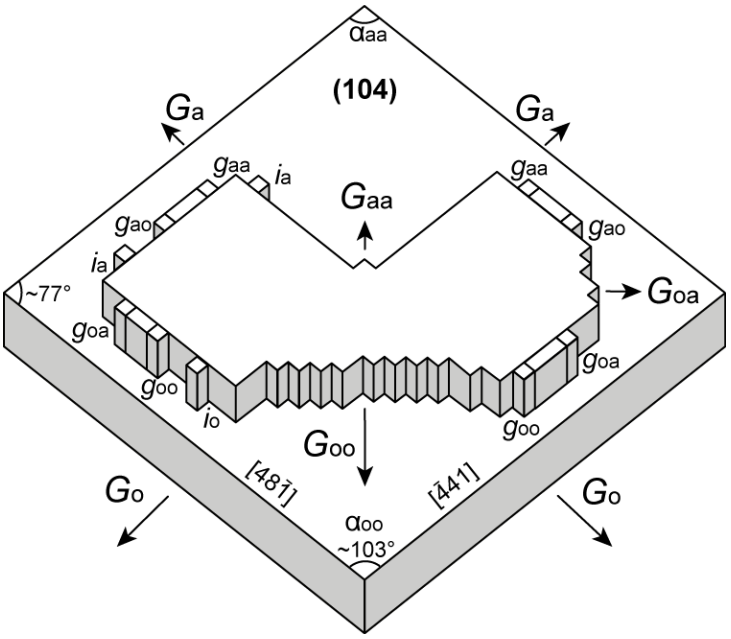

Figure 5.3 – Sketch of a magnesite growth hillock on the $[104]$ surface. The upper step is built out of two merging hillocks in order to illustrate the different "rough" steps that may develop on the [104] surface (see Section 5.3.4). Abbreviations: G = step; g = kink site; i = kink-nucleation site; o = obtuse; a = acute. In the text, g_{xy} is used indistinctly to designate a given kink orientation, or its propagation rate.

In the absence of ligands and as equilibrium is approached, magnesite growth hillocks exhibit a typical rhombic shape delimited by the $[48\bar{1}]$ and $[\bar{4}41]$ crystallographic directions, with two obtuse steps G_o and two acute steps G_a separated by a an angle of theoretically 103° (Jordan *et al.*, 2001). Figure 5.3 presents a sketch of an ideal rhombic magnesite hillock, on which two merging hillocks have been drawn in order to label the different steps and kink sites. Figure 5.4a shows an example of an hillock approaching the rhombic shape.

As the saturation state, and therefore the growth rate, is increased, the kink dynamics (i.e. generation and propagation) along the step is modified, and the island morphology evolves: the transition between acute and obtuse steps gets more rounded, and the angle between the two obtuse steps, α_{oo}, becomes narrower (Saldi *et al.*, 2009; Fig.5.4c). α_{oo} indeed decreases from 97.2° ± 2.6° at $30 < \Omega < 50$ (weighted average of measurements on 4 experiments, this study) to about 89.7° ± 0.8° at $82 < \Omega < 112$ (weighted average of measurements on 8 experiments, this study and Saldi *et al.*, 2009). The acute/acute angle (α_{aa}) is subject to more variability (in particular related to the step source type) but in general widens in the same saturation interval.

Oxalate

At 100°C, with 1 mM oxalate, magnesite growth islands exhibit an increased roughness along all step orientations. Indentations appear at the obtuse/acute transition (Figure 5.4d),

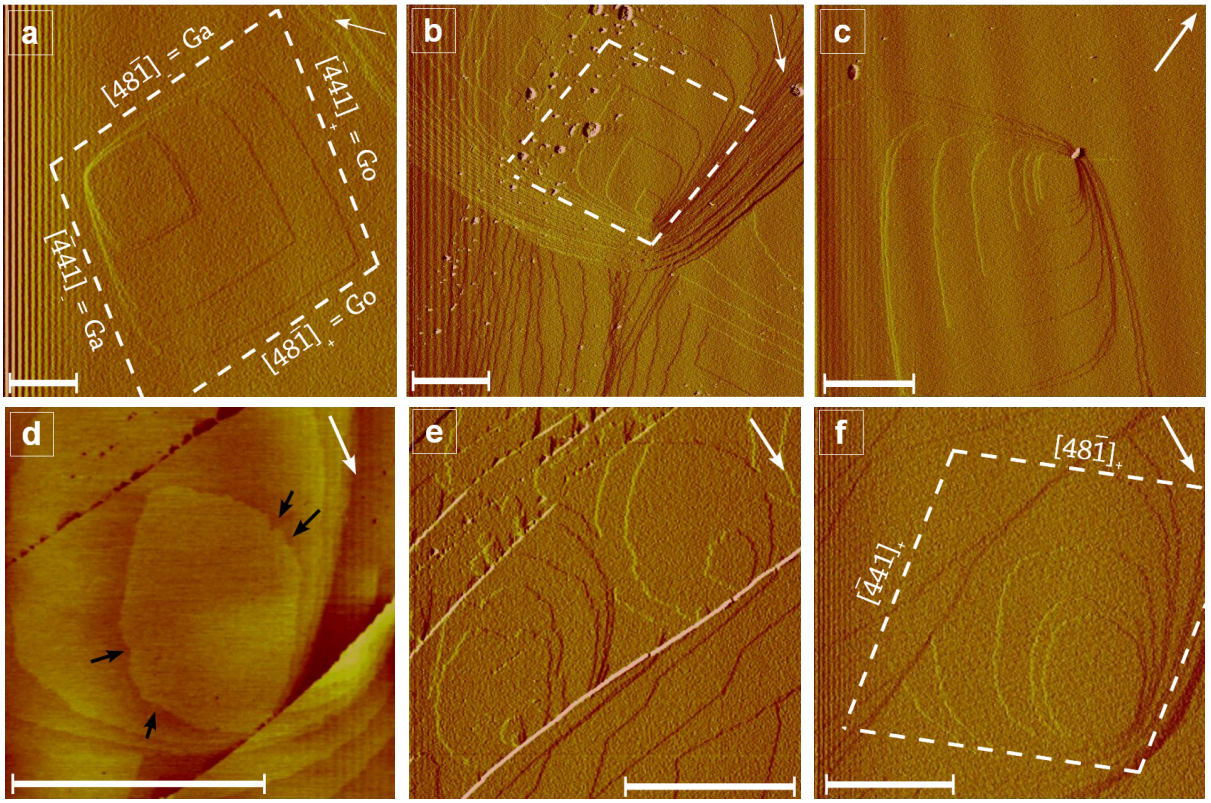

Figure 5.4 – HAFM images of magnesite hillocks in ligand-free conditions (a-c), and in the presence of oxalate (d-f). The white arrows represent the orientation of the c-axis [001] plunging downward into the plane of the page. The scale bars correspond to 1 µm. The rhombus materialized by the dashed white lines represent the shape of an ideal magnesite rhombus and has been drawn for comparison with the actual hillock shape.
(a) Deflection image of a growth hillock at $\Omega = 40$, 100°C. The hillock shape approaches that of the ideal rhombus. (b) Deflection image of a hillock generated by spiral growth at $\Omega = 74$, 100°C. Image courtesy of G. Saldi. The hillock exhibit sharp obtuse and acute tips. Slight vertical elongation is a scanning artefact. (c) Hillock at $\Omega = 112$, 100°C. Image courtesy of G. Saldi. As saturation state increases, the acute tip widens whereas the obtuse one narrows down (see text).
(d) Height image of a hillock generated at a cleavage macrostep, at 100°C, in the presence of 1 mM oxalate. $\Omega = 38$. An increased roughness of the step edges, as well as some indentations (pointed by black arrows) is noticeable. (e) 1 mM oxalate, 80°C, $\Omega = 20$. Islands are rougher than at 100°C. (f) 10 mM oxalate, 100°C, $\Omega = 48$. The shape differs significantly from the ideal magnesite rhombus, with a general rounding of the hillock.

pointed by black arrows). Roughness is more pronounced at 80°C, and islands appear with very irregular shapes (Fig. 5.4e).

As oxalate concentration is increased to 10 mM, at 100°C and $\Omega = 50$, the morphology of the growth hillocks differs markedly from the initial rhombic shape: islands are highly rounded, and step edges are rough at small scale, with all step orientations affected (Figure 5.4f).

These observations clearly indicate that oxalate adsorbs at the magnesite surface, and interacts with step advancement and island spreading. These interactions appear to be unspecific of step orientation.

Citrate

In 0.1 mM citrate solution, no significant change of hillock shape compared to ligand-free solutions is observed. Hillocks appear particularly rhombic, with straight steps (Figure 5.5a).

In the presence of 1 mM of citrate, the shape of magnesite growth islands at 100°C is slightly modified. α_{oo} is not significantly changed, but an apparent elongation along the c-axis is visible as hillocks grow above a few µm in size (Figure 5.5b), corresponding to an increased rounding of the obtuse-acute transition. These shape alterations are less visible at higher saturation states (Fig. 5.5c).

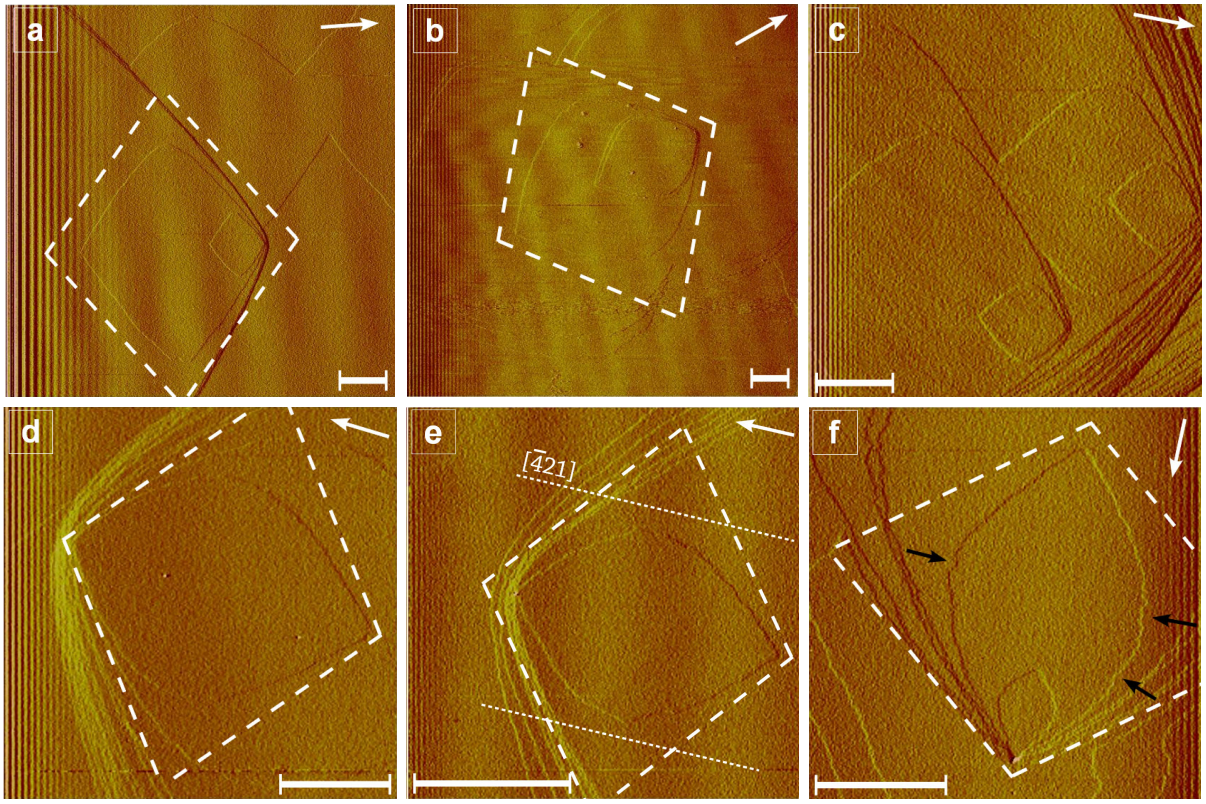

Figure 5.5 – HAFM deflection images of magnesite hillocks in the presence of various concentrations of citrate. The white arrows represent the orientation of the c-axis [001] plunging downward into the plane of the page. The scale bars correspond to 1 µm. The rhombus materialized by the dashed white lines represent the shape of an ideal magnesite rhombus and has been drawn for comparison with the actual hillock shape.
(a) Island generated by spiral growth in the presence 0.1 mM citrate, $\Omega = 65$. The shape approaches closely that of the ideal rhombus. (b) 1 mM citrate, $\Omega = 52$. Some elongation along the c-axis, as well as an increased rounding of the obtuse/acute transition, becomes visible as the monolayers grow bigger. (c) Double spiral, 1 mM citrate, $\Omega = 80$. Hillocks shapes appear less modified than at lower saturation state.
(d) Hillock generated in the presence of 10 mM citrate, $\Omega = 29$. The island clearly appears elongated parallel to the $[\bar{4}21]$ direction. Hillocks imaged in (e) and (f), at $\Omega = 47$, exhibit a similar elongation, with an increased roughness at the transition from obtuse to acute steps (pointed by black arrows).

In the presence of 10 mM citrate, the shape of magnesite growth islands at 100°C is significantly modified. Islands are apparently elongated along $[\bar{4}21]$, as shown in figure 5.5d, e and f. This is due to a delay in the advancement of the obtuse-acute transition step edge, which appears rounded, with an increased roughness (indentations pointed by black arrows in Fig.

5.5f). The obtuse tip remains sharp, but α_{oo} is reduced compared to the ligand-free case: at $\Omega \sim 30$, $\alpha_{oo} = 88.0° \pm 2$, to be compared with $97.2° \pm 3$ in the ligand-free case. The acute tip shows more variability: it is narrow when islands are generated at impurities attaching to the mineral surface (Fig. 5.5a, b), and wider when steps are generated via spiral growth. Reasons for this variability are not well understood yet.

Citrate therefore interacts with magnesite growth in a very different way compared to oxalate. Modifications of shape occur through a progressive rounding and a lesser advancement of the obtuse-acute transition step, producing islands apparently elongated along the $[\bar{4}21]$ orientation.

EDTA

At low concentrations (10 µM to 0.1 mM) and $\Omega \sim 30$, EDTA produced no visible effect on island morphology. Several experiments were performed with a concentration of 10 mM EDTA at 100°C, but at higher supersaturation than in the previously described experiments.

Observed islands had straight steps and sharp obtuse tips. Their morphology departs from that of the ideal magnesite rhombus, with $\alpha_{oo} = 90.5° \pm 1.3$ (weighted average of measurements on 3 different experiments) at $100 < \Omega < 164$, whereas α_{aa} in the same saturation interval is $117.0° \pm 4.1$, therefore significantly wider than the rhombic 103° angle (Figure 5.6). Such features are very comparable to those observed in the absence of any ligands at high saturation state (Section 5.3.2; Fig. 5.4c). At 80°C ($\Omega \sim 60$), the hillock shape gets closer to the rhombic shape. These observations indicate that EDTA does not appreciably affect magnesite growth hillock shape in the investigated conditions.

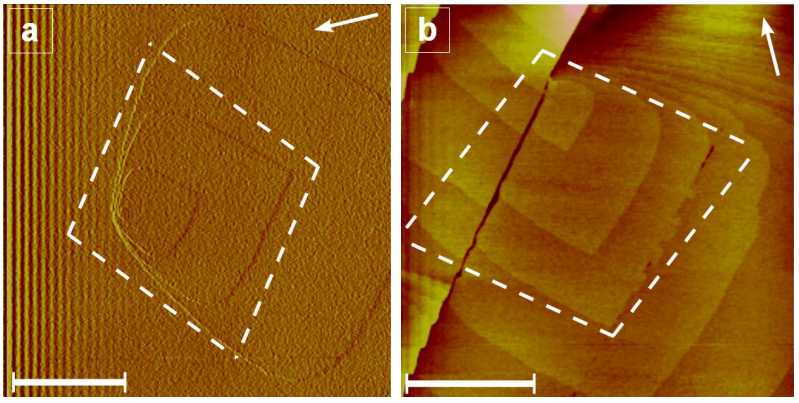

Figure 5.6 – HAFM images of magnesite hillocks at 100°C in the presence of 10 mM EDTA. The scale bars corresponds to 1 µm.
(a) Spiral growth at $\Omega = 164$. Step edges are straight. The obtuse tip is narrower than that of the ideal rhombus, whereas the acute tip is wider.
(b) Propagation of monomolecular steps over a macrostep at $\Omega = 139$. Little modification is observed compared to the ligand-free shape (Fig. 5.4c).

5.3.3 Step velocity

Steps and kink orientations are labelled according to Figure 5.3. Magnesite obtuse step velocity measurements at 100°C, with and without organic ligands, are listed in Table 5.2, and plotted as a function of saturation state in Figures 5.7, 5.8 and 5.9.

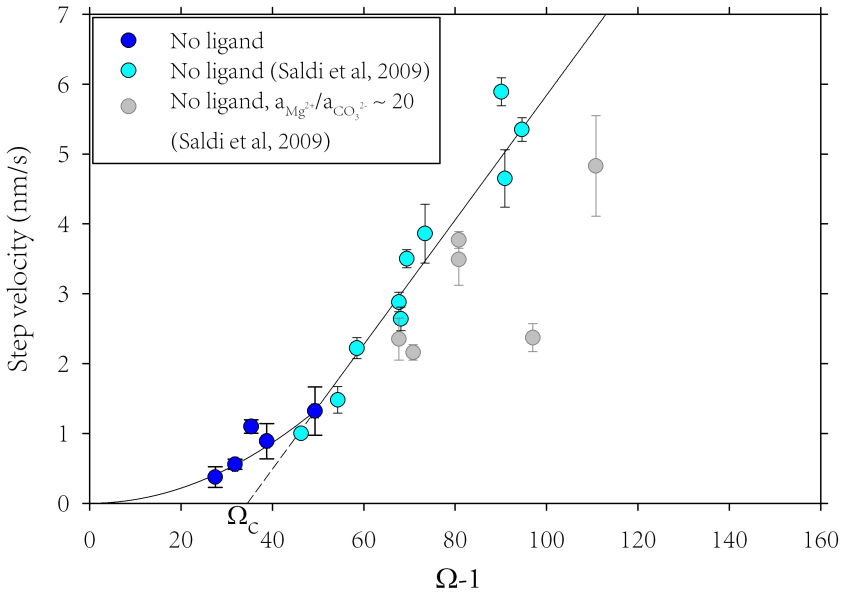

Figure 5.7 – Obtuse step velocity as a function of saturation state, without organic ligands. The fit is linear above $\Omega \sim 50$, in accordance with equation 5.4. The fit crosses the x axis at Ω_c. For $\Omega < 50$, the data have been fitted with an empirical second-order rate law.

In the absence of organic ligands, obtuse step velocities are in good agreement with data from Saldi *et al.*, 2009 at $a_{Mg^{2+}}/a_{CO_3^{2-}}$ ratios close to 1 (Fig. 5.7). Obtuse step velocities exhibit a linear dependence on saturation state above $\Omega \sim 45$, and the rate law can then be expressed as:

$$R(G_o) = k_o(\Omega - \Omega_c) \tag{5.4}$$

where $R(G_o)$ stands for the obtuse step velocity, k_o is the kinetic coefficient of the obtuse steps advancement rate, and Ω_c represents the saturation state at which the linear correlation crosses the x axis. Here $k_o = 0.089 \pm 0.014\ nm.s^{-1}$ and $\Omega_c = 34.5 \pm 2.2$. These data serve as a baseline to evaluate the influence of organic ligands.

Our data suggest that below $\Omega \sim 45$, obtuse step velocities tend towards zero with a super-linear behaviour with respect to saturation state. Such a behaviour has already been reported for calcite (e.g Teng *et al.*, 1999, Davis *et al.*, 2000).

Figure 5.8 represents obtuse step velocity measured in the presence of various concentrations of oxalate and citrate. Oxalate at 1 or 10 mM and citrate at 1 mM do not have a significant effect on obtuse step advancement rates, within measurement uncertainties.

Obtuse step velocity in the presence of 10 mM citrate at $\Omega < 50$ appears to be slightly higher than in ligand-free solutions. This observation needs to be considered with caution, bearing in mind the uncertainties related to chemical speciation calculation in the presence of a high concentration of ligand. Possible reasons for this apparently enhanced obtuse step velocity at moderate saturation state will be discussed later.

On the contrary, at higher saturation state ($\Omega = 132$), one datapoint with 10 mM citrate plots below the ligand-free baseline, which may be due to its relatively high $a_{Mg^{2+}}/a_{CO_3^{2-}}$ ratio of 5.6, compared to ~ 1 in most of the other experiments. Indeed, as shown by Saldi

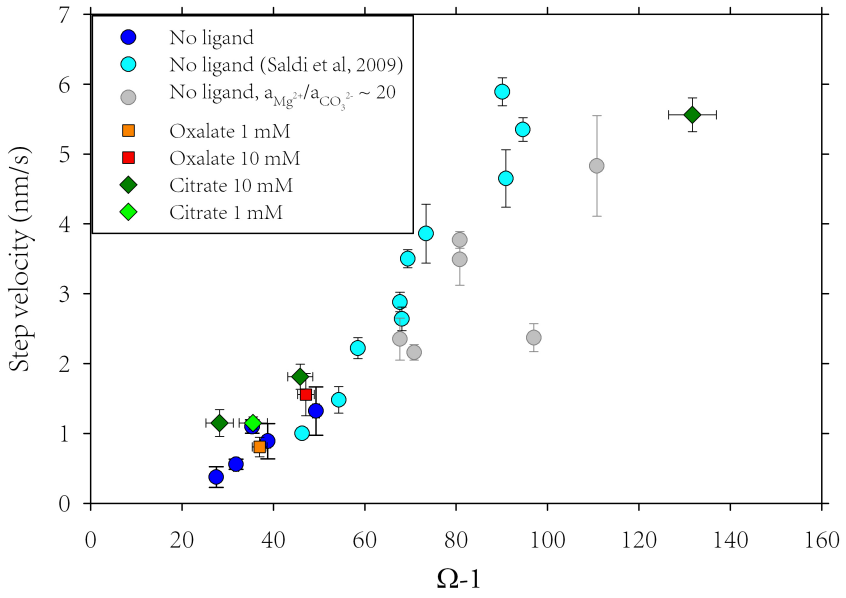

Figure 5.8 – Obtuse step velocity as a function of saturation state, in the presence of various concentrations of citrate and oxalate.

et al., 2009, high $a_{Mg^{2+}}/a_{CO_3^{2-}}$ ratios result in obtuse step velocities that are globally lower than in stoichiometric solutions (see grey points in Fig. 5.8).

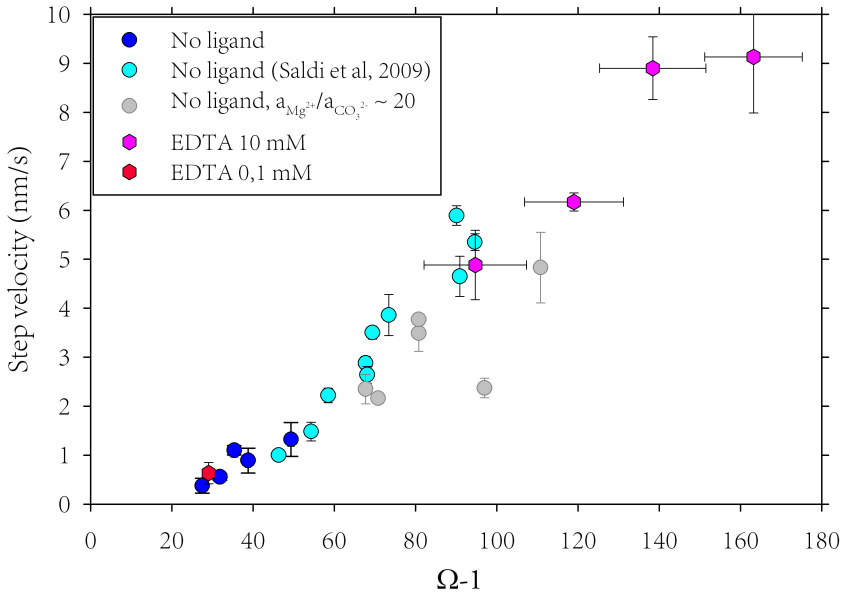

Figure 5.9 – Obtuse step velocity as a function of saturation state, in the presence of various concentrations of EDTA. EDTA does not visibly affect obtuse step advancement rate.

Experiments with 10 mM EDTA were performed at saturation states higher than the range investigated in the absence of ligands. Nevertheless, it can be assessed on Figure 5.9 that obtuse step velocities are not affected by the presence of EDTA, in the concentration range 10

µM to 10 mM.

HAFM resolution was too low for a precise quantification of acute step velocity. Furthermore, shape alteration provoked by citrate and oxalate prevented the development of straight acute steps, rendering more difficult precise velocity measurements. Therefore, acute step velocities reported in Table 5.2 do not allow for a precise comparison between ligand-free and ligand-containing experiments. In general however, the marked anisotropy between obtuse and acute steps always holds, with obtuse steps roughly one order of magnitude quicker than acute steps, in agreement with Jordan *et al.* (2001), Higgins *et al.* (2002), Saldi *et al.* (2009).

5.3.4 Kink dynamics

Step movement results from kink nucleation along step edges, and attachment/detachment of mineral building units to kink sites (Burton *et al.*, 1951; Chernov, 1961). In a supersaturated solution, attachment rates exceed detachment rates, resulting in kink progression and advancement of steps. Following the reasoning of Jordan *et al.* (2001) for magnesite dissolution, the formation of straight steps parallel to the rhombic orientations ($[48\bar{1}]$ and $[\bar{4}41]$) requires that the net attachment rates at the two different kink sites along a step (cf Fig. 5.3) are similar, and faster than the rate of double kink nucleation i. Any deviation from the ideal shape reflects anisotropy in the kinks propagation rates, because kinks with a slower propagation tend to accumulate on a step segment, eventually provoking a change in step orientation. Another possibility for shape modification is an insufficiently fast kink propagation compared to kink nucleation frequency. In both cases, determining the occurrence of kinks along a step therefore permits some qualitative estimation of their reactivity.

Jordan *et al.* (2001, 2007) studied the relative reactivity of the different kink-sites during magnesite dissolution, based on measurements of unbounded steps (G_{oo}, G_{oa} and G_{aa}, see Fig. 5.3 for labelling of corresponding unbounded steps and kink sites during growth) retreat rates at various pH. The following qualitative relationship was proposed:

$$g_{oo} > g_{oa} \sim g_{ao} > g_{aa} \tag{5.5}$$

During our magnesite growth experiments in ligand-free solutions, observations of unbounded steps were scarce, and limited to G_{oo} steps. Indeed, G_{aa} steps were hardly mobile, and G_{oa} configurations were systematically overgrown by quickly advancing obtuse steps. From these observations, it can only be assessed that g_{oo} kinks are by far the most reactive, and that anisotropy with other kink orientations is high.

More informations can be gained from the analyses of hillocks shapes: in ligand-free systems at moderate saturation state, magnesite hillocks shapes depart slightly from the theoretical rhombus, with an angle between acute steps exceeding the ideal value of 103°, whereas the angle between obtuse steps is narrower (Fig. 5.4a, $\alpha_{oo} = 96 \pm 1°$, $\alpha_{aa} = 121 \pm 2°$). These modifications of step orientations become more visible as saturation state increases (Fig. 5.4b, c). Figure 5.10 (top) presents an interpretative sketch of the hillock imaged in Fig. 5.4a, and indicates that changes of step orientation can be interpreted in terms of an accumulation of g_{aa} kinks along acute steps, and g_{oa} kinks along obtuse steps. Because the occurrence of kinks is inversely correlated with their reactivity (Pina *et al.*, 2009), we propose

that $g_{ao} > g_{aa}$ and $g_{oo} > g_{oa}$. Assuming that $g_{oa} \sim g_{ao}$ leads to relationship 5.5, which also holds as the "standard" case for magnesite precipitation.

In the presence of organic ligands, G_{oo} steps were also the only visible unbounded steps, and were significantly faster than other step orientations. g_{oo} kinks can therefore still be considered as most reactive. Hillock shapes in the presence of high oxalate and citrate concentrations reveal significant modifications of kink-sites reactivity:

- Oxalate 10 mM produced rounded islands, with a general increase of step roughness. Such a morphology is indicative of an increase of all kink-sites densities.

- Figure 5.10 (bottom) presents an interpretative sketch of a representative magnesite hillock grown in the presence of 10 mM citrate, at moderate saturation state ($\Omega < 50$, see Fig. 5.5d to f for a comparison). The elongated morphology and the rounded transition from obtuse to acute steps may be explained by an accumulation of g_{oa}/g_{ao} kinks both at obtuse and acute steps. Accumulation of g_{oa} kinks at the obtuse tip of the island also explains the observed reduced α_{oo} angle in the presence of citrate (see paragraph 5.3.2). At the acute tip, α_{aa} is wider than α_{oo}, which indicates less anisotropy between g_{aa} and g_{ao} kinks than between g_{oo} and g_{oa}. Based on the relative occurrence of the different kink sites along the step edges in the presence of 10 mM citrate, the following qualitative relationship can be suggested:

$$g_{oo} > g_{aa} \geq g_{oa} \tag{5.6}$$

which suggests that g_{oa} kinks propagation rates are significantly inhibited by the presence of high citrate concentration.

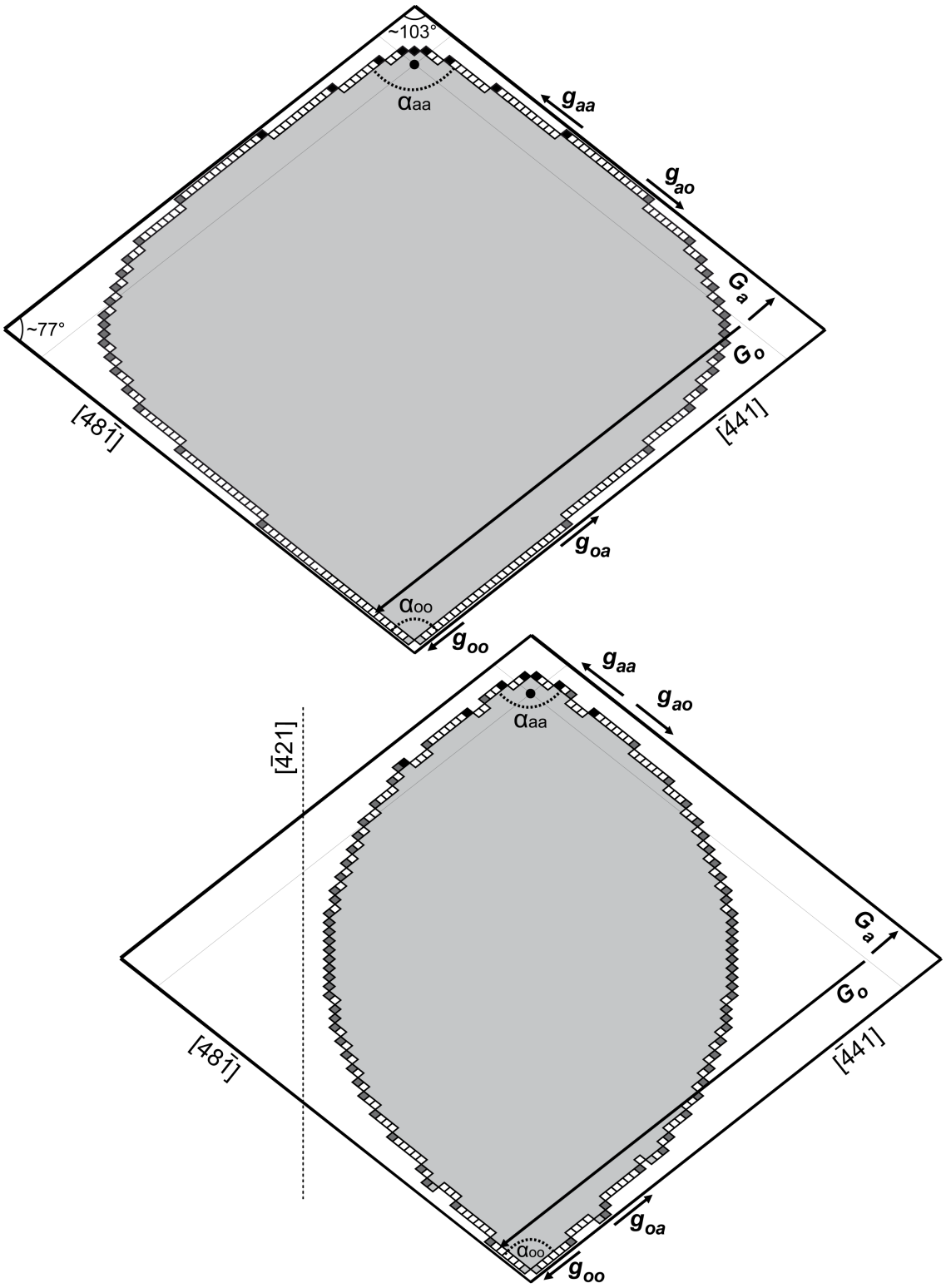

Figure 5.10 – Interpretative sketches of the shape of magnesite hillocks grown at 100°C, (*top*) in the absence of ligands at $\Omega = 40$, and (*down*) in the presence of 10 mM citrate at $30 < \Omega < 50$. The different kink-sites are color-coded: g_{oo}, black; $g_{oa} = g_{ao}$, dark grey; g_{aa}, pale grey; white = no kink-site. The black circle represents the origin of the island, and the enveloping rhombus corresponds to an ideal magnesite hillock with $g_{oo} \approx g_{oa} \approx g_{aa}$. Its size is a measure of the step velocity of acute (G_a) and obtuse (G_o) steps with respect to the origin of the island.
Top : The ligand-free hillock exhibits an accumulation of g_{aa} kinks along the straight portion of acute steps, and an accumulation of g_{oa} kinks along obtuse ones, explaining a wider α_{aa} and a narrower α_{oo} angle compared to the rhombus.
Bottom : In the presence of citrate, accumulation of g_{oa}/g_{oa} kinks along both obtuse and acute steps provokes an apparent elongation along the $[\bar{4}21]$ direction. The relative g_{aa} kinks density is uncertain (see text), as is the velocity of the acute steps compared to the ligand-free case.
Sketches inspired from Pina *et al.*, 2009. Note that the sketches largely underestimate the actual kink density.

Exp.	pH	Ligand type and conc.	Ω	$a(Mg^{2+})$	$a(CO_3^{2-})$	a(free lig.)	$\frac{a(Mg^{2+})}{a(CO_3^{2-})}$	% Mg compl.	% free ligand	G_o (nm/sec)	G_a (nm/sec)	I (layer/sec)	Mec.	R_{AFM} (mol/cm^2/s)
Mgs5	7.98	-	28.5 ± 0.1	$9.70{\cdot}10^{-5}$	$9.07{\cdot}10^{-5}$	-	1.07	-	-	0.38±0.15	n.d.	n.d.	-	-
Mgs3_4	7.99	-	32.8 ± 0.6	$1.09{\cdot}10^{-4}$	$9.32{\cdot}10^{-5}$	-	1.17	-	-	0.56±0.07	0.06±0.01	$1.43{\cdot}10^{-3}$	M	$1.39{\cdot}10^{-12}$
Mgs3_3	8.04	-	36.4 ± 0.7	$1.07{\cdot}10^{-4}$	$1.05{\cdot}10^{-4}$	-	1.03	-	-	1.10±0.10	0.06±0.02	$2.04{\cdot}10^{-3}$	M	$1.99{\cdot}10^{-12}$
Mgs3_1	8.15	-	39.8 ± 0.6	$9.38{\cdot}10^{-5}$	$1.31{\cdot}10^{-4}$	-	0.72	-	-	0.89±0.25	0.17±0.04	$1.30{\cdot}10^{-3}$	M	$1.26{\cdot}10^{-12}$
Mgs2	8.17	-	50.3 ± 0.7	$1.04{\cdot}10^{-4}$	$1.49{\cdot}10^{-4}$	-	0.70	-	-	1.32±0.35	0.13±0.05	$1.66{\cdot}10^{-3}$	Ir.	-
M38B	8.17	-	64.5 ± 0.1	$1.33{\cdot}10^{-4}$	$1.49{\cdot}10^{-4}$	-	0.89	-	-	n.d.	n.d.	$6.10{\cdot}10^{-3}$	Sp.	$5.94{\cdot}10^{-12}$
M38A	8.23	-	65.2 ± 0.1	$1.20{\cdot}10^{-4}$	$1.67{\cdot}10^{-4}$	-	0.72	-	-	n.d.	n.d.	$5.40{\cdot}10^{-3}$	Sp.	$5.26{\cdot}10^{-12}$
M38	8.14	-	99.7 ± 0.4	$2.17{\cdot}10^{-4}$	$1.42{\cdot}10^{-4}$	-	1.52	-	-	n.d.	n.d.	$1.08{\cdot}10^{-2}$	Sp.	$10.5{\cdot}10^{-12}$
Oxl3	8.12	Oxalate 1 mM	38.0 ± 1.6	$9.28{\cdot}10^{-5}$	$1.26{\cdot}10^{-4}$	$1.44{\cdot}10^{-4}$	0.73	42.8%	43.9%	0.81±0.14	0.10±0.01	$1.42{\cdot}10^{-3}$	Ir.	$1.39{\cdot}10^{-12}$
Oxl2	8.16	Oxalate 10 mM	48.1 ± 1.8	$1.03{\cdot}10^{-4}$	$1.45{\cdot}10^{-4}$	$1.18{\cdot}10^{-3}$	0.71	84.7%	41.2%	1.56±0.30	n.d.	n.d.	-	
Cit7E	8.14	Citrate 0.1 mM	57.7 ± 0.2	$1.26{\cdot}10^{-4}$	$1.41{\cdot}10^{-4}$	$8.78{\cdot}10^{-7}$	0.90	15.9%	11.8%	n.d.	n.d.	n.d.	-	
Cit7A	8.07	Citrate 0.1 mM	64.7 ± 0.2	$1.60{\cdot}10^{-4}$	$1.25{\cdot}10^{-4}$	$7.16{\cdot}10^{-7}$	1.27	13.5%	9.6%	n.d.	n.d.	$2.06{\cdot}10^{-3}$	Ir.	-
Cit7D	8.11	Citrate 0.1 mM	81.2 ± 0.2	$1.86{\cdot}10^{-4}$	$1.35{\cdot}10^{-4}$	$6.23{\cdot}10^{-7}$	1.38	11.8%	8.4%	n.d.	n.d.	n.d.	-	
Cit7	8.16	Citrate 0.1 mM	121.4 ± 1.7	$2.47{\cdot}10^{-4}$	$1.52{\cdot}10^{-4}$	$5.06{\cdot}10^{-7}$	1.62	9.6%	6.6%	n.d.	n.d.	$1.47{\cdot}10^{-2}$	Sp.	$14.3{\cdot}10^{-12}$
Cit2	8.04	Citrate 1 mM	36.6 ± 3.1	$1.09{\cdot}10^{-4}$	$1.04{\cdot}10^{-4}$	$1.02{\cdot}10^{-5}$	1.04	69.4%	13.5%	1.15±0.09	0.05±0.02	$1.04{\cdot}10^{-3}$	Sp.	$1.01{\cdot}10^{-12}$
Cit6E	8.05	Citrate 1 mM	51.8 ± 1.0	$1.33{\cdot}10^{-4}$	$1.20{\cdot}10^{-4}$	$8.08{\cdot}10^{-6}$	1.11	63.8%	11.3%	n.d.	n.d.	n.d.	-	
Cit6	8.13	Citrate 1 mM	67.1 ± 1.0	$1.43{\cdot}10^{-4}$	$1.45{\cdot}10^{-4}$	$9.37{\cdot}10^{-6}$	0.98	66.6%	10.7%	n.d.	n.d.	n.d.	-	
Cit6B	8.09	Citrate 1 mM	78.1 ± 1.0	$1.83{\cdot}10^{-4}$	$1.32{\cdot}10^{-4}$	$6.41{\cdot}10^{-6}$	1.39	58.0%	8.6%	n.d.	n.d.	n.d.	-	
Cit6C	8.20	Citrate 1 mM	79.5 ± 1.0	$1.47{\cdot}10^{-4}$	$1.67{\cdot}10^{-4}$	$7.90{\cdot}10^{-6}$	0.88	62.1%	10.4%	n.d.	n.d.	$2.31{\cdot}10^{-3}$	Sp.	$2.26{\cdot}10^{-12}$
Cit6D	8.20	Citrate 1 mM	85.6 ± 1.0	$1.55{\cdot}10^{-4}$	$1.70{\cdot}10^{-4}$	$7.42{\cdot}10^{-6}$	0.91	60.5%	9.9%	n.d.	n.d.	$2.67{\cdot}10^{-3}$	Sp.	$2.61{\cdot}10^{-12}$
Cit1_1	8.06	Citrate 10 mM	29.2 ± 3.0	$8.14{\cdot}10^{-5}$	$1.11{\cdot}10^{-4}$	$1.22{\cdot}10^{-4}$	0.73	96.0%	16.7%	1.15±0.19	n.d.	n.d.	-	
Cit1_2	8.04	Citrate 10 mM	46.9 ± 2.8	$1.38{\cdot}10^{-4}$	$1.05{\cdot}10^{-4}$	$7.99{\cdot}10^{-5}$	1.31	94.5%	10.9%	1.81±0.18	0.05	$9.87{\cdot}10^{-4}$	Sp.	$0.96{\cdot}10^{-12}$
Cit3	7.96	Citrate 10 mM	132.7 ± 5.2	$4.79{\cdot}10^{-4}$	$8.55{\cdot}10^{-5}$	$2.56{\cdot}10^{-5}$	5.61	85.5%	3.5%	5.56±0.24	n.d.	n.d.	-	
Edta7	8.01	Edta 0.01 mM	30.1	$9.56{\cdot}10^{-5}$	$9.72{\cdot}10^{-5}$	$3.95{\cdot}10^{-11}$	0.98	2.9%	< 0.02%	0.63±0.11	n.d.	n.d.	-	
Edta6	8.01	Edta 0.1 mM	30.0	$9.55{\cdot}10^{-5}$	$9.72{\cdot}10^{-5}$	$3.96{\cdot}10^{-10}$	0.98	23.2%	< 0.02%	0.63±0.22	n.d.	n.d.	-	
Edta4	7.97	Edta 10 mM	95.7 ± 12.6	$3.37{\cdot}10^{-4}$	$8.79{\cdot}10^{-5}$	$1.22{\cdot}10^{-8}$	3.83	89.5%	< 0.01%	4.88±0.71	0.58±0.05	n.d.	-	
Edta2	7.95	Edta 10 mM	120.0 ± 12.2	$4.36{\cdot}10^{-4}$	$8.51{\cdot}10^{-5}$	$9.65{\cdot}10^{-9}$	5.13	86.9%	< 0.01%	6.17±0.18	n.d.	$1.40{\cdot}10^{-2}$	Sp.	$13.6{\cdot}10^{-12}$
Edta1	7.97	Edta 10 mM	139.4 ± 13.1	$4.87{\cdot}10^{-4}$	$9.78{\cdot}10^{-5}$	$8.25{\cdot}10^{-9}$	4.98	85.6%	< 0.01%	8.90±0.64	0.82±0.25	$2.49{\cdot}10^{-2}$	Sp.	$24.3{\cdot}10^{-12}$
Edta3	7.95	Edta 10 mM	164.2 ± 12.0	$6.01{\cdot}10^{-4}$	$8.44{\cdot}10^{-5}$	$6.95{\cdot}10^{-9}$	7.12	82.8%	< 0.01%	9.13±1.14	1.04±0.21	$2.18{\cdot}10^{-2}$	Sp.	$21.2{\cdot}10^{-12}$

Table 5.2 – Chemical speciation, measured step velocities and step generation frequencies for HAFM experiments performed in this study. All experiments were performed at 100°C. Reported chemical activities were calculated using PHREEQC (Parkhurst & Appelo, 1999), with its `llnl.dat` database and additional thermodynamic data to account for ligand-cation chelation (see Section 5.2.3). The "free ligand" chemical activity is given for the dominating ligand species in the investigated pH conditions: Oxalate^{2-}, Citrate^{3-}, and HEDTA^{3-}. G_o, G_a and I designate the obtuse and acute step velocity, and the step generation frequency, respectively. The "Mec." column indicate the type of step generation mechanism: M, regular generation at macrosteps; Ir., irregular generation at macrosteps; Sp., spiral growth. The other observations correspond to impurity-aided 2D nucleation, or to cleavage step propagation. R_{AFM} is the macroscopic growth rate calculated according to equation (5.1). Growth rates calculated from irregular step generating mechanisms (Ir.) were considered not representative of the bulk crystal growth, and were not reported here, nor in the corresponding graphs. The uncertainty on I is estimated to be $\sim 5\%$ for spiral growth, and more than 15% in the case of irregular step generation.

5.4 Discussion

5.4.1 Influence of organic ligands on magnesite obtuse step velocity at 100°C: consequence of kink-limited kinetics?

High concentrations of oxalate and citrate provoke pronounced morphological changes of magnesite hillocks (Fig. 5.4, 5.5), but hardly affect obtuse step velocity (Fig. 5.8). Here, we will compare our observations to the classical models of crystal-impurity interaction.

Four main models have been developed to interpret the influence of impurities on crystal growth: the "impurity-incorporation" model, the "surfactant" model, the "step-pinning" (or "Cabrera-Vermileya") model, and the "kink-blocking" model. A short review of their underlying principles can be found in De Yoreo & Vekilov, 2003.

Impurity-incorporation model

A few experimental studies have shown that organic ligands, and in particular citrate, may be co-precipitated during calcite precipitation at ambient temperature (Phillips *et al.*, 2005; Lee & Reeder, 2006). The impurity-incorporation model precisely states that impurities may be incorporated into the growing crystal structure, and alter crystal growth by modifying its solubility.

However, citrate and oxalate are much bigger than the carbonate molecule, so their incorporation into magnesite crystal structure would result in a significant increase of the step height, which has never been observed along the 2.7 Å high monomolecular magnesite steps. Moreover, impurity incorporation is generally associated with an increase of crystal solubility, and therefore provokes a decrease of supersaturation (e.g Davis *et al.*, 2000)[1]. The resulting step velocity is lower than for the corresponding impurity-free step, which was not observed during magnesite growth in the presence of organic molecules.

Therefore, although we cannot rule out that some of the adsorbed organic material may be buried into the precipitating mineral, the impurity-incorporation model is unlikely to explain the observed effect of oxalate and citrate on magnesite growth.

Surfactant model

Within the surfactant model, a step orientation change is due to the adsorption of a "surface-active" molecule, which modifies the orientation dependence of step edge free energy. A step in the presence of a surfactant therefore expresses its new minimum energy shape, which is not necessarily associated with a velocity change (De Yoreo & Vekilov, 2003).

However, the surfactant model is a purely thermodynamic model, which implies that shape modifications should be expressed right from the birth of magnesite islands (e.g Orme *et al.*, 2001). As exposed in Section 5.3.2, in the presence of 1 to 10 mM citrate the shape of magnesite hillocks tends to evolve as they spread, with a fairly rhombic shape at small size, while their steady-state elongated shape is reached when their size exceeds a few µm. These adjustments call for a kinetic, rather than thermodynamic, origin for the observed shapes (Higgins *et al.*, 2002). The surfactant model is therefore unlikely to describe to magnesite growth in the presence of small carboxylic ligands.

[1] A solubility **decrease** was suggested in a few studies on calcite growth (e.g Wasylenki *et al.*, 2005), but only with metallic impurities, at much lower impurity concentrations.

Step-pinning model

The step-pinning model, first proposed by Cabrera & Vermilyea (1958), is based on the assumption that individual steps behave according to the Gibbs-Thomson effect, which states that step excess Gibbs free energy with respect to the solution decreases as step curvature increases. A higher curvature (i.e a smaller curvature radius) therefore results in a lower thermodynamic stability. The Gibbs-Thomson law (GTL) predicts the existence of critical curvature radius r_c for which the step stops because it is at equilibrium with the surrounding solution (Burton *et al.*, 1951):

$$r_c = \frac{bc\,\gamma}{k_B T\, ln\Omega} \tag{5.7}$$

where b is the size of a crystallographic unit along the step, c is the size of the same unit normal to the step (between rows), and γ is the step edge free energy.

Impurities adsorbing to step edges may locally hinder step advancement, causing an increase of step curvature as the unimpeded step segments continue to advance. If the average spacing between two adsorbed impurities is less than $2r_c$, the step is thermodynamically blocked (Fig. 5.11). Impurity adsorption and step-pinning can be specific of certain step orientation, resulting in an overall modified crystal shape (De Yoreo & Vekilov, 2003).

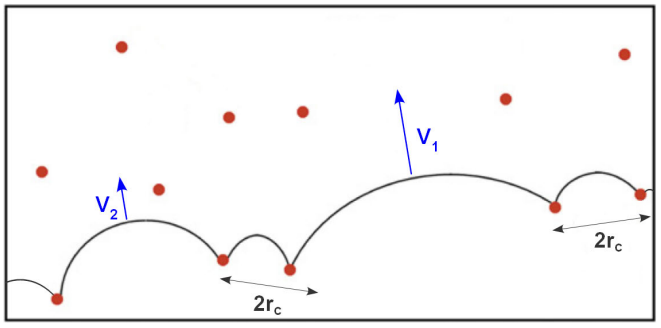

Figure 5.11 – Illustration of the step-pinning model (modified from Weaver *et al.*, 2007). Red dots represent impurities. If the distance between two adsorbed impurities in lower than $2r_c$, the step segment in-between can only advance until its curvature radius reaches r_c. If impurity spacing is larger, the step segments advance at a velocity depending on their curvature ($V_1 > V_2$).

It results from equation (5.7) that the critical radius is inversely correlated to $ln(\Omega)$. Therefore, within the step-pinning model, the step velocity may be unaffected by a given impurity concentration, provided that supersaturation is high enough. In addition, r_c is inversely correlated with temperature (eq. 5.7). Due to the retrograde solubility of magnesite, a lower temperature coincides with a lower supersaturation, for a given solution composition. Assuming the step edge free energy increases with decreasing temperature (Zandvliet *et al.*, 2001), the critical radius is expected to be larger at 80°C than at 100°C, which should result in more step-pinning at 80°C. Hillock observation indeed reveals that steps are highly serrated in the presence of 1 mM oxalate at 80°C (Fig. 5.4e), whereas pinning is much less obvious at 100°C (Fig. 5.4d). Such observations suggest the step-pinning model could indeed apply to magnesite growth.

However, the assumption that steps behave in accordance with the Gibbs-Thomson Law is applicable only if there always is a high density of kinks along step edges, which allow the step segment to quickly equilibrate with its environment (Chernov *et al.*, 2005). This

prerequisite is at the basis of the classical BCF formalism (Burton *et al.*, 1951), which assumes thermal fluctuations always maintain high kink densities.

Several observations prompt us to challenge this "rough step" assumption in the case of magnesite:

- The *high polygonization* of magnesite hillocks (or etch pits) can only be obtained if the rate of kink-nucleation is much lower that the rate of kink annihilation through coalescence of two propagating (or retreating) kinks. As a result, the kink density remains low ("smooth step"), and the step velocity is mostly limited by the rate of kink nucleation, as is observed for calcite (Liang, 1996).
- The low-kink density regime has been shown to result in a *super-linear dependence of step velocity on saturation state*, at low saturation state, as observed in this study for magnesite (section 5.3.3), or for calcite by Teng *et al.* (1999). Indeed, the rate of kink nucleation, which controls step advancement in a low-kink regime, increases non linearly with solution supersaturation (Voronkov, 1968, 1970; Zhang & Nancollas, 1990, 1998). When the maximum kink density along a step is reached, the step velocity can only increase linearly with supersaturation (Voronkov, 1970; De Yoreo & Vekilov, 2003; Vekilov, 2007).
- At the *intersection of straight steps*, rough steps of much higher velocity were observed to form during magnesite growth (this study) and dissolution (Jordan *et al.*, 2001, 2007). The step intersection indeed provides an unlimited source of kinks, and step velocity strongly increases because it is then not limited by a low kink density.

Similar observations were made for a number of sparingly soluble crystals, such as calcite (Teng *et al.*, 1999), barite (Higgins *et al.*, 2000), brushite ($CaHPO_4{\cdot}2\,H_2O$, Chernov, 2004), monoclinic lysozyme (Rashkovich *et al.*, 2002), or KAP (Rashkovich *et al.*, 2003). In these cases, step advancement and crystal growth may not be ruled according to thermodynamical equilibrium, but rather according to non-equilibrium kinetics (e.g Zhang & Nancollas, 1998; Chernov, 2004; De Yoreo *et al.*, 2009 and references therein).

Indeed, the step-pinning model was shown to adequately describe the influence of impurities on the growth of crystals characterized by rough steps and high kink density, such as calcium oxalate monohydrate (Weaver *et al.*, 2007), but failed at explaining the influence of Sr^{2+} or aspartic acid polymers on calcite (Wasylenki *et al.*, 2005 and Elhadj *et al.*, 2005, respectively). Similarly, magnesite step velocity is clearly limited by a low kink density, so its growth kinetics as well as the influence of impurities may be better described by a kinetic approach, than by the step-pinning model.

Kink-blocking model

The **kink-blocking model** precisely follows a kinetic approach. It assumes the blocking of kink propagation due to adsorption of impurities to kink-sites. In the case of rough steps, whose advancement is limited by kink propagation rate, the kink-blocking results in a reduced kinetic coefficient (De Yoreo & Vekilov, 2003 and references therein).

In the case of smooth steps however, the lowering of kink propagation rate may not affect the overall velocity. In a recent study, De Yoreo *et al.* (2009) investigated the consequences of the kink-blocking mechanism on the step speed and morphology of a low-kink density crystal, via kinetic Monte-Carlo modelling. The authors showed that in this model, step

growth can be stopped only via the independent attachment of two impurities on both kink types along a step, therefore blocking the kink propagation in both directions. It results that the step can grow at full speed as long as one kink orientation is free of impurity and able to propagate normally. The amount of impurity necessary to initiate crystal growth inhibition may be higher than in the step-pinning model, but if the impurity concentration is further increased, the step quickly drawns into a "dead zone".

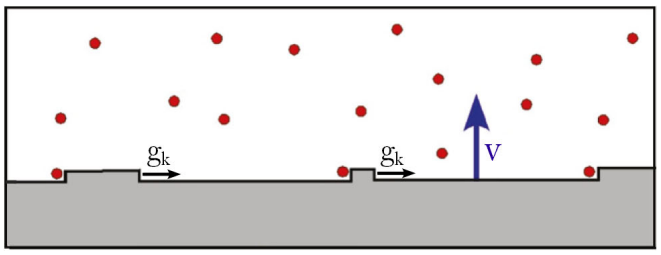

Figure 5.12 – Illustration of the kink-blocking model in the case of smooth steps (modified from De Yoreo *et al.*, 2009). Kinks propagate at the g_k rate, unless they are blocked by an impurity. The step may advance at its impurity-free velocity v as long as one kink orientation is free of impurity. This would ultimately result in a change of step orientation.

The kink-blocking mechanism provides a convincing framework to interpret the evolution of magnesite growth in the presence of organic ligands: first, the step velocity may not be reduced by adsorbed ligands, provided that supersaturation is high enough/surface impurity density is low enough. Second, the model does not predict the apparition of pinned morphologies, but rather an increase of roughness due to blocked kink sites, such as what has been observed with oxalate and citrate. Furthermore, if impurity adsorption is a kink-specific process, step orientation would change as a result of a higher occurrence of the temporarily blocked kink-sites over the unblocked ones, still free to propagate. This has indeed been observed in the presence of citrate (Fig. 5.10).

Only a more thorough study of step velocity as a function of impurity concentration would allow to fully discriminate between the step-pinning model and the kink-blocking model (De Yoreo *et al.*, 2009). This would however require to work at lower saturation state, which is difficult due to the slow magnesite growth and the limited HAFM resolution, or at higher ligand concentrations, which would introduce more uncertainty in the speciation calculation.

Here, we should discuss the possibility that citrate may slightly increase obtuse step velocity. In its steady-state regime (linear increase of the step speed as a function of saturation), the step velocity may be expressed as a function of kink density ρ_k and kink propagation rate g_k (Frank, 1974):

$$v = b\rho_k g_k \tag{5.8}$$

where b stands for the kink depth. Under the classical kink Creation-Propagation-Collision (CPC) model, the kink density is a function of the average kink propagation rate g_k and of the double-kink nucleation rate i_0 (Frank, 1974; Zhang & Nancollas, 1990; Liang, 1996):

$$\rho_k = \sqrt{\frac{2i_0}{g_k}} \tag{5.9}$$

It follows that:

$$v = b\sqrt{2i_0 g_k} \tag{5.10}$$

Within the kink-blocking model, kink propagation is hindered by impurity adsorption. Therefore, the only possibility for v to increase is an increase of the double-kink nucleation rate i_0. Although the processes potentially leading to such an increase are unclear, we may hypothesize that they are related to modifications of the electrostatic field due to citrate adsorption, and/or to ligand-facilitated Mg^{2+} desolvation (e.g Elhadj *et al.*, 2006), or co-adsorption of Mg on adsorbed citrate molecules.

5.4.2 Site-specific adsorption of oxalate and citrate

Oxalate and citrate provoke different shape alterations of magnesite hillocks: in the presence of citrate, hillocks are elongated parallel to the $[\bar{4}21]$ direction, which reveals an increased population of g_{oa}/g_{ao} kinks. This suggests that the reactivity of these kink-sites is specifically inhibited by the ligand. In the presence of oxalate, highly rounded morphologies suggest that inhibition of the kink-sites reactivity occurs more homogeneously.

Similar observations have been made at ambient temperature with simple organic molecules on a variety of (bio)minerals, and particularly calcite, which offers a close chemical and structural match to magnesite. The maleate anion ($^{-}OOC-CH=CH-COO^{-}$) for instance produces highly rounded calcite hillocks at concentrations of 3 mM (Dobson *et al.*, 2006), whereas aspartate ($^{-}OOC-CH_2-CH(NH_2)-COO^{-}$) only provokes a rounding of acute edges (Orme *et al.*, 2001; Elhadj *et al.*, 2005). During calcite dissolution, high concentrations (100 mM) of succinate ($^{-}OOC-CH_2-CH_2-COO^{-}$) or malonate ($^{-}OOC-CH_2-COO^{-}$) provoke the formation of hexagonal pits, with a clear expression of the $[\bar{4}21]$ step direction (Teng *et al.*, 2006; Hong *et al.*, 1997; Wu *et al.*, 2011). Oxalate on the contrary was reported not to have any effect on etch pits morphology (Wu *et al.*, 2011), although it only lacks one aliphatic carbon compared to malonate.

Therefore, small organic molecules relatively close in terms of size and chemical functionality have dramatically different effects on the shapes of hillocks or etch pits. These observations were interpreted based on the long-standing concept of geometrical, stereochemical and electrostatic match between the ligand and the surface structure (e.g Mann *et al.*, 1993; Teng & Dove, 1997; Qiu *et al.*, 2004). Namely, close correspondence between cation spacing at the mineral surface, and carboxylic groups spacing in the carboxylate chain plays a crucial role in the adsorption strength (Wu *et al.*, 2011), and interactions between additional functional groups and the crystal surface determine the surface sites were the organic molecules are best accommodated. The organics inhibit growth (or dissolution) where they preferentially adsorb, and may in addition stabilize the expression of new crystallographic orientations.

In the oxalate molecule, the distance between the carbons of the two carboxylic groups is 2.6 Å (Geffroy *et al.*, 1999; Figure 5.13), which is much less than the minimal distance between Mg ions on magnesite (104) surface ($\sim$ 4 Å). Therefore, it is likely that oxalate is able to bind to only one surface magnesium at a time, forming a bidentate complex (i.e with both carboxylates bounded to the same surface magnesium). Citrate, on the contrary, is a non-planar molecule (Glusker, 1980), with 3.2 Å between adjacent carboxylic groups, and 6.88 Å between the terminal carboxylates (Hu *et al.*, 2010; Fig. 5.13). Therefore, citrate is likely able to bridge independently two surface magnesium, which has been shown to be an important factor in the growth modifying influence of carboxylates (Wu *et al.*, 2011). In addition, its geometry allows for a much greater variety of conformations compared to oxalate when it

Figure 5.13 – Structure of oxalate (left) and citrate (right), with black spheres representing carbons, red spheres, oxygen, and white spheres, hydrogen. Arrows indicate the distances between carboxylic groups (in Å).

adsorbs to a mineral surface (see for example De Leeuw & Rabone, 2007), and its carboxyl and hydroxyl groups provide additional possibilities for stabilizing bonds in a non-planar environment. The hydroxyl group in particular, has been shown to play an important role in the preferential binding of citrate to calcium oxalate monohydrate $[\bar{1}01]$ face acute steps (Qiu *et al.*, 2005).

Therefore, we hypothesize that citrate complex geometry and chemical functionality render it highly specific of particular sites on the magnesite $[104]$ surface. In particular, it preferentially binds to g_{oa}/g_{ao} kinks during magnesite growth, thus blocking their propagation. This explains their higher occurrence, and an apparent elongation of hillocks along $[\bar{4}21]$. Oxalate is likely less influenced by the structural environment of surface magnesium, and may therefore bind rather indistinctly to the different kink sites, which would explain its rather homogeneous influence on surface shape.

Jordan *et al.* (2007) investigated surface processes associated with magnesite dissolution at far from equilibrium conditions in the presence of various organic ligands, in similar conditions compared to the present study (100°C, pH $\sim$ 8, 0.01M NaHCO3). Their observations are quite different from ours: in the presence of 10 mM citrate, the authors reported an accumulation of g_{oa} kinks at the edges of etch pits, and observed an increase of g_{aa} kinks reactivity. On the contrary, oxalate in the same conditions did not appreciably affect the pits shapes, but increased g_{oa} kinks reactivity.

The observed overall increase of dissolution rate suggests a ligand-promoted reaction mechanism (LPRM): ligands adsorb on surface metal cations as inner-sphere mononuclear complexes and labilize their bonds to the mineral, therefore facilitating their detachment from the mineral surface together with carbonate (e.g Ganor *et al.*, 2009 and references therein).

If dissolution enhancement indeed occurs via LPRM, one may expect that during magnesite growth the ligand would increase the rate of kink detachment where it binds, therefore resulting in a lower overall propagation rate of the same kink-sites whose retreat rate was enhanced during dissolution. This is not what we observed: with oxalate, all kink sites exhibit a lowered reactivity, and not only the g_{oa} kinks; with citrate, g_{oa} kinks were most inhibited during growth, whereas the effect on g_{aa} kinks is less clear. In addition, the LPRM mechanism involves the formation of mononuclear surface complexes, whereas

kink-blocking results from the formation of bi- or polynuclear complexes (Ganor *et al.*, 2009).

This apparent discrepancy suggests that oxalate and citrate may exert a different role depending on how they bind to kinks along magnesite step edges:

- Where the ligands bind as mononuclear complexes, kink retreat rates are enhanced through LPRM (i.e g_{aa} kinks for citrate, and g_{oa} kinks for oxalate). This effect is visible during dissolution, but may not be visible during growth at relatively high supersaturation ($\Omega > 20$), where the reversed rate is negligible.
- Where ligand binds in a favorable conformation that allows to bridge several metal centers, kink reactivity is hindered both for dissolution and growth. This is the case for g_{oa} kinks with citrate, which showed an increased occurrence both in dissolution and growth experiment.

Although rough, this analysis may help to reconcile growth and dissolution observations. In addition, we should not forget that our growth solutions have high Mg concentrations compared to the dissolution experiments of Jordan *et al.* (2007), so the proportion of ligand complexed with Mg^{2+} in our experiments is much higher (Table 5.2), and the magnesite surface chemistry may as well be different. Both factors may influence adsorption of the ligand at the mineral surface.

The use of AFM functionalized tips could be useful to better resolve the preferential interactions between organics and different sites at the magnesite surface (e.g Sheng *et al.*, 2005; Friddle *et al.*, 2011). In parallel, molecular dynamics simulations would help to fully unveil the factors controlling citrate and oxalate binding to magnesite steps (e.g Orme *et al.*, 2001; Pina *et al.*, 2004; Qiu *et al.*, 2005). In particular, in addition to stereochemical match, the adsorbed water was suggested to play a significant role in the preferred binding sites of aspartate polymers on calcite (Elhadj *et al.*, 2005). Given the highly hydrated state of magnesite surface (Freeman *et al.*, 2009), such a role could be even more important for magnesite.

5.4.3 How do organic ligands slow down magnesite growth?

As shown by HAFM experiments (section 5.3.1) and MFR experiments (Chapter 4), citrate and oxalate decrease magnesite bulk growth rates, at concentrations equal or higher than 0.2 mM for citrate, and equal or higher than 10 mM for oxalate. We have shown that obtuse step velocities are not decreased in the presence of any ligand, and can therefore not explain the overall growth inhibition. The source of the inhibition therefore lies in the processes controlling spiral growth, which in accordance with Saldi *et al.* (2010) is the dominant magnesite growth mechanism in the investigated conditions.

Within the spiral growth model, the growth rate of a crystal face normal to itself can be expressed as (Burton *et al.*, 1951):

$$R_{face} = h\frac{v_{step}}{\lambda} \tag{5.11}$$

where h is the height of a step, v_{step} is the velocity of a family of parallel steps and λ is the width separating them. It should be noted that in the case of magnesite, the face growth rate is the same for each of the faces of the typical rhomboedra, and R_{face} is linked to the bulk growth rate R (eq. 5.1) through $R = \frac{R_{face}}{V_M}$.

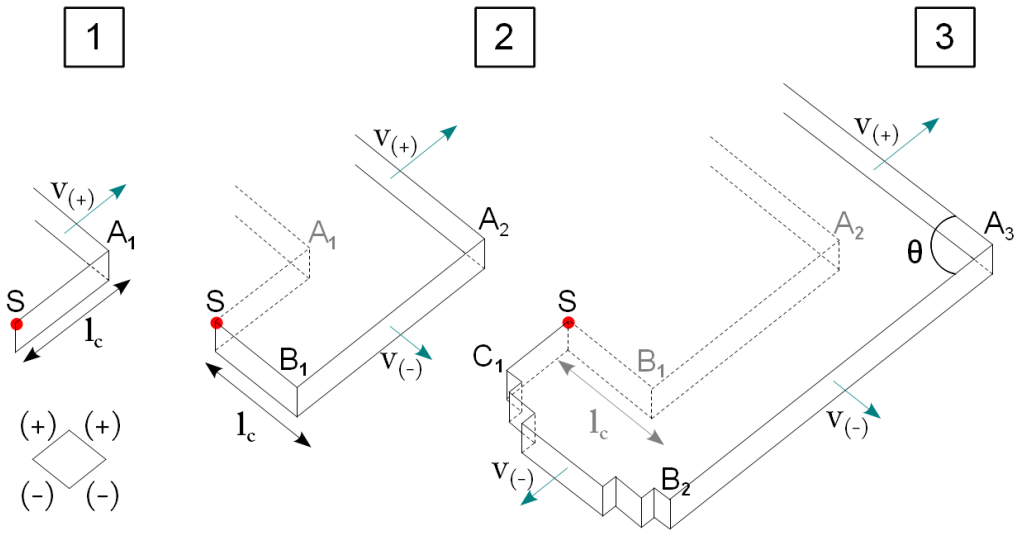

Figure 5.14 – Illustration of the spiral growth process on magnesite [104] surface. The rhombus in the lower left corner represents an ideal magnesite rhombus, and gives the orientation of the sketch. S is the source dislocation giving birth to the spiral (immobile).
In (1), advancement of the obtuse step gives birth to the acute segment SA_1, which cannot advance until it has reached the critical length l_c. When its length exceeds l_c, the acute step segment starts propagating normal to itself at the velocity $v_{(-)}$, and gives birth to the next acute step segment, SB_1 (2). In (3), the SB_1 segment exceeded its critical length, and started to propagate, giving birth to a new obtuse segment SC_1. Kinks have been represented only on the B_2C_1 acute step segment. If kink propagation is hindered by ligand adsorption spiral growth propagation may be inhibited (see text).

Figure 5.14 presents an illustration of the growth of a polygonized spiral. Each of the step segments need to advance a critical length l_c before it can start propagating normal to itself (Chernov, 1961). In the case of an anisotropic spiral, as for magnesite, l_c may be different for the two non-equivalent crystallographic directions, obtuse (+) and acute (−). The terrace width can be expressed as a function of the critical length and the steps velocities, such that for acute steps (Teng *et al.*, 1998):

$$\lambda_{(-)} = 2\,G\,\left[1 + \frac{v_{(-)}}{v_{(+)}}\right]\frac{\langle l_c\rangle}{\sin\theta} \tag{5.12}$$

where G is a constant called "Gibbs factor", $\langle l_c\rangle$ is the mean critical length over the different crystallographic directions, and θ is the angle between two adjacent obtuse and acute step segments (= 77° for magnesite, see Fig. 5.14), and $v_{(-)}$ and $v_{(+)}$ are the acute and obtuse step velocity, respectively.

The bulk growth rate can be expressed as a function of the acute steps parameters:

$$R = \frac{h\cdot v_{(-)}}{V_M\cdot\lambda_{(-)}} = \frac{h\cdot v_{(-)}}{V_M\frac{2\,G}{\sin\theta}\left[1+\frac{v_{(-)}}{v_{(+)}}\right]\langle l_c\rangle} \tag{5.13}$$

It results that there are two ways by which the macroscopic growth rate may be decreased either via a decrease in the acute step velocity $v_{(-)}$, or via an increase in the mean critical length $\langle l_c\rangle$, or both. More precisely, citrate decreases the growth rate by a factor of 3 at a concentration of 1mM. An analysis of eq. 5.13 (Annex 5.5), assuming that acute step velocity

is about one order of magnitude lower than obtuse's in the investigated conditions (Saldi *et al.*, 2009), indicates that in order to explain the influence of citrate, either $\langle l_c \rangle$ is increased by a factor of 3, or $v_{(-)}$ is decreased by a factor of 3.2.

Decrease of the acute step velocity ?

With the current resolution of the HAFM, and given the very low velocity of acute steps, a decrease of their velocity, even by a factor of more than 3, would not be easily measurable. We may however wonder why acute steps may be inhibited, whereas obtuse ones aren't.

Citrate inhibits preferentially g_{ao} kinks during magnesite growth in the investigated conditions. Although its interactions with g_{aa} kinks are less clear, it cannot be excluded that these kinks also are inhibited by citrate to a certain extent. The observation that citrate accelerates g_{aa} kinks retreat rates during magnesite dissolution (Jordan *et al.*, 2007) clearly is a sign that citrate interaction with acute steps is not limited to g_{ao} kinks. Interactions with both kink-sites would certainly lead to an effective reduction of acute step velocity (De Yoreo *et al.*, 2009).

In addition, acute steps have a much lower reactivity compared to obtuse ones. This could come from a lower kink density (caused by a lower kink nucleation rate), and/or from a lower reactivity of the existing kinks. Indeed, on the contrary to obtuse steps, intersections of acute steps, which provide a source of kinks, did not visibly produce any increase of reactivity (G_{aa} steps never developed at such intersections in our experiments). As a result of this lower kink density and/or lower reactivity, the adsorption of a ligand on acute steps could have more pronounced inhibiting effect compared to the same adsorbed amount at obtuse steps. This provides an explanation as to why **oxalate** may inhibit acute step propagation, although its interactions with the step edges appeared to be less specific of a given kink-site.

Finally, precise studies of calcite acute step reactivity as a function of ionic activity ratio (Larsen *et al.*, 2010), or in the presence of various background salts (Ruiz-Agudo *et al.*, 2011), led to the conclusion that growth at acute steps is limited by the rate of carbonate attachment to the kink sites. If the same applies for magnesite, then ligand binding to acute steps could efficiently lower kink reactivity by lowering carbonate anions attachment frequencies for electrostatic reasons.

Given the high anisotropy of magnesite spirals, affecting acute step reactivity always seems a good way to affect the bulk magnesite kinetics (Jordan *et al.*, 2007). Preferential interaction of citrate with acute steps could explain its higher efficiency at inhibiting magnesite growth compared to oxalate.

Increase of the critical length ?

Decrease of the step generation frequency by spiral growth may alternatively, or additionally, be caused by an increase in the average critical length $\langle l_c \rangle$.

It should be noted here that, within the classical BCF formalism (Burton *et al.*, 1951), the critical length l_c is a thermodynamic concept, and is expressed by the Gibbs-Thomson Law (GTL, eq. 5.7):

$$l_c = 2r_c = \frac{2bc\,\gamma}{k_B T\, ln\Omega}$$

However, the GTL has been shown not to describe adequately the development of polygonized spirals on low-kink density crystals such as calcite (Teng *et al.*, 1999), monoclinic

lysozyme (Rashkovich *et al.*, 2002), KAP (Rashkovich *et al.*, 2003), or barite (Higgins *et al.*, 2000). In this case, (Chernov *et al.*, 2005) suggested the critical length could have a kinetic origin (rather than thermodynamic), and developed a formalism to describe step dynamics and spiral growth development under the assumption of a kinetically limited kink density. The "dynamic" critical length could then be expressed as:

$$l_c^* = \frac{2bc\,\gamma_d}{k_B T\, ln\Omega} \tag{5.14}$$

γ_d is a "dynamic step free energy", which differs from γ by a "dynamic step entropy" term depending on the kink density on the step segment. γ_d is an increasing function of the angle of the local step orientation with respect to the close-packed lattice direction (defined by the crystallography of the crystal). Therefore, if the step orientation increasingly differs from its theoretical orientation, as a result for instance of a modified kink reactivity, l_c^* would increase for the given step segment. An overall increase of the average dynamic critical length for the 4 step segments, $\langle l_c^* \rangle$, would result in lower spiral growth rate (eq. 5.13).

Probing the size of the critical lengths is challenging (Higgins & Hu, 2006), and confirming this hypothesis may not be feasible during magnesite growth with the current HAFM resolution. The description nevertheless suggests that even if kink propagation rate on a step segment is reduced in only one direction, and the corresponding step velocity is not decreased, an inhibition of the spiral growth rate is possible if changes in step orientation lead to an increase of the mean critical length.

5.4.4 Interplay between aqueous complexation and surface adsorption

The fact that EDTA has little, if any, influence on magnesite growth at the investigated conditions deserves some attention.

Indeed, EDTA is known to adsorb to surface magnesium of brucite in alkaline conditions much more strongly than oxalate and citrate (Pokrovsky *et al.*, 2005). In addition, EDTA was shown to significantly enhance magnesite dissolution rate at 100°C and pH 8, which was related to an increase of pit nucleation frequency on the [104] surface (Jordan *et al.*, 2007). Therefore, it can be assessed that EDTA has the ability to bind to the magnesite surface.

According to Jones *et al.* (2007), EDTA always adsorbs to the barite surface as the monoprotonated species $HEDTA^{3-}$, which also dominates the speciation of the uncomplexed EDTA in our solutions. However, our speciation calculation indicate that the vast majority of EDTA is complexed to Mg^{2+}, giving activities of $HEDTA^{3-}$ of the order of only 10^{-8} in solution with 10 mM EDTA (Table 5.2). Taking the Langmuir adsorption constant of Pokrovsky *et al.* (2005) for EDTA on brucite at 25°C ($K_L = 10^{4.9} \pm 10^3$), and assuming it applies for magnesite at 100°C, we obtain that less than 0.003% of the surface magnesium are bounded to EDTA in our experiments with the highest EDTA concentration. Because metal-EDTA complexes are generally not adsorbed on mineral surfaces (Davis & Kent, 1990, p.204, and references therein), this high complexation in solution leads to the absence of effect on mineral growth.

Bulk magnesite growth rates as measured with mixed-flow reactors at 120°C indicate a limited growth inhibition in the presence of 1mM EDTA (Chapter 4), which is not observed at 100°C with 10mM EDTA. In both series of experiments, EDTA speciation is largely dominated by $MgEDTA^{2-}$ complexes, so the observed differences cannot be related to the amount of free

EDTA. However, the experiments were performed at lower saturation state at 120°C. We may hypothesize that at lower saturation state, magnesite growth is more sensible to ligand adsorption, due to a lower kink density, and/or a lower kink reactivity. As saturation state increases, the crystal "recovers" from this growth-impeded regime (De Yoreo & Vekilov, 2003; De Yoreo *et al.*, 2009).

Overall, it should be noted that oxalate and citrate are also extensively bonded to Mg^{2+} in our experimental solutions (Table 5.2), which may in part explain their relatively small effect on magnesite growth.

5.5 Conclusion

This is the first AFM study of the influence of organic ligands on mineral growth performed at hydrothermal conditions. We have imaged and measured the growth processes occurring on magnesite $[104]$ surface at 100°C, in the presence of various concentrations of three organic ligands: oxalate, citrate and EDTA, while varying saturation state.

The results indicate that citrate decreases magnesite bulk growth rates by a factor of roughly 3 at concentrations of 1 mM, in accordance with our results acquired with classical mixed-flow reactors. The shape of growth hillocks is strongly modified both by oxalate and citrate, but in different manners: highly rounded islands are observed in the presence of oxalate, while citrate produces islands elongated parallel to the $[\bar{4}21]$ direction. These observations reveal that both ligands adsorb to the magnesite $[104]$ surface, and interact with the growth process. However, due to their different structures, citrate preferentially binds to g_{oa}/g_{oa} kinks and inhibits their progression, while oxalate adsorption is less specific of the kink orientation. On the contrary, EDTA doesn't have any influence on magnesite growth, which is probably due to the fact it is highly complexed with Mg^{2+} in aqueous solution, and only a small amount of free EDTA is available for surface complexation.

Although hillock shapes are significantly modified, surprisingly, obtuse step velocities are not decreased by the presence of oxalate, citrate or EDTA at high concentrations. This observation may be understood within the framework of the De Yoreo *et al.* (2009) model of kink-blocking for low-kink density steps.

Overall, inhibition of bulk magnesite precipitation kinetics by citrate and oxalate likely stems from a reduced rate of step generation by spiral growth, which may proceed either from a decreased velocity of the acute steps, or from larger step critical lengths. The higher inhibition efficiency of citrate compared to oxalate could be related to a preferred interaction of this ligand with acute steps.

Acknowledgments

The financial support of Centre de Coopération Universitaire Franco-Bavarois (CCUFB)/Bayerisch-Französisches Hochschulzentrum (BFHZ) for this study is gratefully acknowledged. QG wishes to thank Université Paris-Est for a mobility grant during his stay at LMU. The authors are grateful to Carole Causserand, who provided technical assistance for chemical analysis, and Giuseppe D. Saldi and Casjen Merkel for insightful discussions throughout the course of this study.

Appendix: How to explain a decrease of step generation rate by spiral growth? An analytical description.

The bulk growth rate of a crystal whose growth is controlled by an isotropic spiral growth is equal to (Burton *et al.*, 1951):

$$R = \frac{h \cdot v_{step}}{V_M \cdot \lambda} \tag{5.15}$$

where h is the height of a step, v_{step} is the velocity of a family of parallel steps and λ is the width separating them.

For the anisotropic spiral of magnesite, step velocities and terrace widths differ for the two step directions: obtuse $(+)$, and acute $(-)$. The expressions for the two terrace widths are (as recalled by De Yoreo & Vekilov, 2003):

$$\lambda_{(+)} = 2G \left[1 + \frac{v_{(+)}}{v_{(-)}}\right] \frac{\langle l_c \rangle}{\sin\theta} \tag{5.16}$$

$$\lambda_{(-)} = 2G \left[1 + \frac{v_{(-)}}{v_{(+)}}\right] \frac{\langle l_c \rangle}{\sin\theta} \tag{5.17}$$

where G is the "Gibbs factor", $\langle l_c \rangle$ is the mean critical length over the different crystallographic directions, θ is the angle between two adjacent obtuse and acute step segments, and $v_{(+)}$ and $v_{(-)}$ are the step velocity of obtuse and acute steps, respectively (see Fig. 5.14).

The bulk growth rate can therefore be expressed as a function of the acute steps velocity and terrace width:

$$R = \frac{h \cdot v_{(-)}}{V_M \cdot 2G \left[1 + \frac{v_{(-)}}{v_{(+)}}\right] \frac{\langle l_c \rangle}{\sin\theta}} \tag{5.18}$$

As outlined above, there are two ways by which the bulk growth rate may be decreased: either via an increase in the mean critical length $\langle l_c \rangle$, or via a decrease of the acute step velocity $v_{(-)}$.

Let's consider R_i the initial growth rate, and R_f a decreased growth rate resulting from inhibition by an additive. The i and f subscripts will define from now on the grandeurs before inhibition and after, respectively.

The bulk growth rate is inversely proportional to $\langle l_c \rangle$, so if growth inhibition was due only to the critical length, the decrease in growth rate from R_i to R_f could be explained by a corresponding increase of $\langle l_c \rangle$ by a factor $\frac{R_i}{R_f}$:

$$\frac{\langle l_c \rangle_f}{\langle l_c \rangle_i} = \frac{R_i}{R_f}$$

A decrease by a factor of 3 of the bulk growth rate as observed with 1mM citrate may therefore be explained by an increase by a factor of 3 of the mean critical length.

Let's now consider the possibility that the growth reduction is due to a reduction of the acute step velocity only. The initial acute step velocity is termed $v_{(-)i}$, and the inhibited acute

step velocity is termed $v_{(-)f}$. The obtuse step velocity is unchanged. Then:

$$\begin{aligned}\frac{R_i}{R_f} &= \frac{v_{(-)i}}{\lambda_{(-)i}} \cdot \frac{\lambda_{(-)f}}{v_{(-)f}} \\ &= \frac{v_{(-)i}}{v_{(-)f}} \cdot \frac{1 + v_{(-)f}/v_{(+)}}{1 + v_{(-)i}/v_{(+)}} \\ &= \frac{v_{(-)i}}{v_{(-)f}} \cdot \frac{B}{1+B} + \frac{1}{1+B}\end{aligned}$$

where $B = \frac{v_{(+)}}{v_{(-)i}}$ is the initial step velocity ratio, and has been introduced for simplicity sake.

It follows that :

$$\frac{v_{(-)i}}{v_{(-)f}} = \frac{R_i}{R_f} \cdot \frac{1+B}{B} - \frac{1}{B} \tag{5.19}$$

Equation 5.19 gives a direct relationship between a given growth rate reduction and the corresponding decrease in acute step velocity, assuming the totality of the growth rate decrease is due to acute step advancement inhibition.

In the case of magnesite and in the investigated conditions, obtuse steps are roughly one order of magnitude faster than acute steps (Saldi *et al.*, 2009 and this study), so $B \sim 10$. **Therefore, in order to obtain a decrease by a factor of 3 of the bulk growth rate as observed with 1mM citrate, acute step velocity needs to be decrease by a factor of 3.2.**

For obtuse steps, one obtains similarly that:

$$\frac{v_{(+)i}}{v_{(+)f}} = \frac{R_i}{R_f} \cdot (B+1) - B \tag{5.20}$$

Interestingly, if the observed growth rate decrease in the presence of citrate was the exclusive consequence of obtuse step advancement inhibition, **obtuse step velocity would have had to decrease by a factor of 23**, which has clearly not been observed.

Bibliography

Blum, A.E., & Lasaga, A.C. 1987. Monte Carlo simulations of surface reaction rate laws. *Aquatic Surface Chemistry*, 255–292.

Bénézeth, P., Saldi, G.D., Dandurand, J.L., & Schott, J. 2011. Experimental determination of the solubility product of magnesite at 50 to 200°C. *Chemical Geology*, 286, 21–31.

Bosbach, D., & Hochella Jr., M.F. 1996. Gypsum growth in the presence of growth inhibitors: a scanning force microscopy study. *Chemical Geology*, 132(1-4), 227–236.

Burton, W. K., Cabrera, N., & Frank, F. C. 1951. The growth of crystals and the equilibrium structure of their surfaces. *Philosophical Transactions of the Royal Society of London. Series A, Mathematical and Physical Sciences*, 243(866), 299–358.

Cabrera, N., & Vermilyea, DA. 1958. Growth and perfection of crystals. *New York*, 393.

Chernov, A.A. 1961. The spiral growth of crystals. *Physics-Uspekhi*, 4(1), 116–148.

Chernov, A.A. 2004. Notes on interface growth kinetics 50 years after Burton, Cabrera and Frank. *Journal of Crystal Growth*, 264(4), 499–518.

Chernov, A.A., Rashkovich, L.N., & Vekilov, P.G. 2005. Steps in solution growth: dynamics of kinks, bunching and turbulence. *Journal of Crystal Growth*, 275(1-2), 1–18.

Davis, J.A., & Kent, D.B. 1990. Surface complexation modeling in aqueous geochemistry. *Reviews in Mineralogy and Geochemistry*, 23(1), 177.

Davis, K.J., Dove, P.M., & De Yoreo, J.J. 2000. The role of Mg^{2+} as an impurity in calcite growth. *Science*, 290(5494), 1134–1137.

De Leeuw, N. H., & Rabone, J. A. L. 2007. Molecular dynamics simulations of the interaction of citric acid with the hydroxyapatite (0001) and $(01\bar{1}0)$ surfaces in an aqueous environment. *CrystEngComm*, 9(12), 1178–1186.

De Yoreo, J.J., & Dove, P.M. 2004. Shaping Crystals with Biomolecules. *Science*, 306(5700), 1301 –1302.

De Yoreo, J.J., & Vekilov, P.G. 2003. Principles of crystal nucleation and growth. *Reviews in Mineralogy and Geochemistry*, 54(1), 57–93.

De Yoreo, J.J., Zepeda-Ruiz, L.A., Friddle, R.W., Qiu, S.R., Wasylenki, L.E., Chernov, A.A., Gilmer, G.H., & Dove, P.M. 2009. Rethinking classical crystal growth models through molecular scale insights: consequences of kink-limited kinetics. *Crystal Growth & Design*, 9(Dec.), 5135–5144.

Didymus, J.M., Oliver, P., Mann, S., DeVries, A.L., Hauschka, P.V., & Westbroek, P. 1993. Influence of low-molecular-weight and macromolecular organic additives on the morphology of calcium carbonate. *J. Chem. Soc., Faraday Trans.*, 89(15), 2891–2900.

Dobson, P.S., Bindley, L.A., Macpherson, J.V., & Unwin, P.R. 2006. Modes of action of a weak acid modifier of calcite growth. *ChemPhysChem*, 7(5), 1019–1021.

Elhadj, S., Salter, E. A., Wierzbicki, A., De Yoreo, J. J., Han, N., & Dove, P. M. 2005. Peptide controls on calcite mineralization: polyaspartate chain length affects growth kinetics and acts as a stereochemical switch on morphology. *Crystal Growth & Design*, 6(1), 197–201.

Elhadj, S., De Yoreo, J.J., Hoyer, J.R., & Dove, P.M. 2006. Role of molecular charge and hydrophilicity in regulating the kinetics of crystal growth. *Proceedings of the National Academy of Sciences*, 103(51), 19237–19242.

Frank, F.C. 1974. Nucleation-controlled growth on a one-dimensional growth of finite length. *Journal of Crystal Growth*, 22(3), 233–236.

Freeman, C. L., Asteriadis, I., Yang, M., & Harding, J. H. 2009. Interactions of organic molecules with calcite and magnesite surfaces. *J. Phys. Chem. C*, 113(9), 3666–3673.

Friddle, R.W., Battle, K., Trubetskoy, V., Tao, J., Salter, E.A., Moradian-Oldak, J., De Yoreo, J.J., & Wierzbicki, A. 2011. Single-molecule determination of the face-specific adsorption of amelogenin's C-terminus on hydroxyapatite. *Angewandte Chemie International Edition*, 50(33), 7541–7545.

Ganor, J., Reznik, I.J., & Rosenberg, Y.O. 2009. Organics in water-rock interactions. *Reviews in Mineralogy and Geochemistry*, 70(1), 259.

Geffroy, C., Foissy, A., Persello, J., & Cabane, B. 1999. Surface complexation of calcite by carboxylates in water. *Journal of Colloid and Interface Science*, 211(1), 45–53.

Glusker, J.P. 1980. Citrate conformation and chelation: enzymatic implications. *Accounts of Chemical Research*, 13(10), 345–352.

Gratz, A.J., & Hillner, P.E. 1993. Poisoning of calcite growth viewed in the atomic force microscope (AFM). *Journal of Crystal Growth*, 129(3-4), 789–793.

Helgeson, H.C. 1969. Thermodynamics of hydrothermal systems at elevated temperatures and pressures. *American Journal of Science*, 267(7), 729–804.

Higgins, S.R., & Hu, X. 2006. Near molecular-scale growth of natural minerals: Experimental methods and errors in length-dependent step speeds with scanning probe microscopy. *Journal of Electron Spectroscopy and Related Phenomena*, 150(2-3), 235–247.

Higgins, S.R., Eggleston, C.M., Knauss, K.G., & Boro, C.O. 1998. A hydrothermal atomic force microscope for imaging in aqueous solution up to 150°C. *Review of Scientific Instruments*, 69, 2994.

Higgins, S.R., Bosbach, D., Eggleston, C.M., & Knauss, K.G. 2000. Kink dynamics and step growth on barium sulfate (001): A hydrothermal scanning probe microscopy study. *Journal of Physical Chemistry B*, 104(30), 6978–6982.

Higgins, S.R., Jordan, G., & Eggleston, C.M. 2002. Dissolution kinetics of magnesite in acidic aqueous solution: A hydrothermal atomic force microscopy study assessing step kinetics and dissolution flux. *Geochimica et cosmochimica acta*, 66(18), 3201–3210.

Hong, Q., Suárez, M. F., Coles, B. A., & Compton, R. G. 1997. Mechanism of solid/liquid interfacial reactions. The maleic acid driven dissolution of calcite: An atomic force microscopy study under defined hydrodynamic conditions. *Journal of Physical Chemistry B*, 101(28), 5557–5564.

Hu, Y.Y., Rawal, A., & Schmidt-Rohr, K. 2010. Strongly bound citrate stabilizes the apatite nanocrystals in bone. *Proceedings of the National Academy of Sciences*, 107(52), 22425–22429.

Johnson, J.W., Oelkers, E.H., & Helgeson, H.C. 1992. SUPCRT92: A software package for calculating the standard molal thermodynamic properties of minerals, gases, aqueous species, and reactions from 1 to 5000 bar and 0 to 1000°C. *Computers & Geosciences*, 18(7), 899–947.

Jones, F., Jones, P., Ogden, M.I., Richmond, W.R., Rohl, A.L., & Saunders, M. 2007. The interaction of EDTA with barium sulfate. *Journal of Colloid and Interface Science*, 316(2), 553–561.

Jordan, G., Higgins, S.R., Eggleston, C.M., Knauss, K.G., & Schmahl, W.W. 2001. Dissolution kinetics of magnesite in acidic aqueous solution, a hydrothermal atomic force microscopy (HAFM) study: step orientation and kink dynamics. *Geochimica et Cosmochimica Acta*, 65(23), 4257–4266.

Jordan, G., Pokrovsky, O.S., Guichet, X., & Schmahl, W.W. 2007. Organic and inorganic ligand effects on magnesite dissolution at 100 C and pH= 5 to 10. *Chemical geology*, 242(3-4), 484–496.

Larsen, K., Bechgaard, K., & Stipp, S.L.S. 2010. Modelling spiral growth at dislocations and determination of critical step lengths from pyramid geometries on calcite $(10\overline{1}4)$ surfaces. *Geochimica et Cosmochimica Acta*, 74(2), 558–567.

Lee, Young J., & Reeder, Richard J. 2006. The role of citrate and phthalate during Co(II) coprecipitation with calcite. *Geochimica et Cosmochimica Acta*, 70(9), 2253–2263.

Liang, Yong. 1996. Interplay between step velocity and morphology during the dissolution of $CaCO_3$ surface. *Journal of Vacuum Science & Technology A: Vacuum, Surfaces, and Films*, 14(3), 1368.

Mann, S., Didymus, J, M., Sanderson, N.P., Heywood, B.R., & Samper, E.J.A. 1990. Morphological influence of functionalized and non-functionalized α,β-dicarboxylates on calcite crystallization. *Journal of the Chemical Society, Faraday Transactions*, 86(10), 1873–1880.

Mann, S., Archibald, D.D., Didymus, J.M., Douglas, T., Heywood, B.R., Meldrum, Fiona C., & Reeves, N.J. 1993. Crystallization at inorganic-organic interfaces: biominerals and biomimetic synthesis. *Science*, 261(5126), 1286–1292.

Meldrum, F. C., & Hyde, S. T. 2001. Morphological influence of magnesium and organic additives on the precipitation of calcite. *Journal of Crystal Growth*, 231(4), 544–558.

Millero, F., Huang, F., Graham, T., & Pierrot, D. 2007. The dissociation of carbonic acid in NaCl solutions as a function of concentration and temperature. *Geochimica et Cosmochimica Acta*, 71(1), 46–55.

Orme, C.A., Noy, A., Wierzbicki, A., McBride, M.T., Grantham, M., Teng, H.H., Dove, P.M., & DeYoreo, J.J. 2001. Formation of chiral morphologies through selective binding of amino acids to calcite surface steps. *Nature*, 411(6839), 775.

Palmer, D.A., & Wesolowski, D.J. 1997. Potentiometric measurements of the first hydrolysis quotient of magnesium (II) to 250 C and 5 molal ionic strength (NaCl). *Journal of solution chemistry*, 26(2), 217–232.

Parkhurst, D.L., & Appelo, CAJ. 1999. User's guide to PHREEQC (version 2): a computer program for speciation, batch-reaction, one-dimensional transport, and inverse geochemical calculations. *US Geological Survey Water-Resources Investigations Report*, 99(4259), 312.

Phillips, B. L., Lee, Y. J., & Reeder, R. J. 2005. Organic coprecipitates with calcite: NMR spectroscopic evidence. *Environmental Science and Technology*, 39(12), 4533–4539.

Pina, C.M, Putnis, C.V, Becker, U, Biswas, S, Carroll, E.C, Bosbach, D, & Putnis, A. 2004. An atomic force microscopy and molecular simulations study of the inhibition of barite growth by phosphonates. *Surface Science*, 553(1-3), 61–74.

Pina, C.M., Merkel, C., & Jordan, G. 2009. On the bimodal effects of silicic acids on calcite growth. *Crystal Growth & Design*, 9(9), 4084–4090.

Pokrovsky, O.S., Schott, J., & Castillo, A. 2005. Kinetics of brucite dissolution at 25°C in the presence of organic and inorganic ligands and divalent metals. *Geochimica et Cosmochimica Acta*, 69(4), 905–918.

Qiu, S. R., & Orme, C. A. 2008. Dynamics of biomineral formation at the near-molecular level. *Chemical Reviews*, 108(11), 4784–4822.

Qiu, S. R., Wierzbicki, A., Orme, C. A., Cody, A. M., Hoyer, J. R., Nancollas, G. H., Zepeda, S., & De Yoreo, J. J. 2004. Molecular modulation of calcium oxalate crystallization by osteopontin and citrate. *Proceedings of the National Academy of Sciences of the United States of America*, 101(7), 1811–1815.

Qiu, S. R., Wierzbicki, A., Salter, E. A., Zepeda, S., Orme, C. A., Hoyer, J. R., Nancollas, G. H., Cody, A. M., & De Yoreo, J. J. 2005. Modulation of calcium oxalate monohydrate crystallization by citrate through selective binding to atomic steps. *Journal of the American Chemical Society*, 127(25), 9036–9044.

Rashkovich, L.N., Gvozdev, N.V., Silnikova, M.I., & Chernov, A.A. 2002. Fluctuations in the step velocity and the generation of a dislocation spiral on the (101) face of monoclinic lysozyme crystals. *Crystallography Reports*, 47(5), 859–866.

Rashkovich, L.N., Petrova, E.V., Shustin, O.A., & Chernevich, T.G. 2003. Formation of a dislocation spiral on the (010) face of a potassium hydrogen phthalate crystal. *Physics of the Solid State*, 45(2), 400–407.

Ruiz-Agudo, E., Putnis, C. V., Wang, L., & Putnis, A. 2011. Specific effects of background electrolytes on the kinetics of step propagation during calcite growth. *Geochimica et Cosmochimica Acta*, 75(13), 3803–3814.

Saldi, G.D., Jordan, G., Schott, J., & Oelkers, E.H. 2009. Magnesite growth rates as a function of temperature and saturation state. *Geochimica et Cosmochimica Acta*, 73(19), 5646–5657.

Saldi, G.D., Schott, J., Pokrovsky, O.S., & Oelkers, E.H. 2010. An experimental study of magnesite dissolution rates at neutral to alkaline conditions and 150 and 200°C as a function of pH, total dissolved carbonate concentration, and chemical affinity. *Geochimica et Cosmochimica Acta*, 74, 6344–6356.

Sheng, X., Jung, T., Wesson, J. A., & Ward, M. D. 2005. Adhesion at calcium oxalate crystal surfaces and the effect of urinary constituents. *Proceedings of the National Academy of Sciences of the United States of America*, 102(2), 267–272.

Shiraki, R., & Brantley, S.L. 1995. Kinetics of near-equilibrium calcite precipitation at 100°C: An evaluation of elementary reaction-based and affinity-based rate laws. *Geochimica et Cosmochimica Acta*, 59(8), 1457–1471.

Teng, H.H., & Dove, P.M. 1997. Surface site-specific interactions of aspartate with calcite during dissolution: Implications for biomineralization. *American Mineralogist*, 82(9), 878–887.

Teng, H.H., Dove, P.M., Orme, C.A., & De Yoreo, J.J. 1998. Thermodynamics of calcite growth: baseline for understanding biomineral formation. *Science*, 282(5389), 724–727.

Teng, H.H., Dove, P.M., & De Yoreo, J.J. 1999. Reversed calcite morphologies induced by microscopic growth kinetics: insight into biomineralization. *Geochimica et Cosmochimica Acta*, 63, 2507–2512.

Teng, H.H., Chen, Y., & Pauli, E. 2006. Direction specific interactions of 1,4-dicarboxylic acids with calcite surfaces. *J. Am. Chem. Soc.*, 128(45), 14482–14484.

Vekilov, P.G. 2007. What determines the rate of growth of crystals from solution ? *Crystal Growth & Design*, 7(12), 2796–2810.

Voronkov, V.V. 1968. Non-equilibrium structure of an elementary step. *Soviet physics, crystallography*, 13(1), 13.

Voronkov, V.V. 1970. The movement of an elementary step by means of the formation of one-dimensional nuclei. *Sov. Phys. Cryst*, 15, 8–13.

Wasylenki, L., Dove, P., Wilson, D., & Deyoreo, J.J. 2005. Nanoscale effects of strontium on calcite growth: An in situ AFM study in the absence of vital effects. *Geochimica et Cosmochimica Acta*, 69(12), 3017–3027.

Weaver, M.L., Qiu, R.S., Hoyer, J.R., Casey, W.H., Nancollas, G.H., & De Yoreo, J.J. 2007. Inhibition of calcium oxalate monohydrate growth by citrate and the effect of the background electrolyte. *Journal of Crystal Growth*, 306(1), 135–145.

Wu, C., Wang, X., Zhao, K., Cao, M., Xu, H., Xia, D., & Lu, J.R. 2011. Molecular modulation of calcite dissolution by organic acids. *Crystal Growth & Design*, 11(7), 3153–3162.

Yoreo, J.J. De, Wierzbicki, A., & Dove, P.M. 2007. New insights into mechanisms of biomolecular control on growth of inorganic crystals. *CrystEngComm*, 9(12), 1144–1152.

Zandvliet, H.J.W., Gurlu, O., & Poelsema, B. 2001. Temperature dependence of the step free energy. *Physical Review B*, 64(7).

Zhang, J., & Nancollas, G.H. 1990. Kink densities along a crystal surface step at low temperatures and under nonequilibrium conditions. *Journal of Crystal Growth*, 106(2-3), 181–190.

Zhang, J., & Nancollas, G.H. 1998. Kink density and rate of step movement during growth and dissolution of an ABCrystal in a nonstoichiometric Solution. *Journal of Colloid and Interface Science*, 200(1), 131–145.

Chapter 6

Hydromagnesite solubility product and growth kinetics in aqueous solution

Sommaire

Hydromagnesite solubility product and growth kinetics in aqueous solution *

Quentin Gautier[1,2], Pascale Bénézeth [1], Vasileios Mavromatis[1], Jacques Schott[1]

[1] Géosciences Environnement Toulouse, Observatoire Midi-Pyrénées, CNRS, Université de Toulouse, 14, avenue Edouard Belin, 31400 Toulouse, France

[2] Université Paris-Est, Laboratoire Navier, 6/8 avenue Blaise Pascal, Champs-sur-Marne, 77455 Marne-La-Vallée, France

Abstract

Hydromagnesite $Mg_5(CO_3)_4(OH)_2{\cdot}4\,H_2O$ is the most widespread form of hydrated Mg-carbonate mineral. In order to better understand the factors controlling the precipitation of hydrated Mg-carbonates, we measured hydromagnesite solubility product at 25 and 50°C and its growth rate between 25 and 75°C, using natural hydromagnesite from caves as seed material.

The obtained solubility products are in the upper range of published values, and confirm the large variability of natural and synthetic hydromagnesite solubility. We show that hydromagnesite surface area normalized growth rates are consistent with transition state theory and may be described through the following equation:

$$R_{\mathrm{Hmgs}} = k_{\mathrm{Hmgs}}(\Omega_{\mathrm{Hmgs}}{}^{\frac{1}{5}} - 1)$$

where Ω_{Hmgs} is the saturation state of the solution with respect to hydromagnesite, estimated based on the newly determined solubility products, and k_{Hmgs} is a rate constant equivalent to $A\exp(-E_a/RT)$, with A a pre-exponential factor equal to $5.12 \cdot 10^{-7}$ mol/cm^2/s, and E_a the activation energy equal to 45.5 ± 9 kJ/mol.

Comparison of hydromagnesite growth rates with recently published magnesite growth rates show that: (1) hydromagnesite apparent growth activation energy is lower by more than 100 kJ/mol compared to magnesite obtuse step advancement, and (2) hydromagnesite growth rates are much higher than corresponding magnesite rates at comparable temperature and saturation state, with highest differences close to equilibrium.
Thus our results confirm the long-standing hypothesis that the slow dehydration kinetics of the Mg^{2+} cation is responsible for the difficulty for magnesite to form at low temperature, and that this kinetic inhibition can be partly eliminated by precipitating hydrated Mg-carbonates.

However, in order to take into account the large differences in solubility between hydromagnesite and magnesite, we performed simulations of their growth rates as a function of solution composition at 90 and 50°C, and pH 7 and 9. These reveal that hydromagnesite will grow more quickly than magnesite in natural or industrial environments only at low

*This article will be submitted for publication to *Chemical Geology* in a revised version.

temperatures and alkaline pH. This explains then why hydromagnesite forms at the expense of magnesite as a result of surface alteration of ultramafic rocks, but does not explain why hydromagnesite may be a precursor of magnesite in high temperature, high P_{CO_2} environments. Better constraining Mg-carbonate phase nucleation kinetics and mineral transformation is a prerequisite to opimize low- and high-temperature CO_2 mineral sequestration under the form of magnesium carbonates.

6.1 Introduction

Despite its structural, chemical and thermodynamic similarity with the very common mineral calcite, magnesite ($MgCO_3$) is known for its reluctance to form at ambient temperature (Lippmann, 1973; Hänchen *et al.*, 2006; Saldi *et al.*, 2009). Magnesite is however the most stable Mg-carbonate mineral in a wide range of temperature (Königsberger *et al.*, 1999; Bénézeth *et al.*, 2011); this reluctance to precipitate is thus interpreted as resulting from a kinetic inhibition, which is widely ascribed to the highly hydrated character of the Mg^{2+} cation (Sayles & Fyfe, 1973; Lippmann, 1973).

The small Mg^{2+} cation indeed has a high charge density, which results in the structuration of tightly bonded hydration shells. The first hydration shell consists of six water molecules in octahedral configuration, while the second hydration shell contains 12 to 13 water molecules (Pavlov *et al.*, 1998; Ikeda *et al.*, 2007; Di Tommaso & de Leeuw, 2010).
Because a metal cation must lose its waters of hydration upon integration in an anhydrous crystal, the "lability" of its hydration spheres is a crucial parameter controlling the cation and its corresponding mineral reactivity (Pokrovsky & Schott, 2002). Mg^{2+} however has a much higher hydration enthalpy than Ca^{2+} (Noyes, 1962), which means that hydration water must overcome a large energy barrier in order to leave Mg^{2+} first hydration shell (Yang *et al.*, 2012). As a result, the water exchange rate constant for Mg^{2+} at ambient temperature is $6.7 \cdot 10^5$ s^{-1} (Bleuzen *et al.*, 1997), three to four orders of magnitude lower than for Ca^{2+} (approximately $2 \cdot 10^9$ s^{-1}, Larentzos & Criscenti, 2008). Mg^{2+} dehydration is thus particularly difficult, which explains why direct magnesite precipitation from aqueous solution is only observed at temperatures higher than ca. 80°C (e.g Giammar *et al.*, 2005; Hänchen *et al.*, 2006; Saldi *et al.*, 2012).

At lower temperature, Mg-carbonates tend to precipitate under the form of various hydrated compounds, whose formation depends on the chemical conditions and temperature (see the recent paper of Hopkinson *et al.*, 2012, and references therein). At temperatures higher than 15°C, hydromagnesite $Mg_5(CO_3)_4(OH)_2{\cdot}4\,H_2O$ is the second most stable and the most widespread Mg-carbonate mineral forming in the Earth's surface environments, followed by nesquehonite $MgCO_3{\cdot}3\,H_2O$ (Königsberger *et al.*, 1999; Marion, 2001). Both minerals may form at ambient temperature (Hänchen *et al.*, 2006; Hopkinson *et al.*, 2012), although it is generally reported that nesquehonite is most readily formed at 25°C, particularly under relatively high CO_2 pressures, while hydromagnesite is obtained at relatively higher temperatures (Hänchen *et al.*, 2006; Wang *et al.*, 2008; Cheng *et al.*, 2009; Cheng & Li, 2010). In addition, artinite $Mg_2(CO_3)(OH)_2{\cdot}3\,H_2O$ may become more stable than hydromagnesite at temperatures lower than 15°C and low P_{CO_2} (Königsberger *et al.*, 1999), while lansfordite $MgCO_3{\cdot}5\,H_2O$ may form at the expense of nesquehonite at temperatures lower than ca. 10°C (Marion, 2001).

To add to the complexity of the system, mineralogical transitions occur between the different Mg-carbonate phase. Nesquehonite is indeed known to transform readily into hydromagnesite, through a transformation possibly mediated by dypingite, $Mg_5(CO_3)_4(OH)_2{\cdot}5\,H_2O$ (Davies & Bubela, 1973; Hopkinson *et al.*, 2008, 2012). A transition between hydromagnesite and magnesite was documented over 100°C by Sayles & Fyfe (1973), Zhang *et al.* (2000) and Hänchen *et al.* (2006), while a direct transformation of nesquehonite into magnesite was

evoked by Schaef *et al.* (2011) and Felmy *et al.* (2012) at moderate temperature (35 to 75°C).

In natural environments, hydrated Mg-carbonate minerals are commonly encountered as weathering products of mafic or ultramafic rocks such as serpentine or basalt (see Deelman, 2011 and references therein). Hydromagnesite is also known to precipitate in microbial mats or stromatolites in alkaline lakes with high Mg/Ca ratio, and thus presents a particular interest as a biomineral (Thompson & Ferris, 1990; Braithwaite & Zedef, 1996; Russell *et al.*, 1999; Renault & Stead, 1990; Power *et al.*, 2007; Kazmierczak *et al.*, 2011; Mavromatis *et al.*, 2012; Shirokova *et al.*, 2012).

In addition, being magnesium carbonate minerals, hydromagnesite and nesquehonite have recently attracted a great deal of interest for their potential capacity to store CO_2 under a mineral form, particularly at low temperature where magnesite does not form. Some experimental studies have addressed the conditions of formation of different Mg-carbonate minerals (Hänchen *et al.*, 2006) and their thermal stability (Frost *et al.*, 2008; Ballirano *et al.*, 2010), while others aimed at precipitating hydromagnesite or nesquehonite as a result of serpentine (Park & Fan, 2004; Teir *et al.*, 2007; Teir *et al.*, 2009) or brucite (Zhao *et al.*, 2009; Schaef *et al.*, 2011) low temperature carbonation. Field studies have proven passive CO_2 sequestration in ultramafic mine tailings located in Canada, through weathering of Mg-silicates and precipitation of hydrated Mg-carbonates, including hydromagnesite, a process susceptible to significantly offset CO_2 emissions for these mining activities (Wilson *et al.*, 2009; Pronost *et al.*, 2011). Similarly, Power *et al.* (2009) suggested using the example of bio-mediated hydromagnesite precipitation in lakes of British Columbia as a biogeochemical model for CO_2 sequestration at the watershed scale.

Thus, there is a wide interest in better understanding the formation and the evolution of hydrated Mg-carbonate minerals. Surprisingly however, not a single study has addressed in detail the question of the kinetics of formation of hydrated Mg-carbonates, as compared to their anhydrous counterpart. This question however has important consequences, both for the fundamental understanding of the role of Mg^{2+} hydration on the formation of various Mg-carbonate phase, and in order to better quantify and optimize the potential role of hydrated Mg-carbonates in low- and high-temperature CO_2 sequestration.

The present study focuses on hydromagnesite, the most widespread Mg-carbonate mineral forming in the Earth's surface environments. We first determined the solubility product of our seed material, a natural hydromagnesite from caves, at 25 and 50°C, and then measured its growth rates under controlled conditions of supersaturation and temperature between 25 and 75°C. The existence of published data on magnesite growth kinetics (Saldi *et al.*, 2009; Saldi *et al.*, 2012; and Chapter 3) allows for an insightful comparison between minerals of similar chemistry but different hydration state.

6.2 Theoretical considerations

Hydromagnesite dissolution and precipitation can be described by the following chemical reaction:

$$Mg_5(CO_3)_4(OH)_2 \cdot 4H_2O_{(cr)} + 6\,H^+ = 4\,HCO_3^- + 5\,Mg^{2+} + 6\,H_2O \tag{6.1}$$

Hydromagnesite solubility product will be defined as the equilibrium constant of reaction 6.1:

$$K_{sp-Hmgs} = \frac{a^5_{Mg^{2+}} a^4_{HCO_3^-} a^6_{H_2O}}{a^6_{H^+}} \tag{6.2}$$

where a_i is the chemical activity of the ith species at equilibrium.
The saturation state of solutions with respect to hydromagnesite is thus defined in the given experimental conditions as:

$$\Omega_{Hmgs} = \frac{a^5_{Mg^{2+}} a^4_{HCO_3^-} a^6_{H_2O}}{a^6_{H^+}} * \frac{1}{K_{sp-Hmgs}} \tag{6.3}$$

The standard state adopted in this study is that of unit activity for pure minerals and H_2O at any temperature and pressure. For dissolved species the standard state is of unit activity in a hypothetical 1 molal solution referenced to infinite dilution at any temperature and pressure.

Aqueous solution speciation, saturation states with respect to solid phases, and solution pH at temperatures higher than 25°C were calculated from measured Mg concentration, alkalinity, and pH measured at room temperature, using the PHREEQC geochemical code (Parkhurst & Appelo, 1999) together with its `llnl.dat` thermodynamic database. As presented in Chapter 3, the database was modified to include the carbonic acid dissociation constants of Millero *et al.* (2007), the thermodynamic constant for Mg^{2+} hydrolysis (Palmer & Wesolowski, 1997), and the newly measured hydromagnesite solubility product from this study (see section 6.4.1), while the activity model used to compute activity coefficients is the Davies model.

Within the classical transition state theory (TST), the rate of mineral formation as a function of saturation state can be expressed (Aagaard & Helgeson, 1982; Schott *et al.*, 2009) as:

$$R = k_{(-)} \left[\prod_i a_i^{m_i} \right] \left(\Omega^{1/\sigma} - 1 \right)^n \tag{6.4}$$

$k_{(-)}$ is the surface area normalized growth rate constant, $[\prod_i a_i^{m_i}]$ expresses the dependency of the forward reaction rate to the solution chemistry, n is the rate order and σ stands for Temkin's average stoichiometric number (Temkin, 1963).

Within TST, σ is equal to the ratio of the rate of destruction of the activated complex controlling the precipitation reaction, with respect to the overall reaction rate (Aagaard & Helgeson, 1982). The underlying assumption is that a single elementary reaction controls the overall rate. The value of σ therefore bears assumption concerning the stoichiometry of this elementary reaction, and the corresponding activated complex (Schott *et al.*, 2009).

Considering that dehydration of the strongly hydrated Mg^{2+} cation is believed to control the kinetics of Mg-carbonate minerals formation (Lippmann, 1973; Pokrovsky & Schott, 2002; Schott *et al.*, 2009), we hypothesize that the rate-controlling activated complex contains one Mg^{2+}. Thus for hydromagnesite which contains five Mg, $\sigma = 5$, and equation 6.4 may be written in a simplified form:

$$R = k_{Hmgs}(\Omega^{\frac{1}{5}} - 1)^{n} \tag{6.5}$$

where the apparent rate constant k_{Hmgs} contains information concerning the dependency of growth rates with respect to solution chemistry.

The parameter n has classically been related to the type of growth-controlling mechanism: $n = 1$ for transport or adsorption controlled growth, $n = 2$ for spiral growth at screw dislocations, while higher orders reveal 2D nucleation-assisted growth (e.g Nielsen, 1984; Blum & Lasaga, 1987; Shiraki & Brantley, 1995). Thus, fitting equation 6.5 to our experimentally determined hydromagnesite precipitation rates should provide information regarding the growth-controlling mechanism in our experimental conditions.

6.3 Materials and Methods

6.3.1 Hydromagnesite seeds

Solubility and precipitation experiments were performed on the same pure natural hydromagnesite originating from the André Lachambre cave network, in the French Pyrénées Orientales.

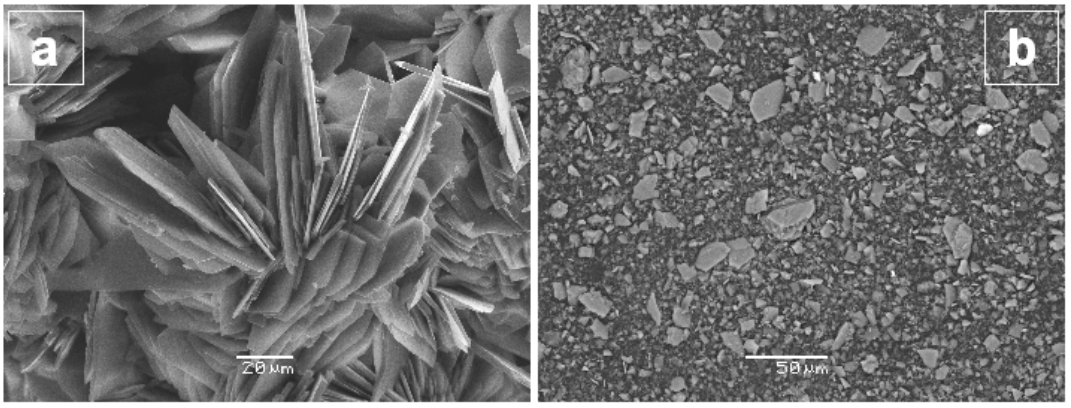

Figure 6.1 – SEM pictures of hydromagnesite seeds and precipitates. (a) Secondary electron (SE) image of a pristine hydromagnesite "flower" from the Lachambre cave network. (b) Backscattered electron (BSE) image of highly divided hydromagnesite fragments obtained after gentle grinding, and used for solubility and growth experiments. Bright spots correspond to aragonite fragments.

SEM observations of the centimeter-sized hydromagnesite "flowers" revealed agglomerates of rectangular to elongated hexagonal-shaped crystals, up to 80 µm long, 60 µm wide, and 2 µm thick (Fig. 6.1a). A few individual crystals of aragonite were present in the initial material. In order to disaggregate hydromagnesite agglomerates, the natural samples were gently grounded in an agate mortar, thus producing a finely divided seed material (Fig. 6.1b), which was used without modification for experiments. The results of electron microprobe analyses performed on hydromagnesite crystals are shown in Table 6.1, and indicate only minor amounts of impurities.

Major oxides (wt %)	
MgO	42.79
CaO	0.04
MnO	0.03
FeO	0.03
SrO	0.01
BaO	-
sum	42.90
SiO_2	0.07

Table 6.1 – Chemical composition of the Lachambre hydromagnesite used in this study, based on 15 EMPA analyses. Note the good agreement between the measured total weight percent of carbonate oxides, and the theoretical value corresponding to hydromagnesite stoichiometry (43.09 %).

The diffractogram of the powdered material provided in Fig. 6.2, performed on an INEL CPS 120 diffractometer using the Cu Kα ray, confirmed the sample was hydromagnesite,

while aragonite was not noticeable.

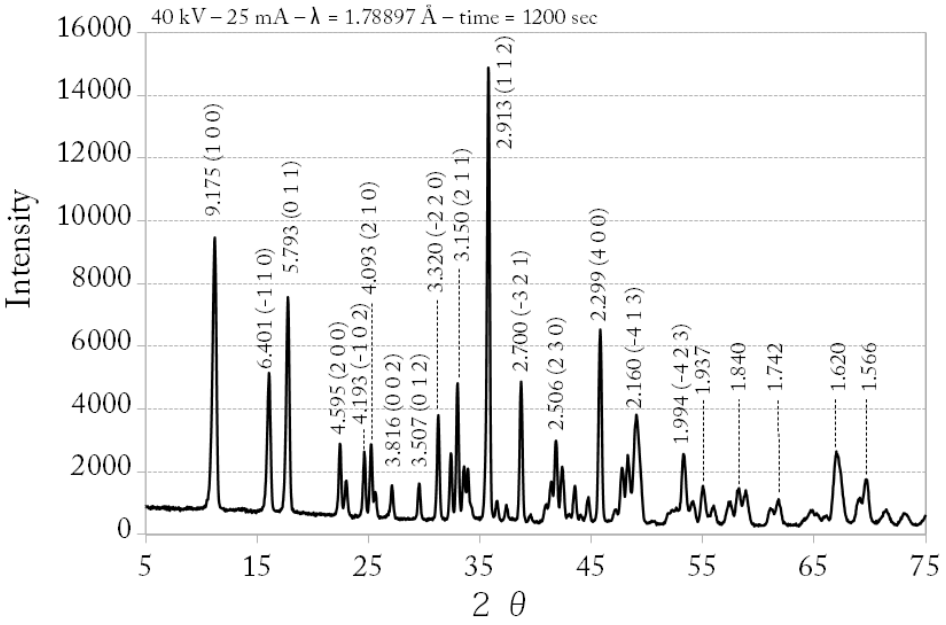

Figure 6.2 – Diffractogram of the powdered seed material with crystallographic indexation of the main peaks. All peaks correspond to hydromagnesite.

The stoichiometry of hydromagnesite has been under debate over the last decades, as to whether its structural formula contained 3 or 4 water molecules (for a review of the controversy, see Hollingbery & Hull, 2010b). However, there seems now to be an agreement on the formula: $Mg_5(CO_3)_4(OH)_2 \cdot 4H_2O$. In order to verify that the stoichiometry of our seed material indeed corresponds to this formula, we performed thermo-gravimetric analyses (TGA) using a Netzsch STA449-F3 TG/DSC Analyser. Analyses were conducted under an argon atmosphere, at a heating rate of 10°C.min^{-1} between 30 and 1000°C, with approximately 800 mg of sample.

Hydromagnesite thermal decomposition proceeds through the following reaction (Beck, 1950; Sawada *et al.*, 1978):

$$Mg_5(CO_3)_4(OH)_2 \cdot 4H_2O \longrightarrow 5\,MgO + 4\,CO_2 + 5\,H_2O \tag{6.6}$$

The four molecules of crystalline water are lost first, above 210°C, leading to a weight loss of 15.4 %. This first step is followed at higher temperature by dehydroxylation, and finally by the loss of four CO_2 molecules. The overall weight loss is theoretically 56.9 %, while the exact decomposition mechanism depends on the heating rate and grain size (Hollingbery & Hull, 2010b).

Results of TGA are provided in Figure 6.3. The overall weight loss is 56.6 %, thus closely matching the expected weight loss of $Mg_5(CO_3)_4(OH)_2{\cdot}4\,H_2O$. The different decomposition steps match with those reported in the literature, with an initial loss of 15.06 % corresponding to 4 H_2O molecules. The rest of the profile exhibits several independent decomposition steps,

and closely resembles the hydromagnesite's TGA at a heating rate of 30°C.min^{-1} reported by Hollingbery & Hull (2012). In particular, the rapid weight loss around 500°C has been interpreted to result from a rapid release of CO_2 from the crystal structure (Khan *et al.*, 2001).

Our TG analysis therefore confirms that our natural hydromagnesite contains four molecule of crystalline water.

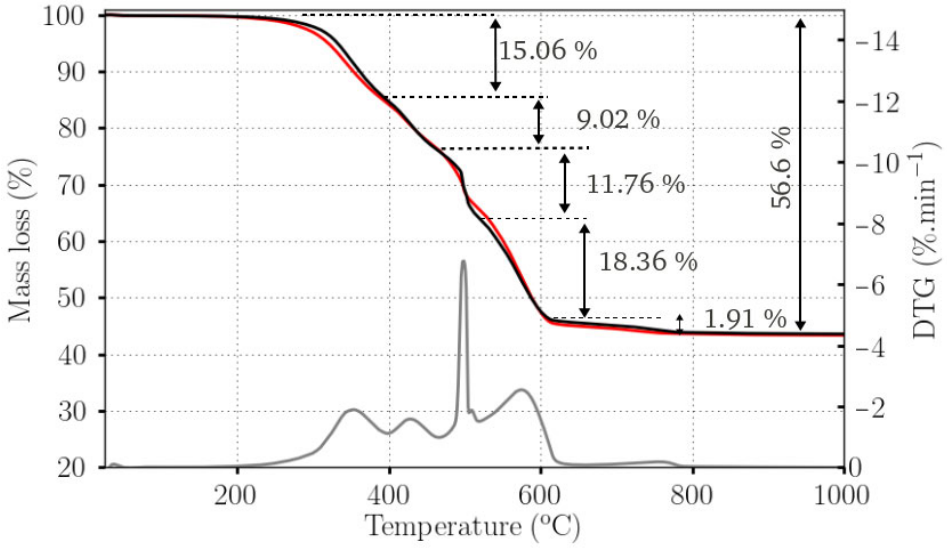

Figure 6.3 – Results of thermo-gravimetric analysis performed on the initial seed material (black curve) as well as on the precipitated material at 25°C (exp. H11, red). The grey curve is the differential thermo-gravimetry (DTG), corresponding to the rate of weight loss. Four main decomposition steps are visible, at 353°C, 428°C, 498°C and 575°C, respectively. The first DTG peak corresponds to loss of four molecules of crystalline water, while the other peaks correspond to non-stoichiometric losses of CO_2 and H_2O.

Finally, the specific BET surface area of hydromagnesite powders was determined by multipoint nitrogen adsorption using an Autosorb 1 (Quantachrome Instruments). Degassing of the samples prior to gas adsorption has been performed at temperatures lower than 90°C so as to not dehydrate the mineral. The measured specific surface area is 3.56 $m^2/g \pm 5\%$ (mean of 3 measurements).

6.3.2 Hydromagnesite solubility experiments

Preliminary growth experiments prepared based on the PHREEQC `llnl.dat` hydromagnesite thermodynamic data, led to the conclusion that the solubility of our seed material was higher than that reported in the database, which is based on the SUPCRT92 model (Johnson *et al.*, 1992). The important variability of published measurements of hydromagnesite solubility product (Langmuir, 1965; Königsberger *et al.*, 1999) prompted us to directly measure the solubility product of our natural hydromagnesite.

Solubility experiments were performed at 25 and 50°C in 250 mL Azlon® polypropylene beakers capped with a tight home-made polypropylene cap and sealed with an O-ring, and placed in thermostated baths maintaining the temperature to within 0.5°C of the goal temperature.

At 25°C, 0.5 g of hydromagnesite powder was placed in three different beakers filled with approximately 220 mL of (1) 0.1 M NaCl solution, (2) 0.01 M NaCl solution, and (3) high purity deionized water (resistivity 18.2 MΩ). At 50°C, two experiments were performed with 0.4 g of powder in either (1) 0.1 M NaCl solution or (2) 0.01 M NaCl solution. The filling solution was heated to the experimental temperature in the beaker prior to hydromagnesite addition. The beakers were then quickly sealed with the polypropylene caps, and placed back into the thermostated bath. Solutions were stirred by Teflon-coated magnetic bars placed in Teflon cages limiting powder grinding.

The caps had two apertures, one closed with a polypropylene screw allowing direct *in situ* pH measurement with a glass electrode, the other obturated by a Teflon-coated silicon septum, maintained with a stainless steel pierced screw allowing sampling. Solution samples (approximately 6 mL) were regularly withdrawn through the septa with polypropylene syringes fitted with 10 cm long needles. The samples were filtered through 0.22 µm Millipore Nylon filters. 2 mL of solution were stored at 4°C for subsequent alkalinity measurements. A small aliquot was used for immediate pH measurement, and the rest of the sample was acidified for later Mg concentration analysis.

At 50°C, solution aliquots had to be cooled down to ambient temperature for pH measurement. To this aim, sampling tubes were kept cold prior to fluid sampling, and the filtrates were placed in a water bath at ambient temperature for approximately two minutes before pH measurement. This way, the temperature of the fluid reached the ambient temperature.

Solubility experiments lasted up to 60 days, during which pH and dissolved Mg concentration measurements allowed to follow the approach of equilibrium. At the end of the experiments, the solids were recovered, filtered through a 0.22 µm Millipore cellulose acetate filter using suction filtration, quickly rinsed with ultrapure deionized water, then frozen at -80°C and freeze dried. The final powders were examined with SEM and XRD, which revealed no visible difference compared to the initial material. We are thus confident that no other hydrated Mg-carbonate phase precipitated during the course of the experiments, and that measured solubility products are truly those of natural hydromagnesite.

6.3.3 Low-temperature growth experiments

At 25°C and 30°C, growth experiments were conducted using a method inspired from Tesoriero & Pankow (1996), hereafter called "discontinuous mixed-flow system". The experimental setup is shown in Fig. 6.4.

In seeded experiments, a weighted amount of powder (0.8 to 1.5 g) was placed in a 1000 mL polypropylene reaction vessel, filled with 500 mL of solution close to equilibrium with hydromagnesite at pH 9.2 at the temperature of interest and at an ionic strength of 0.11 M. A Teflon-coated floating stirring bar was disposed into the reactor, and its rotation controlled by a magnetic stirrer at ∼150rpm. Then the reactor vessel was closed with a polypropylene cap and weighted before placing it in a thermostated bath.

Hydromagnesite precipitation was induced by pumping into the reactors two independent inlet solutions at similar flow rates, one containing dissolved $MgCl_2 \cdot 6\,H_2O$, the other one dissolved Na_2CO_3. The solutions were stored at ambient temperature in compressible polyethylene bags, and flew into the reactors through Tygon tubings passing into one of the apertures

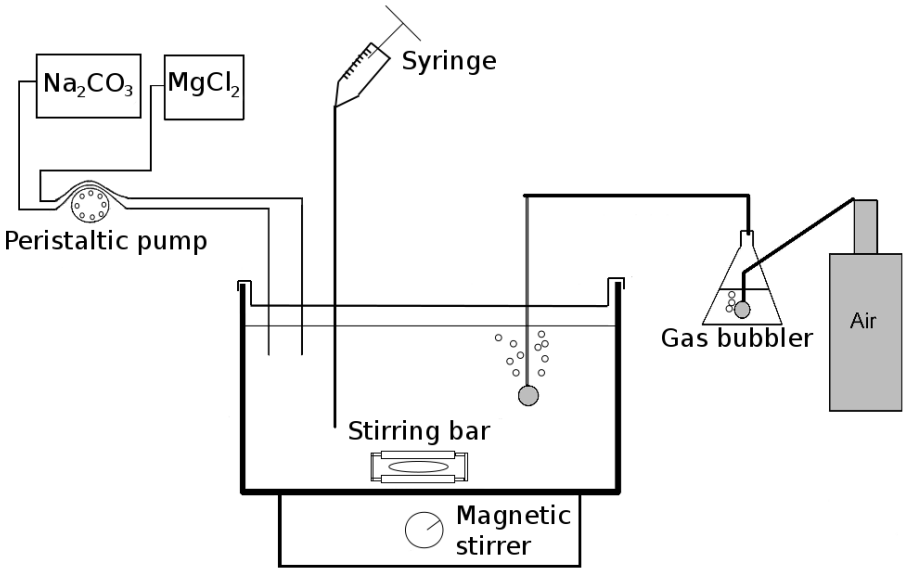

Figure 6.4 – Discontinuous mixed-flow reactor setting used for low temperature hydromagnesite growth experiments. Note that air bubbling was only used in a few preliminary experiments.

in the reactor's caps. The flow rate (9 to 12 mL/day/solution) was maintained constant by peristaltic pumps, which were carefully calibrated at the beginning of the experiments.

Once a day, a volume corresponding to the sum of the volumes added from the inlet solutions was sampled from the reactors with a syringe, thus limiting the solution volume variation to maximum 5 % over a 24 hours time interval. This sampled solution is called thereafter "outlet" solution. Immediately after sampling, solution samples were filtered through a 0.22 µm nylon Millipore filter, and precisely weighted. A sub-sample was used for pH measurement, another one acidified for subsequent Mg concentration analysis, while a last aliquot was stored at 4°C for alkalinity measurement.

At the end of the experiments, the entire reactive solutions were filtered onto 0.22 µm cellulose acetate Millipore filters using suction filtration. The solids were quickly rinsed with ultrapure deionized water, then frozen at -80°C and freeze dried. This drying procedure was chosen so as to preserve the mineralogy and morphology of the final solids, since mineralogical transitions between various forms of hydrated Mg-carbonates are well documented, and occur quickly at temperatures of 60°C or less (Davies & Bubela, 1973; Hopkinson *et al.*, 2008). Dried solids were examined by SEM and XRD.

Over the course of the experiments, addition of inlet solutions increases the reactor solution supersaturation with respect to hydromagnesite, which in turn increases the rate of mineral precipitation. At some point, steady-state growth conditions were established, marked by constant solution Mg concentration and pH (within analytical uncertainties) for a minimum of 6 consecutive days (corresponding to a 20 % renewal of the solution volume). In our experiments, 30 to 35 days were necessary to reach steady-state. Growth rates at steady-state were classically estimated from the change of Mg concentration between the inlet solution

and the sampled fluids:

$$R_{st} = \frac{\mathrm{FR}_{tot} \cdot \Delta[\mathrm{Mg}]_{tot}}{5 \cdot m_{\mathrm{Hmgs}} \cdot S_{\mathrm{BET}}} \tag{6.7}$$

where FR_{tot} represents the total inlet fluid flow rate (equal to the sum of the respective flow rates of each inlet solution), m_{Hmgs} the initial hydromagnesite seeds mass and S_{BET} the initial specific BET surface area. $\Delta[\mathrm{Mg}]_{tot}$ is the change of Mg concentration between the inlet fluid (constituted by the addition of both inlet solutions at their respective flow rates) and the outlet solution. The factor 5 takes into account hydromagnesite stoichiometry with respect to Mg.

In addition to steady-state rates, we calculated daily precipitation rates based on a precise Mg mass balance calculation. Namely, between time steps t_1 and t_2, corresponding to fluid sampling events, the variation of the total dissolved Mg molar quantity in the reactor, $\Delta n_{Mg(tot)}$ is equal to:

$$\Delta n_{Mg(tot)} = n_{Mg(added)} - n_{Mg(sampled)} - n_{Mg(pp)} \tag{6.8}$$

where $n_{Mg(added)}$ is the amount of Mg brought to the reactor from the inlet solution in the same time interval, estimated from the inlet flow rate and initial Mg concentration. $n_{Mg(sampled)}$ is the amount of Mg withdrawn from the reactor at t_2, estimated from the precisely monitored volume of sampled solution and its Mg concentration. $n_{Mg(pp)}$ is the amount of Mg precipitated in the reactor between t_1 and t_2. $\Delta n_{Mg(tot)}$ can be easily calculated from the volume of the reactive solution (updated based on the inlet flow rates and sampled volumes), and its Mg concentration at t_1 and at t_2.

The hydromagnesite precipitation rate between t_1 and t_2 (thereafter called "point-to-point" precipitation rate) can thus be estimated from:

$$R_{(pt\ to\ pt)} = \frac{n_{Mg(pp)}}{5 \cdot (t_2 - t_1) \cdot m_{\mathrm{Hmgs}} \cdot S_{\mathrm{BET}}} \tag{6.9}$$

though with a high uncertainty due to the small variation of Mg concentration between two successive time steps. Additional uncertainty came from a slight (maximum 5 %) decrease of inlet flow rates during the course of the experiment due to aging of the Tygon tubings. Calculated point-to-point precipitation rates were averaged over periods of 3 days, so as to smooth the variability introduced by slight analytical variations. Overall uncertainties reach at least 30 % of the calculated rates.

At the end of the experiments, the reactor was weighted with its cap, stirring bar, reactive solution and precipitated solids, so as to keep track of the changes of mass during the course of the experiment. It was verified that the measured final mass agreed to within 1 g with the final mass calculated from the successive point-to-point mass balance, therefore validating our calculation procedure.

Despite uncertainties, these point-to-point calculations allow to get information about the evolution of hydromagnesite precipitation rates as a function of saturation state during the course of a single experiment, between close to equilibrium conditions and steady-state growth conditions. Given the duration of the experiments, the calculated point-to-point rates can be assumed to represent some steady growth mechanism at the mineral surface.

Solution	T(°C)	Exp. Type	filling slt.		$MgCl_2$ (mol/kgw)	Na_2CO_3 (mol/kgw)	NaCl (mol/kgw)	FR (mL/h) Mg slt.	FR (mL/h) CO_3 slt.
H3	25	unseeded	0.1 M NaCl +	Slt. 1	$2.97{\cdot}10^{-2}$		0.100	0.871	
		air bubbling	7.5 mM Na_2CO_3	Slt. 2		$3.00{\cdot}10^{-2}$	0.100		0.859
H4	25	unseeded	0.1 M NaCl +	Slt. 1	$5.13{\cdot}10^{-2}$		0.100	0.911	
		air bubbling	12.5 mM Na_2CO_3	Slt. 2		$5.00{\cdot}10^{-2}$	0.100		0.906
H9	25	seeded	equil. pH 9.2	Slt. 1	$2.60{\cdot}10^{-2}$		0.037	0.356	
		No air bubbling		Slt. 2		$2.00{\cdot}10^{-2}$	0.056		0.358
H10	25	seeded	equil. pH 9.2	Slt. 1	$3.12{\cdot}10^{-2}$		0.022	0.382	
		No air bubbling		Slt. 2		$2.40{\cdot}10^{-2}$	0.045		0.380
H11	25	seeded	equil. pH 9.2	Slt. 1	$4.11{\cdot}10^{-2}$		-	0.351	
		No air bubbling		Slt. 2		$3.20{\cdot}10^{-2}$	0.030		0.337
H12	25	seeded	equil. pH 9.2	Slt. 1	$5.10{\cdot}10^{-2}$		-	0.370	
		No air bubbling		Slt. 2		$4.00{\cdot}10^{-2}$	0.038		0.372
H6	30	seeded	equil. pH 9.2	Slt. 1	$3.37{\cdot}10^{-2}$		0.022	0.537	
		air bubbling		Slt. 2		$2.40{\cdot}10^{-2}$	0.045		0.519
H8	30	seeded	equil. pH 9.2	Slt. 1	$5.43{\cdot}10^{-2}$		-	0.499	
		air bubbling		Slt. 2		$4.00{\cdot}10^{-2}$	0.038		0.505

Table 6.2 – Inlet solution composition for 25 and 30°C experiments performed using the discontinuous mixed-flow reactor setting. For each experiment, the composition of the two independent inlet solutions is reported. "slt" stands for "solution", "FR" for "flow rate". The "filling solution" column indicates the nature of the solution present in the reactor at the beginning of the experiment.

Table 6.2 provides a list of all experiments performed with the discontinuous mixed-flow reactor experimental setting. In addition to seeded experiments, two unseeded experiments were performed in similar conditions in order to analyze the precipitating phase (H3 and H4 in Table 6.2). In these preliminary experiments, the initial filling solution contained NaCl as well as Na_2CO_3, but no $MgCl_2{\cdot}6\,H_2O$.

These unseeded experiments as well as two seeded experiments (H6 and H8) were performed under continuous air bubbling, in order to maintain a constant P_{CO_2} and pH in the reactor. To minimize evaporation, air was saturated with water vapor by passing through a 0.1 M NaCl solution prior to introduction in the reaction vessel. However, air bubbling resulted in large disequilibrium between Mg^{2+} and CO_3^{2-} activities due to CO_2 degassing, and was therefore not used for subsequent experiments (H9-H12).

6.3.4 Higher temperature growth experiments

Steady-state hydromagnesite growth experiments at 50 and 75°C were performed using the well-known high temperature titanium mixed-flow reactor setting already used for experiments presented in Chapter 4, as well as by Saldi *et al.* (2012) for magnesite precipitation experiments. The experimental setting is presented in Chapter 2. Using the reverse solubility of hydromagnesite, it is possible to use a single inlet solution stored at ambient temperature, which is then undersaturated or only slightly supersaturated with respect to hydromagnesite (not enough though to provoke nucleation events in the mother solution).

At the beginning of the experiments, approximately 1 g of mineral powder was placed in the reactors filled with either deionized water, or with a solution close to saturation with respect to hydromagnesite, at the temperature and pH of interest. Reactors were quickly sealed and heated to the desired temperature, and inlet solution was injected into the reactor from

a 10 L polyethylene compressible bag with the aid of a HPLC pump, at flow rates ranging from 0.25 to 2 mL/min. Inside the reactor, the reactive solution was stirred at 250 rpm with a suspended Parr magnetic stirrer, and kept at constant temperature to within 1°C by a furnace connected to a thermocouple and a Parr temperature control device. The solution left the reactor through a 2 µm titanium frit, and was cooled down with a water refrigerating system before sampling. pH was measured at ambient temperature immediately after sampling. One sub-sample was stored at 4°C for alkalinity measurement; the other sub-sample was acidified and stored for subsequent Mg concentration measurement. Steady-state precipitation rates, indicated by a constant outlet Mg concentration over a minimum of three residence times, were calculated from the variation of Mg concentration between the inlet and the steady-state outlet fluid, $\Delta[Mg]_{\text{tot}}$, using eq. 6.7.

Compared to the low temperature discontinuous mixed-flow reactor setting, this experimental setting allows for a more precise monitoring of the flow rate, which can be directly measured by weighing outlet fluid samples. In addition, saturation state can be simply changed by changing inlet solution or flow rate. In the present case, experiments were run in series of different flow rates on the same seeds, while keeping the same inlet solution composition. Table 6.3 provides a list of inlet solution compositions used for all mixed-flow reactor experiments.

Solution	T(°C)	Exp. Type	filling slt.	inlet pH (25°C)	$MgCl_2$ (mol/kgw)	$NaHCO_3$ (mol/kgw)	NaCl (mol/kgw)	NaOH (mol/kgw)
H504B	50	MFR	mQ water	9.16	$2.59{\cdot}10^{-3}$	$1.06{\cdot}10^{-2}$	0.085	$2.65{\cdot}10^{-3}$
H504C-D	50	MFR	equil. pH 9.45	9.44	$2.62{\cdot}10^{-3}$	$1.06{\cdot}10^{-2}$	0.085	$3.16{\cdot}10^{-3}$
H505A-B	50	MFR	mQ water	9.42	$3.15{\cdot}10^{-3}$	$1.24{\cdot}10^{-2}$	0.084	$3.18{\cdot}10^{-3}$
H506A-E	50	MFR	equil. pH 9.45	9.45	$3.62{\cdot}10^{-3}$	$1.38{\cdot}10^{-2}$	0.076	$3.24{\cdot}10^{-3}$
H75A-C	75	MFR	equil. pH 8.85	8.83	$2.14{\cdot}10^{-3}$	$2.70{\cdot}10^{-2}$	0.071	$1.88{\cdot}10^{-3}$

Table 6.3 – Inlet solution composition for mixed-flow reactor experiments (MFR).

6.3.5 Solution preparation and chemical analysis

All reactive solutions were prepared with high purity deionized water (resistivity 18.2 MΩ), reagent grade NaCl, $MgCl_2{\cdot}6H_2O$, $NaHCO_3$ and high purity 1 M NaOH solutions (throughout the manuscript, the symbol "M" is used for "mol/L"). The NaCl concentration was adjusted to obtain an ionic strength close to 0.1 M in most experiments.

Experiments were performed in alkaline conditions, with solution pH chosen so as to limit supersaturation with respect to brucite and nesquehonite. For mixed-flow reactor experiments, the chemistry of inlet solutions was designed in order to obtain $a_{Mg^{2+}}/a_{CO_3^{2-}}$ ratios close to 1.25, corresponding to the magnesium to carbonate ratio of hydromagnesite structural formula. For low-temperature experiments (discontinuous mixed-flow system), this control was less well achieved (Tables 6.8 and 6.9).

Solution pH was measured with a standard Mettler Toledo glass electrode calibrated against NIST standard buffers (pH 4.01, 6.86, 9.18 at 25°C), with an uncertainty of 0.02 units. For solubility and growth experiments, pH measurements were performed at ambient temperature, and pH at the experimental temperature was recalculated with PHREEQC with the

above-mentioned database. The validity of these calculations was checked during solubility experiments carried out at 50°C: pH was occasionally measured *in situ* right after fluid sampling, with a glass electrode calibrated against buffers at the adequate temperature. It was verified that the pH measured directly at 50°C agreed closely with pH recalculated from ambient temperature pH measurements, Mg concentration and alkalinity.

Experimental solutions were analysed for magnesium concentration by flame atomic absorption spectroscopy using a Perkin Elmer AAnalyst 400 with an uncertainty of ±1% and a detection limit of 6×10^{-7} M. Alkalinity was measured by mean of automatic HCl titration on a Schott TitroLine Alpha Plus titrator, with an uncertainty of ±2% and a detection limit of 5×10^{-5} M.

6.4 Results

6.4.1 Natural hydromagnesite solubility product

Fig. 6.5 presents the evolution of dissolved Mg concentration throughout the course of the solubility experiments performed at 25 and 50°C. Stable Mg concentrations are reached after approximately 1150 hours at 25°C, and solution composition measured in the last two samples of the experiments, reported in Table 6.4, was estimated to be representative of equilibrium between the solution and hydromagnesite. At 50°C, a first plateau at constant pH is reached after 300 hours of experiments. Higher Mg concentrations are however reached after 1150 hours of experiments. All three or four last samples were considered for the calculation of solubility product at 50°C (see Table 6.4).

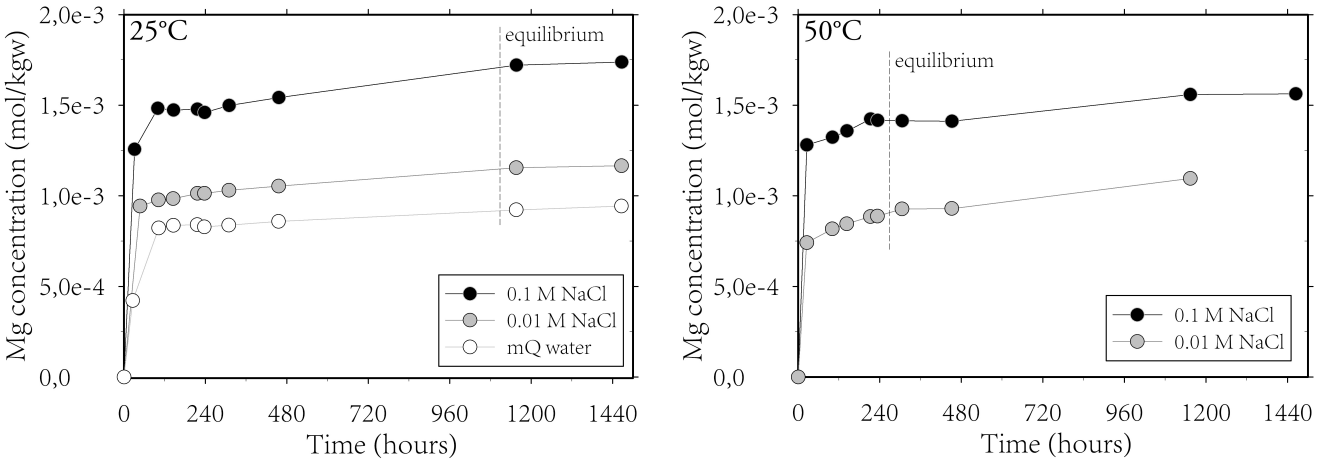

Figure 6.5 – Evolution of Mg concentration during the course of hydromagnesite solubility experiments at 25 and 50°C.

Solution speciation was calculated with PHREEQC based on the reported solution chemistry at equilibrium (Table 6.4). The apparent solubility products for reaction 6.1 at the temperature and ionic strength of interest, defined as

$$Q_{sp-Hmgs} = \frac{m(Mg^{2+})^5 \cdot m(HCO_3^-)^4}{m(H^+)^6} \tag{6.10}$$

are reported in Table 6.5 together with the corresponding ionic strengths and species molalities.

Run #	Time (hours)	T(°C)	NaCl (M)	pH (25°C)	$[Mg^{2+}]$ (mol/kgw)	Alk. (eq/kgw)
Hs25-1i	1157:00	25	0.10	10.40	$1.721 \cdot 10^{-3}$	0.00340
-1j	1467:30	25	0.10	10.32	$1.738 \cdot 10^{-3}$	0.00355
Hs25-2h	1156:25	25	0.01	10.42	$1.155 \cdot 10^{-3}$	0.00279
-2i	1467:00	25	0.01	10.24	$1.166 \cdot 10^{-3}$	0.00380
Hs25-3h	1156:00	25	0	10.60	$9.223 \cdot 10^{-4}$	0.00190
-3i	1466:30	25	0	10.51	$9.431 \cdot 10^{-4}$	0.00204
Hs50-1f	306:00	50	0.10	9.89	$1.424 \cdot 10^{-3}$	0.00307
-1g	452:50	50	0.10	9.90	$1.413 \cdot 10^{-3}$	0.00289
-1h	1154:30	50	0.10	9.90	$1.559 \cdot 10^{-3}$	0.00323
-1i	1465:00	50	0.10	9.93	$1.562 \cdot 10^{-3}$	0.00318
Hs50-2f	305:35	50	0.01	9.97	$9.256 \cdot 10^{-4}$	0.00196
-2g	452:25	50	0.01	9.97	$9.404 \cdot 10^{-4}$	0.00195
-2h	1154:00	50	0.01	9.98	$1.096 \cdot 10^{-3}$	0.00233

Table 6.4 – Chemical composition of samples retained for calculation of hydromagnesite solubility product at 25 and 50°C.

The solubility product can then be calculated from:

$$K_{sp-Hmgs} = Q_{sp-Hmgs} \frac{\gamma^5_{Mg^{2+}} \gamma^4_{HCO_3^-} a^6_{H_2O}}{\gamma^6_{H^+}} \tag{6.11}$$

where γ_i corresponds to the activity coefficient of the subscripted species, estimated from the mean background electrolyte stoichiometric activity coefficient $\gamma_{\pm(NaCl)}$, under the assumption that for an ion of charge z:

$$\gamma|z| = \gamma^{z^2}_{\pm(NaCl)} \tag{6.12}$$

$\gamma_{\pm(NaCl)}$ is derived from the Meissner equation (Meissner & Tester, 1972). The values at the ionic strength and temperature of interest were calculated with a software based on Archer (1992), and are reported in Table 6.5, together with water activity taken from (Busey & Mesmer, 1976) and the calculated solubility products $K_{sp-Hmgs}$. It should be noted that the Meissner activity model gives results that are close to the Davies model used to calculate chemical speciation in the present study.

The calculated $\log K_{sp-Hmgs}$ values have been plotted as a function of reciprocal temperature, together with literature data, in Fig. 6.6. Based on the measured solubility product, the standard molar Gibbs free energy of formation of hydromagnesite was calculated using the standard state properties of aqueous species involved in eq. 6.1. The values are reported in Table 6.6, together with additional values from the literature.

The natural hydromagnesite used in the present study has higher solubility than previously reported data. Its standard state Gibbs free energy of formation is relatively close to the value reported by Robie & Hemingway (1995), but is significantly higher than that of Xiong

(2011). This confirms the large variability of reported hydromagnesite solubility, which may in part be due to differences in cristallinity of the solid. The large differences observed with the data reported by Xiong (2011) may also be due to the lack of control of the actual CO_2 pressure and temperature in the latter experiments.

Run #	T(°C)	pH	I (mol/kgw)	m(Mg^{2+}) (mol/kgw)	m(HCO_3^-) (mol/kgw)	m(H^+) (mol/kgw)	log Qsp	$\gamma_{\pm(NaCl)}$	a_{H_2O}	log $K_{sp-Hmgs}$
Hs25-1i	25	10.40	0.1042	$1.45{\cdot}10^{-3}$	$4.06{\cdot}10^{-4}$	$5.11{\cdot}10^{-11}$	33.99	0.7745	0.996512	31.98
-1j	25	10.32	0.1043	$1.46{\cdot}10^{-3}$	$5.05{\cdot}10^{-4}$	$6.14{\cdot}10^{-11}$	33.91	0.7744	0.996509	31.90
Hs25-2h	25	10.42	0.0136	$8.60{\cdot}10^{-4}$	$4.33{\cdot}10^{-4}$	$4.28{\cdot}10^{-11}$	33.43	0.8894	0.999530	32.52
-2i	25	10.24	0.0142	$8.16{\cdot}10^{-4}$	$8.80{\cdot}10^{-4}$	$6.49{\cdot}10^{-11}$	33.46	0.8875	0.999510	32.53
Hs25-3h	25	10.60	0.0026	$6.81{\cdot}10^{-4}$	$1.99{\cdot}10^{-4}$	$2.66{\cdot}10^{-11}$	32.82	0.9462	0.999910	32.39
-3i	25	10.51	0.0027	$6.87{\cdot}10^{-4}$	$2.74{\cdot}10^{-4}$	$3.27{\cdot}10^{-11}$	32.85	0.9451	0.999906	32.41
									mean 25°C	**32.29** ±0.55 (2 σ)
Hs50-1f	50	9.53	0.1032	$1.22{\cdot}10^{-3}$	$1.22{\cdot}10^{-3}$	$3.81{\cdot}10^{-10}$	30.29	0.7676	0.996553	28.22
-1g	50	9.53	0.1030	$1.22{\cdot}10^{-3}$	$1.14{\cdot}10^{-3}$	$3.80{\cdot}10^{-10}$	30.18	0.7677	0.996557	28.10
-1h	50	9.54	0.1035	$1.33{\cdot}10^{-3}$	$1.26{\cdot}10^{-3}$	$3.72{\cdot}10^{-10}$	30.59	0.7674	0.996543	28.52
-1i	50	9.56	0.1034	$1.33{\cdot}10^{-3}$	$1.20{\cdot}10^{-3}$	$3.55{\cdot}10^{-10}$	30.64	0.7675	0.996544	28.56
Hs50-2f	50	9.54	0.0126	$7.64{\cdot}10^{-4}$	$8.83{\cdot}10^{-4}$	$3.24{\cdot}10^{-10}$	29.13	0.8879	0.999562	28.20
-2g	50	9.54	0.0127	$7.78{\cdot}10^{-4}$	$8.77{\cdot}10^{-4}$	$3.25{\cdot}10^{-10}$	29.15	0.8878	0.999561	28.22
-2h	50	9.57	0.0131	$8.79{\cdot}10^{-4}$	$1.01{\cdot}10^{-3}$	$3.07{\cdot}10^{-10}$	29.82	0.8864	0.999547	28.87
									mean 50°C	**28.38** ±0.55 (2 σ)
									extrapolation to 75°C	**24.90** ±0.65

Table 6.5 – Results of solubility product calculations at 25 and 50°C, and extrapolation to 75°C.

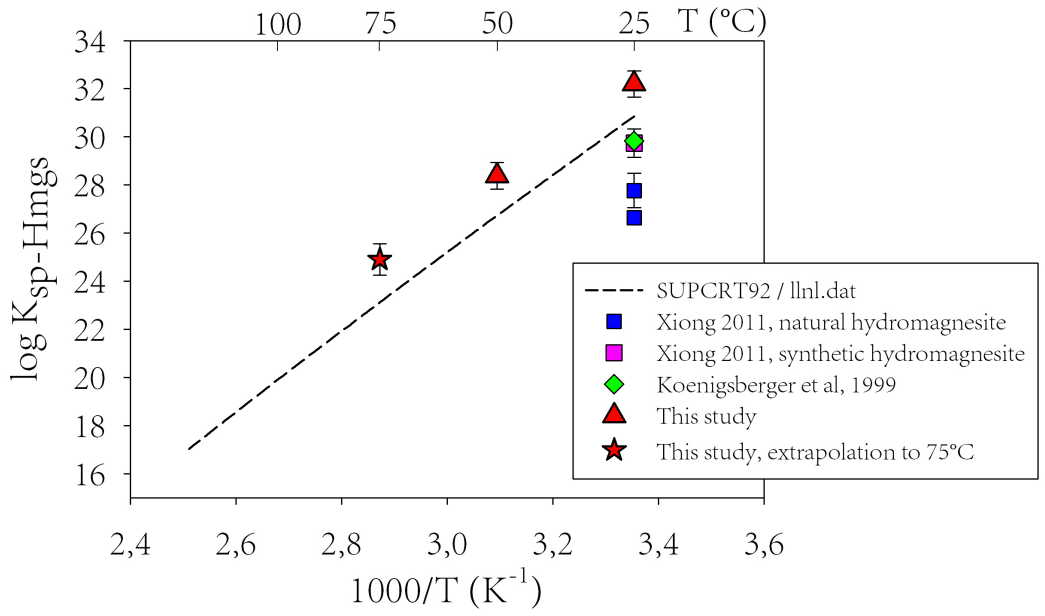

Figure 6.6 – Logarithm of the solubility product of hydromagnesite obtained in this study versus reciprocal temperature, and comparison to literature values.

The mean reaction enthalpy between 25 and 50°C (-287.8 ± 81 kJ.mol^{-1}) is within experimental uncertainty from the value proposed by SUPCRT92, as shown by the similar slopes

on Fig. 6.6. The SUPCRT92 reaction enthalpy at 50°C was therefore used together with the reaction heat capacity at the same temperature to extrapolate our data to 75°C, assuming constant heat capacity between 50 and 75°C. The corresponding data point has been reported in Table 6.5, and plotted in Fig.6.6. Retrieved solubility products were entered into PHREEQC `llnl.dat` database in order to accurately calculate solution saturation state with respect to hydromagnesite.

Hydromagnesite	$\log K_{sp}$ (25°C)	ΔG_f^0 kJ/mol	S_f^0 J/mol/K	ΔH_f^0 kJ/mol	C_p^0 J/mol/K	Reference
	30.85	-5864.66	541.3	**-6514.9**	**571.1**	SUPCRT92, taken from Helgeson (1978)
natural		-5864.2	503.7	-6514.9		Robie & Hemingway (1995)
synthetic		-5871.5				Königsberger *et al.* (1992)
synthetic	29.83	-5870.2	520.0	-6516.0		Königsberger *et al.* (1999)
natural	27.77	-5889 ± 4 (1)				Xiong (2011)
natural	26.63	-5896 ± 2 (1)				Xiong (2011)
synthetic	29.74	-5878 ± 3 (1)				Xiong (2011)
natural	**32.20**	**-5855.6 ± 3**				**This study**
Aqueous species		ΔG_f^0 kJ/mol	S_f^0 J/mol/K	ΔH_f^0 kJ/mol	C_p^0 J/mol/K	
Mg^{2+}		-454.0	-138.1	-466.0	-22.3	Shock & Helgeson (1988)
CO_3^{2-}		-527.98	-50.00	-675.24	-289.53	Shock & Helgeson (1988)
$CO_{2(g)}$		-394.36	213.74	-393.51	37.24	SUPCRT92
HCO_3^-		-586.77	91.2	-691.99	-35.40	Wagman *et al.* (1982)
H_2O		-237.13	69.95	-285.83	75.19	Wagman *et al.* (1982)
OH^-		-157.24	-10.75	-229.99	-148.5	Wagman *et al.* (1982)

Table 6.6 – Values of hydromagnesite solubility product at 25°C and standard state properties of hydromagnesite (25°C, 1 bar) reported in the literature. Bold values in the upper table are the values obtained or used in thise study. The standard state properties of aqueous and gaseous species used for determination of the standard Gibbs free energy of formation of hydromagnesite in the present study are reported in the lower table.
(1) Note that when we recalculated the standard state molar Gibbs free energies of formation of hydromagnesite from Xiong (2011), we obtained values 8 kJ/mol higher than the values obtained by the author and reported here. This is likely due to a different set of standard state properties used to calculate ΔG_f^0, which is not reported by Xiong (2011).

6.4.2 Hydrated Mg-carbonate precipitation kinetics

Control of the precipitating phase

Speciation calculation with PHREEQC indicates that our experimental solutions are not only supersaturated with respect to hydromagnesite, but also with respect to magnesite (Ω_{Mgs} up to 130 in seeded experiments at 25°C) and artinite $Mg_2CO_3(OH)_2{\cdot}3\,H_2O$. Although formation of magnesite is unlikely at temperatures of 75°C and lower (Hänchen *et al.*, 2008; Saldi *et al.*, 2009), and artinite is expected to form only at temperatures lower than ca. 15°C (Königsberger *et al.*, 1999), a variety of hydrated Mg-carbonate minerals may form, whose thermodynamic parameters are poorly known (e.g Davies & Bubela, 1973; Hopkinson *et al.*, 2012). In addition, a few experimental solutions were slightly supersaturated with respect to

brucite at 25°C and 50°C ($\Omega_{brucite}$ up to 3). It was thus important to control the nature of the precipitating mineral phase.

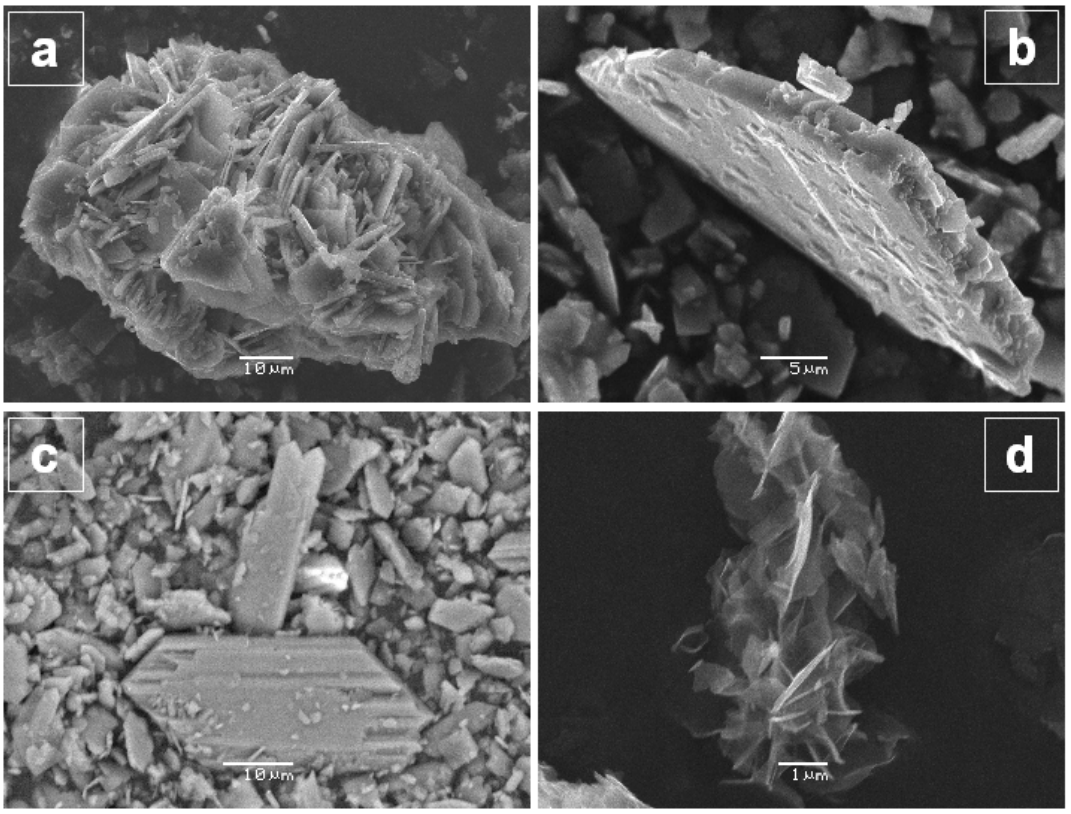

Figure 6.7 – SEM images of seed crystals after growth experiments. (a) Hydromagnesite agglomerate formed during precipitation at 25°C (secondary electrons). (b) Close-up view of the edge of one hydromagnesite crystal grown at 25°C (SE image). (c) BSE image of individual hydromagnesite crystals obtained after growth at 75°C. The (1 0 0) face is clearly visible. (d) SE image of dypingite obtained in unseeded experiments at 25°C.

To this extent, X-ray diffraction, SEM observations and EDS analyses were systematically performed on all solids recovered at the end of the experiments. In seeded experiments, X-ray diffraction patterns only revealed the presence of hydromagnesite. The mineral occurs under the form of agglomerated or individualized single crystals with a "platelet" shape similar to that of the seeds (Fig. 6.7a, b and c). Thermo-gravimetric analyses, performed on a few samples, show patterns similar to the seeds' (Fig. 6.3, red curve). Small variations in the TGA curve may be related to the bigger grain size of the precipitated material (Hollingbery & Hull, 2010b).

Though highly supersaturated with respect to hydromagnesite, unseeded experiments (H3 and H4, Tables 6.2 and 6.8) led to the formation of dypingite only $Mg_5(CO_3)_4(OH)_2 \cdot 5H_2O$, as shown by X-ray diffraction. This is in accordance with experiments performed by Mavromatis *et al.* (2012) in similar abiotic conditions. The less supersaturated experiment H3 produced a poorly crystalline dypingite, with relatively wide peaks. Thermo-gravimetric analysis on H4 precipitate indicates a 59.01 % weight loss upon heating from 30 to 1000°C, in good agreement with the theoretical value of 58.51 % based on dypingite structural formula,

thus confirming the precipitate stoichiometry. A representative SEM picture of the mineral is displayed in Fig. 6.7d.

Evolution of the reactive surface area

Determining the evolution of reactive surface area during the course of growth experiments is critical to correctly normalize growth rates retrieved from long-term experiments as those performed at 25°C, or from series of experiments performed on a single mineral sample as those performed with mixed-flow reactors.

BET measurements performed on the finally recovered minerals indicate that their specific surface area does not vary, within uncertainties, during the course of the experiments. However, upon mineral growth, the mass of seeds increases, thus providing more total surface on which further growth may proceed. In experiment H506 (Table 6.3) for instance, the precipitated mineral mass equals that of the initial seeds, although in most experiments, the gain is between 7 and 50 % of the initial seeds mass. The gain of total surface is thus substantial.

Observations of hydromagnesite pristine crystals morphology reveal that most of their surface is constituted by the (1 0 0) face, which corresponds to the plane surfaces of platelets shown in Fig. 6.1a. This morphology suggests that most of the growth proceeds at the crystal edges. Therefore, it can be hypothesized that crystal growth creates surface mostly through enlargement of the (1 0 0) face, while the reactive surface area constituted by the edges remains to a large extent unchanged.

Upon grinding, many edges growth sites are created by the breaking of pristine crystals (see Fig 6.7b, which shows the fractured aspect of crystal edges). Small crystal fragments have a relatively larger proportion of their total surface constituted by edges, such that the initially measured BET surface area can be assumed to be relatively close from the actual reactive surface area.

At the end of growth experiments, recovered minerals are on average larger in size (and surface) than the initial highly fragmented seed material, while their thickness does not significantly vary. Some crystals exhibit an automorphic shape with a fully developed (1 0 0) face (Fig. 6.7c), which presumably developed from crystal fragments. These observations confirm that growth proceeds mainly from the edges of crystals, which should therefore be considered as the actual reactive surface. A similar conclusion was for instance proposed for the gibbsite mineral by Molis *et al.* (2000), on the basis of ligand-promoted dissolution experiments.

Because estimating the surface represented by edges is a particularly difficult task, we used the specific BET surface area measured on the initial fragmented seed material as a proxy for the "reactive" surface area, which was used to normalize all growth rates. It is however possible that this assumption overestimates the reactive surface area, since possibly unreactive (100) faces still represent a big proportion of the initially measured surface. The important point here, however, is that we assumed that the surface of edges varied negligibly during the course of growth experiments.

Hydromagnesite precipitation rates as a function of saturation state

Fig. 6.8 provides two examples of the evolution of Mg concentration and the approach of steady-state during the course of experiments performed respectively at 25°C in the discontinuous mixed-flow reactor setting, and 50°C in the classical mixed-flow reactor systems.

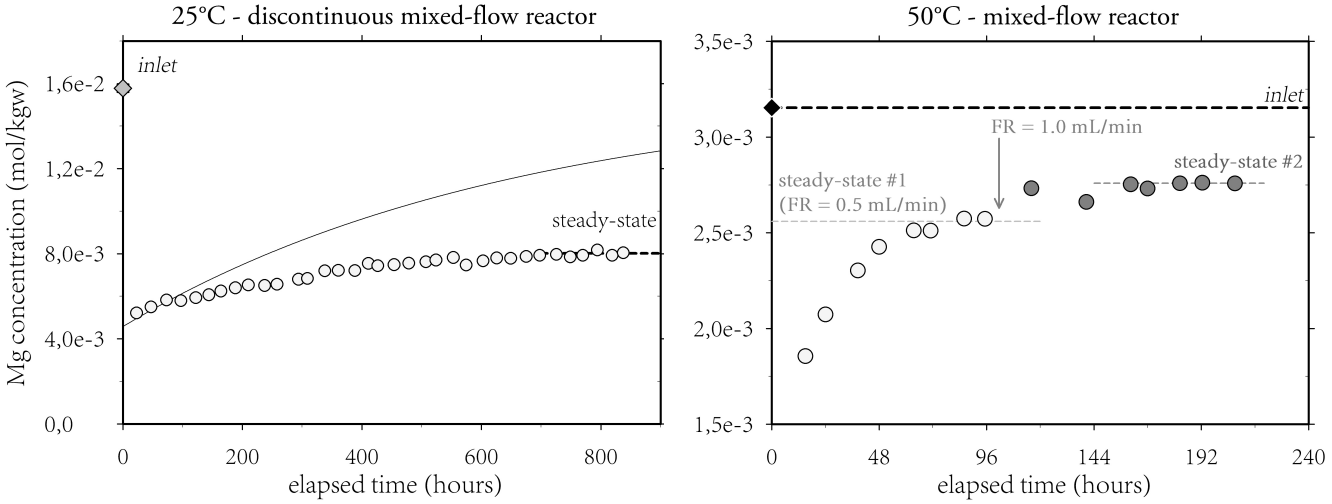

Figure 6.8 – Representative evolution of Mg concentration in the outlet fluid as a function of time during growth experiments performed at 25°C (exp. H10), and at 50°C (exp. H505). At left, the solid line represents the theoretical evolution of Mg concentration if no precipitation was taking place. At right, the graph presents a series of two experiments with different flow rates performed on the same mineral seeds. Analytical uncertainty is smaller than the symbol size.

The results of all steady-state hydromagnesite experiments are summarized in Tables 6.8 and 6.9. The results of "point-to-point" rate calculations from experiments at 25°C are reported in Appendix A.
The logarithm of eq. 6.5 is written:

$$\log R = \log(k_{Hmgs}) + n \log(\Omega^{0.2} - 1) \tag{6.13}$$

Accordingly, the logarithm of hydromagnesite precipitation rates at 25, 30 and 50 and 75°C have been plotted as a function of $\log(\Omega^{0.2} - 1)$ in Fig. 6.9a, b and c. The dashed lines correspond to $n = 1$, and such a rate law satisfyingly fits all the data. The unit rate order indicates that hydromagnesite growth is either diffusion-controlled, or controlled by adsorption of growth units onto mineral surface (Nielsen, 1984). Since experiments were performed in well-mixed conditions, and measured hydromagnesite growth is slow, it is unlikely that the growth rates are controlled by diffusion of reactants from the reactive solution.

The rate constants k_{Hmgs} retrieved with a unit rate order are reported in Table 6.7, together with the best fit parameters for each temperature series. An Arrhenius plot of rates constants obtained with $n = 1$ is shown in Fig. 6.9d, which is consistent with an activation energy of 45.5 ± 9 kJ.mol^{-1}. Note that this activation energy is a lot higher than typical activation en-

ergies for diffusion-controlled processes (10 - 18 kJ/mol, Nielsen, 1984). Therefore, the linear growth rate likely stems from an adsorption-controlled growth mechanism, with subsequent incorporation of crystal units to growth sites presumably existing on hydromagnesite crystals edges.

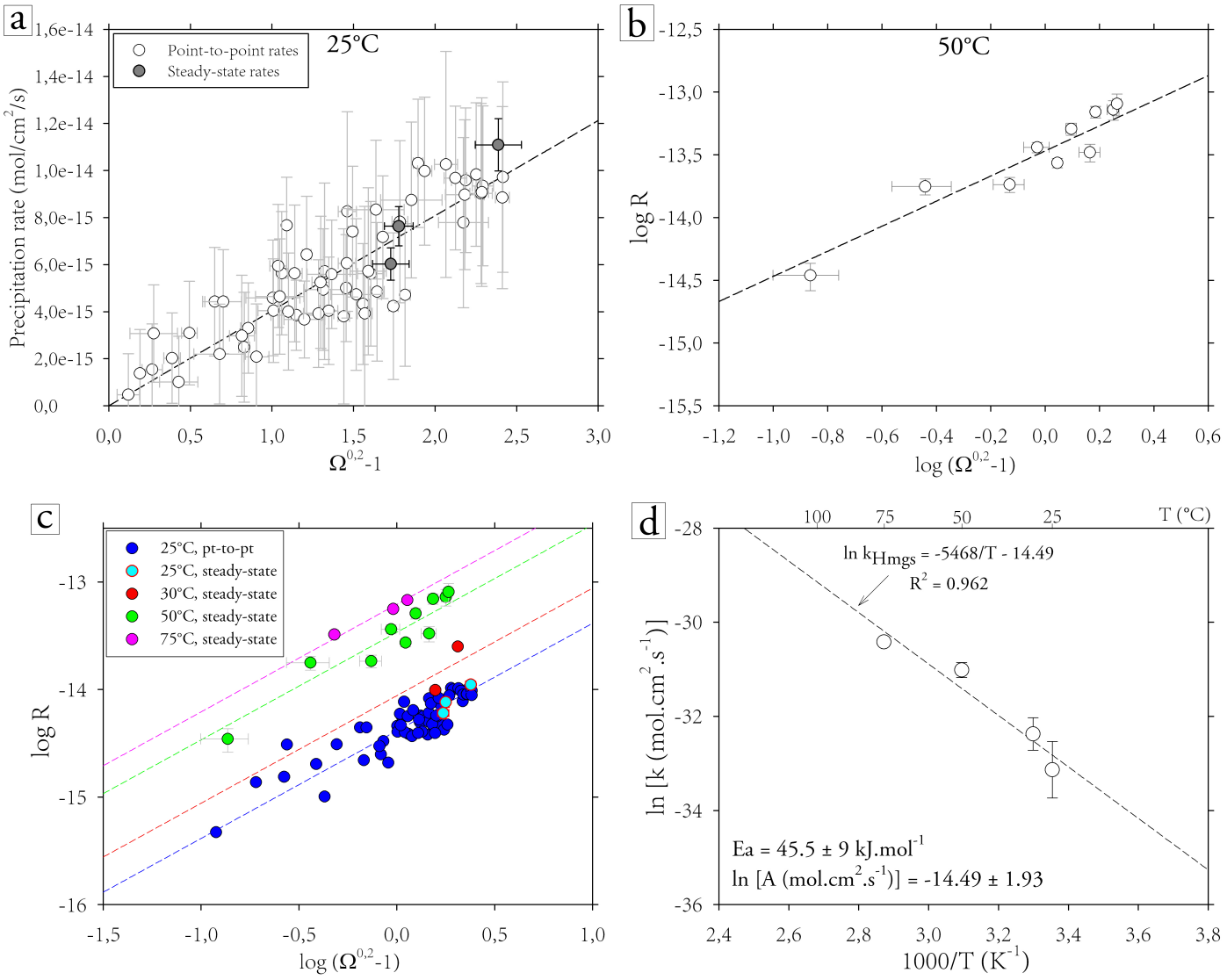

Figure 6.9 – (a) to (c) Plots of measured hydromagnesite growth rates versus supersaturation. Dashed lines slopes correspond to unit rate order. Error bars on "point-to-point" rates at 25°C have been omitted for clarity sake. Unless represented, error bars on "steady-state" rates are smaller than the symbol size. (d) Arrhenius plot of the rate constants obtained for $n = 1$.

T (°C)	n	$\log k_{Hmgs}$ (mol.cm^2.s^{-1})	R^2
25	0.85 $\pm$ 0.06	-14.37 $\pm$ 0.23	0.780
	1	-14.39 $\pm$ 0.26	0.756
30	1	-14.06 $\pm$ 0.15	-
50	1.08 $\pm$ 0.10	-13.46 $\pm$ 0.07	0.916
	1	-13.47 $\pm$ 0.07	0.911
75	0.84 $\pm$ 0.06	-13.22 $\pm$ 0.05	0.996
	1	-13.21 $\pm$ 0.08	0.959

Table 6.7 – Values of rate order n and rate constants k_{Hmgs} obtained from the fit of growth rates plotted in Fig. 6.9. Best fit values and values obtained with $n = 1$ are reported.

Unseeded experiments: dypingite precipitation rate

Unseeded experiment H4 performed at 25°C precipitated dypingite, as determined by X-ray diffraction. Based on steady-state outlet Mg concentration, we calculated a precipitation rate, which was normalized to the final surface area, based on the mass and the BET specific surface area of the seed material recovered at the end of the experiment.

The obtained value, 3.85 $\pm$ 1.57 $\cdot$ 10^{-15} mol.cm^2.s^{-1}, reported in Table 6.8, is of the same order of magnitude as the measured hydromagnesite precipitation rates. However, because dypingite solubility product is not known, it was not possible to calculate the saturation state corresponding to experiment H4. The saturation state with respect to hydromagnesite is particularly high, as reported in Table 6.8, but this information is of little interest to compare dypingite and hydromagnesite precipitation rates, since both minerals may have very different solubilities.

This is however the first measurement of dypingite precipitation rates, and offers the possibility for a comparison between various hydrated Mg-carbonates growth rates as soon as the thermodynamic parameters for dypingite become available.

Exp.	T (°C)	Ω_{Hmgs}	outlet pH (25°C)	Exp. pH (@ T)	I (mol/kgw)	[Mg] inlet (mol/kgw)	Δ [Mg]*10^3 (mol/kgw)	Alk.*10^2 (eq/L)	a(Mg^{2+}) $*10^3$	a(CO_3^{2-}) $*10^3$	$\frac{a(Mg^{2+})}{a(CO_3^{2-})}$	seed mass (g)	FR (mL/h)	Rate * 10^{15} (mol/cm^2/s)
H9	*did not reach steady state*													
H10	25	151.2 ± 33.8	9.66 (2)	9.66	0.090	$1.578{\cdot}10^{-2}$	7.641 ± 0.296	0.879(5)	2.497	0.504	4.95	1.5155	0.766	6.03 ± 0.69
H11	25	165.2 ± 27.7	9.44 (2)	9.44	0.088	$2.149{\cdot}10^{-2}$	10.663 ± 0.357	1.088(2)	3.345	0.464	7.21	1.5214	0.693	7.63 ± 0.83
H12	25	446.0 ± 101.4	9.49 (2)	9.49	0.098	$2.559{\cdot}10^{-2}$	14.419 ± 0.359	1.255(10)	3.330	0.560	5.95	1.5054	0.742	11.09 ± 1.11
H6	30	112.6 ± 15.8	9.20 (1)	9.11	0.120	$1.712{\cdot}10^{-2}$	4.829 ± 0.137	1.406(9)	3.574	0.389	9.18	0.8081	1.057	9.85 ± 1.03
H8	30	263.4 ± 32.8	9.20 (1)	9.11	0.122	$2.697{\cdot}10^{-2}$	12.821 ± 0.256	1.535(6)	4.063	0.411	9.88	0.8016	1.003	25.04 ± 2.39
Unseeded experiments (dypingite precipitation)														
H3	25	6786	9.49 (2)	9.49	0.161	$1.572{\cdot}10^{-2}$	1.216	2.726	3.296	1.131	2.91	*disordered dypingite precipitation*		
H4	25	13836	9.42 (2)	9.42	0.188	$2.604{\cdot}10^{-2}$	8.503	3.428	3.753	1.247	3.01	0.9	1.816	3.85 ± 1.57

Table 6.8 – Results of steady-state precipitation experiments performed with discontinuous mixed-flow reactor settings at 25 and 30°C.

Exp.	T (°C)	Ω_{Hmgs}	outlet pH (25°C)	Exp. pH (@ T)	I (mol/kgw)	[Mg] inlet (mol/kgw)	Δ [Mg]*10^3 (mol/kgw)	Alk.*10^2 (eq/L)	a(Mg^{2+}) $*10^3$	a(CO_3^{2-}) $*10^3$	$\frac{a(Mg^{2+})}{a(CO_3^{2-})}$	seed mass (g)	FR (mL/h)	Rate * 10^{15} (mol/cm^2/s)
H504B	50	1.9 ± 0.3	9.13 (2)	8.85	0.102	$2.591{\cdot}10^{-3}$	0.154 ± 0.030	1.132(1)	0.694	0.314	2.21	1.0314	0.248	3.47 ± 0.85
H504C	50	4.7 ± 1.8	9.35 (2)	9.01	0.102	$2.616{\cdot}10^{-3}$	0.533 ± 0.049	1.172(8)	0.577	0.417	1.39	1.1168	0.396	17.72 ± 2.56
H504D	50	16.0 ± 4.9	9.33 (3)	9.08	0.103	$2.616{\cdot}10^{-3}$	0.318 ± 0.027	1.222(4)	0.620	0.482	1.29	1.1168	0.689	18.34 ± 2.51
H505A	50	41.7 ± 2.7	9.34 (1)	9.09	0.105	$3.150{\cdot}10^{-3}$	0.603 ± 0.020	1.385(8)	0.667	0.556	1.20	1.0317	0.499	27.27 ± 2.31
H505B	50	90.4 ± 26.3	9.38 (3)	9.13	0.105	$3.150{\cdot}10^{-3}$	0.369 ± 0.035	1.426(2)	0.704	0.600	1.17	1.0317	0.988	33.07 ± 5.35
H506A	50	27.1 ± 7.9	9.32 (1)	8.98	0.099	$3.620{\cdot}10^{-3}$	0.893 ± 0.026	1.510(1)	0.727	0.506	1.44	0.9071	0.394	36.29 ± 3.44
H506B	50	57.4 ± 7.4	9.28 (1)	9.03	0.099	$3.620{\cdot}10^{-3}$	0.707 ± 0.041	1.539(2)	0.753	0.557	1.35	0.9071	0.697	50.84 ± 5.64
H506C	50	104.1 ± 11.8	9.32 (1)	9.07	0.099	$3.620{\cdot}10^{-3}$	0.615 ± 0.032	1.557(5)	0.773	0.598	1.29	0.9071	1.095	69.52 ± 7.34
H506D	50	166.4 ± 28.6	9.34 (1)	9.08	0.100	$3.660{\cdot}10^{-3}$	0.471 ± 0.058	1.577(5)	0.819	0.615	1.33	0.9071	1.489	72.46 ± 12.84
H506E	50	184.1 ± 22.1	9.34 (1)	9.09	0.100	$3.660{\cdot}10^{-3}$	0.392 ± 0.057	1.598(1)	0.819	0.628	1.30	0.9071	1.996	80.67 ± 15.92
H75A	75	7.1 ± 0.4	8.67 (0)	8.35	0.102	$2.138{\cdot}10^{-3}$	0.638 ± 0.031	2.695(13)	0.334	0.310	1.08	0.9175	0.498	32.40 ± 3.28
H75B	75	28.8 ± 3.8	8.75 (1)	8.42	0.102	$2.138{\cdot}10^{-3}$	0.549 ± 0.031	2.732(9)	0.370	0.359	1.03	0.9175	1.001	56.06 ± 6.01
H75C	75	44.0 ± 6.0	8.76 (1)	8.43	0.102	$2.138{\cdot}10^{-3}$	0.444 ± 0.019	2.736(1)	0.390	0.368	1.06	0.9175	1.494	67.70 ± 6.38

Table 6.9 – Results of steady-state precipitation experiments performed at 50 and 75°C with titanium mixed-flow reactors.

6.5 Discussion

6.5.1 Comparison with the literature

Our results indicate that hydromagnesite growth rate obeys a linear rate law consistent with the transition state theory. To the best of our knowledge, the only other existing study of hydromagnesite precipitation rates is the one recently published by Wang & Li (2012). The authors studied hydromagnesite nucleation and growth rate at 80°C from highly supersaturated ($\Omega_{\mathrm{Hmgs}} = 10^9$ to 10^{15}), high ionic strength solutions, using a "mixed-suspension mixed-product removal crystallizer".

According to Wang & Li (2012), their growth rates are consistent with the following rate law:

$$G_L\,[\mathrm{m/s}] = 3.42 \cdot 10^{-10} * \left(\Omega^{1/15} - 1\right)^{0.94} \tag{6.14}$$

where $\Omega^{1/15}$ stems from an empirical definition of the saturation state by Nielsen (1984). In order to obtain growth rates directly comparable to our data, it is necessary to divide growth rates reported by Wang & Li (2012) by hydromagnesite molar volume (V_M = 201.57 cm^3/mol). One obtains:

$$R_L\left[\mathrm{mol/cm^2/s}\right] = 1.70 \cdot 10^{-10} * \left(\Omega^{1/15} - 1\right)^{0.94} \tag{6.15}$$

When using a rate law of the type of eq. 6.15 to fit our data at 75°C, we obtain a growth rate constant of $2.29 \cdot 10^{-13}$ $\mathrm{mol/cm^2/s}$ (rate order 0.995), nearly three orders of magnitude lower than the rate constant obtained at 80°C from the data of Wang & Li (2012).
Several factors may explain this important discrepancy:

- Wang & Li (2012) implicitly consider the reactive surface area to be the geometrical surface of pseudo-spherical hydromagnesite agglomerates precipitated in their experiments. However, SEM pictures indicate that the particles are built by "*a large number of thin sheets*", which indicates that the actual reactive surface probably exceeds by far the geometrical surface area.

- Nucleation and growth proceeded at extremely high saturation state in Wang & Li (2012) experiments. Rate law 6.14 indicates a unit rate order, which could reflect a diffusion-limited growth process (Nielsen, 1984). At the mineral surface, it is possible that growth proceeds through spiral growth or two-dimensional nucleation, at a much higher rate than adsorption-controlled growth (Shiraki & Brantley, 1995; Teng *et al.*, 2000).

- High ionic strengths (several mol/kg) used in Wang & Li (2012) experiments decrease water activity, which in turn may facilitate cation dehydration and increase crystal growth rate (e.g Kowacz & Putnis, 2008).

- It cannot be excluded that the mineral originally precipitated by Wang & Li (2012) is actually not only hydromagnesite, but contains nesquehonite or dypingite. The authors indeed reported the presence of nesquehonite in powders precipitated at 25 or 35°C, and dypingite at 70°C. Powders were air-dried at 80°C for 10h before SEM observations and XRD analysis, which could have altered their mineralogy: nesquehonite is known to transform into hydromagnesite within a few tens of hours above 50°C (Davies & Bubela, 1973), with dypingite being a likely intermediate in this transformation (Hopkinson *et al.*, 2008). It is

therefore possible that the nucleation and growth of an additional, more hydrated, Mg-carbonate phase has increased the apparent hydromagnesite growth rates reported by the authors.

6.5.2 Influence of Mg^{2+} dehydration on Mg-carbonates growth rates

Metal cations in aqueous solutions are surrounded by an hydration sphere (Burgess, 1999) which they have to lose prior to incorporation in a crystal edifice. It is widely accepted that this cation dehydration is the rate-controlling step for most ionic crystals precipitation (Nielsen, 1984; Piana *et al.*, 2006; Kowacz *et al.*, 2007). Given the highly hydrated character of Mg^{2+}, numerous authors hypothesized that the reluctance to precipitate the anhydrous form of Mg-carbonates originates in the difficulty to dehydrate Mg^{2+} (e.g Lippmann, 1973; Sayles & Fyfe, 1973; Pokrovsky & Schott, 2002; Hänchen *et al.*, 2006; Romanek *et al.*, 2009; Saldi *et al.*, 2009).

Based on this idea, Lippmann (1973) proposed a correspondence between the activation energy for carbonate mineral precipitation, and the hydration enthalpy of the constituting cation. As such, the author estimated the activation energy of magnesite precipitation to be significantly higher than that of calcite. This idea was verified by Arvidson & Mackenzie (2000) who observed that the activation energy of several Ca-Mg-carbonate minerals scales with the amount of Mg in the crystal structure.

Following Lippmann (1973), we may hypothesize that minerals with similar chemistry but different water contents should exhibit different activation energies. Because hydromagnesite contains 0.8 water molecules per magnesium atom, the lower need for Mg dehydration should result in a lower activation energy.

Our estimation of hydromagnesite activation energy in the temperature range 25°C < T < 75°C amounts to 45.5 ± 9 kJ.mol^{-1}, which is lower by approximately 40 kJ.mol^{-1} than magnesite growth activation energy in the temperature range 100°C < T < 150°C (see Fig. 6.10). However, magnesite growth proceeds through spiral growth (Saldi *et al.*, 2009), whereas hydromagnesite is interpreted to grow through an adsorption-controlled process. It is thus wiser to compare hydromagnesite apparent activation energy with the activation energy for magnesite step advancement, which is controlled as well by the adsorption of growth units onto kinks. Saldi *et al.* (2009) measured the activation energy for obtuse steps advancement in the temperature range 80°C < T < 120°C, and obtained a value of 159 ± 17 kJ.mol^{-1}, which is more than 100 kJ.mol^{-1} higher than the value obtained for hydromagnesite. Thus, our results support the hypothesis that a lesser need for dehydration results in lower activation energy.

Interestingly, Morales *et al.* (2012) compared the activation energy of step advancement for anhydrite ($CaSO_4$) between 60 and 120°C and gypsum ($CaSO_4 \cdot 2\,H_2O$) between 20 and 80°C. In contradiction with Lippmann (1973) hypothesis, it was observed that both activation energies are close to 72 kJ.mol^{-1}. As stated by Morales *et al.* (2012), this suggests that anhydrite growth is not limited by Ca^{2+} dehydration. Besides, the large difference between anhydrite and magnesite step advancement activation energy (about 90 kJ.mol^{-1}) outlines the large differences between Ca^{2+} and Mg^{2+} hydration state and water exchange rates in aqueous solution.

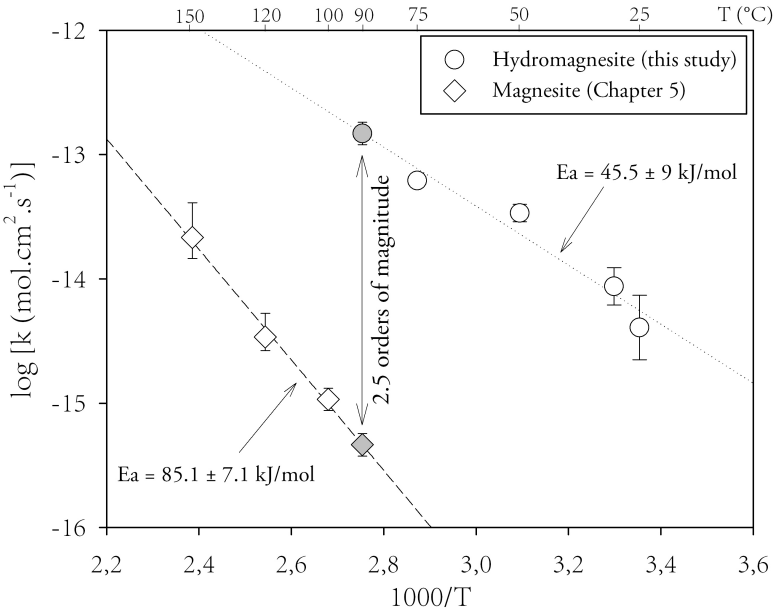

Figure 6.10 – Comparison of Arrhenius plots for magnesite in the temperature range 100°C < T < 200°C and hydromagnesite in the temperature range 25°C < T < 75°C. White datapoints correspond to experimentally retrieved growth rate constants, grey-filled points are extrapolations to 90°C. Hydromagnesite activation energy is significantly lower than magnesite's (see text).

Complete dehydration of Mg^{2+} therefore leads to high activation energies and very low precipitation rates for magnesite. In hydromagnesite, Mg^{2+} dehydration is incomplete; does this result in higher growth kinetics for the hydrated mineral, compared to the anhydrous form?

Kinetic rate constants obtained for hydromagnesite and magnesite growth (Chapter 3) have been plotted on an Arrhenius diagram in Fig. 6.10. On the basis of retrieved Arrhenius parameters, the kinetic rate constants were extrapolated to 90°C. We obtained $\log k_{\mathrm{Hmgs}} = -12.83 \pm 0.21$ and $\log k_{\mathrm{Mgs}} = -15.33 \pm 0.09$. Thus at 90°C, hydromagnesite rate constant is higher by 2.5 orders of magnitude compared to magnesite's. Due to the different "bulk" activation energies, this difference is exacerbated at lower temperatures, and tends to be lowered at higher temperatures.

It should however be noted that the growth rate laws differ for the two minerals. The rate law for hydromagnesite is given by eq. 6.5 with $n = 1$, while that of magnesite is given by (Saldi *et al.*, 2012 and Chapter 3):

$$R_{\mathrm{Mgs}} = k_{Mgs}(\Omega_{\mathrm{Mgs}} - 1)^2 \tag{6.16}$$

Comparing rate constants is therefore not sufficient to grasp the differences in growth rates between magnesite and hydromagnesite. In addition, because hydromagnesite and magnesite have different structural formulae and stoichiometry, it is not straightforward to compare their saturation states.

To solve this issue, we used the chemical affinity concept. The chemical affinity A of a growth reaction is equal to $-RT \ln \Omega$, such that different expressions for Ω result in different and incomparable expressions for A. Therefore, we normalized the chemical affinity for hy-

dromagnesite precipitation to one Mg, in order to compare both growth rates at comparable state of thermodynamic disequilibrium. In addition, hydromagnesite growth rates were multiplied by a factor of 5 in order to normalize rates in terms of mineral Mg content.

Figure 6.11 presents the calculated growth rates of magnesite and hydromagnesite at 90°C as a function of chemical affinity, using for both minerals the rate constants extrapolated to 90°C (Fig. 6.10). Hydromagnesite rates are higher by several orders of magnitude compared to magnesite rates, which indeed supports the idea that Mg^{2+} dehydration limits the rate of magnesite precipitation, and that hydrated minerals are less kinetically inhibited than their anhydrous counterparts. As supersaturation increases (chemical affinity decreases), magnesite growth rate increases faster than hydromagnesite's due to its second-order rate law.
It should also be noted that hydromagnesite precipitation rates remain significantly lower than calcite rates, which are about 6 orders of magnitude higher than magnesite's (Shiraki & Brantley, 1995; Saldi *et al.*, 2009).

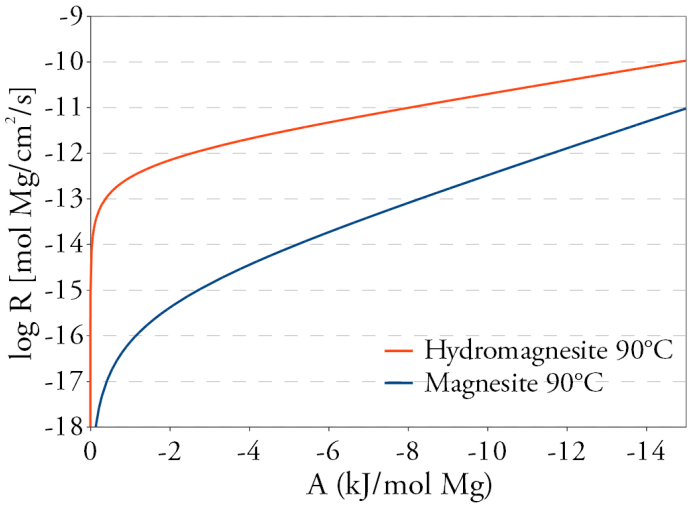

Figure 6.11 – Comparison of surface area-normalized hydromagnesite and magnesite growth rates at 90°C as a function of chemical affinity, normalized to one mole of Mg.

6.5.3 Which consequences for CO_2 mineral sequestration?

Hydromagnesite stores 0.8 moles of CO_2 per mole of Mg precipitated. This ratio is lower than that of magnesite, but because hydromagnesite forms at ambient temperature, it has attracted interest as a potential sink for CO_2 mineral sequestration (e.g Teir *et al.*, 2009; Power *et al.*, 2009; Wilson *et al.*, 2009). Furthermore, because the slow magnesite precipitation has been suggested to limit the process of forsterite carbonation between 100 and 150°C (Saldi *et al.*, 2012), it is important to determine whether hydromagnesite precipitation could accelerate the carbonation process (Guyot *et al.*, 2011).

In the preceding section, we have seen that at comparable saturation states, hydromagnesite precipitates more quickly than magnesite. However, because hydromagnesite is a lot more soluble than magnesite (Königsberger *et al.*, 1999; Bénézeth *et al.*, 2011), such conditions are not representative of natural conditions, or conditions envisioned for mineral carbonation. Therefore, we have simulated the evolution of surface area-normalized hydromagnesite and magnesite growth rates as a function of solution composition, at chosen conditions of

temperature, pH and P_{CO_2}.

Simulations were performed at [pH 9 and atmospheric PCO_2], and [pH 7 and P_{CO_2} = 1bar]. The former conditions are representative of surface alteration of ultramafic rocks, including mine tailings (e.g Bea *et al.*, 2012), while the latter were chosen to assess the influence of a lower pH and higher P_{CO_2} on hydromagnesite growth kinetics. Typical mineral carbonation conditions would however imply a pH around 6 and higher P_{CO_2} (Declercq & Oelkers, 2012). In these conditions however, hydromagnesite is highly soluble, such that its formation is unlikely.

In both cases, simulations were performed at 50 and 90°C so as to observe the interplay between mineral solubility (which decreases with increasing temperature) and growth rate constants (which increase with temperatures). Ionic strength was kept close to 0.1M by adjusting the background NaCl concentration. Magnesite rate constant was extrapolated to 50°C using the activation energy determined in Chapter 3. Note however that this activation energy determined above 100°C is likely not applicable to such low temperatures (Saldi *et al.*, 2009). This extrapolation should thus be viewed as a maximum estimation. The results of these simulations are presented in Fig. 6.12.

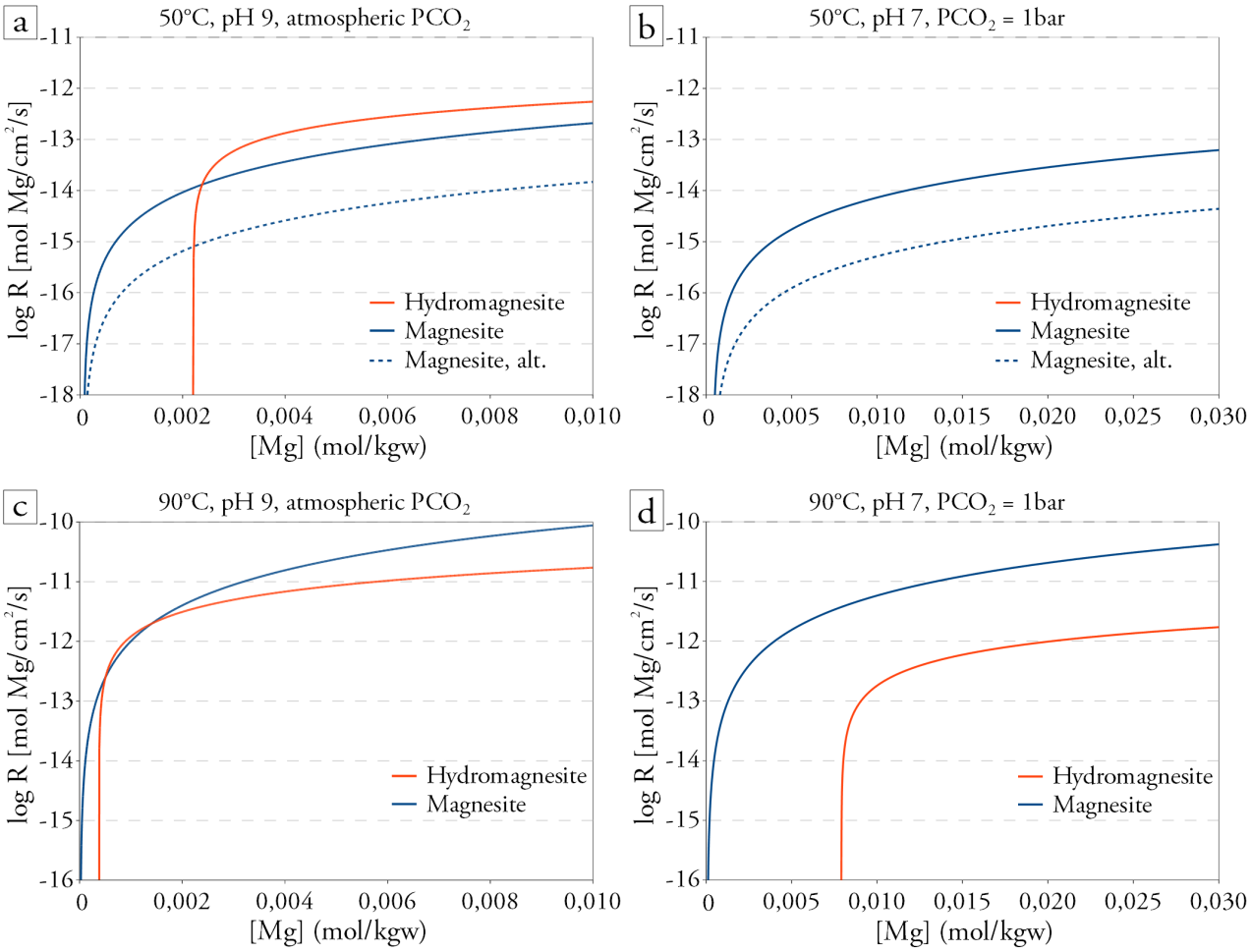

Figure 6.12 – Hydromagnesite and magnesite growth rates as a function of Mg concentration for different case studies (see text). The absence of hydromagnesite curve in graph (b) reveals that hydromagnesite always remains undersaturated in this simulation. The dotted lines in graphs (a) and (b) are magnesite growth rates predicted with a rate constant of 10^{-18} mol/cm^2/s, and materialize the impact of a lower-than-extrapolated magnesite growth rate constant at 50°C.

At pH 9 and 50°C (Fig. 6.12a), hydromagnesite growth rates quickly passes magnesite's after its solubility is reached. The difference in surface area-normalized growth rates remains moderate (half an order of magnitude), but increases if a lower magnesite growth rate is considered (dotted line). At pH 9 and 90°C, magnesite rates remain higher, except for a narrow range of Mg concentration. At pH 7, hydromagnesite solubility is never exceeded in the investigated conditions at 50°C (Fig. 6.12b), while at 90°C, hydromagnesite rates always remain far lower than magnesite rates due to its low saturation state.

Thus these growth rates comparisons reveal that in natural or industrial conditions, hydromagnesite growth rates may exceed magnesite's only at high pH and low temperature, while conditions typical for direct forsterite or serpentine carbonation (i.e, slightly acidic pH and high PCO_2) are clearly unfavourable for hydromagnesite growth.

Surprisingly however, hydromagnesite formation has been observed at temperatures of 120°C and under 3 bars of CO_2 pressure (Hänchen *et al.*, 2008), and up to 160°C in batch

forsterite carbonation experiments performed in slightly alkaline conditions under low CO_2 pressure (King *et al.*, 2010). In these unfavourable conditions for hydromagnesite growth, nucleation kinetics must thus play a crucial role in the apparition of hydromagnesite, which indicates that magnesite nucleation may be even more kinetically inhibited than magnesite growth, as suggested by Lippmann (1973). It is as well likely that hydromagnesite, as an hydrated mineral, has a lower surface free energy compared to magnesite, which would facilitate its nucleation.

According to Hänchen *et al.* (2008), hydromagnesite nucleated at 120°C transforms within a few hours in magnesite. This mineralogical transformation was extensively studied at 126°C by Sayles & Fyfe (1973), and between 110 and 200°C by Zhang *et al.* (2000), who reported time scales of days to weeks for the transformation at temperatures up to 150°C. Thus, at hydrothermal temperatures, hydromagnesite could be a precursor of magnesite formation, even if its growth kinetics are lower than that of magnesite, and its solubility is higher. Understanding magnesite precipitation in hydrothermal conditions requires to better constrain nucleation kinetics of various Mg-carbonate phase, as well as the kinetics and mechanism of phase transformation from hydromagnesite to magnesite.

Though slow, such a transformation is also thought to occur in natural low temperature environments. Deelman (2011), in his monograph, proposed a detailed review of sedimentary occurrences of magnesite, usually found in association with a variety of Mg-carbonate phase, including hydromagnesite, nesquehonite and dypingite, from which it is believed to form (Graf *et al.*, 1961; Renault & Stead, 1990). It should be noted that most of the sedimentary environments where magnesite is found are arid or semi-arid, affected by strong fluctuations of their water content, with high ionic strength evaporitic solutions, and a potential microbial activity (Alderman, 1965; Renault & Stead, 1990), all factors that could ease the hydromagnesite-magnesite transition.

These observations strongly suggest that magnesite can form at ambient temperature over a time scale of years, through the dessication of hydromagnesite or other hydrated Mg-carbonate phase. According to our kinetic analysis, hydromagnesite growth is favored over magnesite at ambient temperature and alkaline pH. Elucidating the mechanisms which allow solid-state transformation from hydromagnesite to the less reactive magnesite could therefore provide a pathway for long-term low-temperature CO_2 sequestration strategies.

6.6 Conclusion

The present study aimed at investigating the precipitation kinetics of hydromagnesite $Mg_5(CO_3)_4(OH)_2 \cdot 4H_2O$ and comparing it to the growth kinetics of magnesite, the anhydrous form of Mg-carbonate. Using thermodynamic parameters determined on purpose from the solubility of natural hydromagnesite samples, we have been studying hydromagnesite growth kinetics as a function of saturation state and temperature from 25 to 75°C.

Hydromagnesite obeys a linear rate law consistent with the transition state theory, which reflects a growth mechanism likely controlled by the adsorption of growth units to active growth sites located on crystal edges. The activation energy is 45.5 $\pm$ 9 kJ.mol^{-1}, which is more than 100 kJ.mol^{-1} lower than the value determined for magnesite obtuse step

advancement between 80 and 120°C by Saldi *et al.* (2009). In addition, hydromagnesite growth rates largely exceed magnesite rates at comparable chemical affinity, the difference being highest at lower saturation states.

These results confirm through direct observations the long-standing hypothesis that Mg^{2+} slow dehydration is responsible for sluggish magnesite precipitation kinetics. If part of this inhibition is removed through precipitation of a hydrated Mg-carbonate such as hydromagnesite, growth rates increase significantly compared to the anhydrous form. Moreover, the observed lower activation energy of hydromagnesite confirms the hypothesis by Lippmann (1973) that for a given growth mechanism, carbonate minerals growth activation energy reflects the extent of cation hydration.

This original dataset shall prove to be useful for various fields of research, including the industrial synthesis of hydromagnesite as a fire retardant (Hollingbery & Hull, 2010a), the understanding of the evolution of MgO or $Mg(OH)_2$-based engineered barriers for CO_2 buffering in nuclear waste repositories (Xiong & Lord, 2008; Zhang *et al.*, 2000), the quantification and optimization of CO_2 sequestration through alteration of ultramafic mine tailings and precipitation of hydromagnesite (Wilson *et al.*, 2009), and the understanding of the role of biofilms and stromatolites in precipitating hydrous Mg-carbonates in alkaline, Mg-rich environments (Walter *et al.*, 1973; Braithwaite & Zedef, 1996; Kazmierczak *et al.*, 2011; Mavromatis *et al.*, 2012; Shirokova *et al.*, 2012). Overall, hydromagnesite growth kinetics at ambient temperature remain slow, and the assumption of its equilibrium precipitation in reactive transport models (e.g Bea *et al.*, 2012) is overly simplifying.

Simulations of hydromagnesite and magnesite growth rates as a function of solution composition indicate that hydromagnesite could grow faster than magnesite only at temperatures lower than ca. 50°C and alkaline pH, which explains its formation as a result of surface alteration of ultramafic rocks. On the contrary, under typical conditions foreseen for CO_2 mineral sequestration by direct carbonation of Mg-silicates, hydromagnesite growth is not favored. However, a literature review indicates that hydromagnesite is often a precursor of magnesite formation, both at ambient and hydrothermal temperatures. Accurate predictions of the formation, growth and evolution of Mg-carbonates in natural as well as industrial systems thus require informations about the respective nucleation kinetics of the different phases, and the kinetics and mechanism of the mineralogical transformation of hydrous phases into the anhydrous, thermodynamically stable magnesite.

Acknowledgments

The authors wish to thank Carole Causserand for help with chemical analysis, Michel Thibaut for performing X-ray diffraction measurements, Alain Castillo for technical assistance with high and low-temperature reactors, and Guillaumbe Lambergé (INSA Toulouse) for kindly performing thermogravimetric analysis. Our gratitude goes to Patrick Cabrol who provided us with pristine natural hydromagnesite samples from the Réseau André Lachambre network. This work was sponsored by the ANR (National Agency for Research), within the framework of the CO2-FIX project under contract ANR-08-PCO2-003.

Appendix

Table 6.10 – Results of "point-to-point" rate calculations from discontinuous mixed-flow reactor experiments performed at 25°C. Uncertainties on saturation state come from analytical uncertainties on pH, Mg concentration and alkalinity, as well as from the averaging of point-to-point rates over three successive days. Uncertainties on growth rates were calculated based on error propagation from different sources of uncertainty (Mg concentration, flow rate, BET surface area).

Exp. #	Ω_{Hmgs}	±	Rate ($mol/cm^2/s$)	±	Exp. #	Ω_{Hmgs}	±	Rate ($mol/cm^2/s$)	±
H9	1.8	0.6	$4.70*10^{-16}$	$1.74*10^{-15}$	H11	5.9	2.9	$1.01*10^{-15}$	$1.94*10^{-15}$
	3.2	0.9	$1.54*10^{-15}$	$1.94*10^{-15}$		14.2	5.4	$4.43*10^{-15}$	$2.21*10^{-15}$
	5.1	1.0	$2.03*10^{-15}$	$1.92*10^{-15}$		25.1	5.4	$2.08*10^{-15}$	$2.24*10^{-15}$
	7.4	1.3	$3.09*10^{-15}$	$2.20*10^{-15}$		35.2	4.7	$5.94*10^{-15}$	$2.62*10^{-15}$
	20.5	2.0	$2.49*10^{-15}$	$2.33*10^{-15}$		44.8	4.9	$5.63*10^{-15}$	$2.91*10^{-15}$
	21.9	2.9	$3.30*10^{-15}$	$1.92*10^{-15}$		53.1	3.3	$6.42*10^{-15}$	$2.49*10^{-15}$
	32.4	15.8	$4.59*10^{-15}$	$2.46*10^{-15}$		64.1	7.7	$5.25*10^{-15}$	$2.81*10^{-15}$
	45.8	19.1	$3.85*10^{-15}$	$1.49*10^{-15}$		90.5	10.7	$8.26*10^{-15}$	$4.24*10^{-15}$
						90.0	10.2	$6.06*10^{-15}$	$2.33*10^{-15}$
						120.1	19.9	$5.61*10^{-15}$	$3.08*10^{-15}$
						138.2	1.9	$7.17*10^{-15}$	$2.61*10^{-15}$
						100.9	35.4	$4.73*10^{-15}$	$3.22*10^{-15}$
						111.8	10.1	$3.92*10^{-15}$	$4.55*10^{-15}$
						96.5	5.2	$7.40*10^{-15}$	$2.78*10^{-15}$
						116.6	27.1	$5.72*10^{-15}$	$3.55*10^{-15}$
						177.1	10.2	$4.71*10^{-15}$	$3.03*10^{-15}$
						167.2	15.0	$7.82*10^{-15}$	$3.45*10^{-15}$
H10	2.4	0.1	$1.38*10^{-15}$	$1.87*10^{-15}$	H12	3.4	2.4	$3.07*10^{-15}$	$2.07*10^{-15}$
	12.2	3.0	$4.43*10^{-15}$	$2.31*10^{-15}$		13.4	7.6	$2.20*10^{-15}$	$2.12*10^{-15}$
	19.7	4.5	$2.98*10^{-15}$	$2.57*10^{-15}$		36.0	15.1	$4.64*10^{-15}$	$2.45*10^{-15}$
	32.8	8.5	$4.04*10^{-15}$	$2.20*10^{-15}$		127.6	47.7	$8.34*10^{-15}$	$2.95*10^{-15}$
	40.9	0.4	$4.01*10^{-15}$	$2.49*10^{-15}$		203.4	10.4	$1.03*10^{-14}$	$2.73*10^{-15}$
	39.9	0.6	$7.67*10^{-15}$	$2.05*10^{-15}$		218.2	16.5	$9.98*10^{-15}$	$3.15*10^{-15}$
	37.1	2.2	$5.64*10^{-15}$	$2.62*10^{-15}$		189.6	71.5	$8.75*10^{-15}$	$3.31*10^{-15}$
	51.3	16.4	$3.67*10^{-15}$	$1.64*10^{-15}$		271.2	32.8	$1.03*10^{-14}$	$4.81*10^{-15}$
	67.5	0.2	$5.72*10^{-15}$	$3.75*10^{-15}$		387.0	39.5	$9.35*10^{-15}$	$3.40*10^{-15}$
	74.1	26.8	$5.59*10^{-15}$	$2.31*10^{-15}$		322.1	85.7	$7.79*10^{-15}$	$3.62*10^{-15}$
	66.4	19.1	$4.94*10^{-15}$	$2.58*10^{-15}$		329.0	47.4	$9.59*10^{-15}$	$3.07*10^{-15}$
	89.2	3.7	$5.01*10^{-15}$	$2.27*10^{-15}$		363.8	6.5	$9.83*10^{-15}$	$3.05*10^{-15}$
	86.5	6.4	$3.80*10^{-15}$	$3.72*10^{-15}$		297.8	34.3	$9.68*10^{-15}$	$3.06*10^{-15}$
	71.4	8.6	$4.04*10^{-15}$	$2.28*10^{-15}$		326.1	65.7	$8.97*10^{-15}$	$3.19*10^{-15}$
	62.4	13.8	$3.92*10^{-15}$	$2.29*10^{-15}$		380.7	41.5	$9.03*10^{-15}$	$3.83*10^{-15}$
	109.6	8.7	$4.33*10^{-15}$	$2.57*10^{-15}$		383.2	24.7	$9.08*10^{-15}$	$4.01*10^{-15}$
	129.3	11.0	$4.85*10^{-15}$	$2.94*10^{-15}$		464.6	8.1	$9.72*10^{-15}$	$4.04*10^{-15}$
	155.7	8.2	$4.23*10^{-15}$	$3.12*10^{-15}$		462.7	29.2	$8.85*10^{-15}$	$3.87*10^{-15}$

Bibliography

Aagaard, P. & Helgeson, H. C. (1982). Thermodynamic and kinetic constraints on reaction rates among minerals and aqueous solutions; I. Theoretical considerations. *American Journal of Science*, 282(3), 237–285.

Alderman, A. R. (1965). Dolomitic sediments and their enviroment in the south-east of south australia. *Geochimica et Cosmochimica Acta*, 29(12), 1355–1365.

Archer, D. G. (1992). Thermodynamic properties of the NaCl+H2O system. II. Thermodynamic properties of $NaCl_{(aq)}$, $NaCl{\cdot}2\,H_2O_{(cr)}$, and phase equilibria. *Journal of Physical and Chemical Reference Data*, 21(4), 793–829.

Arvidson, R. S. & Mackenzie, F. T. (2000). Temperature dependence of mineral precipitation rates along the $CaCO_3$-$MgCO_3$ join. *Aquatic Geochemistry*, 6(2), 249–256.

Ballirano, P., De Vito, C., Ferrini, V., & Mignardi, S. (2010). The thermal behaviour and structural stability of nesquehonite, $MgCO_3{\cdot}3\,H_2O$, evaluated by in situ laboratory parallel-beam x-ray powder diffraction: New constraints on CO2 sequestration within minerals. *Journal of hazardous materials*, 178(1-3), 522–528.

Bea, S. A., Wilson, S. A., Mayer, K. U., Dipple, G. M., Power, I. M., & Gamazo, P. (2012). Reactive transport modeling of natural carbon sequestration in ultramafic mine tailings. *Vadose Zone Journal*, 11(2).

Beck, C. W. (1950). Differential thermal analysis curves of carbonate minerals. *American Mineralogist*, 35, 985–1013.

Bleuzen, A., Pittet, P. A., Helm, L., & Merbach, A. E. (1997). Water exchange on Magnesium(II) in aqueous solution: a variable temperature and pressure ^{17}O NMR study. *Magnetic Resonance in Chemistry*, 35, 765–773.

Blum, A. & Lasaga, A. (1987). Monte carlo simulations of surface reaction rate laws. In *Aquatic Surface Chemistry* (pp. 255–292). New York: John Wiley and Sons.

Bénézeth, P., Saldi, G. D., Dandurand, J.-L., & Schott, J. (2011). Experimental determination of the solubility product of magnesite at 50 to 200°C. *Chemical Geology*, 286, 21–31.

Braithwaite, C. J. R. & Zedef, V. (1996). Hydromagnesite stromatolites and sediments in an alkaline lake, salda golu, turkey. *Journal of Sedimentary Research*, 66(5), 991–1002.

Burgess, J. (1999). *Ions in Solution: Basic Principles of Chemical Interactions*. Woodhead Publishing.

Busey, R. H. & Mesmer, R. E. (1976). The ionization of water in NaCl media to 300°C. *Journal of Solution Chemistry*, 5(2), 147–152.

Cheng, W. & Li, Z. (2010). Nucleation kinetics of nesquehonite $MgCO_3{\cdot}3\,H_2O$ in the $MgCl_2$-Na_2CO_3 system. *Journal of Crystal Growth*, 312(9), 1563–1571.

Cheng, W., Li, Z., & Demopoulos, G. (2009). Effects of temperature on the preparation of magnesium carbonate hydrates by reaction of $MgCl_2$ with Na_2CO_3. *Chinese Journal of Chemical Engineering*, 17(4), 661–666.

Davies, P. J. & Bubela, B. (1973). The transformation of nesquehonite into hydromagnesite. *Chemical Geology*, 12, 289–300.

Declercq, J. & Oelkers, E. H. (2012). Thermodynamic and kinetic constraints on the carbonation of forsterite and serpentine. *submitted*.

Deelman, J. C. (2011). *Low-temperature formation of magnesite and dolomite*. Geology Series. Eindhoven, The Netherlands: Compact Disc Publications, 2.3 edition.

Di Tommaso, D. & de Leeuw, N. H. (2010). First principles simulations of the structural and dynamical properties of hydrated metal ions Me^{2+} and solvated metal carbonates (Me = Ca, Mg, and Sr). *Crystal Growth & Design*, 10(10), 4292–4302.

Felmy, A. R., Qafoku, O., Arey, B. W., Hu, J. Z., Hu, M., Todd Schaef, H., Ilton, E. S., Hess, N. J., Pearce, C. I., Feng, J., & Rosso, K. M. (2012). Reaction of water-saturated supercritical CO_2 with forsterite: Evidence for magnesite formation at low temperatures. *Geochimica et Cosmochimica Acta*, 91, 271–282.

Frost, R. L., Bahfenne, S., Graham, J., & Martens, W. N. (2008). Thermal stability of artinite, dypingite and brugnatellite - implications for the geosequestration of green house gases. *Thermochimica Acta*, 475(1-2), 39–43.

Giammar, D. E., Bruant, R. G., & Peters, C. A. (2005). Forsterite dissolution and magnesite precipitation at conditions relevant for deep saline aquifer storage and sequestration of carbon dioxide. *Chemical Geology*, 217(3-4), 257–276.

Graf, D. L., Eardley, A. J., & Shimp, N. F. (1961). A preliminary report on magnesium carbonate formation in Glacial Lake Bonneville. *The Journal of Geology*, 69(2), 219–223.

Guyot, F., Daval, D., Dupraz, S., Martinez, I., Ménez, B., & Sissmann, O. (2011). CO_2 geological storage: The environmental mineralogy perspective. *Comptes Rendus Geoscience*, 343(2-3), 246–259.

Helgeson, H. C. (1978). Summary and critique of the thermodynamic properties of rock-forming minerals. *American Journal of Science*, 278 A(1).

Hänchen, M., Prigiobbe, V., Baciocchi, R., & Mazzotti, M. (2008). Precipitation in the Mg-carbonate system: effects of temperature and CO_2 pressure. *Chemical Engineering Science*, 63(4), 1012–1028.

Hänchen, M., Prigiobbe, V., Storti, G., Seward, T., & Mazzotti, M. (2006). Dissolution kinetics of fosteritic olivine at 90 - 150°C including effects of the presence of CO_2. *Geochimica et Cosmochimica Acta*, 70(17), 4403–4416.

Hollingbery, L. A. & Hull, T. R. (2010a). The fire retardant behaviour of huntite and hydromagnesite - A review. *Polymer Degradation and Stability*, 95(12), 2213–2225.

Hollingbery, L. A. & Hull, T. R. (2010b). The thermal decomposition of huntite and hydromagnesite: A review. *Thermochimica Acta*, 509(1-2), 1–11.

Hollingbery, L. A. & Hull, T. R. (2012). The thermal decomposition of natural mixtures of huntite and hydromagnesite. *Thermochimica Acta*, 528, 45–52.

Hopkinson, L., Kristova, P., Rutt, K., & Cressey, G. (2012). Phase transitions in the system MgO-CO_2-H_2O during CO_2 degassing of Mg-bearing solutions. *Geochimica et Cosmochimica Acta*, 76, 1–13.

Hopkinson, L., Rutt, K., & Cressey, G. (2008). The transformation of nesquehonite to hydromagnesite in the system CaO-MgO-H_2O-CO_2: An experimental spectroscopic study. *The Journal of Geology*, 116, 387–400.

Ikeda, T., Boero, M., & Terakura, K. (2007). Hydration properties of magnesium and calcium ions from constrained first principles molecular dynamics. *The Journal of Chemical Physics*, 127(7), 074503–074503–8.

Johnson, J. W., Oelkers, E. H., & Helgeson, H. C. (1992). SUPCRT92: a software package for calculating the standard molal thermodynamic properties of minerals, gases, aqueous species, and reactions from 1 to 5000 bar and 0 to 1000°C. *Computers & Geosciences*, 18(7), 899–947.

Kazmierczak, J., Kempe, S., Kremer, B., López-García, P., Moreira, D., & Tavera, R. (2011). Hydrochemistry and microbialites of the alkaline crater lake Alchichica, Mexico. *Facies*, 57(4), 543–570.

Khan, N., Dollimore, D., Alexander, K., & Wilburn, F. (2001). The origin of the exothermic peak in the thermal decomposition of basic magnesium carbonate. *Thermochimica Acta*, 367-368, 321–333.

King, H. E., Plümper, O., & Putnis, A. (2010). Effect of secondary phase formation on the carbonation of olivine. *Environmental Science & Technology*, 44(16), 6503–6509.

Königsberger, E., Königsberger, L. C., & Gamsjäger, H. (1999). Low-temperature thermodynamic model for the system Na_2CO_3-$MgCO_3$-$CaCO_3$-H_2O. *Geochimica et Cosmochimica Acta*, 63(19-20), 3105–3119.

Königsberger, E., Schmidt, P., & Gamsjäger, H. (1992). Solid-solute phase equilibria in aqueous solution. vi. solubilities, complex formation, and ion-interaction parameters for the system Na^+-Mg^{2+}-ClO_4^--CO_2-H_2O at 25°C. *Journal of Solution Chemistry*, 21, 1195–1216.

Kowacz, M. & Putnis, A. (2008). The effect of specific background electrolytes on water structure and solute hydration: Consequences for crystal dissolution and growth. *Geochimica et Cosmochimica Acta*, 72(18), 4476–4487.

Kowacz, M., Putnis, C., & Putnis, A. (2007). The effect of cation/anion ratio in solution on the mechanism of barite growth at constant supersaturation: Role of the desolvation process on the growth kinetics. *Geochimica et Cosmochimica Acta*, 71(21), 5168–5179.

Langmuir, D. (1965). Stability of carbonates in the system MgO-CO_2-H_2O. *The Journal of Geology*, 73(5), 730–754.

Larentzos, J. P. & Criscenti, L. J. (2008). A molecular dynamics study of alkaline earth metal-chloride complexation in aqueous solution. *The Journal of Physical Chemistry B*, 112(45), 14243–14250.

Lippmann, F. (1973). *Sedimentary carbonate minerals*. Springer-Verlag Berlin.

Marion, G. M. (2001). Carbonate mineral solubility at low temperatures in the Na-K-Mg-Ca-H-Cl-SO_4-OH-HCO_3-CO_3-CO_2-H_2O system. *Geochimica et Cosmochimica Acta*, 65(12), 1883–1896.

Mavromatis, V., Pearce, C. R., Shirokova, L. S., Bundeleva, I. A., Pokrovsky, O. S., Benezeth, P., & Oelkers, E. H. (2012). Magnesium isotope fractionation during hydrous magnesium carbonate precipitation with and without cyanobacteria. *Geochimica et Cosmochimica Acta*, 76(0), 161–174.

Meissner, H. P. & Tester, J. W. (1972). Activity coefficients of strong electrolytes in aqueous solutions. *Industrial & Engineering Chemistry Process Design and Development*, 11(1), 128–133.

Millero, F., Huang, F., Graham, T., & Pierrot, D. (2007). The dissociation of carbonic acid in NaCl solutions as a function of concentration and temperature. *Geochimica et Cosmochimica Acta*, 71(1), 46–55.

Molis, E., Barrès, O., Marchand, H., Sauzéat, E., Humbert, B., & Thomas, F. (2000). Initial steps of ligand-promoted dissolution of gibbsite. *Colloids and Surfaces A: Physicochemical and Engineering Aspects*, 163(2-3), 283–292.

Morales, J., Astilleros, J. M., & Fernández-Díaz, L. (2012). A nanoscopic approach to the kinetics of anhydrite (100) surface growth in the range of temperatures between 60 and 120°C. *American Mineralogist*, 97(5-6), 995–998.

Nielsen, A. E. (1984). Electrolyte crystal growth mechanisms. *Journal of Crystal Growth*, 67(2), 289–310.

Noyes, R. M. (1962). Thermodynamics of ion hydration as a measure of effective dielectric properties of water. *Journal of the American Chemical Society*, 84(4), 513–522.

Palmer, D. A. & Wesolowski, D. J. (1997). Potentiometric measurements of the first hydrolysis quotient of magnesium (II) to 250°C and 5 molal ionic strength (NaCl). *Journal of Solution Chemistry*, 26(2), 217–232.

Park, A. H. A. & Fan, L. S. (2004). CO_2 mineral sequestration: physically activated dissolution of serpentine and pH swing process. *Chemical Engineering Science*, 59(22), 5241–5247.

Parkhurst, D. L. & Appelo, C. A. J. (1999). User's guide to PHREEQC (version 2): a computer program for speciation, batch-reaction, one-dimensional transport, and inverse geochemical calculations. *US Geological Survey Water-Resources Investigations Report*, 99(4259), 312.

Pavlov, M., Siegbahn, P. E. M., & Sandström, M. (1998). Hydration of beryllium, magnesium, calcium, and zinc ions using density functional theory. *The Journal of Physical Chemistry A*, 102(1), 219–228.

Piana, S., Jones, F., & Gale, J. (2006). Assisted desolvation as a key kinetic step for crystal growth. *Journal of the American Chemical Society*, 128(41), 13568–13574.

Pokrovsky, O. S. & Schott, J. (2002). Surface chemistry and dissolution kinetics of divalent metal carbonates. *Environmental Science & Technology*, 36(3), 426–432.

Power, I. M., Wilson, S. A., Thom, J. M., Dipple, G. M., Gabites, J. E., & Southam, G. (2009). The hydromagnesite playas of aAtlin, British Columbia, Canada: A biogeochemical model for CO_2 sequestration. *Chemical Geology*, 260(3-4), 286–300.

Power, I. M., Wilson, S. A., Thom, J. M., Dipple, G. M., & Southam, G. (2007). Biologically induced mineralization of dypingite by cyanobacteria from an alkaline wetland near Atlin, British Columbia, Canada. *Geochemical Transactions*, 8, 13.

Pronost, J., Beaudoin, G., Tremblay, J., Larachi, F., Duchesne, J., Hébert, R., & Constantin, M. (2011). Carbon sequestration kinetic and storage capacity of ultramafic mining waste. *Environmental Science & Technology*, 45(21), 9413–9420.

Renault, R. W. & Stead, D. (1990). Recent magnesite-hydromagnesite sedimentation in playa basins of the Cariboo Plateau, British Columbia. *Geological Fieldwork - British Columbia Geological Survey*, (pp. 279–288).

Robie, R. & Hemingway, B. (1995). Thermodynamic properties of minerals and related substances at 298.15 K and 1 bar (10^5 Pascals) pressure and at higher temperatures. *US Geological Survey Bulletin*, 2131.

Romanek, C. S., Jiménez-López, C., Navarro, A. R., Sánchez-Román, M., Sahai, N., & Coleman, M. (2009). Inorganic synthesis of Fe-Ca-Mg carbonates at low temperature. *Geochimica et Cosmochimica Acta*, 73(18), 5361–5376.

Russell, M. J., Ingham, J. K., Zedef, V., Maktav, D., Sunar, F., Hall, A. J., & Fallick, A. E. (1999). Search for signs of ancient life on Mars: expectations from hydromagnesite microbialites, Salda Lake, Turkey. *Journal of the Geological Society*, 156(5), 869.

Saldi, G. D., Jordan, G., Schott, J., & Oelkers, E. H. (2009). Magnesite growth rates as a function of temperature and saturation state. *Geochimica et Cosmochimica Acta*, 73(19), 5646–5657.

Saldi, G. D., Schott, J., Pokrovsky, O. S., Gautier, Q., & Oelkers, E. H. (2012). An experimental study of magnesite precipitation rates at neutral to alkaline conditions and 100-200°C as a function of pH, aqueous solution composition and chemical affinity. *Geochimica et Cosmochimica Acta*, 83, 93–109.

Sawada, Y., Uematsu, K., Mizutani, N., & Kato, M. (1978). Thermal decomposition of hydromagnesite $4MgCO_3$-$Mg(OH)_2$-$4H_2O$ under different partial pressures of carbon dioxide. *Thermochimica Acta*, 27(1-3), 45–59.

Sayles, F. L. & Fyfe, W. S. (1973). The crystallization of magnesite from aqueous solution. *Geochimica et Cosmochimica Acta*, 37(1), 87–99.

Schaef, H. T., Windisch, C. F., McGrail, B. P., Martin, P. F., & Rosso, K. M. (2011). Brucite [$Mg(OH_2)$] carbonation in wet supercritical CO_2: An in situ high pressure X-ray diffraction study. *Geochimica et Cosmochimica Acta*, 75(23), 7458–7471.

Schott, J., Pokrovsky, O. S., & Oelkers, E. H. (2009). The link between mineral dissolution/precipitation kinetics and solution chemistry. *Reviews in Mineralogy and Geochemistry*, 70(1), 207–258.

Shiraki, R. & Brantley, S. L. (1995). Kinetics of near-equilibrium calcite precipitation at 100°C: an evaluation of elementary reaction-based and affinity-based rate laws. *Geochimica et Cosmochimica Acta*, 59(8), 1457–1471.

Shirokova, L. S., Mavromatis, V., Bundeleva, I. A., Pokrovsky, O. S., Bénézeth, P., Gérard, E., Pearce, C. R., & Oelkers, E. H. (2012). Using Mg isotopes to trace cyanobacterially mediated magnesium carbonate precipitation in alkaline lakes. *Aquatic Geochemistry*.

Shock, E. L. & Helgeson, H. C. (1988). Calculation of the thermodynamic and transport properties of aqueous species at high pressures and temperatures: Correlation algorithms for ionic species and equation of state predictions to 5 kbar and 1000°C. *Geochimica et Cosmochimica Acta*, 52(8), 2009–2036.

Teir, S., Eloneva, S., Fogelholm, C., & Zevenhoven, R. (2009). Fixation of carbon dioxide by producing hydromagnesite from serpentinite. *Applied Energy*, 86(2), 214–218.

Teir, S., Kuusik, R., Fogelholm, C., & Zevenhoven, R. (2007). Production of magnesium carbonates from serpentinite for long-term storage of CO_2. *International Journal of Mineral Processing*, 85(1-3), 1–15.

Temkin, M. (1963). The kinetics of stationary reactions. *Akad. Nauk SSR Doklady*, 152, 782–785.

Teng, H. H., Dove, P. M., & De Yoreo, J. J. (2000). Kinetics of calcite growth: surface processes and relationships to macroscopic rate laws. *Geochimica et Cosmochimica Acta*, 64(13), 2255–2266.

Tesoriero, A. J. & Pankow, J. F. (1996). Solid solution partitioning of Sr^{2+}, Ba^{2+}, and Cd^{2+} to calcite. *Geochimica et Cosmochimica Acta*, 60, 1053–1063.

Thompson, J. B. & Ferris, F. G. (1990). Cyanobacterial precipitation of gypsum, calcite, and magnesite from natural alkaline lake water. *Geology*, 18(10), 995–998.

Wagman, D. D., Evans, W. H., Parker, V. B., Schumm, R. H., Halow, I., Bailey, S. M., Churney, K. L., & Buttall, R. L. (1982). The NBS tables of chemical thermodynamic properties. Selected values for inorganic and C1 and C2 organic substances in SI units. *Journal of Physical Chemistry Reference Data*, 11(Suppl. 2), 392.

Walter, M. R., Golubic, S., & Preiss, W. V. (1973). Recent stromatolites from hydromagnesite and aragonite depositing lakes near the Coorong Lagoon, South Australia. *Journal of Sedimentary Research*, 43(4), 1021–1030.

Wang, J. & Li, Z. (2012). Crystallization and agglomeration kinetics of hydromagnesite in the reactive system $MgCl_2$-Na_2CO_3-NaOH-H_2O. *Industrial & Engineering Chemistry Research*, 51(23), 7874–7883.

Wang, Y., Li, Z., & Demopoulos, G. P. (2008). Controlled precipitation of nesquehonite ($MgCO_3 \cdot 3\,H_2O$) by the reaction of $MgCl_2$ with $(NH_4)_2CO_3$. *Journal of Crystal Growth*, 310(6), 1220–1227.

Wilson, S. A., Dipple, G. M., Power, I. M., Thom, J. M., Anderson, R. G., Raudsepp, M., Gabites, J. E., & Southam, G. (2009). Carbon dioxide fixation within mine wastes of ultramafic-hosted ore deposits: examples from the Clinton Creek and Cassiar chrysotile deposits, Canada. *Economic Geology*, 104, 95 –112.

Xiong, Y. (2011). Experimental determination of solubility constant of hydromagnesite (5424) in NaCl solutions up to 4.4 M at room temperature. *Chemical Geology*, 284(3-4), 262–269.

Xiong, Y. & Lord, A. S. (2008). Experimental investigations of the reaction path in the MgO-CO_2-H_2O system in solutions with various ionic strengths, and their applications to nuclear waste isolation. *Applied Geochemistry*, 23(6), 1634–1659.

Yang, Y., Sahai, N., Romanek, C. S., & Chakraborty, S. (2012). A computational study of Mg^{2+} dehydration in aqueous solution in the presence of HS^- and other monovalent anions - insights to dolomite formation. *Geochimica et Cosmochimica Acta*, 88, 77–87.

Zhang, P.-C., Anderson, H. L., Kelly, J. W., Krumhansl, J. L., & Papenguth, H. W. (2000). *Kinetics and Mechanisms of Formation of Magnesite from Hydromagnesite in Brine*. Technical Report SAN099 - 1946J, Sandia National Laboratories, Albuquerque, New Mexico, USA.

Zhao, L., Sang, L., Chen, J., Ji, J., & Teng, H. H. (2009). Aqueous carbonation of natural brucite: relevance to CO_2 sequestration. *Environmental Science & Technology*, 44(1), 406–411.

Chapitre 7

Conclusion Générale et Perspectives

Sommaire

7.1 Conclusions de l'étude

7.1.1 Influence de ligands organiques sur la cinétique et le mécanisme de croissance cristalline de la magnésite

La séquestration minérale du CO_2 par carbonatation de silicates de magnésium passe par la dissolution initiale de la phase silicatée, puis la précipitation d'un minéral carbonaté magnésien. Souvent considérée comme l'étape limitante du processus, la dissolution des silicates magnésiens a fait l'objet d'un grand nombre d'études et a concentré la majeure partie des efforts visant à accélérer le processus de carbonatation de minéraux basiques. Pourtant, la lenteur particulière de la précipitation de la magnésite a conduit à interroger la validité de cette hypothèse de départ (Saldi *et al.*, 2012). À tout le moins, il convient de s'assurer que les solutions proposées pour accélérer la carbonatation n'ont pas un effet néfaste sur la phase de précipitation de la magnésite.

Dans ce contexte, nous nous proposions au début de ce travail de thèse d'évaluer l'influence sur la cinétique de précipitation de la magnésite connus pour leur influence positive sur la dissolution des silicates magnésiens tels que forstérite et serpentine. Les données cinétiques acquises devaient permettre, par le biais d'une modélisation cinétique simplifiée, d'évaluer l'influence de ces ligands sur le processus de carbonatation globale.

Notre étude a porté sur trois ligands organiques courants, l'oxalate, le citrate et l'EDTA. Un préalable important à la conduction de l'étude expérimentale a été la compilation d'une base de données thermodynamique comportant l'ensemble des constantes de complexation des ligands étudiés avec les cations métalliques présents en solution, ainsi que leur évolution en température. Ce travail de revue bibliographique a permis de mettre en évidence de fortes incertitudes sur la constante de complexation du citrate avec Mg^{2+} à haute température. Ceci nous a amené à conduire une expérience de solubilité de la magnésite en présence de citrate, qui a permis de préciser ces données essentielles au calcul rigoureux de la spéciation chimique de nos solutions expérimentales.

De l'échelle macroscopique...

L'étude de la cinétique de croissance cristalline de la magnésite a été conduite par le biais d'expériences en réacteur à flux continu réalisées entre 100 et 146°C, en conditions légèrement alcalines. Les expériences réalisées en conditions inorganiques nous ont amené à réévaluer légèrement les données de cinétique de précipitation de la magnésite acquises par Saldi *et al.* (2012), mais confirment que la magnésite a une loi de croissance parabolique.

Partant de ces données de référence, nous avons évalué l'influence de concentrations croissantes de ligands organiques, entre 10^{-5} M et 10^{-2} M. Nous montrons que les trois ligands étudiés - oxalate, citrate, EDTA - diminuent significativement la vitesse de précipitation de la magnésite, par l'effet combiné de deux mécanismes :

- La complexation du Mg^{2+} en solution aqueuse par les ligands organiques diminue l'activité chimique du cation et entraîne donc une baisse de la saturation des solutions expérimentales, qui conduit à une diminution de la vitesse de précipitation, d'autant plus forte que le ligand est fort et sa concentration importante.
- Bien que la forme de la loi de vitesse soit globalement inchangée en présence de ligands, nous constatons une baisse de la constante cinétique du processus de croissance cristalline,

qui exprime une inhibition de la précipitation de la magnésite à saturation constante. Cette inhibition est observée avec les trois ligands ; elle est maximale dans le cas du citrate, qui à 120°C diminue la constante cinétique de près de 70% avec 0.2 mM de ligand. Dans le cas de l'oxalate, des concentrations de 10 mM sont nécessaires pour observer un effet inhibiteur significatif.

S'il n'est pas exclu que la complexation du Mg^{2+} par des ligands organiques puisse avoir pour conséquence une augmentation de la vitesse d'échange des molécules d'eau autour du cation, cela ne se traduit donc pas par une réactivité accrue de la magnésite.

L'évolution de la constante cinétique de précipitation de la magnésite en présence de ligands à 120°C peut donc être expliquée par l'intermédiaire d'un isotherme d'adsorption de Langmuir, ce qui nous amène à proposer, en accord avec la littérature, que l'inhibition résulte de l'adsorption des ligands à la surface du minéral. Des expériences préliminaires d'adsorption de l'oxalate et du citrate sur la magnésite, réalisées à 120°C dans des conditions proches des expériences de précipitation, suggèrent que l'oxalate s'adsorbe moins que le citrate et que ce dernier a une affinité importante pour un nombre limité de sites surfaciques qui contrôlent le processus de croissance.

...À l'échelle surfacique

L'utilisation de la microscopie à force atomique hydrothermale a permis de conforter ces interprétations initiales. Les vitesses de cristallisation mesurées sur la face (104) de la magnésite à 100°C sont en bon accord avec les cinétiques mesurées à partir des expériences en réacteur à flux continu et confirment que la présence de 1 mM de citrate réduit significativement la constante cinétique. Nos observations indiquent également que le processus de croissance en spirale observé par Saldi *et al.* (2009) demeure le mécanisme contrôlant la cristallisation de la magnésite en présence de ligands organiques.

En revanche, l'oxalate et le citrate affectent de manière sensible la forme des îlots de croissance, ce qui confirme que les ligands s'adsorbent à la surface de la magnésite. L'oxalate conduit à un arrondissement des îlots habituellement rhombiques, tandis que le citrate conduit à leur allongement apparent parallèlement à la direction cristallographique $(\bar{4}21)$. Nous interprétons ces modifications de forme comme résultant d'une adsorption préférentielle du citrate au niveau des "kinks" situés à l'intersection des marches obtuses et aigües, probablement en raison de la géométrie non planaire de la molécule de citrate et de la présence en son sein de trois groupements carboxyliques. L'oxalate semble au contraire interagir de manière indifférenciée avec l'ensemble des "kinks" situés au niveau des marches cristallines. Par ailleurs, l'EDTA n'a pas d'effet significatif sur la forme des îlots ni sur la vitesse de cristallisation. Cela indique que sous la forme ultra majoritaire de chélate $MgEDTA^{2-}$, dans les conditions de nos expériences, l'EDTA interagit peu avec la surface de la magnésite.

La mesure de la vitesse d'avancement des marches *obtuses* révèle de manière surprenante que, malgré les modifications de leur forme observées en présence d'oxalate et de citrate, ces marches ne sont pas ralenties. Cette observation peut être interprétée dans le cadre du modèle de De Yoreo *et al.* (2009) décrivant l'interaction d'impuretés avec les cristaux à faible densité de sites actifs (ou "kinks").

Dès lors, d'où provient la baisse de la vitesse de génération des marches cristallines qui se traduit par la diminution mesurée de la constante cinétique de cristallisation de la magnésite ?

Un examen du mécanisme de croissance en spirale nous permet de proposer deux origines possibles :

- soit une diminution de la vitesse d'avancement des marches *aigües*, qui sont une dizaine de fois plus lentes que les marches obtuses et contrôlent à ce titre la fréquence de rotation des spirales ;
- soit une augmentation de la "longueur critique", distance que doit parcourir un segment de marche cristalline avant d'autoriser la rotation d'une spirale.

Ces deux paramètres sont à ce stade difficilement accessibles à l'expérimentation ; des données plus précises et plus nombreuses sont nécessaires pour conclure précisément quant au mécanisme responsable de l'inhibition de la croissance de la magnésite. Toutefois, la plus grande efficacité inhibitrice du citrate par rapport à l'oxalate pourrait trouver son origine dans l'interaction spécifique du tricarboxylate avec certains sites des marches aigües.

7.1.2 Conséquences pour la séquestration minérale du CO_2 sous la forme de magnésite

Bien qu'originales, les données cinétiques acquises ne permettent pas de construire un véritable modèle de complexation de surface décrivant les interactions entre ligands organiques et surface de la magnésite dans des conditions de pH, de température, de force ionique, de concentration en Mg^{2+} et en CO_3^{2-} variées. Il est toutefois possible, moyennant quelques approximations, d'évaluer l'influence des ligands organiques étudiés sur le processus global de carbonatation des silicates magnésiens.

Notre étude a porté sur le cas de la carbonatation de la forstérite, pour laquelle un modèle de dissolution en présence d'oxalate a été publié par Prigiobbe et Mazzotti (2011). Nous montrons que dans les conditions typiques envisagées pour la carbonatation minérale directe de la forstérite (120°C, 10 bars PCO_2), la présence de 10 mM d'oxalate conduit à une diminution de la vitesse de carbonatation comme de son rendement final, y compris si seule la complexation du Mg^{2+} est prise en compte.

Le cas hypothétique de la carbonatation de la forstérite à pH alcalin permet de se placer dans les conditions attendues d'évolution chimique d'un stockage de CO_2 en roches ultrabasiques. Dans ces conditions, la dissolution de la forstérite, plus lente, devient limitante pour le processus de carbonatation. Il est alors possible que l'oxalate ait une influence positive sur la vitesse de carbonatation, du moins au début de la réaction. Cependant, l'augmentation de la concentration de Mg^{2+} due a la précipitation retardée de la magnésite pourrait conduire à une précipitation accrue de phases silicatées secondaires, susceptibles de diminuer l'étendue de la carbonatation.

Ces résultats peuvent être étendus au citrate et à l'EDTA et nous amènent à conclure que l'utilisation de ligands organiques n'est pas souhaitable pour accélérer la carbonatation de la forstérite, confirmant en cela les résultats expérimentaux récemment obtenus par Bonfils *et al.* (2012). S'il n'est pas exclu que l'influence de ligands soigneusement choisis puisse être positive pour la carbonatation de silicates de magnésium à dissolution plus lente que la forstérite, ces cibles demeurent moins intéressantes pour la séquestration minérale du CO_2.

7.1.3 Influence de l'hydratation du Mg^{2+} sur la réactivité des minéraux carbonatés

Indépendamment de la problématique des ligands organiques, notre étude de la solubilité et de la cinétique de croissance de l'hydromagnésite constitue la première étude quantitative de la réactivité d'un carbonate de magnésium hydraté.

Nous montrons que la cinétique de croissance de l'hydromagnésite peut être décrite par l'intermédiaire d'une loi linéaire conforme à la théorie de l'état transitoire, ce qui suggère que la croissance est contrôlée par l'adjonction d'unités cristallines depuis la solution au niveau de sites actifs nombreux.

La cinétique de croissance de l'hydromagnésite est supérieure de plusieurs ordres de magnitude à celle de la magnésite à affinité chimique comparable. Son énergie d'activation entre 25 et 75°C est de 45.5 $\pm$ 9 kJ.mol^{-1}, plus de 100 kJ.mol^{-1} inférieure à l'énergie d'activation mesurée par Saldi *et al.* (2009) pour la vitesse d'avancement des marches obtuses de la magnésite, processus également contrôlé par l'adsorption d'unités cristallines. Ces deux éléments confirment que la déshydratation complète des ions Mg^{2+} constitue un obstacle majeur à la formation de magnésite à basse température. La déshydratation incomplète du Mg^{2+} dans le cas de l'hydromagnésite permet sa formation à température ambiante.

Toutefois, du fait des différences de solubilité et de composition chimique entre les deux minéraux, la cinétique de croissance de l'hydromagnésite dans les conditions usuelles de carbonatation minérale (température supérieure à 100°C, forte pression de CO_2) demeure inférieure à celle de la magnésite. La précipitation d'hydromagnésite ne peut donc constituer un palliatif à la faible vitesse de précipitation de la magnésite lors de la carbonatation de minéraux basiques à haute température. L'observation pourtant rapportée dans la littérature de la formation d'hydromagnésite à des températures supérieures à 100°C et sous forte P_{CO_2} s'explique ainsi probablement par les fortes disparités de cinétique de nucléation de l'hydromagnésite et de la magnésite.

Ce jeu de données original améliore notre compréhension des facteurs qui contrôlent les relations de phase dans le système des carbonates magnésiens. Il met en évidence les relations complexes entre stabilité thermodynamique, cinétique de nucléation et cinétique de croissance cristalline, qui demeurent largement à explorer. Les données acquises constituent cependant un apport important à la compréhension de la formation de l'hydromagnésite dans les environnements naturels et en vue de mieux quantifier et modéliser la séquestration minérale du CO_2 à basse température, notamment au sein des résidus miniers ultrabasiques.

7.2 Perspectives

La séquestration minérale *ex situ* du CO_2 est-elle une voie prometteuse dans la lutte contre les émissions de gaz à effet de serre ?

À l'issue de cette étude, je ne me prononcerai pas pour l'ensemble des substrats potentiels de carbonatation, mais il est certain que les obstacles à la carbonatation des silicates magnésiens demeurent. En particulier, il apparaît clairement que les ligands organiques proposés pour accélérer la dissolution des minéraux silicatés ne constituent pas une voie prometteuse pour améliorer la cinétique et le rendement de la réaction de carbonatation des silicates magnésiens, en raison de leur influence inhibitrice sur la précipitation de la magnésite. L'étude menée sur l'hydromagnésite et les informations qu'elle livre sur les facteurs qui limitent la précipitation de la magnésite à basse température, fournit en revanche quelques pistes de réflexion sur la manière de progresser vers une précipitation plus rapide des carbonates magnésiens. En outre, l'étude des interactions entre ligands organiques et la croissance cristalline de la magnésite soulève un certain nombre de questions fondamentales que l'on exposera ci-dessous.

7.2.1 Est-il envisageable d'utiliser des additifs organiques pour catalyser la formation de minéraux carbonatés magnésiens ? Et pour accélérer la carbonatation de silicates ?

Nous l'avons vu, la réactivité de la magnésite est limitée par le caractère très hydraté du cation Mg^{2+} en solution aqueuse et son corollaire : une faible vitesse d'échange des molécules d'eau entre la sphère d'hydratation du cation et le reste de la solution. Accélérer la fréquence d'échange des molécules d'eau autour des ions Mg^{2+} est donc crucial pour accélérer la formation de magnésite.

Bien que la calcite précipite beaucoup plus rapidement que la magnésite, la désolvatation du cation Ca^{2+} est également considérée comme l'étape limitante du processus de croissance cristalline du minéral (Nielsen, 1984 ; Hamm *et al.*, 2010). Des études expérimentales ont montré que des protéines naturelles impliquées dans la biominéralisation de la nacre, ainsi que des polypeptides synthétiques riches en résidus acidiques (acide aspartique et acide glutamique) ont la propriété d'accélérer significativement la vitesse de croissance de la calcite, à des concentrations inférieures à 10^{-6} M (Fu *et al.*, 2005, Elhadj *et al.*, 2006). Récemment, il a été démontré que certains peptoïdes, polymères synthétiques de glycines N-substituées, comportant des résidus hydrophiles et hydrophobes, accélèrent la vitesse d'avancement des marches cristallines de la calcite plus de 20 fois à des concentrations de 50 nM (Chen *et al.*, 2011). Cette catalyse de la cristallisation de la calcite proviendrait d'une déshydratation facilitée de Ca^{2+} en présence des biomolécules (Elhadj *et al.*, 2006) et/ou d'une destructuration de l'eau liée à la surface du minéral (Chen *et al.*, 2011).

Si les ligands carboxyliques simples que nous avons utilisés dans cette étude n'ont pas d'effet catalytique visible sur la formation de la magnésite, il n'est pas exclu que des (bio)molécules plus complexes aient un effet accélérateur sur la cinétique de précipitation de la magnésite. Il paraît nécessaire de tester l'influence de polypeptides riches en résidus acidiques ou de peptoïdes, la principale interrogation résidant dans la compatibilité des

fonctionnalités chimiques de telles molécules avec les températures élevées nécessaires aux expérimentations sur la magnésite. De manière générale, une meilleure compréhension des mécanismes moléculaires qui induisent la biominéralisation des minéraux carbonatés magnésiens hydratés ou calciques anhydres pourrait peut-être permettre d'identifier des pistes prometteuses vers la formation à basse température de la magnésite.

À supposer que l'on parvienne à identifier un additif accélérant la formation de magnésite, il est cependant peu probable que le même additif puisse accélérer également la dissolution des silicates magnésiens. En effet, les molécules organiques complexes, notamment composées de longues chaînes hydrocarbonées, ont en général un effet inhibiteur sur la dissolution des silicates (Ganor *et al.*, 2009). À l'inverse, les ligands les plus efficaces pour accélérer la dissolution des minéraux forment des complexes forts avec les cations situés à la surface du minéral, mais également en solution (e.g Schott *et al.*, 2009). De plus, des concentrations importantes (typiquement supérieures 1 mM) de ligand sont nécessaires pour observer un effet significatif sur la cinétique de dissolution (e.g Golubev *et al.*, 2006, Golubev et Pokrovsky, 2006 ; Pokrovsky *et al.*, 2009c) En conséquence, on peut supposer que les ligands accélérant efficacement la dissolution des silicates magnésiens auront *a minima* une influence négative sur la sursaturation des solutions vis-à-vis de la précipitation de magnésite.

Il est donc probable que l'utilisation d'additifs pour accélérer la séquestration minérale du CO_2 ne soit pas envisageable dans le cadre d'un procédé de carbonatation directe. La question de leur utilisation dans le cadre d'un procédé indirect (séparant la phase de dissolution et la phase de précipitation) demeure ouverte.

7.2.2 Formation des carbonates magnésiens : rôle de l'étape de nucléation et des transformations minéralogiques

Mon étude s'est focalisée sur l'étape de croissance cristalline de la précipitation de certains minéraux carbonatés magnésiens. Connaître la cinétique de nucléation est également crucial pour comprendre la succession des phases minérales dans ce système. En particulier, l'observation expérimentale de la formation d'hydromagnésite comme précurseur de la magnésite à haute température (Hänchen *et al.*, 2006 ; King *et al.*, 2010), alors même que les cinétiques de croissance respectives de la magnésite et de l'hydromagnésite suggèrent que la magnésite devrait se former (Chapitre 6), révèle le contrôle exercé par la cinétique de nucléation sur la formation des phases hydratées.

À ce stade, seule la cinétique de nucléation de la nesquéhonite ($MgCO_3 \cdot 3\,H_2O$) a fait l'objet d'une étude détaillée (Cheng et Li, 2010). Il subsiste donc un champ d'étude encore peu investi par la recherche. La technique de suivi *in situ* de la nucléation en conditions hydrothermales et sous forte pression par l'intermédiaire de la spectrométrie Raman, développée par Hänchen *et al.* (2006), pourrait être utilisée pour des études dans un champ large de température.

Par ailleurs, du fait de la grande variété des phases carbonatées magnésiennes hydratées et de leur métastabilité, plusieurs transformations minéralogiques ont été documentées dans la littérature, en particulier de la nesquéhonite à l'hydromagnésite (Davies et Bubela, 1973,

Hopkinson *et al.*, 2008) et de l'hydromagnésite à la magnésite en conditions hydrothermales (Sayles et Fyfe, 1973 ; Zhang *et al.*, 2000). Une étude récente de Montes-Hernandez *et al.* (2012) révèle en outre la transformation directe de dypingite en magnésite en 24h par simple chauffage à 90°C.

Le mécanisme par lequel s'opèrent ces transformations reste mal connu : déshydratation à l'état solide ou dissolution/reprécipitation sont les processus les plus fréquemment évoqués. La compréhension de la cinétique et des facteurs qui influencent ces transitions est toutefois particulièrement importante, car la formation de magnésite à basse température dans les environnements naturels semble être précédée de phases hydratées qui précipitent à partir de solutions aqueuses (voir la discussion du Chapitre 6 ainsi que Deelman (2011)). On pourrait ainsi envisager de favoriser par des moyens physiques (en faisant par exemple varier le taux d'hygrométrie) la transition minéralogique des formes hydratées métastables vers la forme anhydre stable et peu réactive, sans l'apport d'énergie nécessaire à sa précipitation directe en solution aqueuse.

7.2.3 Comprendre l'origine de l'adsorption préférentielle des ligands sur certains sites surfaciques

L'étude HAFM de l'interaction de ligands organiques avec la croissance cristalline de la magnésite révèle l'adsorption préférentielle des ligands sur certains "kink-sites" le long des marches cristallines, grâce à la modification de la forme des îlots de croissance qu'elle induit.

Si la microscopie à force atomique est une technique d'imagerie particulièrement puissante, elle est également une méthode d'étude des propriétés mécaniques et chimiques de tous types de surface. La fonctionnalisation des pointes sondeuses avec des molécules organiques consiste à greffer au bout d'une pointe en silicium ou nitrure de silicium recouverte d'or une molécule ou un simple groupement chimique, en vue d'étudier son interaction avec une surface, une technique appelée "Chemical Force Microscopy" (Noy *et al.*, 1997). Sous l'effet des interactions attractives ou répulsives entre les molécules greffées et la surface, la déflection du microlevier maintenant la pointe varie, renseignant sur l'affinité de la pointe pour la surface. La technique est déjà largemement utilisée en sciences de la vie, par exemple pour l'étude des mécanismes de reconnaissance moléculaire (antigènes-anticorps notamment).

Cette approche a également utilisée en minéralogie. Par exemple, Sheng *et al.* (2005) ont testé l'affinité pour les différentes faces crystallographiques de l'oxalate de calcium monohydraté de groupements chimiques carboxylate et amidine greffés sur des pointes AFM. De manière similaire, Friddle *et al.* (2011) ont utilisé une pointe fonctionnalisée avec une protéine impliquée dans la biominéralisation de l'hydroxyapatite afin de déterminer l'énergie libre de liaison de cette protéine avec les différentes faces du minéral. Hassenkam *et al.* (2009) ont utilisé une technique analogue pour cartographier à l'échelle micrométrique les propriétés de mouillabilité de la surface de coccolithes fossiles, par l'intermédiaire d'une molécule hydrocarbonée hydrophobe. Sous réserve d'une résolution suffisante, la microscopie à force atomique "chimique" pourrait ainsi permettre d'observer in situ les préférences d'adsorption de molécules ou groupements greffés à l'extremités des pointes d'AFM et de confirmer les informations indirectes issues de l'observation des figures de croissance cris-

talline. Jusqu'à présent cependant, cette technique n'a été utilisée qu'a température ambiante.

Quant à la compréhension des facteurs qui conduisent à une adsorption préférentielle de molécules organiques au niveau de certains sites surfaciques, de nombreuses études de simulation numérique de dynamique moléculaire ont prouvé l'utilité de cet outil pour interpréter, voire prédire, l'adsorption de ligands organiques sur une grande variété de systèmes minéraux (e.g de Leeuw et Cooper, 2003 ; Qiu *et al.*, 2004 ; Elhadj *et al.*, 2005 ; Filgueiras *et al.*, 2006 ; Yang *et al.*, 2008). À ce stade, peu d'études ont porté sur la magnésite, mais les capacités techniques existent et les simulations de dynamique moléculaire pourraient certainement aider à identifier d'éventuelles molécules catalysant la précipitation de magnésite.

7.2.4 Inclure le mécanisme de croissance cristalline en présence d'impuretés dans les modèles descriptifs de la croissance minérale

Notre étude de l'influence de ligands organiques sur la croissance de la magnésite ne nous a permis de proposer que des lois cinétiques empiriques décrivant la cinétique de croissance cristalline de la magnésite en présence de ligands pour une chimie de la solution donnée. Ces lois ne sont pas aisément transposables à d'autres conditions chimiques (pH, concentrations ioniques), d'autres concentrations de ligands, ou des températures différentes.

Les modèles de complexation de surface ("surface complexation model", SCM) décrivent la chimie de la surface minérale par l'intermédiaire de groupements surfaciques réactifs et de constantes de protonation, d'hydrolyse et de complexation acquises grâce à une caractérisation précise de l'interface minéral-solution (Schott *et al.*, 2009). Les SCM permettent ainsi de relier la chimie surfacique à la réactivité du minéral. Un tel modèle a été par exemple proposé pour la magnésite à température ambiante par Pokrovsky *et al.* (1999), appliqué à la dissolution de la magnésite par Pokrovsky et Schott (1999), puis étendu à des températures et pressions de CO_2 plus importantes par Pokrovsky *et al.* (2009b) et Saldi *et al.* (2010), et enfin appliqué à la précipitation de la magnésite en conditions hydrothermales par Saldi *et al.* (2012). Ce SCM permet donc de décrire la réactivité de la magnésite dans de vastes intervalles de conditions chimiques, de sursaturation, et de température. Le même SCM a par ailleurs été utilisé par Pokrovsky *et al.* (2009a) d'une manière semi-empirique pour modéliser l'influence de ligands organiques sur la cinétique de dissolution de la magnésite à 60°C, par l'intermédiaire d'une constante de complexation des groupements Mg surfaciques.

On peut voir deux limites principales à ce type de modèle :

- Les SCM usuels considèrent la surface minérale comme une unité plane et uniforme et n'intègrent pas la variété des sites surfaciques et de leurs propriétés chimiques. Par exemple, il a été montré récemment que l'eau adsorbée à la surface de la calcite n'a pas la même acidité selon qu'elle est située au niveau d'une terrasse cristalline (plane) ou d'un "kink" (Andersson et Stipp, 2012). En conséquence, on peut supposer que la plupart des constantes d'équilibre surfaciques dépendent du positionnement de l'atome considéré. L'utilisation de constantes génériques déterminées à partir des propriétés macroscopiques demeure valide tant que la proportion respective des différents sites ne varie pas trop. En revanche dans le cas où une "population" de sites non présents initialement est créée (par exemple

par l'intermédiaire d'une fracture), la description physico-chimique initiale pourrait ne plus être valide. Idéalement, il est donc nécessaire de distinguer les propriétés chimiques de chacun des sites surfaciques.

- Les SCM usuels ne permettent pas de prendre en compte la non-stœchiométrie d'une solution vis-à-vis de la précipitation d'un minéral. En effet, ils considèrent que la cinétique de dissolution ou précipitation dépend essentiellement de la concentration surfacique d'un seul groupement ($>MgOH_2^+$ pour la magnésite en conditions neutres à alcalines), et ne considèrent donc pas, ni ne donnent un moyen de prédire, la dépendance de la vitesse à la stoichiométrie de la solution. L'influence de ce paramètre sur la cinétique de précipitation de a pourtant été démontrée, dans le cas de la calcite, par Stack et Grantham (2010) et Larsen *et al.* (2010).

Une autre "classe" de modèles, basés sur le modèle descriptif de la croissance cristalline dit "BCF" (Burton *et al.*, 1951), s'attache à décrire le mécanisme de la croissance cristalline, en particulier la dynamique des kinks au niveau des marches cristallines, la vitesse d'avancement des marches et le mécanisme de leur génération. Le modèle de Zhang et Nancollas (1998) pour un crystal binaire a ainsi été utilisé pour interpréter les données de cinétiques de précipitation en conditions non-stœchiométriques. En revanche, ce type de modèle ne prend pas en compte la chimie de surface et son influence sur la réactivité et est donc mal adapté pour prédire l'influence d'un ligand s'adsorbant au niveau de certains sites surfaciques.

Nous avons vu que citrate et oxalate s'adsorbent au niveau de sites spécifiques à la surface de la magnésite et que leur influence sur la cinétique de croissance du minéral dépend probablement de l'influence de leur adsorption sur l'étape limitante du processus de croissance cristalline. Afin de pouvoir représenter rigoureusement l'influence de ligands sur la réactivité du minéral, il est donc nécessaire de tenir compte à la fois de la chimie surfacique et des sites d'adsorption préferentielle, ainsi que du processus de croissance cristalline. Comment réconcilier les deux approches de modélisation ?

L'approche proposée récemment par Wolthers *et al.* (2011) pour la calcite est un premier pas dans cette direction : les auteurs intègrent au modèle de Zhang et Nancollas (1998) un SCM très complet distinguant les constantes d'équilibre chimique relatives à trois types de sites surfaciques différents (Wolthers *et al.*, 2008). Le modèle, ajusté sur la base d'études expérimentales sur la dépendance de la cinétique de croissance à la stœchiométrie, peine toutefois à reproduire la grande dispersion des données cinétiques publiées pour la calcite. On pourra remarquer que le modèle est perfectible en ceci qu'il considère la calcite comme un crystal cubique et ne prend donc pas en compte l'existence de marches aigües et obtuses, qui, comme pour la magnésite, ont des réactivités différentes. En outre, la diversité effective des sites surfaciques à prendre en compte excède largement le nombre de trois.

En tout état de cause, la description présentée ici d'un modèle mécanistique "idéal" paraît extrêmement ambitieuse. En effet, la description complète de la croissance d'un minéral nécessite de connaître le mécanisme de croissance du minéral, la fréquence de nucléation des kinks le long de ces différentes orientations cristallographiques, leur vitesse de propagation et certains paramètres thermodynamiques tels que l'énergie libre d'un segment de marche. Par ailleurs, la description physico-chimique complète nécessite de décliner les relations de chimie de surface pour l'ensemble des sites surfaciques pertinents (terrasse, marche et kink,

pour différentes orientations cristallographiques), y compris pour les relations de complexation de surface impliquant des ligands. La majeure partie de ces paramètres sont difficilement accessibles à l'expérimentation, en particulier pour ce qui concerne le modèle de complexation de surface étendu. En revanche, les simulations numériques de dynamique moléculaire, citées à de nombreuses reprises au cours de ce manuscrit, permettent d'obtenir des informations précises à la fois sur la dynamique de croissance des minéraux et sur la réactivité des groupements surfaciques quelle que soit leur position. Ceci pourrait permettre de proposer une description mécanistique cohérente de la croissance cristalline dans de larges gammes de conditions physico-chimiques, y compris en présence de ligands ou molécules de natures variées.

Bibliographie

Andersson, M. P. et Stipp, S. L. S. (2012). How acidic is water on calcite ? *The Journal of Physical Chemistry C*, 116(35), 18779–18787.

Bonfils, B., Julcour-Lebigue, C., Guyot, F., Bodénan, F., Chiquet, P. et Bourgeois, F. (2012). Comprehensive analysis of direct aqueous mineral carbonation using dissolution enhancing organic additives. *International Journal of Greenhouse Gas Control*, 9, 334–346.

Burton, W. K., Cabrera, N. et Frank, F. C. (1951). The growth of crystals and the equilibrium structure of their surfaces. *Philosophical Transactions of the Royal Society of London. Series A, Mathematical and Physical Sciences*, 243(866), 299–358.

Chen, C.-L., Qi, J., Zuckermann, R. N. et DeYoreo, J. J. (2011). Engineered biomimetic polymers as tunable agents for controlling $CaCO_3$ mineralization. *Journal of the American Chemical Society*, 133(14), 5214–5217.

Cheng, W. et Li, Z. (2010). Nucleation kinetics of nesquehonite $MgCO_3{\cdot}3\,H_2O$ in the $MgCl_2$-Na_2CO_3 system. *Journal of Crystal Growth*, 312(9), 1563–1571.

Davies, P. J. et Bubela, B. (1973). The transformation of nesquehonite into hydromagnesite. *Chemical Geology*, 12, 289–300.

de Leeuw, N. H. et Cooper, T. G. (2003). A computer modeling study of the inhibiting effect of organic adsorbates on calcite crystal growth. *Crystal Growth & Design*, 4(1), 123–133.

De Yoreo, J. J., Zepeda-Ruiz, L. A., Friddle, R. W., Qiu, S. R., Wasylenki, L. E., Chernov, A. A., Gilmer, G. H. et Dove, P. M. (2009). Rethinking classical crystal growth models through molecular scale insights : consequences of kink-limited kinetics. *Crystal Growth & Design*, 9, 5135–5144.

Deelman, J. C. (2011). *Low-temperature formation of magnesite and dolomite*. Geology Series. Compact Disc Publications, Eindhoven, The Netherlands, 2.3 édition. E-book first published online in May 2003. Version 2.3 updated in 2011. www.jcdeelman.demon.nl/dolomite/bookprospectus.html.

Elhadj, S., De Yoreo, J. J., Hoyer, J. R. et Dove, P. M. (2006). Role of molecular charge and hydrophilicity in regulating the kinetics of crystal growth. *Proceedings of the National Academy of Sciences*, 103(51), 19237–19242.

Elhadj, S., Salter, E. A., Wierzbicki, A., De Yoreo, J. J., Han, N. et Dove, P. M. (2005). Peptide controls on calcite mineralization : polyaspartate chain length affects growth kinetics and acts as a stereochemical switch on morphology. *Crystal Growth & Design*, 6(1), 197–201.

Filgueiras, M. R. T., Mkhonto, D. et de Leeuw, N. H. (2006). Computer simulations of the adsorption of citric acid at hydroxyapatite surfaces. *Journal of Crystal Growth*, 294(1), 60–68.

Friddle, R. W., Battle, K., Trubetskoy, V., Tao, J., Salter, E. A., Moradian-Oldak, J., De Yoreo, J. J. et Wierzbicki, A. (2011). Single-molecule determination of the face-specific adsorption of amelogenin's C-terminus on hydroxyapatite. *Angewandte Chemie International Edition*, 50(33), 7541–7545.

Fu, G., Qiu, S. R., Orme, C. A., Morse, D. E. et De Yoreo, J. J. (2005). Acceleration of calcite kinetics by abalone nacre proteins. *Advanced Materials*, 17(22), 2678–2683.

Ganor, J., Reznik, I. J. et Rosenberg, Y. O. (2009). Organics in water-rock interactions. *Reviews in Mineralogy and Geochemistry*, 70(1), 259.

Golubev, S. V., Bauer, A. et Pokrovsky, O. S. (2006). Effect of pH and organic ligands on the kinetics of smectite dissolution at 25 °C. *Geochimica et Cosmochimica Acta*, 70(17), 4436–4451.

Golubev, S. V. et Pokrovsky, O. S. (2006). Experimental study of the effect of organic ligands on diopside dissolution kinetics. *Chemical Geology*, 235(3-4), 377–389.

Hamm, L. M., Wallace, A. F. et Dove, P. M. (2010). Molecular dynamics of ion hydration in the presence of small carboxylated molecules and implications for calcification. *The Journal of Physical Chemistry B*, 114, 10488–10495.

Hassenkam, T., Skovbjerg, L. L. et Stipp, S. L. S. (2009). Probing the intrinsically oil-wet surfaces of pores in North Sea chalk at subpore resolution. *Proceedings of the National Academy of Sciences*, 106(15), 6071–6076.

Hänchen, M., Prigiobbe, V., Storti, G., Seward, T. et Mazzotti, M. (2006). Dissolution kinetics of fosteritic olivine at 90 - 150°C including effects of the presence of CO_2. *Geochimica et Cosmochimica Acta*, 70(17), 4403–4416.

Hopkinson, L., Rutt, K. et Cressey, G. (2008). The transformation of nesquehonite to hydromagnesite in the system CaO-MgO-H_2O-CO_2 : An experimental spectroscopic study. *The Journal of Geology*, 116, 387–400.

King, H. E., Plümper, O. et Putnis, A. (2010). Effect of secondary phase formation on the carbonation of olivine. *Environmental Science & Technology*, 44(16), 6503–6509.

Larsen, K., Bechgaard, K. et Stipp, S. L. S. (2010). Modelling spiral growth at dislocations and determination of critical step lengths from pyramid geometries on calcite $(10\bar{1}4)$ surfaces. *Geochimica et Cosmochimica Acta*, 74(2), 558–567.

Montes-Hernandez, G., Renard, F., Chiriac, R., Findling, N. et Toche, F. (2012). Rapid precipitation of magnesite microcrystals from $Mg(OH)_2$-H_2O-CO_2 slurry enhanced by NaOH and a heat-ageing step (from 20 to 90°C). *Crystal Growth & Design*, in press.

Nielsen, A. E. (1984). Electrolyte crystal growth mechanisms. *Journal of Crystal Growth*, 67(2), 289–310.

Noy, A., Vezenov, D. V. et Lieber, C. M. (1997). Chemical force microscopy. *Annual Review of Materials Science*, 27(1), 381–421.

Pokrovsky, O. S., Golubev, S. V. et Jordan, G. (2009a). Effect of organic and inorganic ligands on calcite and magnesite dissolution rates at 60°C and 30 atm pCO2. *Chemical Geology*, 265(1-2), 33–43.

Pokrovsky, O. S., Golubev, S. V., Schott, J. et Castillo, A. (2009b). Calcite, dolomite and magnesite dissolution kinetics in aqueous solutions at acid to circumneutral pH, 25 to 150°C and 1 to 55 atm pCO2 : new constraints on CO_2 sequestration in sedimentary basins. *Chemical Geology*, 265(1-2), 20–32.

Pokrovsky, O. S. et Schott, J. (1999). Processes at the magnesium-bearing carbonates/solution interface. II. Kinetics and mechanism of magnesite dissolution. *Geochimica et cosmochimica acta*, 63(6), 881–897.

Pokrovsky, O. S., Schott, J. et Thomas, F. (1999). Processes at the magnesium-bearing carbonates/solution interface. I. A surface speciation model for magnesite. *Geochimica et cosmochimica acta*, 63(6), 863–880.

Pokrovsky, O. S., Shirokova, L. S., Benezeth, P., Schott, J. et Golubev, S. V. (2009c). Effect of organic ligands and heterotrophic bacteria on wollastonite dissolution kinetics. *American Journal of Science*, 309(8), 731–772.

Prigiobbe, V. et Mazzotti, M. (2011). Dissolution of olivine in the presence of oxalate, citrate, and CO_2 at 90°C and 120°C. *Chemical Engineering Science*, 66(24), 6544–6554.

Qiu, S. R., Wierzbicki, A., Orme, C. A., Cody, A. M., Hoyer, J. R., Nancollas, G. H., Zepeda, S. et De Yoreo, J. J. (2004). Molecular modulation of calcium oxalate crystallization by osteopontin and citrate. *Proceedings of the National Academy of Sciences*, 101(7), 1811–1815.

Saldi, G. D., Jordan, G., Schott, J. et Oelkers, E. H. (2009). Magnesite growth rates as a function of temperature and saturation state. *Geochimica et Cosmochimica Acta*, 73(19), 5646–5657.

Saldi, G. D., Schott, J., Pokrovsky, O., Gautier, Q. et Oelkers, E. H. (2012). An experimental study of magnesite precipitation rates at neutral to alkaline conditions and 100-200°C as a function of pH, aqueous solution composition and chemical affinity. *Geochimica et Cosmochimica Acta*, 83, 93–109.

Saldi, G. D., Schott, J., Pokrovsky, O. S. et Oelkers, E. H. (2010). An experimental study of magnesite dissolution rates at neutral to alkaline conditions and 150 and 200°C as a function of pH, total dissolved carbonate concentration, and chemical affinity. *Geochimica et Cosmochimica Acta*, 74, 6344–6356.

Sayles, F. et Fyfe, W. (1973). The crystallization of magnesite from aqueous solution. *Geochimica et Cosmochimica Acta*, 37(1), 87–99.

Schott, J., Pokrovsky, O. S. et Oelkers, E. H. (2009). The link between mineral dissolution/precipitation kinetics and solution chemistry. *Reviews in Mineralogy and Geochemistry*, 70(1), 207–258.

Sheng, X., Jung, T., Wesson, J. A. et Ward, M. D. (2005). Adhesion at calcium oxalate crystal surfaces and the effect of urinary constituents. *Proceedings of the National Academy of Sciences*, 102(2), 267–272.

Stack, A. G. et Grantham, M. C. (2010). Growth rate of calcite steps as a function of aqueous calcium-to-carbonate ratio : Independent attachment and detachment of calcium and carbonate ions. *Crystal Growth & Design*, 10(3), 1409–1413.

Wolthers, M., Charlet, L. et van Cappellen, P. (2008). The surface chemistry of divalent metal carbonate minerals ; a critical assessment of surface charge and potential data using the charge distribution multi-site ion complexation model. *American Journal of Science*, 308(8), 905–941.

Wolthers, M., Nehrke, G., Gustafsson, J. et van Cappellen, P. (2011). Calcite growth kinetics : Modeling the effect of solution stoichiometry. *Geochimica et Cosmochimica Acta*.

Yang, M., Stipp, S. L. S. et Harding, J. (2008). Biological control on calcite crystallization by polysaccharides. *Crystal Growth & Design*, 8(11), 4066–4074.

Zhang, J. et Nancollas, G. H. (1998). Kink density and rate of step movement during growth and dissolution of an ABCrystal in a non-stoichiometric solution. *Journal of Colloid and Interface Science*, 200(1), 131–145.

Zhang, P.-C., Anderson, H. L., Kelly, J. W., Krumhansl, J. L. et Papenguth, H. W. (2000). Kinetics and mechanisms of formation of magnesite from hydromagnesite in brine. Technical Report SAN099 - 1946J, Sandia National Laboratories, Albuquerque, New Mexico, USA.

Annexe:

"An experimental study of magnesite precipitation rates at neutral to alkaline conditions and 100-200°C as a function of pH, aqueous solution composition and chemical affinity."

Giuseppe D. Saldi, Jacques Schott, Oleg S. Pokrovsky, **Quentin Gautier**, Eric H. Oelkers

Article publié dans la revue *Geochimica et Cosmochimica Acta*

Available online at www.sciencedirect.com

SciVerse ScienceDirect

Geochimica et Cosmochimica Acta 83 (2012) 93–109

Geochimica et Cosmochimica Acta

www.elsevier.com/locate/gca

An experimental study of magnesite precipitation rates at neutral to alkaline conditions and 100–200 °C as a function of pH, aqueous solution composition and chemical affinity

Giuseppe D. Saldi *, Jacques Schott, Oleg S. Pokrovsky, Quentin Gautier, Eric H. Oelkers

Géochimie et Biogéochimie Expérimentale, GET – CNRS – OMP – Université de Toulouse, 14, Avenue Edouard Belin, 31400 Toulouse, France

Received 13 July 2011; accepted in revised form 28 November 2011; available online 8 December 2011

Abstract

Magnesite precipitation rates were measured at temperatures from 100 to 200 °C as a function of saturation state and reactive fluid composition in mixed flow reactors. Measured rates were found to increase systematically with increasing saturation state but to decrease with increasing reactive fluid aqueous CO_3^{2-} activity and pH. Measured rates are interpreted through a combination of surface complexation models and transition state theory. In accord with this formalism, constant saturation state BET surface area normalized magnesite precipitation rates (r_{Mg}) are a function of the concentration of protonated Mg sites at the surface ($>MgOH_2^+$) and can be described using:

$$r_{Mg} = k^-_{Mg}\left(\frac{K_{CO_3}K_{OH}}{K_{CO_3}K_{OH} + K_{OH}a_{CO_3^{2-}} + K_{CO_3}a_{OH^-}}\right)^n \left(1-\Omega^n_{Mg}\right)$$

where k^-_{Mg} represents a rate constant, K_{OH} and K_{CO_3} stand for equilibrium constants, a_i designates the activity of the subscripted aqueous species, n refers to a reaction order equal to 2, and Ω_{Mg} denotes the saturation state of the reactive solution with respect to magnesite. Retrieved values of n are consistent with magnesite precipitation control by a spiral growth mechanism. The temperature variation of the rate constant can be described using $k^-_{Mg} = A_a \exp(-E_a/RT)$, where A_a represents a pre-exponential factor equal to 5.9×10^{-5} mol/cm^2/s, E_a designates an activation energy equal to 80.2 kJ/mol, R denotes the gas constant, and T corresponds to the absolute temperature. Comparison of measured magnesite precipitation rates with corresponding forsterite dissolution rates suggest that the relatively slow rates of magnesite precipitation may be the rate limiting step in mineral carbonation efforts in ultramafic rocks.

Published by Elsevier Ltd.

1. INTRODUCTION

This study is designed to improve our understanding of the precipitation rates of carbonate minerals. The precipitation of carbonate minerals, such as calcite ($CaCO_3$), dolomite ($CaMg(CO_3)_2$), siderite ($FeCO_3$), and magnesite ($MgCO_3$), is often coupled in natural environments to silicate mineral dissolution that releases divalent metal cations to the aqueous phase (e.g. Berner et al., 1983). Similar processes have the potential to sequester carbon-dioxide within carbonate minerals (e.g. Giammar et al., 2005; Oelkers and Schott, 2005; Oelkers and Cole, 2008; Dufaud et al., 2009; Prigiobbe et al., 2009a; Guyot et al., 2011). Ultramafic and basaltic rocks are among the most abundant, reactive,

* Corresponding author. Present address: Earth Sciences Division, Lawrence Berkeley National Laboratory, 1 Cyclotron Road, Berkeley, CA 94720, USA. Tel.: +1 510 486 6856.

E-mail addresses: gdsaldi@lbl.gov (G.D. Saldi), oelkers@get.obs-mip.fr (E.H. Oelkers).

0016-7037/$ - see front matter Published by Elsevier Ltd.
doi:10.1016/j.gca.2011.12.005

and economically available sources of divalent cations for carbonate precipitation (Lackner et al., 1995, 1997; Goldberg et al., 2001; McGrail et al., 2006; Matter et al., 2007, 2009, 2011; Gysi and Stefánsson, 2008; Kelemen and Matter, 2008; Oelkers et al., 2008a; Schaef et al., 2009; Daval et al., 2010; Garcia et al., 2010; Gislason et al., 2010; Wolff-Boenisch et al., 2011). For example, ultramafic rocks contain 30–50% MgO by weight and represent the feedstock material with the highest potential for CO_2 mineral sequestration (Wolff-Boenisch et al., 2006; Marini, 2007). Mg-carbonate formation from the forsterite and serpentine contained within mafic or ultramafic rocks can be described by the following reactions:

$$\underset{\text{Forsterite}}{Mg_2SiO_{4(s)}} + 2CO_{2(g)} + 2H_2O = 2\underset{\text{Magnesite}}{MgCO_{3(s)}} + H_4SiO_{4(aq)} \quad (1)$$

$$\underset{\text{Serpentine}}{Mg_3Si_2O_5(OH)_{4(s)}} + 3CO_{2(g)} + 2H_2O = 3\underset{\text{Magnesite}}{MgCO_{3(s)}} + 2H_4SiO_{4(aq)} \quad (2)$$

where aqueous silica could eventually precipitate as quartz or other silicate minerals. Numerous studies have focused on the application of reactions (1) and (2) to carbon sequestration on an industrial scale (e.g. O'Connor et al., 2000; Wolf et al., 2004; Giammar et al., 2005; Maroto-Valer et al., 2005; Chen et al., 2006; Alexander et al., 2007; Gerdemann et al., 2007; Oelkers et al., 2008a). The optimization of such mineral carbonation efforts is facilitated by the detailed understanding of rates of reactions among fluids, Mg-silicates, and Mg-carbonates. Whereas a large number of studies have focused on quantifying the dissolution rates of Mg-silicates (e.g. Luce et al., 1972; Lin and Clemency, 1981; Schott et al., 1981; Schott and Berner, 1983, 1985; Wogelius and Walther, 1991, 1992; Pokrovsky and Schott, 2000; Rosso and Rimstidt, 2000; Oelkers, 2001a; Oelkers and Schott, 2001; Golubev et al., 2005; Golubev and Pokrovsky, 2006; Hänchen et al., 2006; Saldi et al., 2007; Olsen and Rimstidt, 2008; Prigiobbe et al., 2009b) relatively few studies have focused on Mg-carbonate precipitation rates (Sayles and Fyfe, 1973; Usdowski, 1989; Deelman, 1999, 2003; Hänchen et al., 2008; Saldi et al., 2009). This study attempts to overcome this limitation through the direct measurement of magnesite precipitation rates as a function of saturation state, temperature, CO_2 partial pressure, and reactive fluid chemistry.

Another goal of this work is an improved understanding of the link between mineral dissolution and precipitation rates. The application of transition state theory has led to equations that can accurately describe mineral dissolution rates as a function of aqueous solution composition and saturation state (cf. Berger et al., 1994; Oelkers et al., 1994; Oelkers and Schott, 1995, 1999; Schott and Oelkers, 1995; Oelkers, 2001b; Pokrovsky et al., 2005; Schott et al., 2009). Such models have also been used to predict mineral precipitation rates in geochemical modeling studies (e.g. Steefel and MacQuarrie, 1996; Knauss et al., 2005; Steefel and Maher, 2009; Zhu, 2009; Goddéris et al., 2010; Zhu et al., 2010; Liu et al., 2011), yet the applicability of such models has not been verified in detail and may be inconsistent with what is known about mineral precipitation kinetics (e.g. Nielsen, 1964, 1984; Nancollas and Reddy, 1971; Reddy and Nancollas, 1976; Reddy and Gaillard, 1981; Reddy et al., 1981; Inskeep and Bloom, 1985; Mucci, 1986; Van Cappellen and Berner, 1991; Piana et al., 2006; Kowacz et al., 2007; Vekilov, 2007; Bénézeth et al., 2008; Kowacz and Putnis, 2008; Perdikouri et al., 2009; Vavouraki et al., 2010; Rodriguez-Blanco et al., 2011). In an attempt to explore the link between dissolution and precipitation, magnesite precipitation rates have been measured as a function of chemical affinity and aqueous solution composition using the same solids and experimental methods as used by Saldi et al. (2010) for magnesite dissolution. This study thus allows direct assessment of the link between dissolution and precipitation rates.

2. THEORETICAL CONSIDERATIONS

The standard state adopted in this study is that of unit activity for pure minerals and H_2O at any temperature and pressure. For aqueous species, the standard state is unit activity of a hypothetical one molal solution referenced to infinite dilution at any temperature and pressure. The activity of species at the magnesite surface is assumed equal to their concentration. Aqueous solution speciation and saturation indices, computed with respect to solid phases, were calculated using PHREEQC (Parkhurst and Appelo, 1999), together with the Lawrence Livermore National Laboratory (llnl) thermodynamic database. Additional data for the formation constants of the aqueous complex $MgOH^+$ were taken from Shock et al. (1997).

Magnesite precipitation rates obtained in this study were interpreted using the surface complexation model developed for carbonate minerals by Van Cappellen et al. (1993) and Pokrovsky et al. (1999a,b). At pH >6 the rates of magnesite dissolution, defined by the following reaction:

$$MgCO_{3(c)} = Mg^{2+}_{(aq)} + CO^{2-}_{3(aq)}, \quad (3)$$

were successfully described by the surface complexation model assuming that they are proportional to the surface concentration of protonated magnesium centers, $\{> MgOH_2^+\}$ (Pokrovsky and Schott, 1999, 2002; Schott et al., 2009; Saldi et al., 2010), in accord with

$$r_{Mg} = k^+_{Mg}\{> MgOH_2^+\}^n \cdot \left(1 - \left(\frac{Q_{Mg}}{K_{Mg}}\right)^n\right), \quad (4)$$

where r_{Mg} represents the surface area normalized magnesite overall dissolution rate, k^+_{Mg} denotes a rate constant, n stands for a reaction order, and Q_{Mg} and K_{Mg} refer to the reaction quotient and equilibrium constant for reaction (3). Eq. (4) also can be expressed in terms of surface area normalized forward rate $r_{+,Mg}$ using (cf. Lasaga, 1981; Aagaard and Helgeson, 1982; Oelkers et al., 1994):

$$r_{Mg} = r_{+,Mg}\left(1 - \left(\frac{Q_{Mg}}{K_{Mg}}\right)^n\right) = r_{+,Mg}\left[1 - \exp\left(\frac{-nA}{RT}\right)\right] = r_{+,Mg}(1 - \Omega^n_{Mg}) \quad (5)$$

where R represents the gas constant, T stands for the absolute temperature, A defines the chemical affinity of reaction (3), and Ω_{Mg} designates the saturation state of magnesite $\left(\Omega_{Mg} = \left(\frac{Q_{Mg}}{K_{Mg}}\right)\right)$. Note that $r_{+,Mg}$, the forward reaction rate $\left(r_{+,Mg} = k^+_{Mg}\{> MgOH_2^+\}^n\right)$, corresponds to the

dissolution rates at far-from-equilibrium conditions where $\left(\frac{Q_{Mg}}{K_{Mg}}\right) \ll 1$. The concentration of the $>MgOH_2^+$ surface species can be calculated by assuming that three species dominate magnesium speciation on magnesite surfaces at alkaline conditions: $>MgOH^\circ$, $>MgOH_2^+$, and $>MgCO_3^-$ (Pokrovsky et al., 1999a). Reactions among these species can be written:

$$>MgOH^\circ + H_2O => MgOH_2^+ + OH^-, \quad (6)$$

and

$$>MgCO_3^- + H_2O => MgOH_2^+ + CO_3^{2-}, \quad (7)$$

Combining the laws of mass action for these reactions with the conservation of magnesium surface sites leads to (cf. Saldi et al., 2010)

$$\{>MgOH_2^+\} = \left(\frac{K_{CO_3}K_{OH}}{K_{CO_3}K_{OH} + K_{OH}a_{CO_3^{2-}} + K_{CO_3}a_{OH^-}}\right), \quad (8)$$

where K_{OH} and K_{CO_3} stand for the equilibrium constants for reactions (6) and (7) respectively, and a_i signifies the activity of the subscripted aqueous species. Combining Eqs. (4), (5), and (8) leads to

$$r_{+,Mg} = k_{Mg}^+\left(\frac{K_{CO_3}K_{OH}}{K_{CO_3}K_{OH} + K_{OH}a_{CO_3^{2-}} + K_{CO_3}a_{OH^-}}\right)^n \quad (9)$$

and

$$r_{Mg} = k_{Mg}^+\left(\frac{K_{CO_3}K_{OH}}{K_{CO_3}K_{OH} + K_{OH}a_{CO_3^{2-}} + K_{CO_3}a_{OH^-}}\right)^n\left(1 - \Omega_{Mg}^n\right) \quad (10)$$

In accord with Eqs. (9) and (10) magnesite dissolution rates decrease with increasing pH and $a_{CO_3^{2-}}$ (cf. Saldi et al., 2010). Recall that $r_{Mg} = r_{+,Mg}$ when $\Omega_{Mg} = 0$, such that $r_{Mg} = r_{+,Mg}$ in strongly undersaturated solutions. As Ω_{Mg} is always greater than 1 for supersaturated solutions, r_{Mg} for precipitation never equals $r_{+,Mg}$,, but $r_{Mg} = -r_{+,Mg}$ for $\Omega_{Mg}^n = 2$.

The parameter n in Eqs. (4), (5), (9), and (10) has been attributed to different phenomena in the literature. In the dissolution literature, n is often equated to the reciprocal of Temkin's average stoichiometric number. In this context, n equals the reciprocal of the number of moles of activated or precursor complex in one mole of the dissolving or precipitating mineral (e.g. Aagaard and Helgeson, 1982; Oelkers et al., 1994). In the mineral precipitation literature, n is often related to the precipitation mechanism. It has been argued that, for elementary reactions, $n = 1$ is consistent with transport or adsorption controlled growth and $n = 2$ is consistent with spiral growth (cf. Nielsen, 1964, 1984; Gratz et al., 1993; Shiraki and Brantley, 1995; Teng et al., 2000). If growth is controlled by surface nucleation, rates are quantified via an exponential function of saturation state, i.e. $n > 2$. As emphasized by Temkin (1963), however, the chemical affinity of an overall reaction needs to be normalized to that of the elementary reaction to accurately use reaction orders based on these elementary reaction mechanisms.

The temperature variation of the rate constant, k_{Mg}^+, is commonly described using an Arrhenius equation of the form (e.g. Eyring, 1935; Oelkers and Schott, 1999; Carroll and Knauss, 2005; Oelkers et al., 2008b):

$$k_{Mg}^+ = A_a \cdot e^{-Ea/RT} \quad (11)$$

where E_a corresponds to the activation energy and A_a refers to a pre-exponential factor. The degree to which measured magnesite precipitation rates can be described using Eqs. (10) and (11) will be assessed below.

3. EXPERIMENTAL METHODS

3.1. Magnesite samples

The synthetic magnesite samples used in this study were originally prepared for the magnesite dissolution experiments reported by Saldi et al. (2010). This synthetic magnesite was produced by placing ~20 g of analytical grade hydrated Mg-carbonate (magnesium hydroxide carbonate, Merck Chemicals), 250 ml of deionized water, and 15–20 g of solid CO_2 into a rocking 400 ml Ti-autoclave. The autoclave was sealed and temperature was increased to 200 °C. After 3 weeks, the solids were recovered, rinsed in deionized water, and dried in an oven at 60 °C. The synthesized magnesite powders consisted of 4–40 μm rhombohedral shaped crystals. A SEM photomicrograph of a representative synthetic magnesite powder is shown in Fig. 1a. X-ray diffraction (XRD) and energy dispersive X-ray spectroscopic (EDS) analyses confirm that these powders are pure magnesite. These synthetic magnesite powders were used in the precipitation experiments without further treatment. The specific surface area of all magnesite powders used in the present study was determined by multi-point krypton adsorption according to the BET method (Brunauer et al., 1938). Geometric surface areas of these powders were estimated by laser granulometric analysis, assuming the crystals were cubic. Results of these surface area measurements and calculations are reported in Table 1.

3.2. Experiments and solution analysis

Steady-state magnesite precipitation rates were determined from mixed-flow reactor experiments using the same 200 and 300 ml titanium reactors as previously used by Saldi et al. (2010) to measure magnesite steady-state dissolution rates. Inlet solutions were stored in compressible polyethylene containers and injected into the reactor by a high pressure liquid chromatography (HPLC) pump allowing flow rates ranging from 0.1 to 10 ml/min. The reactive solution inside the reactor was stirred at a constant rate with a Parr magnetic stirrer and kept at constant temperature ±1 °C by a Parr controlled furnace. The fluid left the reactor through a 2 μm titanium filter and was cooled before passing through a back-pressure regulator that maintained a constant pressure throughout the system; this pressure was typically 15–40 bars. There was no evidence that fluid

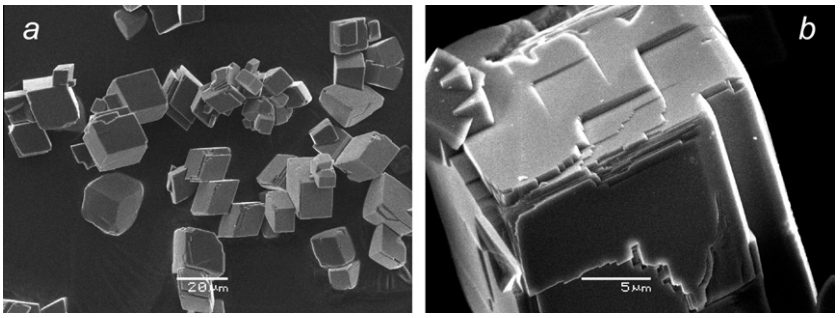

Fig. 1. SEM photomicrographs of synthetic magnesite used in the present study. (a) Example of magnesite powder after synthesis at 200 °C and a CO_2 pressure of 50 bar. (b) Detail of a magnesite crystal after a precipitation experiment performed in a mixed-flow reactor.

Table 1
Values of specific surface area for the magnesite powders used in this study as determined by krypton adsorption (S_{BET}) and by granulometric analysis (S_{GEO}).

$MgCO_3$ powder	S_{BET} (cm^2/g)	S_{GEO} (cm^2/g)
Mgs-I	2241	822
Mgs-II	1723	643
Mgs-III	1610	772
Mgs-V	1791	844
Mgs-VIII	2007	669

stirring led to grain collisions resulting in either fragmentation or grain surface damage.

Inlet solutions were prepared with high purity deionized H_2O (18.2 MΩ cm) and reagent grade NaCl, $MgCl_2$, $NaHCO_3$, HCl, and NaOH. Experiments were performed at ionic strengths varying from 0.1 to 1 mol/kg. The compositions of all inlet solutions used in the experiments are summarized in Table 2. All solutions were analyzed for magnesium concentration and alkalinity. Mg was measured by flame atomic absorption spectroscopy (AAS) with an uncertainty of ±2% and a detection limit of 6×10^{-7} M, whereas the alkalinity was determined by standard HCl titration with an uncertainty of ±2% and a detection limit of 5×10^{-5} eq/L. Solution pH measurements were performed at 25 °C for inlet solutions as well as for outlet solutions immediately after sampling using a standard glass electrode, previously calibrated with 4.01, 6.86, and 9.18 NIST pH buffers. These 25 °C pH measurements were used together with measured fluid compositions and PHREEQC to calculate the pH at the temperatures of the experiments. Solution pH was also measured *in situ* during selected experiments performed at 100, 120, and 150 °C using the pH electrode system described below.

Experiments were run in series. Each series consisted of experiments with distinct fluid flow rates and/or a distinct inlet solution with a single magnesite powder. Each experimental series is noted by a distinct prefix in Tables 2–5. Steady-state precipitation rates, indicated by a constant outlet Mg concentration, were calculated using

$$r_{Mg} = -q \cdot \Delta[Mg]_{tot}/S \quad (12)$$

where q represents the fluid flow rate, $\Delta[Mg]_{tot}$ stands for the difference between the outlet and inlet fluid Mg concentration, and S refers to the total mineral surface area. The surface area used to calculate these rates was the BET surface area of unreacted powders. Post-experiment measurements show that these surface areas changed by no more than 10% during the experimental series.

Constant Mg concentrations in the outlet solution were obtained after an elapsed time of 4 h to 6 days, depending on the flow rate. Steady-state was verified with a minimum of three constant Mg concentrations of the outlet fluid samples taken over several residence times. After all samples at a given set of conditions had been obtained, inlet fluid composition and/or fluid flow rate were changed to the next desired experimental conditions.

3.3. *In situ* pH measurements

The reported pH values were measured *in situ* during many of the experiments performed in this study. *In situ* pH was measured using a solid contact Li–Sn alloy commercial electrode (Potential®, St. Petersburg, Russia) coupled to a Na-selective glass reference electrode. This reference electrode produces a constant standard potential in solutions having constant Na^+ activity; a detailed description of this electrode is provided by Pokrovski et al. (1995). The electrode couple used in this study can be represented as:

Sn–Cu, Li–Sn alloy|H-selective glass|Na-bearing buffer solution|Na-selective glass

The electromotive force of this cell can be described using:

$$E = E^\circ + (2.3RT/F)[\mathrm{Log}a_H - \mathrm{Log}a_{Na^+}], \quad (13)$$

where E stands for the measured electric potential of the system, E° denotes the standard potential determined from the calibration curve, F refers to the Faraday constant, and a_i again designates the activity of the subscripted aqueous solution. This pH-electrode couple was calibrated in aqueous $NaCl/Na_2CO_3$, $NaCl/B(OH)_3/NaOH$, and $NaCl/CH_3COONa/HCl$ solutions at 100, 120, and 150 °C. The pH of these calibration solutions at elevated temperature was calculated using PHREEQC (Parkhurst and Appelo, 1999) and HCh (GIBBS) (Shvarov, 1999) together with association constants for $NaB(OH)_4^\circ$ reported by Pokrovski et al. (1995). This pH electrode couple was not used at temperatures higher than 150 °C because higher temperatures were found to rapidly degrade the

Table 2
Composition of inlet fluid solutions used for magnesite precipitation experiments in the present study.

Experiment	T (°C)	pH (25 °C)	NaCl (mol/kg)	$MgCl_2$ (mol/kg) $\times 10^4$	HCl (mol/kg) $\times 10^3$	NaOH (mol/kg) $\times 10^4$	$NaHCO_3$ (mol/kg)
PM6, PM6A	200	8.11	0.1	1.653	0	0	0.01
PM6B–PM6E	200	8.08	0.1	1.698	0	0	0.01
PM7–PM7B	200	8.26	0.1	0.931	0	0	0.02
PM7C–PM7E	200	8.24	0.1	0.942	0	0	0.02
PM8–PM8E	200	8.36	0.1	0.525	0	0	0.04
PM9, PM9A	200	7.15	0.1	1.712	0	0	0.01
PM9B	200	7.20	0.1	1.692	0	0	0.01
PM12, PM12A	200	6.62	0.1	2.260	20.2	0	0.04
PM12B–PM12D	200	6.45	0.1	1.313	5.20	0	0.01
PM13–PM13E	200	6.12	0.1	1.842	6.50	0	0.01
PM21–PM21D	200	6.55	0.5	2.684	9.75	0	0.02
PM21E, PM21F	200	6.28	0.5	2.729	9.75	0	0.02
PM24–PM24E	200	6.22	1.00	3.841	9.22	0	0.02
PM27, PM27A	200	6.22	1.00	3.513	9.27	0	0.02
PM29–PM29B	200	6.13	0.10	2.657	6.68	0	0.01
PM30–PM30B	200	7.78	0.10	0.550	2.19	0	0.06
PM33, PM33A	200	6.25	1.00	3.708	9.27	0	0.02
PM33B–PM33F	200	6.22	1.00	3.570	9.27	0	0.02
PM35, PM35A	200	7.82	0.10	0.567	2.19	0	0.06
PM35B–PM35F	200	7.86	0.10	0.560	2.19	0	0.06
PM37–PM37C	200	8.83	0.10	0.165	0	0	0.08
PM41, PM41A	200	8.71	0.10	0.202	0	4.00	0.01
PM14A–PM14C	150	7.49	0.08	2.944	4.48	0	0.04
PM16–PM16E	150	7.92	0.1	3.174	1.60	0	0.01
PM17	150	7.07	0.1	3.729	2.79	0	0.02
PM17A–PM17D	150	7.21	0.1	3.930	2.79	0	0.02
PM18–PM18B	150	7.48	0.1	3.174	4.39	0	0.04
PM18C, PM18D	150	7.48	0.1	3.155	4.39	0	0.04
PM19	150	6.68	0.1	6.578	1.21	0	0.006
PM19A–PM19C	150	6.51	0.1	6.679	1.21	0	0.006
PM19D	150	6.60	0.1	6.560	1.21	0	0.006
PM20, PM20A	150	7.46	0.1	2.983	5.73	0	0.06
PM20B, PM20C	150	7.60	0.1	2.922	5.73	0	0.06
PM20D–PM20G	150	7.38	0.1	2.913	5.73	0	0.06
PM22–PM22C	150	6.90	0.5	5.591	3.30	0	0.02
PM23, PM23A	150	7.15	0.5	5.560	3.30	0	0.02
PM23B, PM23C	150	6.93	0.5	5.526	3.30	0	0.02
PM25	120	7.22	0.1	6.716	2.00	0	0.02
PM26	120	7.19	0.1	6.669	1.40	0	0.02
PM26A–PM26D	120	7.38	0.1	6.689	0.730	0	0.02
PM28, PM28A	120	7.66	0.1	6.674	0.695	0	0.02
PM28B–PM28E	120	7.66	0.1	6.537	0.695	0	0.02
PM31, PM31A	120	7.64	0.1	3.876	0.733	0	0.02
PM38, PM38A	120	8.32	0.1	41.66	0	93.0	0.01
PM39, PM39A	120	8.75	0.06	1.193	0	27.2	0.06
PM39B	120	8.70	0.06	1.176	0	27.2	0.06
QM1	120	8.90	0.1	3.752	0	101	0.04
QM2	120	9.12	0.04	0.651	0	101	0.08
QM2A, QM2B	120	9.20	0.04	0.683	0	101	0.08
QM3A, QM3B	120	9.45	0.01	0.323	0	190	0.09

electrodes. The buffer solutions prepared for this high temperature calibration were standardized against NIST pH 4.01, 6.86, and 9.18 buffers at 25 °C using a common pH glass combination electrode prior to their use. An example of high temperature electrode calibration in 0.1 M Na bearing solutions at 100, 120, and 150 °C is illustrated in Fig. 2. The slopes of the calibration lines are close to the corresponding theoretical Nernst slopes. Electrode potentials exhibited high stability over time periods of several days with an accuracy of 0.02 pH units, requiring only a periodic control of pH drift for possible deviation from the original calibration. The pH values obtained using the high temperature electrodes were within ±0.04 units of those calculated using corresponding pH measured at 25 °C at pH >7.6; these values differed by as much as 0.2 units at lower pH.

Table 3
Summary of the results of magnesite precipitation experiments performed in this study at 100 °C. Values listed in this table were previously reported by Saldi et al. (2009). Refer to Table 1 for the BET specific surface area values used to calculate the reported precipitation rates.

Experiment	Ω_{Mg}	pH[a]	I (mol/kg)	Alk (mol/kg) × 100	Δ [Mg] (mol/kg) × 10^4	(aCO_3^{2-} × 10^5)	$MgCO_3$ powder	$MgCO_3$ mass (g)	FR (g/min)	r_p (mol/cm^2/s) × 10^{12}
PM31B	30.0	**7.63**	0.12	1.79	−0.519	4.52	Mgs-II	1.753	0.602	0.17
PM32	32.9	**7.66**	0.12	1.87	−0.582	4.96	Mgs-II	1.753	1.197	0.38
PM32A	34.5	**7.68**	0.12	1.87	−0.545	5.20	Mgs-II	1.753	1.689	0.51
PM32B	39.8	**7.74**	0.12	1.87	−0.424	5.95	Mgs-II	1.753	2.378	0.56
PM32C	39.1	**7.72**	0.12	1.87	−0.332	5.77	Mgs-II	1.753	3.367	0.62
PM34	33.3	**7.70**	0.12	1.85	−1.436	5.50	Mgs-VIII	2.825	0.597	0.25
PM34A	43.8	**7.81**	0.12	1.86	−1.100	7.02	Mgs-VIII	2.825	0.984	0.32
PM34B	33.9	**7.68**	0.12	1.85	−0.484	5.15	Mgs-VIII	2.825	1.481	0.21
PM34C	38.5	**7.74**	0.12	1.86	−0.493	5.90	Mgs-VIII	2.825	2.156	0.31
PM36	25.1	**7.98**	0.12	1.95	−0.931	10.8	Mgs-VIII	1.599	0.491	0.24
PM36A	31.2	**8.04**	0.12	1.96	−0.582	12.2	Mgs-VIII	1.599	1.085	0.33
PM36B	20.1	**8.12**	0.12	1.99	−0.553	14.8	Mgs-VIII	1.599	0.396	0.11
PM36C	23.9	**8.12**	0.12	1.99	−0.235	15.0	Mgs-VIII	1.599	0.987	0.12

[a] All pH values were measured directly using high temperature electrodes.

Table 4
Summary of the results of magnesite precipitation experiments performed in this study at 120 °C. Refer to Table 1 for the BET specific surface area values used to calculate the reported precipitation rates.

Experiment	Ω_{Mg}	pH[a]	I (mol/kg)	Alk (mol/kg) × 100	Δ[Mg] (mol/kg) × 10^4	(aCO_3^{2-} × 10^5)	$MgCO_3$ powder	$MgCO_3$ mass (g)	FR (g/min)	r_p (mol/cm^2/s) × 10^{12}
PM25	30.7	7.46	0.12	1.62	−0.813	2.66	Mgs-II	0.806	0.990	0.97
PM26	29.0	**7.51**	0.12	1.67	−1.780	3.06	Mgs-II	0.795	0.590	1.28
PM26A	34.7	**7.52**	0.12	1.75	−1.130	3.25	Mgs-II	0.795	1.484	2.04
PM26B	40.8	**7.59**	0.12	1.75	−1.009	3.78	Mgs-II	0.795	1.874	2.30
PM26C	43.3	**7.63**	0.12	1.74	−1.165	4.14	Mgs-II	0.795	2.371	3.36
PM26D	44.8	**7.61**	0.12	1.75	−0.723	3.96	Mgs-II	0.795	3.526	3.10
PM28	30.7	**7.61**	0.12	1.73	−2.596	3.96	Mgs-II	0.761	0.493	1.63
PM28A	46.0	**7.68**	0.12	1.75	−1.431	4.67	Mgs-II	0.761	1.780	3.24
PM28B	36.9	**7.53**	0.12	1.76	−0.760	3.33	Mgs-II	0.761	2.390	2.31
PM28C	38.3	**7.53**	0.12	1.77	−0.544	3.34	Mgs-II	0.761	3.973	2.75
PM28D	46.8	**7.63**	0.12	1.76	−0.599	4.17	Mgs-II	0.761	2.994	2.28
PM28E	44.7	**7.59**	0.12	1.76	−0.434	3.86	Mgs-II	0.761	5.487	3.02
PM31	25.1	**7.66**	0.12	1.81	−0.955	4.60	Mgs-II	1.753	1.183	0.62
PM31A	24.2	**7.78**	0.12	1.80	−1.672	5.98	Mgs-II	1.753	0.587	0.54
PM38	70.2	**7.38**	0.12	0.77	−8.57	1.0	Mgs-V	1.803	0.581	5.45
PM38A	96.3	**7.47**	0.12	0.82	−6.09	1.3	Mgs-V	1.803	1.103	7.36
PM39	30.0	8.40	0.12	6.18	−0.73	80.6	Mgs-V	1.803	0.593	0.48
PM39A	47.5	8.40	0.12	6.19	−0.45	79.1	Mgs-V	1.803	1.107	0.55
PM39B	40.1	8.41	0.12	6.18	−0.57	81.9	Mgs-V	1.803	1.602	0.99
QM1	36.3	8.02	0.14	3.88	−2.48	21.7	Mgs-V	1.780	1.198	1.55
QM2	34.7	8.84	0.14	9.03	−0.32	267.6	Mgs-V	1.780	0.584	0.097
QM2A	45.6	8.83	0.14	8.89	−0.24	259.6	Mgs-V	1.780	1.084	0.136
QM2B	50.3	8.83	0.14	8.90	−0.19	259.8	Mgs-V	1.780	1.506	0.153
QM3A	33.4	9.09	0.14	10.9	−0.044	484.1	Mgs-V	1.712	0.500	0.012
QM3B	36.6	9.23	0.14	10.9	−0.026	584.0	Mgs-V	1.712	0.900	0.013

[a] pH values listed in bold were measured directly using high temperature electrodes. All others were calculated for the experimental temperature from the measured 25 °C pH using PHREEQC.

4. RESULTS

A representative example of the approach of a magnesite precipitation experiment to steady-state is shown in Fig. 3. This figure shows the evolution of Mg concentration in the outlet fluid of experiment PM9-B. The fluid flow rate in this experiment was 0.2 g/min. Because the reactor has a volume of 200 ml, the residence time for the experiment was 17 h and the reactor would be expected to attain mechanical steady-state in approximately 75 h. Outlet fluid Mg concentration decreases with time during the experiment attaining a steady-state value after approximately 130 h of elapsed time. This steady-state was confirmed by four additional outlet Mg concentration measurements.

Table 5
Summary of the results of magnesite precipitation experiments performed in this study at 150 °C. Refer to Table 1 for the BET specific surface area values used to calculate the reported precipitation rates.

Run #	Ω_{Mg}	pH[a]	I (mol/kg)	Alk (mol/kg) × 100	Δ[Mg] (mol/kg) × 10^4	(aCO_3^{2-} × 10^5)	$MgCO_3$ powder	$MgCO_3$ mass (g)	FR (g/min)	r_p (mol/cm^2/s) × 10^{12}
PM14A	38.5	**7.80**	0.12	3.41	−2.068	9.53	Mgs-III	0.629	1.593	5.42
PM14B	52.3	**7.75**	0.12	3.40	−1.650	8.60	Mgs-III	0.629	5.392	14.7
PM14C	46.4	**7.85**	0.12	3.40	−1.990	10.8	Mgs-III	0.629	2.728	8.94
PM16	13.4	7.32	0.11	0.743	−0.803	0.704	Mgs-III	0.407	0.445	0.85
PM16A	17.1	7.41	0.11	0.747	−0.663	0.858	Mgs-II	0.407	0.896	1.41
PM16B	19.3	7.43	0.11	0.749	−0.460	0.897	Mgs-II	0.407	1.592	1.74
PM16C	20.2	7.43	0.11	0.751	−0.329	0.899	Mgs-II	0.407	3.189	2.50
PM16D	19.1	7.45	0.11	0.747	−0.597	0.942	Mgs-II	0.407	1.598	2.27
PM16E	26.8	7.55	0.11	0.753	−0.235	1.18	Mgs-II	0.407	4.998	2.79
PM17	35.5	7.50	0.12	1.59	−1.343	2.26	Mgs-II	0.591	2.195	4.82
PM17A	27.3	7.48	0.12	1.59	−2.013	2.16	Mgs-II	0.591	1.490	4.91
PM17B	20.3	7.56	0.12	1.59	−2.721	2.58	Mgs-II	0.591	0.604	2.69
PM17C	27.8	7.67	0.12	1.59	−2.590	3.28	Mgs-II	0.591	1.105	4.68
PM17D	43.6	7.66	0.12	1.59	−1.824	3.27	Mgs-II	0.591	3.960	11.8
PM18	34.5	7.63	0.14	3.41	−2.051	6.46	Mgs-II	0.405	0.886	4.34
PM18A	27.3	7.73	0.14	3.41	−2.444	8.09	Mgs-II	0.405	0.444	2.59
PM18B	67.1	7.76	0.14	3.42	−1.452	8.52	Mgs-II	0.405	3.193	11.1
PM18C	57.9	7.85	0.14	3.41	−1.910	10.6	Mgs-II	0.405	1.588	7.24
PM18D	74.1	7.79	0.14	3.42	−1.357	9.11	Mgs-II	0.405	3.998	13.0
PM19	10.3	7.14	0.11	0.328	−0.897	0.202	Mgs-II	0.592	0.500	0.73
PM19A	8.3	7.00	0.11	0.332	−0.550	0.150	Mgs-II	0.592	0.903	0.81
PM19B	9.2	7.05	0.11	0.330	−0.575	0.168	Mgs-II	0.592	1.496	1.40
PM19C	11.7	7.15	0.11	0.330	−0.430	0.210	Mgs-II	0.592	2.179	1.53
PM19D	6.9	6.90	0.11	0.333	−0.145	0.120	Mgs-II	0.592	3.649	0.87
PM20	25.3	7.80	0.16	5.19	−2.488	14.2	Mgs-II	0.417	0.391	2.25
PM20A	50.1	7.79	0.16	5.20	−1.974	13.7	Mgs-II	0.417	1.590	7.28
PM20B	41.6	7.79	0.16	5.20	−2.095	13.9	Mgs-II	0.417	0.891	4.33
PM20C	54.6	7.74	0.16	5.20	−1.725	12.4	Mgs-II	0.417	1.992	7.97
PM20D	56.4	7.64	0.16	5.20	−1.412	9.85	Mgs-II	0.417	3.208	10.5
PM20E	47.6	7.74	0.16	5.20	−1.869	12.4	Mgs-II	0.417	1.385	6.00
PM20F	67.2	7.68	0.16	5.20	−1.248	10.7	Mgs-II	0.417	4.512	13.1
PM20G	66.6	7.79	0.16	5.20	−1.585	13.9	Mgs-II	0.417	2.493	9.16
PM22	28.4	**7.42**	0.52	1.49	−1.339	1.49	Mgs-II	0.595	2.352	5.11
PM22A	25.6	7.35	0.52	1.49	−1.048	1.25	Mgs-II	0.595	4.453	7.59
PM22B	23.8	7.42	0.52	1.48	−1.960	1.46	Mgs-II	0.595	1.614	5.14
PM22C	18.2	7.62	0.52	1.49	−3.789	2.31	Mgs-II	0.595	0.711	4.38
PM23	28.5	7.52	0.52	1.49	−2.089	1.85	Mgs-II	0.598	1.094	3.70
PM23A	28.7	7.44	0.52	1.49	−1.447	1.56	Mgs-II	0.598	3.604	8.44
PM23B	32.2	7.52	0.52	1.49	−1.576	1.84	Mgs-II	0.596	1.989	5.08
PM23C	27.5	7.37	0.52	1.49	−0.942	1.33	Mgs-II	0.596	4.988	7.62

[a] pH values listed in bold were measured directly using high temperature electrodes. All others were calculated for the experimental temperature from the measured 25 °C pH using PHREEQC.

The summary of the results of all 149 steady-state magnesite precipitation experiments performed during this study is reported in Tables 3–6. Logarithmic plots of magnesite precipitation rates measured in aqueous 0.1 M NaCl solutions at 100, 120, 150, and 200 °C are shown in Fig. 4. The dashed lines in this figure are consistent with $n = 2$, which itself is consistent with magnesite precipitation rates being controlled by a spiral growth mechanism (cf. Saldi et al., 2009). It can be seen that the dashed lines having a slope of 2 are consistent with all data. Although the distribution of the data points at 150 °C suggests rates at this temperature might be better described with somewhat shallower slope, as shown below this is due to the effects of fluid composition other than saturation state on rates. It can be seen in Fig. 4 that, despite scatter, rates tend to decrease with increasing aqueous CO_3^{2-} activity. This is particularly evident for the experiments performed at 120 and 200 °C, which were performed over the widest range of $a_{CO_3^{2-}}$. For example, at 200 °C magnesite precipitation rates measured in solutions having $a_{CO_3^{2-}} > 10^{-3.5}$ are approximately two orders of magnitude slower than those measured in solution having $a_{CO_3^{2-}} < 10^{-5}$. This decrease of rates with increasing $a_{CO_3^{2-}}$ is consistent with Eq. (10) and the role of the $>MgOH_2^+$ surface species on the magnesite precipitation mechanism.

A comparison of magnesite precipitation rates measured in aqueous solutions of various NaCl concentrations is shown in Fig. 5. Again the dashed lines in this figure have a slope of 2, consistent with magnesite precipitation rates

Table 6
Summary of the results of magnesite precipitation experiments performed in this study at 200 °C. Refer to Table 1 for the BET specific surface area values used to calculate precipitation rates.

Experiment	Ω_{Mg}	pH[a]	I (mol/kg)	Alk (mol/kg) × 100	Δ[Mg] (mol/kg) × 10^4	($aCO_3^{2-} \times 10^5$)	$MgCO_3$ powder	$MgCO_3$ mass (g)	FR (g/min)	r_p (mol/cm^2/s) × 10^{12}
PM6A	11.4	7.96	0.11	0.913	−1.479	1.69	Mgs-I	0.306	1.798	6.47
PM6B	14.1	7.96	0.11	0.912	−1.481	1.69	Mgs-I	0.306	2.500	9.01
PM6C	17.1	7.93	0.11	0.915	−1.429	1.61	Mgs-I	0.306	4.007	13.9
PM6D	7.6	7.92	0.11	0.909	−1.577	1.56	Mgs-I	0.306	1.497	5.74
PM6E	19.5	7.92	0.11	0.912	−1.387	1.56	Mgs-I	0.306	7.521	25.4
PM7A	6.5	8.14	0.12	1.91	−0.915	4.84	Mgs-I	0.305	0.691	1.54
PM7B	9.4	8.14	0.12	1.91	−0.883	5.39	Mgs-I	0.305	1.796	3.87
PM7C	7.6	8.13	0.12	1.91	−0.862	5.42	Mgs-I	0.305	2.499	5.26
PM7D	13.2	8.15	0.12	1.89	−0.885	5.22	Mgs-I	0.305	1.999	4.32
PM7E	18.9	8.16	0.12	1.92	−0.845	5.48	Mgs-I	0.305	4.004	8.26
PM8	6.2	8.25	0.14	1.92	−0.806	5.64	Mgs-I	0.305	7.515	14.8
PM8A	8.0	8.26	0.14	3.90	−0.498	14.1	Mgs-I	0.303	1.197	1.46
PM8B	8.6	8.26	0.14	3.90	−0.490	14.4	Mgs-I	0.303	1.793	2.16
PM8C	6.1	8.24	0.14	3.90	−0.488	14.5	Mgs-I	0.303	2.501	2.99
PM8D	11.7	8.29	0.14	3.90	−0.498	13.9	Mgs-I	0.303	1.000	1.22
PM8E	14.3	8.31	0.14	3.90	−0.476	15.4	Mgs-I	0.303	4.017	4.69
PM9	6.7	7.44	0.11	3.90	−0.466	15.9	Mgs-I	0.303	7.508	8.58
PM9A	6.0	7.64	0.11	0.645	−1.430	0.388	Mgs-I	0.305	0.697	2.43
PM9B	4.0	7.47	0.11	0.658	−1.533	0.609	Mgs-I	0.305	0.401	1.50
PM12	12.9	7.36	0.14	1.90	−1.936	0.941	Mgs-III	0.429	0.700	3.27
PM12A	20.2	7.29	0.14	1.90	−1.545	0.575	Mgs-III	0.429	3.509	13.1
PM12B	6.3	7.37	0.11	0.449	−0.802	0.174	Mgs-III	0.429	1.502	2.91
PM12C	11.4	7.47	0.11	0.443	−0.686	0.278	Mgs-III	0.429	3.004	4.97
PM12D	14.5	7.53	0.11	0.442	−0.580	0.315	Mgs-III	0.429	5.516	7.72
PM13	6.3	7.04	0.11	0.315	−0.812	0.076	Mgs-III	0.422	0.699	1.39
PM13A	6.9	6.96	0.11	0.312	−0.494	0.063	Mgs-III	0.422	3.700	4.48
PM13B	7.1	7.05	0.11	0.315	−0.706	0.078	Mgs-III	0.422	1.499	2.59
PM13C	9.3	7.10	0.11	0.312	−0.449	0.084	Mgs-III	0.422	6.015	6.62
PM13D	9.7	7.10	0.11	0.314	−0.402	0.085	Mgs-III	0.422	8.013	7.90
PM13E	9.8	7.24	0.11	0.309	−0.719	0.115	Mgs-III	0.422	2.501	4.41
PM29	8.5	6.93	0.11	0.275	−0.654	0.051	Mgs-II	0.407	1.902	2.96
PM29A	8.6	6.89	0.11	0.278	−0.506	0.047	Mgs-II	0.407	4.012	4.83
PM29B	9.0	6.89	0.11	0.282	−0.410	0.048	Mgs-II	0.407	6.961	6.78
PM30	21.8	8.20	0.16	5.53	−0.463	17.8	Mgs-II	0.407	1.810	1.99
PM30A	26.1	8.23	0.16	5.52	−0.449	18.9	Mgs-II	0.407	4.015	4.28
PM30B	29.1	8.21	0.16	5.52	−0.434	18.0	Mgs-II	0.407	7.511	7.75
PM35	16.6	8.23	1.02	0.954	−2.141	0.307	Mgs-II	0.456	0.566	2.57
PM35A	22.7	8.24	1.02	0.941	−1.989	0.360	Mgs-II	0.456	1.128	4.76
PM35B	17.3	8.24	1.02	0.949	−1.380	0.207	Mgs-II	0.456	1.545	4.52
PM35C	18.5	8.21	1.02	0.945	−1.277	0.266	Mgs-II	0.456	2.098	5.68
PM35D	13.8	8.26	1.02	0.949	−1.020	0.277	Mgs-II	0.456	2.798	6.05
PM35E	19.5	8.22	1.02	0.949	−0.979	0.344	Mgs-II	0.456	3.527	7.32
PM35F	11.4	8.27	1.02	0.950	−0.899	0.327	Mgs-II	0.456	4.355	8.30
PM37	14.9	8.63	0.18	5.68	−0.503	19.4	Mgs-II	0.456	0.598	0.64
PM37A	21.8	8.64	0.18	5.69	−0.480	19.8	Mgs-II	0.456	1.198	1.22
PM37B	25.0	8.62	0.18	5.69	−0.494	19.8	Mgs-II	0.456	1.600	1.68
PM37C	27.2	8.61	0.18	5.69	−0.488	18.8	Mgs-II	0.456	2.196	2.27
PM41	3.4	8.10	0.16	5.69	−0.508	20.6	Mgs-II	0.456	0.400	0.43
PM41A	4.9	8.10	0.16	5.69	−0.485	19.2	Mgs-II	0.456	2.796	2.88
PM21	11.9	7.39	0.52	0.923	−1.826	0.409	Mgs-II	0.398	0.608	2.70
PM21A	15.6	7.43	0.52	0.925	−1.638	0.445	Mgs-II	0.398	1.220	4.86
PM21B	22.0	7.47	0.52	0.930	−1.325	0.490	Mgs-II	0.402	4.266	13.6
PM21C	18.5	7.58	0.52	0.924	−1.746	0.616	Mgs-II	0.402	1.826	7.67
PM21D	20.7	7.60	0.52	0.921	−1.668	0.642	Mgs-II	0.402	2.539	10.2
PM21E	10.7	7.42	0.52	0.934	−2.007	0.444	Mgs-II	0.402	0.405	1.95
PM21F	17.3	7.51	0.52	0.924	−1.738	0.534	Mgs-II	0.402	1.421	5.94
PM24	19.5	7.36	1.02	0.933	−1.739	0.362	Mgs-II	0.401	1.441	6.04
PM24A	17.5	7.23	1.02	0.935	−1.381	0.273	Mgs-II	0.401	3.925	13.1
PM24B	20.4	7.40	1.02	0.929	−1.784	0.390	Mgs-II	0.401	1.855	7.98

Table 6 (*continued*)

Experiment	Ω_{Mg}	pH[a]	I (mol/kg)	Alk (mol/kg) × 100	Δ[Mg] (mol/kg) × 10^4	($aCO_3^{2-} \times 10^5$)	$MgCO_3$ powder	$MgCO_3$ mass (g)	FR (g/min)	r_p (mol/cm^2/s) × 10^{12}
PM24C	17.2	7.26	1.02	0.937	−1.561	0.289	Mgs-II	0.401	2.794	10.5
PM24D	15.5	7.40	1.02	0.922	−2.271	0.387	Mgs-II	0.401	1.236	6.77
PM24E	13.0	7.53	1.02	0.924	−2.828	0.519	Mgs-II	0.401	0.621	4.23
PM27	15.6	7.25	1.02	0.949	−1.437	0.289	Mgs-II	0.413	1.449	4.88
PM27A	12.3	7.40	1.02	0.956	−2.318	0.405	Mgs-II	0.413	0.517	2.81
PM33	12.5	7.28	1.03	0.954	−2.141	0.307	Mgs-II	0.456	0.566	2.57
PM33A	15.9	7.35	1.03	0.941	−1.989	0.360	Mgs-II	0.456	1.128	4.76
PM33B	12.0	7.10	1.03	0.949	−1.380	0.207	Mgs-II	0.456	1.545	4.52
PM33C	15.9	7.22	1.03	0.945	−1.277	0.266	Mgs-II	0.456	2.098	5.68
PM33D	18.4	7.23	1.03	0.949	−1.020	0.277	Mgs-II	0.456	2.798	6.05
PM33E	22.9	7.33	1.03	0.949	−0.979	0.344	Mgs-II	0.456	3.527	7.32
PM33F	22.5	7.31	1.03	0.950	−0.899	0.327	Mgs-II	0.456	4.355	8.30

[a] pH values were calculated for the experimental temperature from the measured 25 °C pH using PHREEQC.

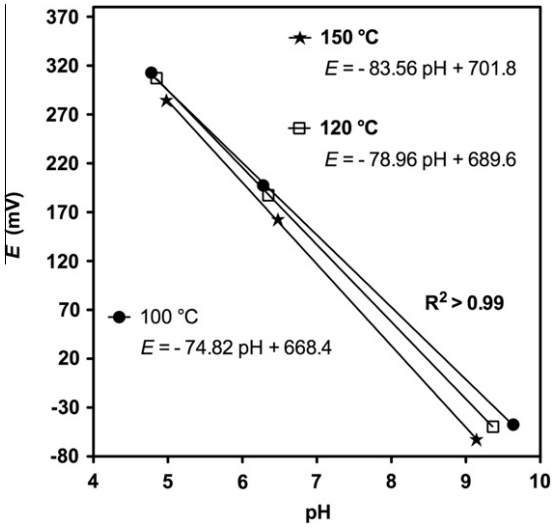

Fig. 2. Examples of the solid contact pH electrode coupled with a Na-selective reference electrode calibration at 100, 120, and 150 °C in aqueous 0.1 M NaCl solutions.

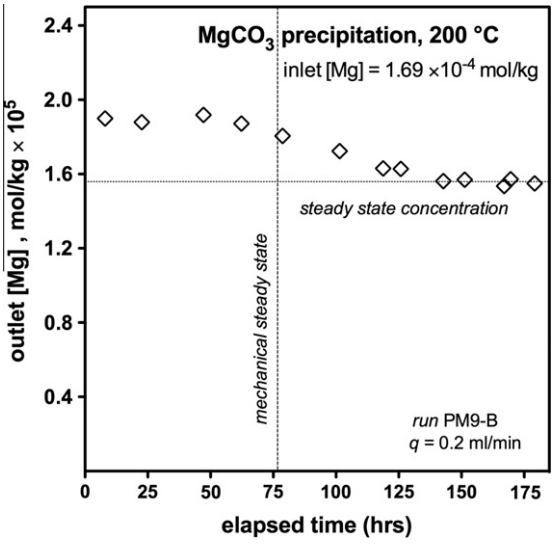

Fig. 3. Evolution of Mg concentration in the outlet fluid as a function of time during experiment PM9. Chemical steady-state is attained shortly after the time required for mechanical steady-state. The analytical uncertainty in the measurements is approximated by the symbol size.

that are controlled by a spiral growth mechanism. Increasing NaCl concentration appears to decrease rates; magnesite precipitation rates measured in solutions having NaCl concentrations $\geqslant$0.5 mol/kg are on average 0.4 log units slower than corresponding rates measured in 0.1 mol/kg NaCl solutions. This result is consistent with the observations made by Pokrovsky and Schott (1999) who observed a moderate decrease of magnesite dissolution rates with increasing ionic strength at alkaline conditions. The increase of ionic strength leads to a decrease in the concentration of the rate controlling $>MgOH_2^+$ species on the magnesite surface thus lowering rates.

The degree to which measured magnesite precipitation rates are consistent with Eq. (10) and thus the surface complexation model described above can be assessed with the aid of Fig. 6. The symbols in this figure represent all the magnesite precipitation rates measured in aqueous 0.1 mol/kg NaCl solutions in this study. Rates in this figure were divided by $\left(1-\Omega_{Mg}^{n}\right)$ to isolate the effects of CO_3^{2-} from that of Ω_{Mg}. By normalizing rates to the degree of supersaturation the effect of aqueous CO_3^{2-} activity is evident at all studied temperatures. The curves, consistent with the symbols in this figure, were generated using Eq. (10), $n = 2$, and the parameters listed in Table 7. The values of K_{CO_3}, K_{OH}, and k_{Mg}^{-}[1] reported in Table 7 were generated through a trial-and-error procedure to obtain the best fit to the data shown in Fig. 6. A comparison between the values of the surface speciation constants, K_{CO_3} and K_{OH}, listed in Table 7 for 150 and 200 °C and those previously retrieved from the regression of measured magnesite dissolution rates by Saldi et al. (2010) indicates that, although retrieved values of K_{CO_3} are essentially identical, those retrieved for K_{OH} in this study are approximately one order of magnitude

[1] This rate constant is reported here as k_{Mg}^{-} rather than k_{Mg}^{+} to distinguish it from rate constants obtained for magnesite dissolution.

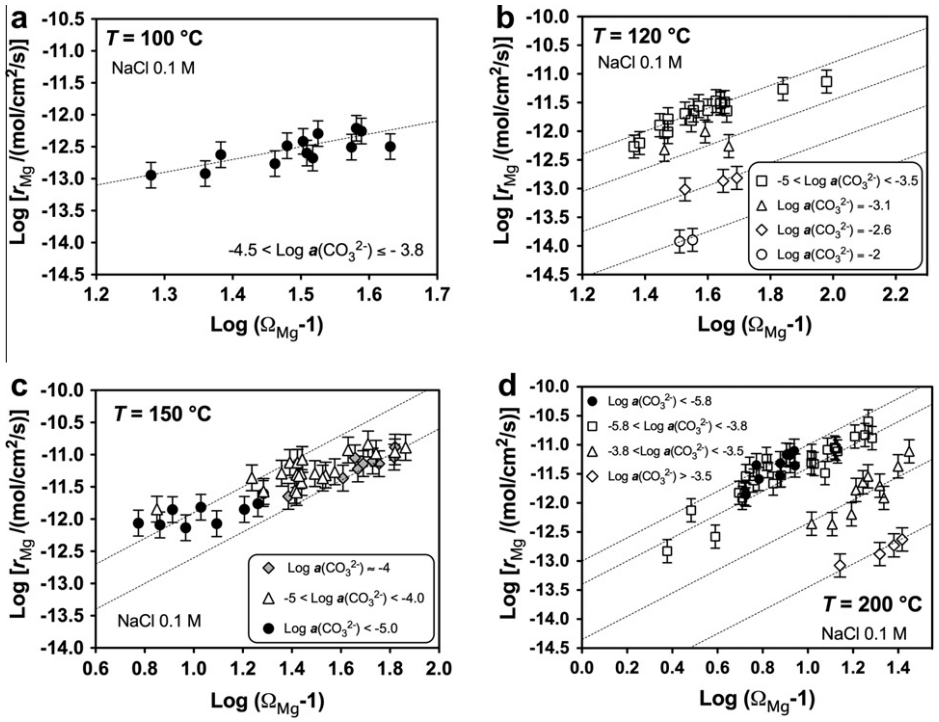

Fig. 4. Logarithmic plots of magnesite precipitation rates measured in fluids containing 0.1 mol/kg NaCl at (a) 100, (b) 120, (c) 150 and (d) 200 °C versus the degree of supersaturation ($\Omega_{Mg} - 1$). The reactive fluid aqueous CO_3^{2-} activity of the experiment is indicated by the symbol as defined in the plots. Dashed lines have a slope consistent with $n = 2$. Error bars correspond to an uncertainty of ± 0.2 logarithmic units.

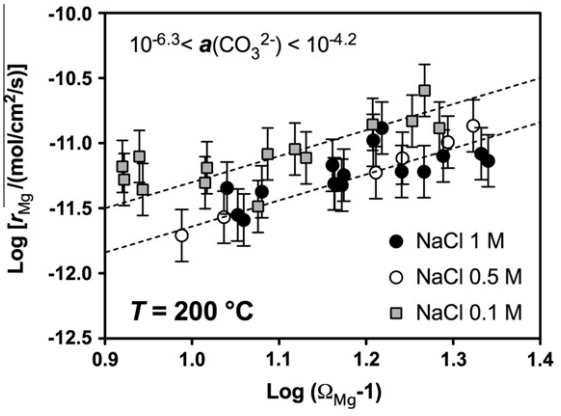

Fig. 5. Logarithmic plot of magnesite precipitation rates measured at 200 °C and in solution having a log aqueous CO_3^{2-} activity between −6.3 and −4.2 as a function of the degree of fluid supersaturation ($\Omega_{Mg} - 1$). The dashed lines have a slope consistent with $n = 2$. The grey squares, open circles, and filled circles correspond to precipitation rates measured in reactive fluids containing 0.1, 0.5, and 1.0 mol/kg NaCl, respectively. Error bars correspond to a ± 0.2 log units uncertainty in measured rates.

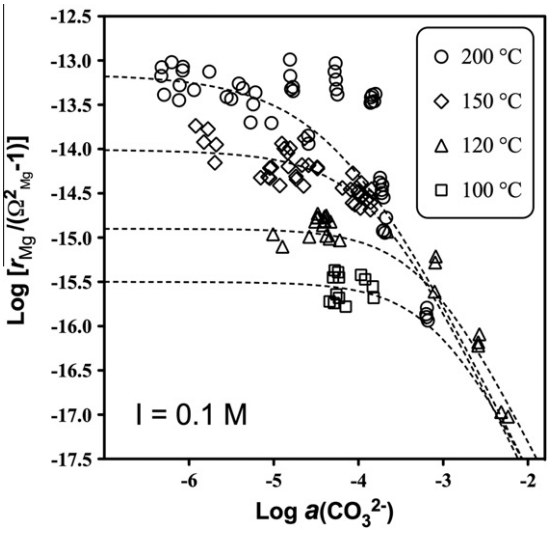

Fig. 6. Logarithmic plot of magnesite precipitation rates divided by ($\Omega^2_{Mg}-1$) as a function of reactive fluid aqueous CO_3^{2-} activity from 100 to 200 °C. Symbols represent experimental data, whereas the dashed curves were calculated using Eq. (10) and the parameters listed in Table 7. Note that only rates obtained in 0.1 mol/kg aqueous NaCl solution are shown in this graph.

larger than those obtained from the dissolution rate measurements. This difference likely stems from the different chemical conditions at which these constants were derived. Both sets of constants were retrieved by fitting the effects of two interdependent chemical parameters, $a_{CO_3^{2-}}$ and a_{OH^-}, on magnesite reaction rates. Precipitation experiments in the present study were conducted at higher total carbon concentrations, higher $a_{CO_3^{2-}}$, and more basic pH than the dissolution experiments of Saldi et al. (2010). Differences in retrieved data for K_{OH} may also stem from uncertainties in aqueous species formation constants, and/or variations in

Table 7
Values of rate constants (k^{-}_{Mg}) and equilibrium constants (K_{OH} and K_{CO_3}) obtained from the regression of rate data obtained in the present study in 0.1 mol/kg NaCl solutions at the indicated temperatures.

T (°C)	Log k^{-}_{Mg} (mol/cm^2/s)	Log K_{CO_3}	Log K_{OH}
100	-15.5 ± 0.2	-3.0 ± 0.2	9.5
120	-14.9 ± 0.1	-3.15 ± 0.2	9.2
150	-14.0 ± 0.3	-3.85 ± 0.2	8.5 ± 0.3
200	-13.15 ± 0.3	-4.2 ± 0.3	8.1 ± 0.2

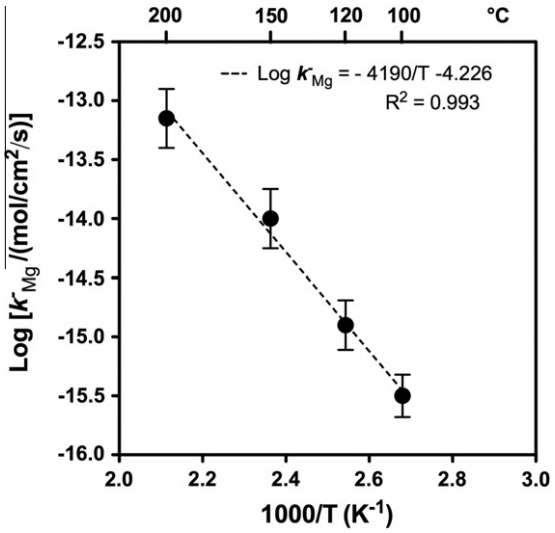

Fig. 7. Arrhenius plot of retrieved rate constants as a function of reciprocal temperature. Filled circles represent rate constants listed in Table 7, whereas the dashed line corresponds to a linear least squares fit of these rate constants. The slope of this line is consistent with $E_a = 80.2$ kJ/mol and $A_a = 5.9 \times 10^{-5}$ mol/cm^2/s.

surface complex activity coefficients (cf. Bénézeth et al., 2011).

An Arrhenius plot of retrieved magnesite precipitation rate constants (k^{-}_{Mg}) is shown in Fig. 7. Retrieved rate constants are consistent with an Arrhenius behavior; the line drawn through the data points corresponds to an activation energy of 80.2 kJ/mol and the intercept is consistent with $A_a = 5.9 \times 10^{-5}$ mol/cm^2/s. Note that it is unlikely that these Arrhenius parameters can be used to extrapolate rates reported in the present study to ambient temperatures because evidence suggests that the magnesite precipitation mechanism changes at temperatures below 80 °C (Saldi et al., 2009).

A further assessment of the quality of the fit of measured rates to Eq. (10) can be made with the aid of Fig. 8. This figure shows the variation with magnesite saturation state of the measured magnesite precipitation rates normalized to the concentration of the rate controlling surface complex, $\{> MgOH_2^+\}$, at 120 and 150 °C. The dashed lines in this figure were calculated using Eq. (10) and the parameters listed in Table 7. Note the slope of these dashed lines is 2, which corresponds to the value of n. A close match can be seen between the magnesite precipitation rates measured at both 120 and 150 °C, and the corresponding dashed line.

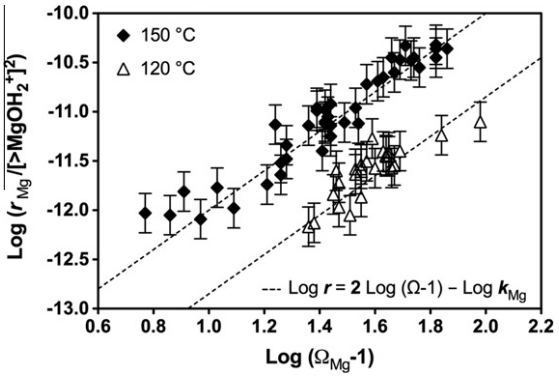

Fig. 8. Logarithmic plot of magnesite precipitation rates measured in fluids containing 0.1 mol/kg NaCl normalized to the square of the concentration of the rate controlling surface species, $[> MgOH_2^+]$, versus $(\Omega_{Mg} - 1)$. The dashed lines were calculated using Eq. (10), $n = 2$ and parameters listed in Table 7 for the corresponding T. Error bars correspond to 0.2 log units.

This coherence confirms that the shallow slope of the 150 °C rate data shown in Fig. 4c stems from a variation of the rate controlling $> MgOH_2^+$ complex concentration on the magnesite surface rather than a lower reaction order.

5. DISCUSSION

5.1. Dependence of magnesite precipitation rates on the aqueous Mg^{++}/CO_3^{2-} activity ratio

A number of past studies have reported that the growth rates of a given mineral can vary significantly as a function of the ion activity ratio at constant degree of supersaturation. For example, Nehrke et al. (2007) and Perdikouri et al. (2009) reported that at constant degree of supersaturation calcite growth rates maximize when $a_{Ca^{2+}}/a_{CO_3^{2-}}$ was equal or close to 1. Stack and Grantham (2010) suggested that this behavior depended on crystal orientation. In contrast, constant saturation state barite growth rates appear to be accelerated by increasing aqueous Ba^{2+} activity even when $a_{Ba^{2+}}/a_{SO_4^{2-}}$ greatly exceeds 1 (Kowacz et al., 2007). Moreover, Saldi et al. (2009) reported that constant saturation state magnesite step advance rates appear to be independent of $a_{Mg^{2+}}/a_{CO_3^{2-}}$. Although the present study was not designed to assess the effect of the $a_{Mg^{2+}}/a_{CO_3^{2-}}$ on magnesite precipitation rates some insight can be obtained. Fig. 9 illustrates the variation of measured magnesite precipitation rates as a function of $a_{Mg^{2+}}/a_{CO_3^{2-}}$ at 150 °C for those experiments performed at $25.3 < \Omega_{Mg} < 27.8$ and 200 °C for those experiments performed at $6.3 < \Omega_{Mg} < 7.1$. In these two cases rate measurements were made at nearly identical Ω_{Mg} but contrasting $a_{Mg^{2+}}/a_{CO_3^{2-}}$. In both cases no dependence of precipitation rates on $a_{Mg^{2+}}/a_{CO_3^{2-}}$ is evident.

5.2. Comparison between magnesite dissolution and precipitation rates

Precipitation rates in the present study were measured using the same reactors, materials, and temperature, and similar reactive fluids as those previously used by Saldi

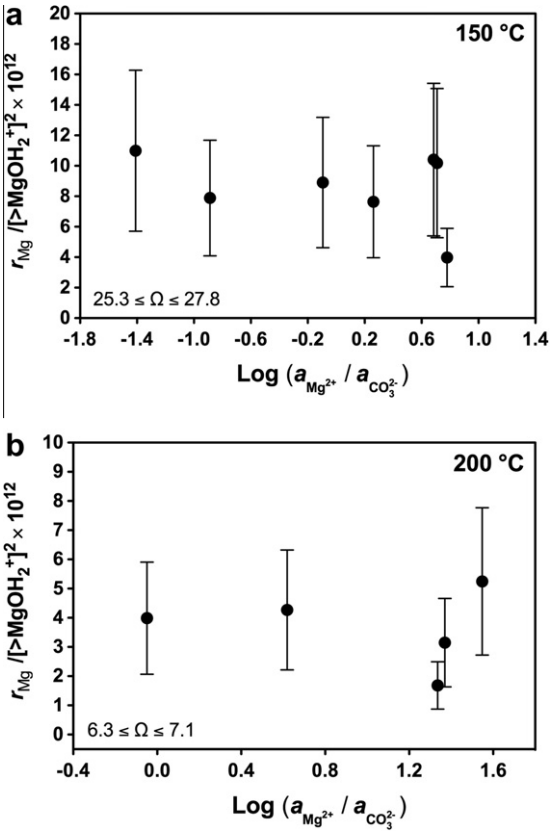

Fig. 9. Magnesite precipitation rates normalized to the square of the corresponding concentration of the rate-controlling species ($>MgOH_2^+$) plotted against the logarithm of the aqueous Mg^{2+}/CO_3^{2-} activity ratio at 150 (a) and 200 °C (b) for the indicated constant degree of supersaturation. Both plots show that magnesite precipitation rates are essentially independent of Mg^{2+} to CO_3^{2-} activity ratio at the considered conditions.

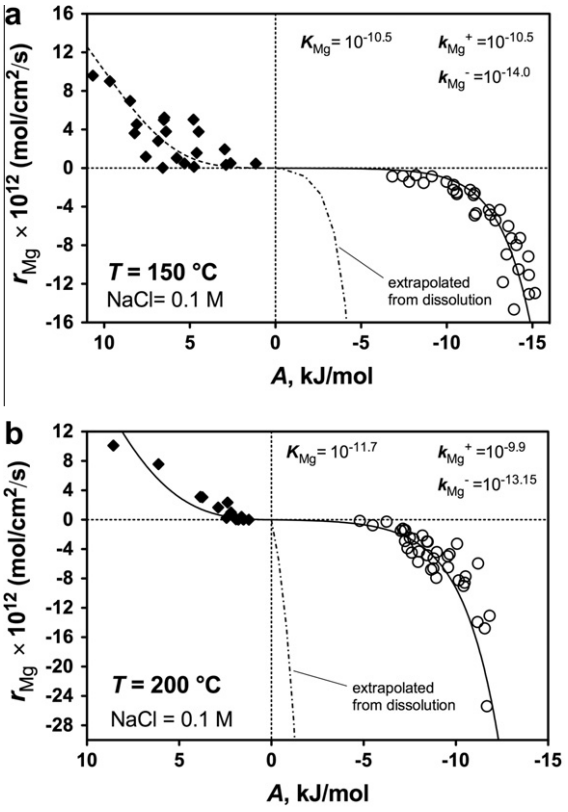

Fig. 10. Comparison of magnesite precipitation rates measured in this study with corresponding dissolution rates reported by Saldi et al. (2010). All rates were measured in 0.1 mol/kg NaCl solutions. The symbols in these plots represent measured rates, but the curves were computed using Eq. (10) together with the parameters reported in Table 7 and Saldi et al. (2010). The curves for precipitation at 150 and 200 °C were generated for a pH equal to 8.0 and 7.0, respectively, and assuming a constant total carbon concentration of 0.01 mol/kg, but those for dissolution were generated by adjusting pH for a solution containing 0.001 mol/kg of total carbon and 1×10^{-5} mol/kg of Mg. The dotted-dashed curves on both plots represent the precipitation rates extrapolated from the dissolution data using Eq. (10) with the parameters provided by Saldi et al. (2010), for solution compositions representative of those used in this study.

et al. (2010) to measure magnesite dissolution rates. As such these studies allow a direct and consistent comparison of magnesite dissolution and precipitation rates. A comparison of the results published in these two studies reveals several interesting similarities and contrasts. First, the variation of magnesite dissolution and precipitation rates with reactive fluid composition suggests that both rates are proportional to the concentration of the same complex present at the magnesite surface: $>MgOH_2^+$, which itself suggests that both are controlled by the same activated complex. Because both rates are proportional to the same surface complex, magnesite dissolution and precipitation rates can be described accurately with an identical rate equation. The only difference in the equations describing magnesite dissolution and precipitation is the identity of the reaction order n, and the value of the rate constants k_{Mg}^+ and k_{Mg}^-. The reaction order for magnesite dissolution was reported to be 4 by both Pokrovsky and Schott (1999) and Saldi et al. (2010). This suggests that the hydration of four adjacent Mg atoms on the magnesite surface is required for dissolution. The reaction order for magnesite precipitation is found to be 2, which is consistent with a spiral growth mechanism.

The observation that the same surface complex controls dissolution and precipitation, but the reaction order with respect to this complex differs, may reflect the fact that this complex needs to be present at different positions on the magnesite crystal to be reactive. Although etch pits are present at the magnesite surface during dissolution (see Jordan et al., 2007), magnesite dissolution appears be dominated by the removal of material from grain edges, which were continuously rounded during the experiments reported by Saldi et al. (2010). Precipitation rates reported in this study and those reported in Saldi et al. (2009) appear to be controlled by a spiral growth occurring at relatively sparse locations on crystal faces. This difference may also be reflected in the relative values of the rate constants retrieved for dissolution versus precipitation. The traditional application of the principle of detailed balancing when applied to elementary reactions requires that the ratio of the forward to reverse rate constant equals the equilibrium constant for the reaction (cf. Schott et al., 2009). If applied

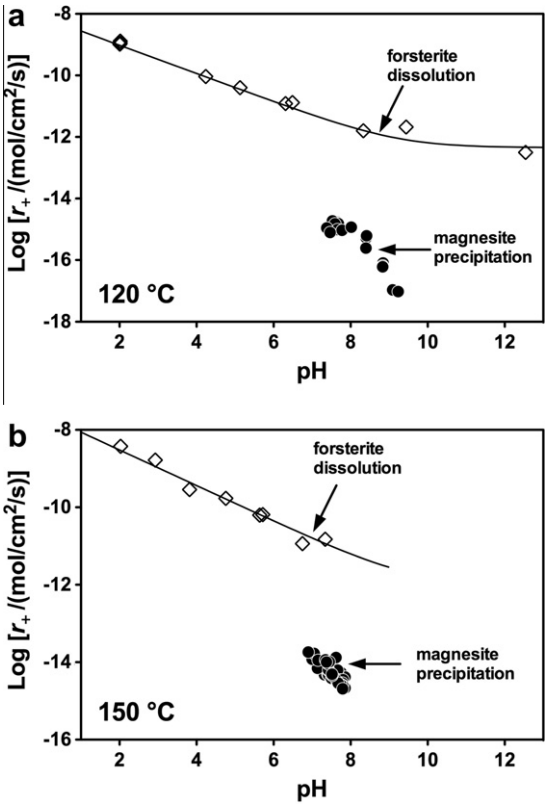

Fig. 11. Comparison of far from equilibrium forsterite dissolution rates reported by Hänchen et al. (2006) with corresponding r_+ values generated from magnesite precipitation rates determined in the present study as a function of pH (see text).

directly to magnesite dissolution and precipitation, this would imply that $k^+_{Mg}/k^-_{Mg} = K_{Mg}$. k^+_{Mg} values reported by Saldi et al. (2010) are $10^{-10.5}$ and $10^{-9.9}$ mol/cm^2/s, at 150 and 200 °C, respectively. Combining these with the corresponding k^-_{Mg} values listed in Table 7 leads to $\left(k^+_{Mg}/k^-_{Mg}\right) = 10^{3.5}$ and $10^{3.25}$ at 150 and 200 °C, respectively. These ratios are orders of magnitude different that the corresponding K_{Mg} values reported by Bénézeth et al. (2011), which are equal to $10^{-10.7}$ and $10^{-11.8}$ at 150 and 200 °C, respectively. The inconsistency of the retrieved rate constants with the principle of detailed balancing for elementary reactions further confirms the difference between the observed dissolution and precipitation mechanisms.

Corresponding magnesite dissolution and precipitation rates are shown as a function of chemical affinity in Fig. 10. There are several caveats that need to be considered when considering Fig. 10. First, in accord with Eq. (10), rates are functions of three independent parameters: the reactive fluid saturation state, carbonate ion activity, and pH. Fig. 10 exhibits rates that were measured over a range of pH and reactive fluid compositions so that the comparison of dissolution versus precipitation rates is not direct. Second, the distribution of rates shown in Fig. 10 is dependent on the limitations of the mixed-flow reactor techniques used in these studies; precipitation rates lower than about $\sim 10^{-13}$ mol/cm^2/s cannot be accurately measured using this reactor system because at such conditions the differences between the chemical composition of the inlet and outlet fluid were too small to compute meaningful rates. Third, the distribution of rates in this figure reflects some experimental bias; many dissolution rates were measured in fluids that were initially magnesium- and carbonate-free, so that reactive fluid saturation state, carbonate activity, and pH co-varied.

Despite these caveats, the distribution of rates in Fig. 10 suggests an asymmetrical magnesite rate behavior. Dissolution rates appear to be faster than precipitation rates close to equilibrium but slower than precipitation rates at far from equilibrium conditions. This observation, no doubt stems from the term $(1 - \Omega^n_{Mg})$ in Eqs. 5 and 10. Ω_{Mg} varies from 0 to 1 in undersaturated solutions, is equal to 1 at equilibrium, and is >1 in supersaturated solution. Because there is no upper bound for Ω_{Mg} in supersaturated solutions, the $(1 - \Omega^n_{Mg})$ term in Eqs. 5 and 10, can continue to decrease as the reactive fluid becomes increasingly supersaturated.

Fig. 10 also presents a comparison of magnesite precipitation rates measured in this study with corresponding rates predicted from the magnesite dissolution rate equation reported by Saldi et al. (2010). Measured precipitation rates are orders of magnitude slower than those predicted from the dissolution rate equation despite the fact that rates were measured on identical mineral powders and using identical experimental techniques. This comparison demonstrates, therefore, that large errors may arise in geochemical modeling calculations if using the commonly adopted assumption that transition state theory based dissolution rate equations can be used to predict mineral precipitation rates.

5.3. The role of magnesite precipitation rates in mineral carbonation

Magnesite precipitation is one of the steps of mineral carbonation, a technology to store anthropogenic CO_2 in solid carbonate phases. Perhaps the most studied mineral carbonation pathway is that described by Eq. (1), which couples forsterite dissolution with magnesite precipitation (e.g. Béarat et al., 2006; Andreani et al., 2009; Prigiobbe et al., 2009a; King et al., 2010; Daval et al., 2011). Forsterite is commonly thought of as the best source of the divalent metal cations required to create carbonate minerals due to its fast dissolution rates and worldwide abundance. Forsterite dissolution has been shown to follow a relatively simple dissolution mechanism (Pokrovsky and Schott, 2000; Oelkers, 2001a); its surface area normalized dissolution rates can be described using:

$$r_{Fo} = r_{+,Fo}(1 - \Omega_{Fo}) \quad (14)$$

where r_{Fo}, $r_{+,Fo}$ and Ω_{Fo} refer to the surface area normalized dissolution rate, forward dissolution rate and saturation state of aqueous solution with respect to forsterite. Forward dissolution rates of forsterite have been reported by Wogelius and Walther (1991), Pokrovsky and Schott (2000), Oelkers (2001a), and Hänchen et al. (2006) as function of reactive fluid pH. At steady state, the stoichiometry of reaction (1) requires:

$$r_{Fo}s_{Fo} = 2r_{Mg}s_{Mg} \quad (15)$$

and thus according to Eqs. 5, 14, and 15, steady state carbonation by reaction (1) requires

$$r_{+,\mathrm{Fo}} S_{\mathrm{Fo}} (1 - \Omega_{\mathrm{Fo}}) = 2 r_{+,\mathrm{Mg}} S_{\mathrm{Mg}} \left(1 - \Omega_{\mathrm{Mg}}^2\right) \quad (16)$$

where S_i refers to the surface area of the subscripted mineral phase. A comparison of forward forsterite dissolution rates and forward magnesite precipitation rates is provided in Fig. 11. Magnesite forward precipitation rates are 3–4 orders of magnitude slower than corresponding forsterite dissolution rates. This observation, together with Eq. (16) indicates that the steady state carbonation in accord with reaction (1) would either require a substantial supersaturation of magnesite ($\Omega_{\mathrm{Mg}} > 50$), $S_{\mathrm{Mg}} \gg S_{\mathrm{Fo}}$ or a combination of the two. In either case, this observation challenges the commonly held assumption that relatively fast dissolution rates are the rate limiting step for mineral carbonation.

6. CONCLUSIONS

The results summarized above represent one of the most comprehensive studies to date of the precipitation rates of a major rock forming mineral. The comparison of these rates with dissolution rates reported in the literature leads to several major conclusions:

(1) Dissolution rate constants and equations cannot in general be extrapolated to predict precipitation rates.
(2) Precipitation rates may not be sufficiently fast such that it can be generally assumed that secondary mineral precipitation occurs at local equilibrium with these phases.
(3) Magnesite precipitation rates are sufficiently slow such that in some instances they may represent the rate limiting step for the carbonation of Mg-rich silicate rocks.

Taken together these observations attest to the critical need to quantify the precipitation rates of the major rock forming minerals for the accurate modeling of chemical mass transfer in natural and industrial processes.

ACKNOWLEDGMENTS

We would like to thank Jean-Claude Harrichoury and Alain Castillo for their scrupulous technical assistance throughout the duration of the experimental work, and Carole Causserand for her generous assistance during the analytical part of the work. We thank also Alain Pages for performing granulometric analyses, and express our gratitude to Andrey Bychkov for his indispensable expertise in developing and improving the system of pH measurement in situ. We are also grateful to Pascale Bénézeth, Jean-Louis Dandurand, Robert Gout, and Stacey Callahan for helpful discussions during the course of this study. Support from Centre National de la Recherche Scientifique, and the European Community through the MIR Early Stage Training Network (MEST-CT-2005-021120) is gratefully acknowledged. This manuscript benefited from insightful review comments provided by Jonathan Icenhower and two anonymous reviewers. We thank Carl Steefel for his careful comments and editorial assistance.

REFERENCES

Aagaard P. and Helgeson H. C. (1982) Thermodynamic and kinetic constraints on reaction rates among minerals and aqueous solutions: I. Theoretical considerations. *Am. J. Sci.* **282**, 237–285.

Alexander G., Maroto-Valer M. M. and Gafarova-Aksoy P. (2007) Evaluation of reaction variables in the dissolution of serpentine for mineral carbonation. *Fuel* **86**, 273–281.

Andreani M., Luquot L., Gouze P., Godard M., Hoise E. and Gibert B. (2009) Experimental study of carbon sequestration reactions controlled by the percolation of CO_2-rich brine through peridotites. *Environ. Sci. Technol.* **43**, 1226–1231.

Béarat H., McKelvy M. J., Chizmeshya A. V. G., Gormley D., Nunez R., Carpenter R. W., Squires K. and Wolf G. H. (2006) Carbon sequestration via aqueous olivine mineral carbonation: role of passivating layer formation. *Environ. Sci. Technol.* **40**, 4802–4808.

Bénézeth P., Palmer D. A. and Wesolowski D. J. (2008) Dissolution/precipitation kinetics of boehmite and gibbsite: application of a pH-relaxation technique to study near-equilibrium rates. *Geochim. Cosmochim. Acta* **72**, 2429–2453.

Bénézeth P., Saldi G. D., Dandurand J.-L. and Schott J. (2011) Experimental determination of the solubility product of magnesite at 50 to 200 °C. *Chem. Geol.* **286**, 21–31.

Berger G., Cadoré E., Schott J. and Dove P. (1994) Dissolution rate of Quartz in lead and sodium electrolyte solutions between 25 and 300°C: effect of the nature of surface complexes and reaction affinity. *Geochim. Cosmochim. Acta* **58**, 541–551.

Berner R. A., Lasaga A. C. and Garrels R. M. (1983) The carbonate–silicate geochemical cycle and its effect on atmospheric carbon-dioxide over the past 100 million years. *Am. J. Sci.* **283**, 641–683.

Brunauer S., Emmet P. H. and Teller E. (1938) Adsorption of gases in multimolecular layers. *J. Am. Chem. Soc.* **60**, 309–319.

Carroll S. A. and Knauss K. G. (2005) Dependence of labradorite dissolution kinetics on $CO_{2(aq)}$, $Al_{(aq)}$ and temperature. *Chem. Geol.* **217**, 213–225.

Chen Z. Y., O'Connor W. K. and Gerdemann S. J. (2006) Chemistry of aqueous mineral carbonation for carbon sequestration and explanation of experimental results. *Environ. Prog.* **25**, 161–166.

Daval D., Hellmann R., Corvisier J., Tisserand D., Martinez I. and Guyot F. (2010) Dissolution kinetics of diopside as a function of solution saturation state: macroscopic measurements and implications for modeling of geological storage of CO_2. *Geochim. Cosmochim. Acta* **74**, 2615–2633.

Daval D., Sissmann O., Menguy N., Saldi G. D., Guyot F., Martinez I., Crovixier J., Garcia B., Machouk I., Knauss K. and Hellmann R. (2011) Influence of amorphous silica layer formation on the dissolution rate of olivine at 90 °C and elevated pCO_2. *Chem. Geol.* **284**, 193–209.

Deelman J. C. (1999) Low temperature nucleation of magnesite and dolomite. *N. Jb. Miner. Mh.* **7**, 289–302.

Deelman J. C. (2003) Note on magnesite formation (Studies on Irreversible Geochemical Reactions **9**). *Carnets de Géologiel Notebooks on Geology*. Maintenon, Letter 2003/03.

Dufaud F., Martinez I. and Shilobeeva S. (2009) Experimental study of Mg-rich silicates carbonation at 400 and 500 °C and 1 kbar. *Chem. Geol.* **265**, 79–87.

Eyring H. (1935) The activated complex in chemical reactions. *J. Chem. Phys.* **3**, 107–115.

Garcia B., Beaumont V., Perfetti E., Rouchon V., Blanchet D., Oger P., Dromart G., Huc A.-Y. and Haeseler F. (2010) Experiments and geochemical modeling of CO_2 sequestration

by olivine. Potential, quantification. *Appl. Geochem.* **25**, 1383–1396.

Gerdemann S. J., O'Connor W. K., Dahlin D. C., Penner L. R. and Rush H. (2007) Ex situ aqueous mineral carbonation. *Environ. Sci. Technol.* **41**, 2587–2593.

Giammar D. E., Bruant R. G. and Peters C. A. (2005) Forsterite dissolution and magnesite precipitation at conditions relevant for deep saline aquifer storage and sequestration of carbon-dioxide. *Chem. Geol.* **217**, 257–276.

Gislason S. R., Wolff-Boenisch D., Stefansson A., Oelkers E. H., Gunnlaugsson E., Sigurdardottir H., Sigfusson B., Broecker W. S., Matter J. M., Stute M., Axelsson G. and Fridriksson T. (2010) Mineral sequestration of carbon-dioxide in basalt: a pre-injection overview of the CarbFix project. *Int. J. Greenhouse Gas Cont.* **4**, 537–545.

Goddéris Y., Williams J. Z., Schott J., Pollard D. and Brantley S. L. (2010) Time evolution of the mineralogical composition of Mississippi Valley loess over the last 10 kyr: climate and geochemical modeling. *Geochim. Cosmochim. Acta* **74**, 6357–6374.

Goldberg P., Chen Z. -Y., O' Connor W., Walters R. and Ziock H. (2001) CO_2 mineral sequestration studies in US. *Presented at the First National Conference on Carbon Sequestration*. Washington, DC, May 14–17, 2001.

Golubev S. V. and Pokrovsky O. S. (2006) Experimental study of the effect of organic ligands on diopside dissolution kinetics. *Chem. Geol.* **235**, 377–389.

Golubev S. V., Pokrovsky O. S. and Schott J. (2005) Experimental determination of the effect of dissolved CO_2 on the dissolution kinetics of Mg and Ca silicates at 25° C. *Chem. Geol.* **217**, 227–238.

Gratz A. J., Hillner P. E. and Hansma P. K. (1993) Step dynamics and spiral growth on calcite. *Geochim. Cosmochim. Acta* **57**, 491–495.

Guyot F., Daval D., Dupraz S., Martinez I., Menez B. and Sissmann O. (2011) CO_2 geological storage: the environmental mineralogy perspective. *Compte Rendu Geosci.* **343**, 246–259.

Gysi A. P. and Stefánsson A. (2008) Numerical modeling of CO_2–water–basalt interaction. *Mineral. Mag.* **72**, 55–59.

Hänchen M., Prigiobbe V., Storti G., Seward T. M. and Mazzotti M. (2006) Dissolution kinetics of fosteritic olivine at 90–150 °C including effects of the presence of CO_2. *Geochim. Cosmochim. Acta* **70**, 4403–4416.

Hänchen M., Prigiobbe V., Baciocchi R. and Mazzotti M. (2008) Precipitation in the Mg-carbonate system – effects of temperature and CO_2 pressure. *Chem. Eng. Sci.* **63**, 1012–1028.

Inskeep W. P. and Bloom P. R. (1985) An evaluation of rate equations for calcite precipitation kinetics at pCO_2 less than 0.01 atm and pH greater than 8. *Geochim. Cosmochim. Acta* **49**, 2165–2180.

Jordan G., Pokrovsky O. S., Guichet X. and Schmahl W. (2007) Organic and inorganic ligand effects on magnesite dissolution at 100° C and pH = 5 to 10. *Chem. Geol.* **242**, 484–496.

Kelemen P. B. and Matter J. (2008) In situ carbonation of peridotite for CO_2 storage. *Proc. Natl. Acad. Sci. U S A* **105**, 17295–17300.

King H. E., Plumper O. and Putnis A. (2010) Effect of secondary phase formation on the carbonation of olivine. *Environ. Sci. Technol.* **44**, 6503–6509.

Knauss K. G., Johnson J. W. and Steefel C. I. (2005) Evaluation of the impact of CO_2, co-contaminant gas, aqueous fluid and reservoir rock interactions on the geological sequestration of CO_2. *Chem. Geol.* **217**, 339–350.

Kowacz M. and Putnis A. (2008) The effect of specific background electrolytes on water structure and solute hydration: consequences for crystal dissolution and growth. *Geochim. Cosmochim. Acta* **72**, 4476–4487.

Kowacz M., Putnis C. and Putnis A. (2007) The effect of cation: anion ratio in solution on the mechanism of barite growth at constant supersaturation: role of the desolvation process on the growth kinetics. *Geochim. Cosmochim. Acta* **71**, 5168–5179.

Lackner K. S., Wendt C. H., Butt D. P., Joyce E. L. and Sharp D. H. (1995) Carbon dioxide disposal in carbonate minerals. *Energy* **20**, 1153–1170.

Lackner K. S., Butt D. P. and Wendt C. H. (1997) Progress on binding CO_2 in mineral substrates. *Energy Convers. Manage.* **38**, S259–S264.

Lasaga A. C. (1981) Transition state theory. *Rev. Min.* **8**, 135–169.

Lin F.-C. and Clemency C. V. (1981) The dissolution kinetics of brucite, antigorite, talc and phlogopite at room temperature and pressure. *Am. Min.* **66**, 801–806.

Liu F., Lu P., Zhu C. and Xiao Y. (2011) Coupled reactive flow and transport modeling of CO_2 sequestration in the Mt. Simon sandstone formation, Midwest USA. *Int. J. Greenhouse Gas Control* **5**, 294–307.

Luce R. W., Bartlett W. B. and Parks G. A. (1972) Dissolution kinetics of magnesium silicates. *Geochim. Cosmochim. Acta* **36**, 35–50.

Marini L. (2007). *Geological sequestration of carbon dioxide: thermodynamics, kinetics and reaction path modeling.* Developments in Geochemistry 11, Elsevier, p. 470.

Maroto-Valer M. M., Fauth D. J., Kuchta M. E., Zhang Y. and Andresen J. M. (2005) Activation of magnesium rich minerals as carbonation feedstock materials for CO_2 sequestration. *Fuel Process. Technol.* **86**, 1627–1645.

Matter J. M., Takahashi T. and Goldberg D. S. (2007) Experimental evaluation of in situ CO_2–water–rock reactions during CO_2 injection in basaltic rocks: implications for geological CO_2 storage. *Geochem. Geophy. Geosys.* **8**, 1–19, Q02001.

Matter J. M., Broecker W. S., Stute M., Gislason S. R., Oelkers E. H., Stefansson A., Wolff-Boenisch D., Gunniangsson E., Alexsson G. and Bjornsson G. (2009) Permanent carbon dioxide storage into basalt: the CarbFix pilot project Iceland. *Energy Proced.* **1**, 3641–3646.

Matter J. M., Broecker W. S., Gislason S. R., Gunniangsson E., Oelkers E. H., Stute M., Sigurdardottir H., Stefansson A., Alfredsson H. A., Aradottir E. S., Alexsson G., Sigfusson B. and Wolff-Boenisch D. (2011) The CarbFix pilot project – storing carbon dioxide in basalt. *Energy Proced.* **4**, 5579–5585.

McGrail B. P., Schaef H. T., Ho A. M., Chien Y. J., Dooley J. J. and Davidson C. L. (2006) Potential for carbon dioxide sequestration in flood basalts. *J. Geophys. Res.-Solid Earth* **111**, 13.

Mucci A. (1986) Growth kinetics and composition of magnesian calcite overgrowths precipitated from seawater: quantitative influence of orthophosphate ions. *Geochim. Cosmochim. Acta* **50**, 2255–2265.

Nancollas G. H. and Reddy M. M. (1971) The crystallization of calcium carbonate. II. Calcite growth mechanism. *J. Colloid Interf. Sci.* **37**, 824–830.

Nehrke G., Reichart G. J., Van Cappellen P., Meile C. and Bijma J. (2007) Dependence of calcite growth rate and Sr partitioning on solution stoichiometry: non-Kossel crystal growth. *Geochim. Cosmochim. Acta* **71**, 2240–2249.

Nielsen A. E. (1964) *Kinetics of precipitation*. Pergamon Press, p. 151.

Nielsen A. E. (1984) Electrolyte crystal growth mechanisms. *J. Crystal Growth* **67**, 289–310.

O'Connor W. K., Dahlin D. C., Nilsen D. N., Rush G. E., Walters R. P. and Turner P. C. (2000) CO_2 storage in solid form: a study of direct mineral carbonation. *Fifth International Conference on*

Greenhouse Gas Control Technologies. Cairns, Australia, August 13–16, 2000.

Oelkers E. H. (2001a) An experimental study of forsterite dissolution rates as a function of temperature and aqueous Mg and Si concentrations. *Chem. Geol.* **175**, 485–494.

Oelkers E. H. (2001b) General kinetic description of multioxide silicate mineral and glass dissolution. *Geochim. Cosmochim. Acta* **65**, 3703–3719.

Oelkers E. H. and Schott J. (1995) Experimental study of anorthite dissolution rates and the relative mechanism of feldspar hydrolysis. *Geochim. Cosmochim. Acta* **59**, 5039–5053.

Oelkers E. H. and Schott J. (1999) Experimental study of kyanite dissolution rates as a function of chemical affinity and solution composition. *Geochim. Cosmochim. Acta* **63**, 785–797.

Oelkers E. H. and Schott J. (2001) An experimental study of enstatite dissolution rates as a function of pH, temperature, and aqueous Mg and Si concentration, and the mechanism of pyroxene/pyroxenoid dissolution. *Geochim. Cosmochim. Acta* **65**, 1219–1231.

Oelkers E. H. and Schott J. (2005) Geochemical aspects of CO_2 sequestration. *Chem. Geol.* **217**, 183–186.

Oelkers E. H. and Cole D. R. (2008) Carbon dioxide sequestration: a solution to a global problem. *Elements* **4**, 305–310.

Oelkers E. H., Schott J. and Devidal J. L. (1994) The effect of aluminum, pH, and chemical affinity on the rates of aluminosilicate dissolution reactions. *Geochim. Cosmochim. Acta* **58**, 2011–2024.

Oelkers E. H., Gislason S. R. and Matter J. (2008a) Mineral carbonation of CO_2. *Elements* **4**, 333–337.

Oelkers E. H., Schott J., Gauthier J.-M. and Herrero-Roncal T. (2008b) An experimental study of the dissolution mechanism and rates of muscovite. *Geochim. Cosmochim. Acta* **72**, 4948–4961.

Olsen A. A. and Rimstidt J. D. (2008) Oxalate-promoted forsterite dissolution at low pH. *Geochim. Cosmochim. Acta* **72**, 1758–1766.

Parkhurst D. L. and Appelo C. A. J. (1999) User's guide to PHREEQC (version 2) – a computer program for speciation, batch-reaction, one-dimensional transport, and inverse geochemical calculations. *US Geological Survey Water-resources Investigation Report 99-4259*. p. 312.

Perdikouri C., Putnis C. V., Kasioptas A. and Putnis A. (2009) An atomic force microscopy study of the growth of a calcite surface as a function of calcium/total carbonate ratio in solution at constant supersaturation. *Cryst. Growth Des.* **9**, 4344–4350.

Piana S., Jones F. and Gale J. D. (2006) Assisted desolvation as a key kinetic step for crystal growth. *J. Am. Chem. Soc.* **128**, 13568–13574.

Pokrovsky O. S. and Schott J. (1999) Processes at the magnesium-bearing carbonates solution interface. II. Kinetics and mechanism of magnesite dissolution. *Geochim. Cosmochim. Acta* **63**, 881–897.

Pokrovsky O. S. and Schott J. (2000) Kinetics and mechanism of forsterite dissolution at 25°C and pH from 1 to 12. *Geochim. Cosmochim. Acta* **64**, 3313–3325.

Pokrovsky O. S. and Schott J. (2002) Surface chemistry and dissolution kinetics of divalent metal carbonates. *Environ. Sci. Technol.* **36**, 426–432.

Pokrovski G. S., Schott J. and Sergeyev A. S. (1995) Experimental determination of the stability constants of $NaSO_4^-$ and $NaB(OH)_4^0$ in hydrothermal solutions using a new high-temperature sodium-selective glass electrode – implications for boron isotopic fractionation. *Chem. Geol.* **124**, 253–265.

Pokrovsky O. S., Schott J. and Thomas F. (1999a) Processes at the magnesium-bearing carbonates/solution interface. I. A surface speciation model for magnesite. *Geochim. Cosmochim. Acta* **63**, 863–880.

Pokrovsky O. S., Schott J. and Thomas F. (1999b) Dolomite surface speciation and reactivity in aquatic systems. *Geochim. Cosmochim. Acta* **63**, 3133–3143.

Pokrovsky O. S., Golubev S. V. and Schott J. (2005) Dissolution kinetics of calcite, dolomite and magnesite at 25 °C and 0 to 50 atm pCO_2. *Chem. Geol.* **217**, 239–255.

Prigiobbe V., Hänchen M., Werner M., Baciocchi R. and Mazzotti M. (2009a) Mineral carbonation processes for CO_2 sequestration. *Energy Proced.* **1**, 4885–4890.

Prigiobbe V., Costa G., Baciocchi R., Hänchen M. and Mazzotti M. (2009b) The effect of CO_2 and salinity on olivine dissolution kinetics at 120 °C. *Chem. Eng. Sci.* **15**, 3510–3515.

Reddy M. M. and Nancollas G. H. (1976) The crystallization of calcium carbonate: IV. The effect of magnesium, strontium and sulfate ions. *J. Cryst. Growth* **35**, 33–38.

Reddy M. M. and Gaillard W. D. (1981) Kinetics of calcium carbonate (calcite)-seeded crystallization: influence of solid/solution ratio on the reaction rate constant. *J. Colloid Interface Sci.* **80**, 171–178.

Reddy M. M., Plummer L. N. and Busenberg E. (1981) Crystal growth of calcite from calcium bicarbonate solutions at constant PCO_2 and 25 °C: a test of calcite dissolution model. *Geochim. Cosmochim. Acta* **45**, 1281–1289.

Rodriguez-Blanco J. D., Shaw S. and Benning L. G. (2011) The kinetics and mechanism of amorphous calcium carbonate (ACC) crystallization to calcite, via vaterite. *Nanoscale* **3**, 265–271.

Rosso J. J. and Rimstidt J. D. (2000) A high resolution study of forsterite dissolution rates. *Geochim. Cosmochim. Acta* **64**, 797–811.

Saldi G. D., Köhler S. J., Marty N. and Oelkers E. H. (2007) Dissolution rates of talc as a function of solution composition, pH and temperature. *Geochim. Cosmochim. Acta* **71**, 3446–3457.

Saldi G. D., Jordan G., Schott J. and Oelkers E. H. (2009) Magnesite growth rates as function of temperature and saturation state. *Geochim. Cosmochim. Acta* **73**, 5646–5657.

Saldi G. D., Schott J., Pokrovsky O. S. and Oelkers E. H. (2010) An experimental study of magnesite dissolution rates at neutral to alkaline conditions at 150 and 200 °C as a function of pH, total dissolved carbonate concentration and chemical affinity. *Geochim. Cosmochim. Acta* **74**, 6344–6356.

Sayles F. L. and Fyfe W. S. (1973) The crystallization of magnesite from aqueous solution. *Geochim. Cosmochim. Acta* **37**, 87–99.

Schaef H. T., McGrail B. P. and Owen A. T. (2009) Dissolution of Columbia River Basalt under mildly acidic conditions as a function of temperature: experimental results relevant to the geological storage of carbon dioxide. *Appl. Geochem.* **24**, 980–987.

Schott J. and Berner R. A. (1983) X-ray photoelectron studies of the mechanism of iron silicate dissolution during weathering. *Geochim. Cosmochim. Acta* **47**, 2233–2240.

Schott J. and Berner R. A. (1985) Dissolution mechanisms of pyroxenes and olivines during weathering. In *The Chemistry of Weathering* (ed. J. I. Drever). D. Reidel Publishing Company, pp. 35–53.

Schott J. and Oelkers E. H. (1995) Dissolution and crystallization rates of silicate minerals as a function of chemical affinity. *Pure Appl. Chem.* **67**, 903–910.

Schott J., Berner R. A. and Sjöberg E. L. (1981) Mechanisms of pyroxene and amphibole weathering. I. Experimental studies of iron-free minerals. *Geochim. Cosmochim. Acta* **45**, 2123–2135.

Schott J., Pokrovsky O. S. and Oelkers E. H. (2009) The link between mineral dissolution/precipitation kinetics and solution chemistry. *Rev. Min. Geochem.* **70**, 207–258.

Shiraki R. and Brantley S. L. (1995) Kinetics of near-equilibrium calcite precipitation at 100°C: an evaluation of elementary reaction-based and affinity-based rate laws. *Geochim. Cosmochim. Acta* **59**, 1457–1471.

Shock E. L., Sassani D. C., Willis M. and Sverjensky D. A. (1997) Inorganic species in geologic fluids: correlations among standard molal thermodynamic properties of aqueous ions and hydroxide complexes. *Geochim. Cosmochim. Acta* **61**, 907–950.

Shvarov Yu. V. (1999) Algorithmization of the numerical equilibrium modelling of dynamic geochemical processes. *Geochem. Int.* **37**, 571–576.

Stack A. G. and Grantham M. C. (2010) Growth rate of calcite steps as a function of aqueous calcium-to carbonate ratio: independent attachment and detachment of calcium and carbonate ions. *Cryst. Growth Des.* **10**, 1409–1413.

Steefel C. I. and MacQuarrie K. T. B. (1996) Approaches to modeling of reactive transport in porous media. *Rev. Min.* **34**, 85–129.

Steefel C. I. and Maher K. (2009) Fluid–rock interaction: a reactive transport approach. *Rev. Min. Geochem.* **70**, 485–532.

Temkin M. I. (1963) Kinetics of stationary reactions. *Doklady Akademii Nauk SSSR* **152**, 156–157.

Teng H. H., Dove P. M. and De Yoreo J. J. (2000) Kinetics of calcite growth: surface processes and relationships to macroscopic rate laws. *Geochim. Cosmochim. Acta* **64**, 2255–2266.

Usdowski E. (1989) Synthesis of dolomite and magnesite at 60 °C in the system Ca^{2+}–Mg^{2+}–CO_3^{2-}–Cl_2^{2}–H_2O. *Naturwissenschaften* **76**, 374–375.

Vavouraki A. I., Putnis C. V., Putnis A. and Koutsoukos P. G. (2010) Crystal growth and dissolution of calcite in the presence of fluoride ions. An Atomic force microscopy study. *Cryst. Growth Des.* **10**, 60–69.

Van Cappellen P. and Berner R. A. (1991) Fluorapatite crystal growth from modified seawater solutions. *Geochim. Cosmochim. Acta* **55**, 1219–1234.

Van Cappellen P., Charlet L., Stumm W. and Wersin P. (1993) A surface complexation model of the carbonate mineral–aqueous solution interface. *Geochim. Cosmochim. Acta* **57**, 3505–3518.

Vekilov P. G. (2007) What determines the rate of growth of crystals from solution? *Cryst. Growth Des.* **7**, 2796–2810.

Wogelius R. A. and Walther J. V. (1991) Olivine dissolution at 25 °C: effects of pH, CO_2 and organic acids. *Geochim. Cosmochim. Acta* **55**, 943–954.

Wogelius R. A. and Walther J. V. (1992) Olivine dissolution kinetics at near-surface conditions. *Chem. Geol.* **97**, 101–112.

Wolf G. H., Chizmeshya A. V. G., Diefenbacher J. and McKelvy M. J. (2004) In-situ observation of CO_2 sequestration reactions using a novel microreaction system. *Environ. Sci. Technol.* **38**, 932–936.

Wolff-Boenisch D., Gislason S. R. and Oelkers E. H. (2006) The effect of crystallinity on dissolution rates and CO_2 consumption capacity of silicates. *Geochim. Cosmochim. Acta* **70**, 858–870.

Wolff-Boenisch D., Wenau S., Gislason S. R. and Oelkers E. H. (2011) Dissolution of basalts and peridote in seawater, in the presence of ligands, and CO_2: implications for mineral sequestration of carbon dioxide. *Geochim. Cosmochim. Acta* **75**, 5510–5525.

Zhu C. (2009) Geochemical modelling of reaction paths and geochemical reaction networks. *Rev. Min. Geochem.* **70**, 533–569.

Zhu C., Peng L., Zheng Z. and Ganor J. (2010) Coupled alkali feldspar dissolution and secondary mineral precipitation in batch systems: 4. Numerical modeling of kinetic reaction paths. *Geochim. Cosmochim. Acta* **74**, 3963–3983.

Associate editor: Carl I. Steefel